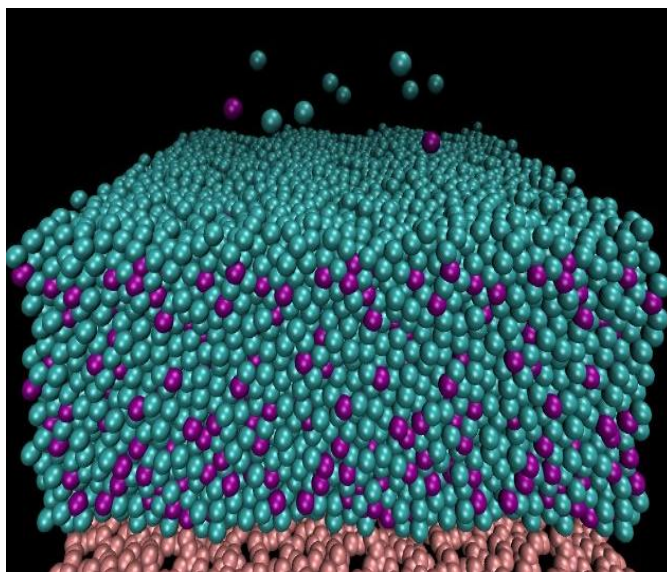
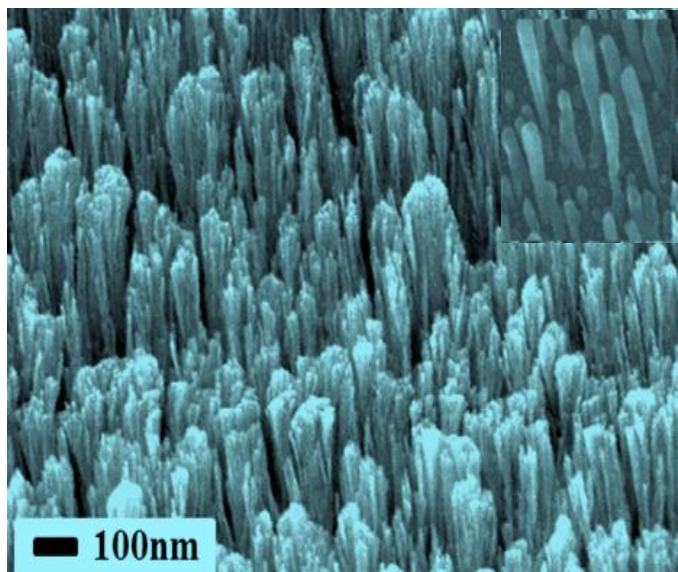
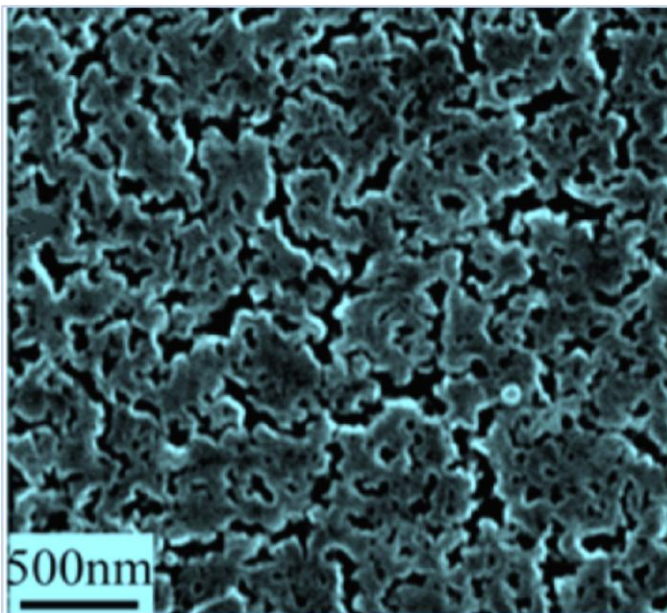
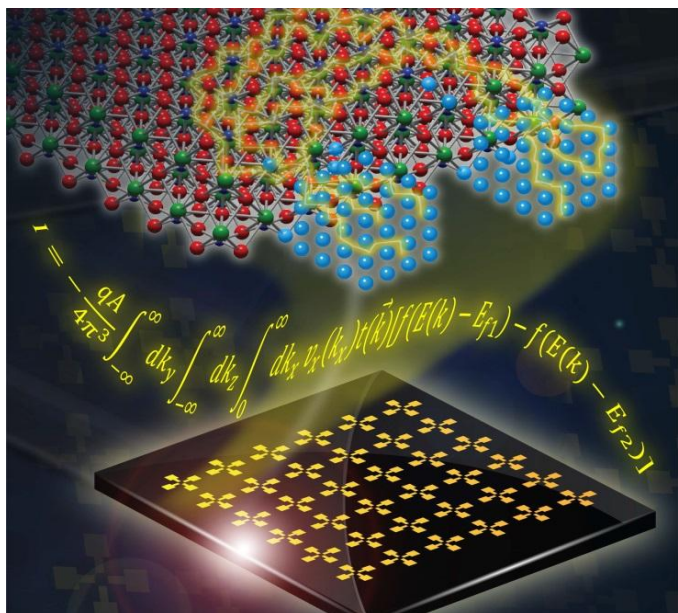


# 2013 Synthesis and Processing Science Principal Investigators' Meeting

Hilton Washington DC North/Gaithersburg, Gaithersburg, MD  
November 17-20, 2013



U.S. DEPARTMENT OF  
**ENERGY**

Office of  
Science

Office of Basic Energy Sciences  
Materials Sciences and Engineering Division

Top Left: Atomistic diagram for crystalline chromium metal (light blue) on SrTiO<sub>3</sub> (top), an equation that describes the transport process (middle), and an array of metal contacts on a SrTiO<sub>3</sub> wafer (bottom). *Advanced Materials*, **25**, 4001 (2013). (Courtesy: Scott Chambers, Pacific Northwest National Laboratory)

Top Right: The figure shows an image of a scanning electron micrograph of high-conduction β-Li<sub>3</sub>PS<sub>4</sub> surface morphology. *Journal of the American Chemical Society*, **135**, 975 (2013). (Courtesy: Chengdu Liang, Oak Ridge National Laboratory)

Bottom Left: Following the theoretical guidance, experiments result in the smallest metallic nanorods ever reported using PVD; ~7 nm for Au. *Physical Review Letters*, **110**, 136102 (2013). (Courtesy: Hanchen Huang, Northeastern University)

Bottom Right: Snapshot of the vapor-deposition process from a computer simulation in which particles are deposited one at a time on a free surface. *Nature Materials*, **12**, 139 (2013). (Courtesy: Mark Ediger, University of Wisconsin-Madison)

---

This document was produced under contract number DE-AC05-06OR23100 between the U.S. Department of Energy and Oak Ridge Associated Universities.

The research grants and contracts described in this document are supported by the U.S. DOE Office of Science, Office of Basic Energy Sciences, Materials Sciences and Engineering Division.

## Table of Contents

<b>Foreword</b> .....	vii
<b>Program Description</b> .....	xi
<b>Agenda</b> .....	xvii
<b>Poster Sessions</b> .....	xxiii
 <b>Laboratory Projects' Abstracts</b>	
<i>Anand Bhattacharya</i> , Argonne National Laboratory: Digital Synthesis: A Pathway to New Materials at Interfaces of Complex Oxides .....	3
<i>Ivan Božović</i> , Brookhaven National Laboratory: Atomic–Layer-by-Layer Molecular Beam Epitaxy Synthesis of Cuprate Superconductors.....	7
<i>Scott A. Chambers</i> , Pacific Northwest National Laboratory: Electronic and Optical Properties of Doped Complex Oxide Epitaxial Films and Interfaces .....	13
<i>Amy J. Clarke</i> , Los Alamos National Laboratory: In-situ Monitoring of Dynamic Phenomena during Solidification.....	18
<i>Nancy J. Dudney</i> , Oak Ridge National Laboratory: Solid Electrolytes to Stabilize High-Voltage Battery Interfaces .....	22
<i>David B. Geohegan</i> , Oak Ridge National Laboratory: Growth Mechanisms and Controlled Synthesis of Nanomaterials (ERKCS81): Synthesis of Nanostructures from Nanoparticle Building Blocks.....	26
<i>Kai-Ming Ho</i> , Ames Laboratory: Development of Order in Deeply Undercooled Liquid Metals.....	31
<i>Matthew Kramer</i> , Ames Laboratory: Predicting and Controlling Phase Selection in Highly Driven Systems .....	35
<i>Chengdu Liang</i> , Oak Ridge National Laboratory: Tailoring Ionic Conductivity in Solids for High-Energy Batteries.....	39
<i>Jun Liu</i> , Pacific Northwest National Laboratory: Molecularly Organized Nanostructural Materials .....	43

<i>Thomas A. Lograsso</i> , Ames Laboratory: Synthesis, Measurement, and Characterization of Functional Materials with Volatile, Reactive, and Toxic Constituents to Address Energy Grand Challenge Problems .....	48
<i>Mikhail I. Mendeleev</i> , Ames Laboratory: Theoretical and Experimental Study of Solid-Liquid Interface Properties of Stoichiometric Compounds .....	53
<i>Cedomir Petrovic</i> , Brookhaven National Laboratory: Exploratory Materials Synthesis and Characterization (EMSC) .....	57
<i>Alex Puzov</i> , Oak Ridge National Laboratory: Growth Mechanisms and Controlled Synthesis of Nanomaterials (ERKCS81): Revealing the Growth Mechanism of Graphene on Catalytic Substrates by Real-Time Optical Diagnostics .....	62
<i>Praveen K. Thallapally</i> , Pacific Northwest National Laboratory: Molecularly Organized Nanostructural Materials – Subtask: Guest Induced Structural Transformation and Nanostructural Materials Synthesis .....	67
<i>Michael C. Tringides</i> , Ames Laboratory: Nanoscale Morphologies to Control Atomic Scale Processes .....	71
<i>Mina Yoon</i> , Oak Ridge National Laboratory: Growth Mechanisms and Controlled Synthesis of Nanomaterials (ERKCS81): Modeling and Characterization of Ultrasmall Nanoparticles .....	76
 <b>University Grants’ Abstracts</b>	
<i>Michael S. Arnold</i> , University of Wisconsin–Madison: Understanding Graphene Crystal Morphology Evolution and Orientation during CVD on Cu; and the Bottom-Up Growth of Graphene Nanostructures with Refined Edges .....	83
<i>Stacey F. Bent</i> , Stanford University: Studies of Surface Reaction and Nucleation Mechanisms in Atomic Layer Deposition .....	88
<i>Yves J. Chabal</i> , University of Texas at Dallas: Novel Theoretical and Experimental Approaches for Understanding and Optimizing Molecule-Sorbent Interactions in Metal Organic Framework Materials .....	92
<i>Eric Chason</i> , Brown University: A Unified Understanding of Residual Stress in Thin Films: Kinetic Models, Experiments and Simulations .....	98
<i>I-Wei Chen</i> , University of Pennsylvania: Electric-Field Enhanced Kinetics in Oxide Ceramics: Pore Migration, Sintering and Grain Growth.....	103

<i>George Chumanov</i> , Clemson University: Coupled Plasmonic Arrays for Real Time Sensing .....	107
<i>Ralph H. Colby</i> , The Pennsylvania State University: Conduction Mechanisms and Structure of Ionomeric Single-Ion Conductors.....	110
<i>Gabor Csathy</i> , Purdue University: Integrated Growth and Ultra-low Temperature Transport Study of the 2 <sup>nd</sup> Landau Level of the Two-Dimensional Electron Gas .....	114
<i>Mark D. Ediger</i> , University of Wisconsin–Madison: High-Throughput Preparation and Characterization of Vapor-Deposited Organic Glasses .....	119
<i>Chang-Beom Eom</i> , University of Wisconsin–Madison: Artificially Layered Superlattice of Pnictide by Design .....	123
<i>Andrei G. Fedorov</i> , Georgia Institute of Technology: Using Energetic Gas Jets to Enable New Modes of Focused Electron Beam Induced Deposition .....	127
<i>Kristen A. Fichthorn</i> , The Pennsylvania State University: Forces, Crystallization, and Assembly in Nanoparticle Suspensions .....	131
<i>Stephen H. Garofalini</i> , Rutgers University: Atomistic Structure, Strength, and Kinetic Properties of Intergranular Films in Ceramics.....	136
<i>Peter F. Green</i> , University of Michigan: Brush-Coated Nanoparticle Polymer Thin Films: Structure-Mechanical-Optical Properties.....	140
<i>Jung Han</i> , Yale University: Evolutionary Selection Growth: Towards Template-Insensitive Preparation of Single-Crystal Layers .....	144
<i>A. John Hart</i> , University of Michigan and Massachusetts Institute of Technology: Understanding and Controlling Nanoscale Crystal Growth using Mechanical Forces .....	148
<i>Joshua L. Hertz</i> , University of Delaware: Improved Electrochemical Performance of Strained Lattice Electrolytes via Modulated Composition.....	153
<i>Hanchen Huang</i> , Northeastern University: Science-Directed Pursue of the Smallest Metallic Nanorods using Physical Vapor Deposition .....	157
<i>Himanshu Jain</i> , Lehigh University: Laser Fabrication of Active Single-Crystal Architecture in Glass.....	161
<i>Ram S. Katiyar</i> , University of Puerto Rico: Development and Understanding of Multifunctional Nanostructured Magnetoelectric and Spintronic Materials.....	165

<i>Carolyn A. Koh</i> , Colorado School of Mines: Investigating the Metastability of Clathrate Hydrates for Energy Storage .....	169
<i>Max G. Lagally</i> , University of Wisconsin–Madison: Synthesis and Processing Research in Group IV Nanomembranes.....	174
<i>Chekesha M. Liddell Watson</i> , Cornell University: Self-Assembly of Non-spherical Colloids: New Reduced Symmetry Crystals and Mesophases for Templating Functional Materials at Fine Scales .....	178
<i>Feng Liu</i> , University of Utah: Strain Engineered Surface Transport in Si(001): Complete Isolation of the Surface State via Tensile Strain .....	183
<i>Richard R. Lunt</i> , Michigan State University: Quasiepitaxial Growth of Organic Crystalline Thin-Films .....	187
<i>Lorenzo Mangolini</i> , University of California at Riverside: Non-equilibrium Effects in the Processing of Materials using Plasmas .....	190
<i>Alexandra Navrotsky</i> , University of California at Davis: How Bulk and Surface Thermodynamics Affects Li Battery Material Properties .....	195
<i>George S. Nolas</i> , University of South Florida: A Fundamental Study of Inorganic Clathrate Open-Framework Materials.....	199
<i>Eugene A. Olevsky</i> , San Diego State University: Study of Spark-Plasma Sintering at Different Scale Levels .....	204
<i>Roberto Paiella</i> , Boston University: Plasmonic Control of Radiation Processes for Enhanced Efficiency and Beam Shaping .....	208
<i>John H. Perepezko</i> , University of Wisconsin–Madison: New Oxide Materials for an Ultra High Temperature Environment.....	213
<i>Pierre F. Poudeu</i> , University of Michigan: Phase Transformations and Equilibria in Complex Half-Heusler/Full-Heusler Nanocomposites .....	217
<i>Bjoern Reinhard</i> , Boston University: New Optoplasmonic Materials for Next Generation Energy Systems.....	221
<i>Darrell G. Schlom</i> , Cornell University: Using Interfaces to Create Strongly Coupled Magnetic-Ferroelectrics.....	226
<i>Theo Siegrist</i> , Florida State University: Discovery and Crystal Growth of New Oxide Phases from Metal Fluxes .....	231

<i>Jay A. Switzer</i> , Missouri University of Science and Technology: Electrodeposition of Cobalt (Hydr)oxide Oxygen Evolution Catalysts for Photoelectrochemical Water Splitting.....	236
<i>Maria C. Tamargo</i> , The City College of New York: Enhanced Materials based on Submonolayer Type-II Quantum Dots.....	240
<i>Salvatore Torquato</i> , Princeton University: Inverse Optimization Techniques for Targeted Self-Assembly .....	245
<i>Peter Voorhees</i> , Northwestern University: Four-Dimensional Analysis of the Evolution of Complex Dendritic Microstructures during Coarsening .....	249
<i>David Wang</i> , Colorado State University: Directed Assembly of Rod-Coil Block Copolymers by Combined External Fields.....	253
<i>Wenyong Wang</i> , University of Wyoming: Quantum Dot Sensitized Solar Cells based on Ternary Metal Oxide Nanowires.....	258
<i>Xudong Wang</i> , University of Wisconsin–Madison: Surface-Reaction-Limited Pulsed Chemical Vapor Deposition for Growing Nanowires inside Highly Confined Spaces.....	262
<i>Boris I. Yakobson</i> , Rice University: Boron-Based Nanostructures: Stability, Functionality and Synthetic Routes .....	267
<i>Francisco Zaera</i> , University of California at Riverside: Atomic Layer Deposition (ALD) of Metal and Metal Oxide Films: A Surface Science Study .....	271
<i>Pengpeng Zhang</i> , Michigan State University: Utilizing Molecular Self-Assembly to Tailor Electrical Properties of Si Nanomembranes .....	275
<i>Qiming Zhang</i> , The Pennsylvania State University: Giant Electrocaloric Effect in Ferroelectric Polymers with Tailored Polar-Nanostructures .....	279
<i>Guangwen Zhou</i> , State University of New York–Binghamton: In Situ Visualization and Theoretical Modeling of Early-Stage Oxidation of Metals and Alloys.....	284
<i>Joshua M. O. Zide</i> , University of Delaware: Growth And Properties of New Epitaxial Metal/Semiconductor Nanocomposites.....	289

**Invited Programs' Abstracts**

*Peter F. Green*, University of Michigan–Ann Arbor, Energy Frontier Research Center:  
Morphology, Carrier Transport and Device Performance of Thiophene-Based Solar  
Cells..... 295

*Jun Liu*, Pacific Northwest National Laboratory, Joint Center for Energy Storage Research:  
Understanding Fundamental Structural Transformation and Electrochemical Reactions  
using In-Situ TEM and NMR ..... 299

*Thomas A. Lograsso*, Ames Laboratory, Critical Materials Institute – A Energy  
Innovation Hub: The Role of Synthesis and Processing in Reducing Criticality ..... 304

**Participant List**..... 307

**Author Index** ..... 311

## FOREWORD

This abstract book comprises the scientific content of the 2013 Synthesis and Processing Science Principal Investigators' Meeting sponsored by the Materials Sciences and Engineering (MSE) division in the Office of Basic Energy Sciences (BES) of the U.S. Department of Energy (DOE). The meeting, held on November 18–20, 2013, at the Washington D.C. North/Gaithersburg Hilton, Gaithersburg, Maryland, is the fourth Principal Investigators' Meeting on this topic and is one among a series of research theme-based Principal Investigators' Meetings being held by MSE division.

The purpose of this Principal Investigators' Meeting is to bring together all of the researchers funded in the Synthesis and Processing Science core research activity so they can get a firsthand look at the broad range of materials science research that is being supported in this important research area. The meeting will serve as a forum for the discussion of new results and research highlights, thus fostering a greater awareness of significant new advances in the field and the research of others in the program. The confidential and collegial meeting environment is intended to provide unique opportunities to develop new collaborations among PIs, and new ideas. In addition, the meeting affords BES program managers an opportunity to assess the state of the entire program at one time on a periodic basis, in order to chart future directions and identify new programmatic needs.

This year's meeting focuses on four topics within the Synthesis and Processing Science portfolio: critical materials for energy applications, basic synthesis science for energy storage, synthesis challenges for film interfaces, and synthesis science for light-matter interaction. While this is one way of organizing and presenting the research within this broad portfolio, there are many other synergies that could be highlighted and will be considered at future meetings.

Let me take this opportunity to express my thanks to all the meeting attendees, for their active participation and sharing their ideas and new research results. Special thanks are given to the Meeting Chairs, Stacey Bent and Matthew Kramer, for their dedicated efforts and invaluable advice towards organizing this meeting. Finally, this meeting would not be possible without the logistical support from Teresa Crockett at DOE-MSE as well as Tammy Click and Verda Adkins-Ferber at Oak Ridge Institute for Science and Education (ORISE).

Bonnie Gersten  
Program Manager, Synthesis and Processing Science  
Materials Sciences and Engineering Division  
Office of Basic Energy Sciences  
U.S. Department of Energy

This page is intentionally blank.

# **Program Description**

This page is intentionally blank.

## 2013 DOE-BES-MSE Synthesis and Processing Science Principal Investigators' Meeting

The 2013 DOE-BES-MSE Principal Investigators' Meeting will focus on the challenges for the Materials Synthesis and Processing Science Program. The meeting will assist in developing the Grand Challenge problems for Basic Energy Sciences pursuant to Synthesis and Processing Science Core Research activities. Some of these challenges have included:

- (1) How do we control materials processes at the level of electrons?
- (2) How do we design and perfect atom- and energy-efficient synthesis of revolutionary new forms of matter with tailored properties?
- (3) How do remarkable properties of matter emerge from complex correlations of the atomic or electronic constituents and how can we control these properties?

New developments in materials synthesis and processing methods are providing unprecedented capabilities to create materials and structures with tailored properties, while advances in *in situ* experimental characterization techniques together with simulation and modeling are leading to important new insights into how to control materials composition and morphologies from the atomic scale to the nanoscale and beyond. Synergies and links between synthesis, *in situ* characterization, and modeling are essential to developing ever-greater capabilities in materials design.

For this meeting, abstracts will be organized within four topical sessions:

**I. Critical Materials for Energy Applications:** *Developing scientific strategies for reducing, reusing, and replacing critical elements in energy production and use-inspired technologies.*

**II. Basic Synthesis Science for Energy Storage:** *Designing new materials with higher energy storage capacity and improved reliability.*

**III. Synthesis Challenges for Film Interfaces:** *Examining synthesis of complex thin films, single crystals, and nanoscale materials with useful physical properties.*

**IV. Synthesis Science for Light-Matter Interaction:** *Investigating approaches for synthesis and processing of materials used to harness light-matter interactions toward energy conversion technologies such as photovoltaics and light emitting diodes.*

Each materials class presents its own challenges; however, several synthesis and processing science themes crosscut all materials systems. They include the following crosscutting issues:

- (1) Developing robust predictive thermodynamic and kinetic tools – How do we accurately incorporate dynamic processes and near-equilibrium into new or existing tools?

- (2) Mesoscale modeling of multi-phase functional materials – What new modeling approaches will enable us to accurately incorporate length scales of functional materials?
- (3) Materials design and fabrication at the atomic scale to achieve tailored properties – How do we manipulate atoms at the atomic scale to achieve new functionality?
- (4) *In situ* characterization of materials synthesis from the atomic to the microstructural scale – How do we measure *in situ* processes at their relevant length and time scales?

Meeting Sessions will be organized to address the following topical areas:

**I. Critical Materials for Energy Applications:** *Developing strategies for reducing, reusing, and replacing critical elements in energy production and utilization technologies.*

Concern for availability of materials critical to advanced technologies and energy efficiency leaped into the forefront in 2010 when the People’s Republic of China significantly restricted their exports of Rare Earth elements. While the ensuing spike in cost in these materials has abated, the underlying challenge of resource availability for certain less-common elements has not gone away, and waiting until the next geopolitical crisis or market disruption is far from prudent. The challenge of mitigating the shortages of these critical materials is summed up in the 3 R’s, reduce, reuse and replace, but the devil is in the details of implementation. Reduction can involve improvements in materials synthesis such as improved nanoparticle synthesis for higher surface area catalysts. Reuse hinges in both capturing waste during production as well as recycling at the end-of-use. However, in many cases the critical element is in very low concentrations and possibly complex chemically bound states, which make their recovery difficult. Recycling of Rare Earth’s from electronics, such as magnets or from electronic displays exemplifies this challenge. Detailed understanding of the thermodynamics of the complex chemistries is required for advanced process modeling necessary for efficient recycling. Replacing existing materials with new, less critical constituents will require more efficient means of materials design and discovery. Most current materials have been refined over the years through “Edisonian” optimization. The pace of global technology development doesn’t allow such luxury at present, especially when natural disasters or geopolitical crises can quickly disrupt markets. Advances in materials genomics has potential to speed up materials discovery, but many approaches are not yet validated nor do they recognize that most technologically useful materials are not in their ground state nor stoichiometric compounds. More challenging is that an alloy’s properties are a finely tuned optimization of multiple phases with varying length scales that are difficult to predict *a priori* with current state-of-the-art simulations. New paradigms in modeling materials processing will be required to accelerate the development of functional materials.

**II. Basic Synthesis Science for Energy Storage:** *Designing new materials with higher energy storage capacity and improved reliability.*

Efficient storage of energy is crucial to development of more fuel efficient transportation technologies and reduced carbon emissions. Current technologies are far from achieving their potential in terms of both storing and converting their fuel to electricity. Moreover, systems reliability is dependent on maintaining a high degree of materials stability and interface integrity over hundreds to thousands of charge-discharge cycles. New or improved anode, cathode and membrane materials will need to be both

robust and inexpensive. Advancements in new materials will require a better understanding of the atomistic to microstructural scale processes that control the rates of ion transport and the materials degradation that accompanies the charge-discharge processes. Materials challenges include, for instance, understanding and control of the transport of ions at the solid/electrolyte interface. Materials degradation due to volumetric changes can be minimized and recharge rates can be increased by controlling particle size and morphology but this must be achieved in materials with appropriate chemical stability and with more abundant constituents that incorporate self-healing, self-regulation, failure-tolerance, and impurity-sequestration. Computational materials design has the promise of discovery of new material compounds, but for more complex architectures for advanced functional materials, innovative fabrication strategies will also be needed. New analytical tools that can monitor changes in the structure and composition of materials in the bulk and at their interfaces are needed to detect and measure changes at the atomic to microstructural level under operating conditions.

### **III. Synthesis Challenges for Film Interfaces:** *Examining synthesis of complex thin films, single crystals, and nanoscale materials with useful physical properties.*

Materials such as thin films, single crystals, and nanoscale objects are central to a wide range of current and future technologies, but meeting the increasingly stringent requirements of property and function will require control of these materials at the atomic scale. Hence, the need for atomically precise synthesis techniques is growing. This session will address some of the latest challenges in developing and understanding methods to carry out atomically controlled synthesis of films and interfaces. This session will focus on understanding general principles that describe how processing affects the resultant material properties. Film deposition techniques such as molecular beam epitaxy (MBE), chemical vapor deposition, atomic layer deposition, pulsed laser deposition and physical vapor deposition provide excellent capabilities. Moreover, patterning by techniques such as lithography or self-assembly is enabling increasing levels of spatial control, yet, many challenges still remain. For example, while MBE has excelled at atomically precise synthesis in which atomic species such as dopants can be placed where desired, other techniques that may be attractive because of higher throughput or lower cost have not yet reached the same level of compositional or structural control. This session will examine what challenges remain in gaining the capability during synthesis to place atoms where we want them in order to generate materials with desired physical properties. Progress in understanding the relationship between processing and properties in a range of important materials and interfaces, such as crystalline solids, ultrathin films, glasses, hybrid materials, and nanostructures, will be reviewed.

### **IV. Synthesis Science for Light-Matter Interaction:** *Investigating approaches for synthesis and processing of materials used to harness light-matter interactions toward energy conversion technologies such as photovoltaics and light emitting diodes.*

Light-matter interactions are at the heart of a number of important energy conversion technologies, including photovoltaics and solid state lighting. Given the inexhaustible size of the solar resource, which exceeds by many times that of other renewable energy sources, plus the need for efficient lighting to reduce energy usage, the conversion of energy between light and electricity as well as between light and chemical energy will continue to be of huge importance in future energy systems. As a result, the need is growing for tailored materials to efficiently carry out these conversions. The variety of energy conversion systems, such as organic light emitting diodes (OLEDs), photovoltaics, and solar fuel devices, utilize a

diversity of materials, including compound semiconductors, organics, hybrid materials, nanoscale materials, and plasmonic-enhanced structures. Many questions and challenges remain in how to meet the materials needs. For example, how can we process these materials so that they have the desired optoelectronic properties? How can we control materials at the appropriate length scales vis-a-vis processing and chemistry? This session will address the challenges of understanding and translating the various universal principles of materials synthesis to affect the way in which the materials interact with light.

**Summary:** Overall, this meeting will endeavor to establish working relationships and collaborations among the investigators through discussion of materials synthesis and processing challenges that crosscut materials classes with an emphasis on coupling theoretical and experimental approaches.

# Agenda

This page is intentionally blank.

# Synthesis and Processing Science

## Principal Investigators' Meeting

Meeting Chairs: **Matthew Kramer** and **Stacey Bent**  
Ames Laboratory / Stanford University

### Sunday, November 17, 2013

3:00 – 6:00pm      **Registration**

### Monday, November 18, 2013

7:30 – 8:30am      \*\*\*\*\***Breakfast**\*\*\*\*\*

8:30 – 8:45am      **Introductory Remarks:**  
Meeting Chairs: **Matthew Kramer** and **Stacey Bent**  
Ames Laboratory / Stanford University

#### **Session 1:      Research on Critical Materials for Energy Applications** Chair: **Matthew Kramer**, Ames Laboratory

8:45 – 9:15am      **Thomas Lograsso**, Ames Laboratory, Critical Materials Institute  
*Critical Materials Institute – A Energy Innovation Hub: The Role of  
Synthesis & Processing in Reducing Criticality*

9:15 – 9:45am      **Theo Siegrist**, Florida State University  
*Discovery and Crystal Growth of New Oxide Phases from Metal Fluxes*

9:45 – 10:15am      **Cedomir Petrovic**, Brookhaven National Laboratory  
*Two-Dimensional Dirac Fermions in Bulk Crystals*

10:15 – 10:45am      \*\*\*\*\***Break**\*\*\*\*\*

10:45 – 11:15am      **Alexandra Navrotsky**, University of California, Davis  
*How Bulk and Surface Thermodynamics Affects Li battery Material Properties*

#### **Session 2:      Topics in Basic Synthesis Science for Energy Storage: Batteries** Chair: **Stacey Bent**, Stanford University

11:15 – 11:45am      **Jun Liu**, Pacific Northwest National Laboratory, Joint Center for Energy  
Storage Research (JCESR)  
*Joint Center for Energy Storage Research (JCESR): Understanding  
Fundamental Structural Transformation and Electrochemical Reactions  
Using In-Situ TEM and NMR*

11:45 – 12:15pm **Chengdu Liang**, Oak Ridge National Laboratory  
*Tailoring Ionic Conductivity in Solids for High-Energy Batteries*

12:15 – 1:15pm \*\*\*\*\***Working Lunch/Poster Introductions**\*\*\*\*\*

1:15 – 2:00pm **Division and Program Updates**  
**Linda Horton**  
Director, Materials Science & Engineering Division, Basic Energy Sciences  
**Bonnie Gersten**  
Program Manager, Synthesis and Processing Science

**Session 2a: Topics in Basic Synthesis Science for Energy Storage: (continued)**  
**Fuel Cells**  
Chair: **Stacey Bent**, Stanford University

2:00 – 2:30pm **Joshua Hertz**, University of Delaware  
*Heterogeneous Thin Films for Tailored Ionic Transport*

2:30 – 3:00pm **I. Wei Chen**, University of Pennsylvania  
*Electric-Field Enhanced Kinetics in Oxide Ceramics: Pore Migration, Sintering and Grain Growth*

3:00 – 3:30pm \*\*\*\*\***Break**\*\*\*\*\*

3:30 – 6:00pm \*\*\*\*\***Poster Session I**\*\*\*\*\*

6:00 – 7:00pm \*\*\*\*\***Working Dinner**\*\*\*\*\*  
(Scientific highlights of the day: discussion and input from attendees)

7:00 – 8:00pm \*\*\*\*\***Poster Session I (continued)**\*\*\*\*\*

## Tuesday, November 19, 2013

7:30 – 8:30am \*\*\*\*\***Breakfast**\*\*\*\*\*

**Session 3: Synthesis Challenges for Film Interfaces**  
Chair: **Anand Bhattacharya**, Argonne National Laboratory

8:30 – 9:00am **Max Lagally**, University of Wisconsin-Madison and **Feng Liu**, University of Utah  
*Synthesis and Processing Research in Group IV Nanomembranes*

9:00 – 9:30am **Ivan Božović**, Brookhaven National Laboratory  
*Atomic-Layer-by-Layer Molecular Beam Epitaxy Synthesis of Cuprate Superconductors*

9:30 – 10:00am **Scott Chambers**, Pacific Northwest National Laboratory  
*Defects in Oxides and at Oxide Interfaces – an Influential and Useful Reality*

10:00 – 10:30am \*\*\*\*\***Break**\*\*\*\*\*

<b>Session 3a:</b>	<b>Synthesis Challenges for Film Interfaces (continued)</b> Chair: <b>Darrell Schlom</b> , Cornell University
10:30 – 11:00am	<b>Stacey Bent</b> , Stanford University <i>Studies of Surface Reaction and Nucleation Mechanisms in Atomic Layer Deposition</i>
11:00 – 11:30am	<b>Eric Chason</b> , Brown University <i>A Unified Understanding of Residual Stress in Thin Films: Kinetic Models, Experiments and Simulation</i>
11:30 – 12:00pm	<b>Hanchen Huang</b> , Northeastern University <i>Science-Directed Pursue of the Smallest Metallic Nanorods Using Physical Vapor Deposition</i>
12:00 – 12:30pm	<b>Michael Tringides</b> , Ames Laboratory <i>Controlling Metal Epitaxial Growth on Graphene and Graphite</i>
12:30 – 1:30pm	***** <b>Working Lunch/Poster Introductions</b> *****
1:30 – 2:15pm	<b>Panel/General Discussion</b>
<b>Session 4:</b>	<b>Early Career Program</b> Chair: <b>Joshua Zide</b> , University of Delaware
2:15 – 2:45pm	<b>Michael Arnold</b> , University of Wisconsin-Madison <i>Understanding Graphene Crystal Morphology Evolution and Orientation During CVD on Cu and the Bottom-Up Growth of Graphene Nanostructures with Refined Edges</i>
2:45 – 3:15pm	<b>PengPeng Zhang</b> , Michigan State University <i>Utilizing Molecular Self-Assembly to Tailor Electrical Properties of Si Nanomembranes</i>
3:15 – 3:45pm	***** <b>Break</b> *****
3:45 – 6:00pm	***** <b>Poster Session II</b> *****
6:00 – 7:00pm	***** <b>Working Dinner</b> ***** (Scientific highlights of the day: discussion and input from attendees)
7:00 – 8:00pm	***** <b>Poster Session II (continued)</b> *****

**Wednesday, November 20, 2013**

7:30 – 8:30am \*\*\*\*\***Breakfast**\*\*\*\*\*

**Session 5: Topics in Basic Synthesis Science for Light-Matter Interaction**

Chair: **Chekesha Liddell Watson**, Cornell University

8:30 – 9:00am **Peter Green**, University of Michigan, EFRC  
*EFRC: Morphology, Carrier Transport and Device Performance of Thiophene Based Solar Cells*

9:00 – 9:30am **Roberto Paiella**, Boston University  
*Plasmonic Control of Radiation Processes for Enhanced Efficiency and Beam Shaping*

9:30 – 10:00am **Jung Han**, Yale University  
*Evolutionary Selection Growth: Towards Template-Insensitive Preparation of Single-Crystal Layers*

10:00 – 10:30am \*\*\*\*\***Break**\*\*\*\*\*

10:30 – 11:00am **Mark Ediger**, University of Wisconsin–Madison  
*High-Throughput Preparation and Characterization of Vapor-Deposited Organic Glasses*

11:00 – 12:00pm **BES Conclusion**  
**Matthew Kramer** and **Stacey Bent**, *Meeting Chairs*  
**Bonnie Gersten**, *Program Manager, Synthesis and Processing Science*

12:00 – 1:00pm **Lunch, Open Discussions, and Adjourning Comments**  
(Optional box lunches available)

# Poster Sessions

This page is intentionally blank.

## Poster Session I

Monday, November 18, 2013

1. *In situ* Monitoring of Dynamic Phenomena during Solidification  
*Amy J. Clarke\**, *S.D. Imhoff*, and *P.J. Gibbs*, *Los Alamos National Laboratory*
2. Four-Dimensional Analysis of the Evolution of Complex Dendritic Microstructures during Coarsening  
*C. Park*, *Katsuyo Thornton*, *University of Michigan* and *J. Gibbs*, *Peter Voorhees\**, *Northwestern University*
3. Predicting and Controlling Phase Selection in Highly Driven Systems  
*Matthew J. Kramer\**, *A. I. Goldman*, *R. E. Napolitano*, *Mikhail I. Mendeleev*, *Kai-Ming Ho*, *R. T. Ott*, *F. Zhang*, *Z. Ye*, *Y. Sun*, *X. Y. Song*, and *C. Z. Wang*, *Ames Laboratory*
4. Development of Order in Deeply Undercooled Liquid Metals  
*F. Zhang*, *Z. Ye*, *Y. Sun*, *X. W. Fang*, *C. Z. Wang*, *Matthew J. Kramer\**, *I. McBrearty*, *Mikhail I. Mendeleev*, *R. E. Napolitano*, *R. T. Ott*, and *Kai-Ming Ho*, *Ames Laboratory*
5. Theoretical and Experimental Study of Solid-Liquid Interface Properties of Stoichiometric Compounds  
*S.R. Wilson*, *Mikhail I. Mendeleev\**, *X.Y. Song*, *R.T. Ott*, *A.I. Goldman*, *R.E. Napolitano* and *M.J. Kramer\**, *Ames Laboratory*
6. Atomistic Structure, Strength, and Kinetic Properties of Intergranular Films in Ceramics  
*Yun Jiang*, *Ying Ma*, *Stephen H. Garofalini\**, *Rutgers University*
7. Laser Fabrication of Active Single-Crystal Architecture in Glass  
*Himanshu Jain\**, *Volker Dierolf\**, *D. Savytskyy*, *P. Gupta*, *B. Knorr*, *Lehigh University*
8. Exploratory Materials Synthesis and Characterization  
*Cedomir Petrovic\**, *Brookhaven National Laboratory*
9. Novel Materials Preparation and Processing Methodologies: Microstructural Refinement and Phase Space Determination of Mg<sub>2</sub>Si-Based Thermoelectric Alloys  
*Yong Liu\**, *Qingfeng Xing\**, and *Thomas A. Lograsso\**, *Ames Laboratory*
10. Novel Materials Preparation and Processing Methodologies: Peculiar Properties of Iron Based Superconductors Disclosed by Heat Treatment and New Synthesis Technology  
*Yong Liu\**, *Qingfeng Xing\**, and *Thomas A. Lograsso\**, *Ames Laboratory*
11. Discovery and Crystal Growth of New Oxide Phases from Metal Fluxes  
*Theo Siegrist\**, *T. Besara*, *D. Ramirez*, *Florida State University*
12. New Oxide Materials for an Ultra High Temperature Environment  
*John H. Perepezko\**, *University of Wisconsin-Madison*
13. Phase Transformations and Equilibria in Complex Half-Heusler/Full-Heusler Nanocomposites  
*Pierre Ferdinand Poudeu\** and *Citrad Uher\**, *University of Michigan* and *Anton Van der Ven*, *University of California Santa-Barbara*

14. A Fundamental Study of Inorganic Clathrate Open-Framework Materials  
*George S. Nolas\**, *University of South Florida*
15. Study of Spark-Plasma Sintering at Different Scale Levels  
*Eugene A. Olevsky\**, *San Diego State University*
16. Electric-Field Enhanced Kinetics in Oxide Ceramics: Pore Migration, Sintering and Grain Growth  
*I-Wei Chen\**, *University of Pennsylvania*
17. Improved Electrochemical Performance of Strained Lattice Electrolytes via Modulated Composition  
*Joshua L. Hertz\**, *University of Delaware*
18. How Bulk and Surface Thermodynamics Affects Li battery Material Properties  
*Alexandra Navrotsky\**, *University of California, Davis*
19. Solid Electrolytes to Stabilize High-Voltage Battery Interfaces  
*Juchuan Li, Yoongu Kim, Chengdu Liang\**, and *Nancy J. Dudney\**, *Oak Ridge National Laboratory*
20. Molecularly Organized Nanostructural Materials  
*Jun Liu\**, *Praveen Thallapally\**, *Yongsoon Shin, Jie Xiao\**, *Xiaolin Li, Yuyan Shao, Maria Sushko, Gregory J. Exarhos, Pacific Northwest National Laboratory*
21. Conduction Mechanisms and Structure of Ionomeric Single-Ion Conductors  
*Ralph H. Colby\**, *Janna K. Maranas, Karl T. Mueller, James Runt and Karen I. Winey, The Pennsylvania State University*
22. Molecularly Organized Nanostructural Materials  
Subtask: Guest Induced Structural Transformation and Nanostructural Materials Synthesis  
*Praveen K. Thallapally\**, *Jian Tian, Jian Liu and Jun Liu\**, *Pacific Northwest National Laboratory*
23. Novel Theoretical and Experimental Approaches for Understanding and Optimizing Molecule-Sorbent Interactions in Metal Organic Framework Materials  
*Nour Nijem, Kui Tan, Y. J. Chabal\**, *University of Texas at Dallas*  
*Haohan Wu, Debasis Banerjee, Jing Li\**, *Rutgers University*  
*Pieremanuele Canepa, Sebastian Zuluaga, Timo Thonhauser, Wake Forest University*
24. Investigating the Metastability of Clathrate Hydrates for Energy Storage  
*Carolyn A. Koh\** and *Amadeu K. Sum\**, *Colorado School of Mines*
25. Forces, Crystallization, and Assembly in Nanoparticle Suspensions  
*Kristen A. Fichthorn\** and *Robert M. Rioux, The Pennsylvania State University*
26. Inverse Optimization Techniques for Targeted Self-Assembly  
*Salvatore Torquato\** and *Frank Stillinger, Princeton University*
27. Directed Assembly of Rod-Coil Block Copolymers by Combined External Fields  
*Qiang (David) Wang\** and *David S. Dandy, Colorado State University*
28. Giant Electrocaloric Effect in Ferroelectric Polymers with Tailored Polar-Nanostructures  
*Qiming M. Zhang\**, *The Pennsylvania State University*

29. Using Energetic Gas Jets to Enable New Modes of Focused Electron Beam Induced Deposition  
*Matthew Henry and Andrei G. Fedorov\**, Georgia Institute of Technology
30. Non-equilibrium Effects in the Processing of Materials using Plasmas  
*Lorenzo Mangolini\**, University of California, Riverside
31. Boron-Based Nanostructures: Stability, Functionality and Synthetic Routes  
*Boris I. Yakobson\** and Pulickel Ajayan, Rice University
32. Growth Mechanisms and Controlled Synthesis of Nanomaterials: Revealing the Growth Mechanism of Graphene on Catalytic Substrates by Real-Time Optical Diagnostics  
*Alex Puretzky\**, Gyula Eres, David B. Geohegan\*, Murari Regmi, Christopher M. Rouleau, Mina Yoon\*, Matthew Chisholm, and Gerd Duscher, Oak Ridge National Laboratory
33. Growth Mechanisms and Controlled Synthesis of Nanomaterials: Modeling and Characterization of Ultrasmall Nanoparticles  
*Mina Yoon\**, David B. Geohegan\*, Alex Puretzky\*, Christopher M. Rouleau, Gyula Eres, Masoud Mahjouri-Samani, Miaofang Chi, and Gerd Duscher, Oak Ridge National Laboratory, and Mengkun Tian, University of Tennessee
34. Growth Mechanisms and Controlled Synthesis of Nanomaterials: Synthesis of Nanostructures from Nanoparticle Building Blocks  
*David B. Geohegan\**, Masoud Mahjouri-Samani, Christopher M. Rouleau, Alex Puretzky\*, Gyula Eres, Mina Yoon\*, Miaofang Chi, and Gerd Duscher, Oak Ridge National Laboratory, and Mengkun Tian University of Tennessee
35. Understanding and Controlling Nanoscale Crystal Growth using Mechanical Forces  
*Mostafa Bedewy<sup>1,2</sup>, Assaf Ya'akovovitz<sup>1</sup>, Kendall Teichert<sup>1</sup>, and A. John Hart\*<sup>1,2</sup>*, <sup>1</sup> University of Michigan, <sup>2</sup> Massachusetts Institute of Technology

## Poster Session II

Tuesday, November 19, 2013

1. Understanding Graphene Crystal Morphology Evolution and Orientation During CVD on Cu; and the Bottom-Up Growth of Graphene Nanostructures with Refined Edges  
*Michael S. Arnold\**, University of Wisconsin
2. Integrated Growth and Ultra-low Temperature Transport Study of the 2<sup>nd</sup> Landau Level of the Two-Dimensional Electron Gas  
*Gabor Csathy\** and *Michael Manfra\**, Purdue University
3. Development and Understanding of Multifunctional Nanostructured Magnetoelectric and Spintronic Materials  
*Ram S. Katiyar\**<sup>1</sup>, *M. Gomez*<sup>1</sup>, *G. Morell*<sup>1</sup>, *L. Fonseca*<sup>1</sup>, *Y. Ishikawa*<sup>1</sup>, *R. Palai*<sup>1</sup>,  
*R. Thomas*<sup>1</sup>, *A. Kumar*<sup>1</sup>, *J. Velev*<sup>1</sup>, *V. Makrov*<sup>1</sup>, *O. Perales*<sup>2</sup>, *M.S. Tomar*<sup>2</sup>, *W. Otaño*<sup>3</sup>,  
University of Puerto Rico, Rio Piedras<sup>1</sup>, Mayaguez<sup>2</sup>, Cayey<sup>3</sup>
4. SISGR—Using Interfaces to Create Strongly Coupled Magnetic Ferroelectrics  
*Craig J. Fennie*, *David A. Muller*, *Darrell G. Schlom\**, Cornell University and *Peter Schiffer*, The Pennsylvania State University
5. Digital Synthesis: A Pathway to New Materials at Interfaces of Complex Oxides  
*Anand Bhattacharya\**, *Sam Bader*, Argonne National Laboratory
6. Electronic and Optical Properties of Doped Complex Oxide Epitaxial Films and Interfaces: Mixed Metal Oxide Corundum-like Materials  
*Scott A. Chambers\**, *Tiffany C. Kaspar\**, *T.C. Droubay*, *Yingge Du\**, *H.K.L Zhang*, *R. Colby*, Pacific Northwest National Laboratory, and *Peter V. Sushko*, University College London
7. Electronic and Optical Properties of Doped Complex Oxide Epitaxial Films and Interfaces: Perovskite Films and Interfaces  
*Scott A. Chambers\**, *Tiffany C. Kaspar\**, *T.C. Droubay*, *Yingge Du\**, *H.K.L Zhang*, *R. Colby*, Pacific Northwest National Laboratory, and *Peter V. Sushko*, University College London
8. Artificially Layered Superlattice of Pnictide by Design  
*Chang-Beom Eom\**, University of Wisconsin–Madison
9. Atomic-Layer-by-Layer Molecular Beam Epitaxy Synthesis of Cuprate Superconductors  
*Ivan Božović\**, *Anthony T. Bollinger* and *Jie Wu*, Brookhaven National Laboratory
10. Studies of Surface Reaction and Nucleation Mechanisms in Atomic Layer Deposition  
*Stacey F. Bent\**, Stanford University
11. Atomic Layer Deposition (ALD) of Metal and Metal Oxide Films: A Surface Science Study  
*Francisco Zaera\**, University of California, Riverside
12. Surface-Reaction-Limited Pulsed Chemical Vapor Deposition for Growing Nanowires inside Highly Confined Spaces  
*Xudong Wang\**, University of Wisconsin–Madison

13. Growth and Properties of New Epitaxial Metal/Semiconductor Nanocomposites  
*Joshua M. O. Zide\*, University of Delaware*
14. A Unified Understanding of Residual Stress in Thin Films: Kinetic Models, Experiments and Simulations  
*Eric Chason\*, Brown University*
15. Electrodeposition of Cobalt (Hydr)oxide Oxygen Evolution Catalysts for Photoelectrochemical Water Splitting  
*Jay A. Switzer\*, Missouri University of Science and Technology*
16. Science-Directed Pursue of the Smallest Metallic Nanorods using Physical Vapor Deposition  
*Hanchen Huang\*, Northeastern University*
17. Nanoscale Morphologies to Control Atomic Scale Processes: Collective Multi-atom Diffusion in Pb/Si(111) at Low Temperatures  
*K.M. Ho, M. Hupalo, P. A. Thiel, Michael C. Tringides\* and C. Z. Wang, Ames Laboratory*
18. Nanoscale Morphologies to Control Atomic Scale Processes: Non-standard Nucleation of Metal Growth on Carbon Rich Surfaces  
*K.M. Ho, M. Hupalo, P. A. Thiel, Michael C. Tringides\* and C. Z. Wang, Ames Laboratory*
19. *In Situ* Visualization and Theoretical Modeling of Early-Stage Oxidation of Metals and Alloys  
*Guangwen Zhou\*, State University of New York, Binghamton*
20. Synthesis and Processing Research in Group IV Nanomembranes  
*Max G. Lagally\* and Mark A Eriksson, University of Wisconsin–Madison with Feng Liu, University of Utah*
21. Strain Engineered Surface Transport in Si(001): Complete Isolation of the Surface State via Tensile Strain  
*Feng Liu\*, University of Utah*
22. Utilizing Molecular Self-Assembly to Tailor Electrical Properties of Si Nanomembranes  
*Pengpeng Zhang\*, Michigan State University*
23. High-Throughput Preparation and Characterization of Vapor-Deposited Organic Glasses  
*S.S. Dalal, D.M. Walters, A. Gujral, and Mark D. Ediger\*, University of Wisconsin–Madison*
24. Quasiepitaxial Growth of Organic Crystalline Thin-Films  
*Richard R. Lunt\*, Michigan State University*
25. Brush-Coated Nanoparticle Polymer Thin Films: Structure-Mechanical-Optical Properties  
*Peter F. Green\*, University of Michigan*
26. Self-Assembly of Non-spherical Colloids: New Reduced Symmetry Crystals and Mesophases for Templating Functional Materials at Fine Scales  
*Chekesha M. Liddell Watson\*, Itai Cohen, Fernando Escobedo, Cornell University*
27. New Optoplasmonic Materials for Next Generation Energy Systems  
*Bjoern Reinhard\*, Boston University*
28. Coupled Plasmonic Arrays for Real Time Sensing  
*George Chumanov\*, Clemson University*

29. Plasmonic Control of Radiation Processes for Enhanced Efficiency and Beam Shaping  
*Roberto Paiella\* and Theodore D. Moustakas, Boston University*
30. Evolutionary Selection Growth: Towards Template-Insensitive Preparation of Single-Crystal Layers  
*Benjamin Leung and Jung Han\*, Yale University*
31. Enhanced Materials Based on Submonolayer Type-II Quantum Dots  
*Maria C. Tamargo\*, Igor K. Kuskovsky, Carlos A. Meriles, City University of New York and I. Cevdet Noyan, Columbia University*
32. Quantum Dot Sensitized Solar Cells Based on Ternary Metal Oxide Nanowires  
*J. Chen, Y. Yang, L. Lu, S. Maloney, Q. Dai, S. Horoz, J. Tang, and Wenyong Wang\*, University of Wyoming*

# **Laboratory Projects' Abstracts**

This page is intentionally blank.

***Program Title:***

**Digital Synthesis: A Pathway to New Materials at Interfaces of Complex Oxides**

***Principle Investigator : Anand Bhattacharya; Co-Investigator: Sam Bader***

***Address: Materials Science Division,***

***Bldg. 223, 9700 S. Cass Ave.,***

***Argonne National Laboratory,***

***Argonne, IL 60657.***

***email: anand@anl.gov***

***(i) Program Scope:***

In our program, we seek to create, characterize and understand novel electronic and magnetic states at interfaces of complex oxides. Our technique for creating these interfaces involves synthesizing ‘digital’ heterostructures of various oxide materials in a single atomic layer-by-layer manner. This allows us to tailor interfaces with great precision and to create superlattices with very short periods, comparable or less than the length scales for charge transfer at the interfaces.

The complex oxides host a very diverse range of collective states of condensed matter. The richness of observed phenomena in these materials, which have also presented some of the greatest challenges to our understanding, are due to their strongly interacting degrees of freedom. Surfaces and interfaces between complex oxides provide a unique environment where these degrees of freedom may ‘reconstruct’ and lead to new properties that are qualitatively different from those of their bulk constituents. Thus, interfaces are a pathway for discovering new materials and phenomena. More specifically, we seek to discover and explore novel states with attributes such as tunability with external electric fields and currents, novel magnetic structures that arise as a result of broken inversion symmetry, and electronic states that arise as a result of strong spin-orbit coupling. These include multiferroic heterostructures, superconductivity at interfaces between materials that may not be superconducting themselves, non-collinear interfacial magnetic structures, and novel two-dimensional electron gases. We seek to explore materials that are known to have interesting phases, such as the manganites and cuprates, where the atoms have been ‘re-arranged’ in simple ways – for example by layering the cations in a manner such that the effects of disorder have been engineered away – to reveal new properties. We create these materials systems using state-of-the-art, ozone-assisted oxide Molecular Beam Epitaxy (MBE) at Argonne, and characterize them using the major DOE facilities for neutron and photon scattering, and at the DOE Nanoscale Science Research Centers.

***(ii) Recent Progress (since 2011):***

***1. Tailoring polarity in a two-dimensional nickelate with single atomic layer control***

Many of the 3d transition metal oxides share a common structural  $MO_6$  building unit—a central transition metal (TM) cation octahedrally coordinated with oxygen nearest neighbors. The electronic states in these materials can be modified by tailoring the  $M-O$  bonds, which typically include the application of epitaxial strain in thin films, or pressure

and isovalent cation substitution in bulk samples. Here, we present a new route to tailor the  $M$ -O bonds without changes to the strain state or stoichiometry in two-dimensional perovskite nickelate ( $n=1$  in the Ruddlesden Popper series). We do this by tailoring the dipolar electrostatic interactions at the unit cell level in nominally non-polar  $\text{LaSrNiO}_4$  via single atomic layer-by-layer synthesis using oxide-MBE. We reconstruct the response of the crystal lattice to the induced polarity using an x-ray phase retrieval technique (COBRA). We find that the response of the O anions to the resulting local electric fields distorts the  $M$ -O bonds, being largest for the apical oxygens ( $\text{O}_{\text{ap}}$ ). It also alters the Ni valence. This structural control strategy has broad implications for tailoring electronic properties in oxides that are sensitive to the  $M$ - $\text{O}_{\text{ap}}$  bond geometry – such as superconductivity in the cuprates. This work is being done in collaboration with Dr. Hua Zhou at the Advanced Photon Source (Argonne) and Prof. James Rondinelli’s group at Drexel University. (Brittany Nelson-Cheeseman et al., *in preparation*)

## 2. Interfacial charge transfer and long range magnetic proximity effects in nickelate/manganite superlattices.

In conventional semiconductors and metals, a mismatch between the chemical potential for charge carriers in two materials at an interface leads to charge transfer. Furthermore, an electric field develops and ‘band bending’ occurs at the interface with profound

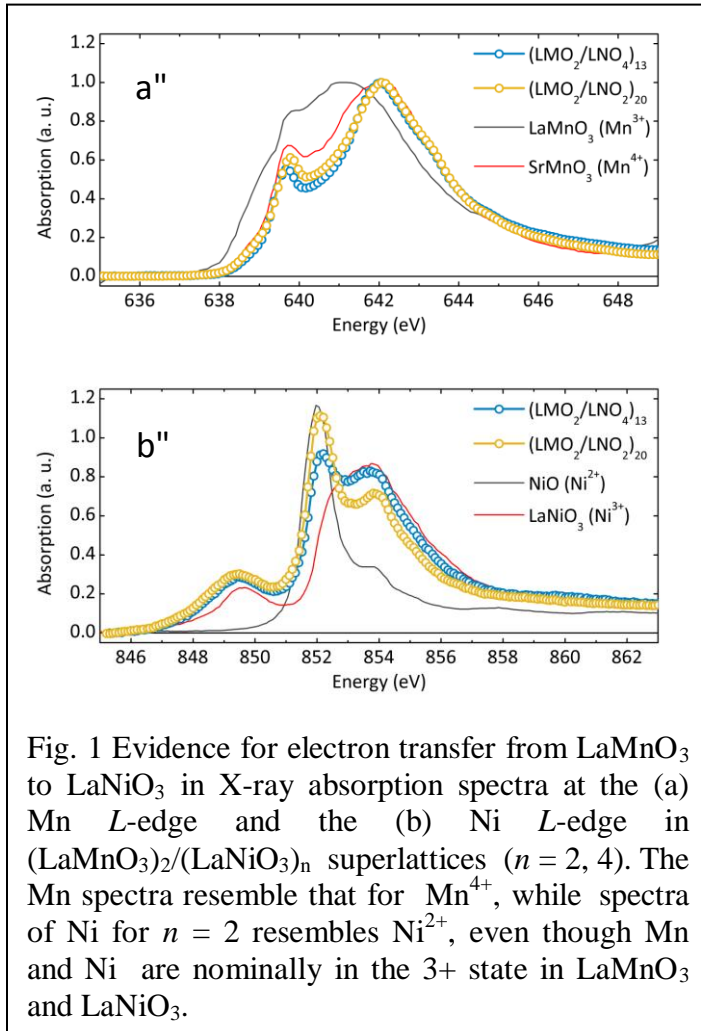


Fig. 1 Evidence for electron transfer from  $\text{LaMnO}_3$  to  $\text{LaNiO}_3$  in X-ray absorption spectra at the (a) Mn  $L$ -edge and the (b) Ni  $L$ -edge in  $(\text{LaMnO}_3)_2/(\text{LaNiO}_3)_n$  superlattices ( $n = 2, 4$ ). The Mn spectra resemble that for  $\text{Mn}^{4+}$ , while spectra of Ni for  $n = 2$  resembles  $\text{Ni}^{2+}$ , even though Mn and Ni are nominally in the 3+ state in  $\text{LaMnO}_3$  and  $\text{LaNiO}_3$ .

consequences. Motivated by the connection between band lineup charge transfer, we investigated the interface between two very dissimilar perovskites,  $\text{LaMnO}_3$  and  $\text{LaNiO}_3$ .  $\text{LaMnO}_3$  is an antiferromagnetic orbital-ordered Mott insulator and  $\text{LaNiO}_3$  is a paramagnetic metal. Using transport and x-ray spectroscopy (collaboration with Dr. John Freeland, Argonne), we were able to demonstrate that there is a significant charge transfer between these materials, with a electrons moving from  $\text{LaMnO}_3$  into  $\text{LaNiO}_3$ . In superlattices of  $(\text{LaMnO}_3)_2/(\text{LaNiO}_3)_n$ , this leads to a metal-insulator transition as  $n$  is varied. The origin of this transition can be traced to the charge transfer between the two constituents (J. Hoffman et al., to appear in *Phys. Rev. B*).<sup>1</sup> This charge transfer is also linked to

interfacial magnetism – the  $\text{LaNiO}_3$  becomes magnetic over approximately the first unit cell in the vicinity of the interface. To explore this further, we made superlattices of  $(\text{La}_{2/3}\text{Sr}_{1/3}\text{MnO}_3)_m/(\text{LaNiO}_3)_n$  where we observed magnetic coupling between  $\text{La}_{2/3}\text{Sr}_{1/3}\text{MnO}_3$  layers separated by  $(\text{LaNiO}_3)_n$ , where  $n$  was as large as 9.<sup>2</sup> This long-range magnetic coupling also leads to a non-collinear magnetic structure, which we have explored in detail using neutron reflectometry (with Dr. Brian Kirby at NIST). We are currently exploring details of magnetic and electronic instabilities in the nickelate layer brought about by proximity to the manganite. (J. Hoffman et al., *in preparation*) We also have an ongoing collaboration with Prof. Jian-Min Zuo group (UIUC) to characterize the interfacial structure and electronic properties using transmission electron microscopy (STEM EELS).

**(iii) Future Plans:**

a.) *Tailoring inversion symmetry materials and M-O<sub>ap</sub> bond lengths:* Motivated by our results in the past few years, we have plans to create and explore a number of materials systems using the synthesis approach that has been outlined earlier. We would like to understand how broken inversion symmetries in crystal structures could be used to tailor the bond between transition metal cations and apical oxygens in layered Ruddlesden Popper materials. In particular, we plan to explore the titanates and cuprates. In the titanates we think that our approach can be used to tailor interesting metallic states made from the Ti  $t_{2g}$  manifold, where we would tailor the Rashba interaction by breaking inversion symmetry via cation ordering. In the cuprates, we hope to tailor the Cu-O<sub>apical</sub> bond length in a systematic way and explore changes in properties.<sup>3</sup>

b) *Interfacial Charge Transfer and Band-lineup in Mott Insulators:* ‘Band bending’ and charge transfer are very general ideas and should occur for a broad range of oxides, beyond the nickelate/manganite interfaces that we are currently exploring. However, a general understanding of what happens at such interfaces is lacking because more often than not the 3d transition metal oxides have narrow bands where the charge carriers are strongly correlated. Here, the ideas of ‘band bending’ have to be considered in light of the dynamic nature of the bands, i.e. the sensitivity of the band structure to filling. Furthermore, interfaces have broken inversion symmetry which can have interesting consequences for interfacial magnetism. Based upon the literature on measurements of band lineup of various 3d oxides, there are systematic though empirical guides to dope materials via charge transfer at interfaces that need to be explored in a controlled manner. We plan to do this work in conjunction with theorists Prof. Andrew Millis (Columbia) and Prof. Peter Littlewood (Argonne/Chicago) who are carrying out a first principles DFT/DMFT based study of this problem.

**(iv) References:**

1. “Charge transfer and interfacial magnetism in  $(\text{LaNiO}_3)_n/(\text{LaMnO}_3)$  superlattices”, J. Hoffman et al., *arXiv:1301.7295v2*, to appear in *Phys. Rev. B* (2013).
2. A long range magnetic coupling was observed in earlier work in manganite/nickelate superlattices – “Oscillatory exchange coupling and positive magnetoresistance in epitaxial oxide heterostructures”, K.R. Nikolaev et al., *Phys. Rev. Lett.* **85**, 3728 (2000).

3. Interfacial apical oxygens can have large distortions in cuprates: "Anomalous expansion of the copper-apical-oxygen distance in superconducting cuprate bilayers." Zhou, Hua, et al. *Proceedings of the National Academy of Sciences* **107**, 8103-8107 (2010).

**(v) Publications supported by Department of Energy, Basic Energy Sciences (since 2011):**

- P1. "Non-volatile ferroelastic switching of the Verwey transition and resistivity of epitaxial  $\text{Fe}_3\text{O}_4/\text{PMN-PT}$  (011)", Ming Liu, J. Hoffman, J. Wang, J. Zhang, B. Nelson-Cheeseman, A. Bhattacharya, *Scientific Reports* **3**, Article No. 1876 (2013) doi:10.1038/srep01876.
- P2. Book Chapter: 'Manganites Multilayers', Anand Bhattacharya, Shuai Dong, and Rong Yu, in "Multifunctional Oxide heterostructures", Eds. E. Y. Tsymbal, E. A. Dagotto, C.-B. Eom and R. Ramesh, Oxford University Press (2012).
- P3. "Interface Magnetism in a  $\text{SrMnO}_3/\text{LaMnO}_3$  superlattice", S. Smadici, B. B. Nelson-Cheeseman, A. Bhattacharya, P. A. Abbamonte, *Phys. Rev. B* **86**, 174427 (2012).
- P4. "Structurally induced magnetization in a  $\text{La}_{2/3}\text{Sr}_{4/3}\text{MnO}_4$  superlattice", Amish B. Shah, Brittany B. Nelson-Cheeseman, Ganesh Subramanian, Anand Bhattacharya, and John C. H. Spence, *Phys. Status Solidi A*, 1–6 (2012) / DOI 10.1002/pssa.201127728.
- P5. "Delta Doping of Ferromagnetism in Antiferromagnetic Manganite Superlattices", T.S. Santos, B.J. Kirby, S. Kumar, S.J. May, J.A. Borchers, B.B. Maranville, J. Zarestky, S. G. E. te Velthuis, J. van den Brink, and A. Bhattacharya, *Phys. Rev. Lett.* **107**, 167202 (2011).
- P6. "Ultrathin  $\text{BaTiO}_3$  templates for multiferroic nanostructures", X.M. Chen, S. Yang, J.H. Kim, H.D. Kim, J.S. Kim, G. Rojas, R. Skomski, H.D. Lu, A. Bhattacharya, T. Santos, N. Guisinger, M. Bode, A. Gruverman, A. Enders, *New Journal of Physics* **13**, 083037 (2011).
- P7. "Control of octahedral rotations in  $\text{LaNiO}_3/\text{SrMnO}_3$  superlattices", S. J. May, C. R. Smith, J. -W. Kim, E. Karapetrova, A. Bhattacharya, P. J. Ryan, *Phys. Rev. B* **83**, 153411 (2011).
- P8. "Cation-ordering Effects in the Single layered Manganite  $\text{La}_{2/3}\text{Sr}_{4/3}\text{MnO}_4$ ", B. B. Nelson-Cheeseman, A. B. Shah, T. S. Santos, S. D. Bader, J.-M. Zuo and A. Bhattacharya, *Appl. Phys. Lett.* **98**, 072505 (2011).
- P9. "Practical Spatial Resolution of Electron Energy Loss Spectroscopy in Aberration Corrected Scanning Transmission Electron Microscopy", A.B. Shah, Q.M. Ramasse, J.G. Wen, A. Bhattacharya and J.M. Zuo, *Micron* **42**, 539 (2011).

## **Atomic-layer-by-layer molecular beam epitaxy synthesis of cuprate superconductors**

Ivan Božović, Anthony T. Bollinger and Jie Wu

*Brookhaven National Laboratory, Upton NY 11973, USA*

### **Program scope**

The mechanism of high-temperature superconductivity (HTS) is one of the most important problems in Condensed Matter Physics. Some basic facts - the dimensionality, the spin and the charge of free carriers, the nature of superconducting transition, the effective interaction that causes electron pairing - are still unclear. To attack these problems, we use atomic-layer-by-layer molecular beam epitaxy (ALL-MBE) to synthesize single-crystal films of cuprates and other complex oxides, as well as multilayers and superlattices with atomically perfect interfaces, enabling novel experiments that were not possible so far.

The program impact is twofold. First, the group is the source of unique samples, including high-quality HTS films and multilayer hetero-structures engineered down to a single atomic layer, that are enabling breakthrough research of few dozen groups at national laboratories and leading universities in US and abroad. Second, our own in-house experiments have also brought in several important results - discovery of HTS interface superconductivity, demonstration of Giant Proximity Effect, HTS in a single  $\text{CuO}_2$  layer, and the (de)localization of electron pairs at the superconductor-insulator quantum phase transition. [1-10] These and future experiments are hoped to provide clear-cut answers to at least some of the above questions, which could significantly impact research on HTS and more broadly on strongly-correlated materials.

### **Recent progress**

In the last two years (FY 2012 and FY 2013) we have performed over 400 ALL-MBE synthesis experiments, most of which produced atomically smooth superconducting films. Every film was characterized by RHEED,  $R(T)$  and/or  $\chi(T)$  measurements and selected ones also by XRD and AFM. Many were patterned into micro- or nano-sized devices and were subject to detailed study of their physical properties and behavior. This resulted in a number of new observations, reported in 25 journal papers and one awarded patent. The highlights are as follows.

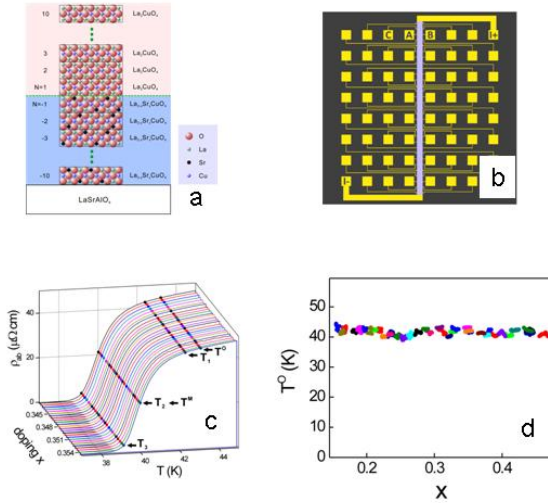


Fig. 1 (a)  $\text{La}_{2-x}\text{Sr}_x\text{CuO}_4 - \text{La}_2\text{CuO}_4$  heterostructure synthesized by ALL-MBE. (b) COMBI library with 32 pixels and 64 contacts for high-throughput measurements of resistivity and Hall effect. (c)  $R(T)$  data from one COMBI library; the composition is scanned in steps of  $\delta x = 0.0003$ . (d)  $T_c$  vs.  $x$  data for over 800 compositions of the bottom (metallic) layer, from  $x = 0.15$  to  $x = 0.47$ .

**Anomalous independence of interface superconductivity on carrier density.** [11] The recent discovery of superconductivity at the interface of two non-superconducting materials has received much attention. In cuprate bilayers, the critical temperature ( $T_c$ ) can be significantly enhanced compared to single-phase samples. [1] Several explanations have been proposed, invoking Sr interdiffusion, accumulation and depletion of mobile charge carriers, elongation of the copper-to-apical-oxygen bond length, or a beneficial crosstalk between a material with a high pairing energy and another with a large phase stiffness. From each of these models, one would predict  $T_c$  to depend strongly on the carrier density in the constituent materials. We studied combinatorial libraries of  $\text{La}_{2-x}\text{Sr}_x\text{CuO}_4 - \text{La}_2\text{CuO}_4$  bilayer samples - an unprecedentedly large set of over 800 different compositions, with the doping level  $x$  spanning a wide range ( $0.15 < x < 0.47$ ) and the measured Hall coefficient varying by one order of magnitude. Nevertheless, across the entire sample set,  $T_c$  stayed essentially constant at about 40 K, see Fig. 1. [11] We inferred that doping up to the optimum level does not shift the chemical potential, unlike in ordinary Fermi liquids, thus posing a new challenge to theory of HTS in cuprates.

**Fluctuating charge density waves in a cuprate superconductor.** [12] Cuprate compounds that host HTS also exhibit various forms of charge and/or spin ordering whose role in the complex cuprate phase diagram is not fully understood. Static charge-density wave (CDW) ordering has been detected so far by diffraction probes only for special doping or in an applied external field. However, dynamic (fluctuating) CDWs may be present more broadly while being difficult to detect by conventional techniques. To observe and characterize fluctuating CDWs in cuprates, and determine whether they favor or compete with HTS, is thus an important open problem. Using a new method, based on ultrafast spectroscopy, the presence was detected and the lifetime measured of CDW fluctuations in cuprates. [12] In an underdoped  $\text{La}_{1.9}\text{Sr}_{0.1}\text{CuO}_4$  film ( $T_c = 26$  K), collective excitations of CDW are observed that persist up to 100 K. This CDW is dynamic; it fluctuates with a

characteristic lifetime of 2 ps at  $T = 5$  K which decreases to 0.5 ps at  $T = 100$  K. In contrast, in an optimally doped  $\text{La}_{1.84}\text{Sr}_{0.16}\text{CuO}_4$  film ( $T_c = 38.5$  K), no signatures of fluctuating CDW are seen at any temperature, favoring the competition scenario.

***Persistence of magnetic excitations in  $\text{La}_{2-x}\text{Sr}_x\text{CuO}_4$  from the undoped insulator to the heavily overdoped non-superconducting metal.*** [13] One of the most intensely studied scenarios of HTS postulates pairing by exchange of magnetic excitations. Indeed, such excitations have been observed up to around optimal doping in the cuprates. In the heavily overdoped regime, neutron scattering measurements indicate that magnetic excitations have effectively disappeared, and this was argued to cause the demise of HTS with overdoping. Resonant inelastic x-ray scattering (RIXS), which is sensitive to complementary parts of reciprocal space, was used to measure the evolution of the magnetic excitations in  $\text{La}_{2-x}\text{Sr}_x\text{CuO}_4$  across the entire phase diagram, from a strongly correlated insulator ( $x = 0$ ) to a non-superconducting metal ( $x = 0.40$ ). For  $x = 0$ , well-defined magnon excitations are observed [13]. These magnons broaden with doping, but they persist with a similar dispersion and comparable intensity all the way to the non-superconducting, heavily overdoped metallic phase. The destruction of HTS with overdoping is therefore caused neither by the general disappearance nor by the overall softening of magnetic excitations; other factor(s), such as the redistribution of spectral weight, must be considered.

***Emergence of superconductivity from the dynamically heterogeneous insulating state in  $\text{La}_{2-x}\text{Sr}_x\text{CuO}_4$ .*** [14] A central issue for copper oxides is the nature of the insulating ground state at low carrier densities and the emergence of HTS from that state with doping. Since this superconductor-insulator transition (SIT) is a zero-temperature transition, magnetoresistance was measured down to very low temperatures, to probe both the insulating state and the presence of superconducting fluctuations in  $\text{La}_{2-x}\text{Sr}_x\text{CuO}_4$  (LSCO) films, for doping levels that range from the insulator to the superconductor ( $x = 0.03$ - $0.08$ ). The charge glass behavior, characteristic of the insulating state, is suppressed with doping, but it coexists with superconducting fluctuations that emerge already on the insulating side of the SIT. This unexpected quenching of the superconducting fluctuations by the competing charge order at low temperatures provides a new perspective on the mechanism of the SIT.

***Spin excitations in a single  $\text{La}_2\text{CuO}_4$  layer.*** [15] The dynamics of  $S = 1/2$  quantum spins on a 2D square lattice lies at the heart of the mystery of the cuprates. In bulk cuprates such as  $\text{La}_2\text{CuO}_4$ , the presence of a weak interlayer coupling stabilizes 3D Neel order up to high temperatures. In a truly 2D system however, thermal spin fluctuations melt long range order at any finite temperature. Further, quantum spin fluctuations transfer magnetic spectral weight out of a well-defined magnon excitation into a magnetic continuum, the nature of which remains controversial. Measurements of the spin response of isolated one-unit-cell thick layers of  $\text{La}_2\text{CuO}_4$  showed that coherent magnons persist even in a single layer of  $\text{La}_2\text{CuO}_4$  despite the loss of magnetic order, with no evidence for resonating valence bond (RVB)-like spin correlations. High-energy continuum is also observed in the isotropic magnetic response; however, these excitations are not well described by two-magnon LSWT, or indeed by any other known theory.

### **Future plans**

First, we plan to complete several major experiments aimed at addressing directly some of the remaining key questions about the mechanism of HTS in cuprates. These include

detailed study of scaling near the critical points, of superconducting fluctuations, interface superconductivity, proximity effects, and new phenomena in HTS nanostructures. Next, our ALL-MBE (“digital”) synthesis technique enables creation of novel artificial, metastable materials. New design opportunities emerge from rich interface physics, which includes massive atomic and electron reconstructions as well as various proximity effects arising from competition between different instabilities and order parameters. This presents a new direction in search for novel superconductors.

## References

1. A. Gozar *et al.*, *Nature* 455, 782 (2008)
2. S. Smadici *et al.*, *PRL* 102, 107004 (2009)
3. G. Logvenov *et al.*, *Science* 326, 699 (2009)
4. V. Butko *et al.*, *Adv. Mater.* 21, 1 (2009)
5. H. Zhou *et al.*, *PNAS* 107, 8103 (2010).
6. A. Suter *et al.*, *PRL* 106, 237003 (2011).
7. I. Sochnikov *et al.*, *Nature Nanotech.* 5, 516 (2010)
8. E. Morenzoni *et al.*, *Nature Comm.* 2, 272 (2011).
9. L. Bilbro *et al.*, *Nature Physics* 7, 298 (2011)
10. A. Bollinger *et al.*, *Nature* 472, 458 (2011).
11. J. Wu *et al.*, *Nature Materials*, 12, 877 (2013).
12. D. Torchinsky *et al.*, *Nature Materials*, 12, 387 (2013).
13. M. Dean *et al.*, *Nature Materials*, published online 08.04.2013.
14. X. Shi *et al.*, *Nature Materials*, 12, 47 (2013).
15. M. Dean *et al.*, *Nature Materials*, 11, 850 (2012).

## DoE Sponsored Publications in the Last Two Years (10.01.2011 – 10.01.2013)

1. M. P. M. Dean, G. Dellea, R. S. Springell, F. Yakhou-Harris, K. Kummer, N. B. Brookes, X. Liu, Y.-J. Sun, J. Strle, T. Schmitt, L. Braicovich, G. Ghiringhelli, I. Bozovic and J. P. Hill, “Persistence of magnetic excitations in  $\text{La}_{2-x}\text{Sr}_x\text{CuO}_4$  from the undoped insulator to the heavily overdoped non-superconducting metal”, *Nature Materials* published online 08.04.2013.
2. J. Wu, O. Pelleg, G. Logvenov, A. T. Bollinger, Y. Sun, G. S. Boebinger, M. Vanević, Z. Radović and I. Božović, “Anomalous independence of interface superconductivity on carrier density”, *Nature Materials* 12, 877-881 (2013).
3. D. H. Torchinsky, F. Mahmood, A. T. Bollinger, I. Božović and N. Gedik, “Fluctuating charge density waves in a cuprate superconductor”, *Nature Materials* 12, 387-391 (2013).
4. X. Shi, D. Popović, C. Panagopoulos, G. Logvenov, A. T. Bollinger and I. Bozovic, “Emergence of superconductivity from the dynamically heterogeneous insulating state in  $\text{La}_{2-x}\text{Sr}_x\text{CuO}_4$ ”, *Nature Materials* 12, 47-51 (2013).

5. Y. Yacoby, H. Zhou, R. Pindak and I. Božović, “Atomic-layer synthesis and imaging uncover broken inversion symmetry in  $\text{La}_{2-x}\text{Sr}_x\text{CuO}_4$  films”, *Phys. Rev. B* **87**, 014108 (2013).
6. E. Stilp, A. Suter, T. Prokscha, E. Morenzoni, H. Keller, B. M. Wojek, H. Luetkens, A. Gozar, G. Logvenov and I. Bozovic, “Magnetic phase diagram of low-doped  $\text{La}_{2-x}\text{Sr}_x\text{CuO}_4$  thin films studied by low-energy muon-spin rotation”, *Phys. Rev. B* **88**, 064419 (2013).
7. G. Dubuis, A. T. Bollinger, D. Pavuna and I. Božović, “On Field Effect Studies and Superconductor-Insulator Transition in High- $T_c$  Cuprates”, (invited paper) *Eur. Phys. J. Special Topics* **222**, 1217–1221 (2013).
8. G. Logvenov, A. M. Gozar and I. Bozovic, “High Temperature Interface Superconductivity”, *Journal of Superconductivity and Novel Magnetism* **6**, 2863-5 (2013).
9. G. Dubuis, A. T. Bollinger, D. Pavuna and I. Božović, “Critical Resistance at the Superconductor-Insulator Transition in Hole-doped Cuprates”, *Journal of Superconductivity and Novel Magnetism* **26**, 749-754 (2013).
10. M. P. M. Dean, R. S. Springell, C. Monney, K. J. Zhou, I. Bozovic, J. Pereiro, B. Dalla Piazza, H. M. Ronow, J. van den Brink, T. Schmitt and J. P. Hill, “Spin Excitations in a single  $\text{La}_2\text{CuO}_4$  layer”, *Nature Materials* **11**, 850-4 (2012).
11. J. Pereiro, J. T. Sadowski, B. Lin, C. Panagopoulos & I. Bozovic, “Low-energy electron microscope study of tobacco mosaic viruses”, *J. Nano Science Letters*, **2**, 29 (2012).
12. V. Gasparov and Božović, “Magnetic field and temperature dependence of complex conductance of ultrathin  $\text{La}_{1.65}\text{Sr}_{0.45}\text{CuO}_4/\text{La}_2\text{CuO}_4$  films”, *Phys. Rev. B* **86**, 094523 (2012).
13. I. Sochnikov, I. Bozovic A. Shaulov and Y. Yeshurun, “Fluxoid quantization effects in high- $T_c$  superconducting double networks”, *Journal of Physics: Conference Series* **400**, 022109 (2012).
14. I. Bozovic, G. Logvenov and A. M. Gozar, “High Temperature Interfacial Superconductivity”, U.S. Patent No. 8,204,564. June 19, 2012.
15. S. Smadici, J. C. T. Lee, A. Rusydi, G. Logvenov, I. Bozovic and P. Abbamonte, “Distinct oxygen hole doping in different layers of  $\text{Sr}_2\text{CuO}_{\square 4}/\text{La}_2\text{CuO}_4$  superlattices”, *Phys. Rev. B* **85**, 094519 (2012).
16. G. Dubuis, A. T. Bollinger, D. Pavuna & I. Božović, “Electric field effect on superconductivity in  $\text{La}_{2-x}\text{Sr}_x\text{CuO}_4$ ”, *J. Appl. Phys.* **111**, 112632 (2012).
17. A. T. Bollinger, J. N. Eckstein, G. Dubuis, D. Pavuna and I. Božović, “Atomic-Layer Engineering of Oxide Superconductors”, in *Oxide-based Materials and Devices III*, edited by F. H. Teherani, D. C. Look and D. J. Rogers, *Proc. SPIE* **8263**, 82631C (2012).
18. X. Shi, D. Popović, C. Panagopoulos, G. Logvenov, A. T. Bollinger and I. Bozovic, “History dependent magnetoresistance in lightly doped  $\text{La}_{2-x}\text{Sr}_x\text{CuO}_4$  thin films”, *Physica B – Cond. Mat. Phys.* **407**, 1915–1918 (2012).

19. J. Pereiro, A. T. Bollinger, G. Logvenov, A. Gozar, C. Panagopoulos and I. Božović, “Insights from study of high-temperature interface superconductivity”, *Phil. Trans R. Soc. A* **370**, 4890–4903 (2012).
20. A. Suter, E. Morenzoni, T. Prokscha, H. Luetkens, B. M. Wojek, G. Logvenov, A. Gozar, and I. Bozovic, “Superconductivity in  $\text{La}_{1.56}\text{Sr}_{0.44}\text{CuO}_4/\text{La}_2\text{CuO}_4$  superlattices”, *Physics Procedia* **30**, 271-274 (2012).
21. S. Smadici, J. C. T. Lee, J. Morales, G. Logvenov, O. Pelleg, I. Bozovic, Y. Zhu, and P. Abbamonte, “Graded orbital occupation near interfaces in a  $\text{La}_2\text{NiO}_4$ - $\text{La}_2\text{CuO}_4$  superlattice”, *Phys. Rev. B* **84**, 155411 (2011).
22. I. Sochnikov, I. Bozovic A. Shaulov and Y. Yeshurun, Uncorrelated behavior of fluxoids in superconducting double networks, *Phys. Rev. B* **84**, 094530 (2011).
23. L. S. Bilbro, R. Valdes Aguilar, G. Logvenov, I. Bozovic, and N. P. Armitage, “On the possibility of fast vortices in the cuprates: A vortex plasma model analysis of THz conductivity and diamagnetism in  $\text{La}_{2-x}\text{Sr}_x\text{Cu}_4$ ”, *Phys. Rev. B* **84**, 100511(R) (2011).
24. M. Beyer, D. Städter, M. Beck, H. Schäfer, V. V. Kabanov, G. Logvenov, I. Bozovic, G. Koren, and J. Demsar, “Photoinduced melting of superconductivity in the high-Tc superconductor  $\text{La}_{2-x}\text{Sr}_x\text{CuO}_4$  probed by time-resolved optical and terahertz techniques”, *Phys. Rev. B* **83**, 214515 (2011).
25. G. Dubuis, A. T. Bollinger, D. Pavuna and I. Božović, “Electric Field Effect on Superconductivity in  $\text{La}_{2-x}\text{Sr}_x\text{CuO}_4$ ”, *J. Appl. Phys.* **111**, 112632 (2011).
26. J. Pereiro, A. Petrovic, C. Panagopoulos and I. Božović, “Interface superconductivity: History, development and prospects”, *Physics Express* **1**, 208-41 (2011).

# Electronic and Optical Properties of Doped Complex Oxide Epitaxial Films and Interfaces

S.A. Chambers (PI)<sup>a</sup>, T.C. Kaspar<sup>a</sup>, T.C. Droubay<sup>a</sup>, Y. Du<sup>a</sup>, H.K.L Zhang<sup>a</sup>, P.V. Sushko<sup>b</sup>, R. Colby<sup>a</sup>

<sup>a</sup>Pacific Northwest National Laboratory, Richland, WA; <sup>b</sup>Department of Physics and Astronomy and London Centre for Nanotechnology, University College London

## I. Program scope

This program focuses on understanding the complex interrelationships that exist between structure, composition and defect densities on one hand, and functional properties on the other hand, for well-defined epitaxial doped oxide films, surfaces and interfaces. The functional properties of interest include electronic, optical, magnetic, magnetoelectronic and photochemical. Our approach is to combine state-of-the-art epitaxial film growth techniques (primarily plasma assisted molecular beam epitaxy (MBE) and secondarily off-axis pulsed laser deposition (PLD)) with definitive materials characterization and functional properties measurements, along with the most advanced theoretical methods, to elucidate defensible cause-and-effect relationships. Materials of interest include oxide films such as (Ga,H):ZnO,  $\alpha$ -(Ti<sub>x</sub>Fe<sub>1-x</sub>)<sub>2</sub>O<sub>3</sub> and  $\alpha$ -(Cr<sub>x</sub>Fe<sub>1-x</sub>)<sub>2</sub>O<sub>3</sub> on  $\alpha$ -Al<sub>2</sub>O<sub>3</sub>(0001), Sr<sub>x</sub>La<sub>1-x</sub>CrO<sub>3</sub> on SrTiO<sub>3</sub>(001) and LaCrO<sub>3</sub>(001), and potentially functional interfaces such as LaCrO<sub>3</sub>/SrTiO<sub>3</sub>(001) and Cr/SrTiO<sub>3</sub>(001), among others.

Much of our research focuses on the properties of defects, broadly defined. Defects in oxides include dopants (a deliberate defect), cation mismatch resulting from departures from ideal stoichiometry, O vacancies, and deviations from perfect abruptness at interfaces due to cation mixing. Detecting and quantifying defects can be extraordinarily difficult. Yet, being cognizant of their presence, and understanding how these defects affect the properties of oxides, is essential to gaining an understanding based in reality. Sometimes defects have exceptionally beneficial effects, as illustrated by section IIA.

## II. Recent Progress

### A. *The power of a few indiffused atoms at epitaxial Cr/SrTiO<sub>3</sub> heterojunctions*

By combining XPS, UPS, STEM/EELS and theory, we have elucidated the detailed characteristics of an exceptionally low-resistance electrical contact to *n*-SrTiO<sub>3</sub>.<sup>1</sup> Most metals create Schottky barriers when deposited on SrTiO<sub>3</sub>. While some Ohmic contacts are known, but they typically involved reactive mixtures of metals that strongly alloy with the SrTiO<sub>3</sub>, and are not amenable to ultra-small (nanometer scale) dimensions. Our detailed investigation shows that the equivalent of 1 - 2 monolayers of Cr diffuse into the SrTiO<sub>3</sub>, occupy interstitial sites, and anchor the remainder of the film to the oxide, resulting in much stronger adhesion than occurs with totally inert metals, such as Au. The in-diffused Cr atoms also transfer electrons to Ti<sup>4+</sup> ions in the top few atomic planes, effectively preventing formation of the Schottky barrier that would otherwise be present if this diffusion and charge transfer had not occurred. The indiffused Cr converts the surface of the SrTiO<sub>3</sub> into a metal. The resulting junction is thus effectively a metal/metal, rather than a metal/semiconductor interface. But, unlike other metal/oxide interfaces with low contact resistance, this junction is structurally and compositionally well-defined and nearly atomically abrupt, making it more suitable for nanoscale device applications.

### B. The effect of Sr doping on the electronic and optical properties of epitaxial LaCrO<sub>3</sub>

Earlier this year, we published a combined experimental and theoretical study of the optical properties of pure LaCrO<sub>3</sub>.<sup>2</sup> This investigation addressed a decades-old debate on the value of the charge transfer (CT) band gap in this material, which ranged from 0.6 eV to 4.5 eV, depending on the theoretical method used. Previous experimental work on bulk polycrystalline material placed the CT gap at ~3.4 eV. Our investigation went considerably beyond what had been done earlier by: (i) carryout measurements on highly pure MBE-grown films, and, (ii) calculating the absorption spectrum from first principles. This combination allowed us to make accurate assignments of the various absorption bands, from which we determined that the CT gap is between 4.75 eV and 4.95 eV, depending on the strain state.

Our broader scientific goal is to see if the band gap of LaCrO<sub>3</sub> can be red-shifted to lower energies by Sr doping on the A site for the purpose of enhancing the visible light harvesting capacity of LaCrO<sub>3</sub>. Indeed, the optical gap is red shifted, and the temperature dependence of the resistivity reveals a transition from insulator at  $x = 0$  to either a metallic state, or a hopping conductive state, as  $x$  increases. However, which transition occurs, and the Sr concentration at which it occurs, depends on the choice of substrate, which determines the strain state of the film. Our data reveal that metallicity, when it occurs, is the result of a change from Cr<sup>3+</sup> ( $3d_{t_2g}^3$ ) to Cr<sup>4+</sup> ( $3d_{t_2g}^2$ ) as Sr<sup>2+</sup> substitutes for La<sup>3+</sup>. However, hopping conductivity occurs as a result of O vacancy ( $V_O$ ) formation.  $V_O$ , which is typically a donor in perovskites, forms as arrays of (111)-oriented planar defects in SrCrO<sub>3</sub> on LaAlO<sub>3</sub>(001).  $V_O$  formation appears to result from two distinct causes: (i) the instability of Cr<sup>4+</sup> ( $3d_{t_2g}^2$ ) in octahedral coordination, and, (ii) lattice strain, which depends on  $x$  and the choice of substrate. The effect of localized  $V_O$  formation on the electronic properties is that the film consists of patches of insulating SrCrO<sub>3- $\delta$</sub>  in which donor electrons from  $V_O$  compensate holes associated with Cr<sup>4+</sup> ( $3d_{t_2g}^2$ ) formation, interspersed with patches of conductive SrCrO<sub>3</sub>. This material structure gives rise to hopping conductivity. Interestingly, when SrCrO<sub>3</sub> on LaAlO<sub>3</sub>(001) is annealed in air at 250°C in a tube furnace, the O vacancies are largely eliminated, and the film becomes metallic as the Cr<sup>3+</sup> ( $3d_{t_2g}^3$ ) is converted back to Cr<sup>4+</sup> ( $3d_{t_2g}^2$ ). Thus, the functional properties of Sr <sub>$x$</sub> La<sub>1- $x$</sub> CrO<sub>3</sub> are driven by the delicate interplay of growth conditions, choice of substrate, and inherent cation stabilities in different coordination environments.

### C. Incommensurate magnetic arrangements drive the structural parameters and modify electronic structure in $\alpha$ -(Cr <sub>$x$</sub> Fe<sub>1- $x$</sub> )<sub>2</sub>O<sub>3</sub>, thereby activating new low-energy photoconductivity channels.

We recently showed that random alloys of Fe and Cr on the cation site in corundum-like epitaxial films of  $\alpha$ -M<sub>2</sub>O<sub>3</sub> leads to a lower band gap than is exhibited by either end member (2.1 eV for  $\alpha$ -Fe<sub>2</sub>O<sub>3</sub> and 3.3 eV for  $\alpha$ -Cr<sub>2</sub>O<sub>3</sub>).<sup>3</sup> Absorption measurements show that the optical gap bows downward significantly with increasing  $x$ , reaching a minimum of 1.8 eV near  $x = 0.5$ . While this result sounds promising for enhanced visible light harvesting in the alloy, it is only useful if optical excitation leads to itinerant carriers. If these new low-energy excitations are caused by *localized*  $d \rightarrow d$  transitions, there is no photocurrent available to do useful light-driven work. However, we have demonstrated using spectral photoconductivity that the threshold for conductivity drops from  $h\nu = 2.1$  eV at  $x = 0$  to  $h\nu = 1.6$  eV at  $x = 0.4$ . Moreover, we were able to make detailed assignments of the various absorption bands by calculating the excited states using time-dependent density functional theory. This analysis reveals that the new- low-energy

excitations that occur in the alloy result from transitions from an occupied band that is strongly Cr  $t_{2g}$  derived to unoccupied bands dominated by Fe  $t_{2g}^*$  and  $e_g^*$  character. The extent of hybridization with O in these bands is sufficiently high that the excited states consist of itinerant carriers, leading to measurable photocurrent.

The overall structure of these  $a$ -( $\text{Cr}_x\text{Fe}_{1-x}$ ) $_2\text{O}_3$  films is driven by several factors, including: (i) the similar ionic radii and identical formal charge of  $\text{Cr}^{3+}$  and  $\text{Fe}^{3+}$ , (ii) the short-range magnetic interactions between  $\text{Cr}^{3+}$  and  $\text{Fe}^{3+}$  in the alloys, (iii) epitaxial strain, and (iv) point defect formation. The similar ionic radii of  $\text{Cr}^{3+}$  and  $\text{Fe}^{3+}$  results in uniform mixing, as is evidenced by STEM images and EELS maps. The magnetic ordering structure has a large effect on the unstrained lattice parameters of ( $\text{Cr}_x\text{Fe}_{1-x}$ ) $_2\text{O}_3$ , which exhibit strong deviations from a linear Vegard's law-like dependence on composition. Although  $\text{Fe}_2\text{O}_3$  and  $\text{Cr}_2\text{O}_3$  are both antiferromagnetic (AFM) in the bulk, the details of their AFM ordering differ. The ( $\text{Cr}_x\text{Fe}_{1-x}$ ) $_2\text{O}_3$  alloys are expected to adopt intermediate spin structures, and DFT calculations confirm that variations in spin structure are primarily responsible for the lattice parameter deviation. Deposition of epitaxial thin films of ( $\text{Fe}_{1-x}\text{Cr}_x$ ) $_2\text{O}_3$  on  $a$ - $\text{Al}_2\text{O}_3$  substrates introduces epitaxial strain and the possibility of point defects, both of which likely impact the band gap of the material. For example, the optical gap for epitaxial thin film  $\text{Cr}_2\text{O}_3$ , which is partially compressively strained to the  $\text{Al}_2\text{O}_3$  substrate, is measured to be 3.07 eV, which is considerably lower than the bulk value. In contrast, the measured optical gap for epitaxial  $\text{Fe}_2\text{O}_3$ , which is fully relaxed, is 2.10 eV, which matches the bulk value. The Cr-rich ( $\text{Fe}_{1-x}\text{Cr}_x$ ) $_2\text{O}_3$  alloy thin films are also partially strained to the substrate, which likely lowers their band gap relative to the unstrained value. In contrast, intermediate-composition alloy films ( $0.3 < x < 0.8$ ) exhibit a lattice expansion, which can be attributed to a slight oxygen over-stoichiometry at these compositions. Further tuning the strain state and point defect formation in ( $\text{Fe,Cr}$ ) $_2\text{O}_3$  epitaxial films, for example by varying the substrate or employing buffer layers, is a promising avenue to optimize the bandgap for efficient solar energy harvesting.

#### *D. Relationship between structure and electronic properties at the $\text{LaCrO}_3/\text{SrTiO}_3(001)$ interface.*

For several years now, the topic of electrical conductivity at the interface of polar and nonpolar perovskites has been vigorously investigated,  $\text{LaAlO}_3/\text{SrTiO}_3(001)$  being the most heavily studied system. Yet, the physical origin of the conductive state remains highly controversial. Some argue that an electronic reconstruction which eliminates the diverging electrostatic potential is the best explanation. Others argue that the conductivity is defect driven. Still others believe that defect-mediated electronic reconstruction is correct. In order to branch expand the knowledge base related to this topic, we have investigated the MBE-grown  $\text{LaCrO}_3/\text{SrTiO}_3(001)$  heterojunction. Even though by all rights, this heterojunction ought to be conductive based on the electronic reconstruction model, it is utterly insulating.<sup>4</sup> In order to probe this mystery, we have carried out a detailed investigation of the interface structure using STEM/EELS, EDS and RBS.<sup>5</sup> The interface is not atomically abrupt. The  $A$ -site cations are found to diffuse across the interface to a greater extent than the  $B$ -site cations, based on high angle annular dark field scanning transmission electron microscopy (HAADF-STEM), energy dispersive x-ray spectroscopy (EDS) and electron energy loss spectroscopy (EELS). The  $B$ -site cation valences are shown to be partially reduced near the interface by analysis of EELS near-edge structures. The location and direction of these electronic modifications do not intuitively

compensate the charge imbalance imposed by uneven cation inter-diffusion. These results highlight the importance of considering both the physical and electronic structure of such complex interfaces in determining their characteristics. Furthermore, the extent of inter-diffusion is shown to increase with increasing LCO film thickness, suggesting a potential mechanism behind the critical thickness for interfacial conductivity in  $\text{LaAlO}_3/\text{SrTiO}_3(001)$  based on the percolation of a continuous layer of electrically active defects on the  $\text{SrTiO}_3$  side of the interface.

### III. Future Plans

Over the next three years, we will continue work on the fundamental properties of doped perovskites and corundums. We will complete our investigation of Sr-doped  $\text{LaCrO}_3$  and start work on Sr-doped  $\text{LaFeO}_3$ . We will also initiate research on N doping of the O lattice in  $(\text{Fe,Cr})_2\text{O}_3$  and  $\text{SrTiO}_3$  as a means of engineering the optical properties. Additionally, we will explore double perovskites of the form  $REMM'O_3$ , such as  $\text{LaCrFeO}_3$  and  $\text{LaMnNiO}_3$ . Here, the structure along the (111) direction is  $(-REO_3-M-REO_3-M')$ .  $\text{LaCrFeO}_3$  and  $\text{LaMnNiO}_3$  have been made as both thin films and bulk polycrystals, and are claimed to exhibit interesting magnetic and optical properties. There are, however, significant discrepancies in the reported properties of these materials. In all these studies, our primary goal remains to establish defensible causal relationships between structure/composition and functional properties.

- 
1. S. A. Chambers, M. Gu, P. V. Sushko, H. Yang, C. Wang and N. D. Browning, *Adv. Mater.* **25**, 4001 (2013).
  2. P. V. Sushko, L. Qiao, M. E. Bowden, G. E. Exarhos, F. K. Urban III, D. Barton and S. A. Chambers, *Phys. Rev. Lett.* **110**, 077401 (2013).
  3. S. E. Chamberlin, Y. Wang, K. Lopata, T. C. Kaspar, A. W. Kohn, D. R. Gamelin, R. Bovind, P. V. Sushko and S. A. Chambers, *J. Phys.: Condens. Matter* **25**, 392002 (2013).
  4. S. A. Chambers, L. Qiao, T. C. Droubay, T. C. Kaspar, B. Arey and P. V. Sushko, *Phys. Rev. Lett.* **107**, 206802 (2011).
  5. R. Colby, L. Qiao, V. Shutthanandan, J. Ciston, H. K. L. Zhang, B. Kabius and S. A. Chambers, *Phys. Rev. B*, in press (2013).

### IV. Sponsored Publications in FY2012 – FY2013

1. S.A. Chambers, L. Qiao, T.C. Droubay, T.C. Kaspar, B. Arey, P.V. Sushko “Band Alignment, Built-in Potential, and the Absence of Conductivity at the  $\text{LaCrO}_3/\text{SrTiO}_3(001)$  Heterojunction”, *Physical Review Letters* **107**, 206802 (2011).
2. Bo Zhao, T.C. Kaspar, T.C. Droubay, J. McCloy, M.E. Bowden, V. Shutthanandan, S.M. Heald, S.A. Chambers, “Electrical Transport Properties of Ti-doped  $\text{Fe}_2\text{O}_3$  (0001) Epitaxial Films”, *Physical Review B* **84**, 245325 (2011).
3. S.A. Chambers, T.C. Droubay, C. Capan, G.Y. Sun, “Unintentional F doping of the Surface of  $\text{SrTiO}_3(001)$  Etched in HF acid – Structure and Electronic Properties”, *Surface Science* **606**, 554 (2012).

4. C. Capan, G.Y. Su, M. Bowden, S.A. Chambers, “Epitaxial Cr on  $n$ -SrTiO<sub>3</sub>(001) – An Ideal Ohmic Contact”, *Applied Physics Letters* **100**, 052106 (2012).
5. T.C. Kaspar, A. Ney, A.N. Mangham, S.M. Heald, Y. Joly, V. Ney, F. Wilhelm, A. Rogaley, F. Yakou, S.A. Chambers, “X-ray “Structure of Epitaxial (Fe,N) co-doped Rutile TiO<sub>2</sub> Thin Films by X-ray Absorption”, *Physical Review B* **86**, 035322 (2012).
6. Y. Du, D. Kim, T. C. Kaspar, S. E. Chamberlin, I. Lyubinetzky, S. A. Chambers, “*In-situ* Imaging of the Growth of Epitaxial Anatase TiO<sub>2</sub>(001) Films on SrTiO<sub>3</sub>(001)”, *Surface Science* **606**, 1443 (2012).
7. D.C. Look, T.C. Droubay, S.A. Chambers, “Stable Highly Conductive ZnO via Reduction of Zn Vacancies”, *Applied Physics Letters* **101**, 102101 (2012).
8. Peter V. Sushko, Liang Qiao, Mark Bowden, Tamas Varga, Gregory J. Exarhos, Scott. A. Chambers, “Multiband Optical Absorption Controlled by Lattice Strain in Thin-film LaCrO<sub>3</sub>”, *Physical Review Letters* **110**, 077401 (2013).
9. L. Qiao, H.L. Zhang, M.E. Bowden, V. Shutthanandan, R. Colby, Y. Du, B. Kabius, P.V. Sushko, S.A. Chambers, “The Impacts of Cation Stoichiometry and Substrate Surface Quality on Nucleation, Structure, Defect Formation and Intermixing in Complex Oxide Heteroepitaxy – LaCrO<sub>3</sub> on SrTiO<sub>3</sub>(001)”, *Advanced Functional Materials* **23**, 2953 (2013).
10. Scott A. Chambers, Meng Gu, Peter V. Sushko, Hao Yang, Chongmin Wang, Nigel D. Browning, “Ultra-low Contact Resistance at an Epitaxial Metal/Oxide Heterojunction Through Interstitial Site Doping”, *Advanced Materials* **25**, 4001 (2013).
11. L. Qiao, H. Y. Xiao, S. M. Heald, M.E. Bowden, T. Varga, G. J. Exarhos, M. D. Biegalski, I. Ivanov, Y. Zhang, W.J. Weber, T.C. Droubay, S.A. Chambers, “The Impact of Crystal Symmetry on the Electronic Structure and Functional Properties of Complex Lanthanum Chromium Oxides”, *Journal of Materials Chemistry C* **1**, 4527 (2013).
12. Tiffany C. Kaspar, Sara E. Chamberlin, Scott A. Chambers, “Surface Structure of  $\alpha$ -Cr<sub>2</sub>O<sub>3</sub>(0001) After Activated Oxygen Exposure”, *Surface Science.*, in press (2013).
13. R. Colby, L. Qiao, V. Shutthanandan, J. Ciston, K.H.L. Zhang, B. Kabius, S.A. Chambers, “Cation Intermixing and Electronic Compensation at the Insulating LaCrO<sub>3</sub>/SrTiO<sub>3</sub>(001) Interface”, *Physical Review B*, in press (2013).

## **In-situ Monitoring of Dynamic Phenomena during Solidification**

**A.J. Clarke, S.D. Imhoff, and P.J. Gibbs**  
**Materials Science and Technology Division,**  
**Los Alamos National Laboratory, Los Alamos, NM 87545**

### **Program Scope**

Solidification is experienced by all metals and provides the first opportunity to influence microstructural development and eliminate defects that may result in failure. By advancing our fundamental understanding of solidification, the development of innovative processing to produce as-cast materials with improved quality is possible, without the need for energy intensive down-stream wrought processing. Traditional inquiry into a metal's microstructure and defects is destructive and occurs after processing under the assumption that the final condition suitably represents an instantaneous condition at an earlier time. Real-time imaging using ultra-brilliant third generation synchrotron and high-energy proton sources now affords direct interrogations of dynamic events during metal melting and solidification from the microscopic to the macroscopic length scale.

We use synchrotron x-ray and proton imaging to observe the role of processing conditions on structure and defect development in metals. Real-time imaging provides important dynamic feedback, which permits us to effectively manipulate relevant sample conditions during melting and solidification. Our imaging experiments are performed using 800 MeV proton radiography (pRad) at Los Alamos National Laboratory's Los Alamos Neutron Science Center [1] and the Sector 32-Insertion Device beamline at Argonne National Laboratory's Advanced Photon Source (APS) [2]. Importantly, protons permit imaging of large volumes of metal ( $> 10,000 \text{ mm}^3$ ) and thick sections (e.g. 6 mm), typically at lower spatial resolution ( $\sim 65 \text{ }\mu\text{m}$  features), whereas x-rays permit the examination of small volumes of metal ( $\ll 1 \text{ mm}^3$ ) and thin sections (e.g. 200  $\mu\text{m}$ ), typically at higher spatial resolution ( $\sim 2 \text{ }\mu\text{m}$  features). Together, these two complementary techniques let us probe over four orders of magnitude in sample volume, allowing for investigations of long range and local solidification phenomena.

### **Recent Progress**

Solidification processing is controlled by large-scale parameters, such as alloy chemistry and the imposed cooling rate and thermal gradient, but the morphology of the solid-liquid interface is simultaneously sensitive to events across multiple length scales. At low solidification velocities, the interface between the liquid and solid phases is planar; however, changing the processing conditions will destabilize the interface, resulting in the development of cellular or tree-like dendritic structures. Figure 1a schematically shows the dependence of imposed thermal gradient ( $G$ ) and solidification velocity ( $V$ ) on solid-liquid interface stability. Destabilization of the planar interface is due to the pileup of solute atoms at the solid-liquid interface, which directly affects local chemistry and morphology and microstructure development and potentially leads to property variations within a casting. The effective prediction of solid-liquid interface stability in metals is thus essential for creating innovative processing and materials by design. Our recent work has focused on direct observations and the control of solid-liquid interface stability in metals during melting and solidification.

Real-time imaging provides a unique opportunity to create process maps for metals, such as that shown in Figure 1a. By varying the imposed solidification conditions, we observe a range of

solid-liquid interface morphologies. Figure 1b highlights three example images collected during real-time x-ray imaging of a 200  $\mu\text{m}$  thick Al-0.6at.%Cu alloy foil at APS. Solidifying the sample in a constant thermal gradient of 85 K/cm with a solidification velocity of 5  $\mu\text{m/s}$  results in a planar solidification front (red symbols, Figure 1). Decreasing the thermal gradient to 65 K/cm, while maintaining the same cooling rate and interface velocity, results in a cellular interface (green symbols, Figure 1), while increasing the interface velocity to 50  $\mu\text{m/s}$  destabilizes the solid-liquid interface to result in dendritic growth (blue symbols, Figure 1). These dynamic processing studies enable the selection of models for interface stability to improve our understanding of solidification microstructure and solute development.

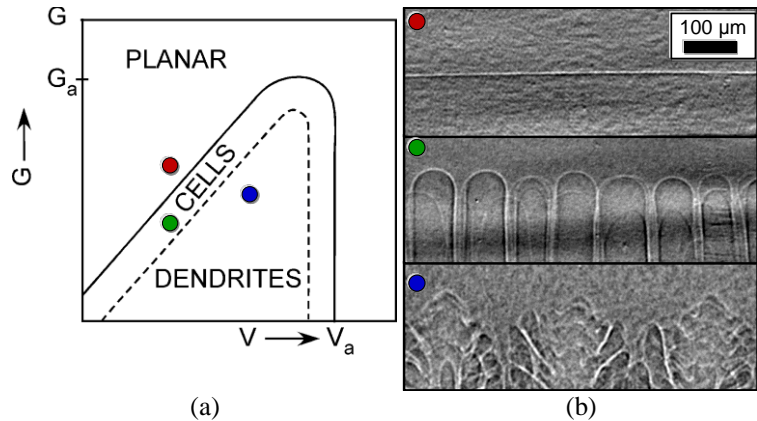


**Figure 1.** a) Processing map for solidification showing solid-liquid interface morphology for a given thermal gradient ( $G$ ) and solidification velocity ( $V$ ) and b) x-ray images of directional solidification in an Al-0.6at.%Cu alloy showing a planar (red symbols), cellular (green symbols), or dendrite (blue symbols) solid-liquid interface for the processing conditions indicated in (a).

We have also explored the use of x-rays to image thin sections of high density metals. Figure 2 shows an example x-ray image obtained during directional solidification of a Sn-27at.%Bi alloy, where the Sn-rich dendrites (the light tree-like structures) are growing into the melt. As these dendrites grow, Bi solute is rejected into the liquid, forming the dark contrast adjacent to the advancing dendrites. Since the Bi-rich liquid is denser than the average liquid density, it begins to flow downward. The thermosolutal and buoyant convection affects the dendritic growth rate and probability of tertiary branching of specific dendrites (e.g. the branches on the right side of the large dendrite in Figure 2 are clearly stunted compared to their counterparts on the left side). These data provide direct evidence toward understanding the role of local transformation conditions and solute on solid-liquid interface stability and morphology evolution.

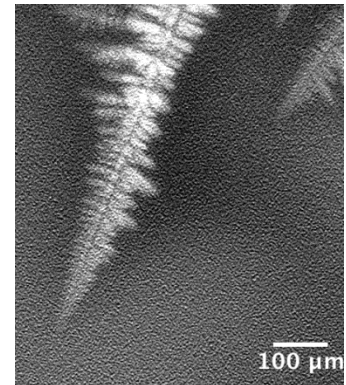
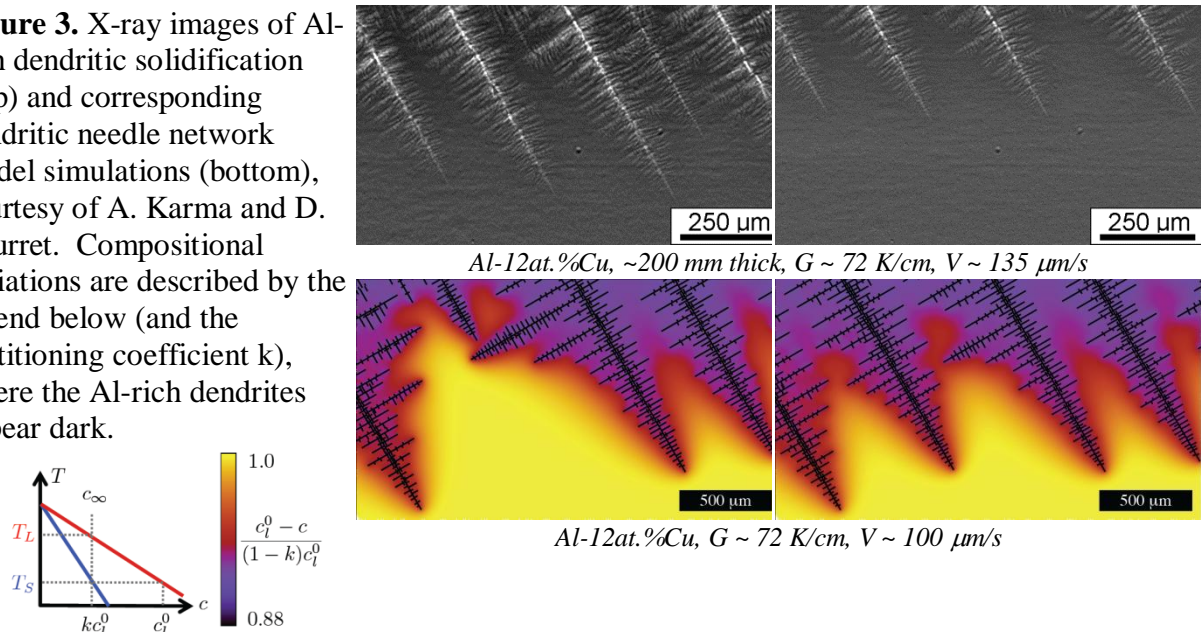


**Figure 2.** X-ray image of Sn-rich dendrites (light) and Bi-rich solute (dark) in the melt during directional solidification of a Sn-27at.%Bi alloy.

Similar results to those shown in Figures 1 and 2 were provided to Professor Alain Karma and Dr. Damien Tournet at Northeastern University to assist in their development and benchmarking of quantitative models for morphology and solute development during processing. Dendritic needle network (DNN) model simulations [3] have been performed for a set of x-ray images obtained from an Al-12at.%Cu alloy during directional solidification. Example x-ray images and early DNN simulation results are shown in Figure 3 for similar processing conditions. The experimental and simulated results both depict early-stage competitive growth (left images) and the eventual development of a stable, Al-rich dendritic array (right images).

**Figure 3.** X-ray images of Al-rich dendritic solidification (top) and corresponding dendritic needle network model simulations (bottom), courtesy of A. Karma and D. Tourret. Compositional variations are described by the legend below (and the partitioning coefficient  $k$ ), where the Al-rich dendrites appear dark.



In addition to the assessment of solid-liquid interface stability in thin sections during directional solidification, we have also studied liquid-liquid phase separation during melting and solidification. Figure 4 shows example complementary proton and synchrotron x-ray images of solidification in an Al-10at.%In alloy [1]. During melting, proton imaging captures the initial macroscopic length scale sedimentation of the denser, In-rich liquid. The dark streaks observed in the proton image during solidification in Figure 4 correspond to the monotectic colony boundaries that contain a higher volume fraction of indium. Complementary x-ray imaging of the same alloy highlights the early meso- and microscopic influence of gravity and thermo-capillarity on fluid flow and In-rich droplet evolution. These real-time observations have permitted subsequent quantification of the formation, coarsening, and complex collective motion of the In-rich liquid droplets within the majority Al-rich liquid at elevated temperatures. An example x-ray image of the In-rich liquid droplets in the melt as the solidification interface sweeps across the field-of-view is also shown in Figure 4. During solidification, the In-rich liquid droplets initially display a coarsening behavior typical of second phase growth. Eventually, the larger particles suddenly change trajectory and accumulate at the advancing solid-liquid interface. These In-rich droplets are then pushed along that interface, or are engulfed in the solidifying Al matrix to create In-rich channels. Understanding the complex motion and coarsening of the In-rich liquid droplets in the melt at smaller length scales may provide a methodology to control how the solidification structure and solute segregation develop,

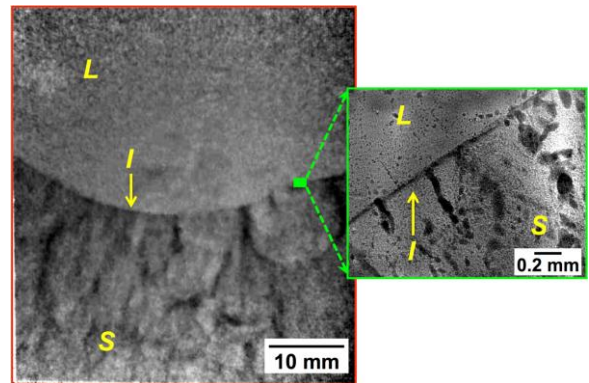


**Figure 4.** Complementary proton (left) and x-ray (right) images of structure evolution in an Al-10at.%In alloy during directional solidification (L, I, and S are liquid, interface, and solid, respectively) that qualitatively highlight the different volumes probed by these two techniques. Note that the proton and x-ray images are from two different samples.

allowing for improved casting quality.

### **Future Plans**

We have highlighted selected results from our recent real-time imaging of metal melting and solidification work, which relates processing changes to micro-, meso-, and macroscopic length scale development. These data provide unique insight into microstructural and defect evolution during solidification, which will allow for advancements in solidification theory. We will continue to use x-ray and proton imaging, coupled with modeling, to understand, predict and control structure and defect development in metals during processing. Experiments at pRad at LANL are scheduled in October 2013, and complementary APS experiments are scheduled in November 2013. We have primarily examined the influence of local conditions on structural development in thin sections and low density metals. However, pRad is a unique tool for extending our experimental understanding of solidification to high density materials and thick sections. Thus, upcoming pRad experiments will focus on solid-liquid interface stability and the role of solute convection in large volumes and high density metals during melting and solidification, whereas our upcoming APS experiments will extend our observations of transient phenomena on structural development in small volumes. In particular, we will use multi-rate solidification to probe grain boundary stability and microscopic solid-liquid interface stability, which is fundamentally relevant to hot-tearing and casting technology. Additionally, we will experimentally observe cyclic crystal growth and dissolution in metals during melting and solidification toward improved understanding of anisotropic growth rates on interface stability.

Although the two dimensional DNN simulations are promising for predicting solidification microstructure development at length scales relevant for casting (e.g. Figure 3), we will continue to provide Professor Alain Karma and Dr. Damien Tournet at Northeastern University real-time imaging results toward the extension of their modeling to three dimensions for improved representation of solidification structure evolution. We will also provide real-time images of grain boundary grooving during directional solidification and hot-tearing in dilute aluminum-copper alloys to theoretically and experimentally understand how hot-tears develop during solidification.

### **References**

- [1] A. Clarke, S. Imhoff, P. Gibbs, J. Cooley, C. Morris, F. Merrill, B. Hollander, F. Mariam, T. Ott, M. Barker, T. Tucker, W.-K. Lee, K. Fezzaa, A. Deriy, B. Patterson, K. Clarke, J. Montalvo, R. Field, D. Thoma, J. Smith, and D. Teter, "Proton radiography peers into metal solidification," *Scientific Reports*, vol. 3, no. 2020, pp. 1–6, 2013, DOI:10.1038/srep02020, <http://www.nature.com/srep/2013/130619/srep02020/full/srep02020.html>
- [2] A.J. Clarke, S.D. Imhoff, J.C. Cooley, B.M. Patterson, W.-K. Lee, K. Fezzaa, A. Deriy, T.J. Tucker, M.R. Katz, P.J. Gibbs, K.D. Clarke, R.D. Field, D.J. Thoma, and D.F. Teter, "X-ray imaging of Al-7at.% Cu during melting and solidification," *Emerging Materials Research*, vol. 2, no. EMR2, pp. 90–98, 2013
- [3] D. Tournet and A. Karma, "Multiscale dendritic needle network model of alloy solidification," *Acta Materialia*, vol. 61, no. 17, pp. 6474–6491, 2013

### **DoE BES Sponsored Publications**

See references [1] and [2] above.

## Solid Electrolytes to Stabilize High-Voltage Battery Interfaces

Juchuan Li, Yoongu Kim, Chengdu Liang, and Nancy J. Dudney

[dudneynj@ornl.gov](mailto:dudneynj@ornl.gov) and [liangcn@ornl.gov](mailto:liangcn@ornl.gov)

Oak Ridge National Laboratory, Oak Ridge, TN 37831

### Program Scope

Practical electrical energy storage for portable and vehicle application require a maximum energy density achieved with high capacity electrode materials coupled to operate at the maximum cell potential. High voltage batteries challenge the phase and electrochemical stability of both the electrode and the electrolyte materials, particularly at the interface. Four and 5V batteries exceed the electrochemical stability window of conventional liquid electrolytes. Fabrication of batteries with solid electrolytes is one route to promote stability at high voltage. In some batteries with liquid electrolytes, stability is achieved when the electrolyte decomposition products form a passivating solid electrolyte interphase (SEI) at one or both electrode/electrolyte interfaces.<sup>1</sup> A more direct approach is to apply a synthetic or artificial SEI as a thin coating at the electrode interface.

The study of how solid electrolytes and SEI coatings affect the stability of battery electrodes is the purpose of this program. A wide variety of mechanisms have been discussed in the literature, but superficial experimental observations fail to provide clear insight into exactly what material properties and processing will lead to the most effective and robust solid electrolyte/electrode interface while maintaining good Li ion transport. Understanding the complex and multiple degradation paths initiated at interfaces will identify how to optimize the composition and processing of the electrolyte coating to best inhibit the aging and decomposition processes. Our approach is to fabricate model materials and electrode structures to extract fundamental understanding.

### Recent Progress

Lipon as an artificial SEI on thin film  $\text{LiNi}_{0.5}\text{Mn}_{1.5}\text{O}_4$  electrodes: Thin-film electrodes are used as a model system to investigate the effect of the artificial SEI composed of lithium phosphorous oxynitride (Lipon). As a model system, the thin-film electrodes have well defined geometry for the interfaces and diffusion lengths, and are free of binders and conducting carbon additives, which could complicate the study. Further, the thickness of the Lipon solid electrolyte coating on a thin film cathode can be varied over a wide range without altering the electronic connection to the current collector. The spinel  $\text{LiNi}_{0.5}\text{Mn}_{1.5}\text{O}_4$  (LMNO) cathode is being investigated due to the reversible lithium exchange at a narrow 4.7V redox potential versus lithium metal.

For LMNO films cycled with a standard organic carbonate electrolyte, we find a conflicting view between the deliverable capacity, which appears stable, and the coulombic efficiency which indicates side reactions. As shown in Fig. 1a, a 2  $\mu\text{m}$

LiNi<sub>0.5</sub>Mn<sub>1.5</sub>O<sub>4</sub> film delivers stable reversible capacity under a rate of 1C for 100 cycles, and the capacity retention is about 99.98(9)%. However, the coulombic efficiency, defined as the ratio between discharge capacity and charge capacity, is below than 98%. The difference between high capacity retention and low coulombic efficiency is caused by charge consumed in oxidation of the electrolyte at high voltage (~2% to 4%), and also that consumed by corrosion of cell hardware (~0.2%).

Building an artificial SEI film on high voltage cathodes is a solution to prevent decomposition of the conventional electrolyte with a limited voltage window. Here, we use Lipon as an example of artificial SEI, which conducts lithium ions and blocks electrons. The ionic conductivity of Lipon is about  $10^{-6}$  S cm<sup>-1</sup> and it has a wide range of stable potential window (0 V to 5.5 V vs. Li/Li<sup>+</sup>). The thickness of Lipon varied from 1 nm to 200 nm and is precisely controlled by deposition conditions. The amount of active materials is reduced to 400 nm thick in order to enlarge the relative signals of irreversible capacity. As seen in Fig. 1b, all samples deliver relatively stable capacity, indicating that Lipon is compatible with LiNi<sub>0.5</sub>Mn<sub>1.5</sub>O<sub>4</sub>. The coulombic efficiency of bare LiNi<sub>0.5</sub>Mn<sub>1.5</sub>O<sub>4</sub> of 400 nm thick is only about 90%, significantly lower compared to that of 2 μm thick films, indicating that we successfully enlarge the signals of unwanted reactions by reducing the amount of the active materials. It is remarkable that with only 1 nm Lipon coating, the coulombic efficiency is increased significantly to about 95%. This indicates that only a very thin film is needed to inhibit electronic conduction, or perhaps to coat reactive sites at the surface. Further increasing Lipon thickness leads to a gradual increase in efficiency, which stabilizes at about 97–98% for the 200 nm of Lipon coating. For batteries with commercial-scale loading, we estimate that the coulombic efficiency should be 99.99% or better for 200 nm Lipon coated LiNi<sub>0.5</sub>Mn<sub>1.5</sub>O<sub>4</sub> spinel.

Optimizing performance of the system requires tuning of the thickness of the artificial SEI: a sufficient thickness is required to provide electrochemical protection during cycling, but the addition of interfaces and a thicker film may increase polarization.

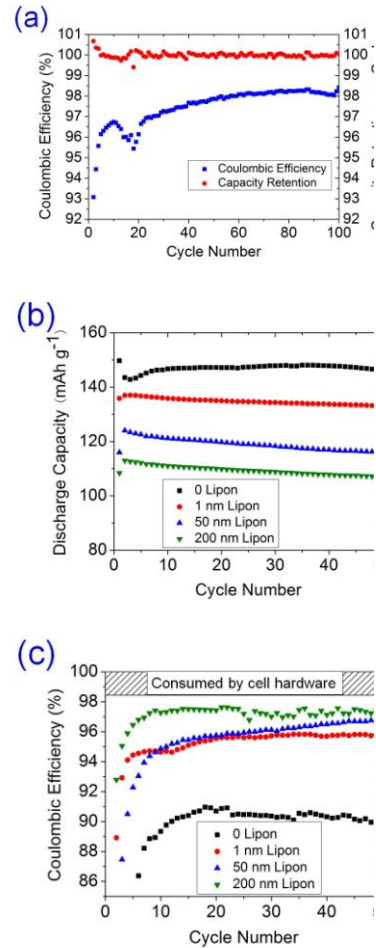


**Figure 1.** (a) Coulombic efficiency and capacity retention of 2 μm LiNi<sub>0.5</sub>Mn<sub>1.5</sub>O<sub>4</sub>. (b) Discharge capacity and (c) coulombic efficiency of Lipon coated 400 nm LiNi<sub>0.5</sub>Mn<sub>1.5</sub>O<sub>4</sub>.

The additional resistance brought by Lipon is quantified using the difference between the oxidation and corresponding reduction peaks. Resistive coatings reduce the energy density and rate performance; in this case the optimum thickness of Lipon artificial SEI should be between 1 and 50 nm.

To our knowledge, this is the first example where the thickness of a synthetic SEI coating has been varied systematically. This work will be presented in the context of our range of studies including: new results for a solid state battery, a variety of spinel, layered and Li-excess cathode powders with ultra-thin Lipon coating, and other thin film cathodes. This begins to provide a perspective from which the mechanisms for stabilization of cathode materials with solid electrolytes and SEI coatings can be understood.

#### **Future Plans:**

The Lipon coating on  $\text{LiMn}_{1.5}\text{Ni}_{0.5}\text{O}_4$  significantly depresses the electrolyte oxidation at high voltage and promotes the cycling performance of cathode materials. These results show that a pre-formed SEI with known structure and ionic conductivity is superior to the spontaneously formed SEI. We will seek to deepen the understanding of the function of solid electrolyte coatings. Key questions are the following: (a) Is there any additional SEI formed on top of the Lipon coating? (b) Can electrons transport through the ultra-thin artificial SEI? (c) What is the potential distribution within a system with artificial SEI? (d) Do other solid electrolyte coatings on the cathode function in a manner similar to the Lipon coating? With a thorough characterization of the electrochemical and chemical aspects of the solid electrolyte coating, we expect to derive a fundamental understanding of the solid electrolyte/cathode interface with which to guide the research of advanced materials for electrical energy storage.

#### **References:**

1. M. Winter, The Solid Electrolyte Interphase - The Most Important and the Least Understood Solid Electrolyte in Rechargeable Li Batteries. *Zeitschrift Fur Physikalische Chemie-International Journal of Research in Physical Chemistry & Chemical Physics*, 223(10-11): 1395-1406. (2009).

#### **DoE Sponsored Publications in the Last Two Years**

1. Juchuan Li, Loïc Baggetto, Surendra K. Martha, Gabriel M. Veith, Jagjit Nanda, Chengdu Liang, Nancy J. Dudney "Artificial SEI Enables the Use of  $\text{LiNi}_{0.5}\text{Mn}_{1.5}\text{O}_4$  5 V Cathode with Conventional Electrolytes," *Advanced Energy Materials* 2013 <http://dx.doi.org/10.1002/aenm.201300378> (online)
2. Yoongu Kim, Nancy J. Dudney, Miaofang Chi, Surendra K. Martha, Jagjit Nanda, Gabriel M. Veith, and Chengdu Liang "A perspective on coatings to stabilize high-voltage cathodes:  $\text{LiMn}_{1.5}\text{Ni}_{0.5}\text{O}_4$  with sub-nanometer Lipon cycled with  $\text{LiPF}_6$  electrolyte" *Journal of the Electrochemical Society*, 2013, 160, A3113-A3125.

- Zhan Lin, Zengcai Liu, Wujun Fu, Nancy J. Dudney, and Chengdu Liang, "Lithium Polysulfidophosphates: A Family of Lithium-Conducting Sulfur-Rich Compounds for Lithium-Sulfur Batteries," *Angewandte Chemie-International Edition* 2013, 52, 7460-7463.
- Zengcai Liu, Wujun Fu, E. Andrew Payzant, Xiang Yu, Zili Wu, Nancy J. Dudney, Jim Kiggans, Kunlun Hong, Adam J. Rondinone, and Chengdu Liang; "Anomalous high ionic conductivity of nanoporous  $\beta$ -Li<sub>3</sub>PS<sub>4</sub>," *Journal of the American Chemical Society*, 2013, 135, 975-978.
- Zhan Lin, Zengcai Liu, Wujun Fu, Nancy Dudney, and Chengdu Liang; "Phosphorous Pentasulfide as a Novel Additive for High-Performance Lithium-Sulfur Batteries," *Advanced Functional Materials*, 2013, 23, 1064-1069 (journal cover)
- Zhan Lin, Zengcai Liu, Nancy Dudney, and Chengdu Liang; "A Lithium Superionic Sulfide Cathode for All-Solid Lithium-Sulfur Batteries," *ACS Nano*, 2013 7, 2829-2833
- Xunli Wang, Ke An, Lu Cai, Zhili Feng, Steve E. Nagler, Claus Daniel, Kevin J. Rhodes, Alexandru D. Stoica, Harley D. Skorpenske, Chengdu Liang, Wei Zhang, Joon Kim, Yue Qi, and Stephen J. Harris; "Visualizing the Chemistry and Structure Dynamics in Lithium-Ion Batteries by In-situ Neutron Diffraction," *Scientific Reports*, 2012, 2, 747.
- Lu Cai, Zengcai Liu, Ke An, Chengdu Liang, "Unraveling Structural Evolution of LiNi<sub>0.5</sub>Mn<sub>1.5</sub>O<sub>4</sub> by In-situ Neutron Diffraction", *Journal of Materials Chemistry A* 2013, 1, 6908-6914.
- Lu Cai, Ke An, Zhili Feng, Chengdu Liang, Stephen J. Harris "In-Situ Observation of Inhomogeneous Degradation in Large Format Li-Ion Cells by Neutron Diffraction," *Journal of Power Sources*, 2013, 236, 163-168.
- Lu Cai, Zengcai Liu, Ke An, and Chengdu Liang; "Probing Li-Ni Cation Disorder in Li<sub>1-x</sub>Ni<sub>1+x-y</sub>Al<sub>y</sub>O<sub>2</sub> Cathode Materials by Neutron Diffraction," *Journal of The Electrochemical Society*, 2012, 159 (7) A1-A5.
- Yi-Chun Lu, Ethan J. Crumlin, Gabriel M. Veith, Jonathon R. Harding, Eva Mutoro, Loïc Baggetto, Nancy J. Dudney, Zhi Liu, and Yang Shao-Horn; "In Situ Ambient Pressure X-ray Photoelectron Spectroscopy Studies of Lithium-Oxygen Redox Reactions," *Nature Scientific Reports*, 2012, 2, 715.

## Growth Mechanisms and Controlled Synthesis of Nanomaterials (ERKCS81): Synthesis of Nanostructures from Nanoparticle Building Blocks

David B. Geohegan,<sup>1</sup> Masoud Mahjouri-Samani,<sup>1</sup> Mengkun Tian,<sup>3</sup> Christopher M. Rouleau,<sup>1</sup>  
Alex Puzetky,<sup>1</sup> Gyula Eres,<sup>2</sup> Mina Yoon,<sup>2</sup> Miaofang Chi,<sup>2</sup> and Gerd Duscher<sup>2,3</sup>

<sup>1</sup>Center for Nanophase Materials Sciences and <sup>2</sup>Materials Science and Technology Division,  
Oak Ridge National Laboratory, Oak Ridge, TN 37831 and  
the <sup>3</sup>Dept. of Materials Science and Engineering, Univ. of Tennessee, Knoxville, 37996

### Program Scope

The overarching goal of the research program is to understand the link between the growth mechanisms and the resulting structure of nanoscale materials. The emphasis is on the development of real-time methods to induce and probe chemical and physical transformations away from thermodynamic equilibrium in order to controllably synthesize nanomaterials with enhanced properties resulting from metastable structures. The approach relies on correlating the real-time diagnostic measurements with predictive theoretical methods and post-growth characterization by imaging, spectroscopy, and atomic-resolution analytical electron microscopy to develop a framework for the deterministic synthesis of nanomaterials with desired properties. A distinguishing feature of the program is the development and application of time-resolved, in situ diagnostics of nanomaterial growth kinetics and a corresponding development of models to understand the underlying kinetic and chemical pathways. Spatial confinement and reactive quenching approaches are developed to explore the synthesis mechanisms of rationally-designed nanostructures with enhanced intrinsic properties, targeting: (1) oxide, carbon, and alloy nanomaterials produced in metastable states by catalyst-free or catalyst-mediated processes, and (2) doped, decorated, and filled nanomaterial hybrids designed to induce permanent electric fields or distribute charge within nanostructures. Theoretical methods are used to understand fundamental mechanisms of synthesis in order to guide the formation of nanostructures tailored to enhance energy storage, catalysis, thermal management, and photovoltaics in support of DOE's energy mission.

### Recent Progress

Here recent work to understand the role of carbon and metal oxide ultrasmall nanosheet and nanoparticle building blocks in the growth of larger nanostructures and thin films is described. During CVD of SWNTs and graphene (see accompanying abstract), characteristic features of autocatalytic kinetics imply that metastable intermediates play key roles as "building blocks" in the synthesis of carbon nanostructures. Here we investigate similar processes that occur in laser vaporization synthesis of carbon and metal oxide nanostructures and thin films by isolating ultrasmall nanoparticle (UNP) building blocks and studying their structural evolution into larger nanostructures and thin films. Understanding how such nanoparticulate and nanosheet building blocks are incorporated into nanostructures and thin films

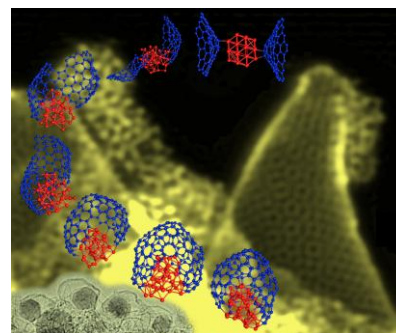


**Figure 1.** The process by which curved nanocones of carbon become encapsulated to form a new hybrid "nanooyster" material (inset) is shown through snapshots of QM/MD simulations. Background is an aberration-corrected, atomic resolution, Z-STEM image of single wall carbon nanohorns and unconverted graphene flakes, which served as the feedstock in the process.<sup>1</sup>

provides new approaches for nanostructure and thin film synthesis and processing using condensed phase feedstock.

### ***Condensed phase growth of nanoysters from Fe-decorated single wall carbon nanohorns***

In the growth of graphene flakes and single-wall carbon nanohorns (SWNHs) by laser vaporization without any metal or substrate, atomic-resolution TEM shows ultrasmall graphene flakes and curved sheets which appear to be involved in the self-assembly process (see Figure 1). Here, these suspected intermediate species were decorated with metals to understand the role of metal catalyst nanoparticles in altering the product distribution. New carbon-metal nanostructures, “nanoysters”, consisting of encapsulated metal nanoparticles inside hollow carbon shells were synthesized by transforming single-wall carbon nanohorns with reactive metals in a rapid, high-temperature annealing process.<sup>1</sup> Hollow single-wall carbon nanohorns were first synthesized in a laser vaporization process from pure carbon, were decorated with metal, and then rapidly heat-treated with a laser to form the nanoysters. State-of-the-art electron microscopy provided atomic-scale characterization of the nanomaterials, revealing (in addition to the SWNHs) single-wall graphene sheets and nanocones which appeared to be “building blocks” in the catalyst-free synthesis of the nanohorns.

To understand how metal nanoparticles could alter the product distribution, Fe nanoparticles were deposited onto the single-wall carbon nanostructures and rapidly laser heated to temperatures of 2000°C. Density functional theory-based calculations showed the mechanism by which metal nanoparticles can assist edge coalescence in the nanooyster shell to form a hollow structure. This demonstration confirms that condensed phase processes can efficiently convert solid carbon into new nanostructures, such as nanoysters, and points the way to the creation of new forms of encapsulated metallic quantum dots within environmentally-compatible carbon shells for novel magnetic, optical, and biological applications. Understanding the way in which metal and carbon

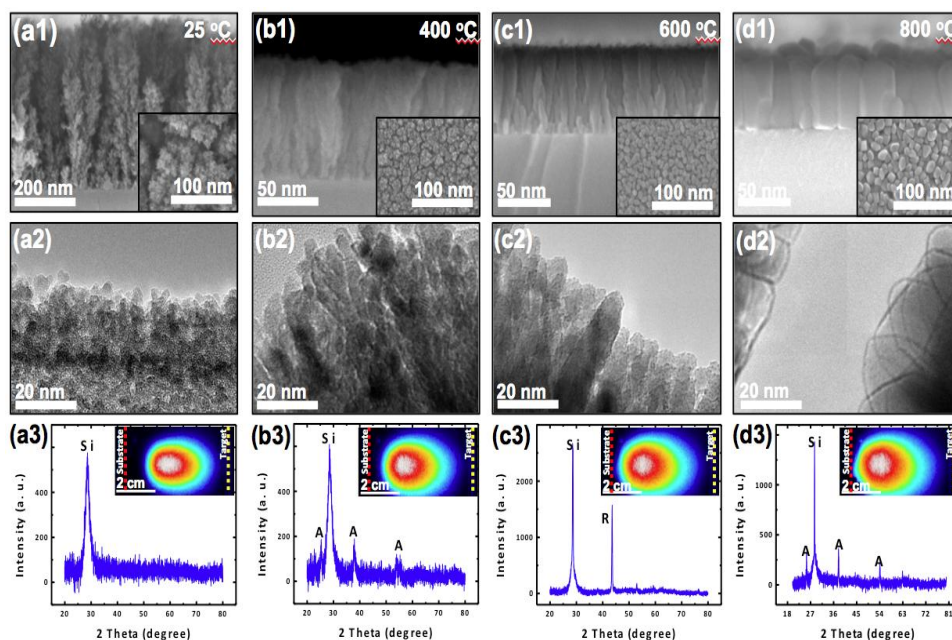


**Fig. 2.** TiO<sub>2</sub> nanostructures assembled from ultrasmall nanoparticles (UNPs) of TiO<sub>2</sub>. The UNPs are formed by laser ablation of TiO<sub>2</sub> in 200 mTorr of O<sub>2</sub> gas en route to deposition at d=5 cm from the target at different growth temperatures of (a) 25°C, (b) 400°C, (c) 600°C, and (d) 800°C. Top row shows SEM cross-sectional images of the deposits (insets are top-views) showing the progression of fractal agglomerates of ultrasmall ‘amorphous’ nanoparticles at room temperature to densified, crystalline (anatase) nanosheet films at 800°C. Second row are corresponding TEM images. Bottom row shows XRD, which indicate the formation of anatase (A) crystallites at 400°C, deposition resulting in crystalline (rutile, R) nanorods at 600°C, and anatase nanosheets at 800°C under very similar plume conditions (insets show plume positions at  $\Delta t = 10 \mu s$  after ablation).

“building blocks” interact to form “nanoysters” required a novel “nano-enabled materials design” approach, wherein theory, synthesis, and characterization were used to unravel the atomistic mechanisms driving the formation of this new type of carbon-metal system.

***Understanding how ultrasmall nanoparticle “building blocks” incorporate into nanorods, nanosheets, and thin films***

It is well known that clusters and nanoparticles are formed by the interaction of pulsed laser ablation plumes with background gases, however their role in the synthesis of thin films and nanostructures has not been made clear. It has been demonstrated that nanoparticles can be used as feedstock to synthesize single-crystal ZnO nanorods by NAPLD (nanoparticle assisted pulsed laser deposition)<sup>2</sup> at few-Torr ambient pressures. However, the processes leading to the self-organization of such nanostructures<sup>3</sup> and their incorporation in thin films grown at lower pressures < 200 mTorr has not been elucidated in PLD. To understand these processes ultrasmall nanoparticle synthesis by laser vaporization was first performed using time-resolved *in situ* diagnostics. Here we concentrate on 3-4 nm diameter TiO<sub>2</sub> UNPs synthesized by laser vaporization of TiO<sub>2</sub> targets into 200 mTorr oxygen ambients and deposited as building blocks for more complex TiO<sub>2</sub> architectures. Detailed electron microscopy and computational characterization of the UNP structure are presented in an accompanying abstract.

Figure 2 summarizes the key findings. Plume imaging and spectroscopy was used to understand the formation times and spatial locations of TiO<sub>2</sub> UNPs at different deposition distances and pressures, and conditions were chosen to optimize the formation and deposition of UNPs (Fig. 2(a)). With increasing substrate temperature, the incorporation of these UNP building blocks into larger nanoparticles, nanorods, and nanosheets was investigated by HRTEM, XRD, and Raman spectroscopy. The data (see caption to Fig. 2) reveals that the UNPs (that have no recognizable phase) transform into larger nanoparticles, nanorods, and nanosheets with anatase or rutile phases depending on the deposition conditions. To understand how the ultrasmall metal oxide building blocks incorporate into larger nanostructures, TiO<sub>2</sub> UNPs were deposited on TEM grids and their morphological and structural evolution was followed during sintering using HRTEM (FEI Titan). These results will be presented. However, although such *in situ* HRTEM measurements reveal interparticle orientational effects on sintering and the kinetics of densification from as-deposited UNP nanostructures, they cannot accurately portray the pulse-by-pulse incorporation that occurs during PLD.

To control and alter the incorporation rate of UNPs into nanostructures, a new approach involving laser sintering was explored, as shown in Fig. 3. In this approach, freshly-deposited UNPs formed in the gas phase by laser vaporization and condensation are incorporated into nanostructures or thin films using energy supplied by a second laser pulse delivered directly to the top surface of the

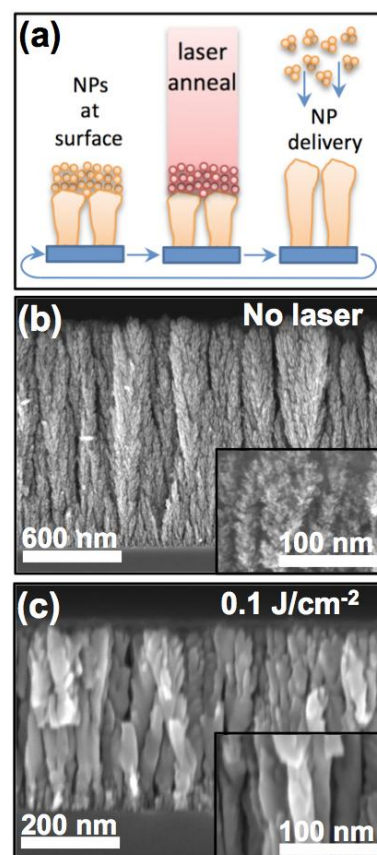


**Figure 3.** (a) Schematic of stepwise incorporation of TiO<sub>2</sub> ultrasmall nanoparticles by laser sintering. Each laser pulse is split, and irradiates nanoparticles that arrived and formed by condensation in the ablation plume on the previous shot (b) unirradiated mesoporous nanoparticle film without laser irradiation (c) Crystalline (anatase) TiO<sub>2</sub> nanosheets formed under identical conditions with laser irradiation.

nanoparticle film. Similar highly-crystalline nanostructures are obtained, and the results will be compared with those of direct nanoparticle-assisted PLD.

## Future Plans

These results indicate that ultrasmall nanoparticle building blocks serve as intermediates in the growth of thin films and nanostructures for both carbon and metal oxide materials, and can be used in new synthesis and processing approaches to form nanostructures and hybrid architectures by nanoparticle-assisted pulsed laser deposition. Pulsed laser vaporization provides a somewhat tunable mixture of atoms, ions, molecules, and clusters with kinetic energies that can both contribute to, or limit, the pulsed laser deposition of thin films and nanostructures. To better control the synthesis and delivery of each component of this flux, a new PLD reactor has been designed and built that incorporates *in situ* imaging and spectroscopic diagnostics and pulsed gas introduction to control the type of species formed by gas collisions (molecules to UNPs) prior to delivery at a substrate located in a separate chamber. This reactor will be used to limit the aggregation of UNPs encountered in typical PLD, and to explore how film properties change as the principal reactants vary from atoms and molecules to nanoparticles. We will explore the synthesis of 2D materials by laser vaporization deposition, exploiting the stoichiometric synthesis of precursor vapors that has been used for many years in PLD, but which is a key limitation in the exploration of new crystalline nanosheets by chemical vapor deposition approaches.

## References

1. K. R. S. Chandrakumar, J.D. Readle, C.M. Rouleau, A.A. Puzetky, D.B. Geohegan, K. More, V. Krishnan, M. Tian, G. Duscher, B. Sumpter, S. Irle, K. Morokuma, *Nanoscale* **5**,1849 (2013).
2. T. Okada, R. Q. Guo, J. Nishimura, M. Matsumoto, and D. Nakamura, *Appl Phys A* **93**, 843 (2008).
3. P. Jensen, *Rev. Mod. Phys.* 71(5), 1695 (1999).

## DoE Sponsored Publications in the Last Two Years

1. K. R. S. Chandrakumar, J.D. Readle, C.M. Rouleau, A.A. Puzetky, D.B. Geohegan, K. More, V. Krishnan, M. Tian, G. Duscher, B. Sumpter, S. Irle, K. Morokuma, "High-temperature transformation of Fe-decorated single-wall carbon nanohorns to nanoysters: a combined experimental and theoretical study", *Nanoscale* **5**,1849 (2013).
2. I.A. Merkulov, M. Yoon, D.B. Geohegan, "How the shape of catalyst nanoparticles determines their crystallographic orientation during carbon nanofiber growth", *Carbon* **60**, 41 (2013).
3. J. Jacimovic, R. Gaal, A. Magrez, L. Forro, M. Regmi, G. Eres, "Electrical property measurements of Cr-N codoped TiO<sub>2</sub> epitaxial thin films grown by pulsed laser deposition", *Appl. Phys. Lett.* **102**, 172108 (2013).
4. A.A. Puzetky, D.B. Geohegan, S. Pannala, C.M. Rouleau, M. Regmi, N. Thonnard, G. Eres, "Real-time Optical Diagnostics of Graphene Growth Induced by Pulsed Chemical Vapor Deposition", *Nanoscale*, **5**, 6507 (2013).
5. S. Dai, B. Guo, X.-G. Sun, P.F. Fulvio, G.M. Veith, R.T. Mayes, S. Brown, J. Adcock, D.B. Geohegan, S.M. Mahurin, A.A. Puzetky, C.M. Rouleau, "Fluorination of "brick and mortar" soft-templated graphitic ordered mesoporous carbons for high power lithium-ion battery", *J. Mater. Chem. A* **1**, 9414 (2013).
6. K. Li, G. Eres, J. Howe, Y.-J. Chuang, X. Li, Z. Gu, L. Zhang, S. Xie, Z. Pan, "Self-Assembly of Graphene on Carbon Nanotube Surfaces", *Scientific Reports* **3**, 2353 (2013).

7. D.B. Geohegan, A.A. Puzetky, M. Yoon, G. Eres, C. Rouleau, K. Xiao, J. Jackson, J. Readle, M. Regmi, N. Thonnard, G. Duscher, M. Chisholm, K. More, "Laser Interactions for the Synthesis and *in situ* Diagnostics of Nanomaterials", Book chapter: in Springer Series in Materials Science (2013).
8. S.-J. Woo, E.-S. Lee, M. Yoon, Y.-H. Kim, "Finite-Temperature Dihydrogen Adsorption/Desorption Thermodynamics Driven by Soft Vibration Modes", *Phys. Rev. Lett.* **111**, 066102 (2013).
9. D.B. Geohegan, I.N Ivanov, A.A. Puzetky, S. Jesse, B. Hu, M. Garrett, B. Zhao, "Transparent conductive nano-composites", US patent 8540542 B2 (2013).
10. A.A. Puzetky, D.B. Geohegan, J. J. Jackson, S. Pannala, G. Eres, C.M. Rouleau, K.L. More, N. Thonnard, J. D. Readle, "Incremental Growth of Short SWNT Arrays by Pulsed Chemical Vapor Deposition", *Small* **8**, 1534 (2012).
11. Y. Liu, C. Brown, D. Neumann, D.B. Geohegan, A.A. Puzetky, C.M. Rouleau, H. Hu, D.J. Styers-Barnett, P.O. Krasnov, B.I. Yakobson, "Metal-Assisted Hydrogen Storage on Pt-Decorated Single-Walled Carbon Nanohorns," *Carbon* **50**, 4953 (2012).
12. K. Lee, K. Berland, M. Yoon, S. Andersson, E. Schroeder, P. Hyldgaard, and B.I. Lundqvist, "Benchmarking van der Waals density functionals with experimental data: potential energy curves for H<sub>2</sub> molecules on Cu(111), (100), and (110) surfaces" *J. of Physics: Condensed Matter* **24**, 424213 (2012).
13. D.B. Geohegan, A.A. Puzetky, C.M. Rouleau, M. Regmi, J.J. Jackson, J. Readle, K. More, G. Eres and G. Duscher, Nonequilibrium Laser Synthesis and Real-Time Diagnostics of Carbon Nanomaterial Growth, *Proceedings of 31st International Congress on Applications of Lasers & Electro-Optics (ICALEO-2012)*.
14. R. Sachan, S. Yadavali, N. Shirato, H. Krishna, V. Ramos, G. Duscher, S. J. Pennycook, A. K. Gangopadhyay, H. Garcia, and R. Kalyanaraman, "Self-Organized Bimetallic Ag-Co Nanoparticles with Tunable Localized Surface Plasmons Showing High Environmental Stability and Sensitivity", *Nanotechnology*, **23**, 275604 (2012).
15. M. Chisholm, G. Duscher, W. Windl, "Oxidation Resistance of Reactive Atoms in Graphene" *Nano Letters*, **12**, 4651 (2012).
16. A. K. Kothari, B. W. Sheldon, G. Eres, "Thickness Limitations in carbon nanotube reinforced silicon nitride coatings synthesized by vapor infiltration", *Acta Materialia*, **60**, 7104 (2012).
17. M. Regmi, M.F. Chisholm, G. Eres, "The Effect of Growth Parameters on the Intrinsic Properties of Large-Area Single Layer Graphene Grown by Chemical Vapor Deposition on Cu", *Carbon* **50**, 134 (2011).
18. D.B. Geohegan, A.A. Puzetky, J.J. Jackson, C. M. Rouleau, G. Eres, K.L. More, "Flux-Dependent Growth Kinetics and Diameter Selectivity in Single-Wall Carbon Nanotube Arrays", *ACS Nano* **10**(5), 8311 (2011).
19. X. Liu, S. Sen, J. Liu, I. Kulaots, D.B. Geohegan, A. Kane, A.A. Puzetky, C.M. Rouleau, K.L. More, G. Tayhas, R. Palmore, R.H. Hurt "Antioxidant Deactivation on Graphenic Nanocarbon Surfaces", *Small* **7**, 2775 (2011).
20. M. Yoon, H. Weitering, Z. Zhang, "First-principles studies of hydrogen interaction with ultrathin Mg and Mg-based alloy films", *Phys. Rev. B* **83**, 045413 (2011).

## Development of Order in Deeply Undercooled Liquid Metals

F. Zhang, Z. Ye, Y. Sun, X. W. Fang, C. Z. Wang, M. J. Kramer, I. McBrearty, M. I. Mendeleev, R. E. Napolitano, R. T. Ott, and K. M. Ho

Division of Materials Science and Engineering, Ames Laboratory USDOE, Ames, IA 50011

### Program Scope

While an overwhelming body of evidence, reported by us and others [1-16], shows that noncrystalline metallic phases (i.e. liquids and glasses) have clear elements of short- and medium-range order, they are not easily defined. From an energetic standpoint, this lack of uniqueness in the description of structural order (and its coupling with chemical order) in noncrystalline metallic phases severely limits our ability to extend the traditional models of Gibbs free energy and associated analyses to understand and predict phase transformations. An accurate description of order parameters for non-crystalline systems would enable predicting the dynamics of phase selection and glass formation in undercooled liquid materials. The thrust of this subtask is a combined experimental and modeling to move beyond traditional descriptions of the short-range order (SRO) and to develop ways of characterizing and quantifying the medium-range order (MRO) that develops from the undercooled liquid and glasses. Some of the key questions which need to be addressed are: (1) What are the prevailing forms of non-crystalline order in liquids and glasses? (2) What is the spatial extent of these more energetically stable interconnected regions within the undercooled liquid? (3) How stable are these features, i.e., do they form and then dissolve over some lifetime? (4) How do these features change in size, temporal stability and chemistry with under cooling? (5) How does the undercooling rate affect these structures? (6) How sensitive are these stable cluster structures to changes in chemistry, including major and minor constituents? and (7) What role do these networks play in nucleation and phase selection during solidification?

### Recent Progress

#### 2.1 Cu-Zr system

The energetic stability of first and second shell packing motifs in noncrystalline structures is central to understanding the short- to medium-range structural order in metallic glasses. We examined the stability of various medium-range structural motifs that represent possible building

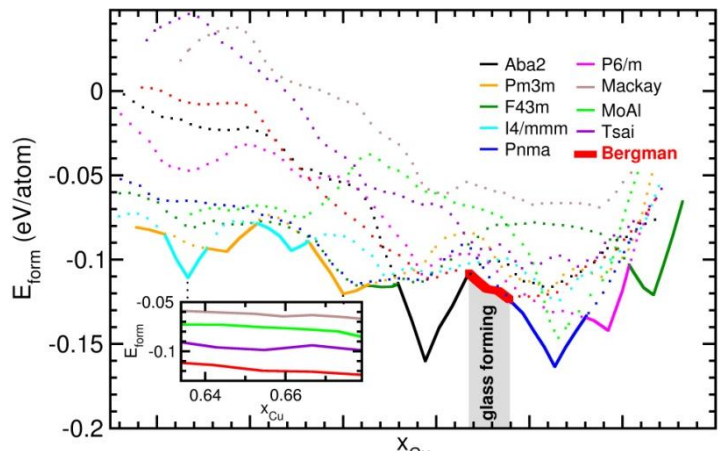


**Figure 1.** Formation energy of the lowest energy structure for each motif, as a function of the Cu compositions. Mackay, MoAl, Tsai, and Bergman are four typical medium-range icosahedral motifs, while other motifs are extracted from known Cu-Zr compounds. The bold red line highlights the composition range where the crystallization-resisting Bergman motif is the most energetically favorable. Inset shows the formation energy of the lowest energy structure with icosahedral motifs in the best glass-forming region:  $0.63 < x_{Cu} < 0.68$ .

blocks for competing glassy and crystalline phases in Cu-Zr system, using a genetic algorithm to efficiently identify the energetically favored decoration of each motif for specific compositions. A Bergman motif with crystallization-resisting icosahedral symmetry is the most energetically favorable motif in the composition range  $0.63 < x_{\text{Cu}} < 0.68$ , which matches the optimal glass-forming range observed experimentally for this binary system (see Fig. 1). The stability of the Bergman motif agrees well with our previous cluster alignment analysis [12].

### 2.2 Al-Sm system

Undercooled Al-Sm liquids represent a typical system driven far from equilibrium and exhibiting a rich behavior of short- to medium-range ordering. For alloys of identical composition (Al-10%Sm), we have found that small differences in the structural order of the glassy materials caused by the different processing conditions lead to vastly different phase selection during thermal annealing. Using ab-initio molecular dynamics (AIMD) simulations, we have examined the atomic packing in the undercooled liquid.

We found that the solute (Sm)-centered clusters display a novel non-icosahedral “3-6-6-1” first-shell motif as shown in the inset Fig.2 (b). The population of this motif grows as the liquid gets more deeply undercooled [see Fig.2 (a)].

Experimentally, Al<sub>9</sub>Sm liquids also exhibit medium-range segregation into nanometer-sized regions with different atomic compositions as shown in the 3D atomic probe of fast-quenched melt-spun material, Fig. 3 (a), where red and white colors represent Sm-rich and depleted regions, respectively. This segregation results in a pre-peak prior to the major peak in the structure factors  $S(q)$  of the undercooled liquid and melt-spun material shown in Fig.3 (b). Our AIMD simulations successfully captured this feature. The calculated  $S(q)$  clearly shows the pre-peak, which compare favorably with that obtained in the experiments. Fig. 3(c) gives a snapshot of the Al<sub>450</sub>Sm<sub>50</sub> liquid at  $T = 1300$  K, where only the Sm atoms (red) and the central Al atoms (blue) of pure first-shell Al clusters are shown. The clustering of Sm-rich and Al-rich regions is evident in Fig. 3(c).

Amorphous Al-Sm alloys also display a complicated crystallization behavior involving multiple unknown meta-stable phases. These unknown phases have been a major obstacle preventing a thorough understanding of the phase selection in liquids and amorphous solids. Using an efficient genetic algorithm for structure determination, we were able to solve *all* the unknown phases that appeared during the crystallization of melt-spun Al<sub>9</sub>Sm samples, including

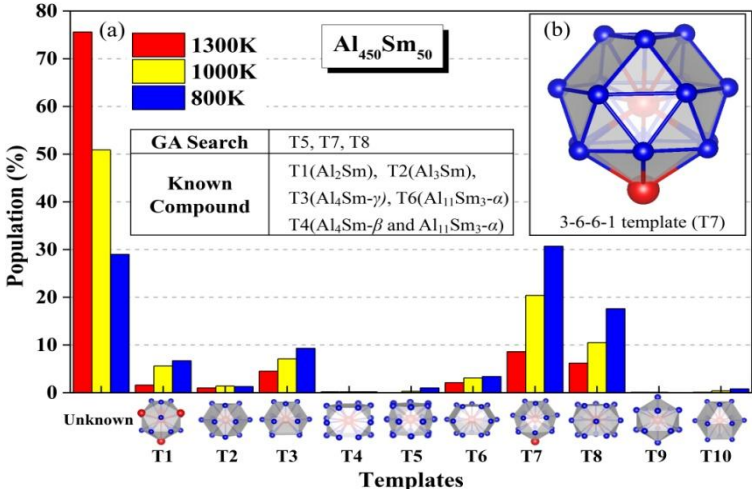


**Figure 2. Population of Sm-centered templates at different temperatures in Al<sub>450</sub>Sm<sub>50</sub> samples. Templates T5, T7 and T8 are identified in genetic-algorithm searches for Al<sub>x</sub>Sm<sub>1-x</sub> compounds with  $x$  close to 0.9 and structure size up to 40 atoms per unit cell. Other templates are extracted from known Al-Sm compounds. The ‘3-6-6-1’ template (T7) has the largest population among all templates.**

a cubic  $A_{60}B_{11}$  phase and a hexagonal  $Al_5Sm$  phase. For the  $A_{60}B_{11}$  phase, A and B refer to two distinct sets of Wyckoff positions, which can be occupied by Al, Sm, or vacancy. The overall Al composition for this phase is close to 0.9. The calculated x-ray diffraction (XRD) patterns match almost perfectly with those of experiments. Interestingly, the cubic  $A_{60}B_{11}$  phase shares the same “3-6-6-1” motif as the undercooled  $Al_9Sm$  liquids. We will show how the bcc unit cell and the “3-6-6-1” motifs pack inside the cubic cell. This topological connection between the undercooled liquid and crystal structures is definitely worth further investigation as a reason why the metastable  $A_{60}B_{11}$  phase appears first in the devitrification of the amorphous melt-spun  $Al_9Sm$  samples but is not observed in devitrification from sputtered thin-film samples.

### Future Plans

Our future work will be focused on the Al-Sm system. We will extend the short range order in undercooled Al-10%Sm liquids, which is characterized as the “3-6-6-1” motif (T7 in Fig.2), to medium-range by studying how these motifs pack in space. While the short-range order can be well-established with AIMD, AIMD in general is not sufficient to study medium-range order due to the spatial and temporal constraints in computationally challenging AIMD. Fortunately, the short-range order, together with other thermodynamic and dynamical information, can be used to calibrate an EAM classical potential. With a well-behaved classical potential, we can perform MD calculations on systems large enough to fully accommodate the medium-range order. We can also study how the medium-range order develops with different cooling processes. With such studies, we intend to identify the pathway from as-quenched amorphous alloy to the cubic metastable phase, and also answer intriguing questions regarding what is the origin of the vastly different devitrification behavior between melt-spun and sputtered samples.

The research proposed above also bridges atomistic and continuum modeling. A proper order parameter extracted from the knowledge about the ordering of the system at the medium-range level will enable us to quantitatively describe the free energy landscapes of disordered systems to enable thermodynamically robust predictions of phase selection and transformation pathway during rapid solidification or devitrification.

### References

1. D. R. Nelson and F. Spaepen, *Solid State Physics*, edited by H. Ehrenreich, F. Seitz and D. Turnbull (academic New York, 1989), Vol **42**, p. 1.
2. Li Huang, C.Z. Wang, S.G. Hao, M.J. Kramer, and K.M. Ho, *Phys. Rev. B* **81**, 014108 (2010).

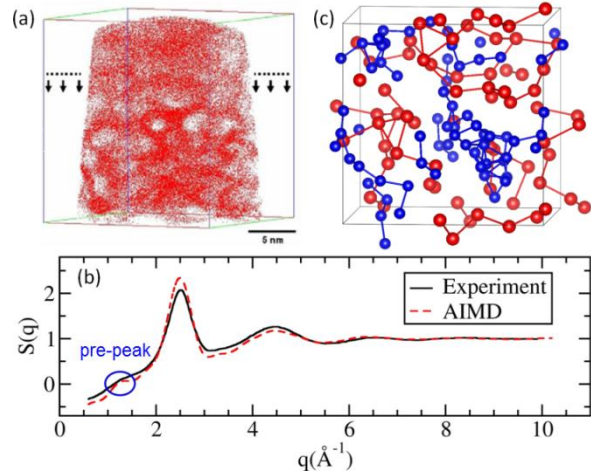


**Figure 3. (a) 3D atom probe of quenched  $Al_9Sm$  alloy. Red and white represent Sm-rich and depleted regions, respectively. (b) Structure factor of  $Al_9Sm$  at  $T = 1273$  K, obtained in both experiments and AIMD simulations. (c) A snapshot collected in AIMD simulations. Only Sm atoms (red) and the central Al atoms (blue) in first-shell Al clusters are shown.**

3. Li Huang, X.W. Fang, C.Z. Wang, M.J. Kramer, Z.J. Ding, and K.M. Ho, Appl. Phys. Lett., 98, 231906 (2011).
4. M. Li, C. Z. Wang, S. G. Hao, M. J. Kramer, and K. M. Ho, Phys. Rev. B, 80, 184201 (2009).
5. H. W. Sheng, W. K. Luo, F. M. Alamgir, J. M. Bai, and E. Ma, Nature 439 419, (2006).
6. Y. Q. Cheng, H. W. Sheng, and E. Ma, Physical Review B 78, 014207 (2008)
7. P. J. Steinhardt, D. R. Nelson, M. Ronchetti, Phys. Rev. B **28**, 784 (1983)
8. J. D. Honeycutt and H. C. Andersen, J. Phys. Chem. **91**, 4950 (1987).
9. J. L. Finney, Nature **266**, 309 (1977); Proc. R. Soc. A **319**, 479 (1970)
10. X. W. Fang, C. Z. Wang, Y. X. Yao, Z. J. Ding, & K. M. Ho, Phys. Rev. B **82**, 184204 (2010)
11. M. I. Mendeleev *et al.* Philos. Mag. **90**, 3795-3815 (2010).
12. X. W. Fang, C. Z. Wang, S. G. Hao, M. J. Kramer, Y. X. Yao, M. I. Mendeleev, Z. J. Ding, R. Napolitano, and K. M. Ho, Nature: Scientific Reports, 1:194 DOI: 10.1038/srep00194 (2011).
13. X. W. Fang, C. Z. Wang, Y. X. Yao, Z. J. Ding, and K. M. Ho, Phys. Rev. B, **83**, 224203 (2011).
14. S. Wu, M. J. Kramer, X. W. Fang, S. Y. Wang, C. Z. Wang, K. M. Ho, Z. J. Ding, and L. Y. Chen, Phys. Rev. B **84**, 134208 (2011).
15. S. Wu, X. W. Fang, S. Y. Wang, C. Z. Wang, Y. X. Yao, K. M. Ho, Z. J. Ding and L. Y. Chen, J. Appl. Phys. **110**, 103518 (2011).
16. X. S. Wu, M. J. Kramer, X. W. Fang, S. Y. Wang, C. Z. Wang, K. M. Ho, Z. J. Ding, and L. Y. Chen, Phys. Rev. B **84**, 134208 (2011).
17. A. Laio and M. Parrinello, PNAS, **99**, 12562 (2002).
18. A. Laio and F. L. Gervasio, Rep. Prog. Phys. **71** 126601 (2008).
19. M. Ji, C. Z. Wang, and K. M. Ho, Phys. Chem. Chem. Phys. **12**, 11617 (2010).

### **Publications resulting from work supported by the DOE project over the last two years.**

- [1] Feng Zhang, Min Ji, Xiao-Wei Fang, Cai-Zhuang Wang, Mikhail I. Mendeleev, M. J. Kramer, Ralph E. Napolitano, Kai-Ming Ho, "Composition-dependent stability of the medium-range order responsible for metallic glass formation: A first-principles study", Phys. Rev. Lett., submitted.
- [2] S. G. Hao, C. Z. Wang, C. Liu, M. I. Mendeleev, M. J. Kramer, R. E. Napolitano, and K. M. Ho, Identification of Order Parameter Describing Liquid-Glass Transition in  $\text{Cu}_{64.5}\text{Zr}_{35.5}$  Alloy", Phys. Rev. B. submitted.
- [3] B. Shen, C. Y. Liu, Y. Jia, G. Q. Yue, F. S. Ke, H. B. Zhao, L. Y. Chen, S. Y. Wang, C. Z. Wang, K.M. Ho, "Molecular dynamics simulation studies of structural and dynamical properties of rapidly quenched Al" J. Non-Crys. Solids. accepted.
- [4] G. Q. Yue, S. Wu, B. Shen, S. Y. Wang, C. Z. Wang, K. M. Ho, M. J. Kramer and L. Y. Chen, "Effects of strontium impurity on the structure and dynamics of  $\text{Al}_{88}\text{Si}_{12}$  liquid", J. Phys. Condensed Matter, **25**, 245102, (2013).
- [5] M. I. Mendeleev, M. J. Kramer, S. G. Hao, K. M. Ho, and C. Z. Wang, "Development of interatomic potentials appropriate for simulation of liquid and glass properties of  $\text{NiZr}_2$  alloy", Phil. Mag. **92**, 4454 (2012).
- [6] S. Wu, X. W. Fang, S. Y. Wang, C. Z. Wang, Y. X. Yao, K. M. Ho, Z.J. Ding, and L. Y. Chen, "Icosahedral short-range order in amorphous  $\text{Cu}_{80}\text{Si}_{20}$  by *ab initio* molecular dynamics simulation study", Intermetallics, **30**, 122 (2012).

## Predicting and Controlling Phase Selection in Highly Driven Systems

M. J. Kramer,<sup>\*#</sup> A. I. Goldman,<sup>\*@</sup> R. E. Napolitano,<sup>\*#</sup> M. I. Mendeleev,<sup>\*</sup> K. M. Ho,<sup>\*@</sup>  
R. T. Ott,<sup>\*</sup> F. Zhang,<sup>\*</sup> Z. Ye,<sup>\*</sup> Y. Sun,<sup>\*</sup> X. Y. Song,<sup>\*%</sup> and C. Z. Wang<sup>\*</sup>

<sup>\*</sup>Division of Materials Science and Engineering Division, Ames Labs DOE

<sup>#</sup>Department of Materials Science and Engineering, Iowa State University

<sup>@</sup>Department of Physics, Iowa State University

<sup>%</sup>Chemistry Department, Iowa State University

### Program Scope

Phase selection for slowly cooled liquids is typically well-described in the framework of equilibrium phase diagrams and the Gibbs' phase rule. For rapid solidification processes (e.g., melt spinning), however, phase selection can deviate from equilibrium(1), and thus, a more comprehensive description of the structure and dynamics of the far-from equilibrium system is required. Since non-equilibrium structures obtained by highly driven phase transformations are becoming increasingly more important for novel materials used in energy critical technologies, it is essential that we develop a detailed understanding of the interconnection between the nanoscale structural/chemical ordering in the undercooled liquid or amorphous solid phases and the resulting phase selection during rapid quenching from the liquid and devitrification from the amorphous phase. Given that the crystalline phases that evolve during these highly driven transformations are often metastable in nature and sometimes not identified experimentally or predicted via simulations, accurate descriptions of their structures and dynamics are quite challenging(2-4). This arises from the fact that many of these metastable phases are simply characterized by a nominal composition and/or a Bravais lattice, but beyond that our understanding of their nascent structural features are absent. To build a comprehensive framework that bridges the interconnection between the structures of the non-equilibrium liquid and amorphous solid of metallic systems with their phase selection during highly driven transformations, we need a combined experimental and computational approach that is rooted in newly developed methodologies for describing far from equilibrium transitions. Specifically, this approach requires:

- (i) considering different non-equilibrium processing routes through non-equilibrium structures with varying degrees of structural/chemical order (e.g., melt spinning vs. physical vapor deposition);
- (ii) developing robust in situ characterization techniques that allow for simultaneous measurement of structural transitions in undercooled liquids and amorphous solids (e.g., combined wide- and small-angle X-ray scattering);
- (iii) formulating appropriate thermodynamic models to quantify the energetic and structural landscapes with suitable "reduced sets" of order parameters that can be quantified through connection to measurable quantities but remain rich enough to characterize the structural-chemical coupling, and;

- (iv) developing a powerful genetic algorithm, which combined with experimental characterization of phase transitions and thermodynamic modeling, will provide the necessary identification of metastable crystalline phases and their relationship with structural features in the undercooled liquid or amorphous solid.

In order to meet such ambitious goals, we have assembled a team with expertise in the critical areas of first-principles investigations of material behavior, classical potentials and molecular dynamics simulations, X-ray scattering and e-beam microanalysis, solution thermodynamics, solid-liquid interfaces, and solidification/transformation dynamics.

### Recent Progress

The goals laid out above are ambitious in nature, but we have applied this multi-tiered approach over the past two years to develop a descriptive framework for complicated non-equilibrium systems. We specifically focused on the Al-RE (RE = Sm or Tb) systems since our previous work has highlighted the complicated crystallization behavior from the undercooled metallic liquid or amorphous solid (1, 5-7). This work along with that of other groups has revealed that the phase selection from highly driven transformations for Al-RE alloys occurs in several steps with competing metastable crystalline phases (8). Unfortunately, many of these phases have not been identified, which significantly limits our ability to understand and control the phase selection in liquids and amorphous solids. In our recent work we have synthesized amorphous solids of Al-RE alloys by both melt spinning and physical vapor deposition (i.e., magnetron sputtering). For alloys of identical composition (Al-10%Sm), we have found that small differences in the structural order of the glassy metal structures caused by the different processing conditions lead to vastly different phase selection during thermal annealing. Fig. 1 shows a comparison of the phase selection processes for the two alloys prepared by the different methods. Two important attributes that should be noted are: (i) the distinctly different non-equilibrium transformations during the initial stages of devitrification; phase separation vs. polymorphic crystallization, and (ii) the unidentified metastable phases that are unique to the processing conditions. Through our combined approach of in situ synchrotron X-ray scattering, advanced electron beam analysis, thermodynamic modeling and ab initio simulations based on a genetic algorithm, we have moved beyond our limited understanding of these complicated

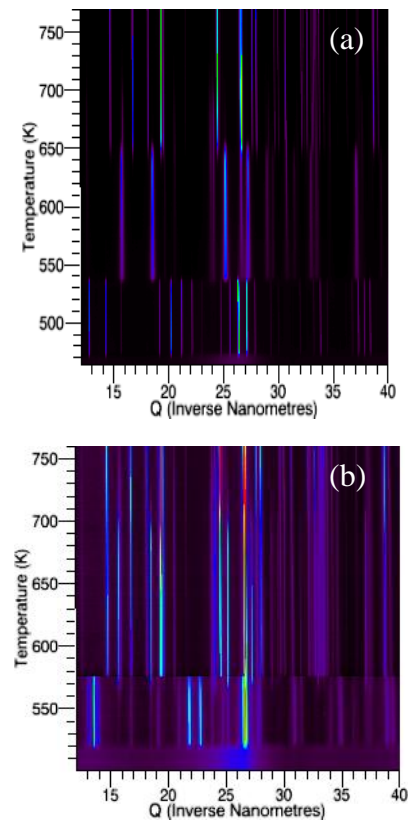


**Figure 1. In situ synchrotron X-ray scattering patterns as a function of temperature showing the different phase selections for amorphous Al-10%Sm alloys prepared by (a) melt spinning of the liquid and (b) magnetron sputtering.**

phase transitions to develop a much more descriptive framework. Performing genetic-algorithm search over a wide range of chemical compositions, we have identified all the well-known equilibrium phases reported in the existing Al-Sm phase diagram. In addition, we also located a number of low-energy metastable phases, which can be stabilized during highly driven transformations in the system (see Fig. 2). By comparing and utilizing experimental X-ray and TEM data, we have identified all observed metastable phases during devitrification of melt-spun amorphous Al-10%Sm alloys. These newly discovered crystal phases will be added into our thermodynamic modeling to obtain a more complete thermodynamic model and eventually, a quantitatively accurate description of how phase selections depend on non-equilibrium processing in this prototypical system. While this methodology has been demonstrated for Al-RE systems, it can be applied to other metallic liquids and amorphous solids to help predicting and controlling phase selection.

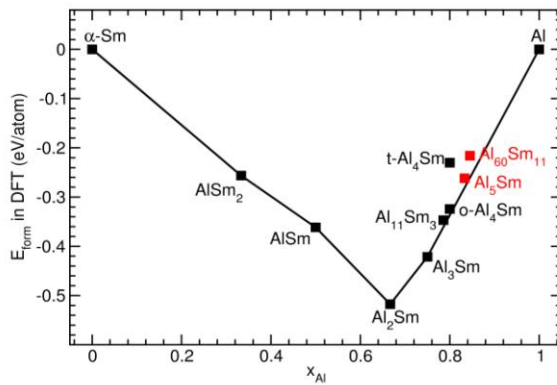


**Figure 2. Formation energy calculated in DFT as a function of the Al composition. Black squares denote the known phases, and red squares denote the two new phases identified with genetic algorithm.**

### Future Plans

Our future research will focus on further developing this methodology to provide critical insight into phase selection in far from equilibrium systems. This work will include identifying the different metastable phases for the Al-RE alloys prepared by magnetron sputtering in order to correlate their dependence on the initial short- and medium-range structural/chemical ordering in the amorphous solid. Understanding this connection is a necessary step in developing predictive models for designing and controlling metastable structures via different processing schemes. Structural and thermodynamic

data from first principles calculations of newly discovered/identified phases will be incorporated into our thermodynamic models to achieve an accurate description of phase selection under highly non-equilibrium processing conditions in the Al-RE system. These data will be also used to develop classical interatomic potentials which then will be utilized in MD simulation of the solid-liquid interface properties in the Al-RE system.

Recent Rietveld analysis of in situ synchrotron data indicates that the newly found  $\text{Al}_{60}\text{Sm}_{11}$  phase with body-centered cubic symmetry contains disordered vacancy or anti-site defects. Typical *ab initio* simulations are performed at  $T = 0$  K, so there is a need to investigate how these defects affect the phase stability at finite temperatures. Beyond this, we know that the crystallization of highly-driven systems is an incredibly complicated process. For example, the devitrification of the Al-Sm sputtered thin film involves two additional unknown meta-stable phases compared with the samples prepared by the melt-spinning technique. Our future work will continue to advance the capabilities of our genetic algorithm approach in order to identify the atomic structures of metastable phases such as those seen in the Al-Sm sputtered films. These model systems will provide an

important basis for understanding complex non-equilibrium transitions. Our experimental efforts will include synthesizing non-equilibrium structures via during processing routes (e.g., melt spinning vs. magnetron sputtering) in order to obtain different degrees of chemical and topological order in the starting amorphous phase. By using advanced characterization techniques such as synchrotron X-ray scattering, electron beam analysis and 3D atom probe tomography, we will better correlate how this order can be incorporated into the genetic algorithm to predict phase selection during devitrification. Through this combined approach we will develop the framework for predicting and controlling phase selection in highly-driven systems.

## References

1. N. Wang, Y. E. Kalay, R. Trivedi, *Acta Materialia* **59**, 6604 (Oct, 2011).
2. Y. Q. Cheng, E. Ma, *Progress in Materials Science* **56**, 379 (May, 2011).
3. Y. Zhang, N. Mattern, J. Eckert, *Journal of Applied Physics* **111**, (Mar, 2012).
4. C. Fan, H. G. Yan, C. T. Liu, H. Q. Li, P. K. Liaw, Y. Ren, T. Egami, *Intermetallics* **23**, 111 (Apr, 2012).
5. Y. E. Kalay, I. Kalay, J. Hwang, P. M. Voyles, M. J. Kramer, *Acta Materialia* **60**, 994 (Feb, 2012).
6. Y. E. Kalay, C. Yeager, L. S. Chumbley, M. J. Kramer, I. E. Anderson, *Journal of Non-Crystalline Solids* **356**, 1416 (Jun, 2010).
7. Y. E. Kalay, L. S. Chumbley, M. J. Kramer, I. E. Anderson, *Intermetallics* **18**, 1676 (Aug, 2010).
8. J. Antonowicz, E. Jezierska, M. Kedzierski, A. R. Yavari, L. Greer, P. Panine, M. Sztucki, *Reviews on Advanced Materials Science* **18**, 454 (Oct, 2008).

## Select publications by this task within our DOE project over the last two years.

- [1] Dahlborg, U., M. J. Kramer, et al. (2013). "Structure of Molten Al and Eutectic Al-Si Alloy Studied by Neutron Diffraction." *Journal of Non-Crystalline Solids* **361**: 63-69.
- [2] Liu, A. C. Y., M. J. Neish, et al. (2013). "Systematic Mapping of Icosahedral Short-Range Order in a Melt-Spun Zr<sub>36</sub>Cu<sub>64</sub> Metallic Glass." *Physical Review Letters* **110**(20): 205505.
- [3] Wu, S., M. J. Kramer, et al. (2012). "Icosahedral short-range order in amorphous Cu<sub>80</sub>Si<sub>20</sub> by *ab initio* molecular dynamics simulation study." *Intermetallics* **30**: 122-126.
- [4] Yue, G. Q., S. Wu, et al. (2013). "Effects of strontium impurity on the structure and dynamics of Al<sub>88</sub>Si<sub>12</sub> liquid." *Journal of Physics-Condensed Matter* **25**(24): 245102.
- [5] Trivedi, R. and N. Wang (2012). "Theory of rod eutectic growth under far-from-equilibrium conditions: Nanoscale spacing and transition to glass." *Acta Materialia* **60**(6-7): 3140-3152.
- [6] Wang, N., Y. E. Kalay, et al. (2011). "Eutectic-to-metallic glass transition in the Al-Sm system." *Acta Materialia* **59**(17): 6604-6619.
- [7] Wang, T. and R. E. Napolitano (2012). "A Phase-Field Model for Phase Transformations in Glass-Forming Alloys." *Metallurgical and Materials Transactions a-Physical Metallurgy and Materials Science* **43A**(8): 2662-2668.

# Tailoring Ionic Conductivity in Solids for High-Energy Batteries

Zengcai Liu, Zhan Lin, Nancy Dudney, and Chengdu Liang\*  
Center for Nanophase Materials Sciences  
Materials Science and Technology Division  
Oak Ridge National Laboratory, Oak Ridge TN, 37831

## Program Scope

From harvesting renewable energies to delivering electricity on various scales for both portable and stationary power sources, greater and more efficient electric energy storage (EES) is in demand.<sup>1</sup> In all EES systems, the movements of electrons and ions are design and controlled to achieve the storage and release of energy at high density, enhanced safety, and high efficiency. To achieve control of charge transfer and ion transport in EES systems, the capability of tailoring the ionic conductivity in solids and interfaces is of paramount importance in the development of new materials for energy storage. This program focuses on the studies of ionic conductivities of solid materials. The goal of the research is to correlate the ionic conductivity of solids to their physical and chemical structures and therefore unravel the underpinning physics for ionic conductivity.

This program encompasses synergistically linked synthesis and characterization approaches: new materials with well-defined structures have been created to derive a deep understanding of the structure/ ionic mobility relationship. Lithium thiophosphates and lithium-sulfur battery systems have been chosen as the model systems for the investigation: The lithium thiophosphates are the most conductive solid electrolytes with respect to lithium ions.<sup>2</sup> The lithium-sulfur batteries promise high-energy density and enhanced safety.<sup>3</sup>

## Recent progress

Nanostructure enhances ionic conductivity:  
Solid electrolytes which conduct lithium ions are promising materials for enabling high-energy battery chemistries and circumventing safety issues of conventional lithium batteries. Achieving the combination of high ionic conductivity and a broad electrochemical window in a solid electrolyte is a grand challenge for the synthesis of battery materials. In recent work, we show an enhancement of room-temperature lithium-ion conductivity of 3 orders of magnitude by creating a nanostructured lithium thiophosphate ( $\text{Li}_3\text{PS}_4$ ). This material has a wide

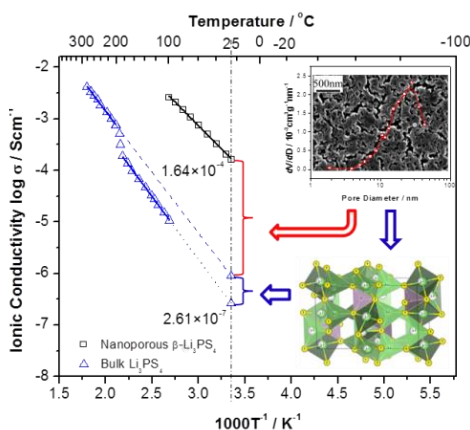


**Figure 1.** Ionic conductivity, SEM, and crystal structure of nanoporous  $\beta\text{-Li}_3\text{PS}_4$

(5 V) electrochemical window and superior chemical stability against lithium metal. The nanoporous structure of  $\text{Li}_3\text{PS}_4$  reconciles two vital effects that enhance ionic conductivity: (1) The reduced dimension to nanometer-sized framework stabilizes the highly conductive beta phase that is formed at elevated temperatures; and (2) The high surface-to-bulk ratio of nanoporous  $\beta\text{-Li}_3\text{PS}_4$  promotes surface conduction. Manipulating the ionic conductivity of solid electrolytes has far-reaching implications for materials design and synthesis in a broad range of applications such as batteries, fuel-cells, sensors, photovoltaic systems, and so forth. **Figure 1** shows the enhanced ionic conductivity of the nanostructured material compared with the bulk material and an SEM image of the nanoporous material.

Core-shell structure imparts high ionic conductivity to  $\text{Li}_2\text{S}$  cathode for Li-S batteries: A core-shell structure of  $\text{Li}_2\text{S}$  nanoparticles with the shell of  $\text{Li}_3\text{PS}_4$  has been developed as a lithium superionic sulfide (LSS) cathode for long-lasting, energy-efficient lithium-sulfur (Li-S) batteries. Given the great potential for improving the energy density of state-of-the-art lithium-ion batteries by a factor of 5, a breakthrough in lithium-sulfur (Li-S) batteries will have a dramatic impact on a broad scope of energy related fields. Conventional Li-S batteries which use liquid electrolytes are intrinsically short-lived with low energy efficiency. These challenges stem from the poor electronic and ionic conductivities of elemental sulfur and its discharge products. Here we show that LSS has an ionic conductivity of  $10^{-7} \text{ S cm}^{-1}$  at  $25^\circ\text{C}$ , which is 6 orders of magnitude higher than that of bulk  $\text{Li}_2\text{S}$  ( $\sim 10^{-13} \text{ S cm}^{-1}$ ). The nanostructure of this core-shell material is crucial for such a dramatic improvement in ionic conductivity. The high lithium-ion conductivity of LSS imparts an excellent cycling performance to all-solid Li-S batteries, which also promises safe cycling of high-energy batteries with metallic lithium anodes. The excellent cyclability demonstrated in **Figure 2** will stimulate great interest for advanced battery materials.

Designed chemical structure conveys ionic conductivity to sulfur-rich compounds: Li-S batteries use the conversion reaction of sulfur and lithium. A well-known long-standing problem of Li-S batteries is the polysulfide shuttle phenomenon. This phenomenon can be eliminated through a solid-state configuration of a battery. Most sulfur compounds are not ionic conductors, therefore cycling the sulfur cathode in the solid state is limited by the poor ionic

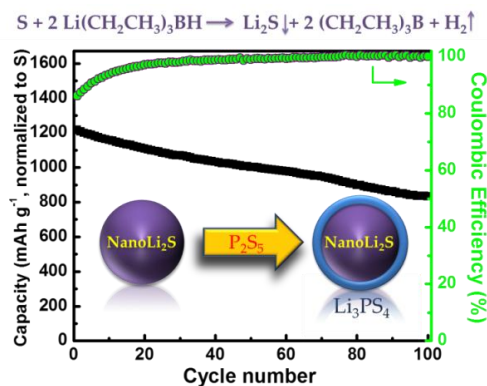


**Figure 2.**  $\text{Li}_2\text{S}@ \text{Li}_3\text{PS}_4$  core shell nanoparticles function as highly reversible cathode materials for Li-S batteries.

conductivity of the cathode materials. Here, we demonstrated that the ionic conductivity of sulfur-rich compounds can be tuned through the sophisticated design of the chemical structure. Lithium polysulfidophosphates (LPSP), a family of sulfur-rich compounds, have been synthesized and characterized as enablers of long-lasting and energy-efficient Li-S batteries. The reaction of  $\text{Li}_3\text{PS}_4$  with  $\text{S}_8$  yields a family of compounds in which the sulfur is attached to the charged terminuses of  $\text{PS}_4^{3-}$ . The resulted compounds have a high intrinsic ionic conductivity. An exemplary LPSP of  $\text{Li}_3\text{PS}_{4+5}$  has an ionic conductivity of  $3.0 \times 10^{-5} \text{ S cm}^{-1}$  at  $25^\circ\text{C}$ , which is 8 orders of magnitude higher than that of  $\text{Li}_2\text{S}$ . The high Li-ion conductivity of an LPSP is the salient characteristic of these compounds that convey the excellent cycling performance to Li-S batteries. In addition, the batteries are configured in an all-solid state that promises the safe cycling of high-energy batteries with metallic lithium anodes. **Figure 3** shows the excellent cyclability of  $\text{Li}_3\text{PS}_{4+5}$  at  $60^\circ\text{C}$ .

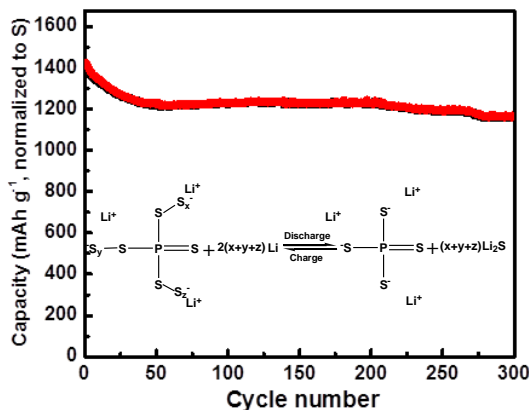


**Figure 3.** Cycling performance and reaction mechanism of  $\text{Li}_3\text{PS}_{4+5}$  at  $60^\circ\text{C}$

### Future direction

This program will focus on the following future directions: (1) the doping effect on the ionic conductivity of sulfide-based solid electrolytes; (2) ion transport at heterogeneous interfaces; and (3) the interplay of ionic and electronic conductivities at the solid state electrode materials.

### References

1. Armand, M.; Tarascon, J. M., Building better batteries. **Nature** 2008, 451 (7179), 652-657.
2. Kamaya, N.; Homma, K.; Yamakawa, Y.; Hirayama, M.; Kanno, R.; Yonemura, M.; Kamiyama, T.; Kato, Y.; Hama, S.; Kawamoto, K.; Mitsui, A., A lithium superionic conductor. **Nat. Mater.** 2011, 10 (9), 682-686.
3. Ji, X. L.; Lee, K. T.; Nazar, L. F., A highly ordered nanostructured carbon-sulphur cathode for lithium-sulphur batteries. **Nat. Mater.** 2009, 8 (6), 500-506.

### DoE Sponsored Publications in the Last Two Years

1. Zhan Lin, Zengcai Liu, Wujun Fu, Nancy J Dudney, and Chengdu Liang, "Lithium Polysulfidophosphates: A Family of Lithium-Conducting Sulfur-Rich Compounds for Lithium-Sulfur Batteries," **Angewandte Chemie-International Edition** 2013, 52, 7460-7463

2. Zengcai Liu, Wujun Fu, E. Andrew Payzant, Xiang Yu, Zili Wu, Nancy J. Dudney, Jim Kiggans, Kunlun Hong, Adam J. Rondinone, and Chengdu Liang; "Anomalous high ionic conductivity of nanoporous  $\beta$ - $\text{Li}_3\text{PS}_4$ ," **Journal of the American Chemical Society**, 2013, 135, 975-978
3. Juchuan Li, Loïc Baggetto, Surendra K. Martha, Gabriel M. Veith, Jagjit Nanda, Chengdu Liang, Nancy J. Dudney "Artificial SEI Enables the Use of  $\text{LiNi}_{0.5}\text{Mn}_{1.5}\text{O}_4$  5 V Cathode with Conventional Electrolytes," **Advanced Energy Materials** 2013 <http://dx.doi.org/10.1002/aenm.201300378> (online)
4. Zhan Lin, Zengcai Liu, Wujun Fu, Nancy Dudney, and Chengdu Liang; "Phosphorous Pentasulfide as a Novel Additive for High-Performance Lithium-Sulfur Batteries," **Advanced Functional Materials**, 2013, 23, 1064-1069 (journal cover)
5. Zhan Lin, Zengcai Liu, Nancy Dudney, and Chengdu Liang; "A Lithium Superionic Sulfide Cathode for All-Solid Lithium-Sulfur Batteries," **ACS Nano**, 2013 7, 2829-2833
6. Xunli Wang, Ke An, Lu Cai, Zhili Feng, Steve E. Nagler, Claus Daniel, Kevin J. Rhodes, Alexandru D. Stoica, Harley D. Skorpenske, Chengdu Liang, Wei Zhang, Joon Kim, Yue Qi, and Stephen J. Harris; "Visualizing the Chemistry and Structure Dynamics in Lithium-Ion Batteries by In-situ Neutron Diffraction," **Nature Scientific Reports**, 2012, 2, 747
7. Lu Cai, Zengcai Liu, Ke An, Chengdu Liang, "Unraveling Structural Evolution of  $\text{LiNi}_{0.5}\text{Mn}_{1.5}\text{O}_4$  by In-situ Neutron Diffraction", **Journal of Materials Chemistry A** 2013, 1, 6908-6914
8. Yoongu Kim, Nancy J. Dudney, Miaofang Chi, Surendra K. Martha, Jagjit Nanda, Gabriel M. Veith, and Chengdu Liang "A perspective on coatings to stabilize high-voltage cathodes:  $\text{LiMn}_{1.5}\text{Ni}_{0.5}\text{O}_4$  with sub-nanometer Lipon cycled with  $\text{LiPF}_6$  electrolyte" **Journal of the Electrochemical Society**, 2013, 160, A3113-A3125.
9. Lu Cai, Ke An, Zhili Feng, Chengdu Liang, Stephen J Harris "In-Situ Observation of Inhomogeneous Degradation in Large Format Li-Ion Cells by Neutron Diffraction," **Journal of Power Sources**, 2013, 236, 163-168.
10. Lu Cai, Zengcai Liu, Ke An, and Chengdu Liang; "Probing Li-Ni Cation Disorder in  $\text{Li}_{1-x}\text{Ni}_{1+x-y}\text{Al}_y\text{O}_2$  Cathode Materials by Neutron Diffraction," **Journal of The Electrochemical Society**, 2012, 159 (7) A1-A5.
11. Yi-Chun Lu, Ethan J. Crumlin, Gabriel M. Veith, Jonathon R. Harding, Eva Mutoro, Loïc Baggetto, Nancy J. Dudney, Zhi Liu, and Yang Shao-Horn; "In Situ Ambient Pressure X-ray Photoelectron Spectroscopy Studies of Lithium-Oxygen Redox Reactions," **Nature Scientific Reports**, 2012, 2, 715.

## Molecularly Organized Nanostructural Materials

Jun Liu, Praveen Thallapally, Yongsoon Shin, Jie Xiao,  
Xiaolin Li, Yuyan Shao, Maria Sushko, Gregory J. Exarhos,  
Pacific Northwest National Laboratory  
Richland, WA 99352

### Program Scope

The overall goal of this project is to investigate a combination of self-assembly and controlled nucleation approaches for synthesizing nanostructured materials with controlled three-dimensional architectures and desired stable crystalline phases of conductive or semiconducting metal oxides suitable for energy applications. Of importance is the understanding of crystallization in self-assembled materials in order to control both resident porosity and pore interconnectivity in these materials because these traits impart certain properties to the material that are underpinning for energy technologies including conversion and storage. The project contains the following components:

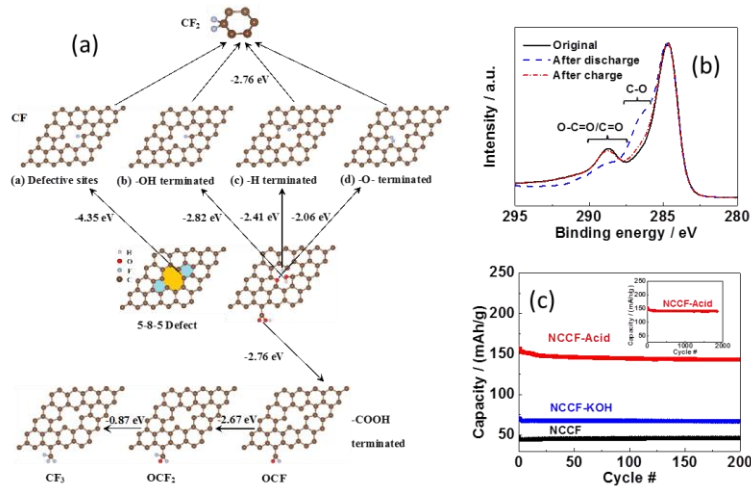
- Manipulation of the kinetics of competing self-assembly and precipitation reactions
- Use of molecular ligands and interfaces to control nucleation and growth
- Multiscale modeling of the self-assembly process in solution
- Structure-property relationships for energy storage applications

### Recent Progress

1. Fundamental understanding of the defect chemistry on the surface the its role on electrochemical properties

Previously we revealed that the defects on carbon surface play a critical role in the nucleation and reactivity of the materials, but the nature of the defects is difficult to characterize and quantify. Functionalized graphene sheets (FGS) comprise of highly reactive defect sites and functional groups that provide an ideal substrate to understand the role of defect chemistry. In particular, we use fluorinated graphene as a model material and prove that the fluorination process on graphene can provide a unique approach to semi-quantitatively probe the defects and functional groups on graphene, given that fluorinated defective sites have different signals that can be accurately captured by Nuclear Magnetic Resonance (NMR). The fluorine content has been modulated to investigate the formation mechanism of different functional groups such as C-F, CF<sub>2</sub>, O-CF<sub>2</sub> and (C=O)F during the fluorination process. The detailed structure and chemical bonds were simulated by density functional theory (DFT) and quantified experimentally by NMR. The results of the DFT and NMR studies show that the lattice vacancies, without oxygen containing groups, provide most of the reactive sites to react with F. FGS also contain COOH, hydroxyl or epoxy groups that contribute to the reaction products with a higher F content.

The understanding and control of the defect on carbon surface provides a powerful approach to develop new electrode materials for energy storage. In the last few years, sodium ion (Na<sup>+</sup>) batteries have attracted increased attention, but their property is hindered by poor intercalation property of Na<sup>+</sup> in electrodes. Since Na<sup>+</sup> intercalation is difficult in most host materials, it is important to consider new storage mechanisms that are not dependent on bulk diffusion and intercalation. We developed a new carbon electrode material by controlling the functional groups on carbon surfaces, explored the surface-driven Na<sup>+</sup> energy storage mechanism based on the reactions between Na<sup>+</sup> and



oxygen functional groups (Nano letters, 2013). The energy storage mechanism is surface-driven reactions between Na<sup>+</sup> and oxygen-containing functional groups on the surface. The surface reaction, rather than a Na<sup>+</sup> bulk intercalation reaction, leads to high rate performance and cycling stability due to the enhanced reaction kinetics and the absence of electrode structure change. The functionalized carbon makes more surface area and surface functional groups available for the Na<sup>+</sup> reaction. It delivers 152 mAh/g capacity at the rate of 0.1 A/g and a capacity retention of 90% for over 1600 cycles.

Figure 1. (a) Simulation of fluorination process on graphene substrate containing different defective sites, along with their individual formation energy of C-F bond at different stages. The experimental and computational study suggests that the divacancy is the most prominent defects on the functionalized graphene surface. (b) Functionalized carbon as a high capacity Na ion storage electrode showing the reversible change of Na ion binding to the carboxylic groups. (c) Highly reversible and stable Na ion storage capacity over long cycles.

## 2. Self-assembly of 3D architectures

We have conducted extensive study on nucleation and self-assembly on two dimensional structures (graphene). Currently we are exploring new approaches to assemble three dimensional architectures from well-controlled nanoscale building blocks. We developed an in situ synthetic strategy for assembling 3D hollow carbon sphere/r-GO (reduced graphene oxide) composite structures, or HCS/r-GO (hollow carbon sphere reduced graphene oxides) (Nanoscale, 2013). The HCS/r-GO composites are prepared via self-assembly of carbon, GO, and spherical alumina-coated silica (ACS) templates, where carbon precursors are polymerized on the alumina catalytic sites of ACS, followed by carbonization at a higher temperature. The GO sheets are folded around the spherical

templates during the catalytic reaction, and the spherical particles can be removed to leave the 3D HCS/rGO composites. We show that a very small amount of r-GO (only 4 wt%) is capable of creating and maintaining the desired hollow pore structure and high surface area in the carbon matrix. Furthermore, by changing the GO content, we can systematically tune the architecture from layered composites to 3D hollow structures to microporous materials. The 3D structures are useful for enhanced transport kinetics in a range of applications. For example, the composites showed a synergistic effect with significantly superior properties than either pure high-surface-area carbon or r-GO. A high specific capacitance of 180 and 154 F g<sup>-1</sup> can be obtained at a current density of 1 and 10 A g<sup>-1</sup>, respectively, with excellent long cycle stability.

### 3. Electrochemical driven reaction at interfaces

This project begins to explore a new direction on how to characterize and understand electrochemical driven nucleation and reactions at liquid-solid interfaces. Preliminary study was conducted at Li-electrolyte interfaces using Li-S chemistry as an example. Numerous studies suggest that continuous contamination of polysulfide species on the Li metal anode is a significant problem, but these reactions are very difficult to control. We developed a new method to provide an artificial surface to control the electrochemical reaction. As such it functions as an artificial reaction surface of Li metal that supplies Li<sup>+</sup> ions on demand while minimizing direct contact between soluble polysulfides and Li metal. Li-S battery incorporating this concept delivers a capacity of more than 800 mAh g<sup>-1</sup> for 400 cycles at a high rate of 1737 mA g<sup>-1</sup>, corresponding to only 11% capacity fade and a Coulombic efficiency above 99%. This simple concept may also provide new lessons for protecting metal anodes in other energy storage devices.

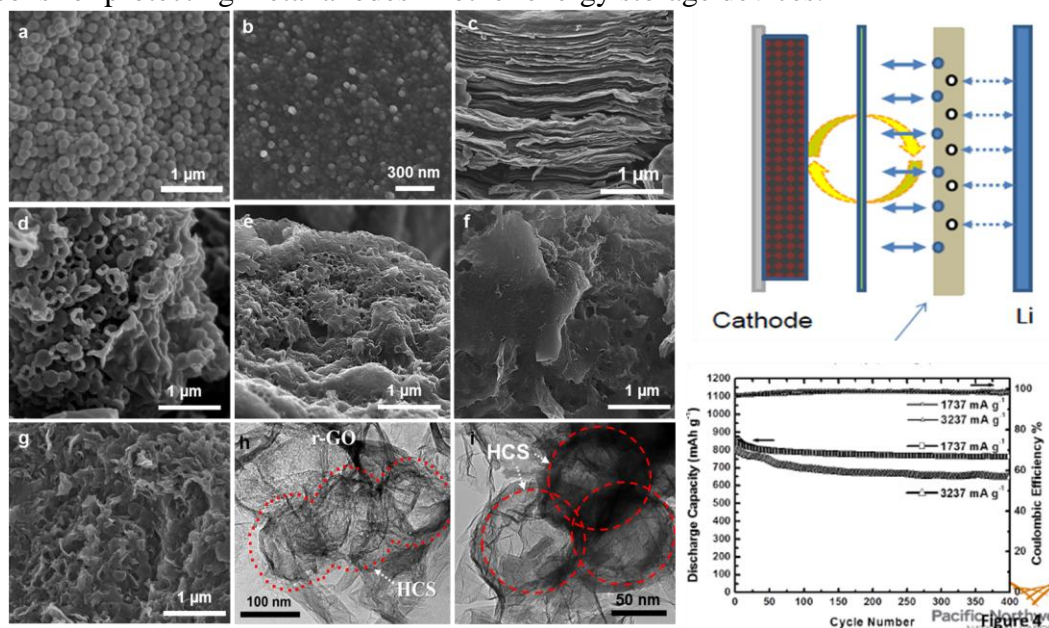


Figure 2. Left panel. Different kind of 3D graphene architectures by self-assembly, from spheres to layers to cages and interconnected architectures. Right panel: Controlling Li-electrolyte interfacial reaction in Li-S chemistry. The top figure shows the artificial

surface on which the reaction takes place. The bottom figure shows the excellent cycling performance of the Li-S battery based on the artificial surface.

### **Future Plans**

The project will follow three important directions: (1) Continuing fundamental study of nucleation and growth of metal and metal oxides on controlled surfaces and nanoscale building blocks, including graphene, carbon nanotubes and other model surfaces; (2) Multiscale nucleation and self-assembly, with control of reaction on both atomic and mesoscale; (3) Electrical field or electrochemical driven nucleation and self-assembly at liquid-solid interfaces.

### **2013 Publications:**

1. "Manipulating the Surface Reactions in Lithium Sulfur Batteries Using Hybrid Anode Structures"  
Cheng Huang, Jie Xiao, Yuyan Shao, Jianming Zheng, Wendy D. Bennett, Dongping Lu, Saraf V. Laxmikant, Mark Engelhard, Liwen Ji, Jiguang Zhang, Xiaolin Li, Gordon L. Graff, Jun Liu, Nature Communication, in revision, 2013.
2. "Molecular Structures of Polymer/Sulfur Composites for Lithium-Sulfur Batteries with Long Cycle Life" Lifen Xiao, Yuliang Cao, Jie Xiao, Birgit Schwenzer, Mark H Engelhard, Laxmikant V. Saraf, Zimin Nie, Gregory J Exarhos, and Jun Liu, J. Materials Chemistry A, in press, 2013.
3. "Opportunities and Challenges of Nanostructured Materials for Rechargeable Energy Storage Devices" Hui Zhan, Jie Xiao, Zimin Nie, Xiaolin Li, Chongmin Wang, Ji-Guang Zhang, Jun Liu, Current Opinions in Chemical Engineering, in press, 2013
4. "Addressing the Grand Challenges in Energy Storage" Jun Liu, ADVANCED FUNCTIONAL MATERIALS, 23, 2013.
5. "Materials Science and Materials Chemistry for Large Scale Electrochemical Energy Storage: From Transportation to Electrical Grid" Jun Liu, Jiguang (Jason) Zhang, Zhengguo Yang, John L. Lemmon, Carl Imhoff, Gordon L. Graff, Liyu Li, Jianzhi Hu; Chongmin Wang, Vish. V. Viswanathan, Suresh Baskaran, Vincent Sprenkle, Xiaolin Li, Yuyan Shao, Birgit Schwenzer, ADVANCED FUNCTIONAL MATERIALS, 23, 929-946, 2013

6. "Making Li-Air Batteries Rechargeable: Material Challenges" Yuyan Shao, Fei Ding, Jie Xiao, Jiguang Zhang, Wu, Xu, Se Park, Jiguang Zhang, Yong Wang, Jun Liu, *ADVANCED FUNCTIONAL MATERIALS*, 23, 987-1004, 2013
7. "Identification of solid-state forms of cucurbit[6]uril for carbon dioxide capture" Jian Tian, Jian Liu, Jun Liu. Praveen K. Thallapally, *CrystEngComm*, 15, 1528-1531, 2013.
8. "Surface-Driven Sodium Ion Energy Storage in Nanocellular Carbon Foams" Yuyan Shao, Jie Xiao, Wei Wang, Mark Engelhard, Xilin Chen, Zimin Nie, Meng Gu, Laxmikant V. Saraf, Gregory Exarhos, Ji-Guang Zhang, Jun Liu, *Nano Letter*, on-line, 2013
9. "Catalytic templating approaches for three-dimensional hollow carbon/graphene oxide nano-architectures" Gun-hee Moon, Yongsoon Shin, Daiwon Choi, Bruce W. Arey, Gregory J. Exarhos, Chongmin Wang, Wonyong Choi, Jun Liu, *Nanoscale*, on-line, 2013.
10. "Non-destructively shattered mesoporous silica for protein drug delivery" Chenghong Lei, Baowei Chen, Xiaolin Li, Wen Qi, Jun Liu, *MICROPOROUS AND MESOPOROUS MATERIALS*, 175, 157-160, 2013.
11. "Nanoscale Phase Separation, Cation Ordering, and Surface Chemistry in Pristine  $\text{Li}_{1.2}\text{Ni}_{0.2}\text{Mn}_{0.6}\text{O}_2$  for Li-Ion Batteries" Meng Gu, Ardra Genc, Ilias Belharouak, Wang, Suntharampillai Thevuthasan, Donald R. Baer, Ji-Guang Zhang, Suntharampillai, Nigel Browning, Jun Liu, Chongmin Wang, *CHEMISTRY OF MATERIALS*, 25, 2319-2326, 2013
12. Formation of the Spinel Phase in the Layered Composite Cathode Used in Li-Ion Batteries, Meng Gu, Ilias Belharouak, Jianming Zheng, Huiming Wu, Xiao, Jie Xiao, Arda Genc, Khalil Amine, Suntharampillai Thevuthasan, Donald R. Baer, Ji-Guang Zhang, Suntharampillai, Nigel Browning, Jun Liu, Chongmin Wang, *ACS NANO*, 7, 760-767, 2013

Novel Materials Preparation and Processing Methodologies  
**Synthesis, Measurement, and Characterization of Functional Materials with Volatile,  
Reactive, and Toxic Constituents to Address Energy Grand Challenge Problems**

Yong Liu, Qingfeng Xing, and Thomas A. Lograsso  
Ames Laboratory, Ames IA 50011

### **Program Scope**

The growth, control and modification of novel materials in single crystal and polycrystalline form is essential for scientific advancement within and across traditional disciplinary boundaries. In support of this mission, the Novel Materials Preparation and Processing Methodologies strengthen the materials synthesis efforts of the Ames Laboratory. The objective of Novel Materials is to quantify and control processing-structure-property relationships: the basic science of how to safely synthesize functional materials containing volatile, reactive, and toxic constituents and how chemical and structural/microstructural features affect properties of novel functional materials; advance the ability to synthesize and characterize high purity, high quality materials, primarily in single crystal form; and develop unique capabilities and processing knowledge in the preparation, purification, and fabrication of metallic elements and alloys. Single crystals are often required to achieve scientific understanding of the origin of various phenomena, whether from intrinsic or extrinsic origins, to elucidate its properties as well as to evaluate a material's full functionality. Our research objectives are: 1) developing synthesis and processing capabilities that support rapid materials discovery using bulk combinatorial approaches, 2) identifying synthesis protocols for specific novel materials through the rapid development and modification of methods to prepare high quality well-characterized single crystals, and 3) elucidating materials phase space and utilizing solidification processing to access metastable states in controlled nanoscale architectures.

### **Recent Progress**

#### **Synthesis of Fe-Based Superconductors**

The important role of understanding synthesis and processing is highlighted by our work on the Fe-based superconductor  $K_xFe_{1.6+y}Se_2$  [A16]. The ability to grow single crystals with reproducible properties is fundamental to the understanding of superconductivity in any material. For  $K_xFe_{1.6+y}Se_2$ , previous work had produced crystals with widely varying properties for a given composition and in the best cases a small superconducting fraction. The commonly accepted

explanation for this phenomenon was that superconductivity was dependent on the degree of Fe vacancy ordering within a single-phase material. We demonstrated that while  $K_xFe_{1.6+y}Se_2$  forms from a homogenous solid solution at the crystal growth temperature, phase segregation into two phases with the same structure, but different compositions, occurs at lower temperature [A16]. While phase segregation on the macroscopic scale had been recognized by previous authors as a problem in obtaining single-phase samples, the fact that there was large temperature dependence to the phase fields and that segregation continued on a microscopic scale into the nominal single-phase region had not been recognized. In materials that are phase segregated on the microscopic scale, the measured superconducting properties are highly dependent on the connectivity of the superconducting phase (Fig. 1). In our work, we determined that the superconducting phase was

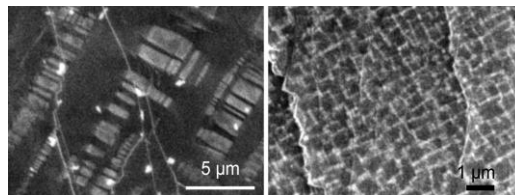


Fig. 1 Back-scattered electron images show differences in the morphology of non-superconductive as-grown single crystal (left) and superconductive crystal quenched from 600 °C (right).

the Fe-rich end member. Furthermore, for flux-grown single crystals, the compositions of the high temperature solid solution which could be accessed, resulted in a phase fraction of the superconducting phase of no more than 10%. We determine that while controlled thermal processing could improve the connectivity and hence the measured superconducting properties of specimen, the volume fraction of superconductor was essentially fixed.

Another Fe-based superconductor where synthesis and processing has been an issue is  $\text{Ba}_{1-x}\text{K}_x\text{Fe}_2\text{As}_2$ , where the size of the single crystal, which could be grown, was limited to several millimeters. This material possess a significant challenge due to the high vapor pressures of K and As at the processing temperature of  $\sim 1130^\circ\text{C}$  necessary to melt the material. In order to maintain the stoichiometry of the melt, the materials must be processed in a sealed crucible. The melt is incompatible with easily sealable crucibles such as Ta and quartz but can be held in high purity alumina crucibles. If the alumina crucible is sealed in a quartz ampoule, the K and As vapors react with the ampoule causing it to fail and release K and As vapors causing the growth to fail and in the absence of secondary confinement releasing hazardous vapors into the environment. To safely manipulate the growth, we developed a technique to use liquid Sn to seal an alumina capsule and thus contain the volatile and toxic K and As vapors when the growth temperature is above the melting point of Sn at  $232^\circ\text{C}$  (Fig. 2). Our liquid-Sn sealing technique is a general approach and can be applied to flux growth of other materials containing volatile and reactive elements. By using this technique and optimizing the growth process, we synthesized  $\text{KFe}_2\text{As}_2$  single crystals with the highest residual resistivity ratio ever reported.

Analysis of the growth morphology in the experiments described above lead us to conclude that the crystals nucleate on the surface of the melt and grow by the reaction of the top surface of the crystal with the contained K and As vapor phase. We were able to promote this reaction by developing an inverted-temperature-gradient method with the colder zone at the top of the crucible [R1]. This method yields higher quality crystals, compared with traditional flux-method, as crystallization from the liquid top can expel impurity phases into liquid during crystal growth. We have harvested crystals with in-plane size up to  $18 \times 10 \text{ mm}^2$  across the whole doping range studied ( $0.21 \leq x \leq 1$ ). In order to sustain a long duration growth at a cooling rate of  $0.5 \text{ K/h}$ , the chemicals were loaded into an alumina crucible, and then sealed in a Ta tube by arc melting.

In summary, we have succeeded in developing new synthesis protocols, optimizing growth processes, and elucidating the material structure to safely manipulate the synthesis process and attain high quality large single crystals of novel functional materials containing volatile, reactive, and toxic constituents. The high quality large single crystals that we synthesized have allowed cut-edge research to be performed [A2-A17].

#### Microstructure control and phase-space elucidation of $\text{Mg}_2\text{Si}$ -based thermoelectric alloys

$\text{Mg}_2\text{Si}$ -based alloys are attractive thermoelectric materials due to their earth-abundance and environmentally green nature [R3]. To improve their thermoelectric properties by creating more

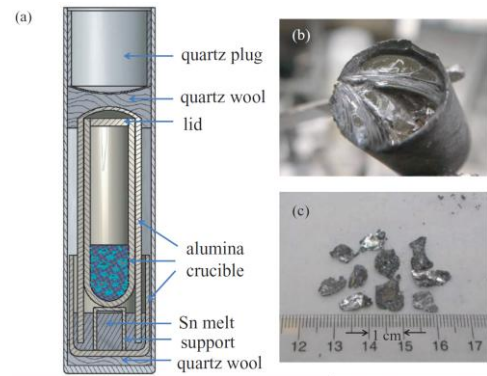


Fig. 2 (a) Crystal growth setup with the liquid Sn-melt technique. (b) Top view of a  $\text{KFe}_2\text{As}_2$  ingot with shiny lamellar-structured crystals. (c)  $\text{KFe}_2\text{As}_2$  single crystals from the ingot.

interfaces inside the materials for phonon scattering, we investigated the microstructure refinement of  $\text{Mg}_2\text{Si}$ -Si eutectic alloys through solidification control. We found only rapid cooling through melt spinning can yield nanometer microstructure (Fig. 3), whereas  $\text{Mg}_2\text{Si}$ -Si eutectic solidification is anomalous and the length scale of eutectic microstructure cannot be refined through directional solidification (Fig. 3).

Partially replacing Si with Sn has been reported to yield improved thermoelectric properties [R4]. However, it is unknown whether the  $\text{Mg}_2\text{Si}_{1-x}\text{Sn}_x$  is a single phase or not. The phase space of Mg-Si-Sn ternary alloys has been debating in literature. We investigated the phase space of Mg-Si-Sn ternary alloys including  $\text{Mg}_2\text{Si}$ - $\text{Mg}_2\text{Sn}$  pseudo-binary alloys and found the  $\text{Mg}_2\text{Si}_{1-x}\text{Sn}_x$  single phase compound in the reported phase-mixture space (Fig. 4). In Fig. 4, the directionally solidified alloy shows Si-rich and Sn-rich  $\text{Mg}_2\text{Si}_{1-x}\text{Sn}_x$  phases across broad compositional ranges (blue), whereas the alloy annealed at 600 °C for 2 wk shows  $\text{Mg}_2\text{Si}_{1-x}\text{Sn}_x$  within a narrower compositional range (red). Further investigations reveals unreported phase transitions in the single phase spaces of the current  $\text{Mg}_2\text{Si}$ - $\text{Mg}_2\text{Sn}$  pseudo-binary phase diagram.

### Future Work

We will continue our evaluation of material phase space to provide a scientific basis for materials synthesis, crystal growth, and microstructure control of novel materials. The field of Fe-based superconductors continues to develop with the commonality of containing volatile and toxic constituents. We will continue to focus our synthesis efforts on these materials as they emerge. One example is the newly discovered  $\text{MgOFeSe}$  compound with neutral PbO-type spacer layers [R2]. At the current time no details are available on the preparation of this compound, however, the intercalation of the PbO layer presents a number of challenges calling for novel but safe synthesis routes for  $\text{MgOFeSe}$ -like crystals from the pure elements or charge neutral compounds. We will investigate the use of electrochemical growth from molten salts or flux growth under moderate conditions: 100~400 °C, ambient pressure, and without using highly toxic solutions. We take advantage of collaborations within the laboratory to perform calculations of the Mg-O-Fe-Se phase diagram to guide the growth development. The development will use our strengths in thermal analysis, X-ray diffraction, and electron microscopy for phase identification and determination to understand the growth process and structure-property relationships.

In our investigation of non-superconducting materials we will complete out the investigation of  $\text{Mg}_2\text{Si}$ -based alloys including Mg-Si-Sn and Mg-Ge-Si alloys.

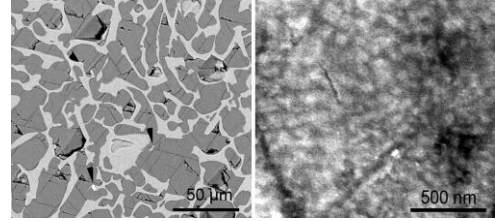


Fig. 3 Back-scattered electron images of  $\text{Mg}_2\text{Si}$ -Si eutectic alloys from directionally solidified (left) and wheel side of melt-spun alloys (right). Si phase is bright while  $\text{Mg}_2\text{Si}$  phase is dark.

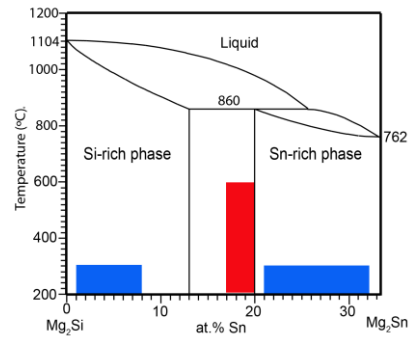


Fig. 4 Published  $\text{Mg}_2\text{Si}$ - $\text{Mg}_2\text{Sn}$  pseudo-binary phase diagram with  $\text{Mg}_2\text{Si}_{1-x}\text{Sn}_x$  phase spaces of an  $\text{Mg}_{44}\text{Si}_{45}\text{Sn}_{11}$  alloy in our work. See text for details.

## References

- R1 Y. Liu, M. A. Tanatar, B. Jensen, K. W. Dennis, R. W. McCallum, R. Prozorov, and T. A. Lograsso, (unpublished).
- R2. X. F. Lu, N. Z. Wang, G. H. Zhang, X. G. Luo, Z. M. Ma, B. Lei, F. Q. Huang, and X. H. Chen, arXiv:1309.3833. 16 Sept 2013.
- R3. J. Tani and H. Hiroyasu Kido, *Physica B*, **364**, 218-224 (2005).
- R4. V. K. Zaitsev, M. I. Fedorov, E. A. Gurieva, I. S. Eremin, P. P. Konstantinov, A. Yu. Samunin, and M. V. Vedernikov, *Physical Review B*, **74**, 045207 (2006).

## Selected Publications during FY2012-FY2013

- A1. A. Jesche, K. W. Dennis, A. Kreyssig, and P. C. Canfield, *Physical Review B*, **85**, 224432 (2012).
- A2. R. Jiang, L. L. Wang, M. L. Huang, R. S. Dhaka, D. D. Johnson, T. A. Lograsso, and A. Kaminski, *Physical Review B*, **86**, 085112 (2012).
- A3. M. Khan, D. L. Schlagel, T. A. Lograsso, K. A. Gschneidner, and V. K. Pecharsky, *Physical Review B*, **84**, 134424 (2011).
- A4. G. Li, G. Grissonnanche, J. Q. Yan, R. W. McCallum, T. A. Lograsso, H. D. Zhou, and L. Balicas, *Physical Review B*, **86**, 054517 (2012).
- A5. H. F. Li, J. Q. Yan, J. W. Kim, R. W. McCallum, T. A. Lograsso, and D. Vaknin, *Physical Review B*, **84**, 220501 (2011).
- A6. J. Ma, J. Q. Yan, S. O. Diallo, R. Stevens, A. Llobet, F. Trouw, D. L. Abernathy, M. B. Stone, and R. J. McQueeney, *Physical Review B*, **84**, 224115 (2011).
- A7. Y. Mudryk, N. K. Singh, V. K. Pecharsky, D. L. Schlagel, T. A. Lograsso, and K. A. Gschneidner, *Physical Review B*, **85**, 094432 (2012).
- A8. G. Petculescu, P. K. Lambert, A. E. Clark, K. B. Hathaway, Q. Xing, T. A. Lograsso, J. B. Restorff, and M. Wun-Fogle, *Journal of Applied Physics*, **111**, 07a921 (2012).
- A9. Y. Ren, J. Q. Yan, J. S. Zhou, J. B. Goodenough, J. D. Jorgensen, S. Short, H. Kim, T. Proffen, S. Chang, and R. J. McQueeney, *Physical Review B*, **84**, 214409 (2011).
- A10. J. B. Restorff, M. Wun-Fogle, K. B. Hathaway, A. E. Clark, T. A. Lograsso, and G. Petculescu, *Journal of Applied Physics*, **111**, 023905 (2012).
- A11. A. Thaler, H. Hodovanets, M. S. Torikachvili, S. Ran, A. Kracher, W. Straszheim, J. Q. Yan, E. Mun, and P. C. Canfield, *Physical Review B*, **84**, 144528 (2011).
- A12. S. L. Bud'ko, Y. Liu, T. A. Lograsso, and P. C. Canfield, *Physical Review B*, **86**, 224514 (2012).
- A13. S. E. Hahn, G. S. Tucker, J. Q. Yan, A. H. Said, B. M. Leu, R. W. McCallum, E. E. Alp, T. A. Lograsso, R. J. McQueeney, and B. N. Harmon, *Physical Review B*, **87**, 104518 (2013).
- A14. T. Q. Li, A. Patz, L. Mouchliadis, J. Q. Yan, T. A. Lograsso, I. E. Perakis, and J. G. Wang, *Nature*, **496**, 69-73 (2013).

- A15. Y. Liu, M. A. Tanatar, V. G. Kogan, H. Kim, T. A. Lograsso, and R. Prozorov, *Physical Review B*, **87**, 134513 (2013).
- A16. Y. Liu, Q. Xing, K. W. Dennis, R. W. McCallum, and T. A. Lograsso, *Physical Review B*, **86**, 144507 (2012).
- A17. M. Ramazanoglu, J. Lamsal, G. S. Tucker, J. Q. Yan, S. Calder, T. Guidi, T. Perring, R. W. McCallum, T. A. Lograsso, A. Kreyssig, A. I. Goldman, and R. J. McQueeney, *Physical Review B*, **87**, 140509(R) (2013).

## Theoretical and Experimental Study of Solid-Liquid Interface Properties of Stoichiometric Compounds

S.R. Wilson, M.I. Mendeleev, X.Y. Song, R.T. Ott, A.I. Goldman,  
R.E. Napolitano and M.J. Kramer

Division of Materials Science and Engineering, Ames Laboratory USDOE, Ames, IA, 50011

### Program Scope

The fundamental nature of structural selection during phase transitions in an undercooled liquid involves the simultaneous action of numerous physical forces, collectively governing the natural evolution of multiscale morphological hierarchy. Considered in concert, the prediction and control of phase selection and morphological dynamics, particularly far from equilibrium, is indeed a formidable task, but recent advances have led to quantitatively accurate predictive modeling methods that can be used to simulate many of the relevant structural and chemical features that evolve upon solidification. These methods, however, rely on accurate parameterization of fundamental thermodynamic and kinetic properties. The present subtask addresses these issues through integrating fundamental thermodynamic measurements<sup>1</sup>, new approaches in bulk thermodynamic modeling<sup>2</sup>, *ab initio* calculations,<sup>3</sup> investigation of bulk and solid-liquid interface (SLI) behavior with molecular dynamics (MD) simulations<sup>4</sup> and investigation of microstructural dynamics through experiments.<sup>5</sup> In this work we combine MD simulations of SLIs with *in situ* X-ray scattering experiments to quantify the SLI kinetics and identify the governing mechanisms. This work represents a significant advancement in our understanding of the fundamental nature of structural dynamics in solid-liquid phase transitions.

### Recent Progress

While SLI properties are key factors affecting nucleation, phase selections, morphology and growth kinetics of crystal phases the actual number of studies where these properties were measured is very limited because of difficulties in performing of such experiments. Molecular dynamics simulations offer an alternative way to obtain these properties but so far the main focus was mostly on pure metals. There are just a few experiments were solutions<sup>6</sup> or stoichiometric compounds<sup>7,8</sup> were studied. Paucity of studies is related to limited availability of appropriate interatomic potentials and with difficulties associated with the MD simulation itself. The latter includes slow kinetics and partitioning during the interface migration such that it is difficult to obtain the steady state interface migration. Stoichiometric compounds represent a special case where there is no partitioning during the SLI migration such that the mechanism of this migration can be studied without accounting for solute redistribution. There are a number of interesting stoichiometric binary compounds because i) they can be very deeply undercooled and in some cases form glasses and ii) the difference in SLI mobility compared to that of pure elements can be several orders of magnitude which may provide insight into why some systems can be so deeply undercooled.<sup>8</sup> Thus the present subtask includes:

- (i) Experimental study of the phase transformation in metallic alloys containing stoichiometric compounds;
- (ii) MD simulation to obtain the main SLI properties;
- (iii) Development of a theoretical underpinning of phase transformation pathways, especially far from equilibrium.

Since experiments serve to verify the theory, we have coordinated the materials selection with this in mind. One model systems we are currently investigating is Zr-Ni, which has a number of stoichiometric compounds. Recently we have used high-energy X-ray scattering experiments to study the liquid to crystalline transformation in  $\text{Ni}_{50}\text{Zr}_{50}$  alloy. These experiments utilized electrostatic levitation technique which eliminates a crucible thus providing deeper undercoolings than typical castings.<sup>9</sup> In spite of the fact that according the phase diagram and electronic structure calculations that the most stable crystalline phase for this alloy is B33, it first solidifies as B2 which then undergoes a solid state transformation to B33 (Fig. 1).

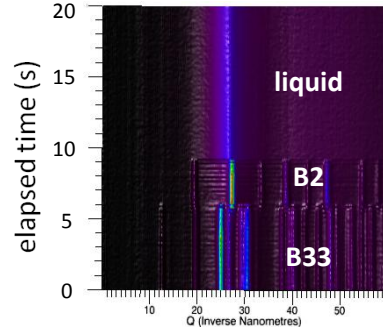


Fig. 1. XRD scattering showing the liquid - B2 - B33 transition in a deeply undercooled

To explain the experimental findings we determined the main SLI free energy for both B2 and B33 using MD simulations. We developed such a potential for Ni-Zr alloys by fitting the potential parameters to the data of our diffraction experiments and *ab initio* calculations<sup>10</sup> to provide correct energetics of stoichiometric compounds and proper liquid structure. Next we employed these potentials to study the SLI properties. To obtain the SLI free energy,  $\gamma$ , and stiffness,  $\gamma + \gamma''$ , we used the capillary fluctuation method (CFM) proposed in.<sup>11</sup> While this study is still in progress, we are already able to explain the experimental results. Figure 2 shows

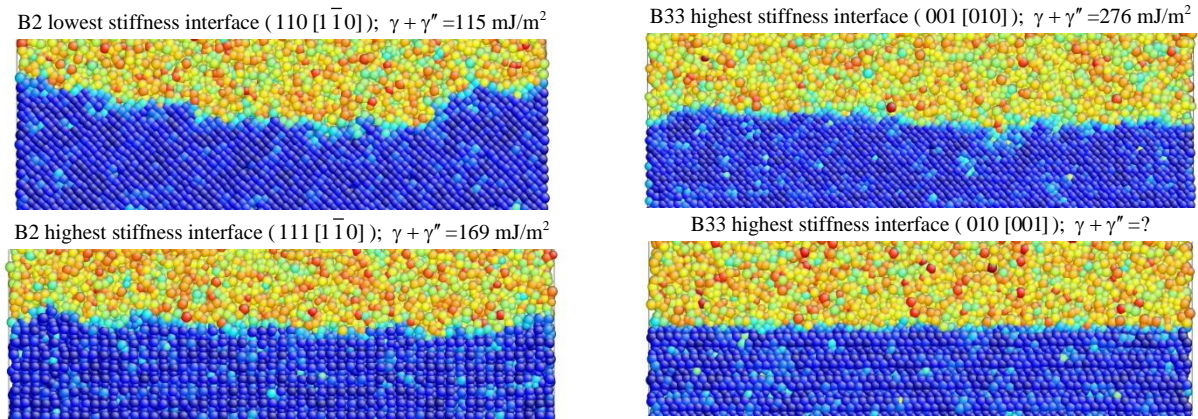


Figure 2. Snapshots of the models containing SLI interfaces for  $\text{Ni}_{50}\text{Zr}_{50}$  B2 and B33 after MD equilibration during 3 ns. The atoms are colored according to the order parameter.

the lowest and highest stiffness interfaces in the  $\text{Ni}_{50}\text{Zr}_{50}$  alloy. Clearly B2 has lower SLI stiffness than does B33 which can be seen from the amplitude of fluctuations in the SLI profile. Moreover, while we obtained the complete orientation dependence of the B2 SLI stiffness, we still could not do the same for B33 because some SLIs have very large stiffness (this is why the highest stiffness SLI looks so flat in Fig. 2). This explains why namely B2 appears first during solidification even although B33 is always more thermodynamically stable than B2.

### Recent Progress on Other Projects

To study the solidification in  $\text{Cu}_{50}\text{Zr}_{50}$  alloy (whose most stable crystal phase at high temperature is B2) we determined the complete map of the SLI properties from MD simulation as shown in Fig. 3 (to our best knowledge this is the first such complete study for a stoichiometric compound). Examination of the obtained data shows that the SLI mobility in  $\text{Cu}_{50}\text{Zr}_{50}$  alloy is 3

orders of magnitudes smaller than in pure metals. However, since the pure metals crystallize at a cooling rate of  $\sim 10^{11}$  K/s<sup>12</sup> this difference in mobility cannot explain why the  $\text{Cu}_{50}\text{Zr}_{50}$  alloy can be vitrified at a cooling rate of  $\sim 10^6$  K/s. Therefore, we should compare the nucleation in the alloy and pure metals. However, the data on the SLI free energy shown in Fig. 3 does not reveal any qualitative difference between the alloy and pure metals. Therefore, the mechanism of the nucleation should be further investigated.

The MD simulation study of the SLI properties requires large computational resources. Therefore, we also develop an alternative approach to estimate these properties using perturbation and density functional theories. We had developed such an approach and applied it to systems with inverse-powers, Lennard-Jones pair potentials as well as to metallic systems with embedded-atom method potentials. For fcc systems, the results are in reasonable agreement with the corresponding ones obtained from molecular dynamics simulations.<sup>13</sup> For bcc systems, our results provide the first reliable estimate for the interfacial free energies of the hard sphere system.

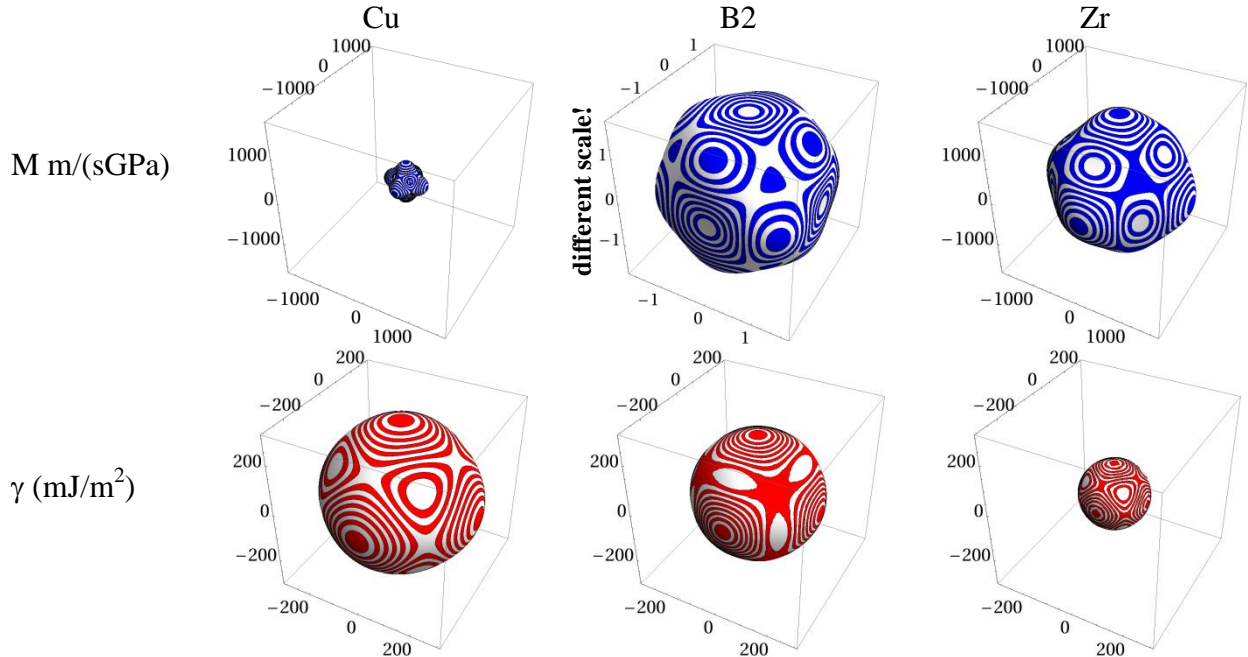


Figure 3. SLI properties in Cu, Zr and  $\text{Cu}_{50}\text{Zr}_{50}$ . Note that the scale of the B2 mobility is 1000 times smaller than that pure elements.

### Future Plans

To understand the phase transformation pathways in metallic alloys we will perform the following studies.

- (i) Perform levitation experiments to directly measure the solidification velocity.
- (ii) Complete our MD study of the SLI properties in  $\text{Ni}_{50}\text{Zr}_{50}$  alloys to explain the phase transformation pathways in Ni-Zr alloys. Next we will perform MD simulations to study the phase transformation of B2 into B33.
- (iii) Perform MD simulation study of SLI properties in  $\text{Al}_{50}\text{Ni}_{50}$  alloy (which solidifies as B2). Having all main SLI properties for  $\text{Cu}_{50}\text{Zr}_{50}$ ,  $\text{Ni}_{50}\text{Zr}_{50}$  and  $\text{Al}_{50}\text{Ni}_{50}$  we will investigate why the SLI mobility in the  $\text{Al}_{50}\text{Ni}_{50}$  alloy is 20 times larger than that in the  $\text{Cu}_{50}\text{Zr}_{50}$  alloy.<sup>8</sup>

- (iv) Investigate nucleation phenomenon in the above three alloys. While we know that Cu<sub>50</sub>Zr<sub>50</sub> alloy never solidifies during MD simulation the authors of <sup>8</sup> reported that the Al<sub>50</sub>Ni<sub>50</sub> alloy easily solidifies during MD simulation.
- (iv) Test the CFM for stoichiometric compounds. Also developing two new methods to determine the stiffness from MD simulation which will be compared to the CFM.

#### References:

- 1 N. Wang, Y. E. Kalay, and R. Trivedi, *Acta Mater.* **59** (17), 6604 (2011).
- 2 S. Wu, M. J. Kramer, X. W. Fang, S. Y. Wang, C. Z. Wang, K. M. Ho, Z. J. Ding, and L. Y. Chen, *Intermetallics* **30**, 122 (2012).
- 3 S. Wu, X. W. Fang, S. Y. Wang, C. Z. Wang, Y. X. Yao, K. M. Ho, Z. J. Ding, and L. Y. Chen, *Journal of Applied Physics* **110** (10) (2011).
- 4 M. I. Mendeleev, *Model. Simul. Mater. Sci. Eng.* **20** (4) (2012).
- 5 Y. E. Kalay, I. Kalay, J. Hwang, P. M. Voyles, and M. J. Kramer, *Acta Mater.* **60** (3), 994 (2012).
- 6 C. A. Becker, D. L. Olmsted, M. Asta, J. J. Hoyt, and S. M. Foiles, *Physical Review B* **79** (5) (2009).
- 7 A. Kerrache, J. Horbach, and K. Binder, *Epl* **81** (5) (2008).
- 8 C. G. Tang and P. Harrowell, *Nature Materials* **12** (6), 507 (2013).
- 9 A. K. Gangopadhyay, G. W. Lee, K. F. Kelton, J. R. Rogers, A. I. Goldman, D. S. Robinson, T. J. Rathz, and R. W. Hyers, *Review of Scientific Instruments* **76** (7) (2005).
- 10 M. I. Mendeleev, M. J. Kramer, S. G. Hao, K. M. Ho, and C. Z. Wang, *Philosophical Magazine* **92** (35), 4454 (2012).
- 11 J. J. Hoyt, M. Asta, and A. Karma, *Phys. Rev. Lett.* **86** (24), 5530 (2001).
- 12 M. I. Mendeleev, M. J. Kramer, C. A. Becker, and M. Asta, *Philosophical Magazine* **88** (12), 1723 (2008).
- 13 Y. Mu, A. Houk, and X. Y. Song, *Journal of Physical Chemistry B* **109** (14), 6500 (2005).

#### Selected DOE Sponsored Publications in 2012-2013 from Current Project

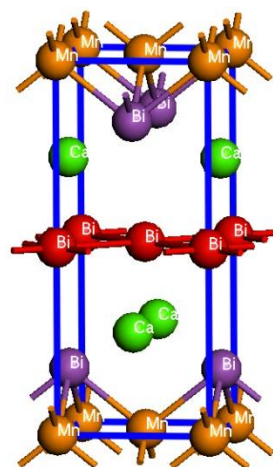
- [1] Y. E. Kalay, I. Kalay, J. Hwang, P. M. Voyles, and M. J. Kramer, Local chemical and topological order in Al-Tb and its role in controlling nanocrystal formation, *Acta Mater.* **60**, 994 (2012).
- [2] X.W. Fang, C.Z. Wang, S.G. Hao, M.J. Kramer, Y. X. Yao, M.I. Mendeleev, Z.J. Ding, R. Napolitano and K.M. Ho, Spatially Resolved Distribution Function and the Medium-Range Order in Metallic Liquid and Glass, *Scientific Reports* **1**, 194 (2011).
- [3] S.K.E. Moorthy, M.I. Mendeleev and J.M. Howe, The influence of spatial and temporal averaging on interpretation of HRTEM images of solid-liquid interfaces, *Ultramicroscopy* **124**, 40-45 (2013).
- [4] M.I. Mendeleev, M.J. Kramer, S.G. Hao, K.M. Ho and C.Z. Wang, Computer simulation of the structure of MZr<sub>2</sub> liquid and amorphous alloys, *Phil. Mag.* **92**, 4098-4112 (2012).
- [5] M.I. Mendeleev, M.J. Kramer, S.G. Hao, K.M. Ho and C.Z. Wang, Development of interatomic potentials appropriate for simulation of liquid and glass properties of NiZr<sub>2</sub> alloy, *Phil. Mag* **92**, 4454-4469 (2012).
- [6] M.I. Mendeleev, Molecular dynamics simulation of solidification and devitrification in a one-component system, *MSMSE* **20**, 045014 (2012).

## Exploratory Materials Synthesis and Characterization (EMSC)

Cedomir Petrovic  
Condensed Matter Physics and Materials Science Department  
Brookhaven National Laboratory, Upton NY 11973

### Program Scope

EMSC program concentrates on exploratory synthesis and characterization of the new model materials of current interest in condensed matter physics. In addition, we often focus on advanced synthesis of known materials in order to enable important physical and structural investigations. We put strong effort in the discovery of new phenomena associated with the correlated behavior of electrons in energy related materials. Most often materials are synthesized in the single crystal form since many observables of interest are tensor quantities and since this allows for the investigation of physical properties that are free of grain boundary influences. We use range of techniques suitable for exploratory materials synthesis and crystal growth: conventional arc melting and powder metallurgical techniques, solution methods, high temperature intermetallic, oxide, sulfide or salt fluxes, chemical vapor transport and deposition. Automated physical and structural characterization is the essential component of the lab. In order to optimize synthesis parameters, it is necessary to characterize structural and physical properties of materials. Quite often the same methods are used to probe and perturb crystal structure, transport, thermodynamic and magnetic properties, sometimes at the extreme conditions. We use environments of high magnetic fields and low temperatures at NHMFL Tallahassee and HZDR Dresden. We also use EXAFS beamlines at NSLS and we are constantly engaged in the buildup of our synthesis and characterization capabilities by custom designing and/or building our materials synthesis and physical characterization tools. We currently pursue several interpenetrating research directions: Quantum criticality in heavy fermions and charge density wave materials, Metal – insulator transitions (MIT) in nearly magnetic materials, Dirac states in bulk crystals and facility development. Our work enhances materials space available to BNL research groups and neighboring universities, with whom there are extensive ties. This program includes training of the next generation of scientists. Students from neighboring universities (Brown, Columbia, Johns Hopkins, Stony Brook) were or are being educated in materials physics, arts and crafts of crystal growth, materials synthesis and characterization.



### Recent progress (examples)

*Exploratory synthesis of new materials.* We have embarked

Fig. 1: (Sr,Ca)MnBi<sub>2</sub> crystal structure. Dirac states are located in quasi-2D Bi layers

on the exploration of Dirac states in bulk crystals. We reported two-dimensional (2D) quantum transport in SrMnBi<sub>2</sub> and CaMnBi<sub>2</sub> single crystals (Fig. 1) [1-2]. The linear energy dispersion leads to nonsaturated linear magnetoresistance (MR) since all Dirac fermions occupy the lowest Landau level in the quantum limit. The transverse MR exhibits a crossover at a critical field B\* from semiclassical weak-field B<sup>2</sup>, to the high-field linear-field dependence. With an increase in temperature, the critical field B\* increases and its temperature dependence is quadratic, attributed to the Landau-level splitting of the linear energy dispersion. The effective magnetoresistant mobility up to  $\mu_{MR} \sim 3400$  cm<sup>2</sup>/Vs is derived. Angular-dependent magnetoresistance and quantum oscillations suggest dominant 2D Fermi surfaces. Our results imply that bulk crystals with Bi square nets can be used to study low-dimensional electronic transport commonly found in 2D materials such as graphene. Notably, we have demonstrated large magnetothermopower effect in bulk crystals with Dirac states. This is attributed to the shift of the chemical potential in the linear bands by magnetic field [3]. The maximum change of thermopower is about 1600% in 9 T and at 10 K.

Small gap semiconductor FeSb<sub>2</sub> shows not only highest known electronic thermoelectric power reported in any material [4], but also pronounced correlated electron phenomena. We recently reported on the emergence of an electronic Griffiths phase in the Te-doped FeSb<sub>2</sub>, predicted for disordered insulators with random localized moments in the vicinity of a metal-insulator transition [5]. Magnetic, transport, and thermodynamic measurements of Fe(Sb<sub>1-x</sub>Te<sub>x</sub>)<sub>2</sub> single crystals show signatures of disorder-induced non-Fermi liquid behavior and a Wilson ratio expected for strong electronic correlations. The electronic Griffiths phase states are found on the metallic boundary between the insulating state (x = 0) and a long-range albeit weak magnetic order (x  $\geq$  0.075).

Similarity with Kondo or Anderson lattices is striking since non-Fermi liquid divergences appear at rather weak randomness and are magnetic field tuned to a Fermi liquid (Fig. 2).

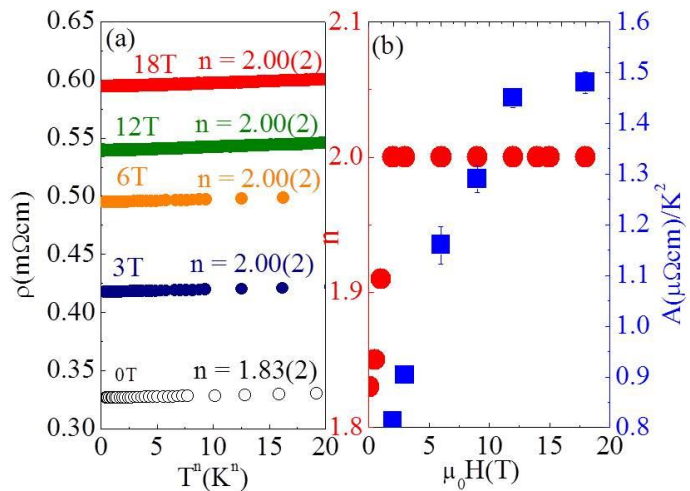


Fig. 2: (a) Resistivity  $\rho(T)$  of Fe(Sb<sub>1-x</sub>Te<sub>x</sub>)<sub>2</sub> for x=0.01 plotted vs  $T^n$  in high fields. (b) Exponent  $n$  from (a) and coefficient  $\rho=\rho_0+AT^2$  as a function of field.

Advanced materials synthesis and crystal growth. Crystals made at EMSC BNL enabled several important STM and neutron studies in the past two years. These include:

a) Vortex lattice reorientation in a heavy fermion superconductor CeCoIn<sub>5</sub>. A single vortex

lattice VL orientation is observed for  $H \uparrow \uparrow [100]$ , while a  $90^\circ$  reorientation transition is found for  $H \uparrow \uparrow [110]$ . The VL form factor shows strong Pauli paramagnetic effects similar to  $H \uparrow \uparrow [001]$ . At high fields, above which the upper critical field becomes a first-order transition, an increased disordering of the VL is observed.

b) First inelastic neutron scattering on a canonical magnetic-field induced quantum critical metal  $\text{YbRh}_2\text{Si}_2$ . Spin fluctuations are reported near the magnetic field –driven quantum critical point (QCP). On cooling, ferromagnetic fluctuations evolve into incommensurate correlations located at  $q_0 = \pm(\delta, \delta)$  where  $\delta = (0.14 \pm 0.04)$  reciprocal lattice units. There is a sharp intradoublet resonant excitation at an energy  $E_0 = g\mu_B\mu_0 H$  with  $g = 3.8 \pm 0.2$  at 0.1 K and in an in-plane magnetic field. Low temperature spin dynamics in the absence of magnetic field is affected by the Fermi surface nesting whereas at high fields and temperatures it resembles Kondo-screened spins above ferromagnetic long range order.

c) Imaging Cooper pairing of heavy fermions in  $\text{CeCoIn}_5$ .  $\text{CeCoIn}_5$  is the highest known  $T_c$  heavy fermion superconductor with  $4f$  magnetic ions. It is also, arguably, the cleanest example of material where superconductivity in nearly magnetic materials can be studied. Hence, it might serve as a test bed for developing theoretical frameworks of magnetically mediating superconductivity. Using Bogolybov quasiparticle interference technique it was possible for the first time to measure the superconducting gap dependence of momentum space  $\Delta(\mathbf{k})$ .

## Future work

In the next period we will pursue several crosscutting directions. These include:

1. Interplay of strong electronic correlations in bulk crystals with Dirac dispersion. In contrast to graphene or simple topological insulators, Dirac states in bulk crystals usually coexist with states derived from other electronic bands at the Fermi level. Hence, due to rich variety of electronic complexity, bulk crystals can be used to understand electron dynamics of the Dirac fermions, i.e. their interactions with other electrons with different values and origin of quasiparticle mass enhancement. There are number of energy relevant materials where Dirac states have been observed, for example  $\text{BaFe}_2\text{As}_2$  with spin density wave (parent compound of Fe-based high- $T_c$  superconductors) [6]. Enhanced thermoelectric properties can also be expected in complex materials with coexisting Dirac and bulk states [7].
2. Heavy fermions (HF) at QCP. We have embarked on the study of QCP characteristics in disordered and doped  $\text{CeCoIn}_5$ . In particular, interlayer transport, phenomena at high magnetic fields and Fermi surface changes will be investigated in an effort to elucidate similarities and differences with Cu-based high  $T_c$  superconductors.
3. Charge fluctuations at the QCP. Recently, firm evidence has been established that the charge order could be an important ingredient in (as opposed to a competitor of) the high  $T_c$  superconductivity in cuprate oxides [8]. We will focus on relatively simple new chalcogenide superconductors with quasi two dimensional conductivity and incipient charge density wave order where such interplay can be observed isolated from long or short range order magnetism.

4. Heavy fermion-like states in *d*- electron metals. We will synthesize and study materials with large quasiparticle mass enhancement in narrow bands, similar to classical *4f*-based HF materials, but without Abrikosov-Suhl resonance. We will focus on investigations of properties near metal-insulator transition with an effort to bring about larger materials class with recently discovered giant thermoelectric power factor [4].

## References

1. Kefeng Wang, D. Graf, Hechang Lei, S. W. Tozer and C. Petrovic, “Quantum transport of two dimensional Dirac fermions in SrMnBi<sub>2</sub>”, Phys. Rev. B 84, 220401 (2011).
2. Kefeng Wang, D. Graf, Limin Wang, Hechang Lei, S. W. Tozer and C. Petrovic, “Two dimensional Dirac fermions and quantum magnetoresistance in CaMnBi<sub>2</sub>”, Phys. Rev. B 85, 041101 (2012).
3. Kefeng Wang, Limin Wang and C. Petrovic, “Large magnetothermopower effect in Dirac materials (Sr,Ca)MnBi<sub>2</sub>”, Appl. Phys. Lett. 100, 112111 (2012).
4. Qing Jie, Rongwei Hu, Emil Boziin, A. Llobet, I. Zaliznyak, C. Petrovic and Q. Li, “Electronic thermoelectric power factor and metal-insulator transition in FeSb<sub>2</sub>”, Phys. Rev. B 86, 115121 (2012).
5. Rongwei Hu, Kefeng Wang, Hyejin Ryu, Hechang Lei, E. S. Choi, M. Uhlarz, J. Wosnitza and C. Petrovic, “Electronic Griffiths Phase in the Te-Doped Semiconductor FeSb<sub>2</sub>”, Phys. Rev. Lett. 109, 256401 (2012).
6. T. Morinari, E. Kaneshita and T. Tohyama, “Topological and transport properties of Dirac Fermions in an antiferromagnetic metallic phase of iron-based superconductors”, Phys. Rev. Lett. 105, 037203 (2010).
7. O. A. Tretiakov, Ar. Abanov, and J. Sinova, “Holey topological thermoelectrics”, Appl. Phys. Lett. 99, 113110 (2011).
8. E. Fradkin and S. A. Kivelson, “Ineluctable complexity”, Nature Physics 8, 864 (2012).

**Publications** (Selected out of 40 total published and 29 supported by this FWP since 09/2011; full list at: <http://www.bnl.gov/cmpmsd/emsc/pubs.asp>)

1. M. P. Allan, F. Masee, D. K. Morr, J. Van Dyke, A. W. Rost, A. P. Mackenzie, C. Petrovic and J. C. Davis, ” Imaging Cooper pairing of heavy fermions in CeCoIn<sub>5</sub>”, Nature Physics 9, 468 (2013).

2. C. Stock, C. Broholm, Y. Zhao, F. Demmel, H. J. Kang, K. C. Rule, and C. Petrovic, “Magnetic Field Splitting of the Spin Resonance in  $\text{CeCoIn}_5$ ”, *Phys. Rev. Lett.* 109, 167207 (2012).
3. Kefeng Wang and C. Petrovic, “Large linear magnetoresistance and magnetothermopower in layered  $\text{SrZnSb}_2$ ”, *Appl. Phys. Lett.* 101, 152102 (2012).
4. C. Stock, C. Broholm, F. Demmel, J. Van Duijn, J. W. Taylor, H. J. Kang, R. Hu and C. Petrovic, “From incommensurate correlations to mesoscopic spin resonance in  $\text{YbRh}_2\text{Si}_2$ ”, *Phys. Rev. Lett.* 109, 127201 (2012).
5. C. Petrovic, P. C. Canfield and J. Y. Mellen, “Growing intermetallic single crystals using in situ decanting”, *Philosophical Magazine* 92, 2448 (2012).
6. P. Das, J. S. White, A. T. Holmes, E. M. Forgan, A. D. Bianchi, M. Kenzelmann, M. Zolliker, S. Gerber, J. L. Gavilano, E. D. Bauer, J. L. Sarrao, C. Petrovic, and M. R. Eskildsen, “Vortex lattice studies of  $\text{CeCoIn}_5$  for H orthogonal to c-axis”, *Phys. Rev. Lett.* 108, 087002 (2012).

**Growth Mechanisms and Controlled Synthesis of Nanomaterials (ERKCS81):  
Revealing the Growth Mechanism of Graphene on Catalytic Substrates  
by Real- Time Optical Diagnostics**

Alex Poretzky,<sup>1</sup> Gyula Eres,<sup>2</sup> David B. Geohegan,<sup>1</sup> Murari Regmi,<sup>2</sup> Christopher M. Rouleau,<sup>1</sup>  
Mina Yoon,<sup>2</sup> Matthew Chisholm,<sup>2</sup> and Gerd Duscher<sup>2,3</sup>

<sup>1</sup>Center for Nanophase Materials Sciences and <sup>2</sup>Materials Science and Technology Division,  
Oak Ridge National Laboratory, Oak Ridge, TN 37831 and the <sup>3</sup>Dept. of Materials Science and  
Engineering, Univ. of Tennessee, Knoxville, 37996

## **Program Scope**

The overarching goal of the research program is to understand the link between the growth mechanisms and the resulting structure of nanoscale materials. The emphasis is on the development of real-time methods to induce and probe chemical and physical transformations away from thermodynamic equilibrium in order to controllably synthesize nanomaterials with enhanced properties resulting from metastable structures. The approach relies on correlating the real-time diagnostic measurements with predictive theoretical methods and post-growth characterization by imaging, spectroscopy, and atomic-resolution analytical electron microscopy to develop a framework for the deterministic synthesis of nanomaterials with desired properties. A distinguishing feature of the program is the development and application of time-resolved, *in situ* diagnostics of nanomaterial growth kinetics and a corresponding development of models to understand the underlying kinetic and chemical pathways. Spatial confinement and reactive quenching approaches are developed to explore the synthesis mechanisms of rationally-designed nanostructures with enhanced intrinsic properties, targeting: (1) oxide, carbon, and alloy nanomaterials produced in metastable states by catalyst-free or catalyst-mediated processes, and (2) doped, decorated, and filled nanomaterial hybrids designed to induce permanent electric fields or distribute charge within nanostructures. Theoretical methods are used to understand fundamental mechanisms of synthesis in order to guide the formation of nanostructures tailored to enhance energy storage, catalysis, thermal management, and photovoltaics in support of DOE's energy mission.

## **Recent Progress**

Non-equilibrium approaches including pulsed laser deposition (PLD), and pulsed chemical vapor deposition (pulsed CVD) are employed to explore the nucleation and growth kinetics of graphene on catalytic substrates and to understand its growth mechanisms. Understanding the mechanisms by which graphene and other 2D nanomaterials grow on different substrates is essential in order to synthesize these nanomaterials with the well-defined numbers of layers and ordered stacking required by many potential applications. Synthesis of graphene and other 2D nanomaterials, e.g., metal chalcogenide nanosheets, have common challenges that include: 1) controlling nucleation density and number of layers, 2) rapid growth over large areas, and 3) growth of large crystalline grains. To address these challenges development of *in situ* diagnostic approaches for controlling and understanding growth mechanisms of these materials are required. Here, we discuss our results on graphene growth by CVD on copper foils, which exhibit very low carbon solubility where surface processes are responsible for graphene formation<sup>1</sup>, and also on Ni films, which has high carbon solubility where both surface and bulk carbon are involved in the growth<sup>2</sup>. The most important parameter for the growth of large graphene single crystals is the nucleation density as defined by the number of nucleation sites per unit area. First, we focus on understanding the kinetic factors that control the nucleation density of graphene on Cu foils.

### Graphene on Cu foils

From the perspective of promoting large area graphene growth the nucleation density determines the largest island size that can be obtained before coalescence causes two or more individual islands to merge into successively larger islands. In thin film epitaxial growth, coalescence is known to be accompanied by incorporation of lattice imperfections, and for growing large area single crystal graphene this is undesirable.

Here we employed a two-step approach for controlling the nucleation step that includes reducing the nucleation site density combined with increasing the reaction barrier at the remaining nucleation sites. These two factors are interrelated and are not easily uncoupled and treated separately. To reduce the nucleation density we use intentional oxidation of the Cu foils in air prior to graphene growth. The role of this step is to remove surface impurities such as carbon contamination and other metallic impurities by oxidation. In addition, the number of structural defects on the surface is reduced and the potential for preferential regrowth of Cu grains exists in the subsequent annealing step in  $H_2$  that is used for reducing the oxidized Cu back to Cu prior to starting graphene growth. We also describe our results on collisional deactivation (CD) for increasing the nucleation barrier at the existing nucleation sites. The effect of CD is to effectively increase the reaction barrier for nucleation by removing enough energy from activated nucleation precursors to bring the reaction below threshold. In practice, we perform CD by using a brief, 10 s duration pulse of Ar at the onset of graphene growth. The use of collisions with inert gases is a familiar approach for changing the rate and the outcome of thermal decomposition reactions of hydrocarbons. Combining these two steps in succession to suppress nucleation in graphene CVD on Cu foils, we demonstrated the growth of large single layer single crystal grains of up to 1.5mm in lateral size (Fig.1).

The Eden cluster model<sup>3</sup>, wherein we assume the methyl radicals act as a generic growth species, was used for interpreting graphene growth in the framework of two-dimensional crystallization governed by kinetic parameters that control the balance between adsorption and desorption of carbon containing intermediates in nucleation and growth of graphene (Fig.2)

### Graphene on Ni films

We also revealed the kinetics and mechanisms of graphene growth on Ni films using a pulsed CVD approach combined with real-time optical diagnostics<sup>2</sup> (Fig 3). *In situ* UV-Raman spectroscopy with simultaneous detection of both the G- and 2D-bands was used to unambiguously detect isothermal graphene growth at high temperatures, measure the growth kinetics with  $\sim 1$ s temporal resolution, and estimate the fractional precipitation upon

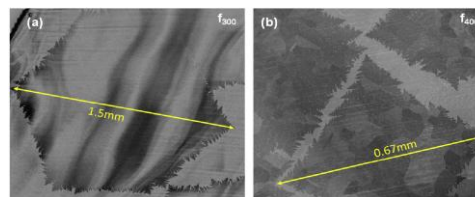


**Figure 1.** Large graphene grains on two different Cu foils f300 and f400. Note that the graphene grains change shape from hexagonal on f300 to rectangular on f400. The Cu foils are designated by “f<sub>T</sub>” where f stands for foil and the subscript T represents the oxidation temperature.

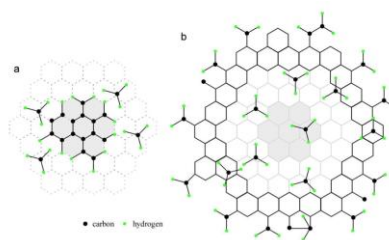


**Figure 2.** (a) The formation of a minimum size stable Eden cluster in graphene nucleation consisting of a 7-member hexagonal ring structure designated by the gray background. (b) An Eden cluster for graphene growth showing a completed compact inner region grown from a minimum cluster illustrated by light gray background and a still growing incomplete outer ring of a graphene island. The methyl radicals in the schematic illustrate a generic growth species.

cooling (Fig. 3). Optical reflectivity and videography provided much faster temporal resolution (Fig. 4). Both the growth kinetics and the fractional isothermal precipitation were found to be governed by the  $C_2H_2$  partial pressure in the CVD pulse for a given film thickness and temperature. Graphene precipitation during cooling was shown to occur above  $600^\circ C$ . Room-temperature Raman spectroscopy and mapping of as-grown and transferred graphene grown by single, sub-second acetylene pulses at low partial pressures and high temperatures is a mixture of *turbostratic bilayer graphene* with low defect density and few-layer graphene patches.

Higher acetylene partial pressures were found to drive larger fractions of isothermal graphene growth and shorter nucleation and growth periods. For example, at  $800^\circ C$  up to 94% of graphene growth occurs isothermally within the  $\sim 1$ -second acetylene gas lifetime in the growth chamber. The possible role of autocatalytic surface chemical reactions should be considered as a growth mechanism (along with dissolution/precipitation) since very similar flux-dependent nucleation and growth kinetics were observed in similar experiments in the pulsed-CVD growth of SWNTs.

However, at lower acetylene partial pressures the bulk of the Ni film was clearly involved in the growth. Isothermal graphene growth was observed  $\sim 10$  seconds *after* the growth gas was cleared from the chamber, and this growth time was shown to significantly shorten when the thickness of the Ni film was reduced. These results were explained in the context of a dissolution/precipitation model incorporating a flux-dependent induction time to form graphene nuclei, and subsequent deposition from dissolved carbon driven by concentration gradients (Fig. 4).

In summary, 1) we employed a two-step approach for suppressing nucleation in graphene CVD on Cu for large area single crystal growth. The combination of oxidation of as received Cu foils to remove low energy nucleation sites and collisional deactivation by an Ar pulse to increase the reaction barrier for nucleation at the remaining sites was used to reduce the overall nucleation density by almost three orders of magnitude. The Eden cluster model was used for interpreting graphene growth in the framework of two-dimensional crystallization governed by kinetic parameters that control the balance between adsorption and desorption of carbon containing intermediates in nucleation and growth of graphene. 2) Real-time optical diagnostics revealed that graphene nucleates and grows rapidly and isothermally on Ni substrates by dissolution and precipitation of carbon with flux-dependent kinetics that indicate autocatalytic reactions. Understanding the mechanisms by which graphene grows on different catalytic metal films is essential in order to synthesize graphene with the well-defined numbers of layers and ordered stacking required by many potential applications.

## Future Plans

These real-time diagnostic techniques are currently being applied to understand the growth mechanisms of other 2D nanomaterials beyond graphene, e.g., metal chalcogenides. These

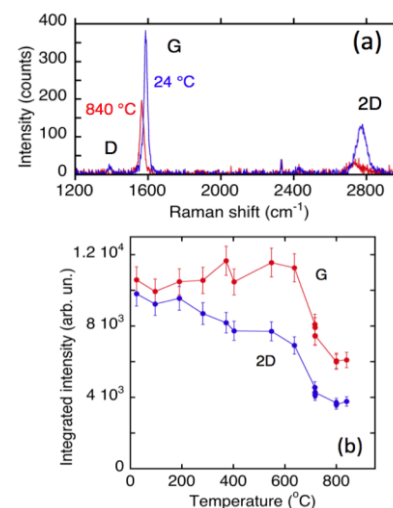


**Figure 3.** (a) UV excitation ( $\lambda_{ex} = 405$  nm) permits Raman spectra of graphene at high temperatures to be measured during isothermal growth ( $> 1$  s resolution) and subsequently by cooling, showing characteristic G and 2D bands. (b) Integrated intensities of the G- and 2D-Raman bands measured during cooling from the growth temperature ( $840^\circ C$ ) to room temperature reveal the fractional graphene precipitation upon cooling.

nanomaterials have very attractive properties, e.g., the band gap of these materials depends on the number of layers, which can be useful for their potential applications. For example, according to our preliminary calculations the band gap of GaS changes from 1.6 eV to 2.5 eV when the number of layers drops from 7 to 1, making them highly amenable to real-time optical diagnostics. We are exploring novel synthesis methods developed for graphene, e.g. pulsed CVD and PLD, conducive with *in situ* Raman scattering, time-resolved reflectivity, and direct imaging during growth of 2D nanosheets on substrates.

## References

1. G. Eres, et al, "Independent Island Growth of Large Area Single Crystal Graphene by Suppressing Nucleation in Chemical Vapor Deposition on Cu" (*in preparation*).
2. A.A. Puzetky, D.B. Geohegan, S. Pannala, C.M. Rouleau, M. Regmi, N. Thonnard G. Eres, *Nanoscale*, **5**, 6507 (2013).
3. O.M. Becker, A. Ben-Shaul, Role and Mechanism of Island Formation in Chemisorption, *Phys. Rev. Lett.*, **61**, 2859 (1988).
4. S.Z. Butler, et al, *ACS Nano* **4**, 2898 (2013).

## DoE Sponsored Publications in the Last Two Years

1. K. R. S. Chandrakumar, J.D. Readle, C.M. Rouleau, A.A. Puzetky, D.B. Geohegan, K. More, V. Krishnan, M. Tian, G. Duscher, B. Sumpter, S. Irle, K. Morokuma, "High-temperature transformation of Fe-decorated single-wall carbon nanohorns to nanoysters: a combined experimental and theoretical study", *Nanoscale* **5**, 1849 (2013).
2. I.A. Merkulov, M. Yoon, D.B. Geohegan, "How the shape of catalyst nanoparticles determines their crystallographic orientation during carbon nanofiber growth", *Carbon* **60**, 41 (2013).
3. J. Jacimovic, R. Gaal, A. Magrez, L. Forro, M. Regmi, G. Eres, "Electrical property measurements of Cr-N codoped TiO<sub>2</sub> epitaxial thin films grown by pulsed laser deposition", *Appl. Phys. Lett.* **102**, 172108 (2013).
4. A.A. Puzetky, D.B. Geohegan, S. Pannala, C.M. Rouleau, M. Regmi, N. Thonnard, G. Eres, "Real-time Optical Diagnostics of Graphene Growth Induced by Pulsed Chemical Vapor Deposition", *Nanoscale*, **5**, 6507 (2013).
5. S. Dai, B. Guo, X.-G. Sun, P.F. Fulvio, G.M. Veith, R.T. Mayes, S. Brown, J. Adcock, D.B. Geohegan, S.M. Mahurin, A.A. Puzetky, C.M. Rouleau, "Fluorination of "brick and mortar" soft-templated graphitic ordered mesoporous carbons for high power lithium-ion battery", *J. Mater. Chem. A* **1**, 9414 (2013).

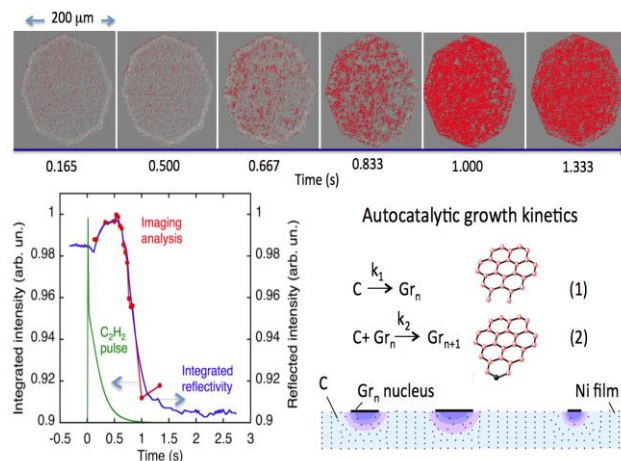


**Figure 4.** *In situ* optical diagnostics reveal the kinetics and mechanisms of CVD graphene growth. (top) Six selected frames from a movie taken through a microscope show how graphene patches (shaded red) nucleate after a delay and then rapidly grow at 800 °C following a single pulse of acetylene (timing lower left). The autocatalytic kinetics measured in this study were acetylene flux-dependent and described in the context of a dissolution/precipitation model (lower right) where subsurface carbon supplies surface graphene nuclei.

6. K. Li, G. Eres, J. Howe, Y.-J. Chuang, X. Li, Z. Gu, L. Zhang, S. Xie, Z. Pan, "Self-Assembly of Graphene on Carbon Nanotube Surfaces", *Scientific Reports* **3**, 2353 (2013).
7. D.B. Geohegan, A.A. Puzetzky, M. Yoon, G. Eres, C. Rouleau, K. Xiao, J. Jackson, J. Readle, M. Regmi, N. Thonnard, G. Duscher, M. Chisholm, K. More, "Laser Interactions for the Synthesis and *in situ* Diagnostics of Nanomaterials", Book chapter: in Springer Series in Materials Science (2013).
8. S.-J. Woo, E.-S. Lee, M. Yoon, Y.-H. Kim, "Finite-Temperature Dihydrogen Adsorption/Desorption Thermodynamics Driven by Soft Vibration Modes", *Phys. Rev. Lett.* **111**, 066102 (2013).
9. D.B. Geohegan, I.N. Ivanov, A.A. Puzetzky, S. Jesse, B. Hu, M. Garrett, B. Zhao, "Transparent conductive nano-composites", US patent 8540542 B2 (2013).
10. A.A. Puzetzky, D.B. Geohegan, J. J. Jackson, S. Pannala, G. Eres, C.M. Rouleau, K.L. More, N. Thonnard, J. D. Readle, "Incremental Growth of Short SWNT Arrays by Pulsed Chemical Vapor Deposition", *Small* **8**, 1534 (2012).
11. Y. Liu, C. Brown, D. Neumann, D.B. Geohegan, A.A. Puzetzky, C.M. Rouleau, H. Hu, D.J. Styers-Barnett, P.O. Krasnov, B.I. Yakobson, "Metal-Assisted Hydrogen Storage on Pt-Decorated Single-Walled Carbon Nanohorns," *Carbon* **50**, 4953 (2012).
12. K. Lee, K. Berland, M. Yoon, S. Andersson, E. Schroeder, P. Hyldgaard, and B.I. Lundqvist, "Benchmarking van der Waals density functionals with experimental data: potential energy curves for H<sub>2</sub> molecules on Cu(111), (100), and (110) surfaces" *J. of Physics: Condensed Matter* **24**, 424213 (2012).
13. D.B. Geohegan, A.A. Puzetzky, C.M. Rouleau, M. Regmi, J.J. Jackson, J. Readle, K. More, G. Eres and G. Duscher, Nonequilibrium Laser Synthesis and Real-Time Diagnostics of Carbon Nanomaterial Growth, *Proceedings of 31st International Congress on Applications of Lasers & Electro-Optics (ICALEO-2012)*.
14. R. Sachan, S. Yadavali, N. Shirato, H. Krishna, V. Ramos, G. Duscher, S. J. Pennycook, A. K. Gangopadhyay, H. Garcia, and R. Kalyanaraman, "Self-Organized Bimetallic Ag-Co Nanoparticles with Tunable Localized Surface Plasmons Showing High Environmental Stability and Sensitivity", *Nanotechnology*, **23**, 275604 (2012).
15. M. Chisholm, G. Duscher, W. Windl, "Oxidation Resistance of Reactive Atoms in Graphene" *Nano Letters*, **12**, 4651 (2012).
16. A. K. Kothari, B. W. Sheldon, G. Eres, "Thickness Limitations in carbon nanotube reinforced silicon nitride coatings synthesized by vapor infiltration", *Acta Materiala*, **60**, 7104 (2012).
17. M. Regmi, M.F. Chisholm, G. Eres, "The Effect of Growth Parameters on the Intrinsic Properties of Large-Area Single Layer Graphene Grown by Chemical Vapor Deposition on Cu", *Carbon* **50**, 134 (2011).
18. D.B. Geohegan, A.A. Puzetzky, J.J. Jackson, C. M. Rouleau, G. Eres, K.L. More, "Flux-Dependent Growth Kinetics and Diameter Selectivity in Single-Wall Carbon Nanotube Arrays", *ACS Nano* **10**(5), 8311 (2011).
19. X. Liu, S. Sen, J. Liu, I. Kulaots, D.B. Geohegan, A. Kane, A.A. Puzetzky, C.M. Rouleau, K.L. More, G. Tayhas, R. Palmore, R.H. Hurt "Antioxidant Deactivation on Graphenic Nanocarbon Surfaces", *Small* **7**, 2775 (2011).
20. M. Yoon, H. Weitering, Z. Zhang, "First-principles studies of hydrogen interaction with ultrathin Mg and Mg-based alloy films", *Phys. Rev. B* **83**, 045413 (2011).

## **Molecularly Organized Nanostructural Materials**

**Subtask:** Guest Induced Structural Transformation and Nanostructural Materials  
Synthesis

Praveen K. Thallapally, Jian Tian, Jian Liu and Jun Liu

[Jun.liu@pnl.gov](mailto:Jun.liu@pnl.gov)

Pacific Northwest National Laboratory  
Richland, WA 99352

**Program Scope:** The overall goal of this project is to investigate a combination of self-assembly and controlled nucleation and growth approaches for synthesizing nanostructured materials with controlled three-dimensional architectures and desired stable crystalline hybrid organic – inorganic nanostructured materials for energy applications.<sup>1-4</sup> Of importance is the understanding of crystallization in self-assembled materials in order to control both resident porosity and pore interconnectivity in these materials because these traits impart certain properties to the material that are underpinning for energy technologies including conversion and storage. The project contains the following components

- Manipulation of the kinetics of competing self-assembly and precipitation reactions
- Use of molecular ligands and interfaces to control nucleation and growth
- Multiscale modeling of the self-assembly process in solution
- Structure-property relationships for energy storage

Nanomaterials with controlled micro, nanoporosities and structural ordering are important for energy storage, catalysis, and many other energy related applications. In this project, we investigate two fundamental approaches to synthesize such materials. The first approach is molecularly directed assembly and crystallization, and the second approach is interfacially controlled nucleation and self-assembly. One class of material, metal-organic frameworks (MOFs) have come to the forefront during the last decade as a new type of well-controlled microporous materials. Fundamental understanding of the formation of such materials and the phase transitions induced by the chemical environments will provide important knowledge regarding the mechanistic of the self-assembly process and the driving force for the structural change.

### **Recent Progress:**

#### **Guest Induced Phase Transformations in Porous MOFs:**

Metal organic frameworks built with flexible ligands have shown to provide some intriguing properties such as breathing phenomena in other words framework expansion and contraction upon guest adsorption and removal. Understanding what causes these

materials to respond to external stimuli can have applications in the development of smart materials. We studied a flexible anionic metal organic framework that transformed into neutral heterobimetallic systems via single-crystal-to-single-crystal processes invoked by cation insertion. These transformations are directed by cooperative bond breakage and formation, resulting in expansion or contraction of the 3D framework by up to 33% due to the flexible nature of the organic linker (Figure 1). These MOFs displays highly selective uptake of divalent transition-metal cations (e.g.,  $\text{Co}^{+2}$  and  $\text{Ni}^{2+}$ ) over alkali-metal cations ( $\text{Li}^+$  and  $\text{Na}^+$ ).



**Figure 1.** A) Structure of the semi-rigid carboxylate linker Tetrakis[4-(carboxyphenyl)oxamethyl]methane acid ( $\text{H}_4\text{L}$ ). Its flexibility arises from twisting of the benzoate moieties around the central quaternary carbon atom (defined as  $\text{C}_{\text{core}}$ ) through etheral links. (C, grey; O: Red); B) Photos of crystals before and after  $\text{TM}^{2+}$  capture; C) Scheme showing the incorporation of  $\text{TM}^{2+}$  cations into the anionic networks to afford neutral and heterobimetallic systems via ligand-directing SC-SC structural rearrangement.

### Gas-Induced Transformation in Porous Organic Lattice:

A well-known organic host, *ris-o*-phenylenedioxy-cyclotriphosphazene (TPP), exists in two polymorphic guest-free forms: the thermodynamic nonporous high-density phase and the kinetic nanoporous low-density phase. Exposure of high density form to solvent vapors often brings a transition to hexagonal inclusion complex, with solvent molecules incorporated into the nanochannels. However, guest-free hexagonal crystals are difficult to obtain by simple evacuation of solvent molecules. Complete removal of the included guest molecules generally causes the collapse of the hexagonal host lattice to nonporous monoclinic phase. We demonstrate that simple pressurization of the high density phase with  $\text{CO}_2$  brings a solid-state transformation to the low density phase with concomitant  $\text{CO}_2$  uptake up to 12 wt% , resulting in significant expansion of the the crystal volume by 23% (Figure 2). Weak

interactions between carbon dioxide and the high-density compound collectively provide sufficient energy to expand the lattice through creation of hexagonal holes as seen in real time by X-ray diffraction measurements.

The primary building block of the lattice, a six-member

phosphazene ring, exists in planar or chair conformations. Gas adsorption induces the conformational transformation that expands the lattice. When the external pressure is released, the gas flows out of the lattice but the porous structure remains unchanged. Moderate heating recovers the initial dense phase. We are currently exploring new avenues to manipulate and control molecular packing in such materials to further enhance their gas adsorption and release properties.

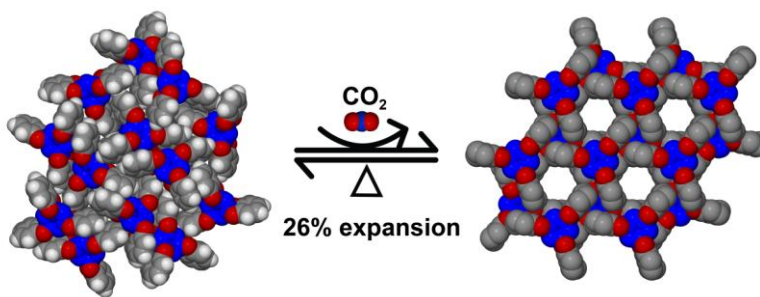


**Figure 2.** Gas-induced conversion of a nonporous high density phase (left) to hexagonal porous phase (right) with moderate pressures of  $\text{CO}_2$ .

### Recent Progress on Other Projects

Three novel crystalline forms of cucurbit[6]uril (CB[6]) have been identified by fine control over the mixing process of the hydrochloride solution of CB[6] with ethanol (Figure 3). The form that exists in nanoplate particles shows permanent porosity upon desolvation and the highest  $\text{CO}_2$  uptake (15 wt%) at 298 K and 1 bar among any known solid-state forms of CB[6]. The high selectivity in adsorbing  $\text{CO}_2$  over  $\text{N}_2$  by CB[6] form II solid can be ascribed to the high charge density at two carbonyl laced portals of CB[6] molecule, which might facilitate local-dipole/quadrupole interactions with  $\text{CO}_2$  that would be absent for  $\text{N}_2$ . In addition, the electron

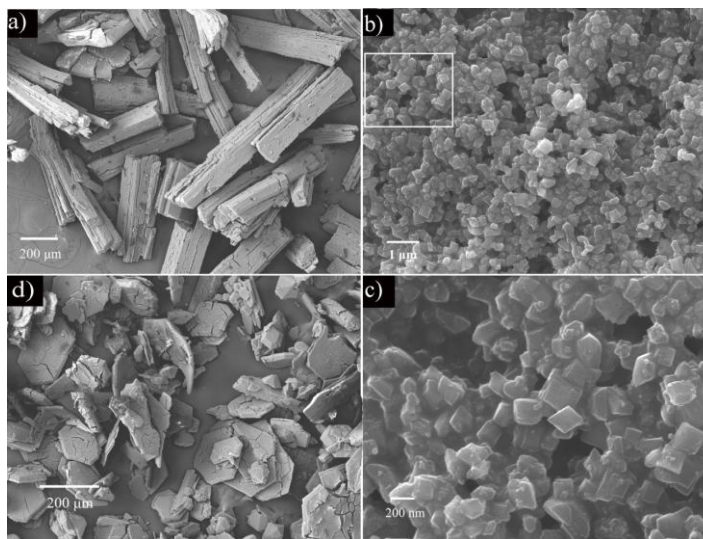


**Figure 3** Scanning electron microscopic (SEM) images of three crystalline forms of CB[6] formed by mixing its HCl solution with ethanol in different ways: (a) crystallized bar-shaped form I crystals; (b) and (c) fast-precipitated form II nanoplate particles with a diameter of 200–300 nm; the white frame in (b) marks the zoomed-in section depicted in (c); and (d) crystallized form III crystals existing as thin hexagonal plates.

lone pairs of nitrogen atoms of CB[6] molecules may have strong interaction with CO<sub>2</sub> molecules that accounts for high uptake. The adsorbed CO<sub>2</sub> in form II solid can be mostly regenerated by the pressure swing process and the remained trace CO<sub>2</sub> can be fully liberated by heating at 50 °C under vacuum.

**Future Plan:** Our future plan will pursue further fundamental understanding of the molecular level interactions by developing and using state-of-the-art characterization and simulation tools. Specifically, we will use molecular simulation and surface sensitive spectroscopy techniques to investigate the molecular interaction of and guest gas molecules such as CO<sub>2</sub> on nanostructural surfaces. The use of more complex molecules will provide more flexibility in synthesizing complex materials. Further studies will be focused on the role of surfactants on the formation of spherical, hexagonal and square shaped nanoparticles and the effect of polymer concentration in the process of nucleation and crystal. Similarly, pore expansion and contraction of metal organic frameworks, the role of functional groups, secondary building blocks and metal centers will be investigated in greater detail. For example, by incorporating photo, electro and magnetic responsive functional groups can we able to control the porosity of metal organic frameworks by applied light and potential will be investigated.

**BES Sponsored Publications in 2011 - 2013 from current subtask**

Total publications = 3, 1 cover art and 2 review articles

- J. Tian, L. V. Saraf, B. Schwenzer, S. M. Taylor, E. K. Brechin, J. Liu, S. J. Dalgarno, and P. K. Thallapally, “Selective Metal Cation Capture by Soft Anionic Metal–Organic Frameworks via Drastic Single-Crystal-to-Single-Crystal Transformations” *J. Am. Chem. Soc.*, 134, 9581–9584 (2012)
- J. Tian, J. Liu, J. Liu and P. K. Thallapally, “Identification of solid-state forms of cucurbit[6]uril for carbon dioxide capture” *CrystEngComm*, 15, 1528-1531 (2013)
- J. Tian, P. K. Thallapally and B. P. McGrail, “Porous organic molecular materials” *CrystEngComm*, 14, 1909-1919 (2012, Highlight).
- J. Liu, P. K. Thallapally, B. P. McGrail, D. R. Brown and J. Liu, *Chem. Soc. Rev.*, “Progress in adsorption-based CO<sub>2</sub> capture by metal–organic frameworks”, 41, 2308-2322 (2012 Critical Review)
- J. Tian, P. K. Thallapally, J. Liu, G. J. Exarhos and J. L. Atwood, “Gas-induced solid state transformation of an organic lattice: from nonporous to nanoporous” *Chem. Commun.*, 47, 701-703 (2011)

## Nanoscale Morphologies to control Atomic scale Processes

K.M. Ho<sup>1,2</sup>, M.Hupalo<sup>1</sup>, P. A. Thiel<sup>1,3</sup>, M.C.Tringides<sup>1,2</sup> and C. Z. Wang<sup>1</sup>

<sup>1</sup> Ames Laboratory, <sup>2</sup> Department of Physics-ISU, <sup>3</sup> Department of Chemistry-ISU  
Ames IA 50011

### Project Scope

The goals of the FWP are to grow epitaxially controllable nanostructures on a variety of substrates and, once controllable morphologies are grown, to study different technologically important problems for which such structures will be useful. Since growth is far from equilibrium and a wealth of metastable structures is possible, control requires better understanding of mass transport (diffusion, nucleation, coarsening etc.). Utilizing its previous expertise, this FWP grows and uses tunable metal morphologies in three areas: (a) to study metal growth on graphene and graphite for improved metal contacts and to determine the extent to which the metal-carbon interaction can modify the electronic structure of graphene. ((b) to grow metal defect-free nanowires on carbon coated surfaces to elucidate the underlying growth mechanisms and optimize the wire geometry for magnetic applications; (c) to investigate enhanced reactivity of adsorbed gases on metal islands (hydrogen adsorption on Mg islands relevant to hydrogen storage). In all three problems the synergistic interaction between theory and experiment is essential to attain understanding and predictability.

### Recent Progress

**Metal growth on graphene/graphite** New properties emerge on the nanoscale that are not present in bulk materials. To exploit these advantages, it is essential to find ways to produce nanostructures of controllable size and morphology since their stability and properties can be tuned to a specific application. In the three problems mentioned previously we aim to identify conditions where the relevant morphology can be realized (layer by layer for graphene, dislocation-free high aspect ratio nanowires and 3-d wedding cake-like growth to

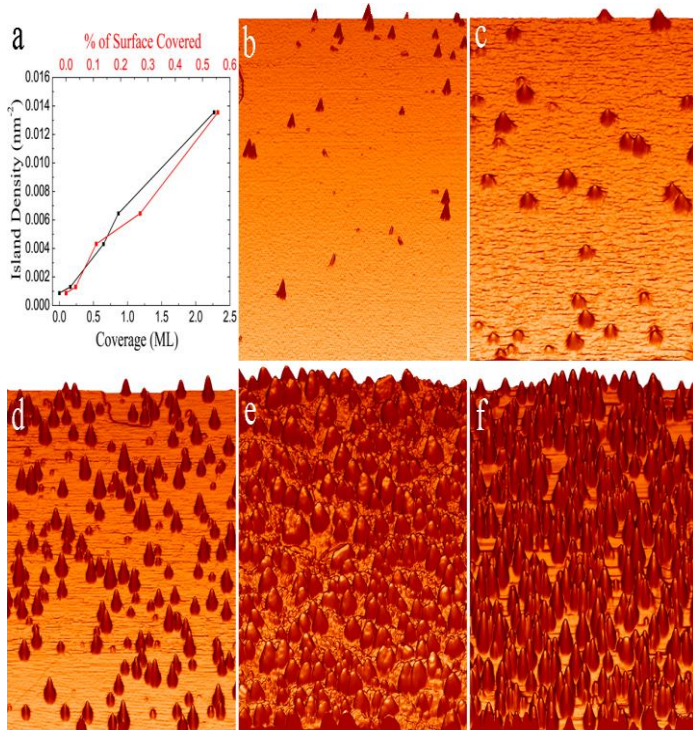


Figure 1: (a) Island density  $n$  vs  $\theta$  for Fe grown on graphene at room temperature showing a monotonic dependence on  $\theta$ . (b-f) Corresponding images at different  $\theta$ ; (b) 0.003ML, (c) 0.16ML, (d) 0.65ML, (e) 0.87ML, and (f) 2.3 ML. All images are 200 x 200 nm<sup>2</sup> except (c) which is 150 x 150 nm<sup>2</sup>.

optimize reactivity etc.). Graphene is a material of recent intensive studies due to its novel electronic and structural properties[G-1]. Metals grown on graphene also have been of interest because of their use as metal contacts in graphene devices, for spintronics applications and for catalysis. Controlled deposition experiments on several metal systems (Fe, Gd, Dy, Eu,Pb) have identified the growth mode.[1,2,4,9,11-14,21,22]. A common method to study the grown morphology is to measure the nucleated island density  $n$  as a function of growth parameters, temperature  $T$ , flux rate  $F$  and coverage  $\theta$ . From these measurements the metal diffusion and adsorption barriers can be extracted. It was found that metal with unfilled inner (Fe, Gd, Dy) have high barriers while s-p metals(Pb) have low barriers and Eu has barriers in between. All metals grow 3-d (except Eu that shows extended terraces) which is not promising for good metal contacts. These experimental results have been fully confirmed with DFT calculations that determine the type of bond and charge transfer between the metal and graphene atoms.

Besides these general results about metal growth some metals show special results. Surprisingly

the growth of Fe on graphene shown in fig.1 is unusual because it does not follow classical nucleation:  $n$  is unexpectedly high, and shows no temperature dependence[12]. These unusual results indicate the presence of long range repulsive interactions. Kinetic Monte Carlo simulations and DFT calculations support this conclusion. Dysprosium was deposited on epitaxial graphene and the majority of the grown islands have triangular instead of hexagonal shapes, expected from its bulk hcp crystal structure. We analyze the island shape distribution and stacking sequence of successively grown islands to deduce that the Dy islands have fcc(111) structure[22].

We have studied the nucleation and growth of Cu on graphite shown in fig.2. We find that Cu decorates step edges and also forms 3-d hexagonal islands on the terraces. A weak dependence of island density on temperature and flux suggests a very low diffusion barrier, in agreement with DFT calculations. Upon annealing, significant coarsening occurs above 600 K. The island density observed at 300 K is too high to be defect-mediated, but is also higher than the maximum value predicted by nucleation theory. The high density is most likely due to a long-range repulsive interaction between Cu atoms, analogous to the interactions for Fe on graphene. The effect of repulsions has been modeled quantitatively with Kinetic Monte Carlo simulations.

**QSE modification in Ag/Si(111) by oxygen** We have used STM to probe the effect of oxygen exposure on an ensemble of Ag islands separated by a Ag wetting layer on Si(111)-(7x7)[15]. Starting from a distribution dominated by islands that are 1 layer high, coarsening at room temperature leads to growth of 2-layer islands, as expected from Quantum Size Effects (QSE). If, however, the sample is exposed to oxygen, coarsening leads to growth of 3-layer islands. Density functional theory supports a model of oxygen adsorbing on top of the Ag islands and changing the height-dependent relative stabilities of the Ag islands.

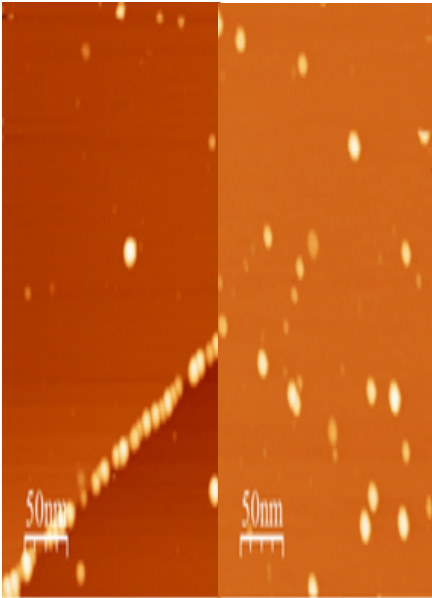


Figure 2: STM image showing preferential nucleation along steps (left). With further deposition the island density is higher, than what expected from the low diffusion barrier, which suggest repulsive adatom interactions.

**Mass transport in Pb/Si(111) and Ag/Si(111)** The Pb/Si(111) wetting layer has shown unusual mobility at low temperatures  $T \sim 180K$  because its motion is superdiffusive  $x \sim t$  not classical  $x \sim t^{1/2}$ . The layer is responsible for the formation of single height 7-layer Pb islands due to QSE[G-2]. This unusual diffusive motion was partially accounted for by using the Frankel Kontorova (FK) model[18]. More recent experiments have shown that in addition to the motion of a steep concentration gradient that moves unperturbed, an oppositely directed and equally sharp front provides the mass required to refill an initially vacant hole[20]. The motions of both fronts and the concentration profiles are highly correlated suggesting an exceptional collective super-diffusive mechanism.

The Ag growth on the Si(111)-Ag( $\sqrt{3} \times \sqrt{3}$ )R30° phase was studied to understand the  $\sqrt{3} \times \sqrt{3}$  nucleation and the role islands and holes differing by one step height play. DFT (implemented as a genetic algorithm search) supported the experimental conclusion that the Si:Ag ratio is always 1:1 under all growth conditions. In addition the diffusion of Ag on  $\sqrt{3} \times \sqrt{3}$  was studied by measuring the nucleated island densities over a wide temperature range[8]. Two different regimes were found. At 50-125 K, islands were small and their density decreased only slightly with increasing temperature. Above 180 K, the islands were larger, and island density decreased strongly with increasing temperature. These temperature dependencies indicate that there is a change of critical size cluster from  $i_c=1$  to  $i_c=4$  around 180 K, and the diffusion barrier of a single Ag atom is 0.22 eV, in excellent agreement with the value calculated by another group[8]. The long diffusion lengths are thus due to a “normal” diffusion barrier and a rather large critical size, with the latter simply preventing Ag islands from being captured on terraces.

## Future work

***Layer by layer growth of metal growth on graphene*** In almost all cases, metal adsorption on graphene was 3-d, confirmed theoretically, since the adsorption energy of a metal atom on graphene is smaller than the metal cohesive energy. For metal contact applications it is important to find ways to grow metals 2-d (layer-by-layer). 2-d growth on graphene was possible with Co films (deposited on graphene grown on Ir(111)) using pulsed laser deposition[G-3]. The 2-d growth was attributed to an effective high flux which promotes interlayer diffusion. High flux rates will be also used in the proposed epitaxial metal studies. Even surfactants will be co-deposited that are known to change 3-d to 2-d growth and this FWP has extensive experience in these issues.

For ideal metal contacts (i.e., 2-d growth and no contact resistance) theoretical studies were performed for Al-and Co- graphene contacts[G-4]. Even under idealized conditions of 2-d growth, the mapping of the Dirac cone structure, as a function of position away from the contacts, shows strong deviations for Co (but not for Al) from ideal graphene. Understanding how the spatial variation of the electronic structure degrades, under the more realistic metal deposition conditions (i.e. for 3-d growth, for strained interfaces, etc.) are questions to be pursued.

The extent to which the unique electronic structure of graphene is modified by the metal-C interaction, requires better understanding of the deposited metal location and distribution. Metal deposition will be carried out in a controlled way: after annealing from low to high temperature T, the changing film morphology and diffusion towards the interface will be correlated with potential changes of the graphene electronic structure. While STM images will provide information about the changing morphology, in collaboration with A. Kaminski we will measure with ARPES the changes in the graphene electronic structure. These experiments are important, because many device applications require operations at high temperatures, so the stability range will depend on how the metal adatoms are distributed at the interface.

***Comparison of metals on carbon-based substrates, and control of metal nanowire growth on C coated Si(111) substrates.*** We have obtained valuable information regarding the energetics that influence diffusion and nucleation of Cu atoms on graphite. We next plan to study growth of Cu on n-layer graphene supported on SiC, in order to determine the influence of the van der Waals forces between carbon sheets on the metal. This in turn will reveal which aspects of metal growth can be tailored by changing the number of carbon layers. We will undertake a similar comparison for Dy, motivated in part by our recent investigation of growth of Dy on graphene[22] and in part by the status of Dy as a prototype magnetic metal. The main experimental approach will be to measure the temperature-and/or flux-dependent island densities and to compare the results with theory. Classically, this provides diffusion barriers, metal-metal bond strengths in small nuclei, and insight into whether nucleation is heterogeneous or homogeneous. We will also study growth and nucleation of metals on amorphous carbon surfaces supported on Si, because these substrates have proven to be effective surfaces for nanowire growth[G-5]. To our knowledge, there is no model to predict nanowire morphology that is based on an iterative combination of theory and experiment such as we will provide. We are also investigating the possibility of transition metal intercalation between carbon sheets on graphite. Preliminary results are in good agreement with predictions from DFT. Understanding transition metal intercalation could provide insight into metal transport between carbon surfaces and underlying materials, such as the amorphous carbon on Si which is effective for metal nanowire growth.

### ***Controllable Mg film morphologies and enhanced H<sub>2</sub> adsorption.***

A more challenging system (compared to O<sub>2</sub> on Mg) is adsorption of H<sub>2</sub> on Mg films, since the process is not possible on bulk Mg(0001). Preliminary experiments on thick Mg films (~15 ML) grown on two substrates Si(111) and W(110) have produced promising controllable morphologies. As expected rougher morphologies are produced on Si(111) than on W(110) because of the larger strain. After deposition at 100 K wedding cakes are produced on both substrates, but the ones on Si(111), are at least twice as steep as the wedding cakes for Mg on W(110).

These nanoscale morphologies will be explored to test if H<sub>2</sub> adsorption can be enhanced on the nanoscale. This is relevant to finding new materials for hydrogen storage[G-6]. With a rich variety of Mg film morphologies, or by using transition metals as catalysts or by possibly QSE-induced reactivity, we plan to carry out several controlled experiments of H<sub>2</sub> adsorption on Mg. We will explore first H<sub>2</sub> adsorption on the open morphologies of wedding-cakes and dislocation networks which have a large fraction of low coordination sites. The importance of steps in promoting H<sub>2</sub> dissociation was shown in earlier experiments on stepped Pt surfaces[G-7]. In addition for uniform height islands or films where QSE are clearly seen, enhancement of H<sub>2</sub> adsorption (as found for O<sub>2</sub>) might be possible.

### General Publications

- G-1. K.S. Novoselov, et al. *Science* 306, 666 (2004).
- G-2 M.C. Tringides, M. Jalochoowski, and E. Bauer, *Phys. Today* 60 (2007): 50
- G-3 C. Vo-Van, et al. *New J. Phys.* **12**, 103040 (2010)
- G-4 S. Barraza-Lopez, et al. *Phys. Rev. Lett.* **104**, 076807 (2010).
- G-6 G. Richter et al. *Nano Lett.* **9**, 3048 (2009).
- G-6 P.T. Sprunger and E. W. Plummer, *Surf. Sci.* **307**, 118 (1994)
- G-7 R.J. Gale, et al. *Phys. Rev. Lett.* **38**, 1027 (1977).

### Publications of the FWP since 2011

1. M. Hupalo S. Binz and M. C. Tringides *JCMP* 23 045005 (2011)
2. M. Hupalo , X. Liu, C. Z. Wang, Wen-Cai Lu, Y. X. Yao, K. M. Ho, and M. C. Tringides *Advanced Materials* 23 2082 (2011)
3. Z. Chvoj, M. C. Tringides, Z. Cromcova *JCMP* 23 215307 (2011)
4. X. Liu, C. et al. *Phys. Rev.B* 83 325411 (2011)
5. M.W. Gramlich, et al . *Phys. Rev. B* 84 075433 (2011)
7. M. Yakes and M. C. Tringides *Jou. of Phys. Chem. A* 115 7096 (2011) invited paper
8. A. Belianinov, B. Ünal, K.-M. Ho, C.-Z. Wang, J. W. Evans, M. C. Tringides, and P. A. Thiel *JPCM* 23 265002 (2011)
- 9 X. Liu, C. Z. Wang, M. Hupalo, W.C. Lu, P. A. Thiel, K. M. Ho, and M. C. Tringides *Phys. Rev. B* 84 235446 (2011)
- 10 D. Vlachos, M. Kamaratos, S.D. Foulis, S. Binz, M. Hupalo and M.C. Tringides *JPCM* 24 095006 (2012)
- 11 T. Li, L. Luo, M. Hupalo, J. Zhang, and M. C. Tringides J. Schmalian. J. Wang *Phys. Rev. Lett.* 108, 167401 (2012)
- 12 S.M.Binz ; M.Hupalo ; X.J. Liu; C. Z. Wang ; W.C.Lu ; P. A. Thiel ;K.M. Ho K; E.H. Conrad ; M.C.Tringides . 2012. *Phys. Rev. Let.* 109:026103.
- 13 X. Liu, C. Z. Wang, Y. X. Yao, W. C. Lu, M. Hupalo, M. C. Tringides, and K. M. Ho *Phys. Chem. Chem. Phys.*, 2012, 14, 9157–9166
- 14 X. Liu, M. Hupalo, C. Z. Wang, Wen-Cai Lu, P. A. Thiel, K. M. Ho, and M. C. Tringides *Phys. Rev. B* 86, 081414(R) (2012)
- 15 D. Shao, X. Liu, N. Lu, C.-Z. Wang, K.M. Ho, M.C. Tringides and P.A. Thiel *Surf. Sci.* 606 (2012) 1871–1878
16. A. Belianinov, B. Ünal, M. C. Tringides, and P. A. Thiel *J. Vac. Sci. Technol. B* 30(5), (2012)
17. T. Duguet and P. A. Thiel 2012. *Progr. in Surf. Sci.* 87:47-62 (2012)
18. Huang L; Wang C Z; Li M Z; Ho K M *Phys. Rev. Let.* 108:026101
19. A. K.Engstfeld, at al .*Phys. Rev. B.* 86:085442 (2012)
20. K. L. Man, M. C. Tringides, M. M. T. Loy, and M. S. Altman *Phys. Rev. Lett.* 110, 036104 (2013)

21. X. Liu ,et al. *Crystals* **2013**, 3(1), 79-111; doi:10.3390/cryst3010079
22. M T Hershberger, M Hupalo, P A Thiel and M C Tringides *JCMP* 25 225005 (2013)
23. Z. Chromcova, M. C. Tringides and Z. Chvoj *J. Phys.: Condens. Matter* *JCMP* 25 (2013) 265003
24. A.V. Matetskiy, L.V. Bondarenko, D.V. Gruznev, A.V. Zotov, A.A. Saranin, and M.C. Tringides *JCMP* 25 (2013) 395006
25. G.P.Zhang, X.J. Liu, C. Z.Wang, Y.X.Yao J. Zhang, K.M. Ho *JCMP* 25:105302 (2013).
26. X. Liu, C. Z. Wang, M. Hupalo, H.Q. Lin, K.M. Ho, and M. C. Tringides *Phys. Rev. Lett.* (submitted).
27. H. Lei , C. Z.Wang , Y. Yao, Y. Wang, M. Huapalo, D. McDougal , M. Tringides, and K.M. Ho *Jou. Chem. Phy.*(submitted).

## Growth Mechanisms and Controlled Synthesis of Nanomaterials (ERKCS81): Modeling and Characterization of Ultrasmall Nanoparticles

Mina Yoon,<sup>1</sup> David B. Geohegan,<sup>1</sup> Alex Puzetzkyy,<sup>1</sup> Christopher M. Rouleau,<sup>1</sup> Gyula Eres,<sup>2</sup>  
Masoud Mahjouri-Samani,<sup>1</sup> Miaofang Chi,<sup>2</sup> Mengkun Tian,<sup>3</sup> and Gerd Duscher<sup>2,3</sup>

<sup>1</sup>Center for Nanophase Materials Sciences and <sup>2</sup>Materials Science and Technology Division,  
Oak Ridge National Laboratory, Oak Ridge, TN 37831 and  
the <sup>3</sup>Dept. of Materials Science and Engineering, Univ. of Tennessee, Knoxville, 37996

### Program Scope

The overarching goal of the research program is to understand the link between the growth mechanisms and the resulting structure of nanoscale materials. The emphasis is on the development of real-time methods to induce and probe chemical and physical transformations away from thermodynamic equilibrium in order to controllably synthesize nanomaterials with enhanced properties resulting from metastable structures. The approach relies on correlating the real-time diagnostic measurements with predictive theoretical methods and post-growth characterization by imaging, spectroscopy, and atomic-resolution analytical electron microscopy to develop a framework for the deterministic synthesis of nanomaterials with desired properties. A distinguishing feature of the program is the development and application of time-resolved, in situ diagnostics of nanomaterial growth kinetics and a corresponding development of models to understand the underlying kinetic and chemical pathways. Spatial confinement and reactive quenching approaches are developed to explore the synthesis mechanisms of rationally-designed nanostructures with enhanced intrinsic properties, targeting: (1) oxide, carbon, and alloy nanomaterials produced in metastable states by catalyst-free or catalyst-mediated processes, and (2) doped, decorated, and filled nanomaterial hybrids designed to induce permanent electric fields or distribute charge within nanostructures. Theoretical methods are used to understand fundamental mechanisms of synthesis in order to guide the formation of nanostructures tailored to enhance energy storage, catalysis, thermal management, and photovoltaics in support of DOE's energy mission.

### Recent Progress

#### *Synthesis and Characterization of Ultrasmall TiO<sub>2</sub> nanoparticles*

TiO<sub>2</sub> nanoparticles were synthesized in the gas phase by pulsed KrF-laser ablation of a ceramic TiO<sub>2</sub> target and subsequent condensation of the laser-induced plume in a background gas. Transmission electron microscopy grids (TEM) were placed 2-7 cm from the target to collect nanoparticles at room temperature from locations within, at the leading edge, and outside the laser induced plume under different oxygen background pressures. It was found that ultrasmall nanoparticles (UNPs) in the range of 2-5nm were produced for a background pressure of 200 mTorr at a distance of 5cm from the target.

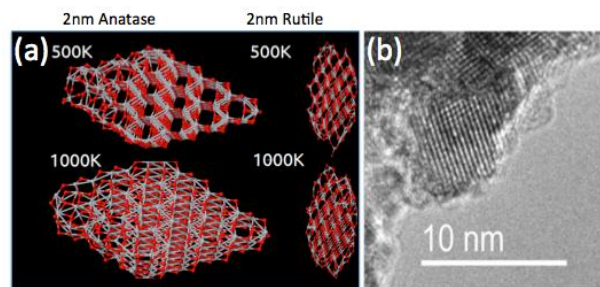


**Figure 1.** (a) Atomic configurations of 2nm anatase and rutile nanoparticles at 500K and 1000K. (b) TEM images of TiO<sub>2</sub> nanoparticles.

The UNPs were studied with high resolution transmission electron microscopy equipped with high resolution electron energy loss spectroscopy to measure their size distribution, crystallinity, phase, and crystal field splitting. Crystal field splitting, and therefore degree to which a particular UNP can be unambiguously ascribed to a particular phase – i.e., anatase or rutile - was observed for nanoparticles in excess of 5nm. For smaller nanoparticles with an unidentifiable phase, the increasing lack of crystal field splitting is currently under investigation using theoretical approaches.

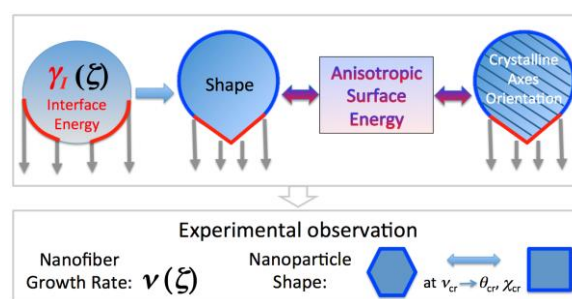
Our theoretical approach combines Monte Carlo simulations that are based on the Matsui-Akaogi force-field [1] and conjugate gradient method to identify the atomic configurations of the UNPs observed experimentally. Our initial configurations were based on the anatase and rutile phase of bulk TiO<sub>2</sub>. The accuracy of our approach has been confirmed against previously published results on the (TiO<sub>2</sub>)<sub>n</sub> (n<10) systems<sup>1,2</sup>, and represents the first step in a screening process that ultimately seeks to produce the global minima for 1 and 2-nm TiO<sub>2</sub> nanoparticles. We applied a hybrid process combining Monte Carlo simulations for large-scale coverage of the energy surface, and a conjugate gradient global optimizer to locate the minima based on the Monte Carlo output.

Figure 1a shows excerpts from simulations that were performed for 2nm anatase and rutile structures at temperatures from 500 to 2000K, and with 2x10<sup>7</sup> Monte Carlo trial steps for sufficient energy convergence. The systems were kept at constant volume and allowed to relax before proceeding with structural optimization using the conjugate gradient technique. At 500K, localized melting was found to occur at the left facet of the anatase structure while most of the remaining crystal remained well-ordered. In general, however, the disorder in bond length density of states was found to increase, but even at 1000K the anatase structure still only melted in localized areas. At 1500K, however, increased localized melting occurred in the anatase structure, extending to both ends and the forward- and rear-facing surfaces. By 2000K, anatase completely melted and rutile was only just showing initial signs of localized melting. Although Collins et al. reports that the melting point of bulk TiO<sub>2</sub> to be 2150K, it is expected that this value will be depressed in smaller scale particles [3].

### ***How the shape of catalyst nanoparticles determines their crystallographic orientation during carbon nanofiber growth***

A theoretical model was developed that explains spontaneous changes in the crystalline orientation of nanoparticles. The changes in crystalline orientation are attributed to the crystal anisotropy of the surface energy of the particles. We consider the case of carbon nanofibers growth, where previous studies have shown that both the catalyst nanoparticle shape and the nanofiber growth rate change with the chemical potential of diluted carbon. The model reveals the mechanism by which the shape and crystallographic orientation of the catalyst nanoparticle are linked to the nanofiber growth rate.

Figure 2 illustrates the physical process responsible for the shape changes and the reorientation of catalyst nanoparticle crystalline axes that have been observed experimentally with changing carbon nanofiber



**Figure 2.** Diagram illustrating the physical process responsible for the shape changes and the reorientation of catalyst nanoparticle crystalline axes that have been observed experimentally.

growth rate. The chemical potential of carbon in the catalyst particle not only determines the nanofiber growth rate, but also determines the interface energy between the catalyst particle and the nanofiber. This interface energy governs the shape of the catalyst nanoparticle, and the crystal anisotropy of the surface energy of the nanocrystalline particles drives the orientation of their crystallographic axes. Thus, the shape and crystallographic orientation of catalyst nanoparticles are governed by the interface energy with the carbon<sup>4</sup>.

### Understanding the nitrogen doping of TiO<sub>2</sub> nanotube arrays

Identification of the phases of ultrasmall nanoparticles (UNPs) is still a challenging experimental task, and although theory sometimes assumes the phase of UNPs mimic those of the bulk, it is not clear whether such phases would indeed be most stable for a nanoscale feature where, characteristically, most of the atoms are exposed. Note that TiO<sub>2</sub> thin films, which also have a large portion of atoms exposed, is not so easily doped with impurity atoms whereas nanoparticles of the same material are.

Given that most of the energetically accessible doping processes occur at the surfaces of nanoparticles and films, we have performed atomistic modeling of the surface structures, and generalize them as atomistic steps, where an infinitely large step would correspond a flat film. We have considered many different types of atomic step-edges of different steps widths and surface terminations (see Fig. 3a,b), and by comparing their energetics we found that the energy of the steps with the least stable edge termination (Fig. 3a) has a dependence on tube diameter, and therefore step-width, shown in the right panel of Fig. 3a. Conversely, the energy of all the other configurations, including the steps with the most stable edge termination (Figure 3b), stays constant with respect to tube diameter, and by extension, step-width size. Interestingly, the energy of the most *unstable* step configurations can become stable only for very small widths – i.e., diameter of less than ~5nm – and indicates that the atomic configurations of nanoscale surfaces of different curvature can have a qualitatively different nature. For nanotube (or nanoparticle) less than 5nm in diameter, it may be chemically very active only because of the atomistic arrangement of its surface.

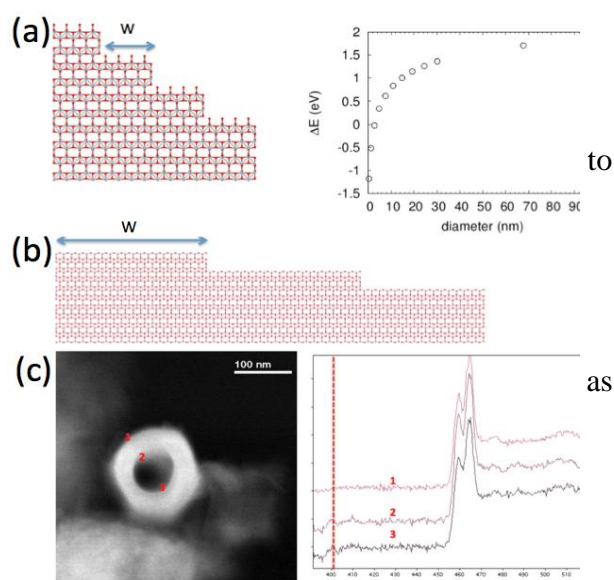


**Figure 3.** Theoretical modeling of TiO<sub>2</sub> nanotube surfaces; the least stable (a) and the most stable (b) edge terminations. Only the most unstable structure has a strong energy dependence on the edge width as shown in the graph. EELS study of individual nitrogen-doped TiO<sub>2</sub> nanotubes along the radial direction (c).

This theoretical study helps to explain the nature of nitrogen doping in the coaxial TiO<sub>2</sub> nanotubes shown in Figure 3c, where a significantly higher doping concentration was found on the inner surface than the outer. Coaxial TiO<sub>2</sub> nanotubes were self-organized during anodization, and had tube diameters ranging from 40 to 150nm, wall thicknesses from 5 to 50nm, and lengths from 1 to 10 μm. Doping was accomplished by post annealing in hydrogen and ammonia. The most interesting feature of the N-doped nanotube arrays is the radial variation in nitrogen doping concentration (see Fig. 3c), which is driven by curvature according to our theory.

## Future Plans

Ultrasmall nanoparticles (UNPs) show very unique features and they can be used as building blocks for synthesis of other nanoscale materials. Therefore, identifying and understanding their structures, phases, and interactions are central to control synthesis of nanowires, nanoparticle assemblies, thin films, and 2D nanosheets from the UNPs. To address this challenge, our theoretical approach to explore a configuration space of molecules by combining efficient total energy calculations and computational optimizer algorithm will be further developed and applied to the UNPs building blocks. Once those intermediates or nanoclusters are identified for a given experimental condition, detailed analysis of their structural and electronic properties will be performed using state-of-the-art first-principles approaches, where theoretical results will be compared with experimental data such as HRTEM, XRD, EELS. Then, we will move forward to model processes of doping of UNPs and process of forming larger nanostructures through melting and sintering UNPs at high temperatures.

## References

1. M. Matsui and M. Akaogi, *Mol. Simul.* **6**, 239 (1991).
2. D. R. Collins and W. Smith, Technical Report DL-TR-96-001: Evaluation of TiO<sub>2</sub> Force Fields; Council for the Central Laboratory of Research Councils (1996).
3. D. R. Collins, W. Smith, N. M. Harrison, and T. R. Forester, *J. Mater. Chem.* **7**, 2543 (1997).
4. I.A. Merkulov, M. Yoon, D.B. Geohegan, "How the shape of catalyst nanoparticles determines their crystallographic orientation during carbon nanofiber growth", *Carbon* **60**, 41 (2013).

## DoE Sponsored Publications in the Last Two Years

1. K. R. S. Chandrakumar, J.D. Readle, C.M. Rouleau, A.A. Puretzky, D.B. Geohegan, K. More, V. Krishnan, M. Tian, G. Duscher, B. Sumpter, S. Irle, K. Morokuma, "High-temperature transformation of Fe-decorated single-wall carbon nanohorns to nanoysters: a combined experimental and theoretical study", *Nanoscale* **5**, 1849 (2013).
2. I.A. Merkulov, M. Yoon, D.B. Geohegan, "How the shape of catalyst nanoparticles determines their crystallographic orientation during carbon nanofiber growth", *Carbon* **60**, 41 (2013).
3. J. Jacimovic, R. Gaal, A. Magrez, L. Forro, M. Regmi, G. Eres, "Electrical property measurements of Cr-N codoped TiO<sub>2</sub> epitaxial thin films grown by pulsed laser deposition", *Appl. Phys. Lett.* **102**, 172108 (2013).
4. A.A. Puretzky, D.B. Geohegan, S. Pannala, C.M. Rouleau, M. Regmi, N. Thonnard, G. Eres, "Real-time Optical Diagnostics of Graphene Growth Induced by Pulsed Chemical Vapor Deposition", *Nanoscale*, **5**, 6507 (2013).
5. S. Dai, B. Guo, X.-G. Sun, P.F. Fulvio, G.M. Veith, R.T. Mayes, S. Brown, J. Adcock, D.B. Geohegan, S.M. Mahurin, A.A. Puretzky, C.M. Rouleau, "Fluorination of "brick and mortar" soft-templated graphitic ordered mesoporous carbons for high power lithium-ion battery", *J. Mater. Chem. A* **1**, 9414 (2013).
6. K. Li, G. Eres, J. Howe, Y.-J. Chuang, X. Li, Z. Gu, L. Zhang, S. Xie, Z. Pan, "Self-Assembly of Graphene on Carbon Nanotube Surfaces", *Scientific Reports* **3**, 2353 (2013).

7. D.B. Geohegan, A.A. Puzetzky, M. Yoon, G. Eres, C. Rouleau, K. Xiao, J. Jackson, J. Readle, M. Regmi, N. Thonnard, G. Duscher, M. Chisholm, K. More, "Laser Interactions for the Synthesis and *in situ* Diagnostics of Nanomaterials", Book chapter: in Springer Series in Materials Science (2013).
8. S.-J. Woo, E.-S. Lee, M. Yoon, Y.-H. Kim, "Finite-Temperature Dihydrogen Adsorption/Desorption Thermodynamics Driven by Soft Vibration Modes", *Phys. Rev. Lett.* **111**, 066102 (2013).
9. D.B. Geohegan, I.N Ivanov, A.A. Puzetzky, S. Jesse, B. Hu, M. Garrett, B. Zhao, "Transparent conductive nano-composites", US patent 8540542 B2 (2013).
10. A.A. Puzetzky, D.B. Geohegan, J. J. Jackson, S. Pannala, G. Eres , C.M. Rouleau, K.L. More, N. Thonnard, J. D. Readle, "Incremental Growth of Short SWNT Arrays by Pulsed Chemical Vapor Deposition", *Small* **8**, 1534 (2012).
11. Y. Liu, C. Brown, D. Neumann, D.B. Geohegan, A.A. Puzetzky, C.M. Rouleau, H. Hu, D.J. Styers-Barnett, P.O. Krasnov, B.I. Yakobson, "Metal-Assisted Hydrogen Storage on Pt-Decorated Single-Walled Carbon Nanohorns," *Carbon* **50**, 4953 (2012).
12. K. Lee, K. Berland, M. Yoon, S. Andersson, E. Schroeder, P. Hyldgaard, and B.I. Lundqvist, "Benchmarking van der Waals density functionals with experimental data: potential energy curves for H<sub>2</sub> molecules on Cu(111), (100), and (110) surfaces" *J. of Physics: Condensed Matter* **24**, 424213 (2012).
13. D.B. Geohegan, A.A. Puzetzky, C.M. Rouleau, M. Regmi, J.J. Jackson, J. Readle, K. More, G. Eres and G. Duscher, Nonequilibrium Laser Synthesis and Real-Time Diagnostics of Carbon Nanomaterial Growth, *Proceedings of 31st International Congress on Applications of Lasers & Electro-Optics (ICALEO-2012)*.
14. R. Sachan, S. Yadavali, N. Shirato, H. Krishna, V. Ramos, G. Duscher, S. J. Pennycook, A. K. Gangopadhyay, H. Garcia, and R. Kalyanaraman, "Self-Organized Bimetallic Ag-Co Nanoparticles with Tunable Localized Surface Plasmons Showing High Environmental Stability and Sensitivity", *Nanotechnology*, **23**, 275604 (2012).
15. M. Chisholm, G. Duscher, W. Windl, "Oxidation Resistance of Reactive Atoms in Graphene" *Nano Letters*, **12**, 4651 (2012).
16. A. K. Kothari, B. W. Sheldon, G. Eres, "Thickness Limitations in carbon nanotube reinforced silicon nitride coatings synthesized by vapor infiltration", *Acta Materialia*, **60**, 7104 (2012).
17. M. Regmi, M.F. Chisholm, G. Eres, "The Effect of Growth Parameters on the Intrinsic Properties of Large-Area Single Layer Graphene Grown by Chemical Vapor Deposition on Cu", *Carbon* **50**, 134 (2011).
18. D.B. Geohegan, A.A. Puzetzky, J.J. Jackson, C. M. Rouleau, G. Eres, K.L. More, "Flux-Dependent Growth Kinetics and Diameter Selectivity in Single-Wall Carbon Nanotube Arrays", *ACS Nano* **10**(5), 8311 (2011).
19. X. Liu, S. Sen, J. Liu, I. Kulaots, D.B. Geohegan, A. Kane, A.A. Puzetzky, C.M. Rouleau, K.L. More, G. Tayhas, R. Palmore, R.H. Hurt "Antioxidant Deactivation on Graphenic Nanocarbon Surfaces", *Small* **7**, 2775 (2011).
20. M. Yoon, H. Weitering, Z. Zhang, "First-principles studies of hydrogen interaction with ultrathin Mg and Mg-based alloy films", *Phys. Rev. B* **83**, 045413 (2011).

# **University Grants' Abstracts**

This page is intentionally blank.

# Understanding Graphene Crystal Morphology Evolution and Orientation During CVD on Cu; and the Bottom-Up Growth of Graphene Nanostructures with Refined Edges

Michael S. Arnold  
msarnold@wisc.edu

Department of Materials Science and Engineering  
University of Wisconsin, Madison, WI 53706

## Program Scope

Graphene has received tremendous attention because of its exceptional properties such as its ultrafast charge transport characteristics<sup>1, 2</sup>; excellent mechanical strength, flexibility, and resilience<sup>3</sup>; outstanding thermal conductivity<sup>4</sup>; and its ultrahigh surface area / volume ratio. The nanostructuring of graphene further enhances its properties by altering its electronic structure, opening an energy gap resulting in semiconducting behavior<sup>5-7</sup>, and increasing the accessibility of the surfaces and the edge density. The exceptional properties of nanostructured graphene materials have the potential to lead to advances in next-generation photovoltaic energy harvesting, energy storage, and semiconductor-based logic and sensing. These technological advances will be possible, however, only if the synthesis of planar nanostructured graphene materials can be realized with high quality and by rationally controllable means.

Traditionally, planar nanostructured graphene materials have been fabricated by growing continuous sheets of graphene and then etching the sheets into nanostructures, from the top-down. However, the top-down nanopatterning of graphene is severely limited by the etching tools that are available, which induce substantial defects, oxidation, and disorder. These defects *degrade* materials performance: for example, the electron mobility in sub-20 nm graphene nanoribbons patterned using reactive ion etching has been shown to be ~1/10,000 of unpatterned graphene due to disorder.<sup>5, 8, 9</sup> Therefore, while the properties of unpatterned graphene materials are exceptional, the properties of nanostructured graphene materials have, thus far, not been exceptional, by most measures.

The overarching scope of this project is to overcome this challenge and to learn how to synthesize both monolayered and multilayered nanostructured graphene materials without highly detrimental etch-induced disorder and with exceptional properties – from the bottom-up via chemical vapor deposition.

## Recent Progress

Recent progress has been made in 3 directions: **(A)** Growing graphene nanostructures from the bottom-up via a newly developed synthetic approach we call barrier-guided CVD (BG-CVD); **(B)** Understanding, more generally, the epitaxy, faceting, and crystal morphology evolution of continuous sheets of graphene on epitaxially oriented Cu thin films during CVD, the results of which tie into developing **(A)** but have much broader implications for growing high quality, continuous graphene

materials; and (C) Repairing defective edges of graphene nanostructures via a newly developed approach based on edge reorganization catalysis.

*(A) Growing graphene nanostructures from the bottom-up via barrier-guided CVD*

We have pioneered a new synthetic method for rationally growing graphene nanostructures from the bottom-up by chemical vapor deposition (CVD) with tailored shape, size, and crystallographic orientation.<sup>DOE1</sup> Our approach called barrier-guided CVD (BG-CVD) confines the crystal growth of monolayered graphene to nm-scale channels and features. In BG-CVD, crystal growth is laterally restricted on planar metal surfaces (Cu) by selectively passivating the Cu with patterned barrier templates (silicon oxide or aluminum oxide) designed to (a) locally limit the generation of intermediate hydrocarbons, and (b) confine their migration. We have demonstrated the bottom-up growth of nanoribbon arrays and nanostructures with 25 nm features on polycrystalline Cu foil substrates using aluminum oxide barriers (Fig. 1). The resulting nanostructures are highly crystalline without appreciable heterogeneous nucleation due to the barriers (as characterized by electron diffraction) and have refined edges compared to those produced via top-down etching (as determined by Raman spectroscopy). Ultimately, because BG-CVD relies on self-limiting crystal growth processes and avoids top-down etch-induced defects, we expect this method will lead to micro- and nanostructured graphene materials with superior performance.

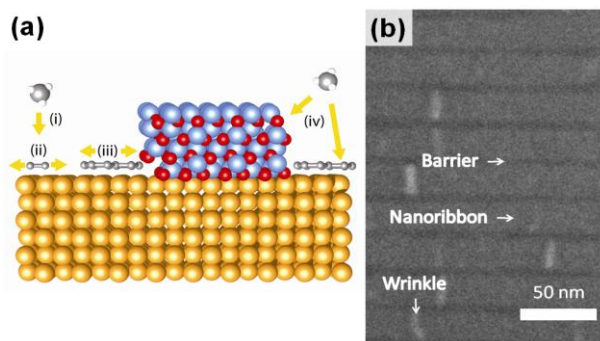


**Fig. 1.** (a) Schematic of BG-CVD: (i)  $\text{CH}_4$  decomposes on Cu into hydrocarbons, which (ii) diffuse and nucleate graphene, (iii) growing to cover the unmasked Cu surface until (iv) the entire surface is covered. (b) Example of graphene nanoribbons grown from the bottom-up via BG-CVD.

*(B) Understanding the epitaxy, faceting, and crystal morphology evolution of graphene during CVD*

In order to learn how to control the crystallographic orientation of graphene nanostructures during BG-CVD, we have conducted fundamental studies on more generally understanding the morphology and shape evolution of continuous graphene crystals during CVD on Cu. In the literature, graphene CVD on Cu has been observed to be complex, yielding different crystal morphologies, including lobes, dendrites, squares, rectangles, stars, and hexagons, of various orientations depending on the CVD conditions. We have comprehensively studied the conditions that lead to these different morphologies and how they evolve.<sup>DOE2</sup> In order to gain unique and unparalleled insight into the problem, growth has been studied on ultrasmooth, epitaxial Cu films instead of the more common polycrystalline Cu foils. Cu enclosures are used to minimize the

evolution of the Cu surface morphology and limit Cu sublimation and to decrease the graphene nucleation density.

We show that at low pressure and low  $H_2:CH_4$  ratio, circular graphene islands initially form. After exceeding  $\sim 1.0 \mu m$ , instabilities develop and evolve into dendrites extending hundreds of micrometers in the 100, 111, and 110 directions on Cu(100), Cu(110), and Cu(111), respectively, indicating mass transport limited growth. At sufficiently higher inter-nucleation density, the

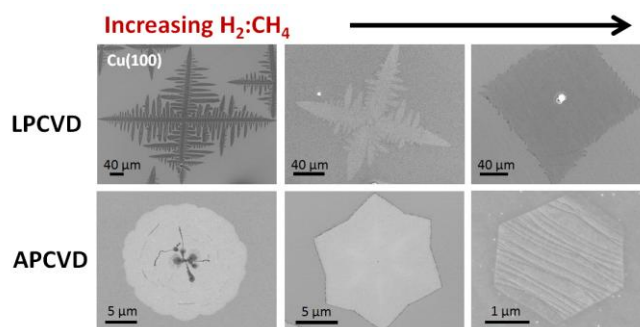


**Fig. 2.** CVD of graphene on Cu 100 as low pressure (LP) and atmospheric pressure (AP) with increasing  $H_2:CH_4$  precursor ratio.

instabilities run together before they can develop into long dendrites, giving rise to lobed structures commonly reported in the literature. Twin boundaries and grain boundaries perturb the preferential growth direction and alter the graphene morphology. Increasing  $H_2:CH_4$  (Fig. 2) results in compact islands that reflect the Cu symmetry (e.g. squares, rectangles, hexagons). In contrast, at atmospheric pressure, increasing  $H_2:CH_4$  results in more hexagonal islands on all surfaces, but with multiple preferred orientations on Cu(100) and Cu(110). At high  $H_2:CH_4$  at both low pressure and atmospheric pressure, a single orientation of graphene is observed on Cu(111). The understanding gained from this study provides a roadmap for rationally tailoring the structure, morphology, and orientation of graphene crystals by controlling the Cu substrate, the CVD chamber pressure, the  $H_2$  and  $CH_4$  partial pressure, and temperature, resulting in fewer defects and enhanced properties.

### *(C) Repairing the defective edges of graphene nanostructures*

We have recently developed an alternative to BG-CVD for creating graphene nanostructures with refined edges, via “edge repair”. We first use top-down lithography and reactive ion etching to create graphene nanostructures with defective edges. We then anneal them on a Cu catalyst substrate for repair. Edge carbon and hydrocarbon intermediate species can detach from the edge and adsorb to the Cu catalyst surface, providing an intermediate location where the species can migrate and then reattach to the edge elsewhere, thereby lowering the kinetic barrier for edge reorganization so that it can be realized  $< 1000 \text{ }^\circ\text{C}$ .

This annealing is only possible at a critical CVD condition in which attachment and detachment are balanced. We have elucidated the conditions for achieving this balance and in particular have identified a critical methane concentration (CMC) for atmospheric-pressure CVD.<sup>DOE3</sup> Above the CMC, graphene both nucleates and grows; below the CMC, it etches; while at the CMC, hydrocarbon intermediate species attach and detach from graphene at equal rates. By studying how the CMC varies with  $[H_2]$  and

temperature, we have identified the conditions necessary for our edge annealing reaction and furthermore elucidated the reaction mechanism. Regarding the latter, we have developed a comprehensive, intermediate hydrocarbon model of atmospheric-pressure CVD of graphene on Cu that describes growth rate and nucleation over a large set of experimental parameters. The model indicates that the growth-limiting intermediate hydrocarbon is CH. Thus, not only do our results provide a roadmap for annealing defects out of graphene nanostructures, but they elucidate the underpinnings of graphene CVD altogether.

## Future Plans

Moving forward, we are working to reduce the feature size of the nanostructures that can be obtained using BG-CVD and edge refinement, to put the nanostructures into a regime (~5 nm) in which quantum confinement effects will open up a more modest electrical bandgap ( $> 0.3$  eV). We are working to better characterize the ordering of nanostructure edges via STM and using polarized Raman spectroscopy. We are working to better understand the factors that control the crystallographic orientation of graphene on Cu using LEEM. And, we are working to correlate edge structure and crystallographic orientation with electronic transport properties (e.g. bandgap and charge transport mobility).

## References

1. J. H. Chen, C. Jang, S. D. Xiao, M. Ishigami and M. S. Fuhrer, *Nat. Nanotechnol.*, 2008, **3**, 206-209.
2. X. Du, I. Skachko, A. Barker and E. Y. Andrei, *Nat. Nanotechnol.*, 2008, **3**, 491-495.
3. C. Lee, X. D. Wei, J. W. Kysar and J. Hone, *Science*, 2008, **321**, 385-388.
4. W. W. Cai, A. L. Moore, Y. W. Zhu, X. S. Li, S. S. Chen, L. Shi and R. S. Ruoff, *Nano Lett.*, 2010, **10**, 1645-1651.
5. M. Kim, N. S. Safron, E. Han, M. S. Arnold and P. Gopalan, *Nano Lett.*, 2010, **10**, 1125-1131.
6. C. Stampfer, J. Guttinger, S. Hellmueller, F. Molitor, K. Ensslin and T. Ihn, *Phys. Rev. Lett.*, 2009, **102**.
7. L. Yang, C. H. Park, Y. W. Son, M. L. Cohen and S. G. Louie, *Phys. Rev. Lett.*, 2007, **99**.
8. M. Kim, N. S. Safron, E. Han, M. S. Arnold and P. Gopalan, *ACS Nano*, 2012, **6**, 9846-9854.
9. N. S. Safron, A. S. Brewer and M. S. Arnold, *Small*, 2011, **7**, 492-498.

## Publications Resulting from Support by DOE Grant over 2 Previous Years

DOE1. Safron, N. S.; Kim, M.; Gopalan, P.; Arnold, M. S., Barrier-Guided Growth of Micro- and Nano-Structured Graphene. *Advanced Materials* **2012**, *24*, 1041-1045.

DOE2. Jacobberger, R. M.; Arnold, M. S., Graphene Growth Dynamics on Epitaxial Copper Thin Films. *Chemistry of Materials* **2013**, 25, 871-877.

DOE3. Safron, N.S.; Arnold, M.S., Experimentally-Determined Model of Atmospheric-Pressure CVD of Graphene on Cu, *Submitted and in Review* **2013**.

DOE4. Huang C.; Kim M.; Wong B.M; Safron N.S.; Arnold M.S.; Gopalan P., Raman Enhancement of A Dipolar Molecule on Graphene, *Submitted and in Review* **2013**.

DOE5. Meng-Yin, W.; Jacobberger, R. M.; Arnold, M. S., Design length scales for carbon nanotube photoabsorber based photovoltaic materials and devices. *Journal of Applied Physics* **2013**, 113, 204504 (15 pp.)-204504 (15 pp.).

## Studies of Surface Reaction and Nucleation Mechanisms in Atomic Layer Deposition

Stacey F. Bent

sbent@stanford.edu

Department of Chemical Engineering  
Stanford University, Stanford, CA 94305

### Program Scope

Atomic layer deposition (ALD) is a method for depositing thin films of numerous semiconducting, insulating and metallic materials using an alternating series of self-limiting reactions between gas phase precursors and the substrate. ALD is proving to be an enabling technique for creating the innovative nanostructured materials needed for future applications, including those in solar energy and photoelectrocatalysis. Despite its growing technological importance, a fundamental, molecular-level understanding of most ALD processes is still lacking.

The aim of this project is to perform both experimental and theoretical studies to uncover surface reaction and nucleation mechanisms active during ALD. A combination of *in situ* and *in vacuo* X-ray photoelectron spectroscopy, infrared spectroscopy, synchrotron radiation photoelectron spectroscopy, and synchrotron radiation X-ray diffraction (XRD) studies are employed, together with complementary theory and modeling. The research focuses on representative ALD systems for the deposition of two categories of material: binary and ternary metal oxides, such as  $\text{SnO}_x$ ,  $\text{ZnO}$ , and  $\text{Zn}_x\text{Sn}_y\text{O}_z$ , and noble metals, such as Pt and Ru. Overall, the main objectives of this study are to develop an improved understanding of the chemical reactions driving both nucleation and steady state growth in ALD, and to provide the scientific foundation required for the ultimate design and synthesis of new materials for applications in energy, electronics, and catalysis.

### Recent Progress

Our recent work has focused on experimental and modeling studies of nucleation in metal ALD. We have also begun theoretical studies of metal oxide ALD. The experimental studies have utilized both laboratory-based and synchrotron-based techniques to elucidate nucleation processes in both Pt and Ru ALD.

The effects of the underlying substrate have a strong influence on ALD nucleation and growth. This effect was investigated using the Pt ALD system on highly ordered pyrolytic graphite (HOPG) as a test case. Pt was deposited by (methylcyclopentadienyl)trimethylplatinum and air. Our results show that Pt nanowires (NWs) form instead of a continuous film (Figure 1). We show that the Pt is deposited only at the step edges of HOPG, where chemically active sites exist, and not on the basal planes, which are chemically inert, leading to the formation of laterally aligned Pt NWs. By TEM measurements, we show that each Pt NW is comprised of a line of single crystalline grains. A

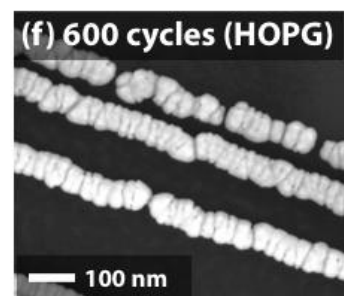


**Figure 1.** Plan-view SEM image of Pt ALD on HOPG, showing the formation of laterally aligned Pt NWs.

growth model involving a morphological transition from 0-D to 1-D structures via coalescence was developed [1]. Our data show that the width of the NWs grows at a rate greater than twice the vertical growth rate. This asymmetry is ascribed to the wetting properties of Pt on HOPG as influenced by formation of graphene oxide, which we aim to detect in future experiments

We also performed *ex situ* thin film diffraction studies at the Stanford Synchrotron Radiation Lightsource (SSRL) on a series of Pt films of differing thicknesses grown on silicon oxide-covered Si(100). Our results allow us to track the Pt ALD growth from initial island nucleation, to island growth, coalescence, and film formation. By using 2D grazing incidence X-ray diffraction (GIXRD), we show that the lattice orientation becomes more [111] oriented during deposition, with a sharp transition occurring during coalescence. We also follow a transition of the in-plane strain of the Pt lattice from compressive strain to tensile strain when the individual islands coalesce into a continuous film.

We looked at a second model metal ALD system, Ru, and studied the competition between Ru and Ru oxide thin film growth by both *in situ* and *ex situ* synchrotron radiation XRD. We had previously shown that Ru can be grown using a new ALD precursor bis(dimethylpentadienyl) ruthenium ( $\text{Ru}(\text{DMPD})_2$ ) and oxygen at an unusually low operating temperature for metal ALD ( $185^\circ\text{C}$ ). Recently, we measured the crystal structure and growth behavior of Ru and  $\text{RuO}_2$  on amorphous  $\text{SiO}_2$  during ALD by  $\text{Ru}(\text{DMPD})_2$ . Our *in situ* XRD studies (Figure 2) suggest that  $\text{RuO}_2$  films grown by  $\text{Ru}(\text{DMPD})_2$  and oxygen at low temperature do not initially nucleate as  $\text{RuO}_2$ . Despite large oxygen exposures during the ALD process, the initial nuclei form as hcp Ru. Then, after higher numbers of ALD cycles, crystalline rutile  $\text{RuO}_2$  begins to appear. The results suggest that a critical Ru nucleus size is required to initiate the growth of  $\text{RuO}_2$ . We speculate that a rate limiting step in the oxidation of Ru, possibly the formation of subsurface oxygen, is dependent upon the size of the Ru nuclei. Although the hcp Ru films are textured with a (002) preference in the growth direction, the rutile  $\text{RuO}_2$  films have no preferential orientation once they nucleate [2].

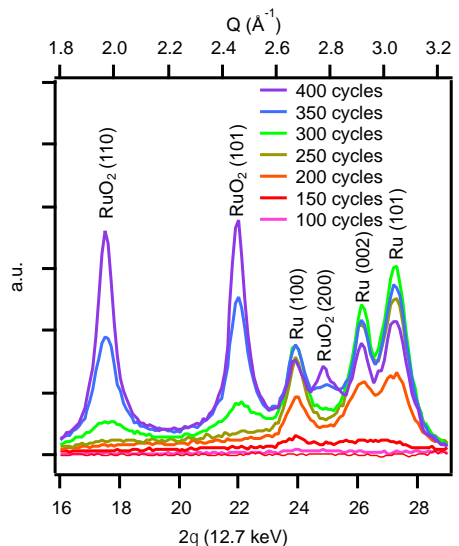


**Figure 2.** *In situ* in-plane diffraction spectra during the growth of  $\text{RuO}_2$  ALD by  $\text{Ru}(\text{DMPD})_2$  and oxygen (10 s at 1000 mTorr). The spectra were collected *in situ* under ALD conditions using a fixed grazing incident angle of  $0.40^\circ$ .

To develop a better understanding of metal oxide ALD, we have begun *ab initio* calculations on tin oxide ALD, a system that we also explore experimentally. The surface chemistry and growth characteristics of  $\text{SnO}_x$  ALD from tetrakis(dimethylamino)tin (TDMASn) and  $\text{H}_2\text{O}$  on OH-terminated silicon were investigated (Figure 3). The reaction pathways that we determine provide the basis for a mechanistic understanding of  $\text{SnO}_x$  ALD on this substrate and facilitate analysis of previous experimental observations. In particular, our previous experiments showed an increase in the growth rate of  $\text{SnO}_x$  at temperatures below  $100^\circ\text{C}$ , for which the role of physisorbed  $\text{H}_2\text{O}$  was suggested. Our calculations provide insight into the origin of this effect by demonstrating that the energetics for the TDMASn reaction with surface OH groups is similar to

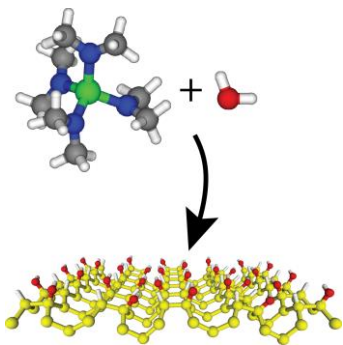


**Figure 3.** Model system for study of ALD chemistry of TDMASn on HO-Si surface.

that with H<sub>2</sub>O molecules. Our results therefore show that the low temperature effect is not due to an especially facile reaction between TDMASn and water. Instead, it is likely caused by an increased density of OH reactions sites due to the physisorbed water species [3]. Future investigations are necessary for understanding the mechanistic details of TDMASn behavior on surfaces that contain both chemisorbed and physisorbed OH groups. The surface chemistry understanding for SnO<sub>x</sub> is expected to be of relevance for the ALD of other technologically promising materials such as zinc tin oxide.

### Future Plans

We plan to extend our studies of metal ALD to better understand the nucleation process under different oxidizing precursors and conditions as well as on different substrates. Attention will be placed on changes in crystal structure, particle orientation, grain size, film strain, and coalescence during the nucleation and growth process. The studies will use our newly built *in situ* XRD instrument at SSRL as well as *ex situ* measurement and modeling. The results from the metal ALD studies are intended to help us to discover strategies for enhancing the nucleation of metal ALD on non-metal surface for production of uniform ultra-thin films, which remains a key challenge in the field. We will also continue to build our program on mechanistic studies of metal oxide ALD, focusing on SnO<sub>x</sub>, ZnO, and zinc tin oxide (ZTO) ALD systems. Our studies aim to answer questions about oxidation state and phase in the deposited metal oxides, the deviations in growth rate and composition in ternary metal oxides, and compositional uniformity in ternary metal oxides. Of special interest in each of these systems are questions about how chemical mechanisms differ during nucleation versus steady state growth, what occurs at temperatures below standard ALD conditions, and what serves as ALD nucleation sites on primarily unreactive surfaces.

### References

- [1] “Growth of Pt nanowires by atomic layer deposition on highly ordered pyrolytic graphite,” H. B. R. Lee, S. H. Baek, T. F. Jaramillo, and S. F. Bent, *Nano Letters*, **13** (2) (2013) 457–463. [x.doi.org/10.1021/nl303803p](https://doi.org/10.1021/nl303803p)
- [2] “Size dependent effects in nucleation of Ru and Ru oxide thin films by atomic layer deposition measured by synchrotron radiation x-ray diffraction,” R. Methaapanon, S. M. Geyer, S. Brennan and S. F. Bent, *Chem. Mat.* **25** (2013) 58–3463. [dx.doi.org/10.1021/cm401585k](https://doi.org/10.1021/cm401585k).

[3] “Insights into the surface chemistry of tin oxide atomic layer deposition from quantum chemical calculations,” J. T. Tanskanen and S. F. Bent, *J. Phys. Chem. C*, **117** (2013) 19056–19062. dx.doi.org/10.1021/jp4063324.

### DoE Sponsored Publications in the Last Two Years

1. “Microstructure-dependent nucleation in atomic layer deposition of Pt on TiO<sub>2</sub>,” H. B. R. Lee and S. F. Bent, *Chem. Mat.*, **24** (2012) 279–286.
2. “Nucleation-controlled growth of nanoparticles by atomic layer deposition,” H. B. R. Lee, M. N. Mullings, X. Jiang, B. M. Clemens, and S. F. Bent, *Chem. Mat.*, **24** (2012) 4051–4059. DOI: 10.1021/cm3014978.
3. “The low temperature atomic layer deposition of ruthenium and the effect of oxygen exposure,” R. Methaapanon, S. M. Geyer, H. B. R. Lee, and S. F. Bent, *J. Mat. Chem.*, **22** (48) (2012) 25154 – 25160. DOI: 10.1039/c2jm35332f.
4. “*In vacuo* photoemission studies of platinum atomic layer deposition using synchrotron radiation,” S. M. Geyer, R. Methaapanon, P. A. Pianetta, and S. F. Bent, *J. Phys. Chem. Lett.*, **4** (1) (2013) 176–179, dx.doi.org/10.1021/jz301475z.
5. “Portable atomic layer deposition reactor for in situ synchrotron photoemission studies,” R. Methaapanon, S. M. Geyer, C. Hagglund, P. A. Pianetta, S. F. Bent, *Rev. Sci. Instrum.* **84** (2013) 015104; doi: 10.1063/1.4773230.
6. “Size dependent effects in nucleation of Ru and Ru oxide thin films by atomic layer deposition measured by synchrotron radiation x-ray diffraction,” R. Methaapanon, S. M. Geyer, S. Brennan and S. F. Bent, *Chem. Mat.* **25** (2013) 58–3463. dx.doi.org/10.1021/cm401585k.
7. “Growth of Pt nanowires by atomic layer deposition on highly ordered pyrolytic graphite,” H. B. R. Lee, S. H. Baeck, T. F. Jaramillo, and S. F. Bent, *Nano Letters*, **13** (2) (2013) 457–463. x.doi.org/10.1021/nl303803p
8. “Insights into the surface chemistry of tin oxide atomic layer deposition from quantum chemical calculations,” J. T. Tanskanen and S. F. Bent, *J. Phys. Chem. C*, **117** (2013) 19056–19062. dx.doi.org/10.1021/jp4063324.

## Novel theoretical and experimental approaches for understanding and optimizing molecule-sorbent interactions in metal organic framework materials

Nour Nijem, Kui Tan, **Y. J. Chabal**, University of Texas at Dallas

Haohan Wu, Debasis Banerjee, **Jing Li**, Rutgers University

Pieremanuele Canepa, Sebastian Zuluaga, **Timo Thonhauser**, Wake Forest University

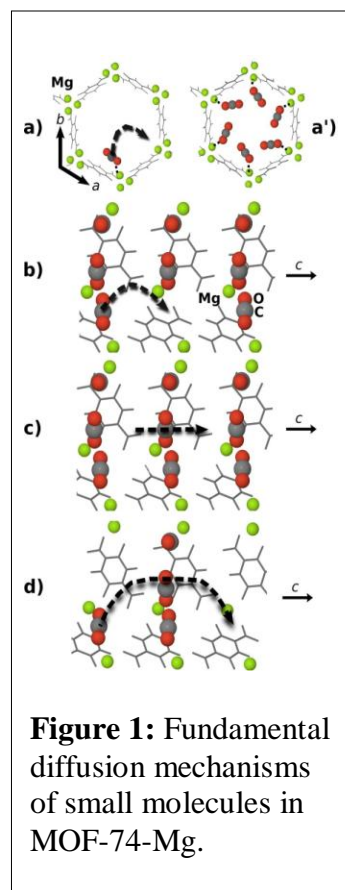
**Program Scope:** The aim of this program is to develop a fundamental mechanistic understanding of the interaction guest molecules (e.g. H<sub>2</sub>, CO<sub>2</sub>, N<sub>2</sub>, CH<sub>4</sub>) in porous metal organic framework (MOF) materials, using a combination of novel synthesis, theoretical analysis and characterization. In particular, we combine high-pressure and low-temperature infrared (IR) absorption and Raman measurements, adsorption isotherms and isosteric heat of adsorption measurements with first-principles calculations based on van der Waals density functional (vdW-DF), to study a number of different MOF materials. One of the goals is to provide insight for the role of unsaturated metal centers in enhancing molecular uptake, selective adsorption and diffusion. The short term impact of the proposed work will result from the control and the understanding of common MOF systems, making it possible to determine the theoretical loading limits and stability of a specific class of materials. The long term impact will involve the development of 1) theoretical and experimental methods to gain a fundamental understanding of molecular interactions within these systems, and 2) new concepts to develop microporous MOFs with tailored molecular binding and selectivity.

### Recent Progress

We have recently focused on two dynamic aspect of gas adsorption in MOFs: diffusion and selective adsorption. To investigate diffusion, we have selected a well-studied system, MOF-74, characterized by unsaturated metal centers with relatively high binding energies. For selective adsorption, we have examined the behavior of a flexible MOF synthesized in our laboratory with interesting structural properties.

**Diffusion:** Combining vdW-DF calculations and time-resolved *in situ* IR spectroscopy, we have studied the diffusion of small molecules in MOF-74-Mg by focusing on the diffusion of H<sub>2</sub>, CO<sub>2</sub>, and H<sub>2</sub>O in MOF-74-Mg.<sup>1</sup> Binding-energy calculations indicate that water binds much more strongly than H<sub>2</sub> and CO<sub>2</sub> and thus is thermodynamically much more likely to occupy metal sites.<sup>2,3</sup> This finding has tremendous importance for storage and capture applications.

To model molecular diffusion in the MOF structure, we coupled climbing-image nudged elastic-band simulations with vdW-DF and identified four important diffusion mechanisms at the atomistic scale. We calculated their corresponding diffusion barriers and were then able to calculate the ratio of diffusion rates for different molecules using the transition-state theory and Arrhenius transport equation. By measuring the asymmetric stretch modes of small molecules over time, we found that MOF loading typically occurs in





identified by the sizeable change of the  $\nu(\text{C}=\text{O})$  mode that disappears at  $1650\text{ cm}^{-1}$  and reappears at  $1616\text{ cm}^{-1}$  in Raman spectra of Fig. 2 (left). This result confirms that stronger hydrogen bonding leads to a lower gate opening pressure and suggests a pressure swing adsorption type separation based on hydrogen bond strength in similar size molecules. This phenomenon also opens the door for the use of strong hydrogen bonding for the detection of traces of acetylene in gas flow for practical applications and as a sealing method for storage of adsorbed molecules in porous materials.

### Future Plans

We plan to examine in detail the competitive adsorption of a variety of molecules in selected MOFs, including the kinetics of site exchange, as for instance,  $\text{H}_2\text{O}$  and  $\text{CO}_2$  in MOF-74. This work will also require the development of vdW-DF methods that can handle systems with spins. We also plan to incorporate catalytic activity within MOFs by incorporating molecular catalysts within the MOF. Whenever possible, best choices for active metal and ligand structures will be guided by *ab initio* simulations.

### References

- (1) Canepa, P.; Nijem, N.; Chabal, Y. J.; Thonhauser, T. *Physical Review Letters* **2013**, *110*, 026102.
- (2) Nijem, N.; Canepa, P.; Kong, L.; Wu, H.; Li, J.; Thonhauser, T.; Chabal, Y. J. *Journal of Physics Condensed Matter* **2012**, *24*, 424203.
- (3) Yao, Y.; Nijem, N.; Li, J.; Chabal, Y. J.; Langreth, D. C.; Thonhauser, T. *Physical Review B* **2012**, *85*, 064302.
- (4) Lan, A.; Li, K.; Wu, H.; Olson, D. H.; Emge, T. J.; Ki, W.; Hong, M.; Li, J. *Angewandte Chemie-International Edition* **2009**, *48*, 2334.
- (5) Nijem, N.; Wu, H.; Canepa, P.; Marti, A.; Balkus, K. J.; Thonhauser, T.; Li, J.; Chabal, Y. J. *Journal of the American Chemical Society* **2012**, *134*, 15201.

### DOE Sponsored Publications in the Last Two Years (9/2011-9/2013)

1. P. Canepa, C.A. Arter, E.M. Conwill, D.H. Johnson, B.A. Shoemaker, K.Z. Soliman, and T. Thonhauser, "High-throughput screening of small-molecule adsorption in MOF." *Journal of Material Chemistry. A*, in print (2013).
2. N. Nijem, P. Canepa, U. Kaipa, K. Tan, K. Roodenko, S. Tekarli, J. Halbert, I.W.H. Oswald, R.K. Arvapally, C. Yang, T. Thonhauser, M.A. Omary, and Y.J. Chabal, "Water cluster confinement and methane adsorption in the hydrophobic cavities of a fluorinated metal-organic framework *Journal of the American Chemical Society*. **135**, 12615 (2013).
3. M. G. Lopez, P. Canepa, and T. Thonhauser, "NMR study of small molecule adsorption in MOF-74-Mg." *Journal of Chemical Physics*, **138**, 154704 (2013).
4. P. Canepa, Y.J. Chabal, and T. Thonhauser, "When metal organic frameworks turn into linear magnets." *Physics Review. B*, **87**, 094407 (2013).
5. P. Canepa, N. Nijem, Y.J. Chabal, and T. Thonhauser, "Diffusion of small molecules in metal organic framework materials." *Physics Review Letter*, **110**, 026102 (2013).
6. A. M. Plonka, D. Banerjee, W. R. Woerner, Z. Zhang, N. Nijem, Y. J. Chabal, J. Li, and J. B. Parise, "Mechanism of Carbon Dioxide Adsorption in a Highly Selective Coordination Network Supported by Direct Structural Evidence." *Angewandte Chemie International Edition*

**52** (6), 1598 (2013), (Selected as inside cover and as “Hot Paper” by *Angew. Chem.*, December 2012).

7. H. Liu, Y. G. Zhao, Z. J. Zhang, N. Nijem, Y. J. Chabal, X. F. Peng, H. P. Zeng, and J. Li, Ligand “Functionalization and Effect on CO<sub>2</sub> Adsorption in Microporous Metal Organic Frameworks.” *Chemistry—An Asian Journal*, **8**, 778-785 (2013). (Selected as featured article) (Selected as inside cover).

8. B. Efremovska, H. H. Wu, J. Vaughn, D. H. Olson, J. Mattai, C. Ortiz, A. Puchalski, J. Li and L. Pan, “Encapsulated Recyclable Porous Materials: An Effective Moisture-Triggered Fragrance Release System, *Chemical Communication.*, **49**, 5724-5726 (2013). (Selected as back Cover).

9. X. J. Zhou, Z. J. Zhang, B. Y. Li, F. Yang, Y. Peng, G. H. Li, Z. Shi, S. H. Feng and J. Li, “Two Three-Dimensional Metal-Organic Frameworks Constructed by Thiazole-Spaced Pyridinecarboxylates Exhibiting Selective Gas Adsorption or Antiferromagnetic Coupling.” *New Journal of Chemistry*, **37**, 425-430 (2013).

10. A. M. Plonka, D. Banerjee, W. W. Woerner, Z. J. Zhang, J. Li, and J. B. Parise. “Effect of Ligand Geometry on Selective Gas Adsorption: The Case of a Microporous Cadmium Metal Organic Framework with V-Shaped Linker.” *Chemical. Communication*, **49**, 7055-7057 (2013).

11. A. Lowe, P. Chittajallu, Q. H. Gong, J. Li, and K. J. Balkus. “Storage and Delivery of Nitric Oxide via Diazeniumdiolated Metal Organic Framework.” *Microporous Mesoporous Materials*, **181**, 17-22 (2013).

12. Z. C. Hu, S. Pramanik, K. Tan, C. Zheng, W. Liu, X. Zhang. Y. C. Chabal and J, Li, “Selective, Sensitive and Reversible Detection of Vapor-Phase RDX and Other High Explosives via 2D Mapping: A New Strategy for MOF Based Sensors.” *Crystal Growth & Design. ASAP* (2013).

13. S. Pramanik, Z. C. Hu, X. Zhang, C. Zheng, S. Kelly, and J. Li, “A Systematic Study of Fluorescence-Based Detection of Nitroexplosives and Other Aromatics in Vapor-Phase by Microporous Metal Organic Frameworks.” *Chemistry -A European Journal, ASAP* (2013).

14. D. Banerjee, ; Z. C. Hu, S. Pramanik, X. Zhang, H. Wang, and J. Li, “Vapor Phase Detection of Nitroaromatic and Nitroaliphatic Explosives by Fluorescence Active Metal Organic Frameworks”, *Cryst. Eng. Comm.* in print (2013).

15. W. Xu, S. Pramanik, Z. Zhang, J. E. Thomas, and J. Li, “Microporous [M<sub>2</sub>(hfipbb)<sub>2</sub>(ted)] (M = Zn, Co): Synthesis, Structure Analysis, Pore Characterization, Small Gas Adsorption and CO<sub>2</sub>/N<sub>2</sub> Separation Properties.” *Journal of Solid State Chemistry*, **200**, 1(2013)

16. Z. Zhang, Y. Zhao, Q. Gong, Z. Li, and J. Li, “MOFs for CO<sub>2</sub> Capture and Separation from Dry and Wet Flue Gas Mixtures: The Effect of Multifunctional Sites on Their Adsorption Capacity and Selectivity.” *Chemical Communications*, **49** (7), 653 (2013).

17. N. Nijem, P. Canepa, L. Kong, H. Wu, J. Li, T. Thonhauser, and Y.J. Chabal, “Spectroscopic characterization of van der Waals interactions in a metal organic framework with unsaturated metal centers: MOF-74-Mg.” *Journal of Physics: Condensed Matter*, **24**, 424203 (2012).

18. R. Sabatini, E. Kucukbenli, B. Kolb, T. Thonhauser, and S. de Gironcoli, “Structural evolution of amino acid crystals under stress from a non-empirical density functional.” *Journal of Physics: Condensed Matter*, **24**, 424209 (2012).

19. Q. Li and T. Thonhauser, "A theoretical study of the hydrogen-storage potential of  $(\text{H}_2)_4\text{CH}_4$  in metal organic framework materials and carbon nanotubes." *Journal of Physics: Condensed Matter*, **24**, 424204 (2012).
20. N. Nijem, H. Wu, P. Canepa, A. Marti, K.J. Balkus Jr., T. Thonhauser, J. Li, and Y.J. Chabal, "Tuning the gate opening pressure of metal-organic frameworks for the selective separation of hydrocarbon." *Journal of the American Chemical Society*, **134**, 15201 (2012).
21. K. Tan, N. Nijem, P. Canepa, Q. Gong, J. Li, T. Thonhauser, and Y.J. Chabal, "Stability and hydrolyzation of metal organic frameworks with paddle-wheel SBUs upon hydration." *Chemistry of Materials*, **24**, 3153 (2012).
22. Y. Yao, N. Nijem, J. Li, Y.J. Chabal, D.C. Langreth, and T. Thonhauser, "Analyzing the frequency shift of physisorbed  $\text{CO}_2$  in metal organic framework materials." *Physics Review B*, **85**, 064302 (2012).
23. B. Li, Z. Zhang, Y. Li, K. Yao, Y. Zhu, Z. Deng, F. Yang, X. Zhou, G. Li, H. Wu, N. Nijem, Y. J. Chabal, Z. Lai, Y. Han, Z. Shi, S. Feng, and J. Li, "Enhanced binding affinity, remarkable selectivity, and high capacity of  $\text{CO}_2$  by dual functionalization of a rht-type metal-organic framework." *Angewandte Chemie International Edition* **51** (6), 1412 (2012).
24. H. Wu, Q. Gong, D. H. Olson, and J. Li, "Commensurate Adsorption of Hydrocarbons and Alcohols in Microporous Metal Organic Frameworks." *Chemical Reviews*, **112** (2), 836 (2012).
25. Q. Li and T. Thonhauser, "A theoretical study of the hydrogen-storage potential of  $(\text{H}_2)_4\text{CH}_4$  in metal organic framework materials and carbon nanotubes." *Journal of Physics: Condensed Matter*, **24** (42), 424204 (2012).
26. J. Y. Lee, H. H. Wu, and J. Li, "An investigation of structural and hydrogen adsorption properties of microporous metal organic framework (MMOF) materials." *International Journal of Hydrogen Energy*, **37**(13), 10473 (2012).
27. Z. Zhang, J. Liu, Z. Li, and J. Li, "Experimental and Theoretical Investigations on the MMOF Selectivity for  $\text{CO}_2$  vs  $\text{N}_2$  in Flue Gas Mixtures." *Dalton Transactions*, **41** (14), 4232 (2012).
28. C. Zou, Z. J. Zhang, X. Xu, Q. H. Gong, J. Li, and C. D. Wu, "A Multifunctional Organic-Inorganic Hybrid Structure Based on  $\text{Mn}^{\text{III}}$ -Porphrin and Polyoxometalate as Highly Effective Dye Scavenger and Heterogeneous Catalyst." *Journal of the American Chemical Society*, **134** (1), 87 (2012).
29. Y. Zhao, H. Wu, T. J. Emge, Q. Gong, N. Nijem, Y. J. Chabal, L. Kong, D. C. Langreth, H. Liu, H. Zeng, and J. Li, "Enhancing Gas Adsorption and Separation Capacity through Ligand Functionalization of Microporous Metal-Organic Framework Structures," *Chemistry - A European Journal*, **17** (18), 5101 (2011).
30. N. Nijem, P. Thissen, Y. Yao, R. C. Longo, K. Roodenko, H. Wu, Y. Zhao, K. Cho, J. Li, D. C. Langreth, and Y. J. Chabal, "Understanding the Preferential Adsorption of  $\text{CO}_2$  over  $\text{N}_2$  in a Flexible Metal-Organic Framework." *Journal of the American Chemical Society*. **133** (32), 12849 (2011).
31. N. Nijem, L. Kong, Y. Zhao, H. Wu, J. Li, D. C. Langreth, and Y. J. Chabal, "Spectroscopic Evidence for the Influence of the Benzene Sites on Tightly Bound  $\text{H}_2$  in Metal-Organic Frameworks with Unsaturated Metal Centers: MOF-74-Cobalt." *Journal of the American Chemical Society*. **133** (13), 4782 (2011).

32. H. Liu, Y. Zhao, Z. Zhang, N. Nijem, Y. J. Chabal, H. Zeng, and J. Li, “*The Effect of Methyl Functionalization on MMOFs’ Capacity and Binding Energy for Carbon Dioxide Adsorption.*” *Advanced Functional Materials* **21** (24), 4754 (2011).

33. L. Kong, Y. J. Chabal, and D. C. Langreth, “First-principles approach to rotational-vibrational frequencies and infrared intensity for H<sub>2</sub> adsorbed in nanoporous materials.” *Physical Review B*, **83** (12), 121402 (2011).

34. K. H. Li, D. H. Olson, and J. Li, “Commensurate Adsorption of Hydrocarbons in Microporous Metal-Organic Frameworks.” *Trends in Inorganic Chemistry*, **12**, 13 (2011).

# A Unified Understanding of Residual Stress in Thin Films: Kinetic Models, Experiments and Simulations

Eric Chason, Brown University, School of Engineering

## Program Scope

Residual stress is a critical reliability issue in thin films. These stresses can be large enough to induce failure and are strongly tied to the processing conditions. For example, Ni films grown at 0.1 nm/s are highly compressive (-600 MPa) while films grown at 20 nm/s are highly tensile (400 MPa) [1]. Although there is a large literature of stress measurements in thin films [2,3,4], the fundamental connection between the film growth process and the resulting stress is not well understood. The goal of the work in this program is to develop a unified framework that can quantitatively explain the residual stress in terms of the underlying kinetic processes and microstructural parameters.

The research consists of projects that integrate experiments with modeling. The initial experiments focus on quantifying the stress in a systematic way that can be compared with the models: different systems (e.g. Cu, Ag, Ni, Fe, Cr), different conditions (temperature, growth rate), different deposition methods (evaporation, electrodeposition) and patterned/randomly-nucleated films. We measure the in-plane stress integrated over the film thickness (called stress-thickness) using a multi-beam wafer curvature system (MOSS [4]) while the film is growing.

The modeling effort utilizes rate equations (described below) to model the stress that develops at the grain boundary as the film is growing. The model describes the evolution of the stress with thickness and its dependence on the grain size ( $L$ ), growth rate ( $R$ ) and effective diffusivity ( $D$ ). The parameters obtained from the modeling will be used to connect the kinetic processes controlling stress with other measurements of parameters such as the surface and grain boundary diffusivity and interfacial energy. Additional modeling will use kinetic Monte Carlo (KMC) simulations to describe the growth of polycrystalline systems based on atomic-level kinetic processes. In the latter part of the project, these experimental and modeling tools will be extended to alloy systems.

## Recent Progress

The current work is centered around a model we have developed that predicts the stress evolution (described more fully in [4]). In brief, the model describes the dynamic balances between stress-generating processes occurring at the grain boundary as the film grows (shown schematically in figure 1). As layers in adjacent grains grow towards each other, they form a new segment of grain boundary that lowers the bond energy,

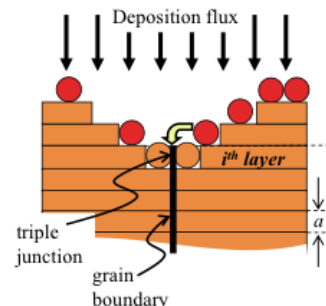


Figure 1. Schematic of film structure around triple junction for model of stress evolution.

even at the expense of inducing tensile stress ( $\sigma_T$ ) in the layer [5]. After the grain boundary forms, the higher chemical potential on the surface can drive atoms into the top of the grain boundary (triple junction) until it is covered over by the layer above it. Balancing these kinetic processes produces a rate equation for the stress in each layer (indexed by  $i$ ) as the film grows:

$$\sigma_i = \sigma_C + (\sigma_T - \sigma_C) \cdot \exp\left(-\frac{\beta D}{L} \frac{\Delta t_i}{a}\right) \quad (1)$$

where  $a$  is the height of an atomic layer and  $\sigma_C$  is the saturation compressive stress. The characteristic time in this equation is related to the rate at which the grain boundary height is changing ( $dh_{gb}/dt = a/\Delta t_i$ ). In the early stage of growth (island coalescence), this can be much faster than the average growth rate of the film. For thick films (steady-state regime) the grain boundary grows at the same rate as the film thickness ( $\Delta t_i = a/R$ ).

*Steady-state stress:* We have measured the steady-state stress as a function of growth rate in Cu layers grown by electrodeposition. This work was a collaboration among multiple labs (Brown, NIST, U. of Limerick) that used different electrolytes but similar growth rates/grain sizes (submitted to a special issue of J. Electrochemical Society on Electrochemical Deposition for Interconnects). The results from the studies for the stress vs deposition rate (multiplied by the grain size) is shown in figure 2. The solid line in the figure is a fit to the model described above, showing that it can account for the measured dependence of the stress on growth rate.

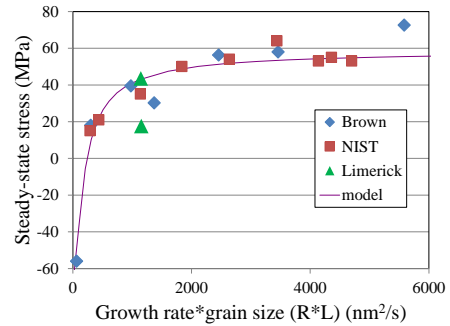


Figure 3. Steady-state stress vs growth rate for data measured at the three laboratories (as indicated in the figure).

*Stress vs thickness in patterned films:* Our model describes the stress in terms of the rate at which the grain boundary height increases (eq. 1). During the coalescence of individual nuclei into a continuous film, this velocity changes greatly as the microstructure evolves. At the initial point of coalescence, the grain boundary grows very rapidly because of the steep contact angle between the coalescing grains and then decreases towards the average rate ( $R$ ) asymptotically. In previous work, we have modeled this in evaporated Ag films by assuming that the islands are semi-circular in cross-section. The change in grain boundary growth rate with thickness explains the measured transition from tensile to compressive stress as the film grows.

However, this shape of islands is only an approximation for grains that have been nucleated randomly. To determine if the model works quantitatively, we have measured the stress evolution during the growth of patterned island arrays in which we know the shape of the islands. Figure 3 shows an SEM image of an array of Ni grains with a

spacing of 22 microns grown in conjunction with S.J. Hearne at Sandia Labs (not yet published). The islands are hemispherical in shape (cross-section in figure 3a) with a

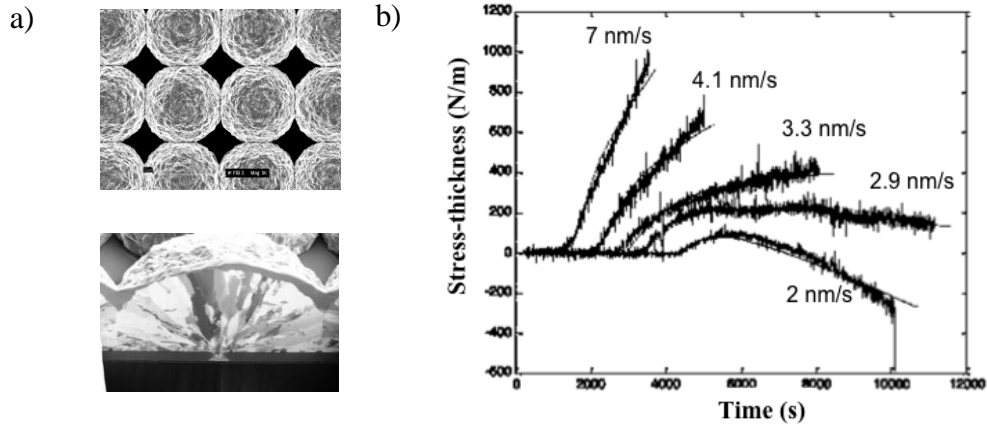


Fig. 3. a) SEM micrographs of patterned array of Ni islands b) Stress-thickness data measured using wafer curvature for electrodeposition at different growth rates (as indicated on figure) Solid lines are fit to stress model described in text.

radius that grows at a uniform rate during electrodeposition. At earlier stages of growth, (not shown) the islands are not touching. As the thickness increases, the film evolves with a geometry that mimics the overlap of hemispheres with increasing radii.

The corresponding measurements of stress-thickness vs time from these island array are shown in figure 3b for different growth rates (as indicated in the figure). The rapid rise in the stress-thickness occurs when the diameter of the spheres is equal to the spacing between them and the spheres start to intersect. Initially, the stress-thickness change is positive (i.e., tensile stress) as the grain boundary height increases rapidly. At longer times, when the grain boundary growth rate decreases toward the average growth rate, the steady-state stress depends on the value of  $R$  (more tensile for faster growth and compressive for slower growth, in agreement with eq. 1).

The solid lines in figure 3b represent a fit to the model, using the intersection of growing spheres to determine the rate at which the grain boundary height is increasing (with the appropriate growth rates ( $R$ ) and island spacing ( $L$ )). The calculations also include the fact that the area of contact increases as the film gets thicker. A single set of fitting parameters ( $\sigma_C = -488$  MPa,  $\sigma_T = 60.8$  MPa, and  $\beta D/aL = 1.85$ ) was used to obtain the results shown.

## Future Plans

In the future, we will extend our measurements of the steady-state stress in Cu to look at the effect of different parameters: grain size, additives to the electrolyte, the electrolyte concentration (exchange current) and deposition method (evaporation). These will enable us to probe different aspects of the model such as the mobility and the grain boundary energy. We will also look at other systems with high and low atomic mobility to further explore the limits of the model's validity. In collaboration with Gery Stafford

at NIST we will use impedance spectroscopy to look at the time constants when growth is turned on and off and relate these to the model parameters. Measurements of the effect of roughness on steady-state stress will be performed to determine quantitatively how this affects the stress. Surface roughness can modify the stress-generating mechanisms included in our model but its effect has not been well measured previously.

Measurements of the evolution of the stress thickness during island coalescence will be studied in patterned and unpatterned films. The patterned films will be grown through a proposal to CINT (Center for Integrated Nanotechnology) at Sandia that was approved this summer. One aspect of this work will be to compare coalescence of hemispheres (2-d) with the coalescence of cylindrical islands (1-d) to relate the difference in stress-thickness evolution to the evolution of the grain boundary. Patterns with different length scales will probe the dependence on  $L$  in the model. Unpatterned films of Cu will be grown by electrodeposition on amorphous substrates to suppress the effects of lattice mismatch and substrate grain structure on the stress evolution. The parameters from modeling the patterned films will be compared with the unpatterned films to determine if they are consistent over different length scales.

Kinetic Monte Carlo simulations of polycrystalline film growth will be performed in collaboration with Luis Zepeda-Ruiz (LLNL) and Hanchen Huang (Northeastern). These will enable the atomistic processes of atom incorporation to be modeled for comparison with the predictions of our rate equations. Although KMC simulations can not directly model the stress, we have described in previous work [6] how we can use the retained vacancy concentration as a surrogate for the stress. In later years, we will extend the experimental and modeling efforts to look at stress evolution in alloy films. These films are important technologically but there is much less known about the phenomenology of stress evolution in these systems. We will study a solid solution (e.g., Ag-Cu) and a phase separating system (e.g., Ag-Ni) to look at how the stress depends on the growth rate. The samples in these studies will be carefully characterized to make sure that we are comparing stress in films with the same grain size(s) and composition. Based on the results we will extend the model to include the different mobility of the two atomic species and the presence of grain boundaries between different phases.

## References

1. S.J. Hearne, J.A. Floro, *J. Appl. Phys.* 97, (2005) 014901.
2. M. F. Doerner, and W.D. Nix, *CRC Crit. Rev. in Sol. State and Mat. Sci.* 14, 225 (1988)
3. R. Koch, *J Phys. Cond. Mat.* 6, 9519, (1994)
4. E. Chason, *Thin Solid Films* 526, 1 (2012).
5. R. W. Hoffman, *Thin Solid Films* 34, 185 (1976).
6. L. Zepeda-Ruiz, E. Chason, G. Gilmer, Y. Wang, H. Xu, A. Nikroo, A. Hamza, *Appl. Phys. Lett.* 95, 151910 (2009).

## DoE Sponsored Publications in the Last Two Years

1. E. Chason, "A kinetic picture of residual stress evolution in polycrystalline thin films", *Thin Solid Films* 526, 1 (2012).

2. E. Chason, A. Engwal, F. Pei, M. Lafouresse, U. Bertocci, G. Stafford, D. N. Buckley, J. A. Murphy, C. Lenihan, "Understanding residual stress in electrodeposited Cu thin films", *J. Electrochemical Soc.*, submitted.

## Electric-Field Enhanced Kinetics in Oxide Ceramics: Pore Migration, Sintering and Grain Growth

I-Wei Chen, [iweichen@seas.upenn.edu](mailto:iweichen@seas.upenn.edu)  
Department of Materials Science and Engineering  
University of Pennsylvania  
Philadelphia, PA 19104-6272

### Program Scope

Although oxide ceramics have been used in many solid state devices in which electric field is high and ion conduction is rapid, there has been little systematic study of the material stability under such conditions. Material stability is usually presumed after initial screening leading to the material selection, but long term operation and device miniaturization may pose new circumstances that challenge the presumption. Prominent solid state ionic devices that are pertinent to energy applications include solid oxide fuel cells and solid oxide electrolysis cells as well as solid state batteries. A large electric field is also utilized in extreme-condition processing such as spark plasma sintering.

This work is an in-depth study of three exotic phenomena not previously known to occur in solid ion-conducting oxides under a large electric current. These phenomena are

- (a) *neutral* objects such as pores and bubbles can move in an uniform electric field without a direct thermodynamic force;
- (b) pore migration and electro-sintering can occur at low temperatures *without* cation lattice/grain-boundary diffusion; and
- (c) grain growth is *position-biased* even though the spatially uniform field is not.

Model electric loading experiments in well defined systems are conducted to define the material parameters that govern these phenomena. The experimental results and theoretical work are combined to elucidate the thermodynamic and kinetic principles of electric-field-induced microstructure evolutions in ion-conducting oxide ceramics.

### Recent Progress

#### In Situ Thermometry and Temperature Surge in Flash Sintering

The relatively large current density investigated in this study may induce Joule heating. This is monitored using impedance spectroscopy, which uses a small AC perturbation over and above a DC current/voltage to probe the impedance change as a result of the DC power. The AC impedance spectroscopy has the ability to simultaneously monitor the real part and the imaginary part of the impedance over an extended range of frequency. This information allows the separation of the impedances from different parts of the electric-loading-train: the line, the electrode, and the ceramic ionic conductor in question, which have different characteristic time constants. Since the microstructure evolution of a ceramic ionic conductor is slow relative to the temperature change caused by Joule heating, the impedance change of the ceramic ionic conductor is solely due to the temperature change. It thus provides a means for *in situ* thermometry. *In situ* thermometry using this method is fast since the frequency scan over many decades can be completed in a few seconds before repeating, continuously in real time. In

practice, a high frequency reading often suffices allowing a time resolution of milliseconds. The method is applicable for both large and small samples. It is even feasible for samples that are out of sight, which is often the case: for example, a small thin disc covered on both sides by electrodes, or a sample housed in an enclosure.

In our standard work, we use a power that is small enough to not cause a significant impedance change, thus assuring the sample temperature to maintain at the same level as that of the furnace. However, to test the limit of this new *in situ* thermometry, we also conducted experiments that simulate the so-called *flash sintering* condition, in which a constant voltage is applied to the sample while the furnace temperature increases at a constant rate. Our experiment demonstrated that this condition invariably led to a thermal runaway with an exponential rise in temperature that cannot be captured, in real time, by conventional thermometry. For example, in a 8 mol%  $\text{Y}_2\text{O}_3$ -stabilized  $\text{ZrO}_2$  (8YSZ) under flash sintering conduction, temperature surges up to  $1500^\circ\text{C}$ , corresponding to a  $1,000\times$  drop in resistance, were recorded under a modest voltage (a few V). The temperature surge is strongly sensitive to the voltage and the sample size/shape: under the same field the surge is larger in larger samples, and in samples with a larger height-to-width ratio.

#### Pore Iono Migration, Electro Sintering, and Pore-Grain Boundary Interaction

We have found under a wide ranging set of electric loading conditions, pores in porous 8YSZ undergo ion-flow-motivated migration, leading to sample dimensional changes (electro sintering) and grain boundary distortions. Sample dimensional changes are best illustrated using an initially uniform disk-shaped sample, which after testing becomes thin in the middle section between two Pt electrodes. Remarkably, the grain size in the sintered region is uniformly small, independent of the temperature of electro sintering, and very close to the initial grain size in the porous sample. This is a remarkable result that is not expected by the prevailing sintering paradigm in ceramics and metals. A more detailed theoretical study further concluded that electro sintering is due to (cation) surface diffusion, which is impossible according to the prevailing paradigm of sintering. Such cation surface diffusion mechanism when coupled to the fast oxygen wind in 8YSZ enables surface reprogramming and pore translation, which accrues to large microstructural changes. Thus, in almost every respect, the electro sintering results are surprising and revealing.

To understand the fate of pores interacting with stationary grain boundaries, we have analyzed the critical conditions for pores to break away from the grain boundary under iono migration condition. This problem was formulated in terms of the thermodynamic condition (the limit of capillarity, which provides pinning force) and the kinetic (the time window for grain boundary bowing, which enables pinning force) condition. Large pores at lower temperature and higher field are found easier to break away. A (pore size-temperature) map for pore-boundary breakaway was constructed for various electric fields. This map was compared with the data obtained in polycrystals of cubic zirconia (8 mol%  $\text{Y}_2\text{O}_3$ -stabilized  $\text{ZrO}_2$  (8YSZ)) and found in reasonable agreement. The above problem has an analogy in classical physical ceramics: during final stage sintering, grain boundary migration may be too fast for pores to follow, resulting in pores breaking away from the grain boundary. The fundamental difference between the two problems is that in classical sintering, it is grain boundary migration that sets the speed limit for pores to follow, whereas in iono migration, it is pore migration that sets the speed limit for grain

boundary to follow. The map for the former is typically in the (pore size-grain size) space since grain size determines the driving force for grain boundary migration. Such a map is not applicable to ionic migration since grain boundary is stationary in practically important cases (e.g., fuel cell and electrolytic cell applications).

To investigate the pore-grain boundary interaction in a well-defined configuration, we used single crystals of cubic zirconia (8YSZ) deposited with a thin layer overcoat of polycrystalline 8YSZ sintered to a relatively high density. After applying an electric current, we observed some residual pores in the thin film to migrate into the single crystal in the direction of oxygen flux but opposite to the direction of electric field. The sole interface between single crystal and polycrystal acts as a pore filter: at a given temperature and electric field only pores of a certain size can pass, which can be used to verify the model prediction. Our data found large pores migrating furthest into the single crystal, which indicates faster electric breakaway of larger pores.

### Modeling Cation Diffusion in 8YSZ

We have resolved a long-standing controversy in ceramic diffusion literature concerning cation diffusivity in 8YSZ and similarly (fluorite) structured ceramics. These ceramics have extensive anion vacancies, which give rise to fast anion diffusivity. However, cation diffusion some  $10^{10}$  times slower than anion diffusion is the mechanism that controls microstructure evolution, processing, and mechanical and irradiation properties. Experimentally, the activation energy of cation diffusivity is found to be around 5 eV according to many studies. Yet all model calculations suggest an activation energy of at least 10 eV for the cation vacancy mechanism, and even higher for various cation interstitial mechanisms. Meanwhile, the dependence of cation diffusion on oxygen pressure is inconsistent with the vacancy mechanism. These discrepancies are already known for over 30 years without a resolution. Our experiments on electrically motivated grain growth in 8YSZ revealed another interesting and perplexing observation: grain growth on the cathode side is orders of magnitude faster than that on the anode side. More recent experiments on electro sintering confirmed the same. This is itself remarkable: since there is no gradient in the electric field to justify a faster migration velocity, it must be grain boundary diffusivity itself that is position sensitive. This sensitivity can only come from a position-sensitivity in defect concentration, yet the concentration of the dominant defect—oxygen vacancy, is essentially constant due to the large concentration of the aliovalent dopant ( $Y^{3+}$ ).

Using first principles simulation, we have found that the activation energy of cation diffusion is highly sensitive to the local structure. Although 8YSZ has a nominally “cubic” fluorite structure, the local atomic structure is far from being cubic, with Zr surrounded by 7 anions instead of 8 anions as in the fluorite, which confirms the local structure determined by EXAFS. First principles simulations found a difference of about 5 eV between the activation energy of a 7-anion-coordinated Zr in “real” 8YSZ and that of a 8-anion-coordinated Zr in “cubic” 8YSZ. This large difference which can largely resolve the controversy has escaped the attention of all the previous investigators because they “habitually” adopted the cubic fluorite structure in their computation.

The result of faster cation diffusivity on the cathode side was also reproduced by first principles simulation which found a higher diffusivity after introducing a small number of supersaturated

oxygen vacancies. Unlike the structural vacancies in 8YSZ, which form because of “acceptor doping” by trivalent  $Y^{3+}$  replacing tetravalent  $Zr^{4+}$ , each supersaturated oxygen vacancy must be charge-compensated by some form of cation reduction. This raises the ground state energy of the reduced cation, which lowers the activation energy.

### Summary

Our experimental findings and first-principles simulation studies have revealed a large set of unexpected and novel results, which challenge prevailing paradigms, resolve long standing controversies, and reveal new kinetic principles and defect thermodynamics, for oxide ceramics that have active ionic conductivity such as YSZ. These results will have a decisive impact on the future course of oxide ceramic studies and applications.

### **Future Plans**

We will report results on electro sintering and pore migration in other oxide ceramics of large ionic conductivity.

### **References**

None.

### **Publications (The Last Two Years)**

W. Zhao, Y. Liu, J. Liu, P. Chen, I-W. Chen, F. Huang and J. Lin, “Controllable Synthesis of Silver Cyanamide as A New Semiconductor Photocatalyst under Visible-Light Irradiation,” *J. Mater. Chem.*, **A1**, 7942-7948 (2013).

S-W. Kim, S-J. L. Kang and I-W. Chen, “Electro-Sintering of Yttria-Stabilized Cubic Zirconia,” *J. Amer. Ceram. Soc.*, **96**[5] 1398-1406 (2013).

S-W. Kim, S-J. L. Kang and I-W. Chen, “Ionomigration of Pores and Gas Bubbles in Yttria-Stabilized Cubic Zirconia,” *J. Amer. Ceram. Soc.*, **96**[4], 1090-1098 (2013).

J. Park and I-W. Chen, “*In Situ* Thermometry Measuring Temperature Flashes Exceeding 1700oC in 8 mol%  $Y_2O_3$ -Stabilized Zirconia Under Constant-Voltage Heating,” *J. Amer. Ceram. Soc.*, **96** [3], 697-700 (2013).

I-W. Chen, S-W. Kim, J. Li, S-J. L. Kang and F. Huang, “Ionomigration of Neutral Phases in Ionic Conductors,” *Adv. Energy Mater.* **2**, 1383-1389 (2012).

S-W. Kim, S G. Kim, J-I. Jung, S-J. L. Kang and I-W. Chen, “Enhanced Grain Boundary Mobility in Yttria-Stabilized Cubic Zirconia under an Electric Current,” *J. Am. Ceram. Soc.*, **94** [12] 4231-4238 (2011).

## Coupled Plasmonic Arrays for Real Time Sensing

George Chumanov

[gchumak@clmson.edu](mailto:gchumak@clmson.edu)

Department of Chemistry

Clemson University, Clemson, SC 29634

### Program Scope

Nanoscale materials attract considerable interest because of their unusual properties and potential for practical applications. Most of the activity in this field is focused on the synthesis of homogeneous nanoparticles from metals, metal oxides, semiconductors, and polymers. It is well recognized that properties of nanoparticles can be further enhanced if they are made as hybrid structures. This research is concerned with the synthesis, characterization, and application of plasmonic Ag nanoparticles (NPs) and structures. One of the emphases is on asymmetric hybrid nanoparticles (AHN). These are composed of a metal plasmonic core with other layers and particles on their surface. The layers and particles are placed on the surface in an asymmetric fashion. These structures exhibit new properties that arise from the interactions between the core and the layers thereby rendering the development of AHNs fundamentally and practically important.

Plasmonic NPs exhibit unique optical properties arising from the excitation of the collective oscillations of the conduction electrons termed plasmon resonances. Plasmon resonances can be tuned across the visible spectral range by varying the particle size, shape, and dielectric environment, as well as by organizing the NPs into arrays. Plasmon excitation in Ag NPs represents the most efficient mechanism by which light interacts with matter. Because of this efficiency, tunability, and photochemical robustness, plasmonic AHNs are ideal for applications involving interaction with light. We design structures for novel optical applications.

### Recent Progress

Irradiation of Ag NPs with light results in the excitation of plasmon resonances. Plasmon resonances can 'enhance' many optical phenomena such as Raman scattering fluorescence, infrared absorption, second harmonic generation, and Rayleigh scattering, via a strong evanescent field associated with the oscillating electrons. Ag NPs can undergo the coherent plasmon coupling when assembled into 2D arrays leading to a sharp cooperative resonance with FWHM of 10-15 nm (Fig.1). In this case, light interacts not with each individual particle in the array but with an ensemble of particles. The ensemble is characterized by the coherent oscillations of the electron density in the particles. The coherent plasmon coupling was discovered in this laboratory and is extensively investigated to understand its fundamental properties and potential practical applications. The strongest coupling, as evident from the sharpest

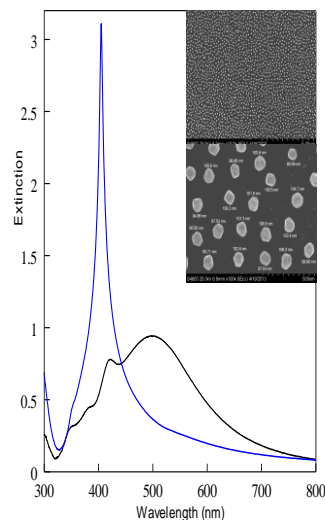


**Fig. 1** Coherent plasmon coupling (blue) and the same Ag NPs in the water (black). Inset: EM images of a coupled 2D array

resonance, occurs at the optimum interparticle distance that depends upon the particle size and dielectric environment. Once the conditions are optimized, the resonant frequency becomes sensitive to small changes in the dielectric environment in the space between the particles and to the presence of different species on the particle surface. This behavior opens opportunity for various sensing applications of the coherent plasmon coupling.

In the last year, we have been developing a sensitive, real time measuring system utilizing the coherent plasmon coupling. The sharpness of the resonance presents an opportunity for differential optical measurements. A coupled 2D array of Ag NPs is simultaneously irradiated with two closely spaced wavelengths selected in such way that they probe the resonance on both sides from its peak. When the resonance shifts to either red or blue side, the extinction at one wavelength increases whereas the extinction at the other wavelength decreases. The sharper the resonance the larger the differential signal is and more sensitive measurements can be performed.

We have developed and constructed an instrument capable of performing the

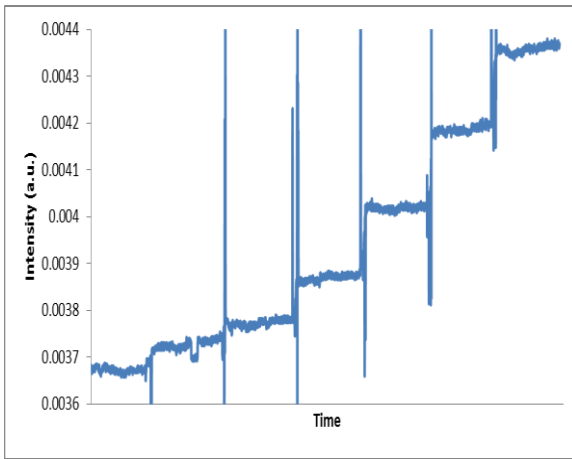


**Fig. 2** Differential signal as a function of the injection of a model compound. Vertical lines correspond to the noise spikes due to the injection. See table for more numerical data.

differential optical measurements. The instrument consists of a monochromator, in which the exit slit was replaced with two small apertures permitting two wavelengths spaced 10 nm apart. The stirring optics crosses the two beams at the coupled 2D array followed by their separation into the two detectors with corresponding electronics. Typical data is presented in Fig. 2, in which the signal change is shown with the injection of a model compound that changes the dielectric environment. As the local dielectric function was increased stepwise, the signal increased accordingly. The table below presents numerical data for the graph shown in Fig. 2. The signal-to-noise ratio in the range of hundreds was obtained in only 10 seconds of the data collection with

the integration time of 300 milliseconds. The detection limit under these conditions was estimated to be in the range of 1E-05 refractive index units. Further improvements are feasible with more optimization and a flow-cell setup.

~5k Data Points Collected Per Change in Refractive Index				
Refractive Index Change	Signal	Noise	S/N	Signal Increase
0	0.0036831	4.2008E-06	876.7615	0
7.00E-05	0.00372299	5.41509E-06	687.5206	3.98832E-05
1.40E-04	0.00377352	6.81662E-06	553.5755	9.04125E-05
3.50E-04	0.00387105	5.7775E-06	670.0219	0.000187951
7.00E-04	0.00401809	5.06459E-06	793.3681	0.000334984
1.05E-03	0.00418738	6.79096E-06	616.6113	0.000504277
1.40E-03	0.00435837	8.28483E-06	526.0668	0.000675269

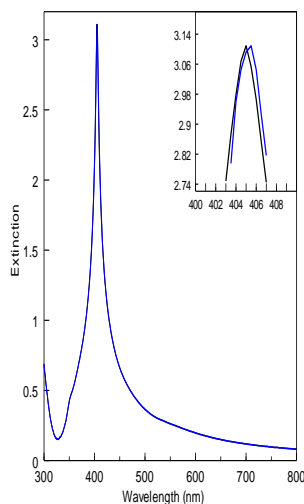


**Fig. 3** Spectral shift of the resonance after changing the refractive index of the medium by  $1.4 \times 10^{-3}$  units and measured using conventional UV-vis spectroscopy. Inset: Magnified region around the peak of the resonance. Even though the shift of the resonance can be detected, it cannot be reliably measured due to the system noise.

To demonstrate the advantage of the differential optical measurements, we have also performed ‘conventional’ measurements on 2D coupled arrays using a standard UV-vis spectrophotometer. The frequency shift of the cooperative resonance can only be detected using this instrument (but cannot be reliably measured) at the maximum ( $1.4 \times 10^{-3}$ ) change of the refractive index (Fig. 3). The differential measurements

have improved the detection limit by at least two orders of magnitude. Another advantage of the differential measurements is that they can be performed in real time.

### **Publications in the Last Two Years with DOE Acknowledgement**

S. Pyshkin, J. Ballato, G. Chumanov, D. Van Derveer, R. Zhitaru, “Long-term and light stimulated evolution of semiconductor properties” *Ceramic Transactions* 235, 113-124, (2012).

Z. Koontz and G. Chumanov “Depolarized Light Scattering From Clusters of Silver Nanoparticles” *Chem.Phys.Chem*, 2013, submitted.

K. D. Dukes, K. A. Christensen, and G. Chumanov “Core-Shell Silver Nanoparticles for Optical Labeling of Cells”, *Analytical Biochemistry*, 2013, in press.

## **Conduction Mechanisms and Structure of Ionomeric Single-Ion Conductors**

**R. H. Colby (PI), J. K. Maranas, K. T. Mueller, J. Runt and K. I. Winey**

### **Program Scope**

We have assembled an active team of scientists to study conduction mechanisms in ionomers. Our focus is on model cation-conducting ionomers that allow systematic variations in polarity, solvating ability, anionic group, alkali metal counterion and ion content. The low- $T_g$  ionomers we have studied thus far – sulfonated polyester ionomers based on poly(ethylene oxide) and polysiloxane backbone ionomers with weak-binding borate anions and either ethylene oxide or cyclic carbonate side chains – have greatly advanced the field of single-ion conducting ionomers. This class of material is expected to play a pivotal role in advanced batteries, as the next generation of battery separator membranes is expected to require single-ion conductors.

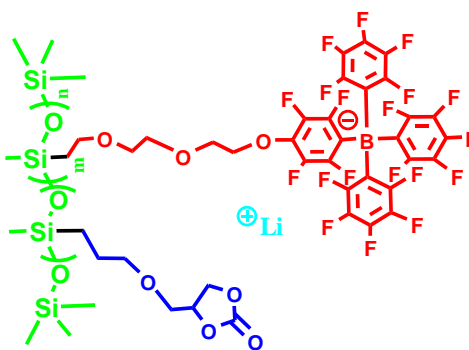
If successful, our fundamental study should lead directly to improved models for cation motion in soft low- $T_g$  ionomers and how that motion is facilitated by changes in ion content, dielectric constant, solvation and cation-anion pair formation energy. Since very similar materials are being considered for advanced batteries, fuel cells, actuators, sensors and super-capacitors, our study of model ionomers will aid in designing superior membranes for these applications. The fact that ionomers only have a single mobile ion makes them ideal for studying conduction mechanisms but it is important to note that these ionomers are *not* intended to be candidate materials for actual battery applications. The understanding we develop will instead drive the field towards superior materials as single-ion conductors for various applications, guided by our Primary Target: What is needed to build a single-ion conducting polymer membrane with high conductivity? That target will be explored via random copolymer ionomers made by RAFT, from various anionic and polar comonomers and blending with various nonionic polar oligomers as nonvolatile plasticizers. Our Second Target will address the question: Can we achieve sufficient mechanical properties without sacrificing conductivity? That question will be addressed by constructing block copolymers having a high- $T_g$  hard block for mechanical strength and a low- $T_g$  soft block for ion conduction.

To accomplish these goals we have a team of five faculty, one post-doc and nine graduate students. Ralph Colby (Materials Science, PSU) has considerable experience with synthesis, dynamics, mechanical properties and charge transport in ionomer melts and polyelectrolyte solutions. Janna Maranas (ChemE, PSU) brings MD simulation expertise and calibration of simulations using quasielastic neutron methods and her force fields have been fully tested for PEO-ionomers. Karl Mueller (Chemistry, PSU) is an expert on multinuclear NMR methods, vital for probing ion surroundings and ion diffusion. Jim Runt (Materials Science, PSU) uses FTIR and dielectric relaxation spectroscopies to study ionomers, with methods developed to extract conducting ion content and mobility. Karen Winey (Materials Science, UPenn) is a world-class expert on characterizing the morphologies of ionomers using X-ray scattering and scanning transmission electron microscopy methods.

## Recent Progress

**Polyanions** We have developed *ab initio* methods (using Gaussian software) to identify ions and polar groups from which to construct single-ion conducting ionomers for facile transport of any particular ion [pub #2]. For transporting  $\text{Li}^+$ , these quantum chemistry calculations have led to constructing ionomers [pub #6] based on polar cyclic carbonate side groups and weak-binding tetraphenyl borate or perfluorinated tetraphenyl borate side chains (see figure below).

We synthesized anionic polysiloxanes with polar carbonate side groups (in blue) and weak-binding tetraphenyl borate or perfluorinated tetraphenyl borate side chains (shown at right in red) and lithium counterions [pub #6], using hydrosilylation. Blending with  $M = 600$  g/mol poly(ethylene glycol) (PEG) improves ion conduction by improved solvation, lower  $T_g$  and homogenization [paper in preparation]. The inherent problem with the neat copolymer ionomers seems to be that while the polar carbonates (blue) solvate  $\text{Li}^+$ , they microphase separate from the borates (red). We also have developed a variety of non-volatile oligomeric plasticizers based on ethylene oxide (for strong solvation of  $\text{Li}^+$ ) and cyclic carbonates (to raise dielectric constant) and blended those with these siloxane-carbonate-borate ionomers. The plasticizers boost ion conductivity greatly, by lowering  $T_g$  and solvating  $\text{Li}^+$ , homogenizing the system and allowing all  $\text{Li}^+$  to contribute to conduction [paper in preparation].



**Polycations** For construction of polycations to transport  $\text{F}^-$  or  $\text{OH}^-$  (other potential lightweight battery ions) we used *ab initio* methods to prove that phosphoniums are both weaker binding and more stable than ammoniums or imidazoliums. The ionomers we have synthesized are the topic of a paper recently submitted to *Chemistry of Materials*. The reason for the weakened ion interactions and improved stability for phosphonium is fully understood. P is less electronegative than C, so the phosphonium has the expected strongly positive P but with weakly negative carbons attached to it that act to shield the positive charge from the small anions and stabilize the carbons by making their protons less acidic. In contrast, nitrogen-containing cations (such as ammonium and imidazolium that we have studied) have N more electronegative than C, making the nitrogen bear a negative charge in these cations, with the attached carbons strongly positive and easily accessible to both the anion (meaning they bind the anion more strongly) and attack on their much more acidic protons (making them less stable).

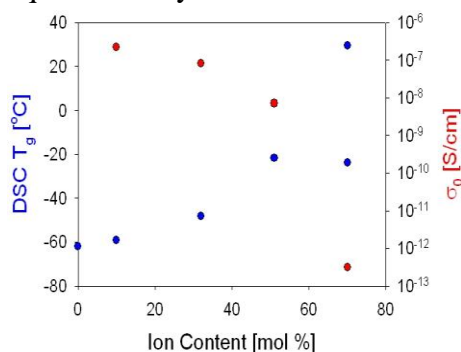
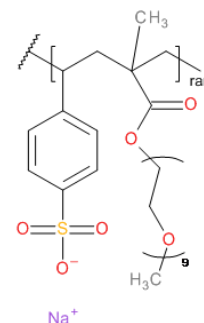
We have used the same hydrosilylation chemistry above to construct cationic polysiloxane ionomers with phosphonium and oligo ethylene oxide side chains, with fluoride, hydroxide or bromide counterions. These anion conductors are potentially useful for  $\text{F}^-$  or  $\text{OH}^-$  conducting membranes for batteries and fuel cells and even at high ion contents these ionomers have very low  $T_g \approx -75$  °C and reasonable ion conductivity without any solvent present. X-ray scattering suggests no ionic aggregation and this helps to keep  $T_g$  low, detailed in our paper recently submitted to *Chemistry of Materials*.

## Future Plans

### RAFT Ionomers

Both polyanions and polycations have been successfully synthesized by our team using Reversible Addition-Fragmentation chain Transfer (RAFT) polymerization methods. One Ph.D. student has been using RAFT for the past 2 years and is developing expertise in this standard polymerization method. Owing to different monomer reactivities, we typically react to 70 or 80% conversion, resulting in quite uniform random copolymers. A strong advantage of RAFT is that, in contrast to our previous polymerization methods, it is straightforward to make ionomers with molecular weight in the  $30,000 < M < 600,000$  g/mol range, with fairly narrow distributions,  $M_w/M_n < 1.2$ .

Nice examples are the random copolymers of sulfonated styrene and methacryl-PEO, such as the one shown at right. Both homopolymers are fully water soluble so the copolymers are easily purified by aqueous dialysis and the counterion can be exchanged by simply

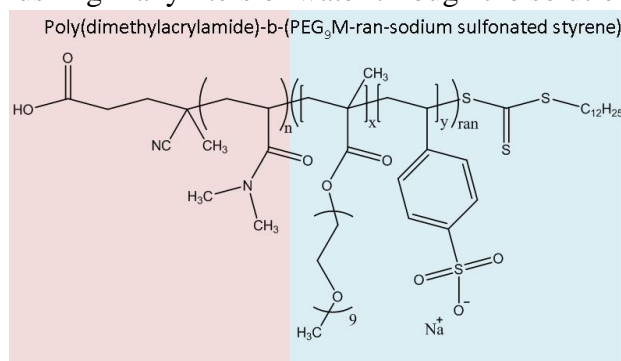


adding a 100x excess of a lithium salt (for example) during dialysis.  $T_g$  stays quite low at low ion content ( $T_g < -40$  °C for less than 40 mol% sulfonated styrene) while  $T_g$  increases more rapidly at higher ion contents, eventually exhibiting two  $T_g$ s in DSC at 70 mol% sulfonated styrene (blue symbols in the plot at left, with 25 °C conductivity in red).

### RAFT Block Copolymer Ionomers

We are now shifting our focus to study block copolymer ionomers made by RAFT. One block is a random copolymer of a sulfonated monomer and methacryl-PEO, such as the one shown above, designed to have low- $T_g$  and high conductivity of cationic counterions such as  $Li^+$  or  $Na^+$ . The second block needs to be high- $T_g$  and impart good mechanical properties. Several candidates have been tried but we are now planning to focus on dimethyl acrylamide as the hard block, with  $T_g = 120$  °C. The enormous advantage of this high- $T_g$  polymer is that it is fully water soluble, allowing our usual method of exhaustive aqueous dialysis, effectively flushing many liters of water through the solution, to remove impurities.

The chemical structure of these block copolymers is shown at right. As with all of our team's work, we plan to use the vast array of experimental materials science methods to fully characterize these materials, emphasizing X-ray scattering (both morphology of ions and microphase separation of the two blocks), dielectric spectroscopy (ion conductivity and segmental polymer motions), linear viscoelasticity (modulus and softening at lower frequency / higher temperature) and <sup>7</sup>Li PGSE NMR to study diffusion of  $Li^+$ .



## Publications in last two years

- 1) D. J. Roach, S. Dou, R. H. Colby and K. T. Mueller, Nuclear Magnetic Resonance Investigation of Dynamics in Poly(Ethylene Oxide) Based Lithium Polyether-ester-sulfonate Ionomers, *J. Chem. Phys.* **136**, 014510 (2012).
- 2) W. Liu, M. J. Janik and R. H. Colby, First Principles Design of Ionomers for Facile Ion Transport, in Polymers for Energy Storage and Delivery: Polyelectrolytes for Batteries and Fuel Cells (K. Page, C. Soles, J. Runt, editors) ACS Symposium Series **1096**, Ch. 2, p. 19-44 (2012).
- 3) G. J. Tudryn, M. V. O'Reilly, S. Dou, D. R. King, K. I. Winey, J. Runt and R. H. Colby, Molecular Mobility and Cation Conduction in Polyether-ester-sulfonate Copolymer Ionomers, *Macromolecules* **45**, 3962 (2012).
- 4) K. Sinha, W. Wang, K. I. Winey, J. K. Maranas, Dynamic Patterning in PEO-based Single Ion Conductors for Li Ion Batteries, *Macromolecules* **45**, 4354 (2012).
- 5) K.-J. Lin and J. K. Maranas, Cation Coordination and Motion in a Poly(ethylene oxide) based Ionomer, *Macromolecules* **45**, 6230 (2012).
- 6) S. Liang, U H. Choi, W. Liu, J. Runt and R. H. Colby, Synthesis and Lithium Ion Conduction of Polysiloxane Single-Ion Conductors Containing Novel Weak-Binding Borates, *Chemistry of Materials* **24**, 2316 (2012).
- 7) K.-J. Lin, K. Li and J. K. Maranas, Differences Between Polymer/Salt and Single Ion Conductor Solid Polymer Electrolytes, *RSC Advances* **3**, 1564 (2013).
- 8) D. J. Roach, S. Dou, R. H. Colby, and K. T. Mueller, Solid state nuclear magnetic resonance investigation of polymer backbone dynamics in poly(ethylene oxide) based lithium and sodium polyetherester-sulfonate ionomers, *J. Chem. Phys.* **138**, 194907 (2013).
- 9) Q. Chen, G. J. Tudryn and R. H. Colby, Ionomer Dynamics and the Sticky Rouse Model, *J. Rheol.* **57**, 1441 (2013).
- 10) K.-J. Lin, K. Li and J. K. Maranas, Does decreasing ion-ion association improve cation mobility in single ion conductors?, *Phys. Chem. Chem. Phys.* **15**, 16143 (2013).
- 11) J.-H. H. Wang and R. H. Colby, Exploring the role of ion solvation in ethylene oxide based single-ion conducting polyanions and polycations, *Soft Matter* DOI: 10.1039/c3sm51460a (2013) published online but no page numbers yet.

## **Title: Integrated Growth and Ultra-low Temperature Transport Study of the 2<sup>nd</sup> Landau Level of the Two-Dimensional Electron Gas**

**Principal Investigators: Gabor Csathy and Michael Manfra**

**Institution: Purdue University**

**Address: 525 Northwestern Ave., West Lafayette, IN 47907**

**E-mail of PIs: gcsathy@purdue.edu, mmanfra@purdue.edu**

### **Program Scope**

We have developed a synergistic experimental program based on systematic growth and ultra-low temperature measurement of high quality GaAs crystals tailored to answering outstanding questions concerning the collective behavior of the correlated electronic ground states of the two dimensional electron gas. Our primary focus is the study of the fractional quantum Hall states and exotic electronic solids of the second Landau level, i.e. corresponding to Landau level filling factors  $2 \leq \nu \leq 4$ . There is mounting theoretical and experimental evidence that several fractional quantum Hall states in this region are not well described by the model of non-interacting composite fermions. For example, the even denominator state at  $\nu=5/2$  may result from an unusual pairing mechanism of the composite fermions described by the Pfaffian wavefunction. Because the pairing is believed to be  $p$ -wave, the  $5/2$  state may resemble other condensed matter systems of current interest such as strontium ruthenate, certain fermionic atomic condensates, and the quantum liquid He-3. Moreover several odd denominator fractional states in the 2<sup>nd</sup> Landau level such as the  $2+2/5$  and  $2+6/13$  states are quite distinct from their well understood lowest Landau level ( $\nu < 2$ ) counterparts.

The study of the  $5/2$  state has been reenergized with the prediction that its excitations obey exotic non-Abelian statistics. The  $\nu=5/2$  and other novel states in the 2<sup>nd</sup> Landau level are not only of fundamental interest as they may manifest behavior not seen in any other physical system, but also may find technological utility in fault-tolerant schemes for quantum computation. These exotic states are, however, fragile and hence they develop only in the highest quality GaAs host crystals and typically only at the lowest electron temperatures.

The goal of our program is to use incisive experimental techniques to generate new insight into the nature of the exotic correlated states of the 2<sup>nd</sup> Landau level. We carry out an integrated growth and experimental study of the two-dimensional electron gas in GaAs in the 2<sup>nd</sup> Landau level by focusing on:

- 1) Growth of ultra-high quality GaAs/AlGaAs heterostructures specifically tailored to study the impact of various material parameters on the stability of the various fractional quantum Hall ground states in the 2<sup>nd</sup> Landau level.
- 2) Application of novel techniques together with transport measurements in the most interesting but technologically difficult ultra low temperature regime ( $T \sim 5\text{mK}$ ). As this regime is still largely unexplored, new and unanticipated results can be expected.

### **Recent Progress**

This project builds on the ongoing collaboration of the PIs and unique experimental capabilities developed at Purdue University. *Our team has recently developed a unique combination of next*

*generation growth and measurement capabilities needed to address several of the outstanding problems in the field of 2D electron physics.*

Manfra has designed and built a highly customized MBE chamber designed for the growth of ultra high mobility GaAs/AlGaAs heterostructures (see Fig.1). Over the past year, Manfra's DOE-related work has focused on 4 primary tasks: 1) improvement of 2DEG samples for examination of exotic 2nd Landau level physics, 2) growth and processing development of in-situ backgated ultra-high mobility 2DEGs, 3) growth and characterization of 2DEGs with controlled disorder, 4) growth of samples specifically designed for DOE-funded external collaborations. Towards these ends several accomplishments are noteworthy.

- a. electron samples with a record high stability of the exotic  $\nu=5/2$  fractional quantum Hall state as measured by the largest energy gap of 569mK. This is an ongoing work, the first results are already published [1,2].
- b. samples in which the 2DEG density can be tuned with an in-situ backgate from  $2 \times 10^{10} \text{cm}^{-2}$  to  $2.7 \times 10^{11} \text{cm}^{-2}$  with a peak mobility of  $17 \times 10^6 \text{cm}^2/\text{Vs}$  at  $T=0.3\text{K}$ .
- c. a series of samples with different strength of the alloy disorder including samples with Al concentrations as low as 0.057% [4].
- d. Manfra's samples have been widely distributed to collaborators, including many DOE-funded researchers. Samples have been grown for approximately 15 independent research groups around the world. Manfra's work with Michael Zudov of the University of Minnesota is a prime example of his external collaborations with DOE-funded researchers [6-8].

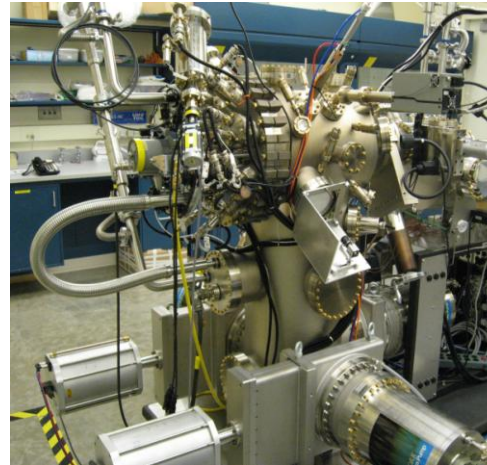


**Fig.1.** Manfra's custom-designed MBE installed at Purdue. This new machine is producing samples of record quality used not only in this current project but also distributed among colleagues, several of which are DOE supported.

Csathy has built a specialized ultra-low temperature refrigerator capable of cooling electrons in semiconductors to 5mK [9,10]. This setup not only cools the electrons but also allows for a reliable magnetic-field-independent temperature measurement of the local bath via He-3 viscometry. His immersion cell is shown in Fig.2. Notable results from his lab supported by this DOE award are:

- a. discovery of a unique experimental signature in the  $R_{xx}$  of the exotic electronic solids called the bubble phases [1].
- b. we have reported unexpected results of the bubble phases in the third Landau level [2].
- c. we have made significant progress with the measurements of samples with alloy disorder [4].

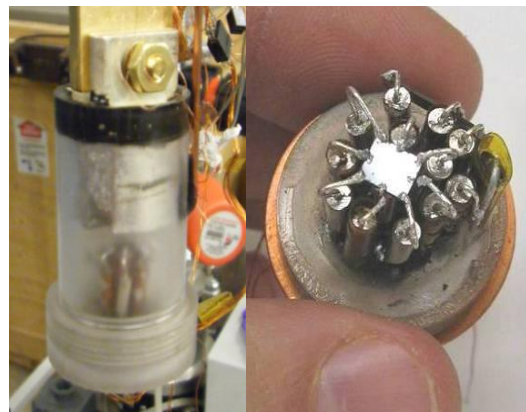


**Fig.2.** Csathy's He-3 immersion cell allows reaching temperatures of 5mK (left). A sample mounted on sintered Silver heat sinks (right). Reliable temperature measurement is achieved using a novel quartz He-3 viscometry [9].

Our progress is evident in the observation of some of the most fragile fractional quantum Hall states [1, 2]. Our electron samples show extremely robust fractional quantum Hall ground states in the lower spin branch of the second Landau level near the filling factor  $\nu=5/2$  [2]. The  $\nu=5/2$  state in one sample grown by Manfra has the largest excitation gap ever reported – close to 0.6 Kelvin. The fine details of the transport features near  $\nu=5/2$  are shown in Fig.3. In particular,

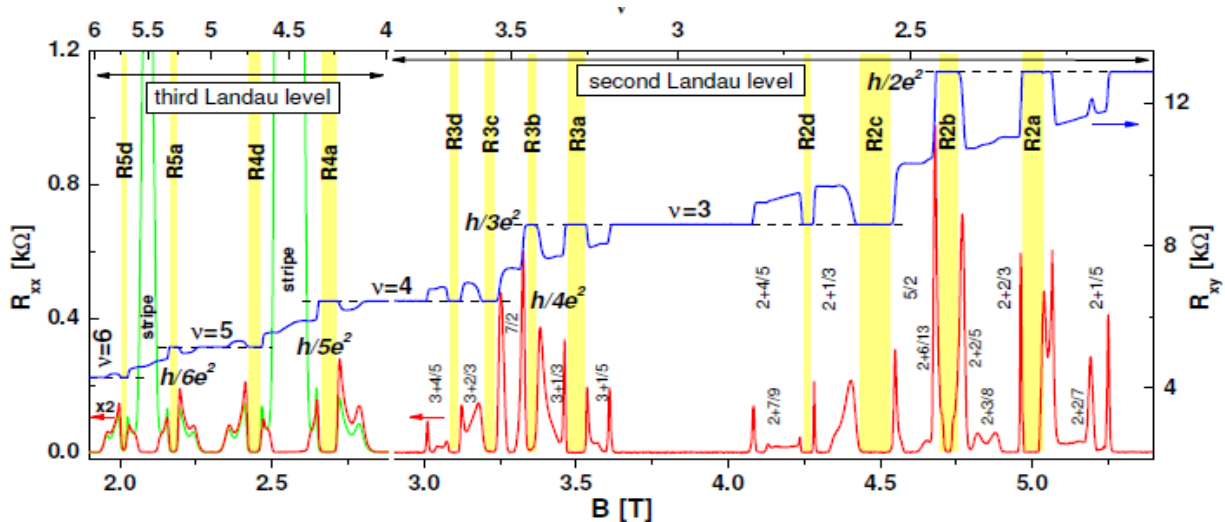


**Fig.3** Magnetotransport in the second and third Landau levels showing the prominent reentrant integer states shaded in yellow and many fractional quantum Hall states marked by their quantum number. See reference [2] for more detail.

we find a completely well-formed  $\nu=2+2/5$  state. This feature has only been reported in 2 samples during the past 6 years, yet it appears quite strong in many of our samples. In addition, we see rich physics in the upper spin branch, near the quantum number  $\nu=7/2$ , and in the third Landau level, near  $\nu=9/2$  and  $11/2$ . The exquisite quality of the data enabled us, for the first time, to investigate the reentrant integer quantum Hall states (RIQHS). In a recently published Phys. Rev. Lett. [1] we report an unexpected sharp peak in the  $R_{xx}$  versus temperature curve of the reentrant integer states, also called the bubble phases. We associated these peaks with the melting of the collective ground state. This allowed us, for the first time, to compare energy scales of various reentrant states [2]. We found that the onset temperatures scale with the Coulomb interaction energy. This comparison allowed us to conclude, that since the interaction energy plays a dominant role in the formation of these phases, the electrons are not randomly localized but form a strongly interacting phases, most likely an exotic electron solid. Furthermore, we found that, contrary to expectations, the onset temperature in the third Landau level is substantially higher than that in the second Landau level. This large discrepancy is not yet understood, but it shows us that there is still much to be learned about these states.

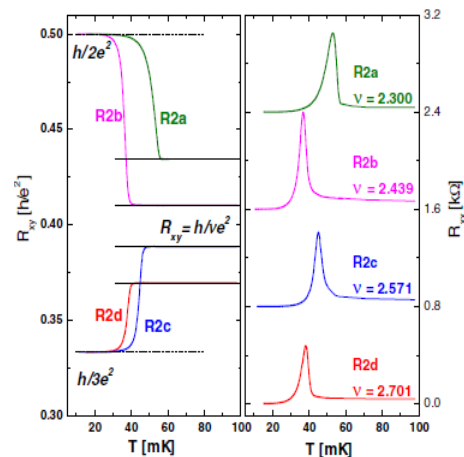


**Fig.4** The prominent changes in both  $R_{xy}$  and  $R_{xx}$  signal the onset of the electronic bubble phases, see reference [1].

Available data suggests that the  $5/2$  state responds differently to different types of disorder. However, in all prior measurements, disorder is uncontrolled as it is the residual disorder from the sample growth process. Manfra has grown a set of samples with deliberate introduction of a specific type of disorder: short range alloy disorder [4]. What is remarkable about these samples is that they host well-developed  $5/2$  states even in the regime in which alloy disorder dominates. The low temperature transport measurements are currently under way.

Under this program, Manfra has also grown high quality two-dimensional hole samples, for which he holds the record for mobility. Manfra's students found that the mobility exhibits an unexpected peak at the relatively low hole density of  $\sim 6 \times 10^{10}/\text{cm}^2$ . Their analysis of known scattering mechanisms was not able to account for the observed behavior leaving the possibility open for an underappreciated mechanism at high densities [3].

### Future Plans

We will continue our effort in studying disorder effects by energy gap measurements in the presence of alloy disorder. We will then extend our studies to other types of well-controlled disorders. We are also investigating the spin polarization of the  $\nu=5/2$  state. Finally, our recent result on the reentrant insulating states calls for their study in high Landau levels. Such investigations involve a coordinated effort between growth and ultra-low temperature measurement and are part of our long term effort aimed at exploring unconventional collective behavior in low-dimensional systems.

### References acknowledging DOE support

1. N. Deng, A. Kumar, M.J. Manfra, L.N. Pfeiffer, K.W. West, and G.A. Csathy, "Collective Nature of the Reentrant Integer Quantum Hall States in the Second Landau Level", *Physical Review Letters* **108**, 086803 (2012)
2. N. Deng, J.D. Watson, L.P. Rokhinson, M.J. Manfra, and G.A. Csathy, "Contrasting Energy Scales of the Reentrant Integer Quantum Hall States", *Rapid Communications, Physical Review B* **86**, 201301 (2012)
3. J.D. Watson, S. Mondal, G. Gardner, G.A. Csathy, and M.J. Manfra, "Exploration of the Limits to Mobility in Two-Dimensional Hole Systems in GaAs/AlGaAs Quantum Wells", *Physical Review B* **85**, 165301 (2012)
4. G.C. Gardner, J.D. Watson, S. Mondal, N. Deng, G.A. Csathy, and M.J. Manfra, "Growth and electrical characterization of  $\text{Al}_{0.24}\text{Ga}_{0.76}\text{As}/\text{Al}_x\text{Ga}_{1-x}\text{As}/\text{Al}_{0.24}\text{Ga}_{0.76}\text{As}$  modulation-doped quantum wells with extremely low  $x$ ", *Applied Physics Letters* **102**, 252103 (2013)
5. E. Kleinbaum and G.A. Csathy, "A Transimpedance Amplifier for Remotely Located Quartz Tuning Forks", *Review of Scientific Instruments* **83**, 126101 (2012)
6. A.T. Hatke, M.A. Zudov, J.D. Watson, and M.J. Manfra, "Magnetoplasmon resonance in a Two-Dimensional; Electron System Driven into a Zero-Resistance State", *Physical Review B* **85**, 121306 (2012)
7. A.T. Hatke, M. A. Zudov, J. D. Watson, M. J. Manfra, L. N. Pfeiffer, and K. W. West, "Effective mass from microwave photoresistance measurements in GaAs/AlGaAs quantum wells", *Journal of Physics: Conference Series* **456**, 012040 (2013)
8. A.T. Hatke, M.A. Zudov, J.D. Watson, and M.J. Manfra, L.N. Pfeiffer, and K.W. West, "Evidence of Effective Mass Reduction in GaAs/AlGaAs Quantum Wells", *Physical Review Letters* **B 87**, 161307 (2013)

## Other references

9. N. Samkharadze, A. Kumar, M.J. Manfra, L.N Pfeiffer, K.W. West, and G.A. Csathy, “Integrated Electronic Transport and Thermometry at milliKelvin Temperatures and in Strong Magnetic Fields”, *Review of Scientific Instruments* **82**, 053902 (2011)
10. A. Kumar, G.A. Csathy, M.J. Manfra, L.N Pfeiffer, and K.W. West, “Nonconventional Odd Denominator Fractional Quantum Hall states in the Second Landau Level”, *Physical Review Letters* **105**, 246808 (2010)

# High-Throughput Preparation and Characterization of Vapor-Deposited Organic Glasses

S.S. Dalal, D.M. Walters, A. Gujral, and M.D. Ediger  
Department of Chemistry  
University of Wisconsin-Madison, Madison, WI 53706

## Program Scope

We discovered recently that organic glasses with high density, low enthalpy, and extraordinarily high kinetic stability can be prepared by physical vapor deposition.<sup>1</sup> Prior to our recent work, these high density/high stability glasses would have been considered to be “impossible materials” in that one would have to age an ordinary glass for thousands of years or more to achieve similar properties. In order to reveal the full potential of these stable vapor-deposited glasses for a variety of applications, and to answer fundamental questions about the amorphous state, we are working to achieve the following objectives: 1) Develop high-throughput methods to characterize the density, surface topology, and molecular packing of vapor-deposited organic glasses. 2) Advance understanding about how the properties of vapor-deposited organic glasses depend upon deposition conditions, substrate, and film thickness. 3) Understand the microscopic packing responsible for the macroscopic anisotropy of some vapor-deposited glasses. 4) Prepare a wide variety of glasses from molecules relevant for organic electronics, both to understand generic features of vapor-deposited glasses and to allow the optimization of deposition conditions for applications in this area. 5) Advance fundamental understanding of amorphous systems by attempting to prepare materials that are equivalent to supercooled liquids equilibrated at very low temperature.

## Recent Progress

We have developed a high-throughput protocol to characterize vapor-deposited organic glasses. Our previous work has shown that substrate temperature can have a significant effect on the physical properties of an organic glass made by vapor deposition.<sup>2</sup> There has been no efficient way to study the effect of substrate temperature in a rapid fashion, significantly hindering progress in understanding structure-property relationships in these materials. In the past year, we have demonstrated a technique which allows the high-throughput characterization of many properties of organic glass-forming materials.<sup>3</sup> In a single experiment, we are able to measure the density, molecular orientation and kinetic stability of a large range of glasses using spectroscopic ellipsometry.

Figure 1 schematically illustrates the experiment. A silicon wafer is suspended between two copper fingers which are at

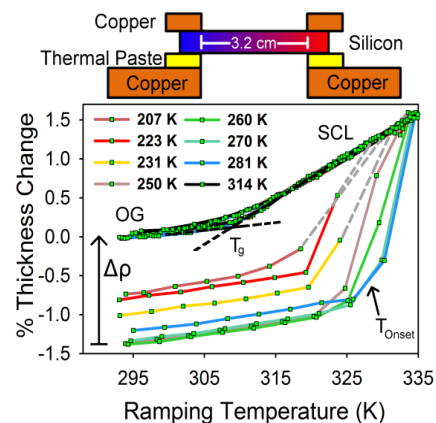


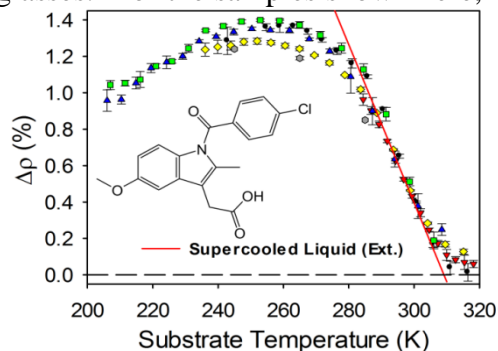
**Figure 1.** Top: A diagram of the temperature gradient sample holder. Bottom: Parallel dilatometry measurements for many different glasses of indomethacin. Different colors indicate different substrate temperatures from the same sample.

different temperatures. This imposes a temperature gradient onto the silicon wafer which is used as a sample substrate during deposition. After deposition, we heat the sample on our ellipsometry stage and perform dilatometry experiments on many different glassy materials simultaneously. As shown in Figure 1, all the different glass samples initially expand linearly as solids. At  $T_{\text{Onset}}$ , which depends on substrate temperature, the glass structurally transforms into the supercooled liquid (SCL), which is identical for all the glasses. For the samples shown here,  $T_{\text{Onset}}$  is up to 18 K greater than the conventional glass transition temperature  $T_g$ , indicating that these materials have achieved significant kinetic stability in comparison to the liquid-cooled ordinary glass (OG). The thickness difference between the as-deposited material and the ordinary glass determines the density of the vapor-deposited glass. The agreement of  $T_g$  and the thermal expansion coefficients of the ordinary glass and supercooled liquid for all the substrate temperatures ensure that all of the transformed materials are in the same state at the end of the experiment.

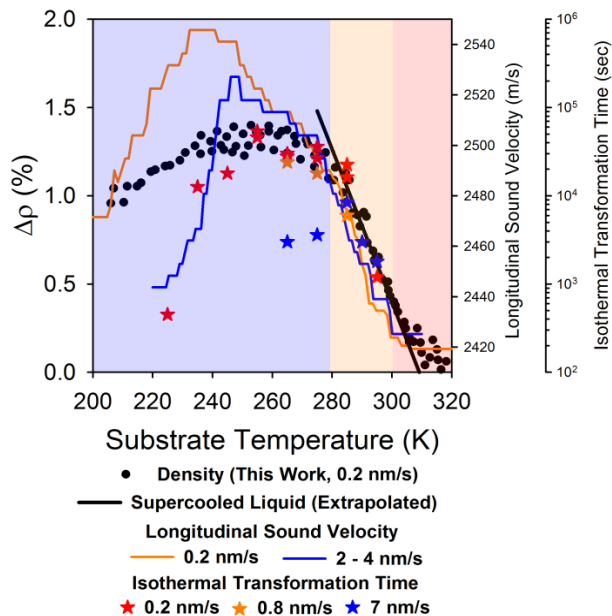
Figure 2 shows the density of as-deposited indomethacin glasses as a function of substrate temperature for several temperature-gradient samples. This data is acquired by mapping the sample before and after transformation into the supercooled liquid.

Figure 3 highlights the influence of kinetic and thermodynamic competition in these materials by comparing measurements of the isothermal resistance to transformation into the supercooled liquid,<sup>4</sup> the longitudinal sound velocity (which is related to the modulus)<sup>5</sup> and the density.<sup>3</sup> The red region indicates where true equilibrium supercooled liquids are prepared. In the yellow region the macroscopic observables follow the equilibrium trend but these materials are structurally anisotropic. In the blue portion of the plot, kinetics dominate the structure of the glasses and the different observables decorrelate. We anticipate materials with interesting and unexpected properties in this domain.

*Glasses have been prepared from molecules relevant for organic electronics.* We used our high-throughput protocol to prepare a variety of glasses of molecules relevant for organic electronics. In order to measure the dichroism of these



**Figure 2.** The density of vapor-deposited indomethacin glasses relative to the ordinary glass, determined for many different substrate temperatures.



**Figure 3.** A comparison of three observables reveals the competition between kinetics and thermodynamics during physical vapor deposition.

molecules, we upgraded our spectroscopic ellipsometry to increase its spectral range to 245-1000nm. We quantify the dichroism using the order parameter,  $S$ , calculated as shown in Equation 1.

$$(1) \quad S = \frac{3}{2} \langle \cos^2 \theta \rangle - \frac{1}{2} = \frac{k_z - k_{xy}}{k_z + 2k_{xy}}$$

By calculating the dichroism for the strong transition dipole moment along the long axis of the molecule, the order parameter describes how the molecules are aligned. Vertically aligned molecules have an order parameter value of 1, horizontally aligned molecules have a value of -0.5, and randomly arranged molecules have value of zero. We observe nearly identical trends in the birefringence and order parameter, suggesting they describe the same type of molecule orientation.

Figure 4 shows how the order parameter depends on the substrate temperature during deposition for several molecules relevant for organic electronics. The general trend is the following: Ordinary glasses, prepared at substrate temperatures above  $T_g$ , are nearly isotropic and have an order parameter of about zero. As the substrate temperature decreases, molecules have a tendency to stand-up and align vertically, as indicated by a positive order parameter. Lower substrate temperatures result in a negative order parameter, indicating horizontal alignment. While it has previously been reported that high aspect ratio molecules tend to show horizontal alignment,<sup>6</sup> vertical alignment and the strong substrate temperature dependence are unexpected and not yet understood.

*High-throughput WAXS.* Previously we have reported that wide angle X-ray scattering (WAXS) can detect short range molecular ordering that depends on substrate temperature in indomethacin glasses.<sup>4</sup> This packing is different from that measured using spectroscopic ellipsometry.<sup>3</sup> This makes WAXS a complementary technique for studying the anisotropic packing of molecules relevant for organic electronics.

We have measured two-dimensional WAXS patterns for a variety of TPD glasses prepared with our high-throughput protocol. Figure 5 shows the integration of a 2D WAXS pattern for TPD glasses from the same sample across a 12 K range in substrate temperature. The signal intensity increases with decreasing substrate temperature  $2\theta = 10^\circ$ . This is indicative of a second length scale important for the packing of TPD molecules.

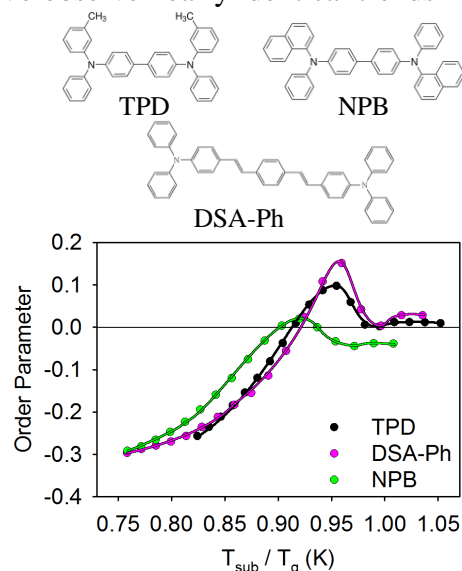


**Figure 4.** Structures and order parameters for molecules used for organic electronics.

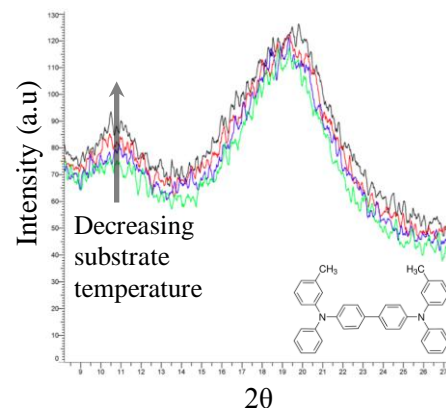


**Figure 5.** Integration of 2D WAXS patterns for TPD. Different colors indicate different substrate temperatures from the same sample.

## Future Plans

In the remaining 20 months of our project, we have these priorities: 1) Complete our ellipsometric investigation of stable glasses of seven molecules utilized in organic electronics. 2) Continue the development of WAXS measurements in conjunction with temperature-gradient samples. 3) Begin IR and AFM characterization of vapor-deposited glasses. 4) For one molecule, likely  $\alpha,\alpha,\beta$ -TNB, prepare temperature-gradient samples at a series of deposition rates. 5) Utilize the temperature-gradient stage to measure transformation growth front velocities as a function of deposition conditions.

## References

- (1) Swallen, S.F; Kearns, K.L.; Mapes, M.K.; Kim, Y.S.; McMahon, R.J.; Ediger, M.D.; Wu, T.; Yu, L.; Satija, S. *Science*. **2007**, *315*, 353.
- (2) Kearns, K.L.; Swallen, S.F; Ediger, M.D.; Wu, T.; Yu, L. *J. Chem. Phys.* **2007**, *127*, 154702.
- (3) Dalal, S.S.; Fakhraai, S.; Ediger, M.D. *J. Phys. Chem. B*. **2013** ASAP. DOI: 10.1021/jp405005n
- (4) Dawson, K.J.; Zhu, L.; Yu, L.; Ediger, M.D. *J. Phys. Chem. B* **2011**, *115*, 455.
- (5) Fakhraai, Z.; Still, T.; Fytas, G.; Ediger, M.D. *J. Phys. Chem. Lett.* **2011**, *2*, 423.
- (6) Yokoyama, D. *J. Mater. Chem.* **2011**, *21*, 19187.

## DOE-sponsored Research Publications

- (1) Dawson, K.; Zhu, L.; Yu, L.; Ediger, M.D. *J. Phys. Chem. B* 2011, *115*, 455.
- (2) Fakhraai, Z.; Still, T.; Fytas, G.; Ediger, M.D. *J. Phys. Chem. Lett.* **2011**, *2*, 423.
- (3) Dawson, K.; Zhu, L.; Kopff, L.A.; McMahon, R.J.; Yu, L.; Ediger, M.D. *J. Phys. Chem. Lett.* **2011**, *2*, 2683.
- (4) C.R. Daley, Z. Fakhraai, M.D. Ediger, and J.A. Forrest, *Soft Matter*, **2012**, *8*, 2206.
- (5) Dawson, K.; Kopff, L.A.; Zhu, L.; McMahon, R.J.; Yu, L.; Richert, R.; Ediger, M.D. *J. Chem. Phys.* **2012**, *136*, 094505.
- (6) Ediger, M.D.; Yu, L. *Nature Materials*, **2012**, *11*, 267.
- (7) Dalal, S.S.; Sepulveda-Marquez, A.; Pribil, G.K.; Fakhraai, Z.; Ediger, M.D. *J. Chem. Phys.* **2012**, *136*, 204501.
- (8) Dalal, S.S.; Ediger, M. D. *J. Phys. Chem. Lett.* **2012**, *3*, 1229.
- (9) Ediger, M.D.; Harrowell, P. *J. Chem. Phys.* **2012**, *137*, 080901.
- (10) Singh, S.; Ediger, M.D.; de Pablo, J.J. *Nature Materials*, **2013**, *12*, 139.
- (11) Dalal, S.S.; Fakhraai, Z.; Ediger, M.D. *J. Phys. Chem. B*. **2013**, ASAP.
- (12) Lyubimov, I.; Ediger, M.D.; de Pablo, J.J. *J. Chem. Phys.*, *accepted*.

## Program Title: Artificially Layered Superlattice of Pnictide by Design

Principle Investigator: Chang-Beom Eom

Mailing Address: Room 2164 ECB, 1550 Engineering Drive, University of Wisconsin-Madison,  
Madison, WI 53706

E-mail: [eom@engr.wisc.edu](mailto:eom@engr.wisc.edu)

### Program Scope

The goals of the program are to grow artificially engineered superlattices of pnictide materials by atomic layer-controlled growth, and to understand how structure property-relationships interact with the novel superconductivity in the pnictides so as to develop new understanding, applications, and devices. The critical scientific issues we will address include growth mechanisms, interaction between superconductivity and magnetism, interfacial superconductivity and physics of flux pinning in pnictide thin film heterostructures. We expect that this goal will also enable an understanding of the fundamental heteroepitaxial growth of intermetallic systems on oxide surfaces and role of interfacial layers in a sufficiently general way that can be applied broadly to many different material systems.

The discovery of superconductivity with transition temperatures of 20K-50K in iron-based materials has initiated a flurry of activity to understand and apply these novel materials. The superconducting mechanism, the structural transitions, the magnetic behavior above and below  $T_c$ , the doping dependence, and the critical current and flux-pinning behavior have all been recognized as critical to progress toward understanding the pnictides. A fundamental key to both basic understanding and applications is the growth and control of high-quality epitaxial thin films and superlattices with atomic layer control. The ability to control the orientation, the strain state, defect and pinning site incorporation, the surface and interfaces, and the layering at the atomic scale, are crucial in the study and manipulation of superconducting properties.

An important characteristic of the Co-doped  $\text{BaFe}_2\text{As}_2$  (Ba-122) material is the relatively low values of doping required to produce superconductivity. This leads to homogeneous films, and similar lattice constants between differently doped films, and great potential for epitaxial superlattices. The 122 materials share the fundamental iron-containing planes that are believed to be responsible for superconductivity, and they potentially all share the same basic mechanism of superconductivity, with a leading candidate being  $s^+$  pairing between electron and hole pockets at the zone center and boundary. All share the five Fe  $3d$ -orbitals important in the electronic structure, leading to a richness that has great potential for manipulation. In addition, the likely coexistence of magnetism and superconductivity for low-doping, and the nearby structural transitions in the intermediate-doping region, offer great flexibility in the design of new superlattices of, for instance, doped 122 and perovskite oxides, 122 layers of different doping levels, and doped 122 layers with the semi-metallic undoped parent compound.

We are guided to the main goals by our understanding developed over the last three years in relating pnictide structural and superconducting properties. The new film growth methods used in this project enables us to not only resolve these uncertainties, but also to design and synthesize new pnictide atomic layered structures that explore the limits of this material's superconducting properties. The **thrusts** of our project are:

- (1) *Atomic-layer-controlled growth of artificially engineered superlattice synthesis*
- (2) *Designing interfacial superconductivity at pnictide and FeSe interfaces.*
- (3) *Investigation of interaction between superconductivity and magnetism by proximity effect*
- (4) *Understanding and control of flux-pinning mechanisms*
- (5) *Study of growth mechanisms of heteroepitaxial superlattices and artificial pinning centers*

## Recent Progress

Artificial layered superlattices offer unique opportunity towards tailoring superconducting properties and understanding the mechanisms of superconductivity by creating model structures which do not exist in nature. We have successfully demonstrated the growth of two different types of artificially engineered superlattices of pnictide superconductor by pulsed laser deposition. First, we have grown a structurally modulated SrTiO<sub>3</sub> (STO) / Co-doped Ba-122 superlattice with sharp interfaces. The epitaxial crystalline quality and modulation wavelength ( $\Lambda$ ) of the superlattices were determined by four-circle x-ray diffraction (XRD). Figure 1a shows the  $\theta$ - $2\theta$  scan of the (STO<sub>1.2 nm</sub> / 8 % Co-doped Ba-122<sub>13 nm</sub>)  $\times$  (n=24) superlattice (STO SL) on 40 nm STO templates deposited on (001) (La,Sr)(Al,Ta)O<sub>3</sub> (LSAT) substrates. Figure 1(b) is a magnification of Fig. 1(a) close to the 002 reflection of the STO SL which clearly shows satellite peaks with calculated modulation length  $\Lambda = 14 \text{ nm} \pm 2 \text{ nm}$  the same as the nominal  $\Lambda$ . We have also grown oxygen-rich undoped BaFe<sub>2</sub>As<sub>2</sub> (Ba-122) / Co-doped Ba-122 compositionally modulated superlattices.

To investigate the microstructure of STO and O-Ba-122 SLs, transmission electron microscopy (TEM) was used. Figure 2a, b show cross sectional low and high magnification high-angle annular dark field (HAADF) images of STO SL. In Fig. 1(c), bright and dark layers correspond to 13 nm Co-doped Ba-122 layer and 1.2 nm STO layer, respectively. We can clearly see that there are 24 STO / Co-doped Ba-122 bi-layers and  $\Lambda$  is 14 nm in accordance with our design and the modulation wavelength determined by x-ray diffraction. Figure 2d is a cross-sectional TEM image of the O-Ba-122 SL, which clearly shows 24 bilayers and the modulation wavelength  $\Lambda=16 \text{ nm}$ . The interface O-Ba-122 layers have grown as laterally aligned but discontinuous second phase nano particles of several nm size. The structure of the O-Ba-122 SL is more desirable than the structure of the STO SL for flux pinning, since the O-Ba-122 SL has structural defects in both *c*- and *ab*-axis directions.

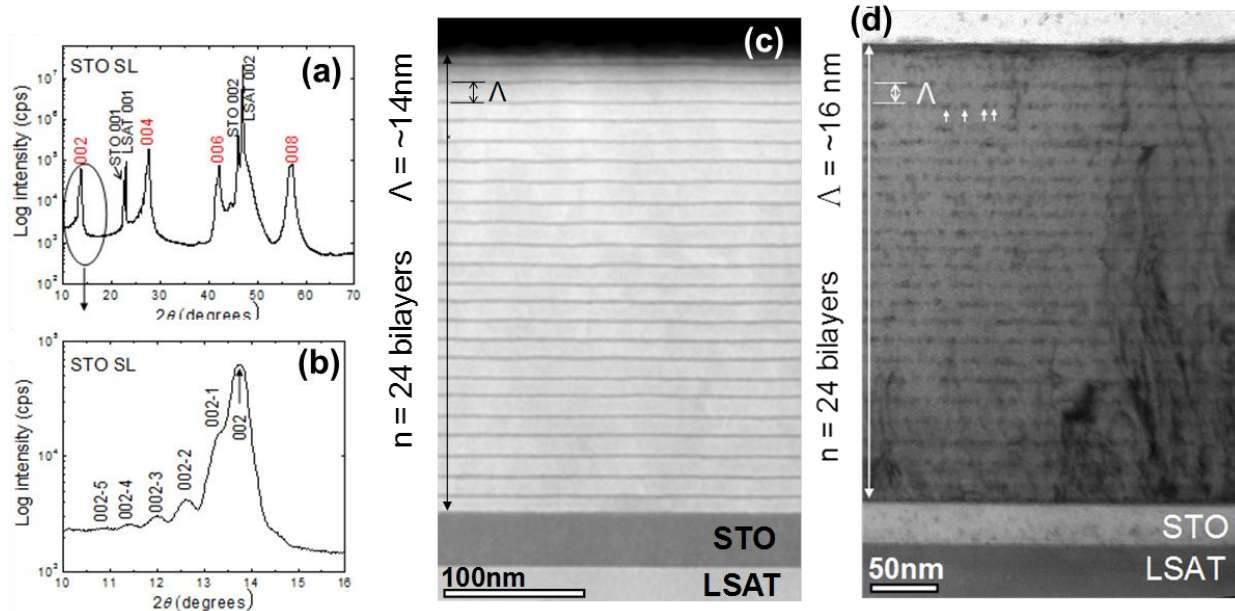


Figure 1. XRD patterns obtained on STO inserted Co-doped BaFe<sub>2</sub>As<sub>2</sub> superlattices (a), Out-of-plane  $\theta$ - $2\theta$  XRD pattern of (STO<sub>1.2 nm</sub>/Co-doped Ba-122<sub>13 nm</sub>) $\times$ 24. (b), Magnified at near 002 reflection of (STO<sub>1.2 nm</sub>/Co-doped Ba-122<sub>13 nm</sub>) $\times$ 24. (c) HAADF image of the  $\langle 100 \rangle$  projection of (STO<sub>1.2 nm</sub>/Co-doped Ba-122<sub>13 nm</sub>) $\times$ 24. **c**, Cross-sectional TEM image of the  $\langle 100 \rangle$  projection of (O-Ba-122<sub>3 nm</sub>/Co-doped Ba-122<sub>13 nm</sub>) $\times$ 24. Arrows indicate nano particle arrays in the O-Ba-122 layer along *ab*-axis.

In order to understand the effect of this nanostructural engineering on  $J_c$  and  $H_{irr}$  we made extensive characterizations at various temperatures, fields and field orientations to the crystal axes. Figure 2(a) shows  $J_c(H)$  for  $H//c$  at 4.2K far from  $T_c$ . It is immediately clear that the two samples with *c*-axis nanorod

pinning defects have much higher  $J_c(H)$  and  $H_{irr}(T)$ . The influence of the  $ab$ -plane defects is revealed in Fig. 2(b) where the  $J_c$  anisotropy for the O-Ba-122 SL and Co-doped Ba-122 single layers at 16K for perpendicular ( $H//c$ ) and parallel ( $H//ab$ ) configurations is compared. Despite these data being affected by their  $T_c$  differences, both samples have the same  $H_{irr} \sim 11$ T for  $H$  parallel to the  $c$ -axis, a result consistent with the lower density of  $c$ -axis pinning centres in O-Ba-122 SL compared to the single layer Co-doped Ba-122. But the really striking result is that the inverted  $H_{irr}$  anisotropy seen for the single layer film with only  $c$ -axis defects ( $H_{irr}$  for  $H//ab$  is less than for  $H//c$ ) is corrected when  $ab$ -plane pins are present in the O-Ba-122 SL film. It is clear that  $H_{irr}$  for  $H//ab$  ( $H_{irr,ab}$ ) of O-Ba-122 SL is approximately doubled from 9 to  $\sim 19$  T, restoring the expected anisotropy of  $H_{irr}$  and  $J_c(H)$  without any degradation to the  $c$ -axis properties. This enhancement is due to the presence of the  $ab$ -plane aligned nanoparticles in the O-Ba-122 SL shown in Fig. 1.

The angular transport  $J_c$  of the STO SL, O-Ba-122 SL, and Co-doped Ba-122 single layer shown in Fig. 2(c) evaluated at a constant reduced temperature  $T/T_c \sim 0.6$  provides further insight into the pinning effects of the nanoparticles. The Co-doped Ba-122 single layer shows only the strong  $c$ -axis pinning produced by the correlated, self-assembled nanopillars, while the  $J_c$  of the STO SL shows only a sharp, few-degrees wide peak when the magnetic field is aligned with the  $ab$ -plane STO superlattice. The  $J_c(\theta)$  of O-Ba-122 SL is higher than the other two samples and shows both strong  $ab$ -plane and  $c$ -axis peaks, which is quite consistent with the  $ab$ -plane aligned second-phase nanoparticles of the bilayer and its  $c$ -axis aligned defects, seen in Fig. 1(d).

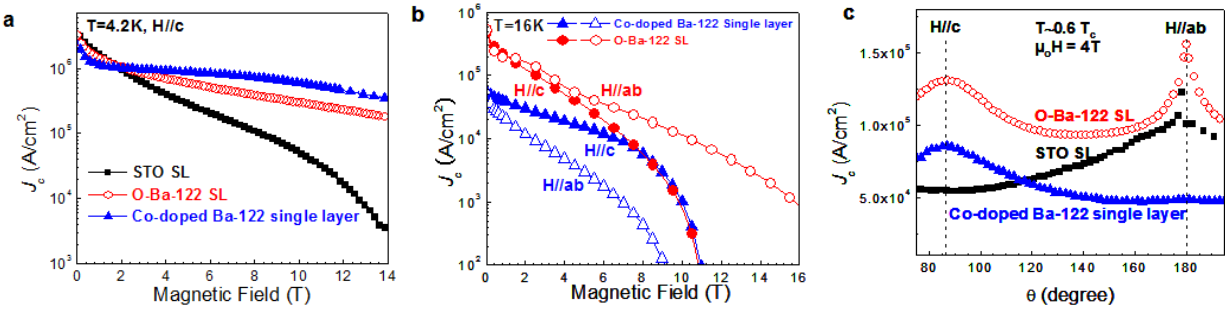


Figure 2.  $J_c$  as a function of magnetic field. a, Magnetization  $J_c$  as a function of magnetic field at 4.2K with the field applied perpendicular to the plane of all three films. b, Transport  $J_c$  as a function of magnetic field at 16K with the field applied perpendicular and parallel to the plane of (O-Ba-122<sub>3 nm</sub>/Co-doped Ba-122<sub>13 nm</sub>) $\times 24$  and Co-doped Ba-122 single layer thin films. c, Angular dependence of transport  $J_c$  at 4T for all three films at a reduced temperature of  $T/T_c \sim 0.6$ .

## Future Plans

### (1) Superconductivity and magnetism at atomically abrupt Pnictide interfaces

The interaction between magnetism and superconductivity is central to the physics of pnictide superconductors, as well as other modern superconductors with potential applications. We have demonstrated that epitaxial heterostructures with sharp interfaces can be made between the optimally-doped material  $\text{Ba}(\text{Fe},\text{Co})_2\text{As}_2$  and other doping levels, as well as insulators such as  $\text{SrTiO}_3$ , and metallic ferromagnets such as Ni, Co, and Fe.

We will compare two different Normal Metal (N) / Superconductor (S) configurations, using the same superconducting layer and changing the N layer properties to determine the interfacial interaction of superconductivity and magnetism. The SC material will be fixed at optimal doping  $\text{Ba}(\text{Fe}_{0.92}\text{Co}_{0.08})_2\text{As}_2$  ( $x=0.08$ ), with maximum  $T_c$  (see Fig. 3, the phase diagram for Ba-122 with Co doping). In the first  $N_u$

(undoped normal metal) /S (superconductor) interface, the normal metal ( $N_u$ ) will be undoped  $BaFe_2As_2$  in which the AFM-SDW correlations dominate. In the second  $N_o$  (overdoped normal metal) /S (superconductor) interface, the normal metal ( $N_o$ ) will be heavily doped Ba122 ( $x=0.20$ ), a paramagnetic metal with no AFM ordering and no SC transition. In Fig. 3 the blue, purple and red arrows represent, respectively, the low doping, optimally doping and over-doping Ba-122 compounds, whose relative interaction we propose to study. Any weakening or enhancement of superconductivity in these systems (i.e., seen as a decrease or increase of  $T_c$ ) will provide a straightforward demonstration of the competitive nature or coexistence of the two long-range orders. The comparison between the two heterostructures will also determine if magnetism has an important role as mediator in the interaction that drives superconductivity in pnictides.

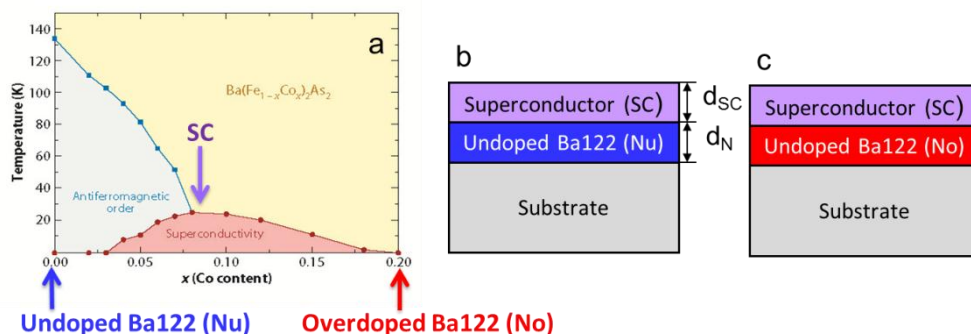


Figure 3. (a) Co-Ba 122 phase diagram, with heterostructure layer doping levels indicated, (b) and (c) two different S/N configurations with undoped ( $x=0$ ) and overdoped ( $x=0.2$ ) normal metals .

## (2) Understanding and control of flux-pinning mechanisms in Pnictide

Pnictide superconductors have potential for high-field superconductivity. The existence of nano-scale columnar second phases and nanoparticles in our artificially engineered superlattices allows a direct probe of fundamental flux-pinning mechanisms in our films as shown in Figure 14(a). We would like to understand the nature of the pinning centers, their origin and growth mechanism, and from that understanding elucidate the physics of flux pinning in pnictide superconductors.

We will address (1) What is the nature of pinning centers in pnictide superlattices? (chemical, structural, and electrical characteristics) (2) What are the intrinsic limits to  $J_c$  and pinning force in pnictides? (3) How do we control the nucleation and growth of pinning centers (4) How do we achieve an ideal pinning center geometry (i.e. optimum size, volume fraction and density of the pinning) to reach a maximum and/or isotropic  $J_c$ ? We propose to answer these questions by controllably altering the nature of pinning in the films, and correlate the electromagnetic and structural characterizations.

## References (which acknowledge DOE support)

1. “Artificially engineered superlattices of pnictide superconductors” S. Lee, C. Tarantini, P. Gao, J. Jiang, J. D. Weiss, F. Kametani, C. M. Folkman, Y. Zhang, X. Q. Pan, E. E. Hellstrom, D. C. Larbalestier, and C. B. Eom, *Nature Materials*, **12**, 392, doi:10.1038/nmat3575 (2013)
2. “Evidence for charge–vortex duality at the  $LaAlO_3/SrTiO_3$  interface” *Nature Communications*, **3**, 955, doi:10.1038/ncomms1959 (2012)
3. “Artificial and self-assembled vortex-pinning centers in superconducting  $Ba(Fe_{1-x}Co_x)_2As_2$  thin films as a route to obtaining very high critical-current densities” C. Tarantini, S. Lee, F. Kametani, J. Jiang, J.D. Weiss, J. Jaroszynski, C.M. Folkman, E.E. Hellstrom, C. B. Eom, D. C. Larbalestier, *Physical Review B*, **86**, 214504 (2012)

# Using Energetic Gas Jets to Enable New Modes of Focused Electron Beam Induced Deposition

Matthew Henry and Andrei G. Fedorov\*

George W. Woodruff School of Mechanical Engineering  
Parker H. Petit Institute for Bioengineering and Bioscience  
Georgia Institute of Technology, Atlanta, GA 30332-0405

## Program Scope

Focused Electron Beam Induced Deposition (FEBID), also referred to as Electron Beam Chemical Vapor Deposition (EB-CVD), is an emerging additive manufacturing (AM) method for “direct writing” of three-dimensional nanostructures from a variety of materials. FEBID has been increasingly used in many applications, ranging from photolithographic mask repair to electrical interconnect fabrication to rapid prototyping of topologically complex opto-electro-mechanical devices.[1] The FEBID advancement as a manufacturing tool remains limited due to low deposition rates, poor deposit purity, and a trade-off between an achievable deposition rate and resulting deposit resolution. The customary method of maximizing precursor supply to the deposit, which is typically the limiting factor for growth rate, is to inject vapor of precursor molecules through a capillary into a vacuum chamber very near the substrate site of deposition. Gas injection as a method of precursor delivery presents many ways in which FEBID may be modified to achieve an improved performance.[2] *One of the most promising and least explored is modulation of the local effective surface temperature of the substrate using energetic jets.* In particular, as we have demonstrated recently, the energy of an inert gas jet impinging upon the surface is sufficient to raise the effective temperature of the surface, to greatly enhance the pre-adsorbed precursor diffusion rate and, in turn, to significantly improve the deposit growth rate and deposit aspect ratio.[3] By further increasing the jet energy, the effective surface temperature rises high enough that desorption becomes dominant and contaminants are cleaned from the surface, which allows a new operating mode of FEBID resulting in formation of deposits free of carbon contamination.

A great deal of fundamental science relevant to gas jet assisted FEBID is not well understood, such as predicting the adsorption probability of impinging molecules onto the surface and the dissociation probability of adsorbed molecules due to secondary electrons.[4] We propose a complimentary modeling and experimental research that would allow us to develop the first principle sticking probability model(s), thus enabling development of comprehensive FEBID simulation tools with minimal empirical inputs. To this end, several fundamentally new and practically useful effects of energetic gas jet impingement are proposed for an in-depth investigation:

- The sticking coefficient of precursor molecules to the surface can be altered due to jet impingement energy, just allowing one to modulate a fraction of precursor molecules sitting on the surface in the state suitable for deposition. What is the physical mechanism of this process and how it can be quantified and modeled?

- Contaminant free radicals at the deposition site may be removed by jet impingement rather than becoming entrapped in the deposit and diminishing its purity. How effective and controllable this process?
- Jet pressure on the deposit is observed to pre-stress FEBID pillars as they are being deposited. If pillars maintain internal stresses when the jet is removed, then structures can be deposited with an adjustable modulus of elasticity. What range of elasticity modulation is possible and for what materials?

It should be noted that a similar deposition process, Focused Ion Beam (FIB) Induced Deposition (FIBID), exists and is often preferred over FEBID due to its higher deposition rate in the beam-limited growth regime and improved “as-deposited” deposit purity with respect to co-deposited carbon contaminants.[2] It has, however, the disadvantages of surface damage, ion implantation, and a generally lower resolution.[2,5] Since both FEBID and FIBID utilize the low energy secondary electrons (SE) generated upon interaction of high energy primary electrons (FEBID) or ions (FIBID) with the precursor molecules to produce a deposit, there is a significant degree of overlap in the fundamental principles and models describing both deposition processes. Therefore, while the proposed research is focused on FEBID its implications are much broader and will impact the advances in FIBID as well.

## Background

The energy of gas jet impingement affects a number of deposition properties/processes, including the precursor sticking coefficient, surface diffusion, surface desorption, and surface temperature. The effective temperature of the surface adsorbed precursor is not necessarily the same as the actual temperature of the substrate it is adsorbed onto. When a gas jet impinges on a substrate it delivers kinetic energy to the adsorbed precursor molecules thereby altering effective surface temperature. Our experiments (Fig. 1) explored the gas-jet effect on surface adsorbed precursor diffusion and desorption, which vary with  $T$ , the effective surface temperature, according to  $D_0 \exp(-E_{dif}/k_B T)$  and  $\nu \exp(-E_{des}/k_B T)$ , where  $E_{dif}$  and  $E_{des}$  are the activation energies for diffusion and desorption, respectively;  $D_0$  is a reference diffusion coefficient;  $\nu$  is the desorption rate constant; and  $k_B$  is the Boltzmann constant. To demonstrate this effect, paraffin was partially dissolved in methanol then applied to a silicon oxide surface of the substrate as the precursor material. At least one day was allowed for the precursor to diffuse uniformly over the surface and for excess molecules to desorb from the surface, thus reaching the equilibrium surface concentration. The reference deposits in Fig. 1a were repeatedly grown on this substrate at a beam current  $\sim 90 pA$  and accelerating voltage  $25 kV$ . A higher beam current did not increase the size of the deposits; therefore, the growth rate is mass transfer (not e-beam) limited. Impingement of an inert gas (argon) jet upon the substrate surface from a  $75 \mu m$  inner diameter capillary with a mass flow rate of  $1.26 \times 10^{-7} kg/s$  enhanced the growth rate of the pillars in Fig. 1b. *The growth rate increased 10-fold over the reference deposits that were grown under the same conditions in the same experiment, but without the gas jet.*

Since no precursor was delivered with the inert gas jet, this indicates that the precursor supply increased due to an enhanced surface diffusion rate. The degree of the enhanced growth rate increases with an increased argon flux to the surface up to a threshold beyond which the growth rate cannot be enhanced further. In the case of a paraffin film on a silicon oxide substrate, the threshold flux to the surface is  $0.05 kg/m^2 s$  for argon gas. Changes in the deposition rate, which were observed to occur immediately in response to applying or removing the inert gas jet

impingement, indicate that the effective surface temperature responds rapidly to the jet. Because the activation energy for desorption is greater than that for diffusion, desorption was not observed with the use of a low energy jet. To increase the impingement energy of the argon jet, the nozzle temperature was increased from 20°C to 140°C using the resistive heating element. The effective surface temperature increased and the resulting deposits in Fig. 1c, while still exhibiting enhanced growth rates, were much diminished in size as compared to the case of the low-energy (diffusion-stimulating) inert gas jet. This is due to some surface adsorbed precursor molecules being depleted by desorption, although the surface diffusion rate was also enhanced.

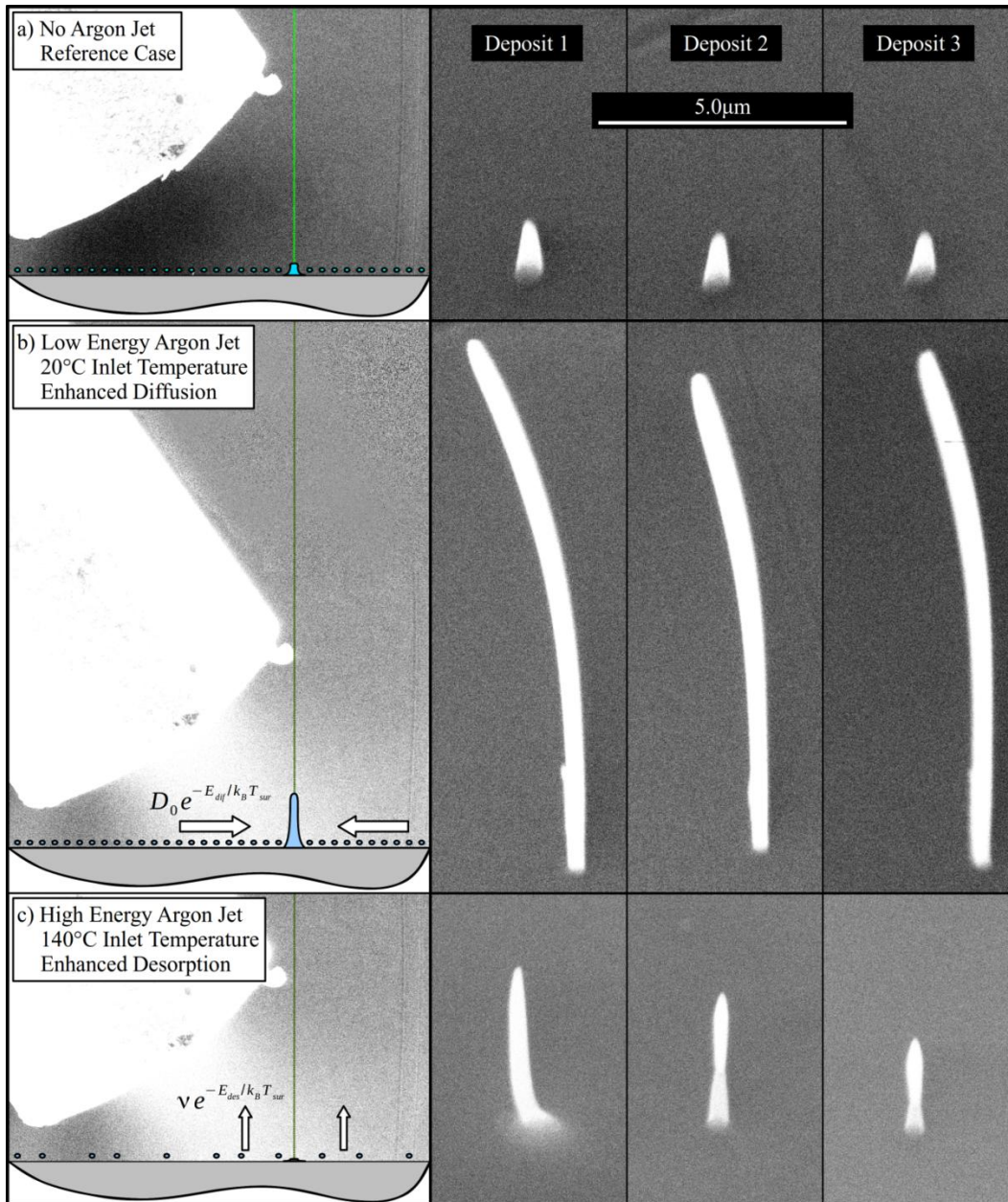


**Fig. 1:** Effect of Increasing Energy of Inert (Ar) Gas Jet on FEBID Deposits (10min Deposition Time, E-beam at 25kV and 90pA). (a) Reference Deposits with No Jet (b) Enhanced Deposits due to Jet Impingement from 20°C Capillary (c) Subsequently Depleted Deposits due to Jet Impingement from the Capillary maintained at 140°C.

## Future Plans

In the course of the three year research program, we plan to (1) investigate the effect of energetic gas jet properties on precursor sticking, diffusing, desorbing – and therefore precursor mass supply rate; (2) verify that precursor mass flux and jet energy can be tuned separately from each other in such a manner as to produce the same heating effect on the surface; (3) fully define the characteristic field properties resulting from jet impingement on the surface (flux distribution, impingement angle distribution, and impingement energy distribution); (4) verify that the effective substrate surface temperature due to jet impingement relates to the gas parameters via kinetic theory; (5) identify the effective mass of a surface adsorption site for use in simulation via the hard-cube model; (6) develop methods to increase deposition purity under enhanced growth conditions; and (7) investigate the possibility of increasing the stiffness of a deposited pillars by pre-stressing it with jet-impingement while it is being grown. This will be done via a complementary theoretical (modeling & simulations) and experimental (model validation and hypothesis generation) approach as depicted in Figure 2.

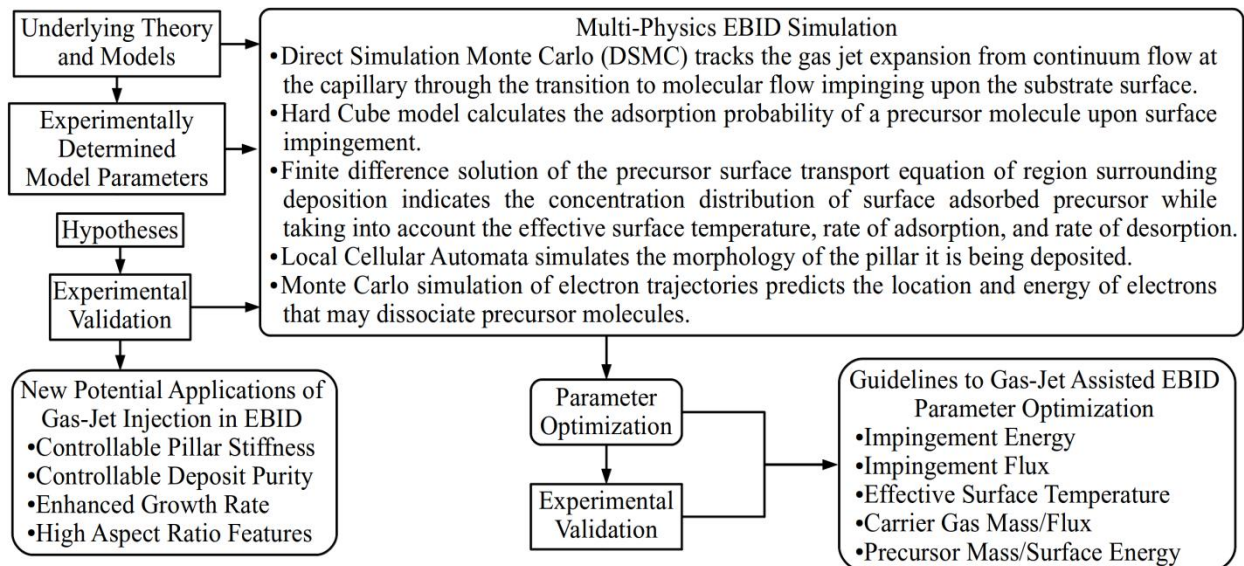


**Fig. 2:** Overview of different aspects of the proposed research, their interactions and expected outcomes.

## References

1. Randolph, S. J., Fowlkes, J. D., and Rack, P. D., Focused, nanoscale electron-beam-induced deposition and etching. *Critical Reviews in Solid State Materials Science*, 2006, **31**, 55–89.
2. Utke, I., Hoffmann, P., and Melngailis, J., Gas-assisted focused electron beam and ion beam processing and fabrication. *Journal of Vacuum Science & Technology B*, 2008. **26**(4): p. 1197-1276.
3. Henry M.R., Kim, S., Rykaczewski, K., and Fedorov, A., Inert gas jets for growth control in electron beam induced deposition. *Applied Physics Letters*, 2011. **98**(26); p. 263109.
4. Fedorov, A., Rykaczewski, K., and White, W., Transport issues in focused electron beam chemical vapor deposition, *Surface & Coating Technology*, **201**, 8808-8812 (2007).
5. Matsui, S., Kaito, T., Fujita, J., Komuro, M., Kanda, K., Haruyama, Y., Three-dimensional nanostructure fabrication by focused-ion-beam chemical vapor deposition. *Journal of Vacuum Science & Technology B*, 2000. **18**(6): p. 3181-3184.

## Forces, Crystallization, and Assembly in Nanoparticle Suspensions

K. A. Fichthorn (PI) and R. M. Rioux (co-PI)

Department of Chemical Engineering

The Pennsylvania State University

University Park, PA, 16802

### Program Scope

In the past decade, an astounding variety of intricate nanostructures, having at least one dimension of 100 nm or less, have been synthesized via solution-phase techniques. These nanostructures will benefit numerous applications in energy technology involving (photo) catalysis, fuel cells, hydrogen storage, and solar cells. In these and many other applications, it has been emphasized that the sizes, shapes, phases, and assembly or dispersion of the nanoparticles can significantly impact their performance. A deep, fundamental understanding of the phenomena that promote shape-selective growth and assembly in these syntheses would enable tight control of nanostructure morphologies in next-generation techniques and allow for the synthesis of more elaborate nanostructures. In certain systems, elaborate nanostructures have been fabricated via oriented attachment (OA), an aggregative growth mechanism that leads to twinned or single-crystal nanostructures. However the mechanisms of OA remain unresolved. In many systems, structure-directing agents (SDAs) are used. These agents can range from small monomer molecules to high-molecular-weight polymers. Although there is a great deal of experimental evidence indicating that SDAs can play a pivotal role in selectively producing various nanostructures, their exact role remains elusive.

In this work, complementary theoretical and experimental methods are used to quantify the binding of SDAs to coinage-metal surfaces and to resolve mechanisms of shape-selective growth. On the theoretical side, first-principles, dispersion-corrected, density-functional theory and classical molecular dynamics (MD) simulations are employed to quantify binding energies, as well as mechanisms by which solution-phase growth occurs. Two experimental platforms – isothermal titration calorimetry and *in-situ*, liquid-phase, high resolution transmission electron microscopy – are being developed and used to quantify SDA binding energies to various nanostructures and provide a real-time, *in-situ* view of nanostructure growth.

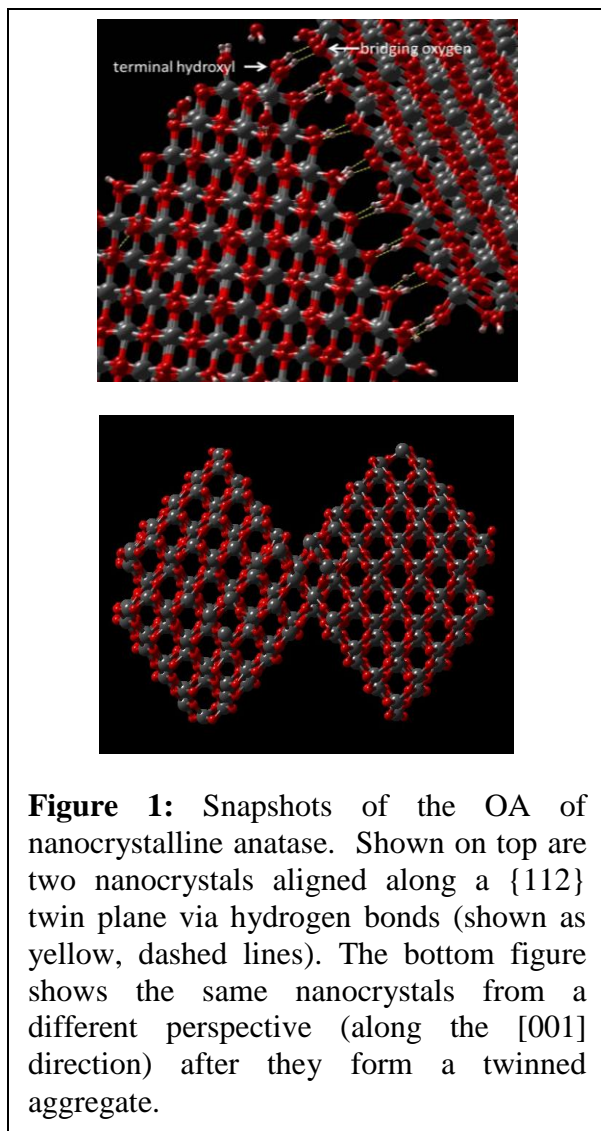
### Recent Progress

The growth of hierarchical nanostructures by OA of molecular clusters and nanocrystals in solution is now widely recognized as an important alternative to the classical crystal growth mechanism by monomer attachment. Crystallization by the aggregation and coalescence of nanocrystals is observed frequently in natural processes and is applied by natural organisms during biomineralization [1], during morphosynthesis of biomimetic inorganic materials [2] and during controlled synthesis of nanocrystals and nanowires [3, 4]. Remarkably, growth by OA occurs in wide variety of organic and inorganic materials exhibiting diverse particle morphologies including spheres, ellipsoids, cubes, platelets, wires, and hybrids, resulting in complex architectures ranging from quasi-one-dimensional nanowires and nanorods to hierarchical two- or three-dimensional superstructures [5]. However, the microscopic origins of OA are still unclear. Atomic-scale investigations with MD could contribute significantly to understanding growth by OA and furnish many details of this mechanism that are not accessible experimentally.

We performed MD simulations using a recently developed<sup>6</sup> and validated<sup>7</sup> ReaxFF reactive force field for TiO<sub>2</sub>/water interactions to study the aggregation of various titanium dioxide (anatase) nanocrystals in vacuum and humid environments. In vacuum, the nanocrystals tend to merge along their direction of approach, resulting in a polycrystalline material. By contrast, in the presence of water vapor, we observed many instances of oriented attachment, which is facilitated by adsorbed water and surface OH in several ways.

First, adsorbed water and OH protect the nanoparticles and prevent the immediate (and relatively misaligned) aggregation that occurs in vacuum. Thus, when two nanoparticles come into close contact, where their surfaces are within Å distances, they are able to bounce and rotate with respect to one another to adjust their relative orientation. Eventually, the particles achieve a configuration with aligned facets, wherein they are loosely associated via a network of hydrogen bonds between the surface hydroxyls on one nanocrystal and the surface oxygens on the other, as shown in Fig. 1, top. The particles shift relative to one another, constantly reconfiguring their hydrogen-bonding network, until they achieve alignment. Subsequently, surface hydroxyls combine with protons to form water, which vacates the inter-particle gap and allows the nanocrystals to aggregate. The result is a single or twinned crystal, as shown in Fig. 1, bottom. We find that OA is dominant on surfaces with the greatest propensity to dissociate water. We, thus, demonstrate the critical role of solvent in nanocrystal aggregation, a finding which opens possibilities for directing nanocrystal growth to fabricate nanomaterials with desired shapes and sizes.

Experimentally, we have utilized isothermal titration calorimetry to determine the thermodynamics of adsorption of small molecules to the surface of solvated nanocrystals. Ultimately, we aim to describe the influence of metal identity, solvent and small molecule (and polymers) on the adsorption thermodynamics. One proposal for shape-control in colloidal synthesis is the facet-dependent adsorption of structure-directing agents. However, there are no quantitative measures of differences in binding energies of SDAs to the surface of solvated nanostructure surfaces. We have utilized isothermal titration calorimetry (ITC) to measure the adsorption thermodynamics of small molecule SDAs in aqueous solutions on the surface of spherical nanoparticles. To demonstrate the capability of ITC to measure the complete thermodynamic profile of adsorption, we chose the model system: carboxylic acid terminated



thiol adsorption to the surface of Au nanoparticles of varying size, and as a function of temperature.<sup>8</sup> **Figure 2** is an example of the adsorption of 3-mercaptopropanoic acid and 6-mercaptophexanoic acid to the surface of 5 nm Au nanoparticles in aqueous solution. With this model system, we were able to demonstrate that ITC is ideally suitable to measure the complete thermodynamics of adsorption since  $K$ ,  $\Delta H$  and  $n$  (binding stoichiometry) can all be measured in a single experiment. An apparent consequence of changing the structure of the thiol (i.e., increasing the number of methylene groups) was a compensation effect between  $\Delta H_{\text{ads}}$  and  $\Delta S_{\text{ads}}$  since  $\Delta G_{\text{ads}}$  was constant amongst the various thiol.<sup>8</sup> A recent manuscript demonstrating a more robust solution to complex adsorption models has been developed.<sup>9</sup>

Recently, we utilized ITC to measure the interfacial thermodynamics of the adsorption of substituted pyrrolidone monomers on Ag nanoparticle surfaces in polar solvents (ethylene glycol and water). Xia and co-workers have demonstrated that Ag nanoparticles of various shapes can be synthesized by altering the conditions of a polyol synthesis, including the use of different SDAs.<sup>10,11</sup> We are utilizing ITC and environmental

transmission electron microscopy to understand the thermodynamics and kinetics associated with nanoparticle growth in the presence of a common SDA, such polyvinylpyrrolidone. We are currently addressing three aspects of silver nanostructure synthesis in the presence of PVP:

- (i) Role of side-chain structure of functionalized pyrrolidone monomers on their adsorption thermodynamics on Ag(111) and (100) surfaces and synthesis of Ag nanostructures by the polyol method in the presence of pyrrolidone monomers.
- (ii) Effect of solvent on the observed thermodynamics of binding – decoupling surface solvation effects to determine intrinsic binding enthalpies.

We anticipate that a detailed understanding of the adsorption thermodynamics under solvated conditions of common SDAs in the Ag system, as well as others, will enable the design of anisotropic nanostructure syntheses utilizing quantitative thermodynamics measured by ITC.

### Future Plans

Experimentally, we will examine binding cooperativity (structure selectivity multivalent effects) during the adsorption of oligomers of vinylpyrrolidone on Ag(111) and (100) surfaces and synthesis of Ag nanostructures by the polyol method in the presence of vinylpyrrolidone (VP) oligomers. The facet-specific surfaces will be synthesized in colloidal form utilizing known recipes and epitaxially-grown on appropriate substrates for determination of facet-specific adsorption thermodynamics. In addition, we are developing an experimental program in liquid-phase environmental TEM to examine the kinetics of nanoparticle growth (in selected systems (Au, Pt) due to their favorable reduction potential) in the presence of various structure directing

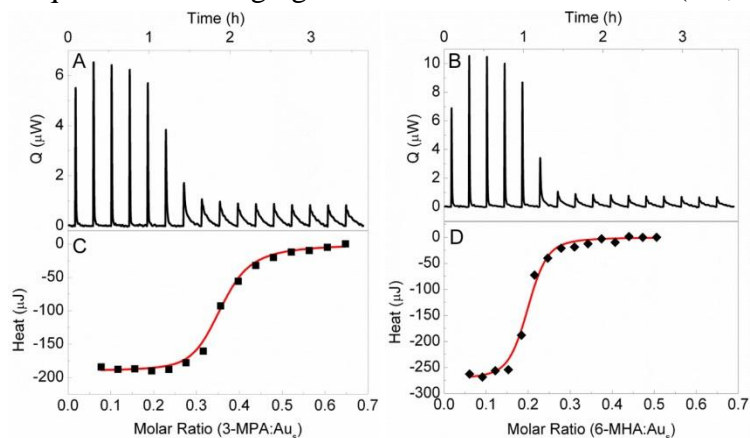


**Figure 2.** Real-time ITC thermograms at pH 6.1 for (A) C<sub>3</sub>-MPA and (B) C<sub>6</sub>-MHA binding to  $5.4 \pm 0.7$  nm Au NPs at 298.15 K with C and D as the respective integrated heat data with an independent model fit.<sup>8</sup>

agents and solvents.<sup>12</sup> In complementary theoretical work, we have developed force fields to describe the interaction of PVP and vinylpyrrolidone oligomers, as well as polyethylene oxide, ethylene glycol, and water with Ag surfaces. MD studies of the binding of PVP and its oligomers to Ag surfaces are underway. These studies are aimed at corroborating experiment and understanding SDA-mediated growth mechanisms of Ag nanostructures.

## References

1. Killian, C. E., Metzler, R. A., Gong, Y. U. T., Olson, I. C., Aizenberg, J., Politi, Y., *et al.* *J. Am. Chem. Soc.* 2009, **131**, 18404-18409.
2. Cölfen H., Antonietti, *Angew. Chemie Int. Ed.* 2005, **44**, 5576-5591.
3. Yuwono V. M., Burrows N. D., Soltis, J. A., Penn, R. L. *J. Am. Chem. Soc.* 2010, **132**, 2163-2165.
4. Schliehe, C., Juarez, B. H., Pelletier, M., Jander, S., Greshnykh, D., Nagel, M., *et al.* *Science* 2010, **329**, 550-553.
5. Niederberger, M., Cölfen, H. *Phys. Chem. Chem. Phys.* 2006, **8**, 3271-3287.
6. Kim, S.-Y., Kumar, N., Persson, P., Sofo, J., van Duin, A. C. T., Kubicki, J. D. *Langmuir* 2013, **29**, 7838-7846.
7. Raju, M., Kim, S.-Y., van Duin, A. C. T., and Fichthorn, K. A. *J. Phys. Chem. C* 2013, **117**, 10558-10572.
8. Ravi, V., Binz, J. M., Rioux, R. M. *Nano Lett.* 2013, **13** 4442-4448.
9. Chang, J. W., Rioux, R. M. Accepted to *Anal. Chem.* (September 2013).
10. Ott, L. S., Finke, R. G. *Coord. Chem. Rev.* 2007, **251** 1075-1100.
11. Ott, L. S., Hornstein, B. J., Finke, R. G. *Langmuir* 2006, **13**, 9357- 9367.
12. Zheng, H. M., Smith, R. K., Jun, Y. W., Kisielowski, C., Dahmen, U., Alivisatos, A. P. *Science* 2009, **324**, 1309-1312.

## DoE Sponsored Publications in the Last Two Years

1. R. Sathiyarayanan, M. Ali-Mohammadi, Y. Zhou, and K. Fichthorn, "The role of solvent in the shape-controlled synthesis of anisotropic colloidal nanostructures", *J. Phys. Chem. C* **115**, 18983-18990 (2011).
2. M. Alimohammadi and K. A. Fichthorn, "A force-field for the interaction of water with TiO<sub>2</sub> surfaces", *J. Phys. Chem. C* **115**, 24206-24214 (2011).
3. W. Al-Saidi, H. Feng, and K. A. Fichthorn, "Adsorption of polyvinylpyrrolidone on Ag surfaces: Insight into a structure-directing agent", *Nano Lett.* **12**, 997-1001 (2012).
4. Y. Zhou and K. A. Fichthorn, "Microscopic view of nucleation in the anatase-to-rutile transition", *J. Phys. Chem. C* **116**, 8314-8321 (2012).
5. W. Al Saidi, H. Feng, and K. A. Fichthorn, "The binding of PVP to Ag surfaces: Insight into a structure-directing agent from dispersion-corrected density-functional theory," *J. Phys. Chem. C* **117**, 1163-1171 (2013).
6. M. Raju, S.-Y. Kim, A. C. T. van Duin, and K. A. Fichthorn, "ReaxFF reactive force field study of the dissociation of water on anatase and rutile surfaces of TiO<sub>2</sub>", *J. Phys. Chem. C* **117**, 10558-10572 (2013).
7. Y. Zhou, W. A. Saidi, and K. A. Fichthorn, "Comparison of the binding of PVP and PEO to Ag surfaces: Elements of a successful structure-directing agent", *J. Phys. Chem. C* **117**, 11444-11448 (2013).
8. K. A. Fichthorn, "Molecular Phenomena in Colloidal Nanostructure Synthesis" (Accepted by *Molecular Simulation*).
9. V. Ravi, J. M. Binz, R. M. Rioux, "Thermodynamic Profiles at the Solvated Inorganic-Organic Interface: The Case of Gold-Thiolate Monolayers", *Nano Lett.* **13** 4442-4448 (2013).

10. J. W. Chang, R. M. Rioux, "Analytical Solutions in Differential Form for Isothermal Titration Calorimetry" (Accepted by *Anal. Chem.*).

# Atomistic Structure, Strength, and Kinetic Properties of Intergranular Films in Ceramics

Yun Jiang, Ying Ma, Stephen H. Garofalini\*  
Department of Materials Science and Engineering  
Rutgers University

## Program Scope

The thin glassy intergranular films (IGFs) present between the crystals in polycrystalline ceramics occupy only a small volume percent of the bulk ceramic but can significantly influence morphology and mechanical, chemical, and optical properties<sup>1,2</sup>. Understanding the atomistic basis for how these IGFs affect material properties has been elusive, although advances in computer simulations<sup>3-5</sup> and recent electron microscopy<sup>6,7</sup> have provided information about the location of atoms at the IGF/crystal interface. Nonetheless, the specific role of these interfacial ions and the important effect of the interfaces on adsorption and their effect on properties have not been quantified from an atomistic perspective.

For instance, HAADF-STEM show that both La-doped and Lu-doped IGFs show the each rare earth (RE) adsorbed onto the prism-oriented surface of  $\text{Si}_3\text{N}_4$ , potentially poisoning the surface and preventing growth, but growth morphology and fracture behavior are quite different. Previous ab-initio calculations could not reproduce the Lu adsorption sites seen experimentally. Our current works provides the cause for the observed behavior as well as the difference between La and Lu adsorption on properties.

We address the detailed atomistic structure and behavior of these IGFs in oxide and nitride ceramics using molecular dynamics computer simulation techniques, with correlations to available experiments using HRTEM, AEM, and HAADF-STEM. The work includes the effect of compositional variations on interface structure as a function of crystal orientation, structure of the interior of the IGF (away from the IGF/crystal interface) as a function of IGF thickness, the role of impurities on the crystal surface, and the effect of these properties on morphology. Our work is being done in conjunction with available experimental verification in collaboration with Dr. Pennycook at ORNL and Professors Phil Batson and Fred Cosandey at Rutgers, as well as interactions with Dr. Christoph Koch at Max-Planck Institut für Metallforschung, Stuttgart for initiating HAADF-STEM images from our simulation data for direct comparison to experimental HAADF-STEM images.

A major thrust of our work is quantifying the important role of *local* IGF composition and bounding crystal surface structures and composition on properties, enabling us to justify the difference seen in La-doped IGFs versus Lu-doped IGFs on properties. We have expanded the simulations to address non-REs of similar size or charge but different interaction strengths.

## Recent Progress

**Our most recent results provide the atomistic mechanism for the difference between La and Lu additives in the IGFs on the adsorption behavior that affects crystal growth, morphology, and strength. The results reproduce the HAADF-STEM data regarding adsorption sites, but also show how such experimental data observe only the ‘end-state’ structures that do not tell the tale of the dynamic behavior during processing that affects morphology and growth behavior.**

ab-initio calculations at ORNL reproduced the La adsorption at sites La1 and La2 as seen experimentally, and Lu at site Lu2, but could not obtain Lu at site Lu1<sup>5</sup>, observing Lu at the incorrect site Lu1’ (see figure 1b). Our MD simulations similarly reproduced the HAADF-STEM data for La at sites La1 and La2 (as well as the experimentally observed La3 and La4)<sup>8,9</sup> (figure

1c), as well as Lu at Lu2; however, initial attempts at reproducing the Lu sites Lu1 on a fully nitrated (N in all anion surface sites) prism surface were, like the ORNL calculations, unsuccessful. We spent quite some time evaluating the interatomic potentials, to no avail.

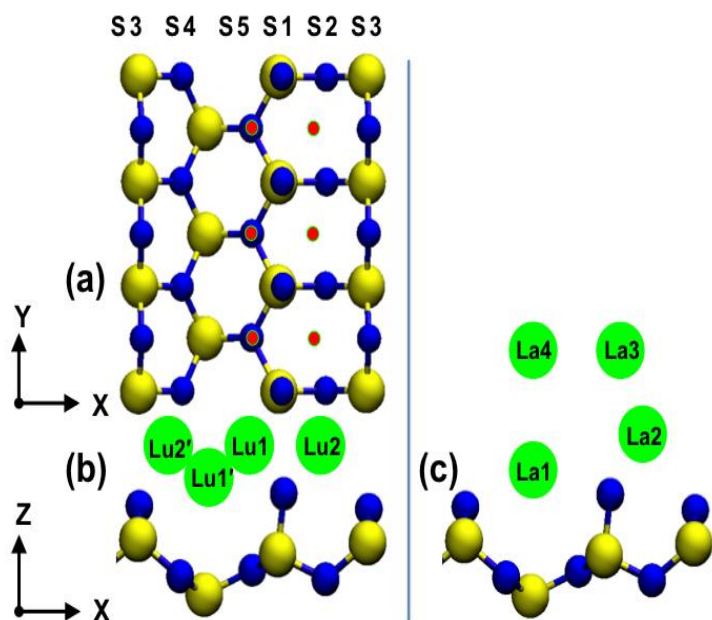


Figure 1 (a) Top view and (b, c) side view of the  $\text{Si}_3\text{N}_4$  prism surface (N in blue spheres, Si in larger yellow spheres). Nitrogen sites are respectively labeled as S3, S4, S5, S1, S2, S3 along the x axis. The red dots in (a) indicate possible Lu1 and Lu2 sites. In (b) are shown Lu adsorption sites Lu1, Lu2, Lu1' and Lu2' (the primed sites are not observed in HAADF-STEM) (c) La adsorption sites La1, La2, La3 and La4 on the  $\text{Si}_3\text{N}_4$  prism surface.

**However, we obtained success after we looked at the effect of oxygen replacing nitrogen on specific sites on the nitride surface on Lu adsorption.**

The presence of O on N-surface sites was shown in EELS studies of an  $\text{SiO}_2$  IGF on the prism  $\beta\text{-Si}_3\text{N}_4$  surface<sup>10</sup> and could be expected in RE-doped IGFs. Figure 1a provides the nomenclature for the different surface N sites that are replaced by O on the prism surface in our MD simulations and VASP calculations in our lab. Placing O at either single sites,  $S_x$ , or double combinations,  $S_x+S_y$ , or triple combinations  $S_x+S_y+S_z$ , where x, y, z are filled with any site numbers from 1 to 6 provided data with regard to the important role of O at specific surface N-lattice sites on Lu and La adsorption.

**We also changed the strength of the La-O vs La-N and Lu-O and Lu-N interactions in our potentials to expand the work beyond just these particular REs to allow for possible application of the results**

**to other non-specific ions with size and charge near these REs but different bond strengths.** In total, 312 samples are studied via molecular dynamics computer simulations with 26 prismatic surface terminations (including single, double and triple O replacements of N), 6 RE potential sets (i.e.  $\text{RE-O} > \text{RE-N}$ ,  $\text{RE-O} \sim \text{RE-N}$ , and  $\text{RE-O} < \text{RE-N}$  for  $\text{RE} = \text{La}$  and  $\text{Lu}$ ) and 2 film thicknesses (6 Å and 18 Å).

Results showed that the positions of Lu siteing at the prism oriented surface is significantly influenced by the presence of O replacing N on the surface lattice sites and the correct Lu siteing similar to HAADF-STEM results can only be obtained if O is present. Importantly, La siteing on the prism oriented surface is unaffected by the presence of O replacing N at these different N surface lattice sites, although the concentration is slightly modified.

The red dots in figure 1a indicate possible adsorption sites Lu1 and Lu2 from the top view. However, previous HAADF-STEM data<sup>6</sup> showed that sites Lu1 and Lu2 are staggered in that they do not have the same y location. The implication is that if one site is filled, the adjacent site with the same y dimension cannot be filled. This is observed in the simulations, and a plot of the interaction energy of Lu over the surface in the presence of a pre-adsorbed Lu provides the

justification. The energy distribution for Lu adsorption onto the N-terminated prism surface versus the S1 O-terminated is shown in figure 2. The surface atoms and one Lu at the Lu2 site given in grey in the figure are kept frozen while a second Lu samples the surface. As shown in figure 2, the second Lu samples a repulsive region surrounding the pre-adsorbed Lu at the Lu2 site (all energies greater than zero were set to zero so that the color bar could be more clear). This repulsive region prevents the second Lu from adsorbing at the Lu1 site at the same y dimension as the occupied Lu2 site (see red dots in figure 1a). The next possible Lu adsorption site would be displaced in y to the second row of red dots in figure 1a.

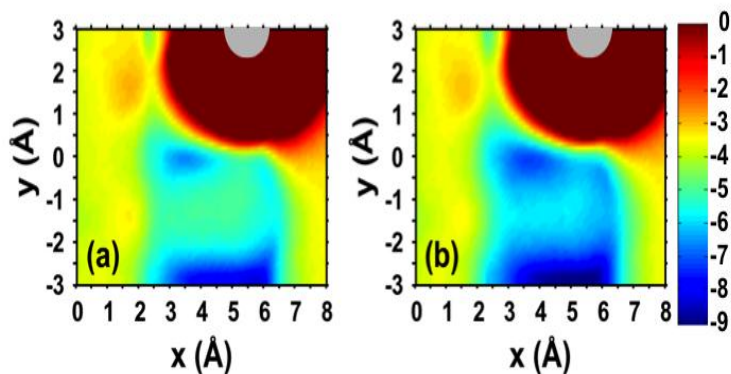


Figure 2. Energy map for Lu on the (a) pure N prism surface and (b) O at the S1 sites. Grey hemisphere at (5.5, 3) is one Lu at site Lu2 that is kept frozen, while a second Lu samples the rest of the adjacent surface sites. Site Lu1 is at (3.5, 0) and a second Lu2 site at (5.5, -3). Color bar gives Lu energy in eV. See text for further details.

Figure 2a shows a well only near (3.5, 0), which is a Lu1 site, indicating both the staggered nature of the siteing and also the lack of another Lu2 site along the same y location (x, 0). The next site would be near (5.5, -3), which is the next available Lu2 site. This lower y-location adsorption site is broader in x because it encompasses both Lu2 and Lu1, but our data shows Lu2 is a deeper well than Lu1, although the color scheme does not show this difference sufficiently well. The actual energetics observed in our simulations show that the Lu binding energy is stronger on the oxidized surface, although it is hard to see in the color scheme in figure 2. A Lu

sampling this  $\sim(x, -3)$  location would naturally fall into the Lu2 site rather than the Lu1 site because our simulations show that there is essentially no barrier between the sites. **Our tabulated energies (not shown here) also show that the adsorption energies at sites on the N-terminated prism surface are clearly weaker than on the O-terminated surface for the S1 and S1-related double replacement sites.**

Finally, HAADF-STEM showed Lu adsorbed onto the prism-oriented surface, similar to La, but Lu did not prevent growth of this surface outward as much as La did, creating the different morphologies of these materials. The HAADF-STEM data was therefore insufficient in providing the mechanism by which La poisoned the surface more than did Lu. Our MD simulations enabled us to view the migration of La or Lu near the prism interface during the melt-quench process to show why one poisoned the surface and the other did not. La adsorbs and sticks to the surface whereas Lu adsorbs but is more easily displaced by Si and N (or O) to allow for normal (outward) growth of the prism surface. However, the Lu remain near the surface and reattached at lower temperatures, reconciling both the growth behavior and the HAADF-STEM results seen experimentally.

### Future work

The project is terminating on April 2014; the student will finish writing the 2 new papers and the dissertation as well as defense of the thesis by the graduate student.

## References

1. P. F. Becher, G. S. Painter, E. Y. Sun, C. H. Hsueh and M. J. Lance, "The importance of amorphous intergranular films in self-reinforced beta-Si<sub>3</sub>N<sub>4</sub> ceramics", *J. Am. Ceram. Soc.* 48, 4493-4499 (2000).
2. P. F. Becher, G. S. Painter, N. Shibata, S. B. Waters and H. Lin, "Effects of Rare-Earth (RE) Intergranular Adsorption on the Phase Transformation, Microstructure Evolution, and Mechanical Properties in Silicon Nitride with RE<sub>2</sub>O<sub>3</sub>+MgO Additives: RE-La, Gd, and Lu", *J. Am. Ceram. Soc.* 91, [7] 2328-2336 (2008).
3. S. H. Garofalini and W. Luo, "Molecular dynamics simulations of calcium silicate intergranular films between silicon nitride crystals", *J. Am. Ceram. Soc.* 86, [10] 1741-1752 (2003).
4. S. Zhang and S. H. Garofalini, "Molecular dynamics simulations of the effect of the composition of calcium alumino-silicate intergranular films on alumina grain growth", *J. Phys. Chem. B* 110, 2233-2240 (2006).
5. G. S. Painter, F. W. Averill, P. F. Becher, N. Shibata, K. Van Benthem and S. J. Pennycook, "First-principles study of rare earth adsorption at beta-Si<sub>3</sub>N<sub>4</sub> interfaces", *Phys. Rev. B* 78, 214206214206, (2008).
6. G. B. Winkelman, C. Dwyer, T. S. Hudson, D. Nguyen-Mahn, M. Doblinger, R. L. Satet, M. J. Hoffmann and D. J. H. Cockayne, "Three-dimensional organization of rare-earth atoms at grain boundaries in silicon nitride", *Appl. Phys. Lett.* 87, 061911-1-3 (2005).
7. N. Shibata, G. S. Painter, P. F. Becher and S. J. Pennycook, "Atomic ordering at an amorphous/crystal interface", *Appl. Phys. Lett.* 89, 051908 (2006).
8. Y. Jiang and S. H. Garofalini, "Molecular dynamics simulations of the locations of La ions in La-Si-O-N intergranular films in silicon nitride", *J. Am. Ceram. Soc.* 93, [11] 3886-3892 (2010).
9. Y. Jiang and S. H. Garofalini, "Molecular dynamics simulations of La<sub>2</sub>O<sub>3</sub>-doped silicate intergranular films in Si<sub>3</sub>N<sub>4</sub>", *J. Mater. Chem.* 20, [46] 10359-10365 (2010).
10. W. Walkosz, R. F. Klie, S. Ogut, B. Mikijelj, S. J. Pennycook, S. T. Pantelides and J. C. Idrobo, "Crystal-induced effects at crystal/amorphous interfaces: The case of Si<sub>3</sub>N<sub>4</sub>/SiO<sub>2</sub>", *Phys. Rev. B* 82, 081412(R), (2010).

## DOE Sponsored Publication from 2011-2013

1. "Role of oxygen on the adsorption of Lu and La on the β-Si<sub>3</sub>N<sub>4</sub> prismatic surface", Y. Jiang, Y. Ma, and S. H. Garofalini, *Acta Mater.* (submitted).
2. "Effect of thickness and composition on the structure and ordering in La-doped intergranular films between Si<sub>3</sub>N<sub>4</sub> crystals", Y. Jiang and S. H. Garofalini, *Acta Mater.* 59 (2011) 5368-5377 (exclusively acknowledges BES-MSE support).
3. "Order in nanometer thick intergranular films at Au-sapphire interfaces", M. Baram, S. H. Garofalini and W. D. Kaplan, *Acta Mater.* 59 (2011) 5710-5715. (exclusively acknowledges BES-MSE support for SHG; the other two authors have support from the Israel Science Foundation)

Two other papers are currently being written regarding the growth behavior induced by the different RE-like atoms in the IGF, providing a possible generic substitute for the RE ions.

## **Brush-Coated Nanoparticle Polymer Thin Films: structure-mechanical-optical Properties**

**Peter F. Green**

**Department of Materials Science and Engineering and Department of Chemical Engineering, Applied Physics**  
University of Michigan, Ann Arbor, MI 48108

### **Program Scope:**

It is now well established that the addition of even small quantities of nanoparticles to polymer hosts to create polymer nanocomposites (PNCs) has the effect of drastically changing physical properties, thereby rendering PNCs useful for diverse applications.<sup>1</sup> Based on the functionality of the polymer and of the nanoparticles, applications include energy conversion, optical behavior, mechanical behavior and a variety of functional environmental and biomedical uses. The major scientific challenges are associated with predictable control and spatial organization of the inorganic nanoparticles within the organic polymer host. Accomplishing this would enable the development of a fundamental understanding of the structure-property behavior of these systems; there is indeed much progress toward accomplishing these goals. One strategy that enables control of the spatial organization metallic nanoparticles within a polymer host is to graft polymer chains onto the nanoparticle surfaces: this enables control of the interactions between the brush layer and the homopolymer host, an otherwise difficult challenge. We established a phase diagram that enabled us to design and control polystyrene (PS) grafted gold nanoparticles in PS hosts for bulk and thin films.<sup>2</sup> This accomplishment enabled us to investigate a series of questions related to structure-property relations in PNCs: (1) NP/block copolymer thin films; (2) coarsening phenomena in NP/BCP systems; (3) surface dynamics of miscible NP/polymer-A/polymer-B systems; (4) surface plasmon processes in thin film PNCs. homopolymer/block copolymer micelle encapsulated brush---coated metallic nanoparticle mixtures.

### **Recent Progress:**

Efforts to develop a unified picture of how various competing interactions at the nanoscale determine the structure-property behavior of polymer nanocomposites (PNCs) continue to be of interest to diverse scientific communities. We established procedures to control the spatial distribution of polystyrene (PS) chain grafted nanoparticles within PS bulk and thin film hosts. <sup>2</sup> In thin films the existence of external interfaces has a profound influence on the structure of the PNC. Thin films are thermodynamically less stable than their bulk analogs due to the preferential attraction between the brush coated nanoparticles and the surfaces. Gains in entropy associated with the interfacial segregation of the grafted nanoparticles compared to the linear host chains as well as van der Waals interactions between the nanoparticles and the interfaces contribute, in part, to this preferential interfacial attraction. Through control of the grafting chain length, host

chain length, film thickness, particle size (and shape), nanoparticle composition and grafting density, significant control of the nanoparticle distribution throughout the homopolymer host is achievable; all this information is quantified in terms of a phase diagram used to guide the structural design of such PNCs. Our prior research laid the foundation to develop rules/procedures to control the nanoparticle organization in block copolymers and block copolymer/homopolymer mixtures. To this end, we provide examples of recent accomplishments.

### Homopolymer/nanoparticle mixtures

Using the aforementioned strategies we designed and fabricated thin films in which nanoparticles of different sizes were organized within thin film polymer hosts: dispersed, phase segregated at interfaces.<sup>3</sup> For nanoparticles dispersed in thin films, Mie theory provided an excellent description of the optical properties. We also showed how the surface plasmon responses of the thin film PNCs manifested features such as particle size, interparticle separation and the proximity to substrates (Fig. 1).

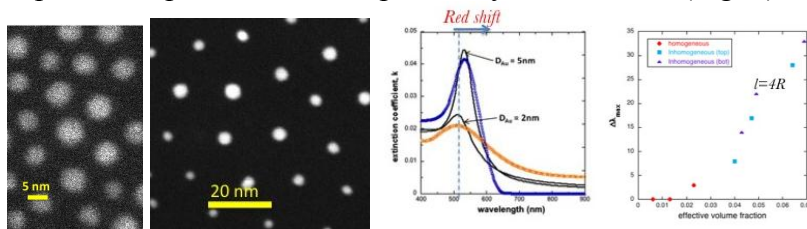


**Figure 1:** (a, b) 2D organization of nanoparticles of different sizes based on design principles; (c) surface plasmon response of particles of different sizes dispersed in a PS host; (d) shifts in the location of the maxima associated with the proximity of interfaces of very different dielectric behavior from the host.

### Block Copolymer Thin Film hosts.

A-b-B diblock copolymers (BCPs) exhibit different phase-separated morphologies, with A and B-phases (spheres, cylinders, lamellae and gyroids) based on the degree of asymmetry between the sizes of the blocks. A common strategy to incorporate NPs within the host includes *in situ* NP synthesis, which has drawbacks, or *ex situ* synthesis of NPs possessing diameters that are small in comparison to the domain dimensions. Sufficiently small NPs will reside in the domains with which they are thermodynamically most compatible, thereby creating a material in which the nanoparticle organization follows the symmetry of the copolymer morphology.

We showed that in BCP thin films defects, dislocations, primarily influence the organization of sufficiently large nanoparticles. Specifically nanoparticles of sufficiently large-sizes that would normally be accommodated within the domains, or form separated phases in bulk BCP, preferentially segregate to the core of edge dislocations. This minimizes the free energy associated with the accommodation of surface relief structures (islands and holes) that form due to a nucleation and growth process in these systems: the chains that comprise the dislocation undergo less stretching and therefore gain conformational entropy when the nanoparticles are located within the dislocation core.<sup>4</sup>



**Figure 1:** (a) Nanoparticles organized around an island; (b) schematic of nanoparticles in a dislocation core; (c) AFM image of an island.

Having demonstrated how to reliably produce these structures we embarked on a problem of particular interest to the field of materials science: coarsening phenomena. Coarsening is a ubiquitous phenomenon: aggregation of aerosol particles, phase separation of liquid-liquid mixtures, structural evolution of alloys.

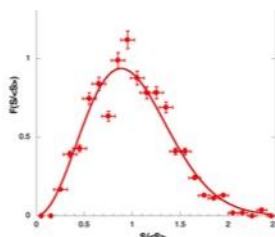
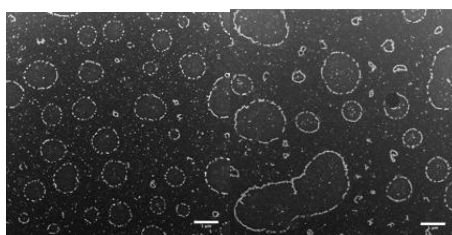


**Figure 3:** (a,b) Nanoparticles surround islands at early and late times. Coarsening of the islands from images in part a to part b. Distribution function describes the organization of nanoparticles (coalescence mechanism)

We investigated how nanoparticles influenced the coarsening of the domains (islands). The main effect, apart from decreasing the dynamics, changed the mechanism from purely coalescence, in the absence of nanoparticles, to a combination of coalescence and Ostwald ripening.<sup>5</sup> The structures of the domains were self-similar and well described by conventional coarsening models.

Having discussed nanoparticle organization in homopolymers and block copolymers, we developed procedures to sequester nanoparticles within BCP micelles in homopolymer hosts.<sup>6</sup> BCP Micelles are formed in A-b-B copolymer/homopolymer-A blends; each micelle possesses an inner core of B-type chains and an outer corona of A-type chain segments. We showed that nanoparticles could be sequestered within the micelles, with an average of one nanoparticle per micelle. The thermodynamics of the systems are described in the publication.

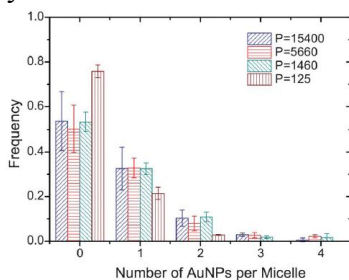


**Figure 4:** the number of nanoparticles per micelle in the BCP/homopolymer mixture. Most micelles are empty. The occupied micelles contain one nanoparticle per micelle.

Finally, other accomplishments included the design of a new class of electrorheological fluids<sup>8</sup> and the study of chain dynamics under various conditions of geometrical confinement.<sup>9</sup>

## References

1. S. Allard A.J. Moule, N.M. Kronenberg, A. Tsami, U. Scherf and K. Meerholz, *Physical Chemistry C* 112, 12583 (2008); J. Henle and S. Kaskel H. Althues, *Chemical Society Reviews* 36, 1454 (2007).
2. Green, P.F., *SOFT MATTER*, Advance Article. 2011, 7, p.7914-7926
3. Kim, J; Yang, H; Green P.F., *LANGMUIR*, 2012, 28(25): p. 9735-9741.
4. Kim, J. and Green, P.F., "Macromolecules, 2010, 43, 10452.
5. Kim, J and Green, P.F., *MACROMOLECULES*, 2012, 45(8): p.3496-3502.
6. Zhao, J; Chen, X.C.; Green P.F., "Nanoparticle Encapsulation in Thin Film Micellar Structures: *SOFT MATTER*, 2013, 9 (26): p.6128.
7. McIntyre, C., Yang, H., Green, P.F., *ACS APPLIED MATERIALS & INTERFACES*, 2013, Article ASAP.
8. McIntyre, C., Yang, H., Green, P.F., *ACS APPLIED MATERIALS & INTERFACES*, 2013, Article ASAP.
9. Yang, H; Chen, X.C.; Jun, G; Green P.F., *MACROMOLECULES*, 2013, 46 p.5036.

## Publications

1. McIntyre, C., Yang, H., Green, P.F., "Electrorheology of Suspensions Containing Interfacially Active Constituents." *ACS APPLIED MATERIALS & INTERFACES*, 2013, Article ASAP.
2. Zhao, J; Chen, X.C.; Green P.F., "Nanoparticle Encapsulation in Thin Film Micellar Structures: A Physical Method for Functional Materials Design." *SOFT MATTER*, 2013, 9 (26): p.6128.
3. Yang, H; Chen, X.C.; Jun, G; Green P.F., "Segmental Dynamics of Chains Tethered at Interfaces of Varying Curvatures." *MACROMOLECULES*, 2013, 46 (12): p.5036.
4. Frieberg, B; Kim, J; Narayanan, S; Green P.F., "Surface Layer Dynamics in Miscible Polymer Blends." *ACS MACRO LETTERS*, 2013, 2 (5): p.388.
5. Kim, J; Yang, H; Green P.F., "Tailoring Refractive Index of Thin Film Polymer Nanocomposites." *LANGMUIR*, 2012, 28(25): p. 9735-9741.
6. Chen, X.C.; Yang, H; Green, P.F., "Micellar Formation and Organization in Thin Film Polymer Blends," *MACROMOLECULES*, 2012, 45(9): p. 3993-4000.
7. Kim, J and Green, P.F., "Time Evolution of the Topography of Structured Hybrid Polymer/Nanoparticle Systems," *MACROMOLECULES*, 2012, 45(8): p.3496-3502.
8. McIntyre, E.C.; Yang, H.; Green, P.F., "Electrorheology of Polystyrene Filler/Polyhedral Silsesquioxane Suspensions," *ACS APPLIED MATERIAL & INTERFACES*, 2012, 4(4), p.2148-2153.
9. Green, P.F.; Oh, H.J.; Akcora, P.; Kumar, S.K. "Structure and Dynamics of Polymer Nanocomposites," *Dynamics of Soft Matter: Neutron Scattering Applications and Techniques*, V.G-S, C.A-Simionescu, S-H. Chen, Editors, Springer, New York Dordrecht Heidelberg London, 2012.

# Evolutionary Selection Growth: Towards Template-Insensitive Preparation of Single-Crystal Layers

Benjamin Leung and Jung Han  
Department of Electrical Engineering  
Yale University, New Haven CT, 06520

## Program Scope

Growth of single crystal semiconductors on amorphous substrates represents both a fundamental conceptual difficulty and a long-standing practical challenge. The ability to form device quality semiconductor material on an amorphous substrate would be outside the realm of typical heteroepitaxial growth methods, where the substrate is expected to provide atomic registry for single crystal growth. In particular, the importance of GaN in opto- and power-electronics is well established. A particular need that has received much attention is the heteroepitaxial integration of GaN with mainstream Si technology. This aspiration faces major challenges including mismatches in lattice and thermal expansion constants, the problem of chemical reactivity, and the current leakage through conductive Si substrates.

The previous approaches of artificial epitaxy, or graphoepitaxy,<sup>1</sup> resorts to surface patterning, typically through electron-beam, interferometric, or photolithography, to create geometric boundary conditions on the length scale of nuclei so their orientations can be influenced, if not dictated, by the shape of the moulds.<sup>2,3</sup> With all the advances in growth and lithography techniques since then however, graphoepitaxy has not produced the level of control required by modern device applications. Within the scope of this project, we explore the possibility of single-crystal growth on amorphous oxide by exploiting a phenomenon in material deposition: evolutionary selection growth.<sup>4</sup> With the successive applications of evolutionary selection (ES) along two perpendicular axes, we work on removing the degrees of freedom in grain orientations, resulting in the preparation of single-crystalline GaN on a SiO<sub>2</sub>/Si(100) template. The conceptual model of ES is confirmed by the modeling of growth dynamics to provide a universal procedure in forming crystalline layers on amorphous substrates.

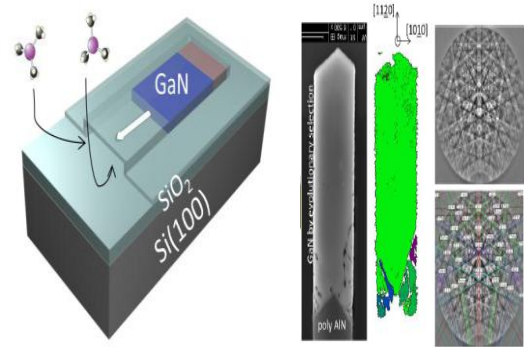


**Figure 1** a) Schematic of confined evolutionary selection growth of GaN in vertically and laterally confined SiO<sub>2</sub> selective area growth mask, and b) Electron backscatter diffraction analysis of GaN crystal grown showing large single crystal evolving from polycrystalline seed, and Kikuchi pattern of single crystal GaN captured ~2 um from end.

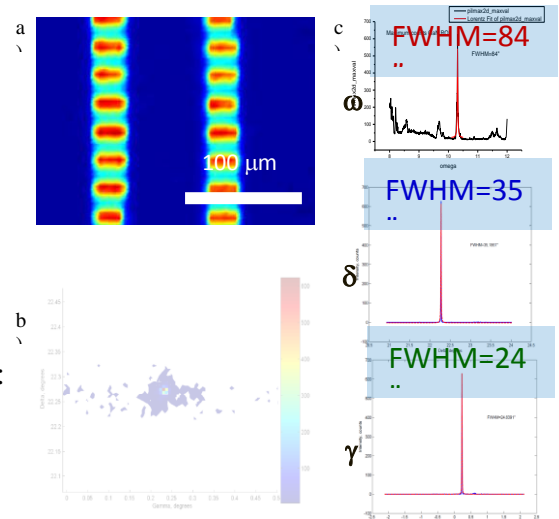


**Figure 2** Micro x-ray diffraction characterization of GaN at Diamond Light Source (synchrotron source, UK) a) AlN (0002) spatial mapping, b) RSM, and c) linewidths showing microstructural quality of GaN comparable to bulk GaN

## Recent Progress

We have recently demonstrated single crystal GaN growth by employing the general phenomenon in film deposition of evolutionary selection.<sup>5</sup> In the concept that has been proposed and demonstrated, evolutionary selection (ES) was employed in first a vertical, then in a lateral direction, allowing a final single crystal of GaN to be formed. This was implemented by deposition of an (0001) oriented AlN layer on a SiO<sub>2</sub>/Si(100) substrate. A SiO<sub>2</sub> confined mask structure is then formed, and subsequent lateral selective area growth of GaN by MOCVD using AlN as a seed, produced site-selected placement of GaN and eliminated the in-plane misalignment.

In this work, the evolutionary selection process is modeled in the context of GaN growth, and the analysis of the deposition conditions that allow this growth process to occur are discussed. Essentially, the concept is enabled by combining evolutionary selection with a selective area growth process. Here, as opposed to typical ELO processes, the surface is predominately covered with dielectric in the regime of very low fill factors, in which the local growth environment is expected to be considerably altered.

Additionally, while the mass transport mechanisms of typical planar SAG has been thoroughly studied, the extension to 3-dimensional masking (vertical and lateral confinement) has not been well explored. By controlled variation of MOCVD growth conditions, in combination with analytic and finite-element modeling of mass transport by gas-phase diffusion (COMSOL), we identify and analyze the major factors in of single-crystal GaN on SiO<sub>2</sub> in this configuration.

There are three influences on the growth condition of GaN in the ES-SAG growth scheme here. The first is necessity of selective growth to prevent unwanted nucleation on the SiO<sub>2</sub> growth surface. While these polycrystals can be removed with subsequent etching of the SiO<sub>2</sub> mask, these large GaN clusters act as sinks for the precursors and grow at a much faster rate since they are not confined within tunnels. The second influence of the growth condition is on the density of nucleation on the AlN seed, which in turn will affect the evolutionary selection mechanism. The ES growth mechanism scales as the density of the initial nucleation, thus the evolution rate will be scaled as well. The third effect of growth condition on the ES-SAG growth is on the

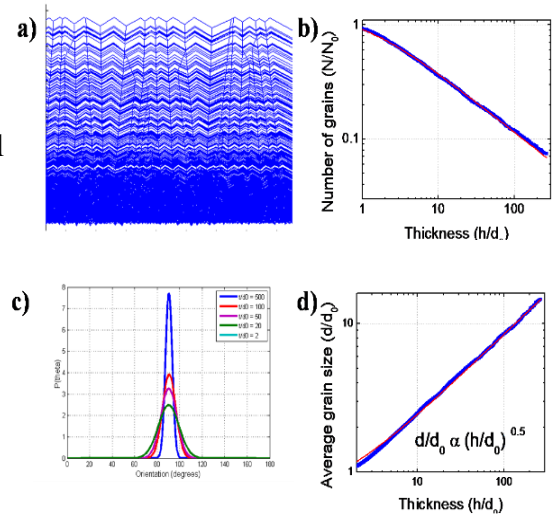


**Figure 1** a) Simulation of competitive growth process of randomly oriented nuclei forming textured film, b) number of grains, c) orientational distribution, and d) grain size distribution dependence on film thickness

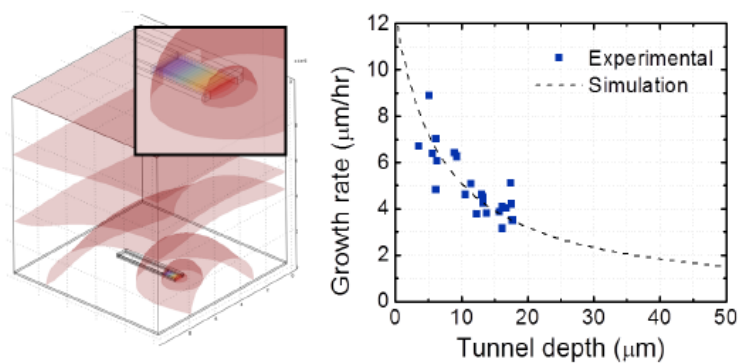


**Figure 3** a) Gas phase concentration profile of precursor modeled by finite element modeling above a single tunnel, b) growth rate dependence on initial depth

growth rate, which will determine the final length of GaN growth in the tunnel in a given growth time. The balance between these considerations will determine the growth conditions used, each of which is investigated in detail.

While growth on planar 2D selective area growth masks have been analyzed in detail, the use of three dimensional masks, i.e. confinement of growth in both in-plane and out-of-plane directions are have been subject to fewer studies . In this case, for analyzing and predicting the mass transport in this growth method, the structures here are modeled as inert rectangular channels of varying dimensions. Typically, a combination of surface and lateral gas phase diffusion takes place, each acting dominantly over different characteristic length scales. Given the large length scales of the SiO<sub>2</sub> mask, the situation is analytically modeled, dominated by gas phase diffusion, as a simple compartment model, described by the reaction-diffusion equation. The solution of such a system has been given, by Deal and Grove<sup>6</sup>, to be

$$\frac{dx}{dt} = \frac{B}{2x_i + A}$$

where x is the length distance from the tunnel opening to the growth front, and the constants A and B are defined by  $A = 2D_{\text{eff}}/k$ ,  $B = 2D_{\text{eff}}C^*/N$ , where  $D_{\text{eff}}$  is the effective diffusion constant inside the tunnel,  $k$  is the reaction rate constant,  $C^*$  is the concentration of precursors outside the tunnel, and  $N$  is the number of precursor molecules incorporated in a unit volume. Using typical constants for MOCVD growth of GaN,  $D_{\text{eff}} = 22 \text{ cm}^2/\text{s}$ ,  $k = 15850 \text{ cm/s}$ ,<sup>7</sup> and  $C^* = 1 \times 10^{-9} \text{ mol/L}$ ,<sup>8</sup> the curve is plotted in Fig 3 and Fig 4, and matches experimental data of growths performed on tunnels etched to different depths. It can be seen that this curve predicts a decreasing growth rate as depth of tunnel increases due to the increased diffusion distance required of the precursors. However, it is found that an appreciable growth rate ( $>1 \text{ } \mu\text{m/hr}$ ) is still possible with tunnel depths of 100  $\mu\text{m}$  and greater.

### Future Plans

We plan to extend the physical dimensions of ES material by further developing fabrication processes and using alternative growth methods such as hydride vapor phase epitaxy to increase growth rate and improve selective area processes. This will allow the possibility of realizing commercial scale light-emitting and electronic devices.

In parallel, extension of the ternary InGaN nanorod concept for long wavelength emitting photonic materials are pursued by the fabrication of 3D scaffolded nanocomposite material. The use of porous GaN will enable a low dislocation density template for high In composition material. The concept of liquid-phase mediated confined growth to produce high In composition InGaN will also be explored.

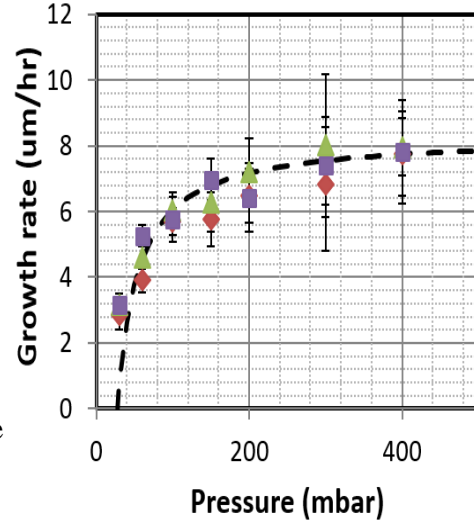


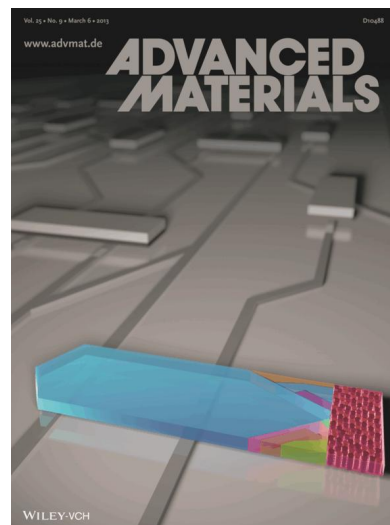
**Figure 4** Analytic compartment model (dashed line) describing growth rate dependence on reactor pressure, with experimental data points shown.

## References

1. E. I. Givargizov, *Thin Solid Films*, **189**, 389 (1990).
2. M. W. Geis, D. C. Flanders, H. I. Smith, *Appl. Phys. Lett.*, **35**, 71 (1979).
3. A. L. Giermann, C. V. Thompson, *Appl. Phys. Lett.*, **86**, 121903 (2005).
4. A. van der Drift, *Philips Res. Rep.*, **22**, 267 (1967).
5. B. Leung, J. Song, Y. Zhang and J. Han, *Adv. Mater.* **25**, 1285 (2013).
6. B. E. Deal and A. S. Grove, *J. Appl. Phys.* **36**, 3770 (1965).
7. M. E. Coltrin and C. C. Mitchell, *J. Cryst. Growth*, **254**, 35 (2003).
8. A. Hirako, K. Kusakabe, and K. Ohkawa, *Jpn. J. Appl. Phys*, **44**, 874 (2005)

## DoE Sponsored Publications in the Last 2 Years

1. J. Song, et al., "Growth, structural and optical properties of ternary InGaN nanorods prepared by selective-area metalorganic chemical vapor deposition", submitted to *Nanotechnology*, (2013).
2. B. Leung, et al., "Using the evolutionary selection principle in selective area growth to achieve single-crystalline GaN on SiO<sub>2</sub>", *International Journal of High Speed Electronics and Systems*, in press, (2013)
3. B. Leung, et al., "Analysis of confined evolutionary growth for single-crystalline GaN layers on SiO<sub>2</sub>", manuscript in preparation, (2013).
4. B. Leung et al., "Evolutionary Selection Growth: Towards Template-Insensitive Preparation of Single-Crystal Layers", *Advanced Materials* **25**, 1285 (2013). [Featured on cover page]
5. B. Leung et al., "Growth evolution and microstructural characterization of semipolar (1122) GaN selectively grown on etched r-plane sapphire" *Journal of Crystal Growth* **341**, 27 (2012).
6. B. Leung, et al., "Using the kinetic Wulff plot to design and control nonpolar and semipolar GaN heteroepitaxy" *Semiconductor Science and Technology* **27**, 024005 (2012).
7. B. Leung, et al., "Optical emission characteristics of semipolar (1122) GaN light-emitting diodes grown on m-sapphire and stripe-etched r-sapphire", *Semiconductor Science and Technology* **27**, 024016 (2012).
8. Q. Sun, et al., "Understanding and controlling heteroepitaxy with the kinetic Wulff plot: A case study with GaN" *Journal of Applied Physics* **110**, 053517 (2011).
9. C. D. Yerino et al., "Shape transformation of nanoporous GaN by annealing: From buried cavities to nanomembranes", *Applied Physics Letters* **98**, 251910 (2011).



# Understanding and Controlling Nanoscale Crystal Growth Using Mechanical Forces

Mostafa Bedewy<sup>1,2</sup>, Assaf Ya' Akobovitz<sup>1</sup>, Kendall Teichert<sup>1</sup>, and A. John Hart<sup>1,2</sup>

<sup>1</sup>Department of Mechanical Engineering, University of Michigan, Ann Arbor, MI

<sup>2</sup>Department of Mechanical Engineering, Massachusetts Institute of Technology, Cambridge, MA

## 1. Program Scope

Growth of one-dimensional nanostructures such as carbon nanotubes (CNTs) and silicon nanowires (SiNWs) is analogous to bulk crystal growth, where a solid is formed by precipitation due to a thermodynamic driving force at an interface. While it is well-known that mechanical stress affects crystal growth, diffusion, and defect migration [1-3], the mechanisms and roles of these phenomena at the nanoscale are not comprehensively understood, and have not been studied with respect to growth of nanostructures. In this program, we are exploring how mechanical stimulation may be used to control the formation rate, geometry, and perfection of one-dimensional nanostructures; and thereby aim to understand how mechanical stress affects the growth of crystals at the nanoscale. We are studying growth of CNTs because their basic growth processes are well-known, yet there is important need to more precisely control the structure and properties of CNTs for many applications. We have constructed micromanipulation systems for application of controlled forces to CNT forests and individual CNTs during growth. Also, we have used comprehensive *in situ* and *ex situ* characterization methods including synchrotron X-ray scattering to construct population-based models of mechanically coupled nanostructure growth, enabling us to relate the measured growth kinetics and structural transformations of the nanostructures to both intrinsically and extrinsically imposed mechanical stimuli.

## 2. Recent Progress

Here we highlight the results of three complementary tasks at the core of the program scope: (1) analysis and modeling of mechanical coupling in CNT forest growth; (2) mechanical perturbation of CNT forest growth using a custom-built CVD reactor; and (3) design and fabrication of MEMS devices for stretching individual CNTs during growth.

### 2.1 Analysis of mechanical and chemical coupling in CNT forest growth

We analyze the mismatch between the apparent forest height kinetics and the calculated diameter-dependent growth kinetics in order to estimate the axial load applied on catalyst nanoparticles by tortuous CNTs in contact. This is based on modeling of the CNTs as curved beams under axial deflection, with geometry derived from X-ray mapping of CNT forests. Using this approach, **Fig. 1A** shows the time evolution of the diameter-dependent compressive force applied on the catalyst nanoparticles. Here, the diameter range of 1-40 nm is assumed to completely represent the CNT population within the forest. The predicted forces increase to reach a maximum 115 seconds after start of growth. Owing to the sign of the growth rate mismatch, the loads change from slightly tensile for diameters smaller than the mode of the diameter distribution to highly compressive for larger diameter CNTs. The compressive stresses applied on the catalyst nanoparticles are then calculated as the force per unit projected area of CNT, based on the measured values for the outer and inner CNT diameters obtained from fitting SAXS linescans. In this figure, positive force means that CNTs are pushing on the catalyst,

and negative means the CNT is pulling on the catalyst. Now, **Fig. 1B** places this information into the collective picture of CNT population growth. Hence, we conclude that growth rate mismatch leads to significant mechanical stresses on individual CNTs that are coupled due to van der Waals forces at contact points. Based on these results, we hypothesize that the maximum density achieved in a forest may be limited by the axial forces acting on the CNT-catalyst interface. Moreover, it is possible that these loads can influence the growth kinetics and structural quality of individual CNTs. The potential influence of mechanical forces on the kinetics and quality of growing CNTs suggests that strategies to improved manufacturing of organized CNTs should consider both chemical and mechanical effects.

Moreover, we propose that during CVD growth of CNTs, the catalytic decomposition of the gaseous precursors at the catalyst surface produces gaseous active species, the concentration of which locally modulates the growth rate of carbon nanotubes by shifting the activation energy. We adopted the mathematical growth model developed by Puretzky et al. [3], to describe the growth kinetics based a set of partial differential equations having reaction constants and activation energies. We use the kinetics of surface carbon generation predicted by this model, and feed this back into the source kinetics of the generation of active species (gaseous by-products). Then the diffusion equation is used to update the spatial distribution of concentration. To close the loop, the activation energy for CNT growth is coupled to this concentration, in such a way that the activation energy is reduced with increasing concentration. We have done experiments and computer simulation, to

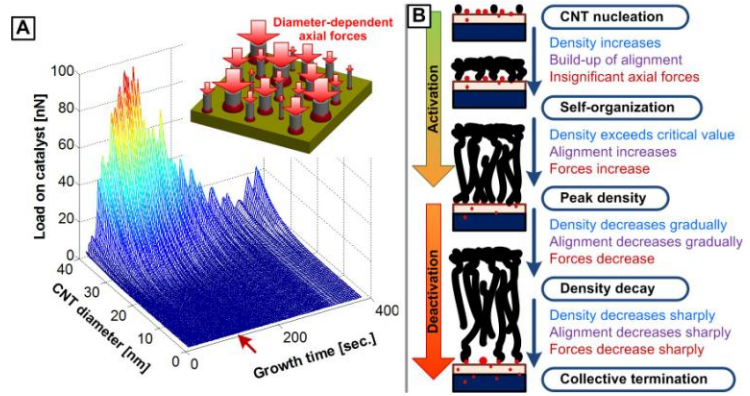


**Fig. 1** (A) Time evolution of the diameter-dependent load exerted by the CNTs on corresponding catalyst particles. (B) Schematic of the successive stages of CNT forest growth showing the evolution of density, alignment and forces along with the competition between CNT activation and deactivation, starting with CNT nucleation and ending with collective growth self-termination.

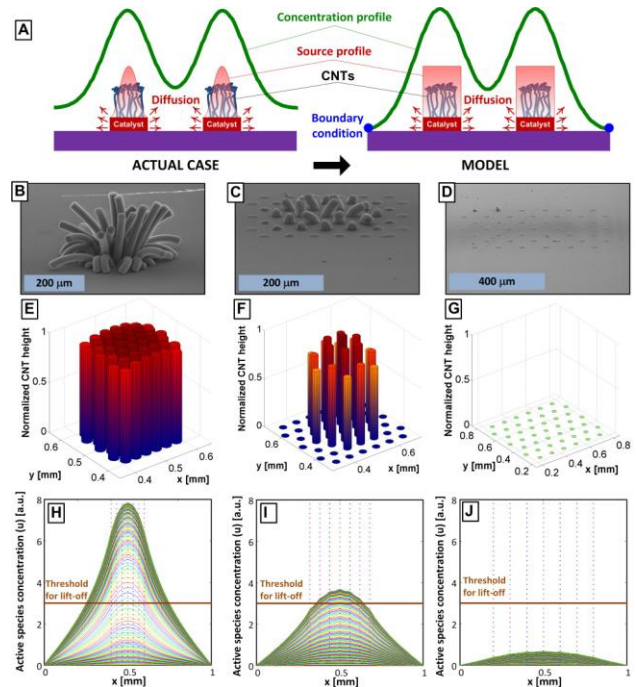


**Fig. 2** (A) Schematic of chemical coupling model, where each catalyst area is considered a source of active species, and this gaseous species diffuses to the surroundings, creating the typical concentration profiles. (B,C,D) SEM images of pillar arrays having diameters of 30 microns and center-distance of 33, 100 and 300 microns respectively. (E, F, G) Simulation results for the same arrays. (H, I, J) Concentration profiles for active gaseous species, showing the threshold value for lift-off.

elucidate and validate this mechanism. As shown in **Fig. 2**, our mathematical model can accurately simulate the experimental results of CNT pillar array growth. At larger spacing, the concentration profiles have lower magnitudes, and when these concentrations are below a certain threshold for lift-off, only a tangled CNT film is obtained.

### 2.2 *In situ* mechanical manipulation of CNT forest growth

We have integrated a custom-built vacuum chamber with a custom-built position/force control module, referred to herein as the "tower", which includes the voice coil actuator, linear flexure bearings, optical encoder, load cell, and the end-effector. First, we apply mechanical compression force to a growing CNT structure by means of pushing rod. The push-rod is connected in series to a load cell and the linear motion system, hence enabling a feedback control on the motion of the rod to track growth while maintaining a constant compressive force (**Fig. 3**). In this experiment, CNT forests grow immediately upon the introduction of acetylene at 800 °C. Initially, there is a gap between the substrate and the probe. However, as soon as CNTs start growing, this gap is bridged by CNTs until contact with the pushing probe. At this point, the load cell starts reading compressive forces, as the voice coil is pushing against the growing CNTs to maintain position. As the load reaches 5 grams, the control scheme is switched from a constant-position feedback loop to a constant force feedback loop, meaning that the load will be held constant at 5 grams, while the actuator moves the probe to compensate for both the CNT growth rate and the thermal expansion of the heater assembly. More recent experiments indicate a non-monotonic relationship between applied (compressive) force and CNT forest growth rate, suggesting different thresholds for mechanical influence on growth kinetics during CNT self-organization and steady collective growth.

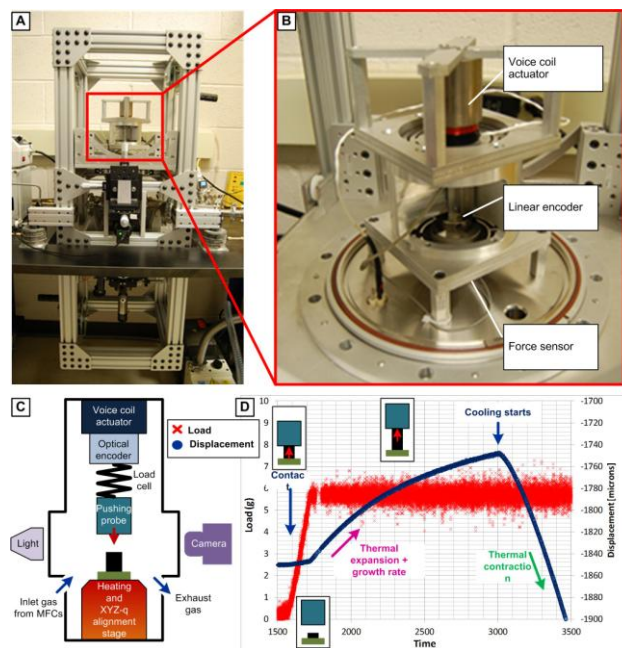


**Fig. 3.** (A,B) Photograph of the custom CVD chamber for mechanically controlled CNT forest growth. (C) Schematic of the *in situ* mechanical manipulation of growing CNT structures. (D) Experimental result for application of constant force during CNT growth using a feedback loop that updates the position of the pushing probe in order to maintain constant force at the contact between the probe and CNT forest.

### 2.3. MEMS devices for applying tension during CNT growth

Last, we have fabricated MEMS devices to enable *in-situ* manipulation of single wall carbon nanotubes (SWNTs), namely to stretch the CNTs after growth across a microfabricated gap. The device consists of an electrostatically actuated MEMS manipulator, aiming to stretch the CNTs, and a heater, that elevates the temperature as necessary to cause CNT growth on the islands. First, the device is actuated in order to reduce the gap between it and the heater. Next, we apply Joule heating and flow of  $C_2H_4$ , in order to cause CNT growth. Finally, the device actuation

voltage is reduced in order to stretch the grown SWCNTs while keeping the growing conditions, i.e. high temperature of the heater and  $C_2H_4$  gas flow, so that the simultaneous presence of carbon feedstock and applied tension can allow mechanically manipulated carbon precipitation. Stretched SWCNTs will be characterized mainly using Raman spectroscopy in order to detect changes in their tension, defects and chirality comparing to a reference un-stretched SWCNTs. Later, we will attempt to integrate the devices with TEM images to observe stretch-induced structural changes in the CNTs. The device shown in **Fig. 4** is fabricated using a SOI wafer, with separate contact electrode paths for the actuator and heater. The device is packaged on a circuit board and the custom-built vacuum chamber holds the device during the growth experiment.

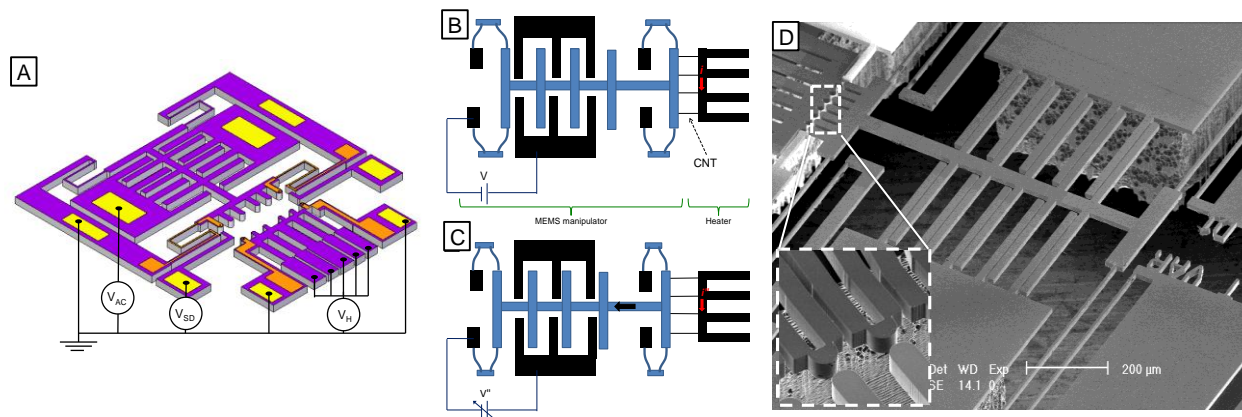


**Fig. 4.** MEMS manipulator for applying tension during SWCNT growth across a gap: (a) 3D model of device indicating material layers and electrical signals applied for resistive heating and electrostatic actuation; (b,c) schematic position of device before and after tension is applied, with SWCNTs spanning gap between heater and actuator module; (d) SEM images of released device, with inset showing islands.

### 3. Future Plans

We plan to investigate the effect of applied forces on the growth kinetics of individual micron sized CNT pillars using the CVD reactor manipulation system described above, by applying both contact forces and non-contact forces (via electrostatics). To understand the effects on the CNT morphology and crystal structure, we will first perform *ex situ* SAXS mapping of the CNT pillars, and therefore extract relationships between applied forces, growth kinetics, and structural quality. We will also use the MEMS devices described above to apply tension to individual CNTs during growth, and relate the applied tension to diameter and defect quality as measured by Raman spectroscopy.

We have also begun to perform in situ TEM studies of CNT growth at Brookhaven National Laboratory (BNL); specifically, we plan to study the mechanism determining CNT growth catalyst activity, quantify the catalyst activation kinetics leading to self-organization, and observe CNT-CNT growth coupling in real time.

Last, we plan to derive a model for nanoscale crystal growth (with adaptation to CNTs and solid nanowires) that includes the effect of applied forces on the crystallization kinetics. This has been postponed to further due to additional findings of our collective growth modeling effort during the past year. We will use this kinetic model in a feedback model of coupled

nanostructure growth, i.e., considering the coupling between CNTs growing at different rates, their elasticity, mechanical instabilities, and mechanically-driven kinetics.

#### 4. References

1. Aziz, M.J., et al., *Crystal growth kinetics of boron oxide under pressure*. Journal of Applied Physics, 1985. **57**(6): p. 2233-2242.
2. Aziz, M.J., *Thermodynamics of diffusion under pressure and stress: Relation to point defect mechanisms*. Applied Physics Letters, 1997. **70**(21): p. 2810-2812.
3. Nygren, E., et al., *Pressure dependence of arsenic diffusivity in silicon*. Applied Physics Letters, 1985. **47**(2): p. 105-107.

#### 5. DoE Sponsored Publications in the Last Two Years

1. M. Bedewy, E.R. Meshot, M.J. Reinker, A.J. Hart. Population growth dynamics of carbon nanotubes. *ACS Nano* 5(11):8974-8989, 2011. <http://dx.doi.org/10.1021/nn203144f>.
2. J. Beroz, M. Bedewy, M. Reinker, V. Chhajer, S. Awtar, A.J. Hart. Four degree of freedom liquid dispenser for direct-write capillary self-assembly with sub-nanoliter precision. *Review of Scientific Instruments* 83:015104, 2012. <http://dx.doi.org/10.1063/1.3673680>.
3. M. Bedewy, E.R. Meshot, A.J. Hart. Diameter-dependent kinetics of activation and deactivation in carbon nanotube population growth. *Carbon* 50(14):5106-5116, 2012. <http://dx.doi.org/10.1016/j.carbon.2012.06.051>.
4. M. Bedewy, A.J. Hart. Mechanical coupling limits the density and quality of self-organized carbon nanotube growth. *Nanoscale* 5:2928-2937, 2013. <http://dx.doi.org/10.1039/C3NR34067H>.
5. A. Ya'akovovitz, D. Copic, J. Beroz, A.J. Hart. Nanoscale displacement measurement of microdevices via interpolation-based edge tracking of optical images. *Journal of Micromechanics and Microengineering* 23:045004. <http://dx.doi.org/10.1088/0960-1317/23/4/045004>.
6. A. Ya'akovovitz, A.J. Hart. High surface capacitance of silicon micropillar arrays. *Submitted for publication*.
7. M. Bedewy, B. Farmer, A.J. Hart. Understanding and control of carbon nanotube forest uniformity via synergetic chemical coupling. *Submitted for publication*.

## **Improved Electrochemical Performance of Strained Lattice Electrolytes via Modulated Composition**

**Joshua L. Hertz**

**Departments of Mechanical Engineering and Materials Science and Engineering  
University of Delaware**

### **Program Scope**

Solid electrolytes, found in batteries, fuel cells, and chemical sensors, are highly (and increasingly) important energy technology components. Nevertheless, the rigid atomic framework of solids provides for relatively few materials with high ionic conductivity, particularly at low temperatures. For example, solid oxide fuel cells typically must be operated at  $\geq 800$  °C in order to obtain sufficient oxygen ion conduction through the electrolyte. These temperatures necessitate the use of expensive components and limit device lifetimes, making them economically unfeasible at this time.

Recently, the use of nanostructured multilayers has been proposed as a means to obtain vastly improved solid state ionic conduction. It is believed that coherency strains and/or differences in defect formation and association energy can cause a redistribution of mobile species, thereby altering the conductivity. Unfortunately, the experimental evidence advocating these techniques has often been controversial. In addition, the materials used in the multilayers are often chosen on an ad-hoc basis, with no general theory to explain how best to optimize conductivity. Further, nearly all of the multilayers demonstrated have used layer materials wherein one of the layers was a poor ion conductor. This latter aspect leads to conduction that is highly anisotropic, with poor conductivity in the through-thickness direction.

In this project, we are studying sputter deposited nanostructured films and multilayers of oxygen ion conductors. We have established means to fabricate zirconia- and ceria-based films where the composition—considering both the Zr/Ce ratio and the dopant content—can be controlled and even modulated with single nanometer resolution. Series of well-controlled compositional modulations enable the determination of the relative importance of strain and defect formation and association energy in spatial redistribution of mobile defects. High resolution TEM and SIMS are being used to physically characterize the specimens. Impedance spectroscopy is being used to determine the effects of the layer spacing and the magnitude of compositional modulation on ionic conductivity. Oxygen ion conductors, with application to SOFCs, are being used in this study; however, the concepts and methods being discovered are applicable to other ionic conduction systems. The research being performed impacts our understanding of the effect of materials nanostructure upon ionic conduction and influences the development of methods to engineer improved conduction.

### **Recent Progress**

In first-stage work on this project, we demonstrated means to produce epitaxial, single-layer films with arbitrary dopant composition and Zr-Ce ratio. Reactive co-sputtering was performed using pure elemental targets of Zr, Ce, and either Y or Gd onto (100) MgO substrates. The use of metal targets allowed for high purity and, by varying the relative sputtering powers and deposition time, controlled composition and thickness of single or multi-layer thin films. X-

ray diffraction (XRD) and transmission electron microscopy (TEM) showed that yttria-stabilized zirconia (YSZ) films deposited on (100) MgO substrates at a substrate temperature of 400 °C were epitaxial with (100) orientation, while gadolinium doped ceria (GDC) films had no preferred orientation. Still, it was found that a YSZ film could be used as a buffer layer to enable epitaxial growth of GDC.

On further testing, YSZ films with thickness ranging from 6 nm to 100 nm were deposited on (0001) Al<sub>2</sub>O<sub>3</sub> substrates and exhibited growth along (111)[110] YSZ // (0001)[10 $\bar{1}$ 0] Al<sub>2</sub>O<sub>3</sub> (Fig. 1). While the thicker films exhibited oxygen ion conductivities similar to bulk samples, the thinnest films exhibited increased ionic conductivity and a reduced activation energy of 0.79 eV between 300 °C - 650 °C. Concomitant with the improved conductivity of the thinner films was an increase in the out-of-plane lattice parameter, matching theoretical expectations regarding tensile strain, and the introduction of edge dislocations, which may additionally assist in-plane ionic conduction. Further evidence for lattice interactions on YSZ ionic conductivity was found in studying films deposited in parallel on MgO and Al<sub>2</sub>O<sub>3</sub> substrates that had polished, ion cleaned, or milled surfaces. Increased substrate surface roughness led to decreases in both the crystallinity and ionic conductivity of the films.

Similar deposition of GDC films on (0001) Al<sub>2</sub>O<sub>3</sub> substrates resulted in columnar, polycrystalline grains with (111) texture. Unlike the YSZ films, which exhibited sharply and monotonically increasing conductivity with decreasing thickness, GDC films achieved highest conductivity at 81 nm thickness with more mild decreases in conductivity for thicker and thinner films. Lattice parameter values never strayed far from equilibrium values, consistent with the lattice strain-based explanation for the prior results.

Multilayer work began with samples of Y-doped CeO<sub>2</sub> thin films where the Y dopants were distributed homogeneously or were condensed into increasingly concentrated layers, to the limit of alternating layers of pure Y<sub>2</sub>O<sub>3</sub> and pure CeO<sub>2</sub> (Fig. 2). Both the entire film thickness and net Y-concentration were kept constant such that only the spatial distribution of dopants was altered. Space charge regions formed at interfaces between regions with varying vacancy concentrations, yielding vacancies trapped within

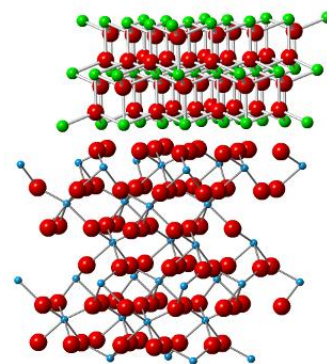
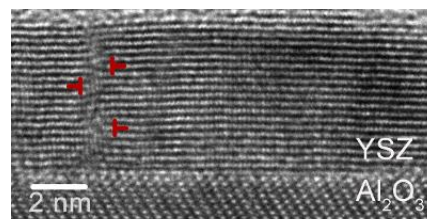


Fig. 1. (Top) HRTEM cross-section of a 6 nm thick YSZ thin film. The red marks indicate edge dislocations. (Bottom) Solid sphere model of the YSZ/Al<sub>2</sub>O<sub>3</sub> interface. Green, blue, and red spheres represent Zr/Y, Al, and O, respectively.

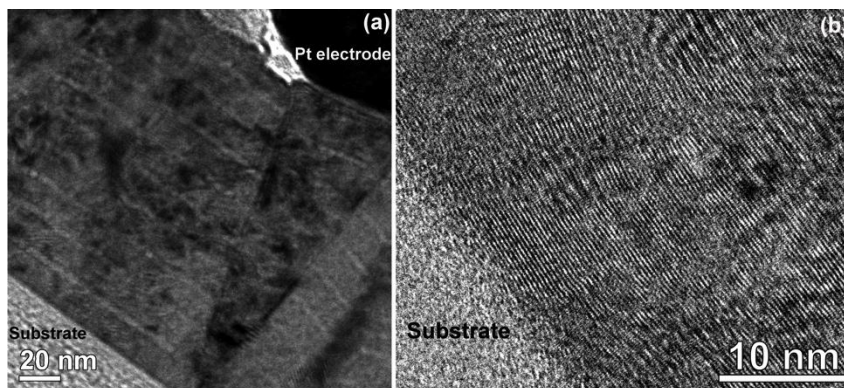


Fig. 2. (a) Bright field and (b) high resolution TEM cross-sections of a heterogeneously doped sample with multilayered 19 nm CeO<sub>2</sub> / 1 nm Y<sub>2</sub>O<sub>3</sub>.

two-dimensional accumulation regions. A Gouy-Chapman model was implemented to understand the distribution of accumulated oxygen vacancies in these regions. Comparison of the measured activation energy of conduction indicates that in films with intermediate dopant condensation, conduction occurred predominantly by vacancies trapped in the Y-containing layers. Conversely, in the film composed of alternating layers of  $\text{Y}_2\text{O}_3$  and  $\text{CeO}_2$ , ionic conduction arises mainly from vacancies trapped in the space charge region. From the Gouy-Chapman model, the total excess conductance of the space charge regions can be analytically determined, thus providing a means to determine the properties of vacancies in ceria in proximity to dopants.

Multilayers composed of  $\text{Ce}_{0.90}\text{Y}_{0.10}\text{O}_{2-\delta}$  (YDC) and  $\text{Ce}_{1-x}\text{Zr}_x\text{O}_{2-\delta}$  (CZO) (Fig. 3) were studied in order to directly quantify the effect of interfacial compressive strains on oxygen ion conduction. CZO solid solutions that adopt a cubic structure ( $x \leq 0.5$ ) were used. Our unique fabrication method allowed different compressive strains to be induced in the YDC layers by controlling the Ce/Zr atomic ratio—and thereby the lattice parameter—in the alternating CZO layers. A key benefit of using CZO other than rare earth oxides is that the lattice parameter of CZO can be continuously varied. First results using  $\text{Ce}_{0.5}\text{Zr}_{0.5}\text{O}_2$  seemed to indicate a sharp reduction in conductivity with compressive lattice strain (Fig. 3). Similar results to those shown in Fig. 3 are found in literature as putative proof of a lattice strain effect. Bulk and interfacial conductivities were distinguished from the dependence of the conductivity on interlayer-spacing. Comparing these values across multilayers using reduced Zr content in the CZO layers—to the limit of pure ceria and thus near-zero lattice strain in the YDC—showed that interfacial conductivity was *not* affected by the amount of lattice strain.

While most of the work performed here has used electrical measurements to determine the oxygen diffusion coefficient,  $D$ , isotopic tracer measurements have also been explored. Recently, there has been concern regarding the ability of this technique to measure  $D$  and/or the surface exchange coefficient,  $k$ , with high precision. By numerically modeling a generalized solution to the diffusion equation, we have derived characteristic parameters related to the exchange time ( $t$ ), material thickness ( $l$ ),

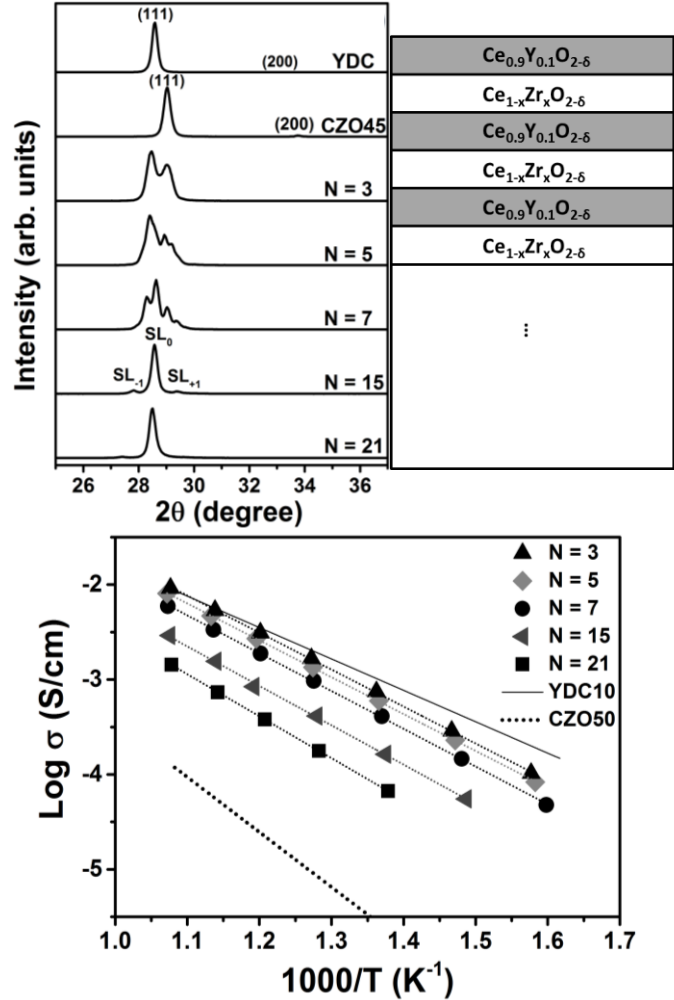


Fig. 3. (Clockwise) XRD patterns, a schematic diagram, and conductivity values of component films and multilayers of YDC and CZO. Total film thickness is 105 nm, with the N value indicating the number of layers within this thickness.

$D$ , and  $k$  that can be used to quantify the range of experimental conditions where  $D$  and/or  $k$  can be precisely determined. Of particular interest was that experiments where  $l \gg \frac{D}{k}$  can be used to robustly determine  $k$  so long as  $5 \cdot 10^{-6} \leq \frac{k^2 \cdot t}{D} \leq 20$ . Experimental validation of the utility of isotope exchange with thin film samples was performed on films of  $\text{LaCoO}_3$  and  $\text{SrCoO}_x$ .

## Future Plans

Three key themes have emerged from the project thus far and will be key focus areas for the future. The first involves the role of substrate-induced lattice parameter changes in single-layer YSZ and GDC films upon ion conduction. These effects clearly depend on the film thickness and the substrate surface and are related to the film's crystallinity. In-depth characterization of the (probably biaxial, and possibly triaxial) strain state and examination of the effects of annealing and dopant content will determine the root cause of these effects and how to engineer improved conduction thereupon. The second theme is the use of heterogeneous doping to study vacancy migration in accumulation region. Because the vacancies are localized to interfacial regions, the identity of the dopant affects the lattice parameter and thus the strain in these same regions. Thus, variation in the thickness and identity of heterogeneous dopant layers will be studied. Third, CZO-based multilayers where strain can be finely tuned will be expanded to look at tensile strained YSZ layers.

## Publications

1. W. Shen, J. Jiang, J.L. Hertz, "Using thin films to investigate heterogeneous defect chemistry," *in preparation* [invited]
2. W. Shen, J.L. Hertz, "Conductivity of ceria-zirconia based strained multilayer films," *in preparation*
3. J. Jiang, D. Clark, J.L. Hertz, "The effects of substrate surface structure on yttria stabilized zirconia thin films," *submitted*
4. J. Jiang, X. Hu, N. Ye, J.L. Hertz, "Microstructure and ionic conductivity of yttria-stabilized zirconia thin films deposited on  $\text{MgO}$ ," *submitted*
5. W. Shen, J. Jiang, C. Ni, Z. Voras, T.P. Beebe, J.L. Hertz, "Two-dimensional vacancy trapping in yttria-doped ceria," *submitted*
6. J. Jiang, J.L. Hertz, "On the variability of reported ionic conductivity in nanoscale YSZ thin films," *J. Electroceramics*, (in press) doi:10.1007/s10832-013-9857-1
7. J. Jiang, W. Shen, J.L. Hertz, "Structure and ionic conductivity of nanoscale gadolinia-doped ceria thin films," *Solid State Ionics*, **249-250**, p. 139 (2013)
8. J. Jiang, X. Hu, W. Shen, C. Ni, J.L. Hertz, "Improved ionic conductivity in strained yttria-stabilized zirconia thin films," *Appl. Phys. Lett.*, **102**, 143901 (2013)
9. E. Fischer, W. Shen, J.L. Hertz, "Measurement of the surface exchange and diffusion coefficients of thin film  $\text{LaCoO}_3$  and  $\text{SrCoO}_x$ ," *J. Electroceramics*, **29**, p. 262 (2012)
10. E. Fischer, J.L. Hertz, "Measurability of the diffusion and surface exchange coefficients using isotope exchange with thin film and traditional samples," *Solid State Ionics*, **218**, p. 18 (2012)
11. J. Jiang, W. Shen, J.L. Hertz, "Fabrication of epitaxial zirconia and ceria thin films with arbitrary dopant and host atom composition," *Thin Solid Films*, **522**, p. 66 (2012)

# Science-directed Pursue of the Smallest Metallic Nanorods using Physical Vapor Deposition

Hanchen Huang

Department of Mechanical and Industrial Engineering  
Northeastern University, Boston, MA 02115

## Program Scope

In growing nanorods, one characteristic length scale is their diameter. This length scale depends on diffusion rates of atoms and on the dynamics of surface steps, among others. In turn, this length scale dictates how small nanorods can be, but does not guarantee such small nanorods will be grown. Another length scale is the separation between neighboring nanorods. If the separation is smaller than the diameter, even if both are small, no nanorods can exist with clear separation; continuous film will then develop.

This project focuses on the theoretical formulation of the characteristic length scales, taking insights from atomistic simulations and physical vapor deposition (PVD) experiments, and relying on PVD experiments for validation. Among all the factors, the atomic diffusion rate over surface steps is the most critical. Based on our earlier studies [1, 2], the atomic diffusion rates over monolayer surface steps and those over multiple-layer surface steps are very different. However, the latter will be meaningful only if the multiple-layer surface steps are kinetically stable. In contrast to the classical theory of Schwoebel and Shipsey [3], which states that the multiple-layer surface steps are not kinetically stable, our recent studies [4] have revealed a positive feedback mechanism that kinetically stabilize multiple-layer surface steps. With the stability established, the remaining questions are how monolayer surface steps cluster and how multiple-layer surface steps dissociate. The competition of clustering and dissociation will dictate the characteristic length scales.

## Recent Progresses

Most relevant to this presentation are three progresses: a closed-form theory of nanorod separation on a homogenous substrate, a closed-form theory of the smallest diameter of nanorods, and a new technology of metallic sealing that has direct benefit to the lifetime of organic solar cells.

In the first progress [5], we derived a closed-form theory of nanorod separation, shown as the blue line in Figure 1. In order to achieve the closed-form theory, several idealized assumptions have to be made in terms of nucleation processes on a substrate. The accompanying Monte Carlo simulations, which do not make these assumptions, verify that these assumptions are valid. In contrast, previous approximations – the lattice approximation and the mean field approximation – are slightly off when compared with the Monte Carlo simulation results. The most important progress here is not the slightly better accuracy of our closed-form theory than the approximations. Rather, the most important progress is the closed-form nature of the new theory. The closed-form theory clearly states how the separation  $L_S$  depends on processing conditions – it scales with  $(\nu/F)^{1/6}$ ; here, the adatom diffusion rate  $\nu$  depends on material type and substrate temperature, and  $F$  is the deposition rate. This explicit expression of dependence will be useful in guiding the design of nanorods, as we will show later in this abstract.

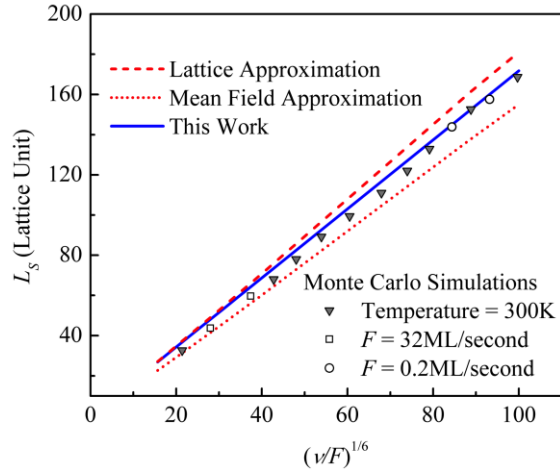


Figure 1: Separation of nanorods  $L_s$  as a function of diffusion rate on substrate  $\nu$  and deposition rate  $F$ .

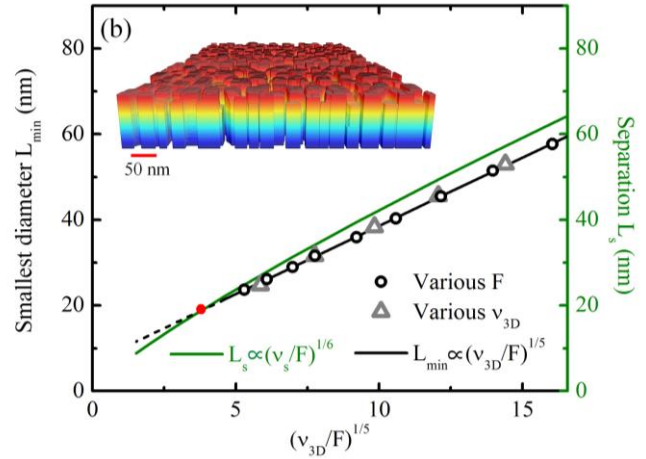


Figure 2: Smallest diameter of nanorods  $L_{min}$  as a function of diffusion rate over multiple-layer surface steps  $\nu_{3D}$  and deposition rate  $F$ .

In the second progress [6], we derived a closed-form theory of the smallest diameter of nanorods. Conceptually, when the top surface of a nanorod is completely bounded by multiple-layer surface steps, the adatom diffusion rate over multiple-layer surface steps  $\nu_{3D}$ , which is slow, dominates. As shown in Figure 2, the smallest diameter scales with  $(\nu_{3D}/F)^{1/5}$ . The accompanying Monte Carlo simulations verify that the closed-form theory is based on realistic assumptions. As substrate temperature and deposition rate change, the two length scales – the separation and the smallest diameter of nanorods – change at different rates. As a result, they cross at a diameter of about 20 nm (for Cu nanorods); Figure 2. The implication is that increasing deposition rate or decreasing temperature will not lead to Cu nanorods that are below 20 nm in diameter, because the separation will be smaller than the diameter. Indeed, this crossing agrees with our experiments [7]; in this case, the theory comes after the experiments, and it provides an explanation instead of prediction.

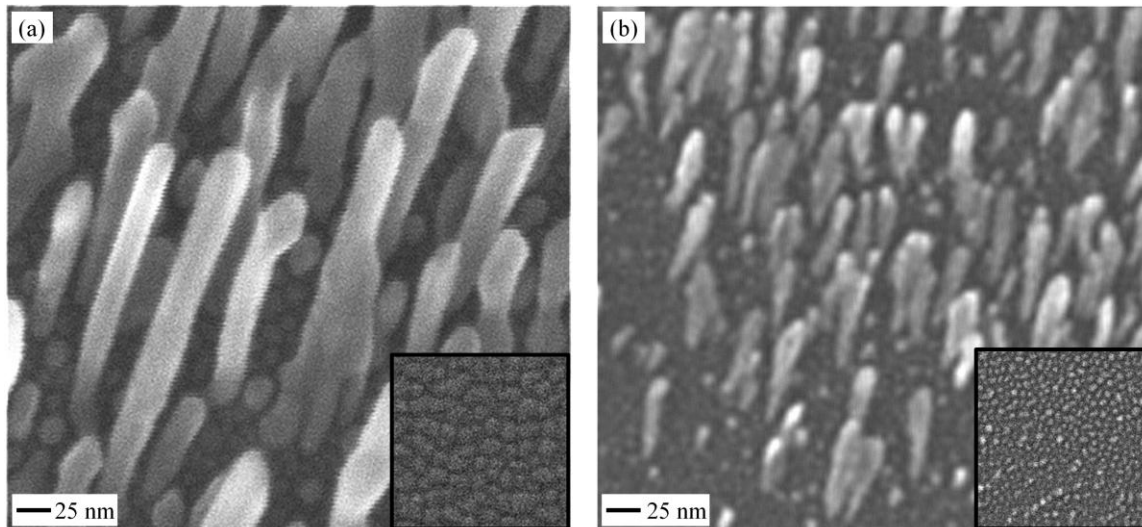


Figure 3: Smallest well-separated nanorods of (a) Cu and (b) Au.

What comes next is a prediction. Based on the closed form theories, we can design to reduce the diameter, for example, by using materials that have smaller  $v_{3D}$  (or larger diffusion barrier); and to increase the separation, for example, by using substrates that are more non-wetting (or larger  $v$ ). Figure 3 shows two such cases of the smallest well-separated Cu and Au nanorods that have ever been achieved using PVD [6].

The third progress [8] takes the results of basic energy science to energy technology. In organic solar cells, one of the primary limiting factors is their degradation due to leakage of water moisture and oxygen; as shown in Figure 4. The polymer-based sealing may block such leakage at the start of operation but degrades fast under sunshine. Metallic sealing would not degrade under the sunshine, but it would require either high temperature or/and high pressure to seal anything with metals. However, when two substrates are decorated with small well-separated nanorods and are brought together, they can easily crosslink. The fast surface diffusion then leads to bridging of the crosslinked nanorods into a continuous film. Our experiments show that the Ag seal forms at room temperature, in air, and under a small pressure of 10 MPa; that is, the condition involves ambient environment only and causes no damage to other components of the solar cells. This Ag seal has a leak rate that is 1000X lower than that of polymer-based seal; and the Ag seal is not expected to degrade under the sunshine.

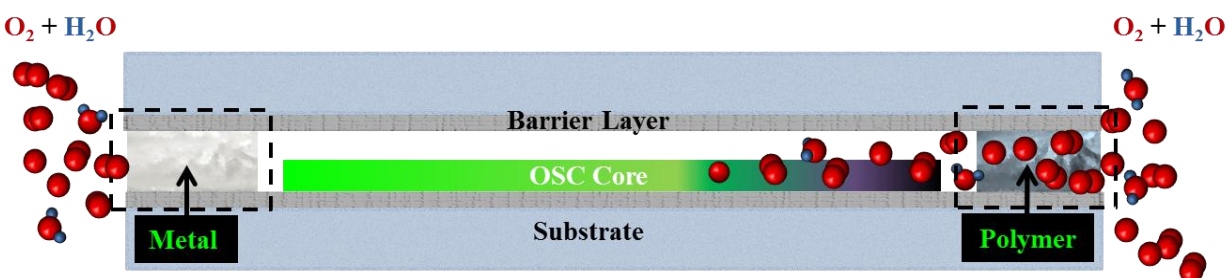


Figure 4: Schematic of metallic sealing vs polymer-based sealing for organic solar cells (OSCs).

### Future Plan

Having established closed-form theories of the smallest diameter and the separation of nanorods, we plan to focus on the dynamics of surface steps. Specifically, we will formulate how multiple-layer surface steps dissociate and how monolayer surface steps cluster. The competition of the two processes will define a length scale that is between the smallest diameter and grain size of thin film. This formulation will rely on insights from atomistic simulations and experiments, and on experiments for validation; as in the previous work. Further, based on the theory of step dynamics (as it is developed), we will also explore mechanisms of controlling the dynamics and thereby controlling the nanorod diameter (and possibly crystal orientations).

### References:

1. S. J. Liu, Hanchen Huang, and C. H. Woo, "Schwoebel-Ehrlich Barrier: From Two to Three Dimensions", **Applied Physics Letters** 80, 3295-3297 (2002).
2. M.G. Lagally and Z.Y. Zhang, "Materials science - Thin-film cliffhanger", **Nature** 417, 907-910 (2002).
3. R. Schwoebel and E. Shipsey, "Step Motion on Crystal Surfaces", **Journal of Applied Physics** 37, 3682-3686 (1966).
4. R. X. Zhang and Hanchen Huang, "Another Kinetic Mechanism of Stabilizing Multiple-layer Surface Steps", **Applied Physics Letters** 98, 221903 (2011).

5. L. G. Zhou and Hanchen Huang, "Critical Separation of Nuclei During Physical Vapor Deposition", **Applied Physics Letters** 100, 141605 (2012).
6. X. B. Niu, S. P. Stagon, Hanchen Huang, J. Kevin Baldwin, and Amit Misra, "Smallest Metallic Nanorods Using Physical Vapor Deposition", **Physical Review Letters** 110, 136102 (2013).
7. Stephen P. Stagon, Hanchen Huang, J. K. Baldwin, and Amit Misra, "Anomaly of Film Porosity Dependence on Deposition Rate", **Applied Physics Letters** 100, 61601 (2012).
8. S. P. Stagon and Hanchen Huang, "Airtight Metallic Sealing at Room Temperature under Small Mechanical Pressure", **Nature Scientific Reports** (2013) under review, and available at <http://arxiv.org/abs/1308.0359>.

**DoE Sponsored Publications in the Last Two Years (2012 and 2013):**

1. S. P. Stagon and Hanchen Huang, "Airtight Metallic Sealing at Room Temperature under Small Mechanical Pressure", **Nature Scientific Reports** (2013) under review, and available at <http://arxiv.org/abs/1308.0359>.
2. X. B. Niu, S. P. Stagon, Hanchen Huang, J. Kevin Baldwin, and Amit Misra, "Smallest Metallic Nanorods Using Physical Vapor Deposition", **Physical Review Letters** 110, 136102 (2013); this paper has been chosen as "Editors' Suggestion", highlighted at the front page of <http://prl.aps.org/>, and highlighted as "Synopsis in Physics" at <http://physics.aps.org/synopsis-for/10.1103/PhysRevLett.110.136102>; and featured on UConn Today (<http://today.uconn.edu/blog/2013/05/uconn-researchers-develop-some-of-the-worlds-smallest-metallic-nanorods/>).
3. S. P. Stagon and Hanchen Huang, "Synthesis and Applications of Small Metallic Nanorods from Solution and Physical Vapor Deposition", **Nanotechnology Reviews** 2, 259-267 (2013).
4. L. G. Zhou and Hanchen Huang, "Controversy over Elastic Constants Based on Interatomic Potentials", **Journal of Engineering Materials and Technology – ASME Transaction** 135, 11010 (2013).
5. L. G. Zhou and Hanchen Huang, "A Response Embedded Atom Method of Interatomic Potentials", **Physical Review B** 87, 45431 (2013).
6. L. G. Zhou and Hanchen Huang, "Critical Separation of Nuclei During Physical Vapor Deposition", **Applied Physics Letters** 100, 141605 (2012).
7. Stephen P. Stagon, Hanchen Huang, J. K. Baldwin, and Amit Misra, "Anomaly of Film Porosity Dependence on Deposition Rate", **Applied Physics Letters** 100, 61601 (2012).
8. Y. F. Zhang and Hanchen Huang, "Design of Twin Structures in SiC Nanowires", **Journal of Computational and Theoretical Nanoscience** 9, 1975-1979 (2012).
9. Hanchen Huang, "A Framework of Growing Crystalline Nanorods", **JOM** 64, 1253-1257 (2012).

# Laser Fabrication of Active Single-crystal Architecture in Glass

H. Jain, V. Dierolf\*, D. Savytsky, P. Gupta, B. Knorr\*<sup>†</sup>

Department of Materials Science and Engineering, Lehigh University, Bethlehem, PA 18015

\*Department of Physics, Lehigh University, Bethlehem, PA 18015

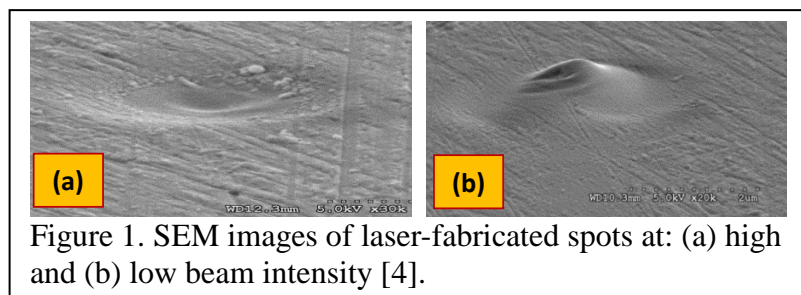
## Program Scope

Nonequilibrium synthesis and processing with energetic particle and photon beams offer new ways to create materials and devices that are not currently possible with established techniques. This project explores a path in this direction, specifically the fabrication of single-crystal architecture in an infrared (IR) transparent glass by a laser beam. Its goal is to develop the enabling science for the formation of active, ferroelectric (single) crystal-in-glass architecture (FCGA), leading to a new class of IR metamaterials that combine exceptional electrical + mechanical + optical functionalities of ferroelectrics (FE) with the robustness, easy formability and low cost of glass. They would provide multiple novel functionalities for micro/nano-opto-electro-mechanical system (M/NOEMS) transducers, sensors; electrically addressable nonlinear waveguides; optical modulators; etc.

The project is focusing on laser-induced single crystal formation in appropriate chalcogenide glasses (ChG), which are IR transparent and devitrify normally to form ferroelectric crystallites. It is building on our proof-of-concept for making FCGAs in a model oxide glass. Sb-S-I glass system is selected as a model of ChG, as it comprises crystals like SbSI and Sb<sub>2</sub>S<sub>3</sub> with excellent potential for energy applications. Upon sufficient understanding of the laser-crystallization process with a continuous wave (CW) laser, in the next step we may exploit femtosecond (fs) laser radiation that can facilitate fabrication in 3D. The special issues of laser-induced fabrication to be addressed include: (a) The controlled single crystal growth by CW (or fs) laser under glass→paraelectric→ferroelectric transformation in a relatively soft ChG, (b) Laser-induced changes in ChG that is usually made of components with very different vapor pressures. (c) The relationship between growth conditions and crystal/domain orientation, and (d) The impact of various photoinduced phenomena (such as photofluidity, photodarkening, photoexpansion, etc.), which are special characteristics of ChG, on its crystal growth process. The mechanism of single crystal growth by laser irradiation is being investigated as a function of laser characteristics with supporting structural information from electron microscopy (especially EBSD), EXAFS, micro-XRD, and micro-Raman spectroscopy. Also the FE state of confined crystals and crystal order at micron and nanometer scales are characterized by novel spectroscopic techniques pioneered in our labs.

## Recent Progress

We have prepared a series of Sb-S-I bulk glasses and established stages of their modification by CW laser: decomposition/ ablation (Fig. 1a),



<sup>†</sup> BK, who helped with the laser irradiation facility, is supported by NSF.

photoexpansion (Fig. 1b) and crystallization (Fig. 2). Laser writing in chalcogenide glasses is found to be inherently more complicated than in oxide glasses due to preferential evaporation and oxidation (if performed in air). For example, we find physical contraction and chemical changes under irradiation with a 488 nm CW Ar<sup>+</sup> laser due to thermal runaway. The wavelength of the laser is well above the bandgap of the SbSI glass and is thus absorbed readily by thin surface layer (several hundred nanometers) of the glass sample. The quasi-eutectic structure of Sb-S-I glasses facilitates decomposition of weak molecular bonds between SbS<sub>3</sub> and SbI<sub>3</sub> eutectic elements and further evaporation of SbI<sub>3</sub> molecules from sample surface under the action of laser beam. The evaporation of this iodine rich phase enriches the remaining supercooled liquid Sb<sub>2</sub>S<sub>3</sub>, which together with volume changes (contraction due to the SbI<sub>3</sub> evaporation) complicates surface crystallization of SbSI phase [1-4].

Notwithstanding the multiple challenges, active ferroelectric SbSI single crystal lines were fabricated by a novel three-stage process as demonstrated by EBSD scan in Fig. 2. To begin, the polycrystalline line was created by translating the laser spot across a previously fabricated line on the surface glass. During this process, a line with few crystal grains was produced. Next, the sample was scanned in a direction perpendicular to the initial “polycrystalline” line, which led to the growth of a single crystal from one of the seed crystals formed earlier. The reason for using seed lines instead of spots is that after a certain distance the process reaches equilibrium and the remainder of the line becomes homogeneous in composition and morphology, thereby providing reproducible nucleation sites for subsequent growth of crystal lines [2].

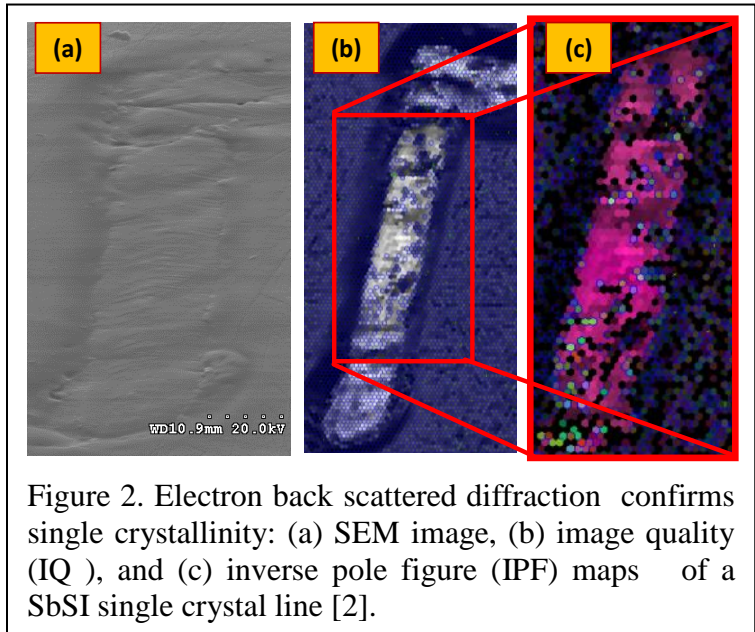


Figure 2. Electron back scattered diffraction confirms single crystallinity: (a) SEM image, (b) image quality (IQ), and (c) inverse pole figure (IPF) maps of a SbSI single crystal line [2].

Very small laser power (0.5-5 mW) is required to induce crystallization in Sb-S-I glasses because of their low crystallization temperature. The control of laser power at these low levels has been difficult with the Ar<sup>+</sup> laser high power laser. The fluctuations in intensity have been a major source of problems in making reproducible structures [1, 2]. Therefore, we have switched to a more stable, low power, energy efficient diode laser instead of the Ar<sup>+</sup> laser. In addition to stability, a diode laser is providing much more precise electrical control of the output power compared to the manual control for the Ar<sup>+</sup> laser.

Surface heating of the SbSI stoichiometric glass induced by a 520 nm CW semiconductor diode laser shows two contracted regions: needle-like crystalline formations at low temperature and bulk crystallization at high temperature. The analysis of observed phenomena and differential calorimetry (DSC) results (Fig. 3) suggest two different kinds of crystallization of the SbSI phase: one-dimensional crystallization at low temperature which starts from the sample surface, and three-dimensional bulk crystallization that continues the transformation to crystalline state at higher temperatures. The origin of the two different crystallizations can be

traced to the strong anisotropy of the SbSI crystal structure due to the weak Van der Waals interaction between covalent-ionic chains  $(\text{Sb}_2\text{S}_2\text{I}_2)_n$  [5].

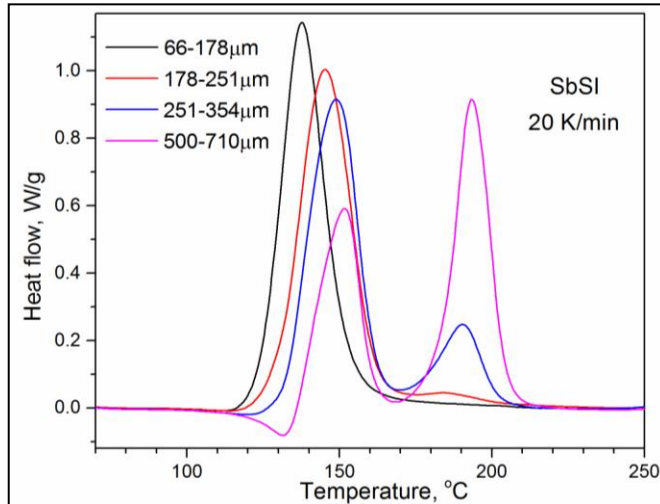


Figure 3. DSC data for different size particles of the SbSI glass with heating rate 20°/min.

Laser writing by 520 nm diode laser beam of circular cross-section was used also on off-stoichiometric  $82\text{SbSI}-18\text{Sb}_2\text{S}_3$  chalcogenide glass to produce crystalline architecture on the sample surface. It was found that  $\text{Sb}_2\text{S}_3$  single crystal spots with elliptic cross-section were produced with the  $\langle 001 \rangle$  direction parallel to major axis of the ellipse and surface of glass matrix (Fig.4). The crystallized lines of  $\text{Sb}_2\text{S}_3$  grew in the same  $\langle 001 \rangle$  orientation with respect to the laser scanning direction. An explosive change in line morphology was observed within such lines during the writing process. Its cause was identified to be the oxidation of  $\text{Sb}_2\text{S}_3$  crystalline phase, which releases huge amounts of reaction

energy (similar to commercial fireworks based on  $\text{Sb}_2\text{S}_3$ ). The oxidation of the laser-induced  $\text{Sb}_2\text{S}_3$  crystals can be eliminated by flow of nitrogen gas over the laser-illuminated zone.

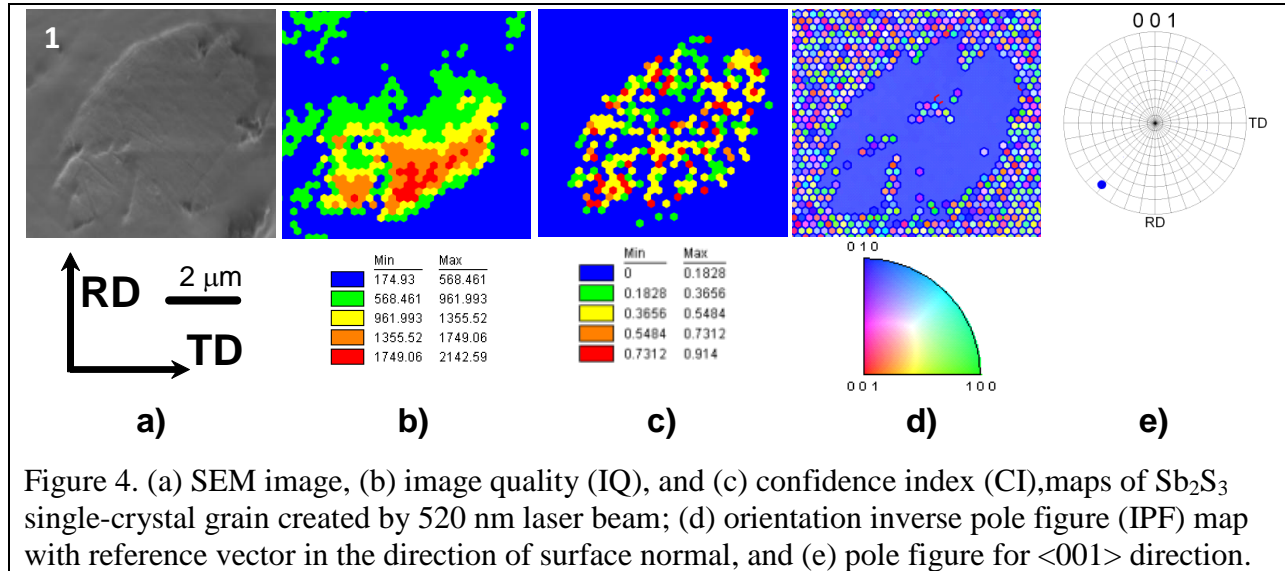


Figure 4. (a) SEM image, (b) image quality (IQ), and (c) confidence index (CI), maps of  $\text{Sb}_2\text{S}_3$  single-crystal grain created by 520 nm laser beam; (d) orientation inverse pole figure (IPF) map with reference vector in the direction of surface normal, and (e) pole figure for  $\langle 001 \rangle$  direction.

The discovery of laser-induced shrinkage and expansion in combination with crystallization of SbSI as well as  $\text{Sb}_2\text{S}_3$  ferroelectric phases has opened a way to produce and integrate different types of passive (optical waveguides, Bragg gratings, microlenses, lens arrays) as well as active (electro-optic modulators, wavelength convertors) micro-optical elements in the same glass substrate using appropriate laser irradiation.

### Future Plans for the Current Year

The quasi-eutectic structure of Sb-S-I glasses facilitates decomposition of weak molecular bonds between  $\text{SbS}_3$  and  $\text{SbI}_3$  eutectic structural units, and preferential evaporation of

SbI<sub>3</sub> molecules from sample surface under the action of laser beam. The evaporation SbI<sub>3</sub> enriches the glass in Sb<sub>2</sub>S<sub>3</sub> phase. We plan to establish an optimal chemical composition of the starting glass, which would account for the evaporation and thereby allow the formation of SbSI/Sb<sub>2</sub>S<sub>3</sub> ferroelectric crystals upon laser irradiation. Alternatively, the thermal runaway evaporation of SbI<sub>3</sub> can be reduced also by choosing the laser beam of longer wavelengths (for example, 637 nm) with lower absorption and correspondingly deeper penetration in the glass. As a result, we hope to identify conditions for forming SbSI crystals more reproducibly.

During current experiments, crystallization starts below the surface of the glass, which makes the characterization of such crystals by EBSD impossible. So we need to expose the crystal formed under the surface by careful polishing/sputtering, and then perform EBSD analysis of the exposed crystal architecture. It will be a challenge to remove the top glass layer without affecting the structure of underlying crystalline region. To circumvent this problem, we plan to conduct scanning X-ray microdiffraction (microSXRD) experiments at BL 12.3.2. beamline of Advanced Light Source (ALS), Lawrence Berkeley National Laboratory (LBNL), which appears suitable for characterizing the crystallinity of laser written lines. In contrast to EBSD, which we have exploited extensively so far, the ultra-brilliant X-ray beam is able to penetrate materials to a distance greater than one hundred microns. We will be interested also in developing a faster alternative to microdiffraction for characterizing the crystal line such as micro-Raman spectroscopy.

### Publications and Patents

1. P. Gupta, A. Stone, N. Woodward, V. Dierolf, H. Jain, "Laser fabrication of semiconducting ferroelectric single crystal SbSI features on chalcogenide glass", *Optical Materials Express* **1** (2011) 652-657. Published online: <http://dx.doi.org/10.1364/OME.1.000652>
2. D.Savytskii, B. Knorr, V. Dierolf, H. Jain, "Formation of Laser-induced SbSI Single Crystal Architecture in Sb-S-I Glasses" *J. Non-Cryst. Solids* **377** (2013) 245-249. Published online: <http://dx.doi.org/10.1016/j.jnoncrysol.2013.01.018>
3. R. Golovchak, L. Calvez, E. Petracovschi, B. Bureau, D. Savytskii, H. Jain, "Incorporation of Ga into the structure of Ge-Se glasses", *Materials Chemistry and Physics* **138** (2013) 909-916. Published online: <http://dx.doi.org/10.1016/j.matchemphys.2012.12.084>
4. D. Savytskii, B. Knorr, V. Dierolf, and H. Jain "Challenges of CW laser-induced crystallization in a chalcogenide glass" *Optical Materials Express*, **3** (2013) 1026-1038. Published online: <http://dx.doi.org/10.1364/OME.3.001026>
5. D. Savytskii, M. Sanders, R. Golovchak, B. Knorr, V. Dierolf, and H. Jain "Crystallization of stoichiometric SbSI glass", Submitted to *Journal of the American Ceramic Society*.
6. *U.S. Provisional Patent Application: Method to Write High-Resolution Single Crystal Architecture on Glass Using Electron Beam*. Inventors: P. Gupta, J. Poplawsky, H. Jain and V. Dierolf, Application No: 61/552,780, October 28, 2011.

# Development and Understanding of Multifunctional Nanostructured Magnetolectric and Spintronic Materials

R.S. Katiyar<sup>1</sup>, M. Gomez<sup>1</sup>, G. Morell<sup>1</sup>, L. Fonseca<sup>1</sup>, Y. Ishikawa<sup>1</sup>, R. Palai<sup>1</sup>,  
R. Thomas<sup>1</sup>, A. Kumar<sup>1</sup>, J. Velev<sup>1</sup>, V. Makrov<sup>1</sup>, O. Peralas<sup>2</sup>, M.S. Tomar<sup>2</sup>, W. Otaño<sup>3</sup>.  
University of Puerto Rico, Rio Piedras<sup>1</sup>, Mayaguez<sup>2</sup>, Cayey<sup>3</sup>

## Program Scope

Magnetolectric (ME) multiferroics and spintronics combine standard microelectronics with spin-dependent effects that arise from interactions between electrons and magnetic field. The spin dependent phenomena become challenging at the nanoscale where new physical effects emerge affecting the spin injection, transport, and switching times. The goals of this project are to develop CMOS compatible multifunctional materials to meet the near future demand of miniaturization of Si based technology and for the next generation technology beyond Si. For this advancement, however, a fundamental understanding of science is needed to develop materials, e.g. high-k gate oxides (for 22 nm node technology and beyond), ME multiferroics, and dilute magnetic semiconductors (DMS) materials at room temperature. Such materials have the potential to form the basis of a new generation of energy efficient nanoscale electronic devices that are fast responding, have low power consumption, and high integration density.

The aim of this research is the synthesis and characterization of various functional oxides and silicides to accomplish the above goal. We have studied different systems, namely, i) spintronic nanostructures we have synthesized thin film of: Co, V-doped ZnO, rare earth (Er and Yb) doped GaN,  $\text{Fe}_x\text{Co}_y\text{Si}$  nanowires (NWs) by CVD and ion implantation; ii) resistive switching phenomenon in Oxides for Memory Devices (high-k gate oxide:  $\text{LaGdO}_3$ , and  $\text{Bi}_{1-x}\text{Sm}_x\text{FeO}_3$ ); iii) Magnetolectric Multiferroics: Pb based Perovskite single phase magnetolectric multiferroic (ME-MF) solid solutions: We have reported extensive studies on  $\text{Pb}(\text{Fe},\text{M})_x(\text{Zr},\text{Ti})_{1-x}\text{O}_3$  [M=Ta, Nb] and pure & doped  $\text{BiFeO}_3$ ; iv) Composites and Heterostructures: PFN-NZFO composites, Tunnel Electroresistance effect in Pt/PZT/LSMO junctions, PZT/LSMO superlattices, v) Novel High-k gate oxide for Logic Devices:  $\text{LaGdO}_3$  (LGD); vi) Theoretical Studies: Elect- Bias dependence of tunneling magnetoresistance (TMR) in  $\text{Co}/\text{Al}_2\text{O}_3$  granular multilayers, formation and properties of the two-dimensional electron gas (2DEG) at  $\text{ZnO}/\text{Zn}(\text{Mg})\text{O}$  (0001) interfaces.

## Recent Progress

**Resistive switching (RS) in High-k gate oxide,  $\text{LaGdO}_3$  (LGD):** The unipolar RS properties of the amorphous LGO thin films deposited by pulsed laser deposition (PLD) have been investigated. The Pt/LGO/Pt MIM stack geometry required a forming voltage of  $\sim 7\text{V}$  to initiate the switching process. After forming process reliable and repeatable nonvolatile switching of the resistance of these devices was obtained between two well defined states of low/high resistance (LR/HR) with nearly constant resistance ratio of  $\sim 10^6$  and non-overlapping switching voltages in the range of  $\sim 0.6\text{-}0.75\text{ V}$  and  $2.5\text{-}4\text{ V}$  respectively. The current conduction mechanism of the device in LR/HR states were found to be dominated by the Ohmic behavior and Poole-Frenkel emission respectively.

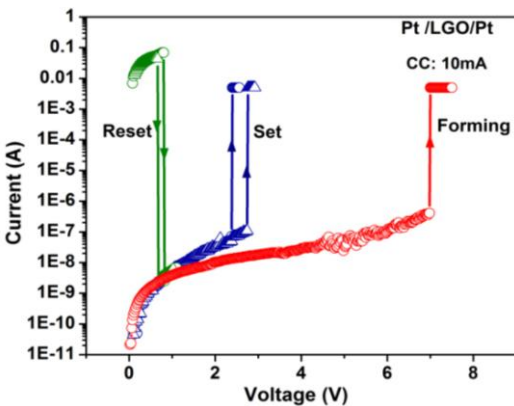


**Fig. 1:** Resistive Switching behavior of LR/HR states of the film showed no obvious degradation for up to  $\sim 12$  hours indicating good retention. The switching between LR/HR states was attributed to formation and rupture of conductive filaments.

**Pb based Perovskite single phase magnetoelectric multiferroic (ME-MF) solid solutions:** Studies on  $\text{Pb}(\text{Fe},\text{M})_x(\text{Zr},\text{Ti})_{1-x}\text{O}_3$  [ $\text{M}=\text{Ta},\text{Nb}$ ] family of perovskite oxides that are ferroelectric (FE) as well as ferromagnetic (FM) and show magnetoelectric properties at ambient temperatures.  $\text{Pb}(\text{Fe}_{0.5}\text{Nb}_{0.5})_x(\text{Zr}_{0.53}\text{Ti}_{0.47})_{(1-x)}\text{O}_3$  (PFN<sub>x</sub>-PZT<sub>(1-x)</sub>) and  $\text{Pb}(\text{Fe}_{0.5}\text{Ta}_{0.5})_y(\text{Zr}_{0.53}\text{Ti}_{0.47})_{(1-y)}\text{O}_3$  (PFT<sub>y</sub>-PZT<sub>(1-y)</sub>) ( $0.1 \leq x, y \leq 0.4$ ), were synthesized in both ceramic and thin films by conventional solid state reaction route and PLD technique respectively. PFT-PZT ceramic samples exhibited ME-MF properties: saturated FE loop with  $P_r \sim 10\text{--}20 \mu\text{C}/\text{cm}^2$ , well defined FM loop with saturation magnetization of about  $0.02\text{--}0.06 \text{ emu}/\text{gr}$ , and the ME effect with  $\alpha = \mu_0 \Delta M / \Delta E = 1.3 \times 10^{-11} \text{ S}/\text{m}$ . Single phase highly oriented thin films of PFT<sub>x</sub>-PZT<sub>(1-x)</sub> were grown on  $\text{La}_{0.67}\text{Sr}_{0.33}\text{CoO}_3$  coated oriented MgO substrates. The films showed MF properties with well saturated FE hysteresis having  $P_r \sim 43\text{--}48 \mu\text{C}/\text{cm}^2$  and magnetization saturation value as  $M_s \sim 6\text{--}17 \text{ emu}/\text{cm}^3$ .

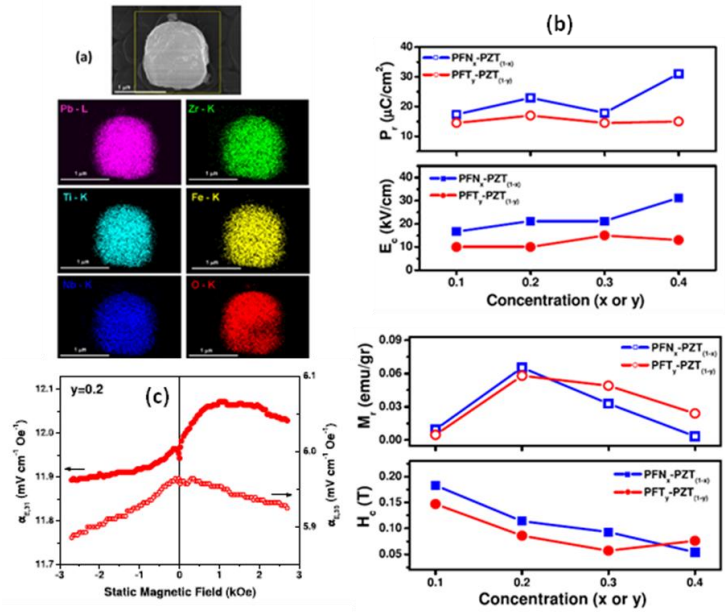


**Fig. 2.** (a) SEM image for  $\sim 1 \mu\text{m}$  grain of PFN<sub>x</sub>-PZT<sub>(1-x)</sub> ( $x = 0.2$ ) with the respective elemental concentration maps. (b) Remanent polarization/magnetization and the respective electric/magnetic coercive field (upper/lower) for PFN<sub>x</sub>-PZT<sub>(1-x)</sub> and PFT<sub>y</sub>-PZT<sub>(1-y)</sub> as a function of the concentration ( $x$  or  $y$ ). ME coefficient as a function of the bias magnetic field in longitudinal ( $\alpha_{E,33}$ ) and transverse ( $\alpha_{E,31}$ ) modes for PFT-PZT ( $y=0.2$ ) at 1 kHz at RT.

**Tunnel Electroresistance effect in Ferroelectric Tunnel Junction in structures with ultrathin ferroelectric  $\text{PbZr}_{0.52}\text{Ti}_{0.48}\text{O}_3$  (PZT) barrier:** We have studied thickness effect of FE PZT films with thickness from 7 to 3 nm on  $\text{La}_{0.67}\text{Sr}_{0.33}\text{MnO}_3$ (LSMO)/ $(\text{LaAlO}_3)_{0.3}(\text{Sr}_2\text{AlTaO}_6)_{0.7}$ (LSAT) (001) substrates deposited by pulsed laser deposition technique. The x-ray diffraction analysis revealed that the PZT and LSMO films were well oriented (001) perovskite structures. Piezo force microscopy (PFM) shows phase and amplitude loop and a clear and reversible out-of-plane phase contrast, above  $\pm 2.5 \text{ V}$  that indicates the FE character of PZT/LSMO films (Fig. 3(a) and its inset). Tunneling conductance mechanism was observed in parabolic behavior of conductance vs. voltage curve obtained from Current-Voltage measures (Fig 3(b)). Switching from low resistance state (LRS) to high resistance state (HRS) and vice versa by sweeping the voltage from negative to positive and back, at zero bias show HRS/LRS was  $\sim 100$ . These junctions demonstrate highly reproducible resistance switching which happens above  $+2.5\text{V}$ , not switching was observed below this voltage. These results indicate resistance switching observed in IV can be due to ferroelectric nature of the barrier (Fig 3(c)).

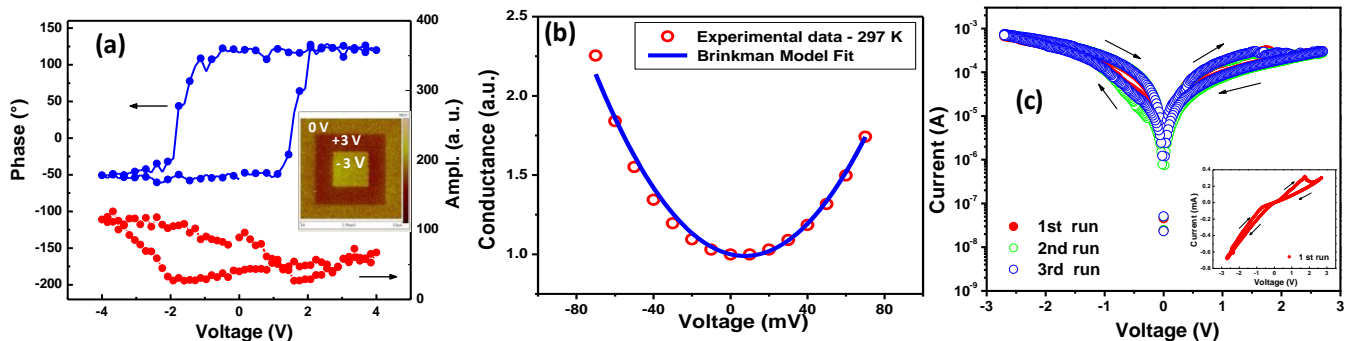


**Fig. 3.** PZT-5nm/LSMO-30nm: (a) PFM shows a clear and reversible out-of-plane phase contrast at 3 V that indicates the FE character of PZT/LSMO films (b) The  $G(V) = dI/dV$  curve show parabola-like behavior, as expected for transport dominating direct tunneling. (b) This junction demonstrates highly reproducible resistance switching which happens at about  $+2.5\text{V}$ .

**Advanced high-k gate dielectric amorphous LaGdO<sub>3</sub> gated metal-oxide-semiconductor devices:** Careful selection of PLD conditions was executed to achieve sub-nanometer EOT (equivalent oxide thickness) in amorphous LGD based high-k/metal gate stacks. The lowest EOTs attained were  $\sim 5.4$  Å and  $8.4$  Å with and without quantum mechanical correction, respectively. The electrical measurements yielded a high permittivity of  $20.56 \pm 2.4$ , a thin bottom interfacial layer of thickness  $4.561$  Å, and interface ( $\text{cm}^{-2} \text{eV}^{-1}$ ) and fixed ( $\text{cm}^{-2}$ ) charge densities of  $\sim 10^{12}$ . Analysis of temperature dependent leakage currents revealed that gate injection current was dominated by Schottky emission below  $1.2$  MV/cm and quantum mechanical tunneling above this field. The physical origin of substrate injection was found to be a combination of Schottky emission and trap assisted tunneling

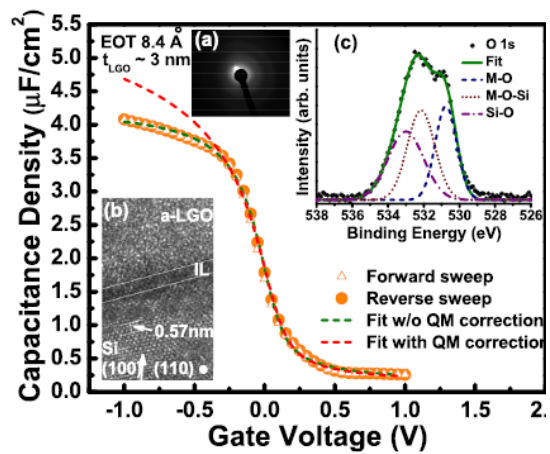


**Fig 4.** *C-V characteristics of Pt/LGO/p-Si n-MOS devices measured at 100 kHz including its Hauser fit with and without quantum mechanical correction (a) SAED image of a-LGO. (b) Cross-sectional TEM images of LGO thin film fabricated at 300 °C. (c) Ex-situ O1s XPS peak from  $\sim 8$  nm thick LGO layer on Si after Ar+ sputtering etches.*

## Future Plans

We will continue working on the synthesis and characterization of single phase materials and heterostructures suitable for spintronics and multiferroic applications. A few proposed studies in this area are: **(1)** synthesis of multiferroic tunnel junction (MF-TJ) using PLD deposition technique, i.e.  $\text{Pb}(\text{ZrTi})\text{O}-\text{Pb}(\text{Fe,Ta})\text{O}_3$  (PZTFT)/ $\text{La}_{2/3}\text{Sr}_{1/3}\text{MnO}_3$  (LSMO), with PZTFT thickness  $\sim 2-7$  nm on (001) LSAT:  $(\text{LaAlO}_3)_{0.3}(\text{Sr}_2\text{AlTaO}_6)_{0.7}$ . We plan the characterization of the electron transport properties of F/MF-TJ, such as current-voltage characteristic, temperature dependencies of conductance, and tunnel electroresistance, magnetoresistance properties, in collaboration of Nebraska University. **(2)** We will be focused on growth and characterization of Yb and Er doped InGaN thin films and fabrication and testing of MTJ using RE-doped III-Nitrides. We also use X-ray magnetic circular dichroism (XMCD), X-ray absorption fine structure (EXAFS), and X-ray near edge spectroscopy (XANES) in collaboration with Brookhaven Nation Laboratory (BNL) for the better understanding of origin of magnetic properties and atom specific magnetic properties. **(3)** Related to theoretical work, we will further pursue the work on dilute magnetic semiconductors, including investigating the effect of rare-earth doping on the electronic structure of ZnO and GaN. The work in 2DEGs continues in several directions including an investigation of the formation of polarization-discontinuity 2DEG at GaN/Ga(Al)N interfaces and the formation of spin-polarized 2DEG as  $\text{GaTiO}_3/\text{SrTiO}_3$  interfaces. The work on the MTJs with asymmetric interfaces continues in the direction of investigating the effect of asymmetric barrier modifications on the spin transfer torque (STT).

## DoE Sponsored Publications in the Last Two Years

The number of reviewed scientific publications from our DOE sponsored project (Award #DE-FG02—08ER46526) is 70 in the last two years but in what follows due to space limitation we are reporting only a few most significant ones:

1. Impedance spectroscopy analysis of  $\text{Ba}_{0.7}\text{Sr}_{0.3}\text{TiO}_3/\text{La}_{0.7}\text{Sr}_{0.3}\text{MnO}_3$  heterostructure, R. Martínez, Ashok Kumar, R. Palai, J. F. Scott, and R. S. Katiyar, *J. App. Phys.D*, **44**,105302 (2011).
2. Effect of the periodicity and the composition in artificially  $\text{BaTiO}_3/(\text{Ba,Sr})\text{TiO}_3$  superlattices, N. Ortega, Ashok Kumar, O. A. Maslova, Yu. I. Yuzyuk, J. F. Scott, and R. S. Katiyar, *Phys. Rev. B*, **83** 144108 (2011)
4. Magnetic control of ferroelectric interfaces, S. Dussan, Ashok Kumar, R. S. Katiyar, Shashank Priya, and J. F. Scott, *J. Phys.: Condens. Matter*, **23** 202203 (2011)

14. Photovoltaic effect in a wide-area semiconductor-ferroelectric device, R.K. Katiyar, Ashok Kumar, G. Morell, J.F. Scott, and R.S. Katiyar, *App. Phys. Lett.*, **99**, 092906 (2011)
15. Electric control of magnon, phonon and magnetic moment in BiFeO<sub>3</sub>: direct evidence of magneto-electric coupling, Ashok Kumar, J.F. Scott, and R.S. Katiyar, *App. Phys. Lett.*, **99**, 062504 (2011)
16. Biferroic relaxors, Ashok Kumar, J.F. Scott, and R.S. Katiyar, *App. Phys. Lett.*, **99**, 042907 (2011)
17. Symmetries and multiferroic properties of new room-temperature magnetoelectrics: lead iron tantalate-lead zirconate titanate (PFT/PZT), Dilsom A. Sánchez, N. Ortega, Ashok Kumar, R. Roque-Malherbe, R. Polanco, J. F. Scott, and R. S. Katiyar, *AIP Advances*, **1**, 042169 (2011).
19. Studies of photovoltaic properties of nanocrystalline thin films of CdS-CdTe, Rajesh K. Katiyar, Satyaprakash Sahoo, A.P.S. Gaur, Arun Kumar Singh, G. Morell and R.S. Katiyar, *J. of Alloys and Compounds*, **509** [41], 10003 (2011)
22. Optical properties of amorphous high-k LaGdO<sub>3</sub> films and its band alignment with Si, S. P. Pavunny, R. Thomas, A. Kumar, E. Fachini, and R. S. Katiyar, *Journal of Applied Physics* **111**, 044106 (2012).
25. Dielectric Properties and Electrical conduction of high-k LaGdO<sub>3</sub> Ceramics, S. P. Pavunny, R. Thomas, A. Kumar, N. M. Murari, and R. S. Katiyar, *Journal of Applied Physics*, **111**, 102811 (2012)
36. Observation of strong magnetoelectric effects in Ba<sub>0.7</sub>Sr<sub>0.3</sub>TiO<sub>3</sub>/La<sub>0.7</sub>Sr<sub>0.3</sub>MnO<sub>3</sub> thin film heterostructures, R. Martinez, A. Kumar, R. Palai, G. Srinivasan, and R. S. Katiyar, *J. Appl. Phys.* **111**, 104104 (2012).
38. Structural and magnetic properties of N doped ZnO thin films. Kajal Jindal, Monika Tomar, R. S. Katiyar, and Vinay Gupta. *J. App. Phys* **111**, 102805 (2012).
42. Optical Dielectric Function Modeling and Electronic Band Lineup Estimation of Amorphous High-k LaGdO<sub>3</sub> Films, S. P. Pavunny, R. Thomas, A. Kumar, J. F. Scott, and R. S. Katiyar, *ECS Journal of Solid State Science and Technology* , **1**(4), N53-N57 (2012).
47. Room-Temperature Single Phase Multiferroic Magnetoelectrics: Pb(Fe, M)<sub>x</sub>(Zr,Ti)<sub>(1-x)</sub>O<sub>3</sub> [M = Ta, Nb]. Dilsom A. Sanchez, Nora Ortega, Ashok Kumar, G. Sreenivasulu, Ram S. Katiyar, J. F. Scott, Donald M. Evans, Miryam Arredondo-Arechavala, A. Schilling<sup>5</sup>, and J. M. Gregg. *J. Appl. Phys.* **113**, 074105 (2013).
52. Advanced high-k gate dielectric LaGdO<sub>3</sub> based MOS devices with sub-nanometer equivalent oxide thickness. S. P. Pavunny, P. Misra, R. Thomas, A. Kumar, J. F. Scott and R. S. Katiyar. *Appl. Phys. Lett.* **102**, 192904 (2013).
53. Effect of oxygen on Jahn-Teller distortion and magnetization dynamics in Pr<sub>0.9</sub>Ca<sub>0.1</sub>MnO<sub>3</sub> thin films. S. Majumdar, H. Huhtinen, P. Paturi, and R. Palai. *J. Phys.: Condens. Matter*, **25**, 066005 (2013).
55. Ferromagnetism in Nanocrystalline Powders and Thin Films of Cobalt-Vanadium co-doped Zinc Oxide. Marco Gálvez-Saldaña, Gina Montes-Albino and Oscar Perales-Perez *MRS Proceedings*, 1449 mrss12-1449-bb06-15 (2012). doi:10.1557/opl.2012.794.
57. Study on the Structural, Electrical and Magnetic Properties of Pure and (Pr<sup>3+</sup>, Co<sup>2+</sup>)-Doped BiFeO<sub>3</sub> Powders and Thin Films. Gina Montes Albino, Marco Gálvez-Saldaña and Oscar Perales-Pérez. *Jap. J. Appl. Phys.* **51**, 11PG06-1-4 (2012).
58. Electric-field-induced magnetization changes in Co/Al<sub>2</sub>O<sub>3</sub> granular multilayers. Sahadevan, A. Kalitsov, G. Kalon, C. Bhatia, J. Velev, and H. Yang, , *Phys. Rev. B* **87**, 014425 (2013).
59. On the Resistive Switching and Current Conduction Mechanisms of Amorphous LaGdO<sub>3</sub> Films Grown by Pulsed Laser Deposition, P. Misra, S. P. Pavunny and R. S. Katiyar, *ECS Transactions*, **53** (3) 229-235 (2013).
62. Spin-polarized state quantum filter used to measure spin-polarized state relaxation time and g-factor. Vladimir I. Makarov<sup>1</sup> and Igor Khmelinskii. *J. Appl. Phys.* **113**, 084304 (2013).
65. Temperature-Dependent Raman Studies and Thermal Conductivity of Few-Layer MoS<sub>2</sub>, Satyaprakash Sahoo, Anand P. S. Gaur , Majid Ahmadi , Maxime J.-F. Guinel , and Ram S. Katiyar, *J. Phys. Chem. C* **117**, 9042 (2013).
68. Free standing graphene-diamond hybrid films and their electron emission properties. Varshney, Deepak; Rao, Chitturi Venkateswara; Guinel, Maxime J.-F.; Weiner; Brad R.; Morell, Gerardo; *J. Appl. Phys.* **110**, 044324 (2011),
69. Conformal coating of ferroelectric oxides on carbon nanotubes; F. Mendoza, A. Kumar, R. Martínez, J.F. Scott, B. Weiner, R.S. Katiyar, G. Morell; *European Physics Letters* **97**, 27001, 2012.
70. Multiferroic properties of Bi<sub>4-x</sub>Nd<sub>x</sub>Ti<sub>3</sub>O<sub>12</sub>/CoFe<sub>2</sub>O<sub>4</sub> composite Film. D. Barrionuevo, S.P. Singh, and M.S. Tomar, *Integrated ferroelectrics* **124**, 48-52 (2011).

# Investigating the Metastability of Clathrate Hydrates for Energy Storage

PIs: Carolyn A. Koh and Amadeu K. Sum

Center for Hydrate Research, Chemical & Biological Engineering Department  
Colorado School of Mines, Golden, CO 80401

## Program Scope

Fundamental investigations are being performed on clathrate hydrate materials and the key processes controlling the synthesis, and structure-property relations of clathrate hydrates containing hydrogen, methane, and other guest molecules for energy storage. Molecular level interactions between guest and host molecules in clathrate hydrates are being probed to advance our understanding of clathrate hydrate metastability related to synthesis, structure, and composition of clathrate hydrates. Addressing questions on metastability is pivotal in all energy applications of clathrate hydrates, including energy storage, energy transportation, and energy recovery. Molecular tools, including Raman spectroscopy, powder X-ray diffraction, and molecular dynamics simulations are being applied to investigate clathrate hydrate energy storage materials with respect to: structure/phase metastability, including coexistence/transitions of metastable phases; metastable cage composition/occupancy, including variable cage occupancy and dynamics. The results from these studies are advancing the knowledge of clathrate hydrate formation and decomposition processes in energy storage and other energy applications.

## Recent Progress

### (I) Discovery of Key Clathrate Hydrate Building Blocks

Direct molecular dynamics simulations probing the formation pathways of structure I (sI) CH<sub>4</sub> hydrate [1] have identified metastable (amorphous) clusters and seven common cages [2] during clathrate hydrate nucleation (Fig. 1). In thermodynamically stable sI structures, only two types of cages are observed. Therefore, the appearance of seven cages suggests metastable cage environments may be present during early stages of clathrate hydrate formation. It was discovered that these seven elementary cage types comprise 95% of all cages present in the nucleating trajectories [2]. These new findings open up the possibility that many of these incipient cages could be also present in sII or other clathrate hydrate nucleation trajectories.

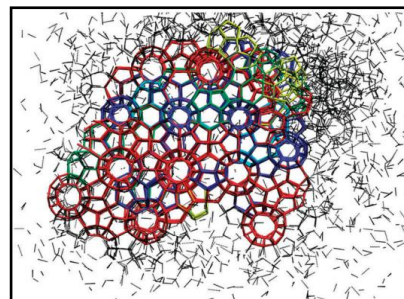
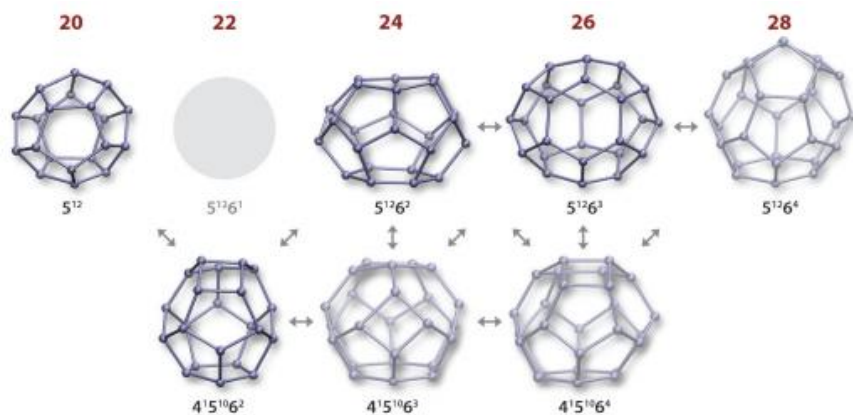


**Figure 1.** Seven dominant cages (left) and amorphous cluster (top) formed during sI clathrate hydrate nucleation<sup>2</sup>

## (II) Discovery of New Metastable Phase Present During Hydrate Structural Transitions

Experiments examining clathrate hydrate structural transition pathways were performed on the structure VI to structure II (sII) transition [3]. It was observed that as sVI clathrate frameworks begin to transition to sII, due to a composition induced change in the equilibrium structure after the addition of  $H_2$  (g), a new intermediate phase [4] was formed prior to the transformation to sII (Fig. 2). The intermediate environment was studied using in-situ and ex-situ Raman spectroscopy and powder X-ray diffraction, and it was found that the spectral width of the intermediate environment ranged from  $\sim 4120$  to  $4182\text{ cm}^{-1}$ , covering  $\sim 62\text{ cm}^{-1}$  (Fig. 3A). The lack of distinct spectral features and relatively large width of the intermediate band compared to the other known structures (Fig. 3B-D) suggests that the metastable intermediate states are likely comprised of many unique environments enclathrating molecular hydrogen. To provide a more detailed characterization of these unique environments quantum mechanical calculations with density functional theory (DFT/B3LYP/6-31++G\*\*) were performed to compute the  $H_2$  Raman shifts of all of the stable cages in structures I, II, and VI. Based upon the  $62\text{ cm}^{-1}$  Raman peak width of this intermediate environment, in-situ Raman and X-ray analysis, DFT calculations, and comparisons to other known clathrate environments, we show that this intermediate  $H_2$  environment is not consistent with any known thermodynamically stable cage type and thus propose we are observing  $H_2$  enclathration into a metastable clathrate-like intermediate phase.

This recent experimental confirmation of metastable intermediate structures could lead to the potential discovery of an entirely new class of clathrate hydrate structures that, if stabilized, may have potential for energy storage and/or other energy applications. Furthermore, on a fundamental level, the isolation of these metastable transition cages exposes new insight into the clathrate hydrate formation pathways and mechanisms. These new experimental findings are closely aligned with our molecular simulation discoveries of metastable cage dynamics occurring during clathrate hydrate nucleation and growth [2].

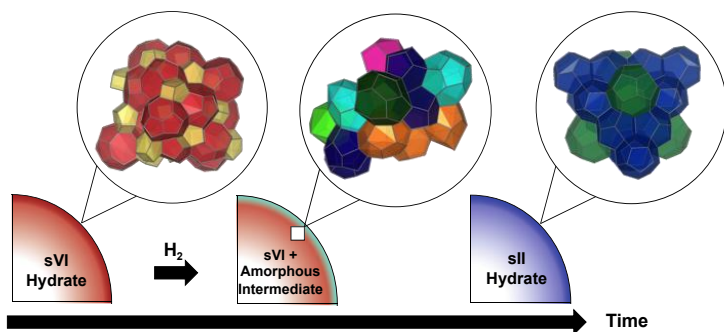
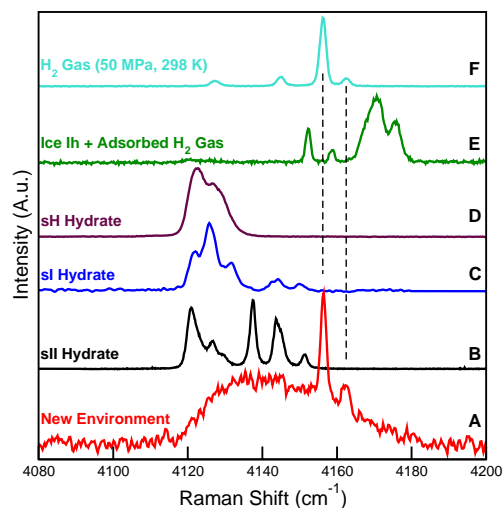


**Figure 3:** Raman spectral data of  $H_2$  in known environments of sI, sII, sH, ice Ih, gas phase compared to  $H_2$  in the metastable intermediate environment, highlighting differences in peak position and width. Raman spectra were measured at 0.1 MPa and 118 to 83 K.

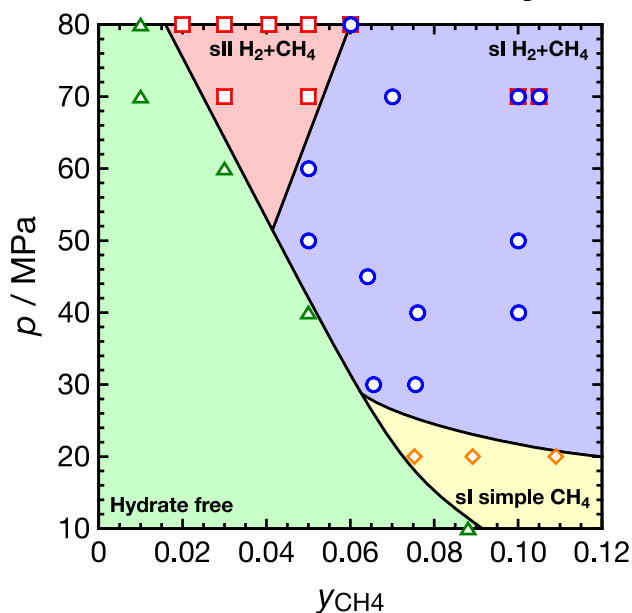
**Figure 2:** Suggested pathway for structural transition from sVI to sII after addition of  $H_2$  guest molecule [4].



### (III) Structure-Synthesis Relations of CH<sub>4</sub> + H<sub>2</sub> Binary Hydrates

To reduce the extreme thermodynamic requirements for stabilizing pure H<sub>2</sub> clathrate hydrate systems, small amounts of a second larger guest are typically added to better stabilize the clathrate hydrate structure [5]. A common binary hydrogen hydrate system is the H<sub>2</sub>+tetrahydrofuran (THF) mixed hydrate, where the binary hydrogen hydrate can be stabilized at more moderate conditions compared to pure H<sub>2</sub> hydrate. Specifically, pure H<sub>2</sub> hydrates form at around 150 MPa and 270 K, while H<sub>2</sub>+THF binary hydrates form at around 10 MPa and 280 K. However, the trade off is typically that only a limited amount of H<sub>2</sub> can be enclathrated in the mixed clathrate hydrate, because THF molecules tend to occupy all 5<sup>12</sup>6<sup>4</sup> (large) cages and H<sub>2</sub> molecules can then only occupy the 5<sup>12</sup> (small) cages. For clathrate hydrates to be considered for practical energy applications, including as a storage medium, it is important to achieve a high energy density at relatively mild conditions.

We show that, like THF, CH<sub>4</sub> may also serve as a thermodynamic promoter, but unlike THF, CH<sub>4</sub> is small enough that H<sub>2</sub> may compete effectively for occupancy in the larger cages, resulting in an overall increase in H<sub>2</sub> enclathration. Furthermore, H<sub>2</sub>+CH<sub>4</sub> binary hydrates are expected to have a higher overall energy density than H<sub>2</sub>+THF hydrates because CH<sub>4</sub> serves as an additional source of energy, unlike THF. When compared to the H<sub>2</sub>+THF binary hydrate, clathrate hydrates incorporating H<sub>2</sub> and CH<sub>4</sub> are comparatively underexplored, with some authors suggesting enclathration of H<sub>2</sub>+CH<sub>4</sub> as *impossible* [6]. We report that the formation of binary H<sub>2</sub>+CH<sub>4</sub> hydrates can be achieved, where the final structure of the system is dependent on at least three thermodynamic variables: the initial mole fraction of mixed gas, pressure, and synthesis formation period (Fig. 4). Hydrate crystal structures and cage occupancies of guest species were obtained from powder X-ray diffractometry (PXRD) and Raman spectroscopy, respectively. The results revealed that compared to THF+H<sub>2</sub> binary hydrates, the storage potential is higher in the case of CH<sub>4</sub>+H<sub>2</sub> and should be explored further, possibly in combination with the self-



preservation effect. These new findings can open up the potential to further investigate other binary co-fuel systems in different clathrate hydrates.

**Figure 4:** Experimentally observed clathrate hydrate structures over a range of pressures ( $p$ ) and initial gas compositions ( $y_{\text{CH}_4}$ ) in the H<sub>2</sub>+CH<sub>4</sub>+water system at  $t = 72$  h and 263 K. Squares: H<sub>2</sub>+CH<sub>4</sub> sII hydrate, diamonds: H<sub>2</sub>+CH<sub>4</sub> sI hydrate, triangles: simple CH<sub>4</sub> sI hydrate, circles: hydrate free.

## Future Plans

Our recent experimental and molecular simulation studies have revealed that during periods of clathrate hydrate structural change (e.g. nucleation or growth), metastable environments not present in thermodynamically stable hydrates may persist for hours or days. Using in-situ Raman spectroscopy, neutron diffraction, and molecular simulations, we will further characterize the nature of these new metastable environments. These new discoveries may potentially reveal an entirely new class of structures. Furthermore, this new environment has been only investigated for the structure VI to structure II clathrate transition using tert-butylamine and H<sub>2</sub> as guest molecules. In future work, we plan to investigate the presence of potentially unique intermediate states in other structures/systems. Fundamental molecular studies of binary co-fuel systems will be also investigated using in-situ Raman spectroscopy, neutron and X-ray diffraction, and molecular simulations.

## References

1. M. R. Walsh, C. A. Koh, E. D. Sloan, A. K. Sum, D. T. Wu, *Science*, **326**, 1095-1098 (2009)
2. M. R. Walsh, J. D. Rainey, P. G. Lafond, D.-H. Park, G. T. Beckham, M. D. Jones, K.-H. Lee, C. A. Koh, E. D. Sloan, D. T. Wu, A. K. Sum. *Phys. Chem. Chem. Phys.* **13**, 19951-19959 (2011).
3. P. S. R. Prasad, T. Sugahara, E. D. Sloan, C. A. Koh, A. K. Sum, *J. Phys. Chem.A*, **113**, 11311-11315 (2009).
4. R. G. Grim, Y. Matsumoto, E. D. Sloan, A. K. Sum, C. A. Koh, *Proc. Am. Chem. Soc.*, Hydrogen Production, Storage, and Utilization, Pub# 725, New Orleans, LA, (April, 2013).
5. L. J. Florusse, C. J. Peters, S. Joop, J. Schoonman, K. C. Hester, C. A. Koh, S. F. Dec, K. N. Marsh, E. D. Sloan, *Science*, **306**, 469-471 (2004).
6. S. S. Skiba, E. G. Larionov, A. Y. Manakov, B. A. Kolesov, V. I. Kosyakov, *J. Phys. Chem. B*, **111**, 11214–11220 (2007).

## DOE Sponsored Publications in the Last Two Years

1. R. G. Grim, P. B. Kerkar, E. D. Sloan, C. A. Koh, A. K. Sum, *J. Chem. Phys.*, **136**, 234504 (2012).
2. R. G. Grim, P. B. Kerkar, M. Shebowich, M. Arias, E. D. Sloan, C. A. Koh, A. K. Sum, *J. Phys. Chem. C.*, **116**, 18557-18563 (2012).
3. Z. M. Aman, S. Joshi, E.D. Sloan, A.K. Sum, C.A. Koh, *J. Colloid Interface Sci.*, **376**, 283-288 (2012).
4. Z. M. Aman, K. Olcott, K. Pfeiffer, E. D. Sloan, A. K. Sum, and C. A. Koh, *Langmuir*, **29**,

- 2676-2682 (2013).
5. M. R. Walsh, J. D. Rainey, P. G. Lafond, D.-H. Park, G. T. Beckham, M. D. Jones, K.-H. Lee, C. A. Koh, E. D. Sloan, D. T. Wu, A. K. Sum, *Phys. Chem. Chem. Phys.* **13**, 19951-19959 (2011).
  6. M. R. Walsh, G. T. Beckham, C. A. Koh, E. D. Sloan, D. T. Wu, A. K. Sum, *J. Phys. Chem. C*, **115**, 21241-21248 (2011).
  7. Z. A. Aman, E. P. Brown, E. D. Sloan, A. K. Sum, C. A. Koh, *Phys. Chem. Chem. Phys.*, **13**, 19796-19806 (2011).
  8. C. A. Koh, E. D. Sloan, A. K. Sum, and D. T. Wu, *Annual Review of Chemical and Biomolecular Engineering*, **2**, 237-257 (2011).
  9. Y. Matsumoto, R. G. Grim, N. M. Khan, T. Sugahara, K. Ohgaki, E. D. Sloan, C. A. Koh, A. K. Sum, *J. Phys. Chem. C*. (In Preparation).
  10. R. G. Grim, C. A. Koh, A. K. Sum, *Science* (In Preparation).

## Synthesis and Processing Research in Group IV Nanomembranes

Max G. Lagally and Mark A Eriksson  
University of Wisconsin-Madison, Madison, WI 53706  
(with Feng Liu, Utah)

### Program Scope

Single-crystal semiconductor sheets present a platform for entirely new science and technology. They may form the basis for devices relevant in energy harvesting, transformation, and conservation. The novelty of thin crystalline sheets lies in the following. 1) They are **thin**; a factor that brings many new phenomena. The very high interface-to-volume ratio makes surfaces or interfaces, and their chemical and structural properties, very important contributors to unique membrane electrical, thermal, and mechanical behavior. 2) Thin sheets can be **strained** to a high degree, effectively allowing lattice constant choice. Many of the most fundamental materials properties are influenced by the lattice and distortions of the lattice. 3) They are easily **stackable** and **bondable**, introducing the potential for an entirely new set of composite materials that change their properties vertically on the scale of 10s to 100nm. Because of this property, **interface effects** can be significant, but readily investigated. Additionally sheets are compatible with all top-down processing that is conventional in the semiconductor device industry.

Our work has been in Group IV-based nanomembranes, but the platform is extendable to other materials and a range of structures and functions, using the materials processing approaches we have developed. The platform of single-crystal semiconductor sheets offers the choice of nano-size in one, two, or three dimensions, as well as the formation of structures with mixed dimensions, but the true advantage is working at the nanoscale in one dimension, while the other two dimensions are at the mesoscale or macroscale. Our work provides excellent prospects for modifying and enhancing materials properties, and new areas of NM processing that can act as technology drivers.

The program scope includes:

- Investigations of
  - electronic transport in surfaces of crystalline sheets, including new orientations of semiconductor NMs and graphene bonded to such NMs
  - strain engineering of new structures, including local and global lattice strain, externally applied strain, and thermal mismatch strain
  - surface modification to affect the kinetic barrier for defect formation during stress application
  - novel interfaces, including structure and thermal/electrical transport through NM stacks, twist boundaries in stacked graphene, and periodically bent NMs
- Fabrication of our own unique NMs, make novel materials via NM strain engineering
- Application of theory to quantify the outcomes of our synthesis and processing efforts
- Focus on structure and defects, electronic band structure, electronic and thermal transport, and mechanical behavior.

## Recent Progress

We are actively investigating a number of research topics at the forefront of NM science. Our core competencies are making NMs via thinning, release, etching and transfer; MBE and CVD growth at very high purities; charge transport measurements; structural and strain measurements; and surface characterization. We have focused in the last two years on

- Surface charge transport in clean and H covered Si(001). Corresponding theoretical work is performed by Feng Liu on surface charge transport in tensilely strained Si(001)
- Use of strain engineering to make defect free Si-Ge crystals and their use for multiple-quantum well growth of Si/SiGe heterostructures and strained-Si 2DEGs
- Mechanical strain of Ge for band engineering
- Charge transport in graphene on semiconductors
- Strain engineering of patterned NMs of high-modulus materials on “soft” substrates to create periodic local 3D structures.
- Thermal transport through stacked-NM interfaces

Work on surface charge transport has recently been published.<sup>1</sup> For this research we developed a back-gated van der Pauw method that is compatible with ultrahigh vacuum. In a thin semiconductor sheet, the simple existence of surfaces can have significant impact on the “bulk” conductance of the sheet by providing states, via a mechanism called “surface transfer doping”. But the surface may itself conduct, independent of the bulk, through extended electronic states at the surface, an important function in many current nanostructure investigations that is quite difficult to measure. We use an electrode at the back of the wafer to fully deplete the “bulk” of the thin Si layer, revealing the non-zero conductivity in the surface bands, caused by the 2x1 reconstruction of the clean surface. A change in NM thickness modifies the coupling strength between the front free surface and the back gate. Any changes in the front surface then act as an additional gate to counter or enhance the effect of the back gate. The NM “bulk” conductance is continuously tunable by the back gate voltage and hence can be made negligible relative to the surface contribution.

We made conductance measurements in UHV on thin SiNMs ranging in thickness from 40nm to 200nm. From the shape of conductance plots as a function of back gate voltage, we conclude that electron transport must occur through the surface bands themselves. Simulations are able to reproduce the experimental results with high precision, and they allow an extraction of the surface band mobility, which for all samples is on the order of 50 cm<sup>2</sup>/Vs. The shape of the curves for the (2x1) surface termination indicates the presence of Fermi level pinning, which we attribute to type-C defects at the surface. For H-terminated Si, the surface bands are destroyed and the minimum conductance becomes much lower, because there is no surface conductance. Temperature dependence measurements on the latter suggest surface states that pin the Fermi level 0.2 eV below the conduction band edge, consistent with F contamination introduced in HF removal of the oxide, which leaves the Si(001) surface H terminated. These studies form the basis for continuing work, see below under Future Work.

The basis for the study described by the second bullet was research published just outside the two-year window of the publication list.<sup>2</sup> Using nanomembrane strain engineering methods, we demonstrate the fabrication of fully elastically relaxed Si<sub>1-x</sub>Ge<sub>x</sub> nanomembranes (NMs) for

use as growth substrates for new materials. To do so, we grow defect-free, uniformly and elastically strained SiGe layers on Si substrates and release the SiGe layers to allow them to relax this strain completely as free-standing NMs. These SiGe NMs are transferred to new hosts and bonded there. We confirm the high structural quality of these new materials and demonstrate their use as substrates for technologically relevant epitaxial films by growing strained Si layers and thick, lattice-matched SiGe alloy layers on them. Current work is focused on producing better-quality SiGe NMs. Past ones, grown in CVD, contain pinholes, which we expect to be able to avoid using MBE. Pinholes are a significant problem for multilayer stacks in which vertical charge transport is required. A manuscript that compares the structural behavior of SiGe thick films grown on SiGe NMs and strain graded SiGe is under review.<sup>3</sup> It shows that significant improvements are obtained using NMs as substrates.

In an entirely different vein, we are looking for surface modification methods, through functionalization, surface coating, immersion, or encapsulation that increase the barrier for the nucleation or motion of cracks and dislocations in very thin crystalline sheets. The motivation is that significant band structure modification occurs in semiconductors with strain. We want to extend the range of tensile strain we can apply to Ge, because it can be made direct-band-gap, and thus emit light.<sup>4</sup> By increasing the strain we could tune the light emission wavelength and also increase efficiency of light emission.

## Future Plans

For the surface transport measurements we will be looking at SOI(111). There is continuing discussion on the nature of surface conduction in this surface, but only our approach can address what may actually be the case and under what circumstances. Beyond that, theoretical studies will suggest if it is feasible to make a surface-based topological insulator.

For both the surface transport and the SiGe NM substrate and growth studies, we will attempt to fabricate step-free mesas. Many years ago we and others have shown with LEEM that it is possible to make mesas at least 20 microns wide on Si(001). We need to extend this to SiGe and to wider mesas. For surface transport this is important because we can eliminate steps and thus dimer row orientation as causes for limited surface mobility. For the growth studies it is important because steps influence the behavior of a strained-Si 2DEG.

Work on functionalization of Ge to inhibit crack formation will continue. We will also initiate other procedures to attempt to extend the range of strain to be more like the theoretical breaking strain.

We have begun to investigate the combination of graphene and semiconductor substrates. There are significant scientific and technical reasons why one may wish to do so.

We will continue the very difficult work on thermal transport through stacked-NM interfaces. The goal is to find out how such interfaces act as thermal impedance and potentially how a limited phonon spectrum can relate to the nanoscale thickness of both the crystalline sheets and the interfaces between them.

## References

1. W. Peng, Z. Aksamija, S.A. Scott, J.J. Endres, D.E. Savage, I. Knezevic, M.A. Eriksson, and M.G. Lagally, *Nature Communications* **4**, 1339 (2013).

2. “Defect-Free Single-Crystal SiGe: A New Material from Nanomembrane Strain Engineering”, D. M. Paskiewicz, B. Tanto, D. E. Savage, and M.G. Lagally, *ACS Nano* **5**, 5814 (2011).
3. “Strain and crystalline-tilt uniformity in strained-Si/SiGe heterostructures grown on elastically relaxed SiGe nanomembranes”, D. M. Paskiewicz, D. E. Savage, M. V. Holt, P. G. Evans, and M. G. Lagally, *Nature Sci. Reports*, under review
4. C. Boztug, J.R. Sánchez-Pérez, F. F. Sudradjat, F. Chen, D. M. Paskiewicz, RB Jacobson, M.G. Lagally, and R. Paiella, *Small* **9**, 622 (2013).

### Publications (since September 2011)

5. “Semiconductor Nanomembranes: Synthesis, Assembly, and Applications”, J.A. Rogers, **M.G. Lagally**, and R.G. Nuzzo, *Nature* **477**, 45 (2011) (invited review).
6. “Electron Tunneling Induced Periodic Nucleation and Growth of Nanoparticles: Physical Basis of Chemical Reduction”, F. Chen, H.-J. You, S.-C. Yang, Z.-M. Yang, X.-P. Song, **M.G. Lagally**, and B.-J. Ding, *Crystal Growth and Design* **11**, 3707 (2011).
7. “Direct-bandgap light-emitting germanium in tensilely strained nanomembranes”, J. R. Sánchez-Pérez, C. Boztug, F. Chen, F. F. Sudradjat, D. M. Paskiewicz, RB Jacobson, **M.G. Lagally**, and R. Paiella, *Proc. Nat. Acad. Sci.* **108**, 18893 (2011).
8. “Semiconductor Nanomembranes: A Platform for New Properties via Strain Engineering”, F. Cavallo and **M. G. Lagally**, *Nanoscale Research Letters* **7**, 628 (2012) (invited review)
9. “InAs islands on free-standing Si nanomembranes: towards coherent growth”, Chr. Deneke, A. Malachias, A. Rastelli, L. das Mercês Silva, M.H. Huang, F. Cavallo, O.G. Schmidt, and **M. G. Lagally**, *ACS Nano* **6**, 10287 (2012).
10. “Probing Semiconductor Surface Electronic Structure with Charge Transport in Nanomembranes”, W. Peng, Z. Aksamija, S.A. Scott, J.J. Endres, D.E. Savage, I. Knezevic, **M.A. Eriksson**, and **M.G. Lagally**, *Nature Communications*, **4**, 1339 (2013).
11. “Fast flexible electronics with strained silicon nanomembranes”, Han Zhou, Jung-Hun Seo, D. M. Paskiewicz, Ye Zhu, P. M. Voyles, W.D. Zhou, **M. G. Lagally**, and Z.Q. Ma, *Nature Scientific Reports* **3**, 01291 (2013).
12. “Tensilely strained germanium nanomembranes as infrared optical gain media”, C. Boztug, J.R. Sánchez-Pérez, F. F. Sudradjat, F. Chen, D. M. Paskiewicz, RB Jacobson, **M.G. Lagally**, and R. Paiella, *Small* **9**, 622 (2013).
13. “Strain-engineered SiGe quantum-well nanomembranes for far-infrared intersubband device applications”, P. Sookchoo, F. F. Sudradjat, A. M. Kiefer, H. Durmaz, R. Paiella, and **M.G. Lagally**, *ACS Nano* **7**, 2326 (2013).
14. “Excitation of a Si/SiGe quantum dot using an on-chip microwave antenna”, E. Kawakami, P. Scarlino, L. R. Schreiber, J. R. Prance, D. E. Savage, **M. G. Lagally**, **M. A. Eriksson**, and L. M. K. Vandersypen, *Appl. Phys. Letters* **103**, 132410 (2013).
15. “Facile fabrication of ordered microstructures on flexible substrates”, F. Cavallo, K.T. Turner, and **M.G. Lagally**, *Advanced Functional Materials*, in press
16. “Semiconductor Quantum Dot Qubits”, **M.A. Eriksson**, S.N. Coppersmith, and **M.G. Lagally**, *MRS Bulletin*, in press
17. “Long-Term Reduction in Poly(dimethylsiloxane) Surface Hydrophobicity via Cold-Plasma Treatments”, B.J. Larson, S.D. Gillmor, J.M. Braun, L.E. Cruz-Barba, D.E. Savage, F.S. Denes, and **M.G. Lagally**, *Langmuir*, accepted.

# **Self-Assembly of Non-Spherical Colloids: New Reduced Symmetry Crystals and Mesophases for Templating Functional Materials at Fine Scales**

**Chekesha M. Liddell Watson  
Itai Cohen  
Fernando Escobedo**

**Department of Materials Science and Engineering  
Cornell University, Ithaca, NY  
Department of Physics  
Cornell University, Ithaca, NY  
Department of Chemical and Biomolecular Engineering  
Cornell University, Ithaca, NY**

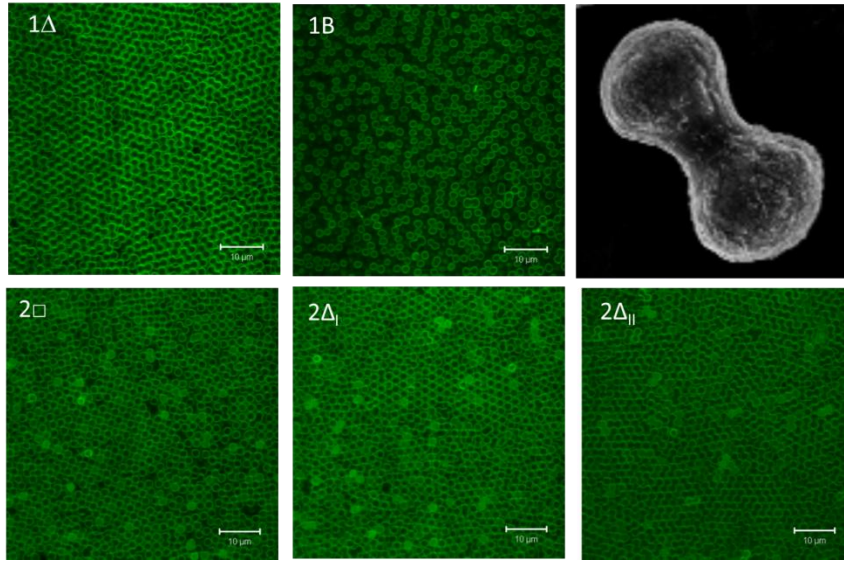
## **Program Scope**

Mesoscale control of light-matter interactions as a route to enhance performance in a range of technologies is a central aim in colloidal materials science and engineering. Increasing focus on atypical colloidal structures is uncovering novel partial order mesophases, quasicrystals, and superlattices with dramatic effects on photon dispersion relations. This work explores processing-microstructure relationships for the self-organization of nonspherical colloids under confinement and exposed to shearing conditions. How nonspherical particle mesophases adapt in the presence of surfaces and how shear forces drive development of structure and rheological behavior in these systems is investigated. Wedge cell and parallel plate confinement techniques and shear-assisted assembly provide a platform to understand the role of thermodynamic and non-equilibrium effects including dynamic flow behavior on the formation of complex colloidal structures. Inorganic precipitation and seeded emulsion polymerization are employed to synthesize tailored collapsed particle morphologies from hemispheres to bulbous mushroom caps as well as faceted polyhedra and peanut shapes. Real space quantitative analysis of structural evolution as a function of shape parameters, volume fraction and confinement height is conducted using ultra-fast confocal microscopy to track particle motions. A custom confocal rheometer setup is utilized to map structural and rheological behavior as a function of confinement gap size and shear rate at a variety of volume fractions. Computational studies on phase behavior of anisotropic particles, kinetics and mechanisms of ordering transitions and rheology of ordered phases is conducted to complement experiments. For this purpose, advanced molecular simulation methods are used including, forward flux sampling (to probe the kinetics of phase transitions) and non-equilibrium iso-stress molecular dynamics (to detect yield stress behavior).

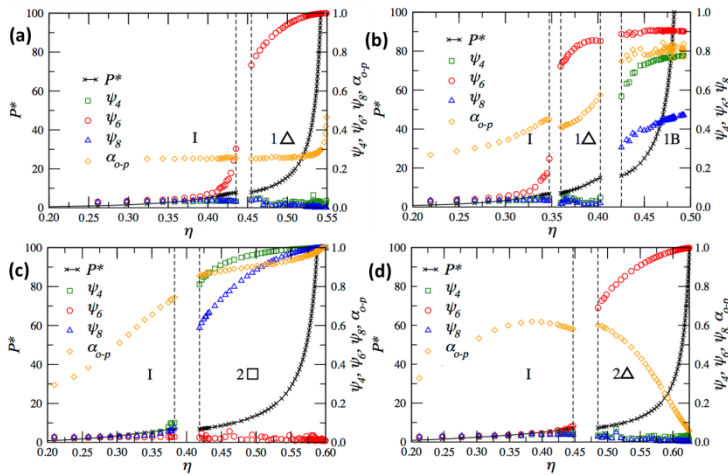
## **Recent Progress**

Colloidal self-assembly has been demonstrated as a prime method for the fabrication of multidimensional photonic materials.[1] Particle ‘shape programming’ can be combined with physical confinement of colloid suspensions to access and stabilize a rich diversity of quasi-2D transition structures as material templates for optical band gap and anomalous refraction

properties.[2-3] Here, wedge-cell confinement was employed to study colloidal phase behavior of hollow fluorescent silica dimers (peanut-shaped) as a function of confinement height. Suspensions of hollow silica peanut-shaped particles were investigated in confinement cells using confocal microscopy, particle tracking, and video-image analysis. Five distinct transitions were discovered in the range from one to two layers of in-plane oriented dimers. Specifically, each configuration found is a degenerate crystal tiling of the corresponding sphere-based structure along the descriptive order sequence  $1\Delta \rightarrow 1B \rightarrow 2\Box \rightarrow 2\Delta$  where,  $\Delta$  and  $\Box$  indicate layers with triangular and square symmetry, respectively. In this scheme the ‘buckled’ phase is indicated by 1B. Two distinct  $2\Delta$  phases were determined for the dimer case, depending on the degree of out-of-plane tilted tiling. Mostly out-of-plane colloidal units in  $2\Delta_I$  re-assemble to



form two layers of predominantly in-plane lying dimers for  $2\Delta_{II}$ . These arrangements can be predicted simply from closest packing arguments for incommensurate layer heights and are in agreement with findings from Monte Carlo simulations. Order parameters and distribution functions for positional and bond orientational order, voronoi constructions for detecting intrinsic defects and number of nearest



neighbors, and fast Fourier transforms (FFT) quantitatively characterize each phase from confocal image analysis. The experimental microscopy and theoretical phase diagram will be presented. Figure 1 (top) illustrates the phases and (bottom) ideal characteristics for monodisperse dimer colloidal building blocks.

We further explored mixed particle systems of spheres and peanut-shaped dimers (Figure 2). Hollow

Figure 1. Top: Confocal images of phase sequence with cell height. Bottom: Equation of state and characteristics of simulated phases  $1\Delta \rightarrow 1B \rightarrow 2\Box \rightarrow 2\Delta$  where,  $\Delta$  and  $\Box$  indicate layers with triangular and square symmetry, respectively. The buckled phase is indicated by 1B. Two distinct  $2\Delta$  phases were determined for the dimer case, depending on the degree of out-of-plane tilted tiling. Mostly out-of-plane colloidal units in  $2\Delta_I$  re-assemble to form two layers of predominantly in-plane lying dimers for  $2\Delta_{II}$ .

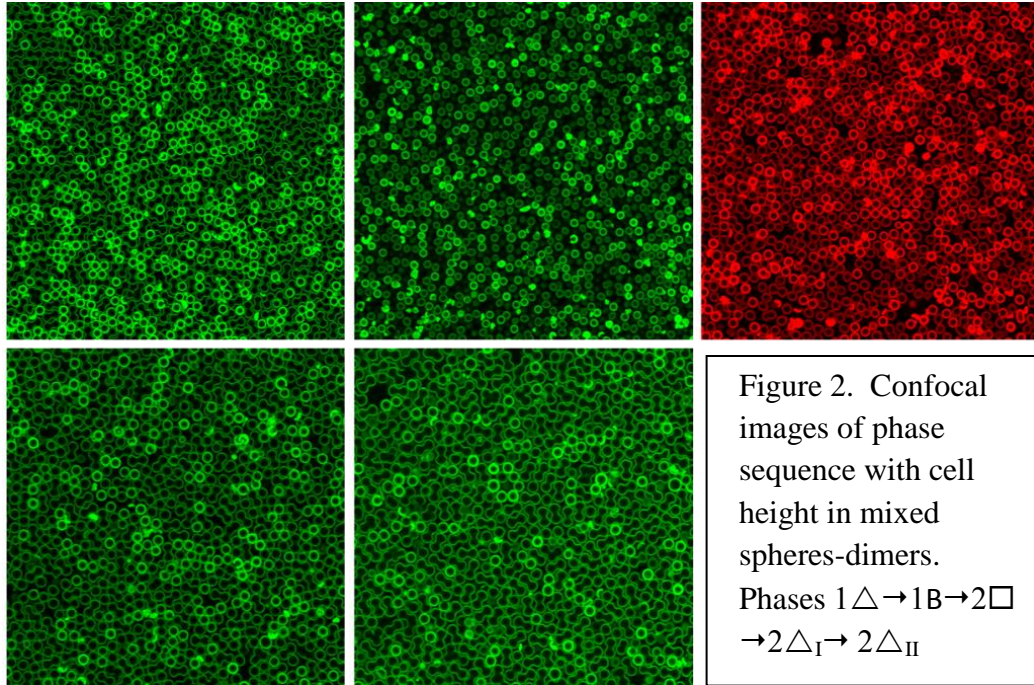


Figure 2. Confocal images of phase sequence with cell height in mixed spheres-dimers. Phases  $1\Delta \rightarrow 1B \rightarrow 2\Box \rightarrow 2\Delta_I \rightarrow 2\Delta_{II}$

silica spheres were prepared by a two stage burn out of polystyrene from core-shell colloids. Hollow peanut-shaped particles were templated on hematite iron oxide dissolved through the sol gel synthesized silica coating using hydro-

chloric acid. Hollow shells were coated with layers of rhodamine isothiocyanate (RITC) labeled silica for fluorescence.[4] The phase behavior of binary systems based in size or charge characteristics has been reported in studies toward the aim of structural diversity in colloids.[5] Shape diversity has rarely been studied using only entropic, excluded volume effects. For roughly equal dimer lobe diameters relative to the sphere diameter, we obtained an isomorphous structure analog where both spheres and dimers tiled the same phase sequence as a function of height in wedge cell confinement. Spheres mixed into the dimer crystals and are substitutional defects in the dimer tiling. Several conditions support the adoption of isomorphous phases at the atomic level. The Hume-Rothery rules suggest that components which have the same crystal structure, size difference less than 15% in radius, and chemical similarity (valence and electronegativity) lead to structures with unlimited solid solubility.[6] Spheres and dimers in this colloidal analog experiment exhibited hard interactions and lobe-based size similarity.

## Future Plans

Future plans include studying the effect of relative size difference, relative concentration, and material type on variations in the phase behavior of sphere-dimer mixtures under confinement. We also plan to investigate the phase behavior of mushroom cap-shaped particles (cut-spheres) and sphere mixtures using quantitative analysis of confocal microscopy imaging. The potential for positional control of topological defects has been a goal in the photonic crystal field due to the ability to confine or guide light through defect engineering. Spheres and dimers, for example, can be prepared from different materials and ‘defect’ placement (i.e., minority particle population) would be restricted to the allowed positions in phases  $1\Delta$ ,  $1B$ ,  $2\Box$ ,  $2\Delta$ . We will continue simulations to elucidate the kinetics and mechanism of the order-disorder transition for dimer and mixed particles in confinement. The synthesis of polymethylmethacrylate (PMMA) nonspherical particles that are easily index matched is being developed for thick suspension studies. In addition, studies on the non-linear structural response of liquid state colloidal

suspensions of spherical particles under oscillatory shear will be refined. Experimental results suggest that hydrodynamic effects may be important at high shear rates to explain certain non-linear responses not observed in the simplified Brownian dynamic simulations. Hence solvent explicit simulations will be implemented in order to more realistically account for hydrodynamic interactions and the rheology in such particle suspensions. Other recent work, demonstrating enhancement of rotational diffusion under shear, focused on diffusion of anisotropic particles in the limit of single particles and dilute suspensions. This work will be expanded to investigate rotational and translational diffusion in semi-dilute and dense suspensions of anisotropic particles. Denser suspensions may provide additional control over particle interactions, diffusion, and assembly. Sheared suspensions of spherical particles doped with anisotropic particles will also be studied. Additionally, the rheology of semi-dilute and dense suspensions of anisotropic particles will be correlated to the suspension structure. Previous work has focused on the rheology of dilute suspensions of anisotropic particles under continuous shear. However, the interplay between suspension structure and applied shear is poorly understood in dense rod-like suspensions. Preliminary results have shown that even for spherical particles, different structures can be created in oscillatory shear depending on the shear amplitude.

## References

1. A. Imhof. “Three-Dimensional Photonic Crystals Made from Colloids” in *Nanoscale Materials*, Springer: New York, 2004, p. 423-454.
2. E. K. Riley, E. Y. Fung and C. M. Liddell Watson. “Buckled Colloidal Crystals with Nonspherical Bases for 2D Slab Photonic Band Gaps.” *Journal of Applied Physics*, 11 (2012): 093504.
3. E. K. Riley and C. M. Liddell. “Confinement-Controlled Self Assembly of Colloids with Simultaneous Isotropic & Anisotropic Cross-Section.” *Langmuir*, 26 (2010): 11648-11656.
4. S. H. Lee, S. J. Gerbode, B. S. John, F. A. Escobedo, I. Cohen, C. M. Liddell. “Synthesis & Assembly of Nonspherical Hollow Silica Under Confinement.” *Journal of Materials Chemistry*, 18 (2008): 4912-4916.
5. A. van Blaaderen, “Colloids Get Complex.” *Nature*, 439 (2006): 545-546.
6. B. C. Carter and M. G. Norton, *Ceramic Materials*, Springer: New York, 2007.

## DOE Sponsored Publications in the Last Two Years

1. C. Avendano, C. M. Liddell Watson, F. A. Escobedo. “Directed Self-Assembly of Spherical Caps via Confinement.” *Soft Matter*, 9 (2013): 9153-9166.
2. B. D. Leahy, X. Cheng, D. C. Ong, C. Liddell-Watson, I. Cohen. “Enhancing Rotational Diffusion Using Oscillatory Shear.” *Physical Review Letters*, 110 (2013): 228301-1 — 228301-5.
3. E. Y. Fung, K. Muangnapoh, C. M. Liddell Watson. “Anisotropic Photonic Crystal Building Blocks: Colloids Tuned from Mushroom-Caps to Dimers.” *Journal of Materials Chemistry*, 22 (2012): 10507-10513.
4. X. Cheng, X. Xu, S. A. Rice, A. R. Dinner, I. Cohen. “Assembly of Vorticity-Aligned Hard-Sphere Colloidal Strings in a Simple Shear Flow.” *Proceedings of the National Academy of Science*, 109 (2012): 63-67.

5. U. Agarwal, F. A. Escobedo. “Yielding and Shear Induced Melting of 2D Mixed Crystals of Spheres and Dimers.” *Soft Matter*, 8 (2012): 5916-5922.

# Strain Engineered Surface Transport in Si(001): Complete Isolation of the Surface State via Tensile Strain

Feng Liu (fliu@eng.utah.edu)  
Department of Materials Science & Engineering  
University of Utah, Salt Lake City, UT 84112

## Program Scope

This theoretical project is carried out in close interaction with an experimental project led by Prof. Lagally at UW-Madison, entitled “Group IV Nanomembranes, Nanoribbons, and Quantum Dots: Processing, Characterization, and Novel Devices”. We address a broad range of topics from atomic structure, stability, and mechanical properties, to electronic, optoelectronic, and charge transport properties of various nanoarchitectures in the context of Si and other solid nanomembranes. These are done by using combinations of different theoretical and computational approaches, ranging from first-principles calculations and molecular dynamics simulations to finite-element analyses. The project focuses on four research areas: (1) Calculations of electronic structure and transport properties of Si nanomembranes, (2) Electronic and topological properties of Si(111) surfaces with adsorbed high-Z and magnetic elements, (3) Electronic and optoelectronic properties of Si and Ge “strain” superlattices and “strain” quantum dots, and (4) Calculations of growth and mechanical properties of nanomembranes.

## Recent Progress

Silicon in the (001) orientation provides the foundation for modern semiconductor devices. The atomic and electronic structures of the Si(001) surface have been thoroughly investigated and are well understood [1]. Engineering surface transport in Si(001) has attracted much recent interest for quantum information processing and surface-state based devices. Local surface conduction has been achieved by atom manipulation using scanning tunneling microscopy [2]. In the widely used (001)-oriented silicon-on-insulator (SOI) system, experiments [3] have shown that global ‘electron’ transport is possible in a very thin clean Si sheet via surface conduction, even in the absence of

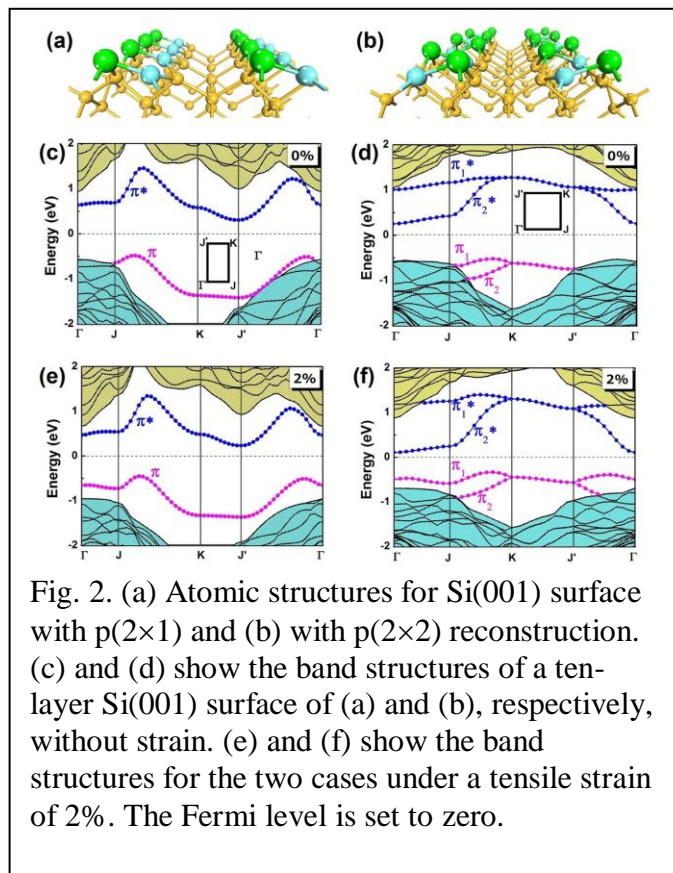


Fig. 2. (a) Atomic structures for Si(001) surface with p(2 $\times$ 1) and (b) with p(2 $\times$ 2) reconstruction. (c) and (d) show the band structures of a ten-layer Si(001) surface of (a) and (b), respectively, without strain. (e) and (f) show the band structures for the two cases under a tensile strain of 2%. The Fermi level is set to zero.

bulk doping. This is enabled by the thermal excitation of electrons from the bulk valence band (VB) to the surface  $\pi^*$  state. However, to achieve surface conduction via ‘holes’ in addition to electrons (i.e., p-type surface), it is desirable to isolate the surface  $\pi$  band in energy from the bulk VB, so that electron excitation and transport could occur principally between the surface  $\pi$  and  $\pi^*$  states.

Strain engineering of the Si bulk band structure is well understood [4] and practically employed in practice to improve the performance of Si electronics. Recently, we demonstrate a hybrid approach of combining surface engineering with strain engineering to manipulate Si(001) surface states, relative to the bulk bands, to an unprecedented level. We extend strain engineering of Si from bulk to surface by systematically studying the effects of strain on the electronic band structures and transport properties of the Si(001) surface with p(2×1) and p(2×2) reconstructions, using first-principles band calculations and quantum transport simulations. We show that sufficient tensile strain can effectively remove the overlap between the surface valence state and the bulk valence band (see Fig. 1), because of the drastically different deformation potentials (see Fig. 2). Isolation of the surface valence state is possible with a tensile strain of ~1.5%, a value that is accessible experimentally.

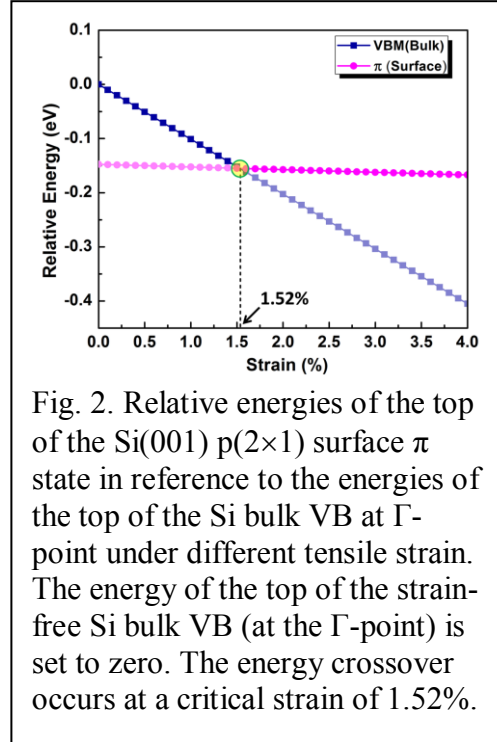


Fig. 2. Relative energies of the top of the Si(001) p(2×1) surface  $\pi$  state in reference to the energies of the top of the Si bulk VB at  $\Gamma$ -point under different tensile strain. The energy of the top of the strain-free Si bulk VB (at the  $\Gamma$ -point) is set to zero. The energy crossover occurs at a critical strain of 1.52%.

Furthermore, quantum transport simulations of a chemical sensing device based on strained Si(001) surface confirm the isolation of dominating surface conductance, giving rise to an enhanced molecular sensitivity within the energy window of Si bulk band gap. We tested NO<sub>2</sub> as an example to show the sensing mechanism of a device based on the strained Si(001) surface. Quantum transport calculations are performed for a six-layer Si(001) p(2×1) surface without and with a

2% tensile strain upon NO<sub>2</sub> adsorption. Various adsorption geometries are considered, and the I-V curves of the most stable configurations are shown in Figs. 3(a), under the bias within the energy window of Si bulk band gap (from -0.6 to 0.6 eV) within which

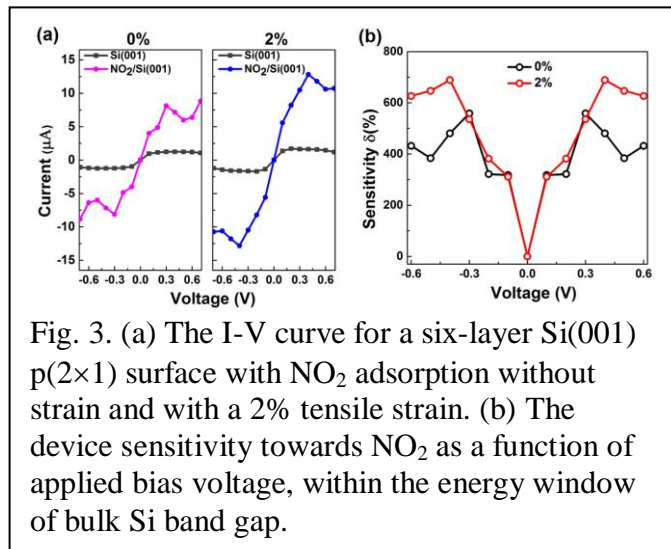


Fig. 3. (a) The I-V curve for a six-layer Si(001) p(2×1) surface with NO<sub>2</sub> adsorption without strain and with a 2% tensile strain. (b) The device sensitivity towards NO<sub>2</sub> as a function of applied bias voltage, within the energy window of bulk Si band gap.

the isolated surface bands reside. One clearly sees the current increase upon NO<sub>2</sub> adsorption is larger in the strained surface. This translates into a substantial strain-increased device sensitivity by ~200%, as shown in Fig. 3(b). Here, we define the sensitivity  $\delta = (I_{ad} - I_0)/I_0 * 100\%$ , with  $I_{ad}$  ( $I_0$ ) being the current with (without) molecular adsorption at a given bias voltage. Our results show the promise for combining surface engineering with strain engineering to further our ability to manipulate surface states for quantum information processing and surface-state based devices.

### Future Plans

We will continue to expand our current studies as described above, the planned research topics include:

- (1) Effect of strain on Si(001) surface band structure.
- (2) Effect of defect and surface adsorption on strained-Si(001) surface band structure.
- (3) Band structures of graphene on Si(001), Ge(001), and Si(111).
- (4) Electronic and topological properties of Si(111) surfaces with adsorbed high-Z and magnetic elements.
- (5) Kinetic growth modeling of self-assembly of Ge QDs on freestanding SiNMs.
- (6) Finite-element analysis of underside growth of SiN on SiNM windows.

### References

1. F. Liu, M. Hohage, and M.G. Lagally, Surfaces and Interfaces, Structure of, Encyclopedia of Appl. Phys., eds. H. Immergut and G. Trigg, Supplement Volume, 321-352 (1999).
2. B. Weber, S. Mahapatra, H. Ryu, S. Lee, A. Fuhrer, T. C. G. Reusch, D. L. Thompson, W. C. T. Lee, G. Klimeck, L. C. L. Hollenberg, and M. Y. Simmons, Science 335, 64 (2012).
3. P. P. Zhang, E. Tevaarwerk, B. N. Park, D. E. Savage, G. K. Celler, I. Knezevic, P. G. Evans, M. A. Eriksson, and M. G. Lagally, Nature 439, 703 (2006).
4. Z. Liu, J. Wu, W. H. Duan, M. G. Lagally, and F. Liu, Phys. Rev. Lett. 105, 016802 (2010).

### The DOE funded publications in the last two years

1. “Spatially separated spin carriers in spin-semiconducting graphene nanoribbons”, Z. F. Wang, S. Jin and Feng Liu, *Phys. Rev. Lett.* **111**, 096803 (2013).
2. “Robustness of two-dimensional topological insulator states in bilayer bismuth against strain and electrical field”, L. Chen, Z. F. Wang, and Feng Liu, *Phys. Rev. B* **87**, 235420 (2003).
3. “Prediction of a Two-Dimensional Organic Topological Insulator”, Z. F. Wang, Ninghai Su, and Feng Liu, *Nano Letters*, **13**, 2842 (2013).
4. “Flat Chern Band in a two-dimensional organometallic framework”, Z. Liu, Z. F. Wang, J.-W. Mei, Y. Wu and Feng Liu, *Phys. Rev. Lett.* **110**, 106804 (2003).
5. “Quantum anomalous hall effect in 2D organic topological insulator”, Z. F. Wang, Z. Liu and Feng Liu, *Phys. Rev. Lett.* **110**, 196801 (2013).
6. “Organic topological insulators in organometallic lattices”, Z. F. Wang, Zheng Liu and Feng Liu, *Nature Commun.* **4**, 1471 (2013).

7. "Quasiparticle Dynamics in Reshaped Helical Dirac Cone of Topological Insulators", L. Miao, Z. F. Wang, W. Ming, M. Yao, M. Wang, F. Yang, F. Zhu, A. V. Fedorov, Z. Sun, C. L. Gao, C. Liu, Q. Xue, Feng Liu, D. Qian, J. Jia, *PNAS*, **110**, 2758 (2013).
8. "Creation of Helical Dirac Fermions by Interfacing Two Gapped Systems of Ordinary Fermions", Z.F. Wang, M.-Y. Yao, W. Ming, L. Miao, F. Zhu, C. Liu, C. L. Gao. D. Qian, J.F. Jia, and Feng Liu, *Nature Commu.*, **4**, 1384 (2013).
9. "Electronic strengthening of graphene by charge doping", C. Si, W. Duan, Z. Liu, and Feng Liu, *Phys. Rev. Lett.* **109**, 226802 (2012).
10. "Anisotropic Strain Enhanced Hydrogen Solubility in bcc Metals: The Independence on the Sign of Strain", H.-B. Zhou, S. Jin, Y. Zhang, and G.-H. Lu, and Feng Liu, *Phys. Rev. Lett.* **109**, 135502 (2012).
11. "Mechanical properties of graphene oxides", L. Liu, J. Zhang, J. Zhao and Feng Liu, *Nanoscale* **4**, 5910 (2012).
12. "Growth Instability of Strained Film: An Elastic Green's Function Force Monopole Approach", H. Hu and Feng Liu, *Proceeding of IUTAM Symposium Surface Effects in the Mechanics of Nanomaterials and Heterostructures*, IUTAM Bookseries, Volume 31, 59-70 (2013), DOI: 10.1007/978-94-007-4911-5\_6
13. "Interplay between quantum size effect and strain effect on growth of nanoscale metal thin films", M. Liu, Y. Han, L. Tang, J. Jia, Q. Xue, and Feng Liu, *Phys. Rev. B* **86**, 125427 (2012).
14. "Quantitative Model of Heterogeneous Nucleation and Growth of SiGe Quantum Dot Molecules", H. Hu, H. Gao, and Feng Liu, *Phys. Rev. Lett.* **109**, 106103 (2012).
15. "Strain-less directed self-assembly of Si nanocrystals on patterned SiO<sub>2</sub> substrate", J. Ren, H. Hu, Feng Liu, S. Chu, and J. Liu, *J. Appl. Phys.*, **112**, 054311 (2012).
16. "Spin-enhanced organic bulk heterojunction photovoltaic solar cells", Y. Zhang, T. P. Basel, B. R. Gautam, X. Yang, D. J. Mascaró, Feng Liu & Z. V. Vardeny, *Nature Communications* **3**, 1043 (2012).
17. "Fractal Landau-Level Spectra in Twisted Bilayer Graphene", Z. F. Wang, Feng Liu, and M. Y. Chou, *Nano Lett.*, **12**, 3833 (2012).
18. "Quantum Electronic Stress: Density-Functional-Theory Formulation and Physical Manifestation", H. Hu, M. Liu, Z. F. Wang, J. Zhu, D. Wu, H. Ding, Z. Liu, and Feng Liu, *Phys. Rev. Lett.* **109**, 055501 (2012).
19. "Spatial and Energy Distribution of Topological Edge States in Single Bi(111) Bilayer", F. Yang, L. Miao, Z. F. Wang, M.-Y. Yao, F. Zhu, Y. R. Song, M.-X. Wang, J.-P. Xu, A. V. Fedorov, Z. Sun, G. B. Zhang, C. Liu, Feng Liu, D. Qian, C. L. Gao, and J.-F. Jia, *Phys. Rev. Lett.* **109**, 016801 (2012).
20. "Topological and electronic transitions in a Sb(111) nanofilm: The interplay between quantum confinement and surface effect", P. Zhang, Z. Liu, W. Duan, Feng Liu, and J. Wu, *Phys. Rev. B* **85**, 201410 (R) (2012).
21. "Simulation of self-assembled compositional core-shell structures in In<sub>x</sub>Ga<sub>1-x</sub>N nanowires", X. B. Niu, G. B. Stringfellow, Young-Ju Lee and Feng Liu, *Phys. Rev. B* **85**, 165316 (2012).
22. "Edge Stability of BN sheets and Its Application for Designing Hybrid BNC Structures", B. Huang, H. Lee, B.-L. Gu, Feng Liu, and W. Duan, *Nano Res.* **5**, 62 (2012).

## Quasiepitaxial Growth of Organic Crystalline Thin-Films

Richard R. Lunt  
Department of Chemical Engineering and Materials Science,  
Department of Physics  
Michigan State University, East Lansing, MI

### Program Scope:

The presence of excitons in organic semiconductors at room temperature distinguish them from traditional semiconductors, providing exceptional opportunities for manipulating energy in a range of structures from light emitting diodes, lasers, transparent photovoltaics, and optical switches. Indeed, organic semiconductors have already shown superior performance in the light emitting diode (LED) field. However, control over crystalline order, orientation, and defect formation are crucial to the fabrication and optimization of these excitonic organic electronics. For organic growth, lattice matching is not strictly required as with inorganic epitaxy, and the modes of epitaxy are therefore uniquely distinct. For example, unmistakable azimuthal relationships have been observed for many organic molecules grown on inorganic crystals that are consistent with theoretical energetic minima, despite a lack of true commensurate “epitaxial” relationship (hence the term “quasi-epitaxy”). While there is a growing body of literature on organic quasiepitaxy (QE) on inorganic substrates, very little is known about organic-organic QE needed to push excitonic electronics to their full potential. Indeed, very little is even known about homo-epitaxial vapor-phase growth. This is due, in large part, to 1) a lack of high quality starting (single) crystalline organic layers, 2) limited implementation of real-time probing methods and 3) a lack of understanding governing organic-organic QE selection rules. Moreover, there have been few examples of preserved-ordering during multilayer crystalline organic growth despite the keen interest in the novel physics afforded by crystalline organic semiconductors. Accordingly, there is a wealth of opportunities for this unexplored regime of organic crystalline growth phenomena. The overarching goal of this project is to understand and explore bottom-up vapor-deposition routes to the growth of large-area organic single crystalline films with controlled thickness, doping, and defect concentration.

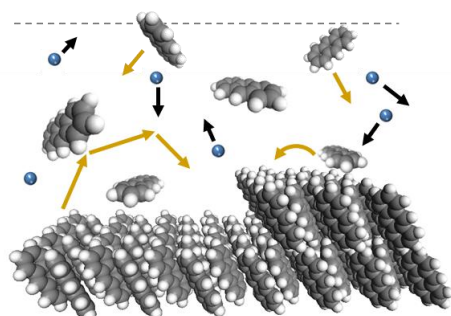


**Figure 1.** (a) Illustration of homo-epitaxy of vapor deposition of anthracene molecules

### Future Plans

Our specific aims are to: 1) Determine and map available growth modes from the vapor phase for archetypal homo-epitaxial (see Figure 1) and hetero-quasiepitaxial systems (see Figure 2), monitored with both real-time and *in situ* diffraction techniques; 2) Elucidate predictive energetic design rules for multilayer sustained quasi-epitaxial ordering; and 3) Model energetically driven QE relationships, and simulate molecular diffusion to gain insight into the intrinsic growth mode energy scaling for homo-epitaxial and hetero-QE systems. We anticipate

that organic homoepitaxial systems will exhibit analogous 2D and 1D inorganic homoepitaxial growth modes under favorable kinetic and thermodynamic conditions<sup>1</sup> and by matching organic crystal surface energies (as opposed to lattice matching with inorganic crystals) it will be possible to grow organic crystalline multilayer hetero-QE architectures from the bottom up.<sup>2</sup> Homo-epitaxy and hetero-QE vapor growth will be explored by utilizing single crystalline organic films grown from both the vapor and the melt for subsequent templating and growth of layers directly from the vapor. Studies will be performed to understand the role of vapor-phase growth in achieving sustained QE utilizing real-time *in situ* diffraction techniques and *ex situ* morphology characterization to provide surface sensitive information on the structural evolution, growth mode, and surface diffusivity of thin-film crystalline formation directly on crystalline organic substrates.<sup>3, 4</sup> Experiments will focus on canonical systems such as short-chain linear acenes, diamanes, and perylene derivatives to gain insight into the energy scaling for the kinetic growth processes and growth modes. We choose these class of materials as they have already found relevance in polariton lasers,<sup>5</sup> solar cells,<sup>6</sup> high mobility transistors, singlet fission applications,<sup>7</sup> and light emitting diodes.<sup>8, 9</sup> Specifically we will utilize materials we have shown in preliminary data to form large-area single crystals from the melt including anthracene, diphenyl anthracene (DPA), *N,N'*-Di-[(1-naphthyl)-*N,N'*-diphenyl]-1,1'-biphenyl)-4,4'-diamine (NPD), and rubrene. To understand these growth modes we will model the key equilibrium (energetic) and kinetic factors to gain insight into the factors governing the intrinsic growth modes. We will model surface diffusion as a function of surface energy matching (molecular pairings) using forcefield-based classical molecular dynamics (MD). These simulations will be extended to both the homo-epitaxial and hetero-QE systems.

The ability to grow quasiepitaxial organic films systems from the vapor-phase will afford crystalline, doped-crystalline, and multilayer single-crystalline structures to be grown from the bottom up. This understanding will enable a new class of organic electronics with unique excitonic tunability and will be used as a platform to study organic crystalline quantum wells, explore exciton confinement effects in the absence of high-defect densities, and determine upper limits for energy transport.

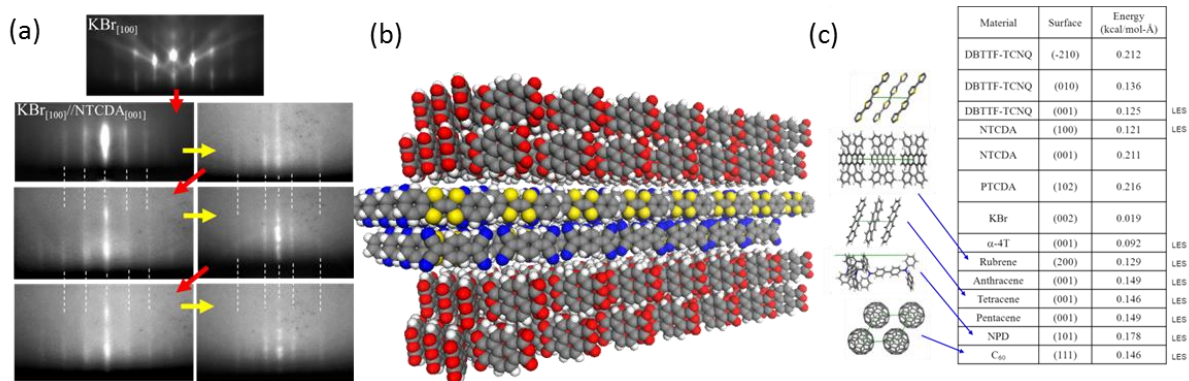


**Figure 2.** (a) Demonstration of sustained quasi-epitaxial multilayer growth monitored in-situ and in real-time via reflection high energy electron diffraction (HP-RHEED); Patterns of the first, second, and third pair growth of NTCDA(5nm)/DB-TCNQ(5nm), left column NTCDA pattern, right column is DB-TCNQ. (b) Schematic structural model of the multilayer NTCDA (red)/DB-TCNQ (blue, yellow) crystalline quantum well. (c) Calculated surface energies of various archetypal organic crystals used to identify surface-matched QE pairing. Lowest energy surfaces (LES) are marked accordingly.

## References

- 1 S. R. Wagner, R. R. Lunt, and P. Zhang, *Phys. Rev. Lett.* **110**, 086107 (2013).
- 2 R. R. Lunt, K. Sun, M. Kroger, J. B. Benziger, and S. R. Forrest, *Phys. Rev. B* **83**, 064114 (2011).
- 3 R. R. Lunt, J. B. Benziger, and S. R. Forrest, *Appl. Phys. Lett.* **90**, 181932 (2007).
- 4 R. R. Lunt, S. Kena-Cohen, J. B. Benziger, and S. R. Forrest, *Phys. Rev. Lett.* **102**, 065504 (2009).
- 5 S. Kena-Cohen and S. R. Forrest, *Nat Photonics* **4**, 371 (2010).
- 6 G. P. Kushto, W. H. Kim, and Z. H. Kafafi, *Organic Photovoltaics V* **5520**, 118 (2004).
- 7 M. B. Smith and J. Michl, *Chemical Reviews* **110**, 6891 (2010).
- 8 R. R. Lunt, B. E. Lassiter, J. B. Benziger, and S. R. Forrest, *Appl. Phys. Lett.* **95**, 233305 (2009).
- 9 H. H. Huang, S. Y. Chu, P. C. Kao, and Y. C. Chen, *Thin Solid Films* **516**, 5669 (2008).

# **Non-equilibrium effects in the processing of materials using plasmas**

PI: Lorenzo Mangolini

Department of Mechanical Engineering  
Materials Science and Engineering Program  
University of California, Riverside

## **Program Scope**

The ability of deposit, synthesize or treat materials under strong non-equilibrium conditions is a well-known properties of non-thermal plasmas. The interaction between non-equilibrium discharges and materials has already been investigated for several systems (most notably, for amorphous silicon thin films). In the last few years, it has become obvious that non-thermal plasmas are also an excellent route for the synthesis and processing of free-standing silicon nanoparticles. Silicon nanoparticles have many interesting properties and relevant applications [1], and have been successfully integrated in nanoelectronics [2], light emitting devices [3, 4] and photovoltaic devices [5]. They are excellent candidates for bio-related applications [6, 7]. Nanostructures based on silicon are potentially compatible with large-scale applications, since silicon is the second most abundant element on Earth. Silicon nanoparticles have successfully been produced using non-thermal plasma reactors deliberately optimized for the production of nanoparticles [8-11]. Non-thermal plasma continuous flow reactors convert silane into silicon nanocrystals sufficiently small to show quantum confinement effects [12]. The particle structure can be tuned from amorphous to crystalline depending on the power input into the plasma (see figure 5 in [13]). This has important consequences on the particle optical properties [14], which are critically important for many applications. Despite the fact that plasma-based techniques are promising candidates for the large volume synthesis of silicon nanocrystals, a detailed understanding of the correlation between plasma properties and nanoparticle structure is missing. The question remains of how the continuous flow reactor introduced in [9] fully converts the silane precursor into particles with a crystalline structure within few milliseconds. The goal of this program is to address this open issue and to investigate the interaction between non-thermal plasmas and silicon nanoparticles dispersed within it, with the goal of understanding the influence of plasma parameters of nanoparticle properties such as surface passivation and structure.

## **Recent Progress**

We have started this project by focusing on the conditions that lead to the formation of crystalline silicon particle. The PI in [15] found that the interaction between reactive species generated by the discharge (ions and radicals) with the particle surface leads to substantial

heating of the nanoparticles. This suggests that plasma-induced heating may lead to the formation of high-quality nanocrystals in the plasma because of a thermal annealing effect.

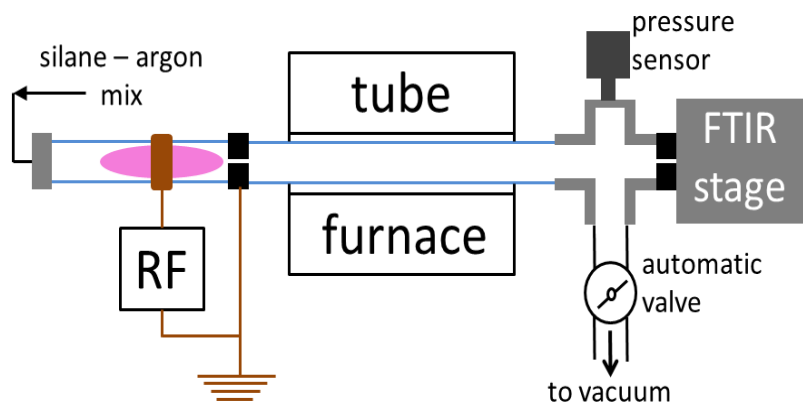


Figure 1. Schematic of experimental system

We have decided to verify the hypothesis that crystallization is due to a thermal effect by performing in-flight annealing experiments on silicon nanoparticles which are deliberately created with an amorphous structure. The experimental apparatus, shown in figure 1, consists of two in-line reactors, a first reactor for

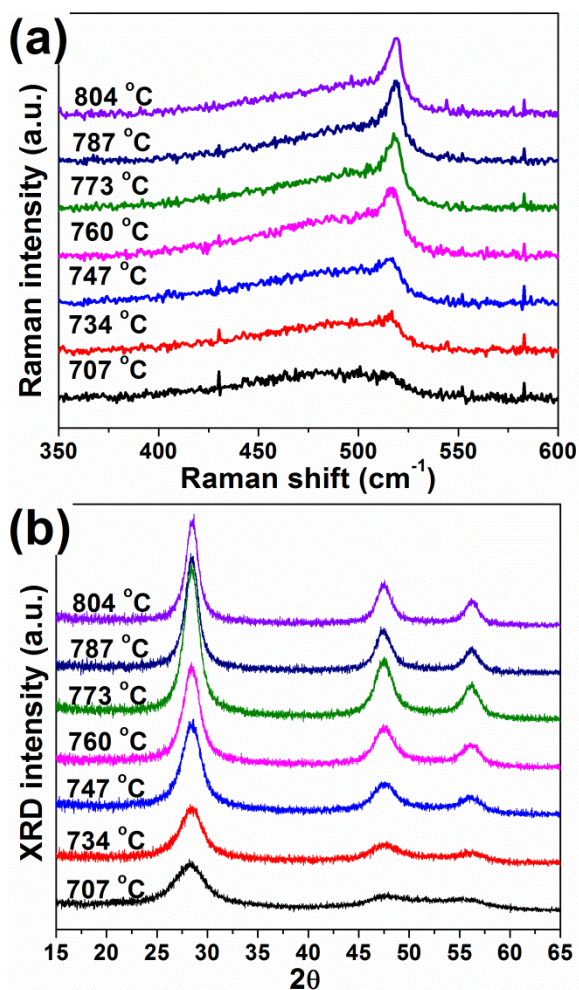


Figure 2. Evolution of Raman (a) and XRD (b) spectra as a function of in-flight annealing temperature for <10 nm silicon particles.

the synthesis of the amorphous powder and a second reactor for its in-flight annealing. The first reactor consists of a non-thermal plasma continuous flow system based on the design described in [9]. An orifice is placed between the first stage of the apparatus (powder production) and the second stage (powder annealing). The second reactor consists of a 60 cm Pyrex tube with a diameter of 2.54 cm, also connected with Ultra-Torr vacuum fitting. The second reactor is placed in a Lindberg tube furnace, which has a 40 cm heated length, and is capable of reaching temperatures of 1000 °C. Extensive characterization of the plasma-produced and in-flight annealed nanoparticles by TEM, XRD, Raman will be presented and discussed. An example of the Raman and XRD spectra obtained from this material as the temperature in the annealing stage is increase is shown in figure 2.

Using the data shown in figure 2 we can quantify the kinetic with which structural evolution takes place during the in-flight annealing step. A necessary step to achieve this is to measure the fraction of crystalline volume in the material as a function of annealing temperature. Both Raman and XRD data have been used for this

purpose. In particular we have used several different models that account for phonon-confinement effects to correctly fit the measured Raman spectra. We have found that the use of either Raman or XRD leads to obtaining the same value of activation energy for crystallization ( $E_a$ ). This result alone is quite interesting, since it is well-known that Raman cannot provide a reliable measurement of crystalline fraction for the case of silicon, because of the effects of strain which modulates the Raman response of the material. In our case we perform Raman characterization on small free-standing particles which are strain-free.

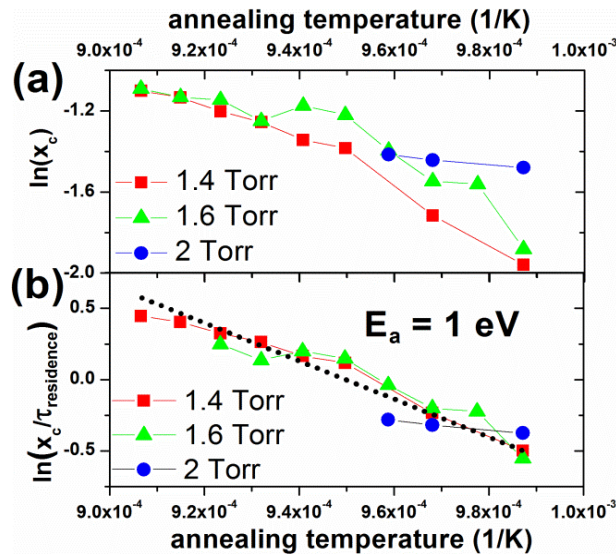


Figure 3. (a) Arrhenius plot of crystalline fraction as a function of annealing temperature for different process parameters. (b) Same as (a) but normalized over residence time in the annealing stage.

crystallization rate, such as the presence of hydrogen on the particle surface and their coalescence rate during the annealing stage, will be presented. The major finding of this study is that the crystallization kinetics is not just a function of temperature and time but is also dependent on geometry and size. The group of Giulia Galli [17, 18] recently predicted using molecular dynamic simulations that the crystallization rate is expected to be enhanced for the case of nanostructures, because of the ability of high surface-to-volume ratio systems of accommodating the stress induced by phase transformation.

If we use the nanoparticle temperature history in a plasma predicted by the PI in [15], and calculate the change in crystalline fraction using the empirical values obtained by the Arrhenius plot shown in figure 3, we find that a negligible fraction of the particles is crystallized. This indicates that the formation of crystalline particles in non-thermal plasmas is not due to simple thermal effects.

The activation energy for crystallization has been obtained by plotting the values of crystalline fraction in an Arrhenius plot, such as the one shown in figure 3. Values of crystalline fraction for different annealing temperatures and pressure in the second stage of the reactor are shown in figure 3a. The values of crystalline fraction, normalized over the pressure-dependent residence time in the annealing stage, are plotted in figure 3b. For sub-10 nm particles we measure an activation energy for crystallization of 1 eV.

This value is substantially lower than 2 eV, which is considered the theoretical minimum value for the activation energy for crystallization for the case of bulk amorphous silicon [16]. An extensive discussion of the various parameters that can affect the

## Future Plans

We are currently performing *in-situ* FTIR measurement on the silane-containing non-thermal plasma to obtain a quantitative measurement of the rate with which the precursor, silane, is consumed in the plasma. Preliminary data will be presented suggesting that there is a correlation between the particle nucleation rate and their structure, with higher nucleation and growth rates leading to the formation of nanocrystals. Additional studies will also be performed using *in-situ* FTIR to characterize the correlation between the plasma parameters and the nanoparticle surface. We will in particular monitor the evolution of surface hydride species as a function of plasma input power. Parameters such as plasma density and hydrogen radical density will be measured using a combination of electrostatic probes and optical emission spectroscopy. By using well-established kinetic rates for reaction of silicon surfaces with various reactive species, we will be able to provide a reliable measurement of the temperature of very small (<10 nm) nanoparticles suspended in a non-thermal plasma.

## DOE sponsored publications

Lopez, T. and Mangolini, L., “Crystallization Kinetics of Plasma-Produced Amorphous Silicon Nanoparticles”, Proceedings of the 2013 MRS Spring Meeting.

Lopez, T. and Mangolini, L., “Low activation energy for the crystallization of amorphous silicon nanoparticles”, under review.

## REFERENCES

1. Mangolini, L., *Synthesis, properties, and applications of silicon nanocrystals*. Journal of Vacuum Science & Technology B: Microelectronics and Nanometer Structures, 2013. **31**(2): p. 020801.
2. Oda, S., *Neosilicon materials and silicon nanodevices*. Materials Science and Engineering, 2003. **B101**: p. 19-23.
3. Cho, K.-S., et al., *High efficiency visible electroluminescence from silicon nanocrystals embedded in silicon nitride using a transparent doping layer*. Applied Physics Letters, 2005. **86**: p. 071909.
4. Cheng, K.-Y., et al., *High-Efficiency Silicon Nanocrystal Light-Emitting Devices*. Nano Letters, 2011. **11**(5): p. 1952-1956.
5. Liu, C.-Y., Z.C. Holman, and U.R. Kortshagen, *Hybrid solar cells from P3HT and silicon nanocrystals*. Nano letters, 2009. **9**(1): p. 449-452.
6. Erogbogbo, F., et al., *Bioconjugation of luminescent silicon quantum dots to gadolinium ions for bioimaging applications*. Nanoscale, 2012. **4**(17): p. 5483-5489.
7. Erogbogbo, F., et al., *In Vivo Targeted Cancer Imaging, Sentinel Lymph Node Mapping and Multi-Channel Imaging with Biocompatible Silicon Nanocrystals*. ACS Nano, 2011. **5**(1): p. 413-423.
8. Bapat, A., et al., *A plasma process for the synthesis of cubic-shaped silicon nanocrystals for nanoelectronic devices*. J. Phys. D: Appl. Phys., 2007. **40**: p. 2247-2257.
9. Mangolini, L., E. Thimsen, and U. Kortshagen, *High-yield plasma synthesis of luminescent silicon nanocrystals*. Nano Letters, 2005. **5**(4): p. 655-659.

10. Mariotti, D. and R.M. Sankaran, *Microplasmas for nanomaterials synthesis*. Journal of Physics D-Applied Physics, 2010. **43**(32).
11. Dogan, I., et al., *Ultra-high throughput plasma processing of free standing silicon nanocrystals with lognormal size distribution*. Journal of Applied Physics, 2013. **113**(13).
12. Jurbergs, D., et al., *Silicon nanocrystals with ensemble quantum yields exceeding 60%*. Applied Physics Letters, 2006. **88**: p. 233116 1-3.
13. Yasar-Inceoglu, O., et al., *Silicon nanocrystal production through non-thermal plasma synthesis: a comparative study between silicon tetrachloride and silane precursors*. Nanotechnology, 2012. **23**(25): p. 255604.
14. Anthony, R. and U. Kortshagen, *Photoluminescence quantum yields of amorphous and crystalline silicon nanoparticles*. Physical Review B, 2009. **80**(11).
15. Mangolini, L. and U. Kortshagen, *Selective nanoparticle heating: another form of nonequilibrium in dusty plasmas*. Physical review E, 2009. **79**(2): p. 026405.
16. Spinella, C., S. Lombardo, and F. Priolo, *Crystal grain nucleation in amorphous silicon*. Journal of Applied Physics, 1998. **84**(10): p. 5383-5414.
17. Li, T.S., D. Donadio, and G. Galli, *Nucleation of tetrahedral solids: A molecular dynamics study of supercooled liquid silicon*. Journal of Chemical Physics, 2009. **131**(22).
18. Li, T.S., et al., *Surface-induced crystallization in supercooled tetrahedral liquids*. Nature materials, 2009. **8**(9): p. 726-730.

## How bulk and surface thermodynamics affects Li battery material properties

Alexandra Navrotsky

Peter A. Rock Thermochemistry Laboratory and Nanomaterials in the Environment,  
Agriculture and Technology Research Unit  
University of California, Davis, CA 95616

### Program Description

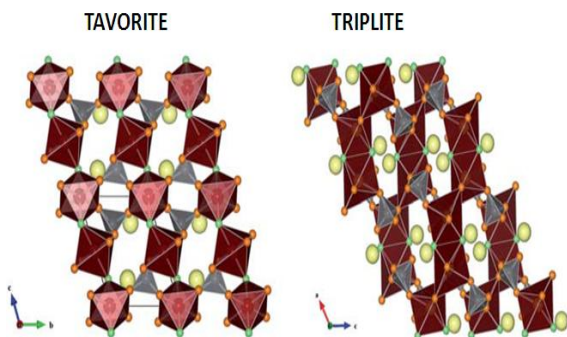
This project, “**Thermochemistry of Oxides with Electrochemical and Energy Applications**”, Alexandra Navrotsky, PI, represents a renewal, continuation, and redirection of a program emphasizing the thermodynamics of materials relevant to energy. The major objectives are: (a) to advance and use unique calorimetric capabilities to determine the energetics of oxide materials relevant to energy applications, with an emphasis on new materials for batteries and fuel cells, (b) to understand, in terms of both macroscopic energetics and microscopic structure and bonding, the interplay of defect chemistry, oxidation-reduction, and size effects at the nanoscale in determining the properties of oxides. In addition to completing work on ionic conductors and continuing to pioneer calorimetric studies of refractory materials above 1500 oC, this project will emphasize mixed ionic - electronic conducting materials containing transition metals of variable valence, especially perovskites ( $A_xRE_{1-x}M_yM'_{1-y}O_3$  (A = alkaline earth, RE = rare earth, M and M' = Mn, Fe, Co) and lithium containing rocksalt, spinel, olivine, and fluorosulfate phases with M = Mn, Fe, Co, Ni. In addition, thermochemical studies of purely ionic conductors (Bi<sub>2</sub>O<sub>3</sub> - based fluorite structured electrolytes, co-doped rare earth ceria, apatites) will be continued. The major and unique technique employed is high temperature oxide melt solution calorimetry, with careful attention to materials synthesis and characterization. Direct *in situ* studies of refractory oxides above 1500 oC by levitation melting and crystallization, synchrotron – based diffraction, and improved differential scanning calorimetry will probe structure and phase transitions in refractory oxides.

The materials under study find important applications in solid oxide fuel cells, gas separation membranes, catalysts, batteries, as well as nuclear energy and aerospace applications. Thus they are directly relevant to one of the Department of Energy’s basic missions, namely the development of more efficient energy sources and energy utilization. Fundamental and systematic thermodynamic data are essential for predicting possible new materials, for determining materials compatibility and longevity in use, for developing efficient synthesis and processing, and for assessing environmental impacts. From the point of view of basic science, this work addresses a number of DOE grand challenges as well as use-inspired fundamental questions. Understanding the relations of thermodynamics, structure and bonding addresses the grand challenge of “*how do we design and perfect atom- and energy-efficient synthesis of revolutionary new forms of matter with tailored properties?*” In addition, the project trains students and postdocs in careful measurements and rigorous data analysis and in working in a large multi-disciplinary group to prepare them for careers in the materials science of energy.

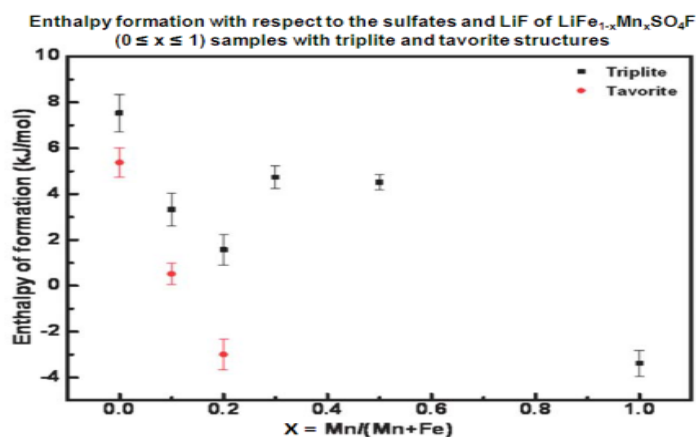
### Recent Progress

New cathode materials containing mixed anions (oxide, fluoride, sulfate, hydroxide) offer possible advantages in voltage and transport. Isothermal acid solution calorimetry was employed to investigate the relative thermochemical stabilities of two polymorphs of the  $LiFe_{1-x}Mn_xSO_4F$  ( $0 < x < 1$ ) solid solution series having triplite and tavorite structures. These compounds have

shown promise as lithium-ion battery cathodes, and a fuller understanding of their thermodynamics will aid in synthesis and their practical application. The linear energetic trends



indicate greater stabilization of each of these structures from the binary components with increase in manganese content and suggest a negligible heat of mixing of Fe and Mn ions. The tavorite phase, formed for  $x < 0.2$ , appears energetically more stable than the triplite. The formation of the disordered triplite structure appears to be entropy driven, and the factors that increase the disorder of the system (e.g. rapid phase formation) favor the triplite structure. Further, the free energy change associated with the tavorite to triplite transformation obtained by calculating configurational entropies using measured enthalpies was almost zero at ambient temperature but becomes exothermic at 500 °C. This suggests that both tavorite and triplite (with random cation distribution) are equally stable at ambient temperature but the tavorite to triplite transformation is thermodynamically favored at high temperatures because of entropy. The triplite phase is a better cathode material than the tavorite and this work confirms its stability under processing and



operating conditions.

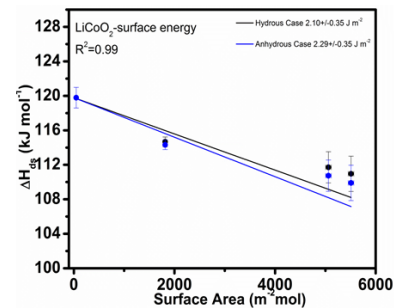
In the drive to obtain high charge/discharge rates in rechargeable lithium ion batteries (LIB), researchers have reduced electrode materials to the nanoscale. However, deleterious “nano effects” occur which may be due to altered surface structure (atomic arrangement, transition metal oxidation state, and electronic structure), which in turn may be strongly reflected in surface energetics which can affect lithium insertion. This work reports calorimetric measurements of surface energy and adsorption energy of H<sub>2</sub>O on nanophase stoichiometric LiCoO<sub>2</sub>. The experimental surface energies corroborate recent DFT calculations, supporting the concept of a change in cobalt coordination and spin state near the surface. The measured surface

### Surface energy of LiCoO<sub>2</sub>

Energy of hydrous surface  $2.10 \pm 0.35 \text{ J m}^{-2}$   
 Energy of anhydrous surface  $2.29 \pm 0.35 \text{ J m}^{-2}$   
 almost no stabilization by hydration

### Compare to CoO

Energy of hydrous surface  $2.82 \pm 0.20 \text{ J m}^{-2}$   
 Energy of anhydrous surface  $3.57 \pm 0.30 \text{ J m}^{-2}$



DFT calculations, Shirley Meng group (2012), give 2.1 J/m<sup>2</sup> for anhydrous surface, influenced by coordination geometry and spin state of Co<sup>3+</sup>

energy of  $\text{LiCoO}_2$  is much lower than values for other rocksalt oxides ( $\text{CoO}$ ,  $\text{NiO}$ ) and correlates with its lower affinity for water, as evidenced by its much lower enthalpy of water adsorption. The labile surface water may aid in transfer of lithium ions across the electrolyte - electrode interface. These observations suggest that strategies for further developing LIB electrodes should focus on the search for materials with low surface energies.

### Future Plans

We are continuing work on surface and hydration energies of nanophase battery related oxides to test the above hypothesis relating functionality and surface and hydration energetics. We are studying a series of hydroxysulfate battery materials provided by Tarascon in France. Mahboob Hosseini has completed her dissertation on apatite structured materials and we are preparing the remaining papers for publication. She has left for a job at Chevron. Salih Buyokkilic is completing his thesis on codoped ceria and we are writing papers. He will leave for a job at Intel by the end of 2013. Post doc Tien Tran has left for a teaching position at University of the Pacific and we are completing publications on bismuth oxide based materials.

### Publications

1. A. Sjastad, H. Fjellvag, K. Helean, and A. Navrotsky, "Enthalpy of Formation of  $\text{Ln}_2\text{O}_2\text{CO}_3$  II ( $\text{Ln} = \text{La}, \text{Nd}, \text{Eu}$ ) and Thermodynamics of Decomposition Equilibria" *Thermochim. Acta*, **550**, 76-82 (2012).
2. T. Tran and A. Navrotsky, "Energetics of Dysprosia-Stabilized Bismuth Oxide Electrolytes" *Chem. Mater.*, **24**, 4185-4191 (2012).
3. S. V. Ushakov and A. Navrotsky, "Experimental Approaches to the Thermodynamics of Ceramics Above  $1500^\circ\text{C}$ " *J. Am. Ceram. Soc.*, **95**, 1463-1482 (2012).
4. W. Zhou, S. V. Ushakov, and A. Navrotsky, "Yttria Stabilized Hafnia: Thermochemistry of Formation and Hydration of Nanoparticles" *J. Mater. Res.*, **27**, 1022-1028 (2012).
5. S. Buyokkilic, T. Shvareva, and A. Navrotsky, "Enthalpies of Formation and Insights into Defect Association in Ceria Singly and Doubly Doped with Neodymia and Samaria" *Solid State Ionics*, **227**, 17-22 (2012).
6. N. Kemik, S. V. Ushakov, M. Gu, N. Schichtel, C. Korte, N. D. Browning, Y. Takamura, and A. Navrotsky, "Yttria Stabilized Zirconia (YSZ) Crystallization in  $\text{Al}_2\text{O}_3/\text{YSZ}$  Multilayers" *J. Mater. Res.*, **27**, 939-943 (2012).
7. P. S. Maram, S. V. Ushakov, and A. Navrotsky, "Fluorite-Pyrochlore Transformation in  $\text{Eu}_2\text{Zr}_2\text{O}_7$  - Direct Calorimetric Measurement of Phase Transition, Formation and Surface Enthalpies" *Roy. Soc. Chem. Advances.*, **2**, 3328-3334 (2012).
8. A. Navrotsky, "Calorimetric Studies of the Stability of Perovskites Relevant to Electroceramics" *Electr. Chem. Soc. Trans.*, **45**, 11-17 (2012).

9. A. V. Radha, J. D. Furman, M. Ati, B. C. Melot, J. M. Tarascon, and A. Navrotsky, "Understanding the Stability of Fluorosulfate Li-ion Battery Cathode Materials: A Thermochemical Study of  $\text{LiFe}_{1-x}\text{Mn}_x\text{SO}_4\text{F}$  ( $0 \leq x \leq 1$ ) Polymorphs" *J. Mat. Chem.*, **22**, 24446-24452 (2012).
10. S. M. Hosseini, T. Shvareva, and A. Navrotsky, "Energetics of Lanthanum Silicate Apatite: Influence of Interstitial Oxygen and Cation Vacancy Concentrations in  $\text{La}_{9.33+x}(\text{SiO}_4)_6\text{O}_{2+3x/2}$  and  $\text{La}_{10-x}\text{Sr}_x(\text{SiO}_4)_6\text{O}_{3-0.5x}$ " *Solid State Ionics*, **233**, 62-66 (2013).
11. K. I. Lilova, R. Hord, L. Alff, B. Albert, and A. Navrotsky, "Thermodynamic Study of Orthorhombic  $T^x$  and Tetragonal  $T'$  Lanthanum Cuprate,  $\text{La}_2\text{CuO}_4$ " *J. Solid State Chem.*, **204**, 91-94 (2013).
12. S. K. Rakshit, S. C. Parida, K. Lilova, and A. Navrotsky, "Thermodynamic Studies of  $\text{CaLaFe}_{11}\text{O}_{19}(\text{s})$ " *J Solid State Chem.*, **201**, 68-74 (2013).
13. A. Tavakoli, H. Kondo, Y. Ukyo, and A. Navrotsky, "Stabilizing Effect of Mg on the Energetics of the  $\text{Li}(\text{Ni},\text{Co},\text{Al})\text{O}_2$  Cathode Material for Lithium Ion Batteries" *J. Electrochem. Soc.*, **160**, A302-A305 (2013).
14. L. Vradman and A. Navrotsky, "Surface Energetics of Nanoscale  $\text{LaMnO}_{3+\delta}$  Perovskite" *J. Am. Ceram. Soc.* (2013 Early View).
15. P. S. Maram, G. C. C. Costa, and A. Navrotsky, "Experimental Confirmation of Low Surface Energy in  $\text{LiCoO}_2$  and implications for Lithium Battery Electrodes" *Angew. Chem. Int. Ed.* (2013 In Press)

## A Fundamental Study of Inorganic Clathrate Open-Framework Materials

George S. Nolas (gnolas@usf.edu)

Department of Physics, University of South Florida, Tampa, 33620

### Program Scope

For many materials the preparation of high-quality single crystals by traditional techniques is especially challenging. Examples include cases where the elemental constituents have greatly differing melting points and/or vapor pressures, when the desired compound is thermodynamically metastable, or where growth with participation of the melt is generally not possible. A variety of synthetic techniques have been successfully employed in the preparation of intermetallic compounds [1, 2] however these approaches are typically not possible for the majority of new or metastable phases. As such, conventional crystal growth techniques are here generally inapplicable. New crystal growth techniques and apparatus are therefore essential in investigating the intrinsic and fundamental properties of new and novel materials. In this project we successfully initiated new approaches for the crystal-growth of intermetallic materials, including inorganic materials with clathrate-hydrate crystal structures and other “open-framework” materials, that allowed for a fundamental investigation of their intrinsic properties, in many cases for the first time. Compounds with the clathrate-II structure type, in particular, have not been previously investigated in detail due to the formidable task of synthesizing high-purity specimens. This material system is therefore ideal for testing new crystal growth techniques and/or apparatus. In addition, the rich variety of compositional variations found in these materials allow for a fundamental investigation into the properties of group 14 elements in novel crystal structures and bonding schemes. The intellectual merit of investigating this material system is very closely tied with its novel structure and the corresponding physical properties it exhibits, and aims to develop important fundamental research towards potential applications in power-conversion and energy storage technologies.

### Recent Progress

Synthetic techniques employed in the preparation of intermetallic compounds [1, 2] are typically inapplicable for the preparation of the majority of new and metastable phases, especially those with elements and/or properties that are not compatible with standard, well-known crystal-growth techniques, as described above. New crystal growth techniques and apparatus are therefore essential. Here we describe three crystal growth techniques developed under this DOE project, and optimized within the last two years. Together with our modified degassing approach we described previously,[3] these four synthetic techniques allow for the synthesis of new inorganic clathrate compounds as well as an investigation of the intrinsic properties of many of these materials for the first time.[4-9] The fundamental investigation and optimization of these techniques, namely spark plasma sintering (SPS), vapour-phase intercalation and ionic-liquid synthesis, represent a key aspect of our most recent efforts, and are outlined below.

#### *Spark Plasma Sintering for Synthesis and Crystal Growth*

Although initially developed for high temperature densification of refractory materials, [10] within the past two years we have employed SPS for the synthesis and crystal-growth, and subsequent measurement of the intrinsic physical properties, of several different clathrate and other compositions since first demonstrating the utility of this approach by growing single

crystals of  $\text{Na}_{24}\text{Si}_{136}$ . [11] Figure 1 outlines the technique. Published most recently [12] is a fundamental investigation of SPS crystal growth as a function of applied pressure, temperature and time. In this study, [12] the selective synthesis of clathrate-I  $\text{Na}_8\text{Si}_{46}$  and clathrate-II  $\text{Na}_{24}\text{Si}_{136}$  was achieved at different temperatures (450 and 600 °C, respectively). Moreover, the size of the crystals increased with increasing pressure, while microcrystalline powders were obtained at relatively low pressures. This study also revealed that an increase in reaction time resulted in an increase in yield. This investigation initiated, for the first time, a study of the affect of the SPS parameters on crystal growth and phase formation. SPS was also successfully employed for the synthesis of a clathrate-I Si-Ge alloy clathrates. SPS processing of a  $\text{Na}_4(\text{Si,Ge})_4$  precursor at 450 °C resulted in the synthesis of  $\text{Na}_8\text{Ge}_{2.8}\text{Si}_{40}\square_{3.2}$ . An investigation into the synthesis of Si-Ge clathrates and the subsequent investigation of the physical properties of these interesting compositions continues within this project.

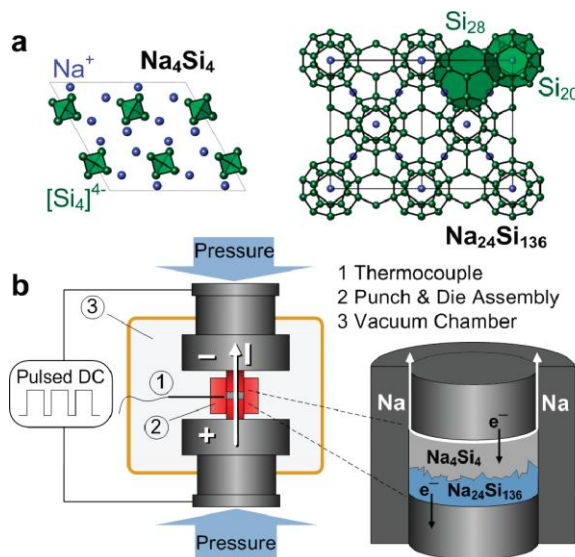


**Figure 1** Illustration of the SPS crystal growth technique. (a) Crystal structures of the  $\text{Na}_4\text{Si}_4$  precursor and  $\text{Na}_{24}\text{Si}_{136}$  crystals, with  $\text{Si}_{20}$  and  $\text{Si}_{28}$  polyndra which form the clathrate-II structure type and the  $\text{Si}_4$  tetrahedrons that form the precursor highlighted and (b) the SPS setup illustrating the growth of  $\text{Na}_{24}\text{Si}_{136}$  crystals along the current direction. Reversing the polarity of the current reverses the crystal growth, thus demonstrating that current induces the redux reaction to form the clathrate phase.

### *Vapour Phase Intercalation Technique*

In this approach, Na vapour, released from the  $\text{Na}_4\text{Si}_4$  precursor, reacts with the spatially separated graphite forming intercalation compounds  $\text{Na}_x\text{C}$  (see Figure 2). Powder X-ray diffraction of the graphite flakes recovered after the reaction confirms the presence of a mixture of stages of Na intercalated graphite. Presumably, the vapour pressure of Na over the intercalated graphite is less than that over  $\text{Na}_4\text{Si}_4$  such that the intercalation of the graphite results in further release of Na from the precursor in order to locally maintain the Na vapour pressure over the precursor. Continued reaction to form  $\text{Na}_x\text{C}$  continuously drives the composition in the precursor Si rich. Nucleation of the respective clathrate phase ensues as the Na content of the sintered body is reduced, and the continuously applied uniaxial pressure facilitates mass transport between precursor and growing crystal. The rate of these dynamic processes is expected to be limited by mass exchange through the vapour phase, as well as diffusion of Na out of the precursor and the reaction kinetics of  $\text{Na}_x\text{C}$  formation. We have applied our approach to different precursors, using

similar conditions to those described, to selectively grow single-crystals of clathrate-I and clathrate-II compounds. This approach was recently patented.[13]

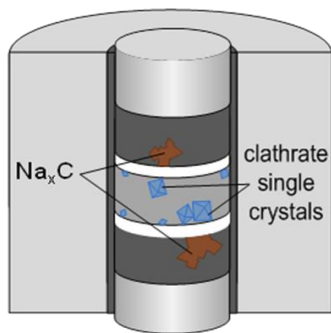


**Figure 2** Schematic illustrating crystal growth by our vapour phase intercalation technique. The precursor, under uniaxial pressure in the custom-designed punch and die assembly, is heated thereby resulting in a local composition change and nucleation of the clathrate phase. The formation of intercalated graphite demonstrates that the carbon, outside of the NaCl “sandwich”, helps to stabilize the Na vapor pressure thus promoting crystal growth.

### *Selective synthesis of clathrates by oxidation of precursors from ionic liquid decomposition*

The selective synthesis of  $\text{Na}_8\text{Si}_46$  and  $\text{Na}_{24}\text{Si}_{136}$  without clathrate impurity phases and in relatively high yield was achieved by oxidation of  $\text{Na}_4\text{Si}_4$  from the byproduct of the decomposition of the ionic liquid (IL) n-dodecyltrimethylammonium chloride (DTAC) combined with  $\text{AlCl}_3$ . [14] Maintaining separation of the IL from the precursor together with careful control of the synthetic parameters, temperature and time in particular, allowed for the synthesis of both clathrate structure types without need for further annealing.

The technique is straight forward. DTEC was combined with  $\text{AlCl}_3$  in a 1:1 molar ratio in a dry nitrogen glove box. The quartz vial that contained the  $\text{Na}_4\text{Si}_4$  precursor was placed inside the quartz tube, before sealing this tube, with the IL mixture at the bottom in order to ensure that the precursor is spatially separated from the IL. Unlike previous studies [15] we separate the IL from the precursor. This was essential in order to avoid secondary clathrate or amorphous phases. Moreover, in order to form the desired clathrate phases, the reaction temperature must be high enough for mass transport to occur in order to allow for structural rearrangements, but also low enough that the oxidation rate is not too high so as to prevent substantial removal of the sodium from the precursor. The low partial pressure of ILs achieves this oxidation rate balance. As the temperature increases so does the partial pressure thereby allowing for relative control of the oxidation rate and thus reducing the sodium content of the precursor. Structure refinement analyses from the X-ray diffraction data indicate full Na and Si occupancy for the  $\text{Na}_8\text{Si}_{46}$  and  $\text{Na}_{24}\text{Si}_{136}$  clathrates (see Figure 3). [14]

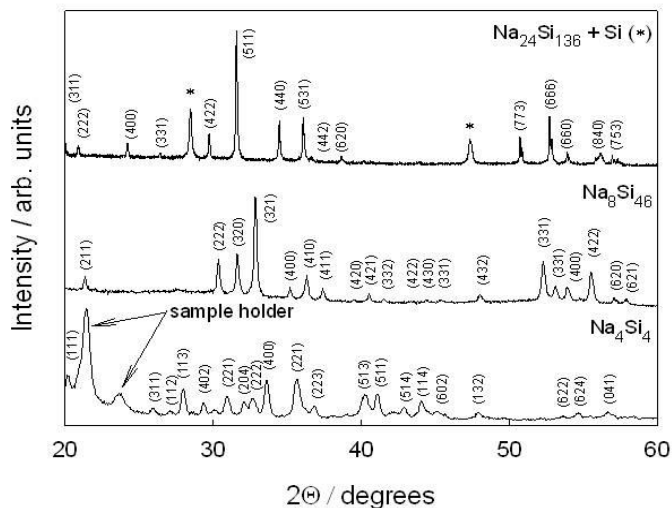


**Figure 3.** Powder XRD spectra of the  $\text{Na}_4\text{Si}_4$  precursor,  $\text{Na}_8\text{Si}_{46}$ , and  $\text{Na}_{24}\text{Si}_{136}$ . The Si peaks are marked with (\*). When the precursor  $\text{Na}_4\text{Si}_4$  was reacted for a period of 24 hours at temperatures of 210 to 240 °C, the result was the clathrate-II phase  $\text{Na}_{24}\text{Si}_{136}$ . Reactions at similar temperatures for 8 hours result in clathrate-I  $\text{Na}_8\text{Si}_{46}$  formation. Reactions for longer than 24 hours resulted in  $\alpha$ -Si formation and possibly amorphous phases. The highest yield of  $\text{Na}_{24}\text{Si}_{136}$ , 20% by weight, was achieved by reacting at 210 °C for 24 hours. Phase pure clathrate-I  $\text{Na}_8\text{Si}_{46}$  was obtained with a similar yield at 240 °C and a reaction time of 8 hours.

## Future Plans

The development of new and novel synthetic methods will allow for the investigation of new materials, and was a key focus under our DOE project. This effort also directly addresses the Synthesis and Processing Science focus area under DOE's Materials Science and Engineering Division, as well as allows for an investigation into the intrinsic structural and transport properties of these unique materials. We will continue and expanded on the investigation on Si-Ge clathrates, materials that are of interest for photovoltaic and thermoelectrics applications, and the subsequent measurements of their physical properties. In addition, theoretical input and guidance will be sought in providing input to identify other specific compositions that are of interest, based on their expected properties. Along with experimental analyses and feedback, an in-depth investigation of new materials with unique properties will be pursued.

## References

1. DOE/BES Workshop, "Future Directions of Design, Discovery and Growth of Single Crystals for Basic Research", Ames Laboratory, Iowa State University, Ames, IA, Oct 10-12, 2003.
2. "Frontiers of Crystalline Mater: From Discovery to Technology", National Academies Press, 2009.
3. M. Beekman, E.N. Nenghabi, K. Biswas, C.W. Myles, M. Baitinger, Y. Grin and G.S. Nolas, *Inorg. Chem.* 49, 5338 (2010).
4. M. Beekman, W. Schnelle, H. Borrmann, M. Baitinger, Yu. Grin and G.S. Nolas, *Phys. Rev. Letter* 104, 018301 (2010).
5. M. Beekman, R.P. Hermann, A. Mochel, F. Juranyi and G.S. Nolas, *J. Phys.: Cond. Matter* 22, 355401 (2010).
6. S. Stefanoski, J. Martin and G.S. Nolas, *J. Phys.: Condens. Mater* 22, 485404 (2010).
7. S. Stefanoski, M. Beekman, W. Wong-Ng, P. Zavalij, and G. S. Nolas, *Chem. Mater.* 23, 1491 (2011).
8. S. Stefanoski and G. S. Nolas, *Crystal Growth & Design* 11, 4533 (2011).
9. S. Stefanoski, C.D. Malliakas, M.G. Kanatzidis, and G.S. Nolas, *Inorg. Chem.* 51, 8686 (2012).
10. M. Tokita, *J. Soc. Powder Tech. Jpn.* 30, 790 (1993).
11. M. Beekman, M. Baitinger, H. Borrmann, W. Schnelle, K. Meier, G.S. Nolas, Y. Grin, *J. Amer. Chem. Soc.* 131, 9642 (2009).
12. S. Stefanoski, M.C. Blosser, and G.S. Nolas, *Cryst. Growth Des.* 13, 195 (2013).
13. M. Beekman and G.S. Nolas, "Novel Methods for Solid State Crystal Growth", US Patent 8,414,858, April 9, 2013.
14. M. C. Blosser and G.S. Nolas, *Mater. Lett.* 99, 161 (2013).
15. A.M. Guloy, R. Ramlau, Z. Tang, W. Schnelle, B. Bohme, M. Baitinger, Y. Grin, *Eur. J. Inorg. Chem.* 17, 2455 (2009).

## DOE sponsored publications (one text, two patents and 8 journal articles) over the last two years:

- 1) A.D. Ritchie, M.B. Johnson, J.F. Niven, M. Beekman, G.S. Nolas, J. Gryko, and M.A. White, 'Influence of Guest Loading on Thermal Properties of  $\text{Na}_x\text{Si}_{136}$  Clathrates', *J. Physics Condens. Matter*, in press (2013).
- 2) Z. Ge, K. Wei, and G.S. Nolas, 'Synthesis and Low Temperature Transport Properties of Polycrystalline  $\text{NiSe}_2$ ', *Phys Status Solidi A*, in press (2013).

- 3) S. Stefanoski, Y. Dong, and G. S. Nolas, 'Structural characterization and low-temperature physical properties of p-type single-crystal  $K_8Ga_{8.5}Sn_{37.5}$  grown by self-flux method', *J. Solid State Chem.* 204, 166 (2013).
- 4) M. C. Blosser and G.S. Nolas, 'Synthesis of  $Na_8Si_{46}$  and  $Na_{24}Si_{136}$  by oxidation of  $Na_4Si_4$  from ionic liquid decomposition', *Mater. Lett.* 99, 161 (2013).
- 5) S. Stefanoski, M. C. Blosser, and G.S. Nolas, 'Pressure Effects on the Size of Type-I and Type-II Si-Clathrates Synthesized by Spark Plasma Sintering', *Crystal Growth & Design.* 13, 195 (2013).
- 6) A.N. Mansour, J. Martin, W. Wong-Ng, and G. S. Nolas, 'Electronic and atomic structure of  $Ba_8Ga_{16}Ge_{30-x}Si_x$  type I clathrates: Ge and Ga XAFS study', *J. Phys. Cond. Matter* 24, 485503 (2012).
- 7) S. Stefanoski, C.D. Malliakas, M.G. Kanatzidis, and G.S. Nolas, 'Synthesis and Structural Characterization of  $Na_xSi_{136}$  ( $0 < x \leq 24$ ) Single Crystals and Low-Temperature Transport of Polycrystalline Specimens', *Inorg. Chem.* 51, 8686 (2012).
- 8) A. Chaturvedi, S. Stefanoski, M.H. Phan, G.S. Nolas, and H. Srikanth, 'Table-like magnetocaloric effect and enhanced refrigerant capacity in  $Eu_8Ga_{16}Ge_{30}$ -EuO composite materials', *Appl. Phys. Lett.* 99, 162513 (2011).
- 9) M. Beekman and G.S. Nolas, "Novel Methods for Solid State Crystal Growth", US Patent 8,414,858, April 9, 2013.
- 10) G.S. Nolas, S. Witanachchi and P. Mukherjee, "Method of Manufacturing a Clathrate Compounds", US Patent 8,211,400, July 3, 2012.
- 11) *The Physics and Chemistry of Clathrates*, edited by G.S. Nolas, Springer, Berlin, to be published in early 2014.

## Study of Spark-Plasma Sintering at Different Scale Levels

Eugene A. Olevsky  
Department of Mechanical Engineering  
San Diego State University, San Diego, CA

### Program Scope

Spark-plasma sintering (SPS) gains particular prominence in connection with its unique capabilities of processing very hard-to-deform materials, which would typically require lengthy consolidation times at significantly elevated temperatures under conditions of conventional powder pressing or sintering. SPS consists essentially of conjoint application of fast heating rates, high axial pressure and field (electric current - based) assisted sintering. The electric current passing through a powder specimen (Fig.1) or, in case of a non-conductive specimen, through a conductive die-punch tooling, generates Joule heat, which provides the conditions of hot compaction; the electric current also enhances densification and improves the final grain structure in quite a remarkable way. This approach significantly advances the processing time- and quality-wise. In particular, it carries the potential of maintaining the nano and sub-micron structure in nano-powder-based materials after consolidation. Practical implementations of the spark-plasma sintering's bright potential, however, are limited by the lack of theoretical concepts enabling the process to be predicted and optimized.

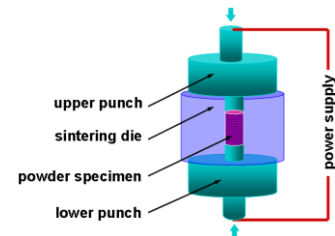


Fig. 1 Spark-Plasma Sintering schematics

The main fundamental issues addressed in the program are: what is the influence of rapid heating? Can the “flash” sintering effect be explained by the thermal runaway? Is there a so-called “non-thermal field effect” involved during SPS? How is the microstructure developed during SPS? How do the various processing parameters influence the microstructure and consequently the physical properties?

The main applied aspects of the present proposal are concerned with exploring the previously non-investigated utilization of the SPS and FPSPS techniques to the fabrication of porous materials, which are of great interest for nuclear fuel and other energy-related applications. This part of the project will involve interactions between PI's research group at San Diego State University and General Atomics.

### Recent Progress

We have analyzed the influence of SPS processing on the inter-particle contact area growth [1] and on densification [2].

We investigated the inter-particle neck growth kinetics of vanadium carbide powder during initial stages of conventional and spark-plasma sintering. Vanadium carbide ( $V_8C_7$ ) micron-size powder has been subjected to both Free Pressureless Spark Plasma Sintering (FPSPS – Fig. 2)) and conventional sintering dilatometry [1]. While the latter resulted not to be effective in the consolidation process, FPSPS procedure proved to be successful in terms of the initial stages of densification and inter-particle neck evolution, even without applying an external load. FPSPS was conducted with and without holding time, in order

to obtain experimental data on the inter-particle contact growth for different temperature regimes. The neck sizes derived from scanning electron microscopy observations (Fig. 3) were utilized in the inverse regression of the surface diffusion equation and led to the calculation of the value of the surface diffusion activation energy for the vanadium carbide powder, which resulted to be 210 kJ/mol. The proximity of the latter value to the previously known magnitude of the surface diffusion activation energy in Vanadium carbide systems indicates that the conventional surface diffusion models may be applicable to the description of the inter-particle neck growth kinetics at the initial stages of FPSPS-based consolidation.

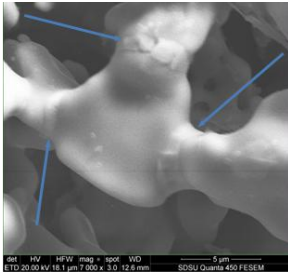


Fig.3 Neck growth in vanadium carbide powder during FPSPS

process. While at the initial stage particle re-arrangement appears to be the major densification rate-controlling factor, at the final stage the dominant creep mechanism, such as grain-boundary sliding may be responsible for the consolidation kinetics. The high heating rate and the field factors of SPS may promote the grain size retention, which is favorable for both particle re-arrangement and grain-boundary sliding. In particular, the interplay between surface diffusion and external pressure-imposed creep, if properly controlled, enables the optimal pore morphology and thus provides for the better efficiency of the SPS process (Fig.4). It is also possible that SPS-specific factors cause the decrease of the transitional porosity value, thereby accelerating the densification by prolonging the more consolidation-efficient initial stage of processing. On the other hand, the application of the external pressure may cause the excessive inter-particle contact growth at the “less desirable” process stages, leading to the decrease of the local stresses at the contact areas and, in turn, causing the process deceleration. The interplay of these factors may be the reason of the ambiguous SPS vs. hot pressing experimental comparative analyses’ outcomes.

The interaction of various consolidation-controlling factors may be different for different material classes. For ceramic materials with limited ductility, the application of the external pressure at the initial low-temperature stages of process, while not causing any substantial densification, may, however, lead to the formation of the inter-particle bonds, hindering particle rearrangement. For metal powder with high plasticity reserve at ambient temperatures, the early application of the external pressure, while causing substantial densification, may cause a topologically favorable shape evolution of the pores, when the contact areas size does not substantially increase.

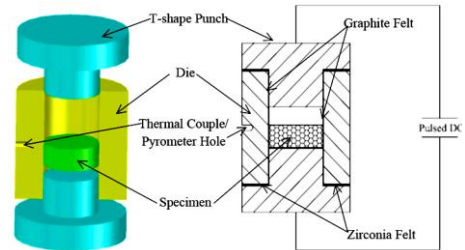


Fig. 2 Free Pressureless Spark Plasma Sintering (FPSPS) schematics

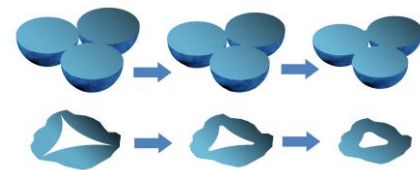


Fig. 4 Inter-particle contact area growth and evolution of pore morphology due to surface diffusion

Thus, while for ceramic powders, a gradual increase of the applied external pressure towards the final stage of the process may be recommended, for metal powders, the application of high pressure from the process start appears to be the optimal spark-plasma sintering strategy.

The above-mentioned discussion indicates also that the traditional model framework for the description of hot pressing processes needs to be updated to describe the true SPS kinetics: models involving the contact area-related parameters, besides the usually employed porosity, should be utilized for this purpose.

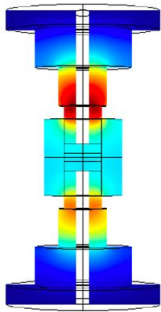


Fig.5 Finite-element modeling of SPS tooling overheating

The constitutive phenomena at the level of particle contacts impact the macroscopic behavior of powder materials subjected to SPS.

We have developed a three-dimensional coupled electrical, thermal, mechanical finite element macro-scale modeling framework of Spark Plasma Sintering (SPS) and applied it to the analysis of an actual problem of SPS tooling overheating, encountered during SPS experimentation [3]. The overheating phenomenon was analyzed by varying the geometry of the tooling that exhibits the problem, namely by modeling various tooling configurations involving sequences of disk-shape spacers with step-wise increasing radii (Fig. 5). The analysis was conducted by means of finite element simulations, intended to obtain temperature spatial distributions in the graphite press-forms, including punches, dies and spacers; to identify the temperature peaks and their respective timing, and to propose a more suitable SPS tooling configuration with the avoidance of the overheating as a final aim.

Electric currents-based Joule heating, heat transfer, mechanical conditions and densification were imbedded in the model, utilizing the finite-element software COMSOL™, which possesses a distinguishing ability of coupling multiple physics. Thereby the implementation of a finite element method applicable to a broad range of SPS procedures was carried out, together with the more specific optimization of the SPS tooling design when dealing with excessive heating phenomena.

## Future Plans

We plan on exploring the flash SPS concept considering thermal runaway phenomena to be its physical basis. We will study both the micro- and macroscopic aspects of flash SPS employing both theoretical analyses and model experiments.

We will further consider the challenge of SPS tooling optimization with the purpose of uniformization of temperature spatial distribution important for process stability.

The elaborated FPSPS will be employed along with regular SPS approaches for the consolidation of porous monocarbide powder specimens targeting energy applications.

## References

1. D. Giuntini, X. Wei, A.L. Maximenko, L. Wei, A.M. Ilyina, E.A. Olevsky Initial stage of free pressureless spark-plasma sintering of vanadium carbide: Determination of surface diffusion parameters, *Int. J. Refract. Met Hard Mater.*, 41, 501-506 (2013)
2. E. Olevsky, I. Bogachev, A. Maximenko, Spark-plasma sintering efficiency control by inter-particle contact area growth: A viewpoint, *Scripta Mater.*, 69(2), 112–116 (2013)

3. D. Giuntini, E. A. Olevsky, C. Garcia-Cardona, A. L. Maximenko, M. S. Yurlova, C.D. Haines, D. G. Martin, and D. Kapoor, Localized overheating phenomena and optimization of spark-plasma sintering tooling design, *Materials*, 6(7), 2612-2632 (2013)

### **DoE Sponsored Publications in the Last Two Years**

1. A.V. Kuzmov, E.A. Olevsky, E.V. Alexandrova, Micro-heterogeneity of powder heating under electric field-assisted sintering and its influence on shrinkage kinetics, *Powd. Met. Metal. Ceram.*, 11/12, 50-60 (2012)
2. D. Lahiri, E. Khaleghi, S. R. Bakshi, W. Li, E. A. Olevsky, and A. Agarwal, Graphene-induced strengthening in spark plasma sintered tantalum carbide-nanotube composite, *Scripta Mater.*, 68, 285-288 (2013)
3. K. I. Rybakov, E. A. Olevsky, and E. V. Krikun, Microwave sintering: Fundamentals and modeling, *J. Am. Ceram. Soc.*, 96, 1003–1020 (2013)
4. E. Olevsky, I. Bogachev, A. Maximenko, Spark-plasma sintering efficiency control by inter-particle contact area growth: A viewpoint, *Scripta Mater.*, 69(2), 112–116 (2013)
5. D. Giuntini, E. A. Olevsky, C. Garcia-Cardona, A. L. Maximenko, M. S. Yurlova, C.D. Haines, D. G. Martin, and D. Kapoor, Localized overheating phenomena and optimization of spark-plasma sintering tooling design, *Materials*, 6(7), 2612-2632 (2013)
6. D. Giuntini, X. Wei, A.L. Maximenko, L. Wei, A.M. Ilyina, E.A. Olevsky Initial stage of free pressureless spark-plasma sintering of vanadium carbide: Determination of surface diffusion parameters, *Int. J. Refract. Met Hard Mater.*, 41, 501-506 (2013)
7. E.A. Olevsky, A.L. Maximenko, and E.G. Grigoryev, Ponderomotive effects during contact formation in microwave sintering, *Model. Simul. Mater. Sci Eng.*, 21, 055022, (2013)

# Plasmonic Control of Radiation Processes for Enhanced Efficiency and Beam Shaping

**R. Paiella<sup>\*</sup> and T. D. Moustakas**

*Department of Electrical Engineering and Photonics Center, Boston University, Boston, MA 02215*

*\* Phone: 617-353-8883, Fax: 617-353-1283, Email: rpaiella@bu.edu*

## **1. Program Scope**

This research program is focused on the development of novel plasmonic nanostructures designed to engineer the radiation and absorption properties of nearby semiconductor photonic materials for enhanced efficiency and functionality. By virtue of their strongly confined plasmonic resonances, metallic nanoparticles (NPs) can concentrate incident radiation into sub-wavelength “hot spots” of highly enhanced field intensity [1], thereby increasing optical absorption by suitably positioned nanoscale absorbers. By reciprocity, the same NPs can also dramatically increase the spontaneous emission rate of radiating dipoles located within these hot spots. In this case, the far-field properties of the emitted light (including polarization and directionality) are then determined by the nature of the NP plasmonic excitations involved in the radiation process, rather than of the original dipole sources. The NPs can therefore be used to enhance the light-emission efficiency of the underlying active material and at the same time control the output radiation far-field profile.

The study of these phenomena can address a number of basic questions related to the optical properties of metallic nanostructures, including their ability to exchange energy with nearby absorbing or radiating species through resonant near-field interactions, the nature of plasmonic dissipation (i.e., scattering versus absorption), and the far-field radiation properties of plasmonic excitations. The same phenomena may also pave the way to new device concepts and applications in a wide range of disciplines, including optoelectronics, sensing, spectroscopy, photovoltaics, and quantum information science.

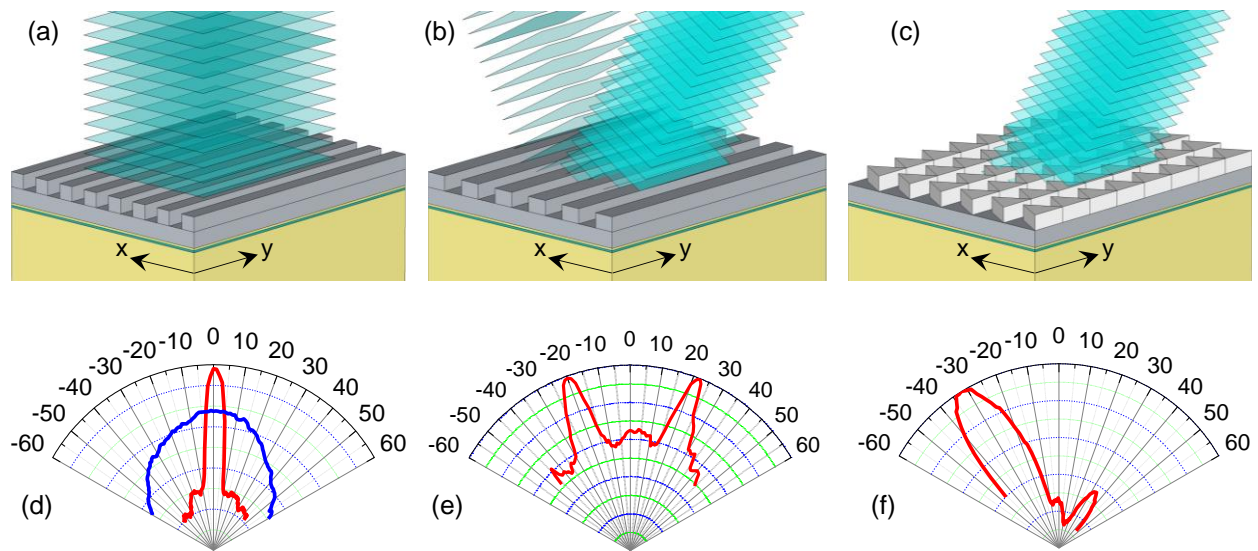
The specific semiconductor active materials employed in this project involve quantum-well (QW) and quantum-dot (QD) samples based on the InGaN materials system. Nitride semiconductors in general provide an ideal solid-state platform for the proposed studies, because of their widely tunable bandgap energies across the visible spectrum (where the plasmonic resonances of typical metallic nanostructures occur) and favorable near-surface optical properties. Furthermore, these materials are technologically important for a wide range of optoelectronic device applications, including LEDs for solid-state lighting, which could benefit strongly from the proposed plasmonic interactions. The use of highly localized QDs will also allow us to directly probe the giant optical-field enhancements produced by metallic NPs in their hot spots.

## **2. Recent Progress**

Earlier work in this project has focused on the use of square periodic arrays of Ag nanocylinders to increase the radiative efficiency of InGaN/GaN QWs emitting at blue/green visible wavelengths [2, 3]. The arrays were designed using finite difference time domain (FDTD) simulations, and fabricated on the top surface of the QW active material using electron-beam lithography. The resulting samples were investigated via cw and time-resolved

photoluminescence (PL) measurements, showing a substantial decrease in the QW recombination lifetime and a strong increase in the overall PL intensity brought about by the plasmonic nanostructures. These observations reveal a picture of plasmon-enhanced light emission, where strongly increased exciton recombination takes place in the QW regions immediately below the NPs via the near-field excitation of the NP plasmonic resonances. Particularly large (up to nearly 5 $\times$ ) PL intensity enhancements were obtained with diffractive NP arrays, based on the coupling between the QW excitons and lattice surface modes of mixed plasmonic and photonic character [3].

More recent activities have focused on the development of plasmonic nanoantenna arrays designed to control the far-field radiation pattern of similar QW light emitting samples [4]. The underlying physical mechanism involves the near-field excitation by the QW electron-hole pairs of propagating surface plasmon polaritons (SPPs) on an ultrathin metal film, which are then diffractively scattered by an array of metallic NPs periodically arranged on the film. In the experimental samples, all metallic nanostructures were based on Ag and were fabricated on the top surface of the QW active material with a combination of electron-beam evaporation and electron-beam lithography. The Ag film is sufficiently thin (40 nm) to enable strong coupling and hybridization between the SPPs supported by its bottom and top surfaces and the localized



plasmonic resonances of the overlaying NPs [5].

**Fig. 1.** Plasmonic nanostructures designed to provide beaming of luminescence (a) along the sample surface normal, (b) along two equal and opposite directions, and (c) along a single oblique direction. (d), (e), (f) Red traces: experimental  $p$ -polarized far-field radiation patterns measured with representative samples based on the geometries of (a), (b), and (c), respectively. The blue trace in (a) is the  $p$ -polarized far-field radiation pattern of the bare QW sample.

Within this general context, a particularly simple geometry consists of a one-dimensional array of rectangular Ag ridges on the Ag film, as illustrated in Figs. 1(a) and 1(b). In this case, if the grating period  $\Lambda$  is chosen so that  $2\pi/\Lambda$  is equal to the wavenumber  $k_{SPP}$  of the excited SPPs,

first-order diffraction of these surface waves results in (one-dimensional) beam collimation along the sample surface normal [Fig. 1(a)]. Vice versa, if the grating period is detuned from the SPP wavelength  $2\pi/k_{SPP}$ , diffraction of forward and backward propagating SPPs leads to the emission of two output beams along equal and opposite angles with respect to the surface normal [Fig. 1(b)].

The experimental demonstration of these ideas is shown in the polar plots of Figs 1(d) and 1(e), where the red traces correspond to the  $p$ -polarized far-field intensity patterns measured with two samples of grating period  $\Lambda = 400$  nm and 600 nm, respectively. These traces were obtained via angle-resolved PL measurements, with the sample region underneath the array pumped at normal incidence through the backside. The resulting PL signal was then measured from the metal-coated top surface, with the collection optics rotated about the excitation spot.

The expected behavior is clearly observed in these plots. For  $\Lambda = 400$  nm [Fig. 1(d)], strong collimation along the sample surface normal is obtained, indicating that the corresponding grating wavenumber  $2\pi/\Lambda$  closely matches  $k_{SPP}$ . A divergence angle as small as  $12^\circ$  (full width at half maximum) is obtained in this case; by comparison, a value of about  $120^\circ$  is measured with the same QW samples without any metallic nanostructure, as shown by the blue trace in Fig. 1(d). At larger grating periods, the far-field pattern consists of two output beams propagating along equal and opposite angles [as illustrated in Fig. 1(e)], whose absolute value increases with increasing  $\Lambda$ . In all these grating samples, the  $s$ -polarized emission was also found to be substantially weaker than the  $p$  component, and as a result it only adds a small pedestal to the overall intensity profile. The reason is that  $s$ -polarized light in this geometry originates from the in-plane components of the excitonic dipoles, whose coupling to the Ag-film SPPs is much weaker than that of the out-of-plane component [1].

Within the same context, we have then demonstrated the ability to generate a well collimated optical beam that emerges from the sample surface along a single geometrically tunable direction (off-axis unidirectional beaming), based on the use of more complex array geometries. Specifically, we have shown that, if grating lines with an asymmetric shape in the direction of the periodicity are employed [such as the lines of triangular NPs in Fig. 1(c)], forward diffractive scattering can be suppressed in favor of backward diffraction (or vice versa), leading to predominant emission in a single direction. A top-view SEM image of a representative sample is presented in Fig. 2, where the various geometrical parameters that can be used to control the NP scattering cross section are also indicated.

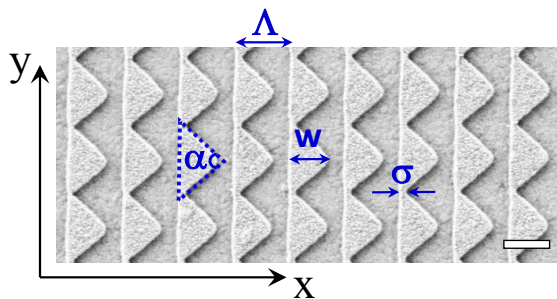


**Fig. 2.** Top-view SEM image of an array of triangular Ag NPs fabricated on an ultrathin Ag film on a QW light-emitting sample to demonstrate plasmonic off-axis unidirectional beaming of luminescence. The scale bar is 500 nm.

In Fig. 1(f) we show the  $p$ -polarized far-field radiation pattern measured with one of these samples, with  $w = 410$  nm,  $\sigma = 50$  nm,  $\alpha = 68^\circ$ , and  $\Lambda = 550$  nm. A strongly asymmetric profile is clearly obtained, with most of the output light emitted in a single beam at a nonzero angle (about  $32^\circ$ ) with respect to the sample surface normal. By varying the relevant geometrical parameters (particularly  $\Lambda$  and  $\alpha$ ), this angle can be tuned over a wide range, as also shown in our recent work [4]. These experimental results are well reproduced by FDTD simulations based on the principle of reciprocity, which were used to develop a detailed picture of the underlying beaming mechanism.

It should be noted that this demonstrated ability to obtain unidirectional beaming at geometrically tunable oblique angles provides a new functionality in the context of planar light-emitting samples of arbitrary spatial extent. Our approach is also fundamentally different from recent reports of plasmonic beam shaping from nanoscale sources, which rely instead on an optimized positioning of the emitter relative to a single antenna or metallic grating [6]. In contrast, the present approach can be applied to a continuous distribution of randomly oriented dipoles over a wide surface area (as is commonly encountered in typical optoelectronic devices), thanks to the extended nature of the SPPs involved in the beamed emission. As a result, this approach may be used to control the output light directionality of a wide range of luminescent devices, with a spatial resolution that simply would not be possible with bulk optics.

### 3. Future Plans

Future activities will focus on three related thrusts. First, we will continue to investigate the use of phased arrays of asymmetric nanoantennas coupled to ultrathin metal films to engineer the far-field radiation properties of extended-area light emitters. Specific opportunities in this context include the demonstration of two-dimensional beaming (i.e., with respect to both the  $y$ - $z$  and the  $x$ - $z$  planes of Fig. 1), beaming accompanied by plasmon-enhanced light emission, and (by reciprocity) direction-sensitive photodetection. Second, we will develop InGaN QD-based samples that can be used to fully investigate and exploit the giant optical field enhancements produced by metallic NPs in their hot spots, by virtue of the QDs highly localized nature. These samples will be grown via self-assembly techniques based on molecular beam epitaxy, followed by the fabrication of metallic NPs accurately aligned to individual QDs, and by the investigation of the resulting highly enhanced exciton-plasmon coupling. Finally, NP arrays on high-density QD samples will be developed to investigate plasmon-enhanced absorption and photocurrent generation based on intraband transitions between the QD bound states and the conduction-band continuum of the barrier material. These processes are important for the demonstration of high-efficiency photovoltaic energy conversion based on the intermediate-band device concept – a potentially transformative application for which the band-structure properties of InGaN QDs are ideally suited.

### 4. References

- [1] S. A. Maier, *Plasmonics: Fundamentals and Applications* (Springer: New York, NY, 2007).
- [2] J. Henson, E. Dimakis, J. DiMaria, R. Li, S. Minissale, L. Dal Negro, T. D. Moustakas, and R. Paiella, *Opt. Express* **18**, 21322 (2010).
- [3] J. Henson, J. DiMaria, E. Dimakis, T. D. Moustakas, and R. Paiella, *Opt. Lett.* **37**, 79-81 (2012).
- [4] J. DiMaria, E. Dimakis, T. D. Moustakas, and R. Paiella, in preparation.

[5] J. DiMaria and R. Paiella, *J. Appl. Phys.* **111**, 103102 (2012).

[6] A. G. Curto, G. Volpe, T. H. Taminiau, M. P. Kreuzer, R. Quidant, and N. F. Van Hulst, *Science* **329**, 930-933 (2010).

### **5. Publications supported by this grant over the last two years**

T. D. Moustakas, "The Role of Extended Defects on the Performance of Optoelectronic Devices in Nitride Semiconductors," *Phys. Status Solidi A* **210**, 169 (2013).

J. DiMaria and R. Paiella, "Plasmonic Dispersion Engineering of Coupled Metal Nanoparticle-Film Systems," *J. Appl. Phys.* **111**, 103102 (2012).

J. Henson, J. DiMaria, E. Dimakis, T. D. Moustakas, and R. Paiella, "Plasmon-Enhanced Light Emission Based on Lattice Resonances of Silver Nanocylinder Arrays," *Opt. Lett.* **37**, 79-81 (2012).

R. Paiella, J. Henson, J. DiMaria, E. Dimakis, R. Li, S. Minissale, L. Dal Negro, and T. D. Moustakas, "Plasmon-Enhanced Near-Green Light Emission from InGaN/GaN Quantum Wells," 220<sup>th</sup> ECS Meeting, paper 2084 (**invited**), Boston (MA), Oct 2011; full article published in *ECS Trans.* **41**, 73 (2011).

# **New Oxide Materials for an Ultra High Temperature Environment**

**J.H. Perepezko**

**University of Wisconsin-Madison**

**Department of Materials Science and Engineering**

**1509 University Ave. Madison, WI 53706**

## **Program Scope**

The development of ceramics that provide a robust performance in an aggressive high temperature environment is a continuing challenge. Materials for high temperature environments must satisfy several stringent requirements that dictate a high melting temperature and stability in an oxidizing environment that often contains water vapor as well as other compatibility issues. The available ceramics such as zirconates, sialons, diborides or carbides satisfy some of the requirements such as high melting temperature, but they also exhibit limitations such as a high oxidation rate or surface decomposition especially in the presence of water vapor

What is needed for enhanced high temperature capability are new oxide materials. From the existing experience we are pursuing a new strategy that involves internal modification control of the outer surface of diborides to promote enhanced oxidation resistance. The internal modification focuses upon the development of a new oxide type based upon HfTaO and ZrTaO superstructures which lowers the oxidation rate. The oxide superstructures are metastable in the binary Hf-O and Zr-O systems, but preliminary experiments confirm that they can be stabilized by Ta additions.

The research focus is on a systematic fundamental study of the phase stability, defect structure and reaction kinetics of the oxide superstructures. The program also includes an investigation of the oxide superstructures constitution, the development of a microstructure based kinetics model for the oxidation behavior of multicomponent boride composites and an evaluation of the thermal barrier characteristics.

## **Background**

The heightened interest in energy generation and efficiency has highlighted the long standing importance of high temperature ceramic materials that exhibit reliable performance in aggressive environments. At the same time, it is also well established that the properties and performance of oxides as oxidation resistant coatings that act to impede oxygen diffusion is closely linked to their structure. Similarly, in another important application of oxides to function as thermal barrier coatings, their performance is determined by structural characteristics as well as their thermodynamic and mechanical compatibility with an underlying substrate [1].

As the drive for higher temperature use continues, the number of available materials shrinks drastically. While a few candidates have been identified such as zirconates, sialons and diborides, most of the recent attention has been focused on diborides ( $ZrB_2$  and  $HfB_2$ ) for high

temperatures due to a number of attributes such as favorable mechanical and thermal properties [2]. However, the diborides such as  $ZrO_2$  do not exhibit acceptable oxidation behavior as monolithic material since the oxidation reaction at high temperature yields a volatile  $B_2O_3$  and a porous skeleton of  $ZrO_2$ . This has been addressed, in part, by composite designs where SiC is incorporated with the diboride to provide an outer  $SiO_2$  layer during oxidation. However, there are limitations to this approach. For example,  $SiO_2$  decomposes to  $SiO(g)$  above about  $1800^\circ C$  and the reaction is enhanced at lower temperature in a combustion environment with water vapor[3]. In order to achieve an enhancement of the oxidation resistance a number of different additives have been examined with the aim of altering the defect structure of  $ZrO_2$  [4]. While there have been some improvements with this approach, the oxidation attack is still significant.

In another important application of oxides to function as thermal barrier coatings (TBC) their performance is determined again by structural characteristics as well as their thermodynamic and mechanical compatibility with an underlying substrate. Many oxides have a low thermal conductivity including yttria stabilized zirconia (YSZ). However, the drive for a further increase in operating temperature has motivated an effort to identify oxides with even lower thermal conductivity than YSZ. As a result of this effort rare earth oxides (REO) have emerged as one of the leading candidates to supplant YSZ. However, there are some technical issues concerning the performance of REOs as well as the issue of sufficient availability.

What is needed for enhanced high temperature capability are new materials either in the form of new oxides or new surface coatings. There are a large number of ternary and higher order oxides involving two or more metal components. The multicomponent oxide structures develop at much higher additive levels than those typically involved in doping, but the structural modifications can also have a significant impact on oxygen transport. For example, in the case of transition metals, the characteristic multiple valence states are associated with different oxide structures. This characteristic behavior suggests a possible route to identify new high temperature oxides that can also inhibit oxygen transport.

From the existing experience, we have started to examine a new strategy that involves internal modification and control of the outer surface to promote enhanced oxidation resistance. The internal modification focus is based upon the development of a new oxide type based upon HfTaO and ZrTaO superstructures which can lower the oxidation rate. Our approach to identifying and understanding the science-based design principles is focused upon a systematic experimental program to identify the kinetic and thermodynamic pathways governing oxide synthesis and performance. The incorporation of the governing thermodynamic and kinetic relationships provides the basis for an integrated coating structure.

In preliminary work we have confirmed the development of oxide superstructures on Hf-Ta alloys as shown in figure 1 following an exposure to  $1650^\circ C$  for 10 min. There is a clear trend of decreasing oxide thickness with increasing Ta level up to 27wt %Ta. During oxidation a well bonded oxide develops that shows thermal shock resistance and freedom from breakaway failure modes. Moreover, the micrographs of oxidized sample cross sections in figure 2 reveal the development of an intermediate reaction zone between the outer surface oxide and the alloy

substrate. X-ray diffraction analysis was employed to identify the structure in the reaction zone product as the  $\text{Hf}_7\text{Ta}_2\text{O}_{19}$  oxide superstructure with reduced mobility for oxygen transport. This is a new result that suggests that the improvement in the oxidation resistance is also accompanied the conversion of the monoclinic  $\text{HfO}_2$  into one type of the homologous  $\text{Hf}_{1/2(n-5)}\text{Ta}_2\text{O}_n$  ( $n=15,17$  and 19) oxide superstructures. However, the mechanism by which tantalum can be added into Hf-based known oxides (which include monoclinic, tetragonal as well as cubic structural

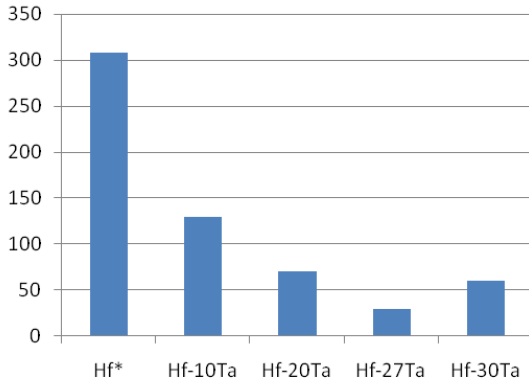


Figure 1. Oxide scale thickness ( $\mu\text{m}$ ) for  $1650^\circ\text{C}$  exposure for 10 min showing the effect of tantalum substitution for Hf in Hf-Ta alloys.

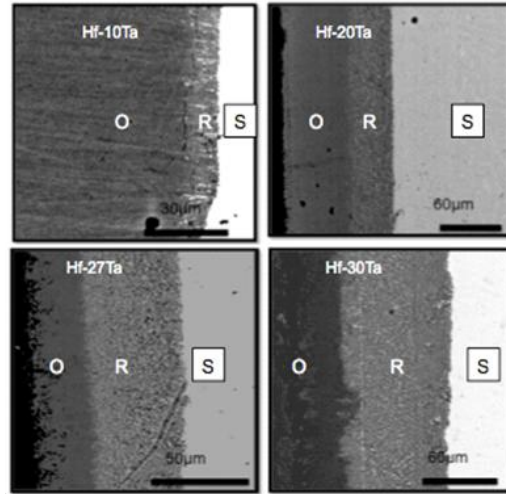


Figure 2.  $1650^\circ\text{C}$  exposure-sample cross section (O-oxide scale, R-reaction zone, S-alloy substrate).

variants) to synthesize the oxide superstructures is not clear and there is very limited available data on the pseudo-binary of  $\text{HfO}_2 - \text{Ta}_2\text{O}_5$ .

## Future Plans

The initial period of the program will aim at synthesizing multicomponent boride systems, evaluating the phase stability of the homologous series oxide superstructures and measuring selected thermodynamic properties (i.e.  $C_p$  and  $\alpha$ ). For the sample synthesis we will develop  $(\text{Hf},\text{Ta})\text{B}_2$  solid solutions through a sintering process or by a reaction synthesis. The reported phase diagrams of Hf-Ta-B and Zr-Ta-B systems show that there is a *continuous* solid solution of  $\text{HfB}_2/\text{ZrB}_2$  and  $\text{TaB}_2$ . For the development of the  $(\text{Hf},\text{Zr})\text{TaO}$  oxide superstructures we will expose the diboride solid solutions to oxidation at different oxygen partial pressures. For the phase stability evaluation an available high temperature furnace can be used to detect whether there is an onset to melting up to the furnace limit of  $2500^\circ\text{C}$ . Similarly, the high temperature XRD facility can be used to determine if there is a solid state structural transition up to  $2200^\circ\text{C}$  and provide measurements of the expansion coefficient. The heat capacity can also be determined up to  $1500^\circ\text{C}$  in a high temperature DSC. For the phase equilibria between the

homologous oxide superstructures another approach will be used based upon the examination of diffusion couples. By varying the base alloy composition in the diffusion couples, different oxide structures will develop through different diffusion pathways. The composition profile across the diffusion couple and oxygen diffusivity can be determined by electron probe and ion beam microanalysis.

### **References**

1. A.G. Evans, D.R. Mumm, J.W. Hutchinson, G.H. Meier and F.S. Petit, *Prog. Mater. Sci.*, vol. 46 (2001) 505-553.
2. W.G. Fahrenholtz, G. E. Hilmas, I.G. Talmy and J.A. Zaykoski, *J. Am. Ceram. Soc.*, vol. 90 (2007) 1347-1364
3. E.J. Opila, *J. Am. Ceram. Soc.*, vol.86 (2003) 1238-1248.
4. E.J. Opila, S.Levine, J. Lorincz, *J. Mat. Sci.*, vol. 39 ( 2004) 5969-5977.

## Phase Transformations and Equilibria in Complex Half-Heusler/Full-Heusler Nanocomposites

- ❖ **Dr. Pierre Ferdinand Poudeu; Materials Science and Engineering, University of Michigan**
- ❖ **Dr. Ctirad Uher; Department of Physics, University of Michigan**
- ❖ **Dr. Anton Van der Ven; Materials Department, University of California Santa-Barbara**

### Program Scope

This project focuses on the development of innovative synthetic strategies for the fabrication of bulk nanocomposites, which consist of a semiconducting half-Heusler (HH) matrix containing metallic full-Heusler (FH) sub-ten nanometer inclusions coherently embedded within the matrix. The embedded FH nano-inclusions are expected to act as “energy filters” to low energy carriers leading to spectacular enhancements of the thermoelectric figure of merit of the HH/FH nanocomposite materials. The synthesized nanocomposites will be structurally characterized using electron microscopy and X-ray diffraction and their thermal and electronic properties at various temperatures will be investigated. The goals are to study the mechanism of phase formation and transformations leading to the stability of FH inclusions within the HH matrix and to elucidate the mechanism by which the embedded inclusions govern electronic transport within the HH matrix and induce large enhancements of the thermoelectric properties.

### Recent Progress

During the first year of this project, we focused our attention on the synthesis, structural characterization, and evaluation of the thermal and electronic transport in n-type  $(\text{Ti,Zr})\text{Ni}_{1+x}\text{Sn}$  and p-type  $\text{Ti}_{0.5}\text{Hf}_{0.5}\text{Co}_{1+x}\text{Sb}_{0.9}\text{Sn}_{0.1}$  nanocomposites. In addition, we have studied the effect of synthesis and processing methods on the microstructure and electronic transport of bulk half-Heusler phases.

#### ***1) The n-type $(\text{Ti,Zr})\text{Ni}_{1+x}\text{Sn}$ and p-type $\text{Ti}_{0.5}\text{Hf}_{0.5}\text{Co}_{1+x}\text{Sb}_{0.9}\text{Sn}_{0.1}$ half-Heusler (HH) / full-Heusler (FH) composite systems***

Several  $(\text{Ti,Zr})\text{Ni}_{1+x}\text{Sn}$  (varying x values) compositions were synthesized using high temperature solid-state reactions and their crystal structure and microstructures were investigated using X-ray diffraction and TEM. Electronic and thermal transports of the synthesized composites were evaluated and correlations between the observed transport behavior and the microstructures were established [1]. X-ray powder diffraction (XRD) data (Figure 1) of the as-synthesized  $\text{Ti}_{0.1}\text{Zr}_{0.9}\text{Ni}_{1+x}\text{Sn}$  (x = 0.02, 0.04 and 0.1) materials suggested the formation of HH product as all diffraction peaks were indexed in the cubic  $\text{MgAgAs}$  structure type (space group:  $F-43m$ ). However, transmission electron microscopy (TEM) study performed on selected specimens revealed the presence of spherical FH precipitates with the size ranging from 10 to 60 nm forming coherent interfaces with the HH matrix.

Electronic transport data on the synthesized nanocomposites indicated a large decrease in the carrier density when compared to that of the pristine of  $\text{Ti}_{0.1}\text{Zr}_{0.9}\text{NiSn}$  (HH) matrix, leading to simultaneous large enhancements of the thermopower (up to 200%). Interestingly, a significant increase in the carrier mobility was also observed which minimized the drop in the electrical conductivity. This unusual behavior of the electronic transport was rationalized by introducing

the concept of carrier culling at the HH/FH phase boundaries. We proposed that the embedded FH-QD forms a potential barrier at the interface with the matrix due to the offset of their conduction band minima (CBM) (Figure 2). This potential barrier discriminates existing charge carriers from the conduction band of the matrix with respect to their relative energy leading to simultaneous large enhancements of the thermopower (up to 200%) and carrier mobility (up to 43%) of the resulting  $\text{Ti}_{0.1}\text{Zr}_{0.9}\text{Ni}_{1+x}\text{Sn}$  nanocomposites.

The improvement in  $S$  with increasing mole fraction of the FH-QDs arises from a drastic reduction (up to 250%) in the effective carrier density coupled with an increase in the carrier's effective mass ( $m^*$ ), whereas the

surprising enhancement in the mobility ( $\mu$ ) is attributed to an increase in the carrier's relaxation time ( $\tau$ ). This strategy to manipulate the transport behavior of existing ensembles of charge carriers within a bulk semiconductor using QDs is very promising and could pave the way to a new generation of thermoelectric materials with high figure of merit.

This atomic scale engineering of the electronic transport within a HH matrix using nanometer scale second phases with FH structure was also successfully applied to the p-type  $\text{Ti}_{0.5}\text{Hf}_{0.5}\text{Co}_{1+x}\text{Sb}_{0.9}\text{Sn}_{0.1}$  HH/FH nanocomposite systems [2]. We found that the coherently embedded nanometer scale FH inclusions greatly altered the electronic transport behavior of the existing ensemble of free charge carriers within the p-type HH matrix ( $\text{Ti}_{0.5}\text{Hf}_{0.5}\text{Co}_{1+x}\text{Sb}_{0.9}\text{Sn}_{0.1}$ ) [2].

## 2) Correlation between Processing Conditions, Microstructure and Charge Transport in Half-Heusler Alloys

To fully understand the effect of synthesis and processing methods on the microstructure and electronic transport of half-Heusler phases, we have performed a systematic investigation of

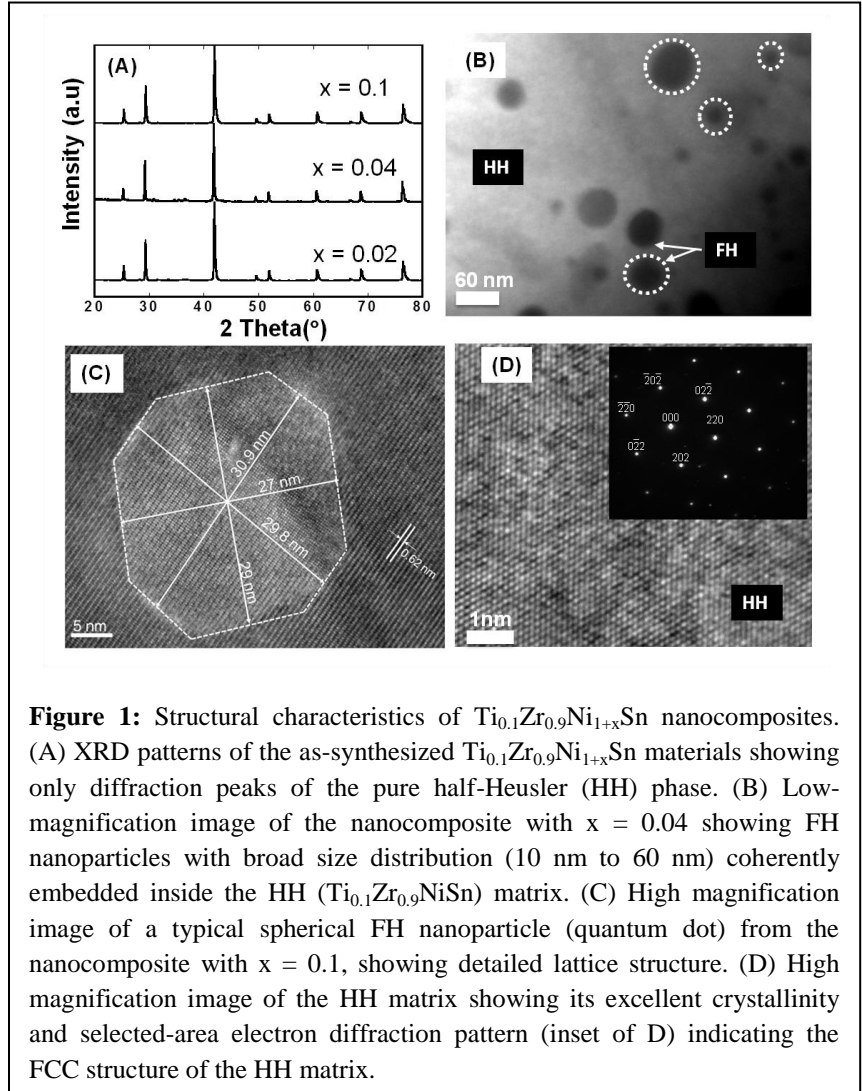


**Figure 1:** Structural characteristics of  $\text{Ti}_{0.1}\text{Zr}_{0.9}\text{Ni}_{1+x}\text{Sn}$  nanocomposites. (A) XRD patterns of the as-synthesized  $\text{Ti}_{0.1}\text{Zr}_{0.9}\text{Ni}_{1+x}\text{Sn}$  materials showing only diffraction peaks of the pure half-Heusler (HH) phase. (B) Low-magnification image of the nanocomposite with  $x = 0.04$  showing FH nanoparticles with broad size distribution (10 nm to 60 nm) coherently embedded inside the HH ( $\text{Ti}_{0.1}\text{Zr}_{0.9}\text{NiSn}$ ) matrix. (C) High magnification image of a typical spherical FH nanoparticle (quantum dot) from the nanocomposite with  $x = 0.1$ , showing detailed lattice structure. (D) High magnification image of the HH matrix showing its excellent crystallinity and selected-area electron diffraction pattern (inset of D) indicating the FCC structure of the HH matrix.

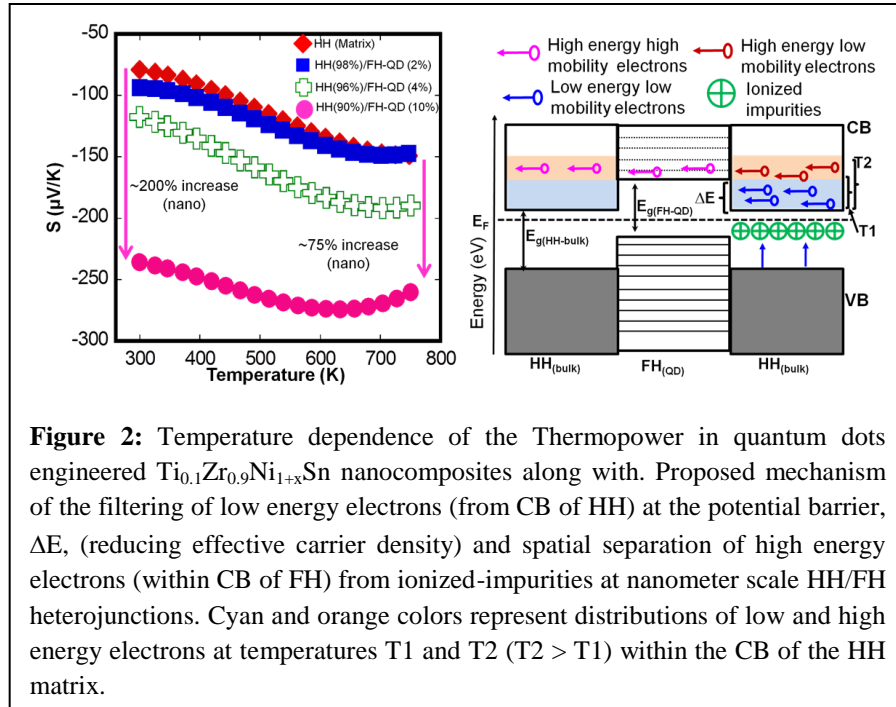


**Figure 2:** Temperature dependence of the Thermopower in quantum dots engineered  $\text{Ti}_{0.1}\text{Zr}_{0.9}\text{Ni}_{1-x}\text{Sn}$  nanocomposites along with. Proposed mechanism of the filtering of low energy electrons (from CB of HH) at the potential barrier,  $\Delta E$ , (reducing effective carrier density) and spatial separation of high energy electrons (within CB of FH) from ionized-impurities at nanometer scale HH/FH heterojunctions. Cyan and orange colors represent distributions of low and high energy electrons at temperatures  $T_1$  and  $T_2$  ( $T_2 > T_1$ ) within the CB of the HH matrix.

mechanically alloyed before consolidation by hot pressing (SS-MA-HP). X-ray powder diffraction and transmission electron microscopy revealed that all SS specimens (SS-SPS, SS-HP, SS-MA-HP) are single-phase HH alloys, whereas the MA sample (MA-SPS) contains metallic nanoprecipitates. Electronic and thermal transport measurements showed that the embedded nanoprecipitates induce a drastic increase in the carrier concentration ( $n$ ), a large decrease in the Seebeck coefficient ( $S$ ), and a marginal decrease in the lattice thermal conductivity ( $\kappa_l$ ) of the MA-SPS sample leading to lower  $ZT$  values when compared to the SS-HP samples. Constant values of  $S$  are observed for the SS series regardless of the processing method. However, a strong dependence of the carrier mobility ( $\mu$ ), electrical conductivity ( $\sigma$ ), and  $\kappa_l$  on the processing and consolidation method is observed (Figure 3).

For instance, mechanical alloying introduces additional structural defects which enhance electron and phonon scattering leading to moderately low values of  $\mu$  and large reduction in  $\kappa_l$ . This results in a net 20% enhancement in the figure of merit ( $ZT=0.6$  at 775K). HH specimens of the

correlation between processing conditions, microstructure and charge transport in Half-Heusler Alloys [3]. Five bulk samples of  $n$ -type  $\text{Zr}_{0.25}\text{Hf}_{0.75}\text{NiSn}_{0.975}\text{Sb}_{0.025}$  HH alloy were fabricated by reacting elemental powders via (1) high temperature solid state (SS) reaction and (2) mechanical alloying (MA), followed by densification using spark plasma sintering (SPS) and/or hot pressing (HP). A portion of the sample obtained by SS reaction was

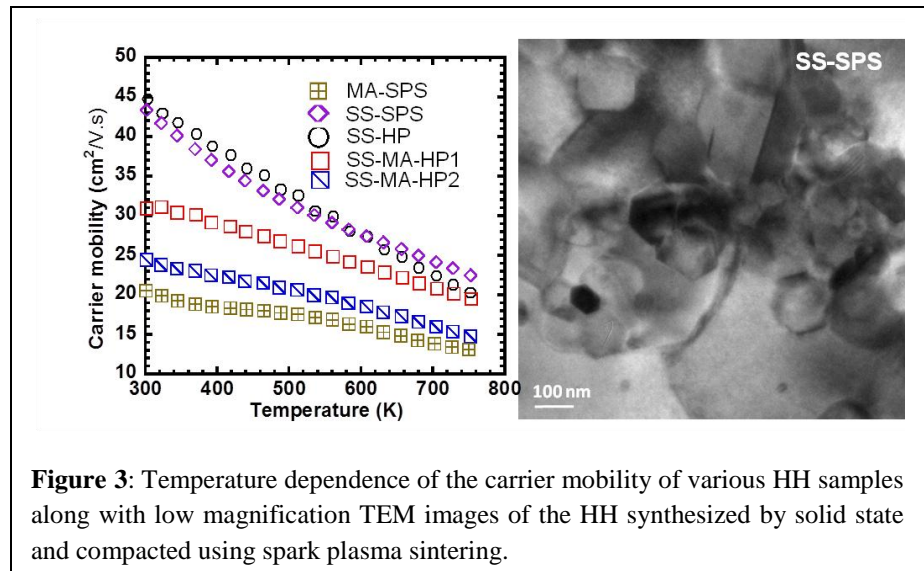


**Figure 3:** Temperature dependence of the carrier mobility of various HH samples along with low magnification TEM images of the HH synthesized by solid state and compacted using spark plasma sintering.

same nominal composition with higher ZT is anticipated from a combination of SS reaction, MA, and SPS (SS-MA-SPS).

### Future Plans

- 1) Determination of the time-temperature-transformation diagrams for the (Ti,Zr)Ni<sub>1+x</sub>Sn and (Zr,Hf)Co<sub>1+x</sub>Sb Half-Heusler/ Full-Heusler systems.
  - (i) Fabrication of various non-crystalline compositions (varying Ni or Co content) using induction melting, Arc melting, etc.
  - (ii) Annealing of several specimens from each composition at various temperatures and times to promote growth of FH nanostructures of different sizes
  - (iii) Study the microstructure of each specimen using electron diffraction to extract relationships between, composition - annealing (time and temperature) - size and distribution of FH nanostructures
- 2) Measurements of Hall effect, electrical conductivity, and thermopower of various HH/FH nanocomposites
- 3) Investigate the theoretical and experimental phase diagrams of (Ti,Zr)Ni<sub>1+x</sub>Sn and (Zr,Hf)Co<sub>1+x</sub>Sb Half-Heusler/ Full-Heusler systems.
- 4) Study and predict the kinetic of HH/FH phase formation and segregation
- 5) First-principles statistical mechanical study of phase stability and order-disorder of Ni and vacancies in Half-Heusler compounds as a function of Ni concentration.

### Publications

- 1) Yuanfeng Liu, Pranati Sahoo, Julien P. A. Makongo, Xiaoyuan Zhou, Sung-Joo Kim, Hang Chi, Ctirad Uher, Xiaoqing Pan and Pierre F. P. Poudeu; Large Enhancements of Thermopower and Carrier Mobility in Quantum Dots Engineered Bulk Semiconductors; *J. Am. Chem. Soc.* **2013**, 135, 7486–7495.
- 2) Pranati Sahoo, Julien P. A. Makongo, Xian-Li Su, Sung Joo Kim, Yuanfeng Liu, Nathan Takas, Hang Chi, Ctirad Uher, Xiaoqing Pan, Pierre F. P. Poudeu, Full-Heusler Nanostructures Boost Thermopower and Hole Mobility in Bulk p-type Half-Heuslers, *Nanoscale* **2013**, DOI: 10.1039/c3nr03145d.
- 3) J.P.A. Makongo, X. Zhou, D. K. Misra, C. Uher, and P.F.P. Poudeu, Correlation between processing conditions, microstructure and charge transport in half-Heusler alloys, *J. Solid State Chemistry* **2013**, 201, 280–287.
- 4) P. Maji, J.P.A. Makongo, X. Zhou, H. Chi, C. Uher, and P.F.P. Poudeu, Thermoelectric performance of nanostructured p-type Zr<sub>0.5</sub>Hf<sub>0.5</sub>Co<sub>0.4</sub>Rh<sub>0.6</sub>Sb<sub>1-x</sub>Sn<sub>x</sub> half-Heusler alloys, *J. Solid State Chemistry* **2013**, 202, 70–76.

# New Optoplasmonic Materials for Next Generation Energy Systems

Bjoern Reinhard

Department of Chemistry and The Photonics Center, Boston University, Boston, MA

## Program Scope

Non-radiative energy transfer between nanoobjects is limited to distances of only a few nanometers, making photons the most attractive long-distance signal carriers. However, once the photon is emitted by a donor quantum emitter, the probability of its absorption through one specific absorber becomes negligibly small.[1] Therefore, realizing efficient and controllable on-chip interactions between single photons and single quantum absorbers and emitters, which are crucial for future quantum information technologies, remains challenging. This problem is mitigated by **photonic atoms (PhAs)** - such as optical microcavities - which can significantly boost the probability of a photon re-absorption through acceptor molecules[2] *via* efficient trapping and re-circulating of photons.[3] PhAs also strongly modify radiative rates of emitters at select frequencies corresponding to cavity modes, which can provide local density of optical states (LDOS) exceeding that of the free space by orders of magnitude.[4-6] In turn, **plasmonic atoms (PIAs)** can enhance the emission of free-space photons by excited molecules (effectively acting as nano-analogs of radio antennas)[7, 8-13] or facilitate relaxation by coupling to surface plasmons (SPs)[14-15]. Consequently, both PIAs and PhAs can enhance the electric field intensity and modify the LDOS.[16, 17] The PhA approach suffers, however, from limited opportunities for light focusing into nanoscale volumes and for engineering efficient spatial overlap between PhA-enhanced electromagnetic fields (and LDOS) and quantum emitters. PIAs, on the other hand, efficiently localize light into nanoscale volumes, but suffer from high dissipative losses in the metal.

The primary scope of this program is to overcome the respective material limitations of PhAs and PIAs for optical signal / energy transfer and routing by the development of

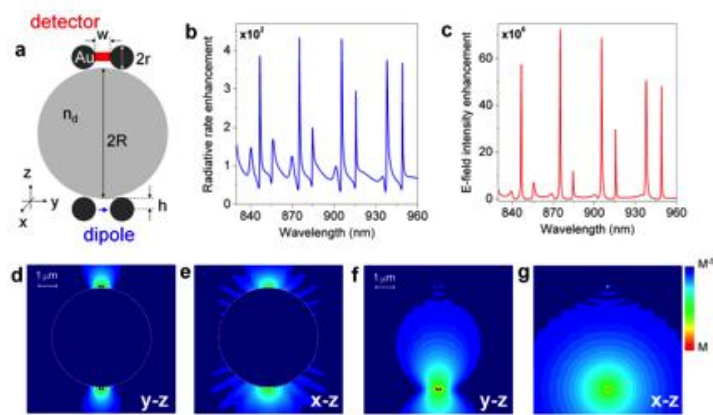


Figure 1: Resonant amplifying superlens. a) A schematic of the optoplasmonic superlens composed of a polystyrene microsphere and two gold NP dimers ( $R=2.8\mu\text{m}$ ,  $n_d=1.59$ ,  $r=75\text{nm}$ ,  $w=25\text{nm}$ ,  $h=80\text{nm}$ ). The structure is excited by an electric dipole positioned at the center of the gap of one of the dimers (shown as blue arrow). b) Radiative rate enhancement of the dipole (over the free-space value) as a function of wavelength. c) Electric field intensity enhancement in the gap of the second dimer (over the value generated by a free-space dipole at the same position). d,e) Electric field intensity distribution in the y-z (d) and x-z (e) planes (log scale) at one of the resonant peaks in (b,c) ( $\lambda=905.4\text{nm}$ ). f,g) Electric field intensity distribution at the same wavelength in the y-z (f) and x-z (g) planes (log scale) in the absence of the microsphere. Boriskina and Reinhard, PNAS 108, 3147 (2011).

optoplasmonic materials that combine plasmonic and dielectric building blocks into hybrid structures in which both components synergistically interact (Figure 1).[1]

### Recent Progress

We have introduced a new class of optoplasmonic materials and have implemented a fabrication strategy that allows the positioning of discrete plasmonic antennas in the equatorial plane of a 2  $\mu\text{m}$  diameter polystyrene or  $\text{SiO}_2$  sphere (Figure 2).[18] The optoplasmonic molecules were generated through a guided self-assembly strategy in which the optical microspheres (OMs) were immobilized in binding sites generated by quartz or silicon posts that contained plasmonic nanoantennas on their tips. Control of the post height facilitated an accurate positioning of the plasmonic antennas into the evanescent field of the whispering gallery modes located in the equatorial plane of the OM. The spectroscopic characterization of the novel materials indicates that photonic and plasmonic modes couple to generate hybrid modes that are sharp but still show substantial localization at the plasmonic nanoantennas.

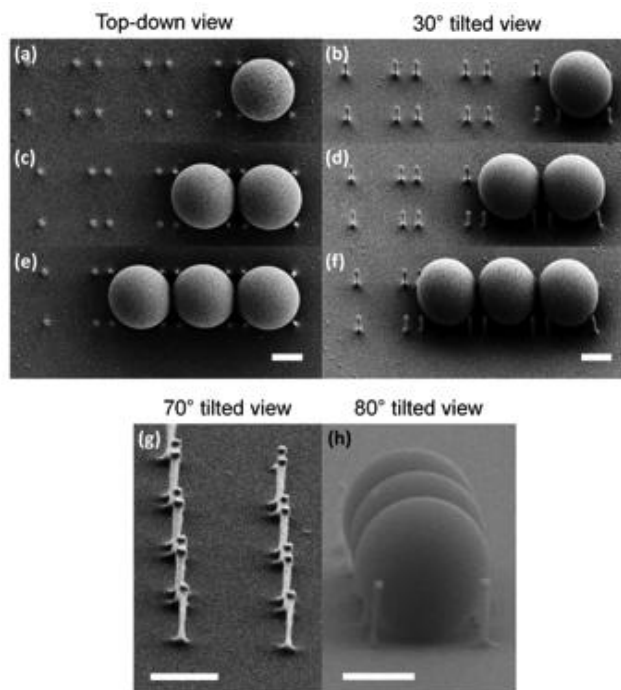


Figure 2. SEM images of optoplasmonic structures that contain one (a, b), two (c, d), or three (e, f) 2.048  $\mu\text{m}$  diameter PS microspheres. The edge-to-edge distance between the pillars of two neighboring binding cavities is  $d_p = 330 \text{ nm}$ , and the height of the pillars is  $h = 870 \text{ nm}$ . The tilted SEM images (g, h) show that spherical Au NPs with a diameter of  $d = 148 \text{ nm}$  are located in the equatorial plane of the PS microspheres trapped in the pillar cavities (scale bars = 1  $\mu\text{m}$ ). W. Ahn et al, ACS Nano 6, 951 (2012). Copyright American Chemical Society.

In a second study, Cy3 dyes were tethered to the plasmonic antennas through oligonucleotide spacers to act as on-chip light sources. We experimentally validated that these optoplasmonic structures achieve an efficient directed photon transfer from the dye functionalized antennas into the microsphere (Figure 3).[19] The fluorescent dyes preferentially emitted into the OM, which efficiently trapped and recirculated the photons. We experimentally determined a relative photon transfer efficiency of 44% in non-optimized self-assembled optoplasmonic molecules.

### Future Plans

After the development of template guided self-assembly strategies for optoplasmonic molecules and successful demonstration of directed photon transfer from plasmonically enhanced emitters into the microcavity resonator, our next step is to experimentally

demonstrate and quantify long-range energy transfer. One experimental structure that we will explore for that purpose is that of a 5.6  $\mu\text{m}$  silica sphere integrated in a set of post supported gold NP dimers. Given the large distance between the two gold NP dimers on opposing sides of the microsphere, we can selectively excite the QD functionalized NP dimer on one side of the optoplasmonic structure using a focused laser beam. The concept of the resonant amplifying superlens [1] predicts that the light emitted by the QD is transferred to the “detector” NP dimer at the opposing side of the PhA, where it can efficiently outcouple into free space photons. Our simulations show clearly (compare **Figures 1d&e** with **1f&g**) that only in the case of an efficient energy transfer through the microcavity resonator, a measurable signal emanates from the detector at the opposing side of the microsphere. The detection of signal intensity at the receiver dimer using conventional confocal fluorescence microscopy would therefore validate the concept of the resonant amplifying superlens. While fluorescence imaging is sufficient to verify the energy transfer across the PhA, we will apply a spectral analysis of the light emitted at the detector to quantify the predicted fluctuations in the dipole radiative rates.

We will use PbS QDs in these experiments that have emission spectra with a width of approximately  $\sim 150$  nm. Based on the discrete resonances in the radiative rate enhancement spectrum in **Figure 1b**, we expect strong intensity modulations in the QD emitter spectrum received and then subsequently re-radiated at the “detector” NP dimer. We will experimentally verify the emission spectra simulated for different superlens configurations by measuring the frequencies and widths of the resonance peaks obtained in self-assembled resonant amplifying optoplasmonic superlenses, which have been structurally characterized by SEM.

After a successful characterization of the long-range photon transfer in optoplasmonic molecules and an elucidation of the engineering principles to control it through the morphology of the structure, we will start to implement active optoplasmonic structures,

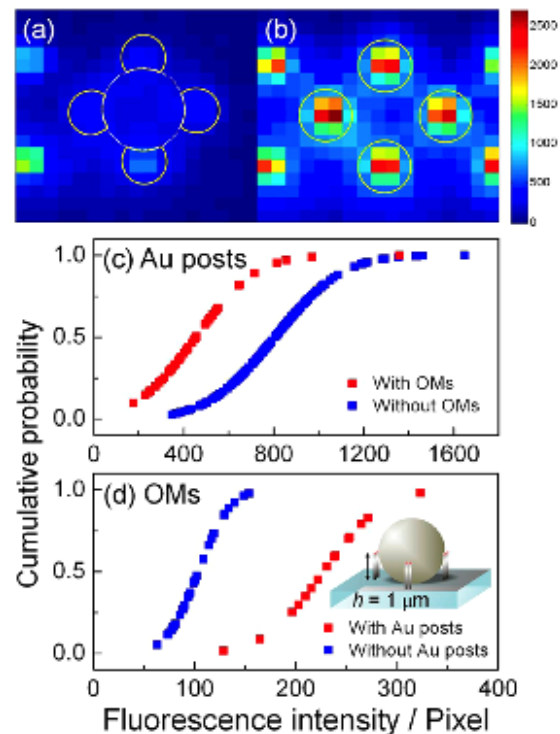


Figure 3. Comparison of fluorescence intensity of Cy3-functionalized gold NP dimer antennas in the presence (a) and absence (b) of an OM. A dotted white circle in (a) indicates the OM inserted into the binding site, and solid yellow circles in (a) and (b) enclose gold posts. Cumulative intensity plots of gold posts (c) and OMs (d) in the presence (red) and absence (blue) of OMs (c) and gold posts (d), respectively. All optoplasmonic structures contain gold NP-functionalized posts with a height of  $h = 1 \mu\text{m}$ . The inset in (d) illustrates the geometry of the investigated structure. W. Ahn et al, ACS Nano 7, 4470 (2013). Copyright American Chemical Society.

such as multiplexers, demultiplexers etc. that allow for a frequency-dependent guiding of light.

#### 4) References

1. Boriskina SV, Reinhard BM (2011) Spectrally and Spatially Configurable Superlenses for Optoplasmonic Nanocircuits. *PNAS* 108: 3147-3151.
2. Folan LM, Arnold S, & Druger S (1985) Enhanced energy transfer within a microparticle. *Chemical Physical Letters* 118:322-327.
3. Vahala KJ (2003) Optical microcavities. *Nature* 424:839-846.
4. Englund D, *et al.* (2005) Controlling the spontaneous emission rate of single quantum dots in a two-dimensional photonic crystal. *Physical Review Letters* 95:013904.
5. Badolato A, *et al.* (2005) Deterministic coupling of single quantum dots to single nanocavity modes. *Science* 308:1158-1161.
6. Aoki T, *et al.* (2006) Observation of strong coupling between one atom and a monolithic microresonator. *Nature* 443:671-674.
7. Halas NJ (2009) Connecting the dots: Reinventing optics for nanoscale dimensions. *Proceedings of the National Academy of Sciences of the U.S.A* 106:3643-3644.
8. Bharadwaj P, Deutsch B, & Novotny L (2009) Optical Antennas. *Advances in Optics and Photonics* 1:438-483.
9. Kuehn S, Hakanson U, Rogobete L, & Sandoghdar V (2006) Enhancement of single-molecule fluorescence using a gold NP as an optical nanoantenna. *Physical Review Letters* 97:017402.
10. Kinkhabwala A, *et al.* (2009) Large single molecule fluorescence enhancements produced by a bowtie nanoantenna. *Nature Photonics* 3:654-657.
11. Alu A & Engheta N (2008) Tuning the scattering response of optical nanoantennas with nanocircuit loads. *Nature Photonics* 2:307-310.
12. Muhlschlegel P, Eisler HJ, Martin OJF, Hecht B, & Pohl DW (2005) Resonant optical antennas. *Science* 308(5728):1607-1609.
13. Cubukcu E, Kort EA, Crozier KB, & Capasso F (2006) Plasmonic laser antenna. *Applied Physics Letters* 89:093120-093123.
14. Akimov AV, *et al.* (Nature) Generation of single optical plasmons in metallic nanowires coupled to quantum dots. *Nature* 450:402-406.
15. Bergman DJ & Stockman MI (2003) Surface plasmon amplification by stimulated emission of radiation: quantum generation of coherent surface plasmons in nanosystems. *Physical Review Letters* 90:027402.
16. Barth M, *et al.* (2010) Nanoassembled Plasmonic-Photonic Hybrid Cavity for Tailored Light-

- Matter Coupling. *Nano Letters* 10:891-895.
17. Devilez A, Stout B, & Bonod N (2010) Compact metall-dielectric optical antenna for ultra directional and enhanced radiative emission. *ACS Nano* 4:3390-3396.
  18. Ahn W., Boriskina SV, Hong Y, Reinhard BM (2012) Photonic-Plasmonic Mode Coupling in On-Chip Integrated Optoplasmonic Molecules. *ACS Nano* 6:951-960.
  19. Ahn W, Hong Y, Boriskina SV, Reinhard BM (2013) Demonstration of Efficient On-Chip Photon Transfer in Self-Assembled Optoplasmonic Networks, *ACS Nano* 7:4470-4478.

## SISGR—Using Interfaces to Create Strongly-Coupled Magnetic-Ferroelectrics

Craig J. Fennie#, David A. Muller#, Peter Schiffer\*, Darrell G. Schlom

School of Applied and Engineering Physics#, Department of Materials Science and Engineering, Cornell University, Ithaca, NY 14853

\*Department of Physics, The Pennsylvania State University, University Park, PA 16802

### I. PROGRAM SCOPE

Our SISGR objective is to create a ferromagnetic ferroelectric that can be deterministically switched between symmetry equivalent states using an electric field. The electric-field switching of a magnetization between  $180^\circ$  symmetry equivalent states has not been demonstrated in any material. The required coupling between ferroelectric and ferromagnetic domains allowing such switching is a missing feature in most multiferroics and is key to advancing the field both scientifically and technologically. Starting at the level of electrons and atoms our goal is to rationally design complex oxide heterostructures and interface-materials with this targeted emergent behavior. This is not a matter of simply optimizing material parameters, but rather begins with understanding a mechanism to control the interplay between the diverse microscopic degrees of freedom prevalent in complex oxides in order to achieve this desired behavior, and ends with the design of new material realizations. These realizations are in turn created with atomic-layer precision, structurally assessed to see that they are the intended realization, and finally their relevant properties are measured. In this program we will develop the scientific ideas necessary to apply this design paradigm to the creation of multiferroics with unprecedented coupling between ferroelectric and magnetic order parameters, i.e., strongly-coupled magnetic-ferroelectrics.

### II. RECENT PROGRESS

Our SISGR recently developed a way to grow single-phase epitaxial films of  $\text{LuFe}_2\text{O}_4$  by MBE in an adsorption-controlled regime.<sup>i</sup> When it comes to high temperature multiferroics,  $\text{LuFe}_2\text{O}_4$  stands out because it has been reported to be simultaneously ferrimagnetic and ferroelectric at the highest temperature of any known material.<sup>ii</sup> It magnetically orders at 250 K,<sup>ii</sup> has a saturation magnetization of about  $1.4 \mu\text{B}/\text{Fe}$  at  $T=0$  K,<sup>iii</sup> and is ferroelectric below 330 K.<sup>ii</sup> The ferroelectricity arises from a rather unusual mechanism—charge ordering of  $\text{Fe}^{2+}$  and  $\text{Fe}^{3+}$  ions.<sup>iv</sup> If true, this would make  $\text{LuFe}_2\text{O}_4$  an improper ferroelectric<sup>v</sup> that develops a polarization through charge-ordering and as such does not restrict the coexistence of magnetism. This is the first time that single-phase  $\text{LuFe}_2\text{O}_4$  films have been achieved by any technique; the only prior report of epitaxial  $\text{LuFe}_2\text{O}_4$  films contained significant inclusions of  $\text{Fe}_2\text{O}_3$  and  $\text{Fe}_3\text{O}_4$ .<sup>vi</sup> We used thermodynamics to identify an adsorption-controlled regime in which excess iron could be supplied during growth and all but that needed to form the  $\text{LuFe}_2\text{O}_4$  film would desorb. Such growth conditions are analogous to the way in which III-V and II-VI compound semiconductors are routinely grown by MBE.<sup>vii-xiv</sup> We have identified and utilized adsorption controlled growth conditions extensively for the growth of single-phase films of numerous complex oxides containing volatile constituents by MBE including  $\text{PbTiO}_3$ ,<sup>xv</sup>  $\text{Bi}_4\text{Ti}_3\text{O}_{12}$ ,<sup>xvi</sup>  $\text{BiFeO}_3$ ,<sup>xvii</sup>  $\text{BiMnO}_3$ ,<sup>xviii</sup> and  $\text{EuO}$ .<sup>xix</sup> In the case of  $\text{LuFe}_2\text{O}_4$ , single-phase epitaxial (0001) oriented films were obtained by our SISGR team on (111)  $\text{MgAl}_2\text{O}_4$ , (111)  $\text{MgO}$ , and (0001)  $\text{SiC}$  substrates.

Having achieved single-phase thin epitaxial films of  $\text{LuFe}_2\text{O}_4$ , we used electron energy loss spectroscopy on an aberration-corrected scanning transmission electron microscope to map the

elemental composition and bonding environment with atomic resolution.<sup>xx</sup> A two-dimensional analysis of the fine structure of the O-K edge yielded distinct signals for the two inequivalent oxygen sites in the crystal. Comparison to an *ab initio* simulation showed that these two components can be interpreted in terms of the differing hybridization of the O *p* orbitals to the Lu and Fe *d* orbitals, thus producing an atomic-resolution map of the local oxygen bonding environment.

Recently our SISGR demonstrated reversible control of magnetic interactions by electric field in strained EuTiO<sub>3</sub> films.<sup>xxi</sup> Such magnetoelectric coupling has the potential to control the magnetic state of a material with an electric field, an enticing prospect for device engineering. In our work we demonstrated a large magnetoelectric cross-field control in a tetravalent titanate film. In bulk form, EuTiO<sub>3</sub> is antiferromagnetic. Both anti- and ferro-magnetic interactions coexist, however, between different nearest europium neighbors. In thin epitaxial films, strain was used to alter the relative strength of the magnetic exchange constants. We not only showed that moderate biaxial compression precipitates local magnetic competition, but also demonstrated that the application of an electric field at this strain condition switches the magnetic ground state. Using first-principles density functional theory, we resolved the underlying microscopic mechanism resulting in *G*-type magnetic order and illustrated how it is responsible for the observed large magnetoelectric effect.

Our team also showed how polar octahedral rotations could serve as a path to new multifunctional materials.<sup>xxii</sup> ABO<sub>3</sub> oxides with the perovskite structure display an amazing variety of phenomena that can be altered by subtle changes in the chemistry and internal structure, making them a favorite class of materials to explore the rational design of novel properties. We have reported that rotations of the BO<sub>6</sub> octahedra give rise to a novel form of ferroelectricity—hybrid improper ferroelectricity. Octahedral rotations also strongly influence other structural, magnetic, orbital, and electronic degrees of freedom in perovskites and related materials. Octahedral rotation-driven ferroelectricity consequently has the potential to robustly control emergent phenomena with an applied electric field.

We formulated a complete theory for a novel form of ferroelectricity, whereby a spontaneous and switchable polarization emerges from the destruction of an antiferroelectric state due to octahedral rotations and ordered cation sublattices. A materials design framework was further constructed based on crystal-chemistry descriptors rooted in group theory,<sup>xxiii</sup> which enables the facile design of artificial oxides with large electric polarizations, *P*, simultaneous with small energetic switching barriers between +*P* and -*P*. The theory is validated with first principles density functional calculations on more than 16 perovskite-structured oxides, illustrating it could be operative in any materials classes exhibiting two- or three-dimensional corner-connected octahedral frameworks. The principles governing materials selection of the “layered” systems are shown to originate in the lattice dynamics of the *A* cation displacements stabilized by the pervasive BO<sub>6</sub> rotations of single phase ABO<sub>3</sub> materials, whereby the latter distortions govern the optical band gaps, magnetic order and critical transition temperatures. This approach provides the elusive route to the practical control of octahedral rotations, and hence a wide range of functional properties, with an applied electric field.

Finally, using a combination of symmetry arguments and first-principles calculations to explore the connection between structural distortions and ferroelectricity in the perovskite family of materials, we have answered the question of why there are so few perovskite ferroelectrics.<sup>xxiv</sup> We explain the role of octahedral rotations in suppressing ferroelectricity in these materials and show that, as the tolerance factor decreases, rotations alone cannot fully suppress ferroelectricity. Our results show that it is cation displacements (“hidden” in Glazer notation) that accompany the

rotations, rather than the rotations themselves, that play the decisive role in suppressing ferroelectricity in these cases. We use the knowledge gained in our analysis of this problem to explain the origin of ferroelectricity in  $R3c$  materials such as  $\text{FeTiO}_3$  and  $\text{ZnSnO}_3$  and to suggest strategies for the design and synthesis of new perovskite ferroelectrics. Our results have implications not only for the fundamental crystal chemistry of the perovskites but also for the discovery of new functional materials.

### III. FUTURE PLANS

We plan to study the temperature dependence of antiferroic distortions by electron diffraction and direct imaging using a new, high-resolution double-tilt heating holder, and correlate with the ferroelectric phase. The first system we intend to target is  $\text{Ca}_3\text{Mn}_2\text{O}_7$  whose octahedral tilts are critical to rotationally-driven ferroelectric state. We also plan to establish the intrinsic magnetic properties of hexagonal  $\text{LuFeO}_3$ . This will be performed by SQUID measurements on phase-pure samples grown by MBE and assessed structurally by XRD and STEM. The magnetic order will be established by neutron diffraction. Finally, we are growing  $(\text{ABO}_3)_1/(\text{A}'\text{BO}_3)_1$  superlattices with  $B=\text{Fe}$  and  $A$  and  $A'$  being different rare-earth ions. The parent constituents are perovskites with space group  $Pnma$ . Our calculations indicate that this ordered superlattice is a hybrid improper multiferroic (both ferroelectric and weakly ferromagnetic) at room temperature. We will synthesize these superlattices and measure their properties including whether they can be switched, whether switching them with an electric field leads to deterministic switching of their magnetization, and their linear magnetoelectric performance.

### IV. REFERENCES

- <sup>i</sup> C.M. Brooks, R. Misra, J.A. Mundy, L.A. Zhang, B.S. Holinsworth, K.R. O'Neal, T. Heeg, W. Zander, J. Schubert, J.L. Musfeldt, Z.K. Liu, D.A. Muller, P. Schiffer, and D.G. Schlom, *Appl. Phys. Lett.* **101** (2012) 132907.
- <sup>ii</sup> N. Ikeda, H. Ohsumi, K. Ohwada, K. Ishii, T. Inami, K. Kakurai, Y. Murakami, K. Yoshii, S. Mori, Y. Horibe, and H. Kito, *Nature* **436** (2005) 1136–1138.
- <sup>iii</sup> J. Iida, Y. Nakagawa, S. Takekawa, and N. Kimizuka, „ *J. Phys. Soc. Jpn.* **56** (1987) 3746-3747.
- <sup>iv</sup> J. van den Brink and D. I Khomskii, *J. Phys.: Condens. Matter* **20** (2008) 434217.
- <sup>v</sup> S-W. Cheong and M. Mostovoy, *Nature Materials* **6** (2007) 13-20.
- <sup>vi</sup> J. Liu, Y. Wang, and J. Y. Dai, *Thin Solid Films* **518** (2010) 6909-6914.
- <sup>vii</sup> J. R. Arthur, Jr., *J. Appl. Phys.* **39** (1968) 4032-4034.
- <sup>viii</sup> A. Y. Cho, *Surf. Sci.* **17** (1969) 494-503.
- <sup>ix</sup> A. Y. Cho, *J. Appl. Phys.* **41** (1970) 2780-2786.
- <sup>x</sup> A. Y. Cho, *J. Appl. Phys.* **42** (1971) 2074-2081.
- <sup>xi</sup> R. Heckingbottom, G. J. Davies, and K. A. Prior, *Surf. Sci.* **132**, (1983) 375-389.
- <sup>xii</sup> H. Seki and A. Koukitu, *J. Cryst. Growth* **78** (1986) 342-352.
- <sup>xiii</sup> J. Y. Tsao, *J. Cryst. Growth* **110** (1991) 595-603.
- <sup>xiv</sup> J. Y. Tsao, *Materials Fundamentals of Molecular Beam Epitaxy* (Academic Press, Boston, 1993) pp. 65-88.
- <sup>xv</sup> C. D. Theis, J. Yeh, D. G. Schlom, M. E. Hawley, and G. W. Brown, *Solid Films* **325** (1998) 107-114.
- <sup>xvi</sup> C. D. Theis, J. Yeh, D. G. Schlom, M. E. Hawley, G. W. Brown, J. C. Jiang, and X. Q. Pan, „ *Appl. Phys. Lett.* **72** (1998) 2817-2819.
- <sup>xvii</sup> J. F. Ihlefeld, A. Kumar, V. Gopalan, D. G. Schlom, Y. B. Chen, X. Q. Pan, T. Heeg, J. Schubert, X. Ke, P. Schiffer, J. Orenstein, L. W. Martin, Y. H. Chu, and R. Ramesh, *Appl. Phys. Lett.* **91** (2007) 071922.
- <sup>xviii</sup> J. H. Lee, X. Ke, R. Misra, J. F. Ihlefeld, X. S. Xu, Z. G. Mei, T. Heeg, M. Roeckerath, J. Schubert, Z. K. Liu, J. L. Musfeldt, P. Schiffer, and D. G. Schlom, *Appl. Phys. Lett.* **96** (2010) 262905.

- 
- <sup>xix</sup> R. W. Ulbricht, A. Schmehl, T. Heeg, J. Schubert, and D. G. Schlom, *Appl. Phys. Lett.* **93** (2008) 102105.
- <sup>xx</sup> J.A. Mundy, Q.Y. Mao, C.M. Brooks, D.G. Schlom, and D.A. Muller, “Atomic-Resolution Chemical Imaging of Oxygen Local Bonding Environments by Electron Energy Loss Spectroscopy,” *Appl. Phys. Lett.* **101** (2012) 042907.
- <sup>xxi</sup> P.J. Ryan, J.-W. Kim, T. Birol, P. Thompson, J.-H. Lee, X. Ke, P.S. Normile, E. Karapetrova, P. Schiffer, S.D. Brown, C.J. Fennie, and D.G. Schlom *Nat. Commun.* **4** (2013) 1334.
- <sup>xxii</sup> N.A. Benedek, A.T. Mulder, and C.J. Fennie, *J. Solid State Chem.* **195** (2012) 11–20.
- <sup>xxiii</sup> A.T. Mulder, N.A. Benedek, J.M. Rondinelli, and C.J. Fennie, *Advanced Functional Materials* (in press, 2013). DOI: 10.1002/adfm.201300210.
- <sup>xxiv</sup> N.A. Benedek and C.J. Fennie, *The Journal Physical Chemistry C*, DOI: 10.1021/jp402046t, 2013.

## V. PUBLICATIONS RESULTING FROM THIS WORK

1. Y. Zhu, A. Soukiassian, D.G. Schlom, D.A. Muller, and C. Dwyer, “Towards Artifact-Free Atomic-Resolution Elemental Mapping with Electron Energy-Loss Spectroscopy,” *Applied Physics Letters* **103** (2013) 141908.
2. X. Ke, T. Birol, R. Misra, J.-H. Lee, B.J. Kirby, D.G. Schlom, C.J. Fennie, and J.W. Freeland, “Structural Control of Magnetic Anisotropy in a Strain-Driven Multiferroic  $\text{EuTiO}_3$  Thin Film,” *Physical Review B* **88** (2013) 094434.
3. A.T. Mulder, N.A. Benedek, J.M. Rondinelli, and C.J. Fennie, “Turning  $\text{ABO}_3$  Antiferroelectrics into Ferroelectrics: Design Rules for Practical Rotation-Driven Ferroelectricity in Double Perovskites and  $\text{A}_3\text{B}_2\text{O}_7$  Ruddlesden-Popper Compounds,” *Advanced Functional Materials* **23** (2013) 4810–4820.
4. T. Birol and C.J. Fennie, “Origin of Giant Spin-Lattice Coupling and the Suppression of Ferroelectricity in  $\text{EuTiO}_3$  from First Principles,” *Physical Review B* **88** (2013) 094103.
5. N.A. Benedek and C.J. Fennie, “Why Are There So Few Perovskite Ferroelectrics?,” *Journal of Physical Chemistry C* **117** (2013) 13339–13349. Note, this will appear as the Cover of the July 4, 2013 issue.
6. A. Melville, T. Mairoser, A. Schmehl, T. Birol, T. Heeg, B. Holländer, J. Schubert, C.J. Fennie, and D.G. Schlom, “Effect of Film Thickness and Biaxial Strain on the Curie Temperature of  $\text{EuO}$ ,” *Applied Physics Letters* **102** (2013) 062404.
7. P.J. Ryan, J.-W. Kim, T. Birol, P. Thompson, J.-H. Lee, X. Ke, P.S. Normile, E. Karapetrova, P. Schiffer, S.D. Brown, C.J. Fennie, and D.G. Schlom “Reversible Control of Magnetic Interactions by Electric Field in a Single-Phase Material,” *Nature Communications* **4** (2013) 1334.
8. N.A. Benedek, A.T. Mulder, and C.J. Fennie, “Polar Octahedral Rotations: A Path to New Multifunctional Materials,” *Journal of Solid State Chemistry* **195** (2012) 11–20.
9. L.W. Martin and D.G. Schlom, “Advanced Synthesis Techniques and Routes to New Single-Phase Multiferroics,” *Current Opinion in Solid State and Materials Science* **16** (2012) 199–215.
10. T. Birol, N.A. Benedek, H. Das, A.L. Wysocki, A.T. Mulder, B.M. Abbett, E.H. Smith, S. Ghosh, and C.J. Fennie, “The Magnetoelectric Effect in Transition Metal Oxides: Insights and the Rational Design of New Materials from First Principles,” *Current Opinion in Solid State and Materials Science* **16** (2012) 227–242.

11. C.M. Brooks, R. Misra, J.A. Mundy, L.A. Zhang, B.S. Holinsworth, K.R. O'Neal, T. Heeg, W. Zander, J. Schubert, J.L. Musfeldt, Z.K. Liu, D.A. Muller, P. Schiffer, and D.G. Schlom, "The Adsorption-Controlled Growth of  $\text{LuFe}_2\text{O}_4$  by Molecular-Beam Epitaxy," *Applied Physics Letters* **101** (2012) 132907.
12. M. Stengel, C.J. Fennie, and P. Ghosez, "Electrical Properties of Improper Ferroelectrics from First Principles," *Physical Review B* **86** (2012) 094112.
13. K. Kathan-Galipeau, P.P. Wu, Y.L. Li, L.Q. Chen, A. Soukiassian, Y. Zhu, D.A. Muller, X.X. Xi, D.G. Schlom, and D.A. Bonnell, "Direct Determination of the Effect of Strain on Domain Morphology in Ferroelectric Superlattices with Scanning Probe Microscopy," *Journal of Applied Physics* **112** (2012) 052011.
14. P. Cueva, R. Hovden, J.A. Mundy, H.L. Xin, and D.A. Muller, "Data Processing for Atomic Resolution Electron Energy Loss Spectroscopy," *Microscopy and Microanalysis* **18** (2012) 667-675.
15. J.A. Mundy, Q.Y. Mao, C.M. Brooks, D.G. Schlom, and D.A. Muller, "Atomic-Resolution Chemical Imaging of Oxygen Local Bonding Environments by Electron Energy Loss Spectroscopy," *Applied Physics Letters* **101** (2012) 042907.
16. J.M. Rondinelli and C.J. Fennie, "Octahedral Rotation-Induced Ferroelectricity in Cation Ordered Perovskites," *Advanced Materials* **24** (2012) 1961–1968.
17. S. Kamba, V. Goian, M. Orlita, D. Nuzhnyy, J.H. Lee, D.G. Schlom, K.Z. Rushchanskii, M. Ležaić, T. Birol, C.J. Fennie, P. Gemeiner, B. Dkhil, V. Bovtun, M. Kempa, J. Hlinka, and J. Petzelt, "Magnetodielectric Effect and Phonon Properties of Compressively Strained  $\text{EuTiO}_3$  Thin Films Deposited on  $(001)(\text{LaAlO}_3)_{0.29}(\text{SrAl}_{1/2}\text{Ta}_{1/2}\text{O}_3)_{0.71}$ ," *Physical Review B* **85** (2012) 094435.
18. N.A. Benedek and C.J. Fennie, "Hybrid Improper Ferroelectricity: A Mechanism for Controllable Polarization-Magnetization Coupling," *Physical Review Letters* **106** (2011) 107204.

## Discovery and Crystal Growth of New Oxide Phases From Metal Fluxes

T. Siegrist<sup>1,2</sup>, T. Besara<sup>2</sup>, D. Ramirez<sup>1,2</sup>

<sup>1</sup>Department of Chemical and Biomedical Engineering  
FAMU-FSU College of Engineering  
and  
National High Magnetic Field Laboratory  
Florida State University, Tallahassee, FL, 32310

### Program Scope

Discovery and growth of crystalline materials is one of the key areas in materials research. New materials, and engineering of their properties, have produced tremendous progress; and the search for new materials with novel properties remains an ongoing activity. Of the many oxide single crystal growth methods, flux growth has proven to be an excellent method for exploratory synthesis work that also will yield crystals large enough for structural and physical characterization. Using metal fluxes to grow oxide phases produces a unique crystal growth environment, where oxygen is now a minority constituent. The low melting point of certain metal fluxes in use allows low temperature synthesis, and gives access to potentially metastable and hard to crystallize phases. We are investigating single crystal oxide growth from alkaline earth metal fluxes, where the sizable oxygen solubility as well as good solubility of lanthanides is used to discover new phases. The reactivity of the flux can be tailored to provide reducing conditions for oxide growth by using alkaline earth mixtures, or the flux material can also be incorporated into the oxide. In particular, the low temperature eutectic mixtures of magnesium with calcium, strontium and barium provide control not only over crystal growth temperatures, but also the reactivity of the flux and its power to reduce lanthanide oxides. Furthermore, alkaline earth metal fluxes have simultaneous solubility for oxides, halides, hydrides, and chalcogenides, therefore new phases are expected to form under unusual conditions.

### Recent Progress

Our research activities resulted in the discovery of two new phases,  $Ba_2OTe$  and  $Ba_3Yb_2O_5Te$ , both mixed oxides that have not been reported previously. In addition, we managed to obtain a series of phases of  $CaV_2O_4$ -type,  $BaLn_2O_4$  ( $Ln$ =lanthanide), in single crystal form. These phases were synthesized previously in powder form. In addition, we also obtained  $BaCe_2O_4$ , a compound that is not accessible using traditional solid state reactions. The ferromagnetic semiconductor  $EuO$  has been successfully grown from a barium/magnesium flux.

*BaLn<sub>2</sub>O<sub>4</sub> (Ln = lanthanide)*

The CaV<sub>2</sub>O<sub>4</sub>-type phases of BaLn<sub>2</sub>O<sub>4</sub>, with Ln = La to Yb were successfully grown as single crystals from molten barium fluxes. In BaLn<sub>2</sub>O<sub>4</sub>, the lanthanide ions are arranged on ladders with a trigonal arrangement. In Figure 1, the ladders are running along the c-axis, and are oriented out of the plane, with lanthanide ions octahedrally coordinated by oxygen. It is therefore expected that magnetic frustration can occur in these phases if the magnetic interaction is

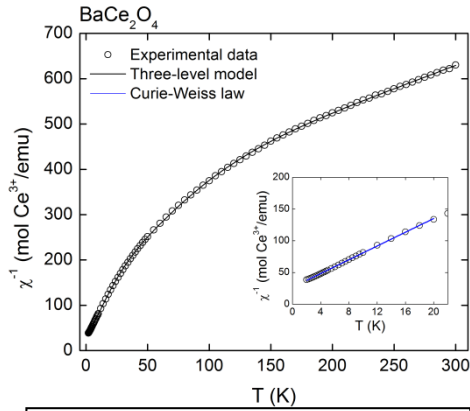


Fig. 2: inverse susceptibility of BaCe<sub>2</sub>O<sub>4</sub>. The data is fit with a 3-level model.

based on a superexchange mechanism. It was possible to synthesize BaCe<sub>2</sub>O<sub>4</sub> crystals for the first time and obtain a magnetic susceptibility measurement. Since the material is transparent, the cerium ion is expected to be Ce<sup>3+</sup>, with a magnetic moment of  $\mu = 2.54\mu_B$ . The magnetic coupling is antiferromagnetic as derived from high temperature data, but no phase transition to an ordered state is observed above 2K. Furthermore, the low temperature susceptibility can be fit with a Curie-Weiss law with a small Weiss temperature of -4.95K and a moment of 1.215  $\mu_B$ . This points towards a potentially frustrated magnetic system with crystal field splitting. As the phases in this series are all charge compensated, they are insulators/semiconductors with a large band gap. The magnetic properties of a majority of the phases follow Curie-Weiss behavior, with antiferromagnetic order below 10K.

*Ba<sub>3</sub>Yb<sub>2</sub>O<sub>5</sub>Te*

We synthesized the new oxy-telluride Ba<sub>3</sub>Yb<sub>2</sub>O<sub>5</sub>Te, a system that combines two structural moieties: double pyramidal perovskite-type Ba<sub>2</sub>Yb<sub>2</sub>O<sub>5</sub> layers and BaTe CsCl-type layers (structure is shown in Fig. 3). This phase is grown as a single crystal from an alkaline earth metal flux, where simultaneously oxygen, tellurium as well as ytterbium are soluble, showing the versatility of the flux. This system is closely related to the well-known Ruddlesden-Popper phases, where perovskite-type layers are combined with rock salt (NaCl) layers. Structurally, the perovskite layers are highly strained, since

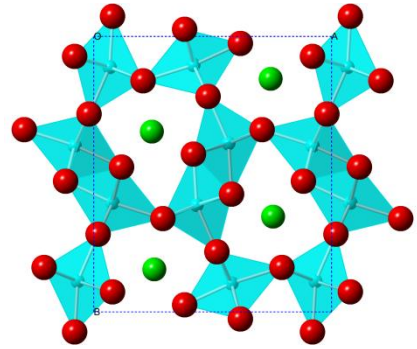


Figure 1: Crystal structure of BaCe<sub>2</sub>O<sub>4</sub>. Barium atoms are green, oxygen red, lanthanides blue with coordination octahedra.

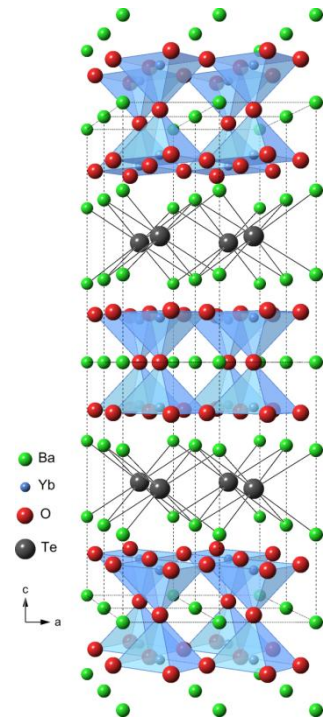


Figure 3: Crystal structure of Ba<sub>3</sub>Yb<sub>2</sub>O<sub>5</sub>Te.

perovskite-type systems with a lanthanide atom on the B site expand the lattice formed by oxygen. Therefore,  $ABO_3$  perovskite related phases with a lanthanide atom on the B-site are not common. We found that  $Ba_3Yb_2O_5Te$  is antiferromagnetic, with a transition in the vicinity of 4K. However, the Weiss constant is larger than expected. Low temperature specific heat measurements showed that at the antiferromagnetic transition, the entropy release is  $R \ln 2$ , indicating that the ytterbium ion f-electrons require inclusion of the crystal electric field. The f-levels are split into three levels, with a  $\Gamma_6$  crystal field split ground state.  $Ba_3Yb_2O_5Te$  is the first demonstration that alkaline earth metal fluxes show sizable simultaneous solubility for two different anions, in this case oxygen and tellurium. This allows further exploration of lattices with two different kinds of anions. Based on DFT calculations, the valence band is formed by oxygen and tellurium orbitals, with mostly tellurium character at the valence band edge.

### *EuO*

The ferromagnetic semiconductor EuO can be grown as a single crystal using a barium/magnesium flux. A flux composed of barium only is not able to reduce the starting material  $Eu_2O_3$  to EuO, but the addition of magnesium allows formation of EuO. Flux inclusion is, unfortunately, not negligible, but the ferromagnetic transition of single crystals grown in this fashion is of the order of 62K. The MH-loop measured at 20K shows saturation at 1.2T. Cube shaped crystals with edge length of the order of 2mm have been obtained so far. Further growth optimization is in progress.



Fig.4: EuO

### *Nb<sub>3</sub>Pd<sub>0.7</sub>Se<sub>7</sub>*

Superconductivity in  $Nb_3Pd_{0.7}Se_7$  was observed at low temperatures at 1.44K.  $Nb_3Pd_{0.7}Se_7$  is low-dimensional system with quasi-one-dimensional ribbons running along the monoclinic b-axis. Despite this low transition temperature, the material has a large upper critical field  $H_{c2}$  of the order of 14T. Such a high  $H_{c2}$  is not expected, since the energy scale should be set by the superconducting transition temperature. Additionally, the upper critical field shows a large anisotropy of the order of 6. Band structure calculations show the Fermi surface in this system to be composed of quasi-one dimensional and quasi-two dimensional sheets with hole character, as well as three-dimensional sheets of both hole- and electron character. The superconductivity in this system is likely due to a strongly correlated electron gas, with an unconventional origin of the superconducting

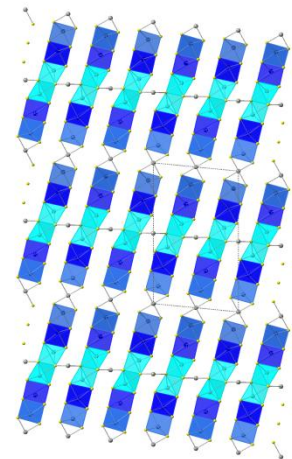


Fig.5  $Nb_3Pd_{0.7}Se_7$

coupling that is reflected in the large ratio between  $H_{c2}$  and  $T_c$ . (Collaboration with L. Balicas, DOE-BES grant DE-SC0002613)

### Molecular Quantum Dots

The structural and physical characterization of novel supramolecular assemblies comprising molecular quantum dots is studied in collaboration with the “Center for Re-Defining

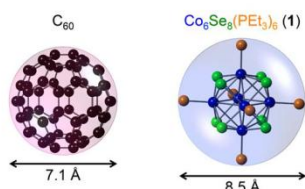
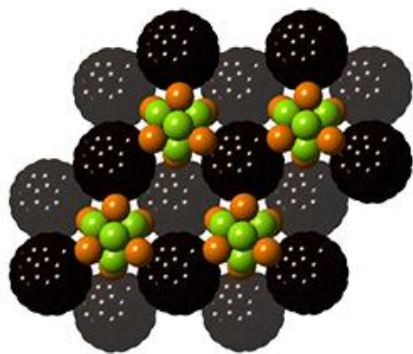


Fig. 6:  $C_{60}$  and  $Co_6Se_8(PEt_3)_6$  cluster

Photovoltaics: Efficiency through Molecular-Scale Control” (EFRC, DE-SC0001085). Novel solid state materials that form the binary assemblies  $[Co_6Se_8(PEt_3)_6][C_{60}]_2$  and  $[Cr_6Te_8(PEt_3)_6][C_{60}]_2$  related to the  $CdI_2$  structure type have been synthesized. These systems can be considered as atomically precise solid-state compounds and form mono-disperse nano-particles of the order of 0.8nm. Co-crystallization assembles these building blocks into structures with substantial charge transfer, forming a supramolecular “ionic crystal”



comprised of these clusters in a 1:2 ratio. The overall arrangement of the clusters is related to the  $CdI_2$ -type structure, where the iodine anion forms a hexagonal close packed lattice and the cadmium cation occupies half of the octahedral interstitial sites. In the supramolecular assembly, the role of the cation is played by the  $Co_6Se_8(PEt_3)_6$  cluster, while  $C_{60}$  plays the role of the anion, since  $C_{60}$  is an electron acceptor molecule. The same arrangement is observed for the supramolecular assembly of  $[Cr_6Te_8(PEt_3)_6][C_{60}]_2$ , where a also a charge transfer is observed. This charge transfer from the  $Co_6Se_8(PEt_3)_6$  cluster to the  $C_{60}$  clusters is responsible for the enhanced electronic conductivity that results in a small band gap of the material.

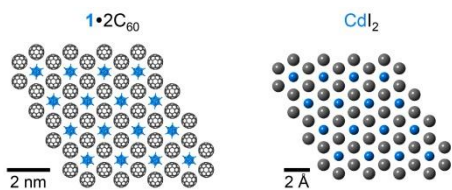


Fig. 7:  $[Co_6Se_8(PEt_3)_6][C_{60}]_2$  and  $CdI_2$

The cluster assembly,  $[Ni_9Te_6(PEt_3)_8][C_{60}]$  crystallizes in the rock-salt type structure, and also shows electron transfer from the  $Ni_9Te_6(PEt_3)_8$  cluster to the  $C_{60}$  cluster. In this case, the charge transfer results in low temperature ferromagnetic order ( $T_c \approx 4K$ ).

### Future Plans

The capability of the flux to dissolve transition elements will be explored. For this, the flux composition will be varied to include aluminum and copper as a starting point. Experiments indicate that transition elements have some small solubility in the alkaline earth metals, but crystal growth has not been optimized. Combining lanthanides and transition elements in this flux environment is expected to yield novel structures with potentially interesting magnetic properties.

### **DoE Sponsored Publications in the Last Two Years**

J. B. Whalen, T. Besara, R. Vasquez, F. Herrera, J. Sun, D. Ramirez, R. L. Stilwell, S. W. Tozer, T. D. Tokumoto, S. A. McGill, M. Davidson and T. Siegrist, "A new oxytelluride : Perovskite and CsCl intergrowth in  $Ba_3Yb_2O_5Te$ ", 203, 204 - 211, (2013).

Q. R. Zhang, D. Rhodes, B. Zeng, T. Besara, T. Siegrist, M. D. Johannes and L. Balicas, "Anomalous metallic state and anisotropic multiband superconductivity in  $Nb_3Pd_{0.7}Se_7$ ", 88, 024508, (2013).

X. Roy, C. H. Lee, A. C. Crowther, C. L. Schenck, T. Besara, R. A. Lalancette, T. Siegrist, P. W. Stephens, L. E. Brus, P. Kim, M. L. Steigerwald and C. Nuckolls, "Nanoscale Atoms in Solid-State Chemistry", 341, 157-160, (2013).

# Electrodeposition of Cobalt (Hydr)oxide Oxygen Evolution Catalysts for Photoelectrochemical Water Splitting

Jay A. Switzer

Department of Chemistry & Materials Research Center

Missouri University of Science and Technology

Rolla, MO 65409-1170

[jswitzer@mst.edu](mailto:jswitzer@mst.edu)

## Program Scope

The kinetic bottleneck of electrochemical and photoelectrochemical water splitting is the four-electron oxygen evolution reaction (OER)<sup>1,2</sup>. OER catalysts include transition metal oxides such as RuO<sub>2</sub>, IrO<sub>2</sub>, PtO<sub>2</sub>, MnO<sub>2</sub>, and Co<sub>3</sub>O<sub>4</sub>.<sup>3</sup> Although the most active of these catalysts are the expensive noble metal oxides RuO<sub>2</sub>, IrO<sub>2</sub>, and PtO<sub>2</sub>, there is interest in developing OER catalysts based on earth-abundant metals such as Co and Ni. Co<sub>3</sub>O<sub>4</sub> is slightly less active than the noble metal oxides for water oxidation in alkaline solution.<sup>3</sup> Kanan and Nocera have also shown that an *amorphous* cobalt-phosphate (CoPi) OER catalyst can be electrodeposited, which works in neutral solution.<sup>4</sup> Our focus is on the electrodeposition of *crystalline* thin films of cobalt-based OER catalysts such as Co<sub>3</sub>O<sub>4</sub>, Co(OH)<sub>2</sub>, and CoOOH.<sup>5,6</sup> We argue that by studying crystalline materials with known crystal structures we then have a better chance of understanding the mechanism of the catalysis of the oxygen evolution reaction.

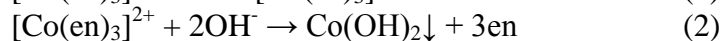
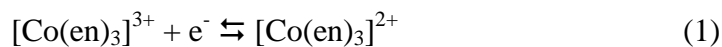
Electrodeposition is a bottom-up processing method in which solid films are assembled on an electrode surface from molecular and ionic precursors in solution. The rate of the reaction is precisely controlled through the applied potential, and microstructure and orientation of the film can often be controlled through solution additives. In our lab, we have studied the epitaxial electrodeposition of metal oxide thin films onto single-crystal substrates for several years. We hope that by depositing films with controlled crystallographic orientations it will be possible in future work to compare the catalytic activity of various well-defined surfaces.

## Recent Progress

We are interested in electrodepositing oxides and hydroxides of cobalt that are active catalysts for the oxygen evolution reaction (OER). We are particularly interested in depositing *crystalline* materials with well-characterized structures. Here, we present results on the electrodeposition of Co<sub>3</sub>O<sub>4</sub> and Co(OH)<sub>2</sub>.<sup>5,6</sup> Because Co(OH)<sub>2</sub> can be electrochemically converted to CoOOH, and thermally converted to CoO and Co<sub>3</sub>O<sub>4</sub>, this gateway material gives us the opportunity to directly compare the catalytic activity of the oxides, hydroxides, and oxyhydroxides of cobalt. We are also able to deposit epitaxial films of these materials, so it may be possible to compare the catalytic activities of various surfaces of the materials. We show that epitaxial films of Co(OH)<sub>2</sub> on Au can be converted to epitaxial films of CoOOH and Co<sub>3</sub>O<sub>4</sub>. The catalytic activity of Co<sub>3</sub>O<sub>4</sub>, Co(OH)<sub>2</sub>, and CoOOH will be compared in this talk. Preliminary results will be presented on the electrodeposition of CoOOH onto n-Si for the photoelectrochemical splitting of water.

We have recently reported on the electrodeposition and OER activity of  $\text{Co}_3\text{O}_4$ .<sup>5</sup> The films were deposited by electrochemically oxidizing a tartrate complex of Co(II) in alkaline solution at reflux temperatures. The crystalline films deposit with the normal spinel structure with a lattice parameter of 0.8097 nm and a crystallite size of 26 nm.

In order to electrodeposit  $\text{Co}(\text{OH})_2$  films,<sup>6</sup> we exploit the well-known coordination chemistry that Co(III) favors nitrogen ligands over oxygen ligands, whereas Co(II) favors oxygen ligands over nitrogen ligands.  $[\text{Co}(\text{en})_3]^{3+}$  is nearly 35 orders of magnitude more stable than  $[\text{Co}(\text{en})_3]^{2+}$  (en = ethylenediamine). The formation constants for  $[\text{Co}(\text{en})_3]^{3+}$  and  $[\text{Co}(\text{en})_3]^{2+}$  are  $10^{48.69}$  and  $10^{13.94}$ , respectively. Co(III) complexes are also substitutionally inert, whereas Co(II) complexes are substitutionally labile in aqueous solution. Hence,  $[\text{Co}(\text{en})_3]^{3+}$  is stable in an alkaline solution, but  $[\text{Co}(\text{en})_3]^{2+}$  reacts with excess  $\text{OH}^-$  to produce  $\text{Co}(\text{OH})_2$ . The formation constant of  $\text{Co}(\text{OH})_2$  is  $10^{14.96}$ . The  $\text{Co}(\text{OH})_2$  films were deposited according to equations 1 and 2. Films were deposited at room temperature at a potential of -1 V vs. Ag/AgCl in a solution of 45 mM  $[\text{Co}(\text{en})_3]^{3+}$  in 2 M NaOH.<sup>6</sup> The  $\text{Co}(\text{OH})_2$  deposits with a dense microcone morphology (Fig. 1). It has with the brucite layered structure with measured lattice parameters of  $a = b = 0.3179$  nm and  $c = 0.4658$  nm.



Electrodeposited  $\text{Co}(\text{OH})_2$  is a potent catalyst for the OER.<sup>6</sup> Linear sweep voltammograms (LSVs) at a scan rate of 1 mV/s on a Ti electrode (blue) and a  $\text{Co}(\text{OH})_2$ -coated Ti electrode (red) in unstirred 1 M KOH at room temperature are shown in Fig. 2. The LSV measured on electrodeposited, crystalline  $\text{Co}_3\text{O}_4$  film, which is an active OER catalyst, is also shown (black) because the surface chemistry of both materials during OER is similar. The onset of OER on  $\text{Co}(\text{OH})_2$  is 0.51 V<sub>Ag/AgCl</sub> which is about 50 mV higher than that measured on  $\text{Co}_3\text{O}_4$ . However, current densities, based on the geometric area of the electrodes, are much higher on the  $\text{Co}(\text{OH})_2$  film at more positive potentials. X-ray and Raman studies show that the surface of the  $\text{Co}(\text{OH})_2$  is converted to  $\text{CoOOH}$  at the potentials of the OER. We have also found that electrodeposited films of Co metal can be electrochemically converted to  $\text{CoOOH}$ . The catalytic activity of all of these species for the OER is compared in Tafel plots in Fig. 3. Note that  $\text{Co}_3\text{O}_4$  is the most active OER catalyst in this group. All of the catalysts in this

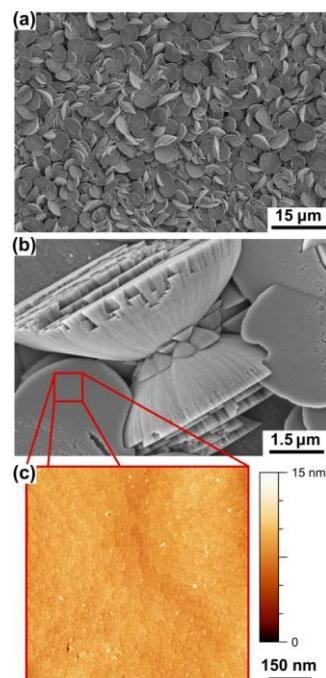


Fig. 1 - Morphology of electrodeposited  $\text{Co}(\text{OH})_2$ . (a) and (b) SEM images. (c) AFM image of a flat disk surface

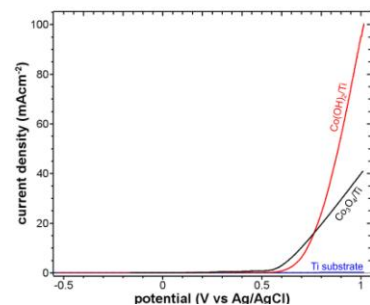


Fig. 2- Comparison of the catalytic activity for OER of  $\text{Co}_3\text{O}_4$  and  $\text{Co}(\text{OH})_2$  in 1 M KOH

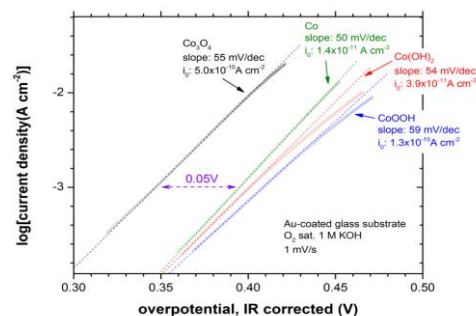


Fig. 3 - Tafel plots for various OER catalysts

study are considerably more active than the previously reported, amorphous CoPi catalyst.<sup>4</sup>

We have exploited the fact that Co can be converted to an active OER catalyst to produce a photoelectrochemical cell for photo-assisted water splitting. A very thin layer of Co metal was electrochemically deposited onto n-Si(100) and then electrochemically converted to CoOOH. A chopped light voltammogram of the n-Si/Co/CoOOH heterojunction in 1.0 M NaOH is shown in Fig. 4. The cell shows a 0.4-0.5 V up-conversion compared with the best of the catalysts in this study, and has impressive photocurrents for the oxygen evolution reaction in the 20 mA/cm<sup>2</sup> range. Our initial studies show that the photoanode is stable for at least several hours under illumination. The band diagram for the n-Si/Co interface is shown in Fig. 5. The photoanode acts like a metal/semiconductor Schottky barrier with a barrier height of 0.7 eV in series with the CoOOH OER catalyst.

### Future Plans

We would like to develop a method to measure the active area of the OER catalysts so that the catalytic activity can be compared more quantitatively. The areas are too low to measure by standard BET measurements. We are attempting to do differential capacitance measurements to compare the double layer capacitance of the various materials. We also plan to try quantitatively adsorbing and desorbing dyes with a known adsorption footprint area onto the surface.

We plan to do cross-sectional TEM studies of the n-Si/Co/CoOOH heterojunction before and after extended water-splitting experiments. Is there an interfacial layer of CoSi<sub>2</sub>? Does an insulating layer of SiO<sub>2</sub> form after the photo experiments? Can the stability be improved by purposely producing a cobalt silicide layer between the Si and Co by introducing a thermal anneal step?

The catalytic activity of Ni and NiCo, NiFe, and CoFe alloys will be explored. The most active of these alloys will then be electrodeposited onto n-Si to produce a photoanode.

Other, more stable, n-type semiconductors such as TiO<sub>2</sub> and Fe<sub>2</sub>O<sub>3</sub> will be modified with our most active OER catalysts for photoelectrochemical water splitting.

### References

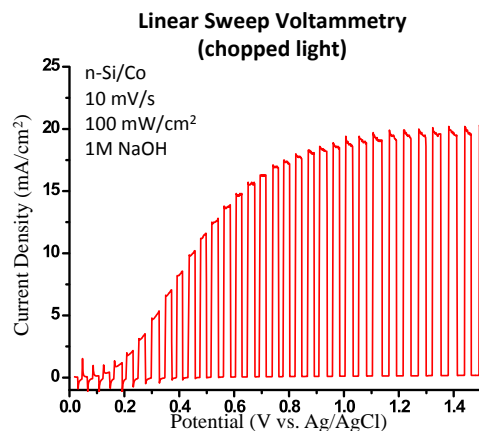


Fig. 4 - Photoelectrochemistry on an n-Si/Co/CoOOH heterojunction in 1.0 M NaOH

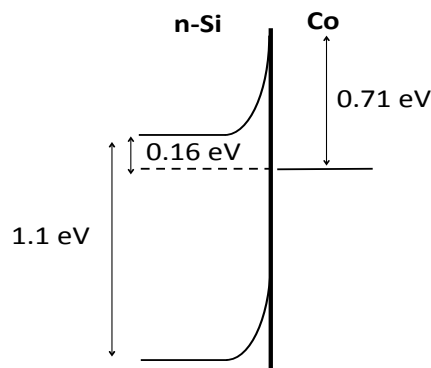


Fig. 5 - Band diagram for n-Si/Co heterojunction

1. M. G. Walter, E. L. Warren, J. R. McKone, S. W. Boettcher, Q. Mi, E. A. Santori, and N. S. Lewis, *Chem. Rev.* **110**, 6446 (2010).
2. D. K. Zhong and D. R. Gamelin, *J. Am. Chem. Soc.* **132**, 4202 (2010).
3. S. Trasatti, *Electrochim. Acta* **29**, 1503 (1984).
4. M. W. Kanan and D. G. Nocera, *Science* **321**, 1072 (2008).
5. J. A. Koza, Z. He, A. S. Miller, and J. A. Switzer, *Chem. Mater.* **24**, 3567 (2012).
6. J. A. Koza, C. M. Hull, Y.-C. Liu, and J. A. Switzer, *Chem. Mater.* **25**, 1922 (2013).

### **Publications over the past two years resulting from work supported by the DOE project**

1. R. V. Gudavarthy, S. Gorantla, G. Mu, E. A. Kulp, T. Gemming, J. Eckert, and J. A. Switzer, "Epitaxial electrodeposition of Fe<sub>3</sub>O<sub>4</sub> on single-crystal Ni(111)," *Chem. Mater.* **23**, 2017-2019 (2011).
2. R. V. Gudavarthy, N. Burla, E. A. Kulp, S. J. Limmer, E. Sinn, and J. A. Switzer, "Epitaxial electrodeposition of chiral CuO films from copper(II) complexes of malic acid on Cu(111) and Cu(110) single crystals," *J. Mater. Chem.* **21**, 6209-6216 (2011).
3. Z. He, R. V. Gudavarthy, J. A. Koza, and J. A. Switzer, "Room-temperature electrochemical reduction of epitaxial magnetite films to epitaxial iron films," *J. Am. Chem. Soc.* **133**, 12358-12361 (2011).
4. J. A. Koza, Z. He, A. S. Miller, and J. A. Switzer, "Resistance switching in electrodeposited VO<sub>2</sub> thin films," *Chem. Mater.* **23**, 4105-4108 (2011).
5. J. Koza, Z. He, A. S. Miller, and J. A. Switzer, "Electrodeposition of crystalline Co<sub>3</sub>O<sub>4</sub> – a catalyst for the oxygen evolution reaction," *Chem. Mater.* **24**, 3567-3573 (2012).
6. J. A. Switzer, "Atomic layer electrodeposition," *Science* **338**, 1300-1301 (2012).
7. Z. He, J. A. Koza, G. Mu, A. S. Miller, E. W. Bohannon, and J. A. Switzer, "Electrodeposition of Co<sub>x</sub>Fe<sub>3-x</sub>O<sub>4</sub> epitaxial films and superlattices," *Chem. Mater.* **25**, 223-232 (2013).
8. J. A. Koza, C. M. Hull, Y.-C. Liu, and J. A. Switzer, "Deposition of β-Co(OH)<sub>2</sub> films by electrochemical reduction of tris(ethylenediamine)cobalt(III) in alkaline solution," *Chem. Mater.* **25**, 1922-1926 (2013).
9. J. A. Koza, E. W. Bohannon, and J. A. Switzer, "Superconducting filaments formed during nonvolatile resistance switching in electrodeposited δ-Bi<sub>2</sub>O<sub>3</sub>" *ACS Nano*, submitted, manuscript #nn-2013-038207, accepted (2013).
10. Y.-C. Liu, J. A. Koza, and J. A. Switzer, "Comparison of the catalytic activity of electrodeposited Co(OH)<sub>2</sub>, CoOOH, and Co<sub>3</sub>O<sub>4</sub> for the oxygen evolution reaction," *Electrochim. Acta*, in preparation (2013).

## Enhanced Materials Based on Submonolayer Type-II Quantum Dots

M. C. Tamargo, I. K. Kuskovsky, C. A. Meriles and I. C. Noyan  
Department of Chemistry, The City College of New York, NY, NY 10031

Department of Physics, Queens College of CUNY, Queens, NY 11367

Department of Physics, The City College of New York, NY, NY 10031

Department of Applied Physics and Applied Mathematics, Columbia University, NY, NY 10027

### Program Scope

During the past few years we have investigated a nanostructured material that we refer to as submonolayer type-II QDs made from wide bandgap II-VI semiconductors. Our goal is to understand and exploit their tunable optical and electrical properties, by taking advantage of the type-II band alignment and quantum confinement effects.<sup>1</sup> Type-II ZnTe quantum dots (QDs) in a ZnSe host are particularly interesting because of their relatively large valence band and conduction band offsets.<sup>2</sup> Exploring the potential for designing new materials with enhanced properties was the primary motivation of our most previous award. During that time we advanced our understanding of these novel nanostructures and our ability to control and manipulate their structural properties and we obtained materials with new and enhanced properties. We also developed an experimental approach to characterize the structures with high precision and insight. In this program we aim to develop enhanced materials based on the submonolayer type-II QDs, with emphasis on materials that may be advantageous for photovoltaic and spintronics applications. We also expand the structural characterization of these materials by refining our X-ray diffraction methodologies.

Intermediate band solar cells (IBSCs) are substantially more efficient than conventional solar cells.<sup>3,4</sup> IBSCs rely on multi-photon absorption with an assistance of an intermediate band in the mid-gap region of the semiconductor material used for the solar cell fabrication. The formation of the intermediate band by means of quantum dots (QDs) is thought to be one of the best approaches to fabricate IBSCs.

We have shown that the material system with multi-layers Zn(Cd)Te/ZnCdSe submonolayer QDs has the ideal material parameters for this particular application.<sup>5,6</sup> The band gap of host ZnCdSe lattice matched to InP is  $\sim 2.1$  eV and the intermediate band can be engineered at  $\sim 0.7$  eV using hole confinement levels in the Zn(Cd)Te QDs. These parameters are the best match to the optimal IBSC parameters proposed by Luque and Marti. Additionally, the submonolayer QDs grown via migration enhanced epitaxy (MEE) grow without the formation of wetting layers, which is known to be detrimental for device fabrication due to the introduction of strain. Moreover, the type-II band alignment is expected to improve carrier extraction process due to reduced radiative recombination within QDs.

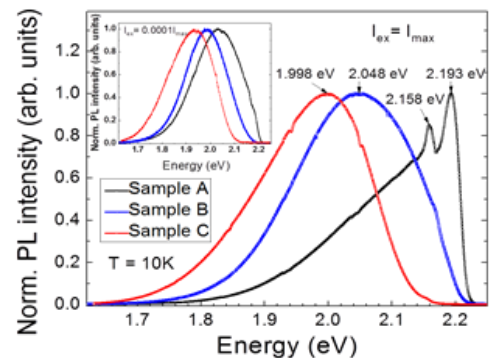


**Figure 1:** Photoluminescence (PL) at 10K for samples A, B and C. Inset shows PL data at lower excitation intensity.

## Recent Progress

Initial attempts to grow the ZnTe/ZnCdSe structures showed a typical type-II behavior, as shown in Figures 1 and 2. Below band gap absorption was observed in the samples which can further be enhanced by increasing the QD size and density, which can be controlled by adjusting Te flux used during the growth. However, detailed analysis of the HRXRD showed a relatively high lattice mismatch between the zeroth order SL peak and the substrate peak. This lattice mismatch was found to be due to the formation of an unintentional strained ZnSe-rich layer at the QD-barrier interface as confirmed by the HRXRD simulations. To avoid potential degradation issues, optimization of growth parameters of these multilayer

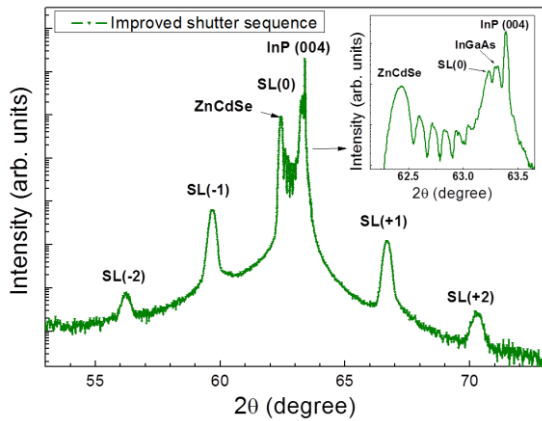


**Figure 3:** HRXRD plot of the sample obtained by the improved shutter sequence.

map (RSM) analysis was performed in order to extract structural information about the submonolayer QDs.<sup>7</sup> RSM along (002) as well as (004) orientations showed a clear elongation in  $q_x$  direction for sample with higher Te fraction and thus with larger and denser QDs, as shown in Figure 4. This indicated enhanced vertical alignment of larger submonolayer QDs case of sample E.

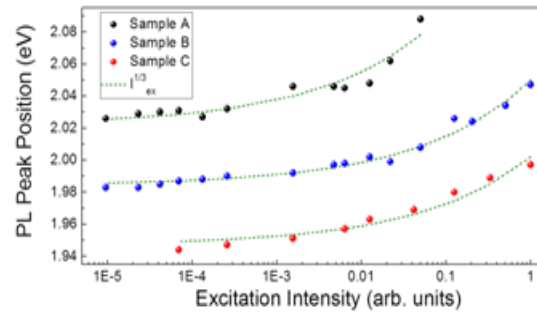


**Figure 2:** Excitation intensity dependence of the PL peak energy.

structures was performed. Optimization was achieved first by modifying the shutter sequences used during MEE to grow QDs in group-II-rich conditions and secondly by strain balancing technique through the growth of intentional Cd-rich spacers. Improved HRXRD data is shown in Figure 3. The type-II nature and therefore long radiative recombination lifetimes remained unchanged after structural improvements.

In order to investigate the possibility of vertical coupling of the QDs, and thus miniband formation, as needed for the IBSC application, two structures grown by the improved shutter sequence with different QD sizes were investigated. HRXRD based reciprocal space

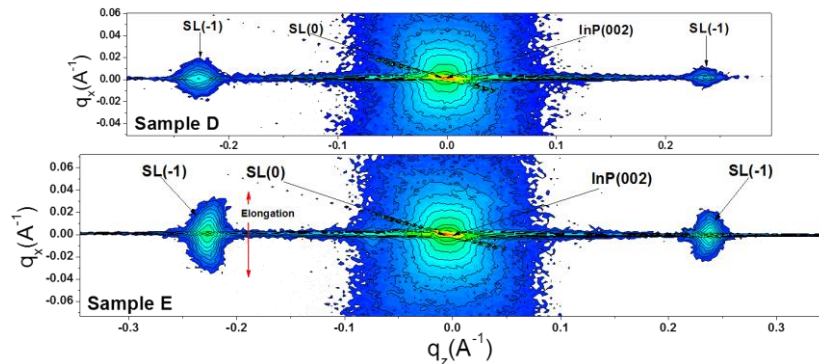


**Figure 4:** Reciprocal space map of two samples showing enhanced vertical correlation for the sample with the larger QDs.

Systematic analysis of RSMs by fitting the experimental data to a theoretical model shows that ~90% QDs in the sample with larger QDs are vertically correlated, which is important to ensure sufficient overlap of the QD confined hole wave functions to facilitate the miniband formation. Formation of miniband is an important prerequisite for successful operation of an IBSC to increase below band gap absorption and to reduce non-radiative recombination.

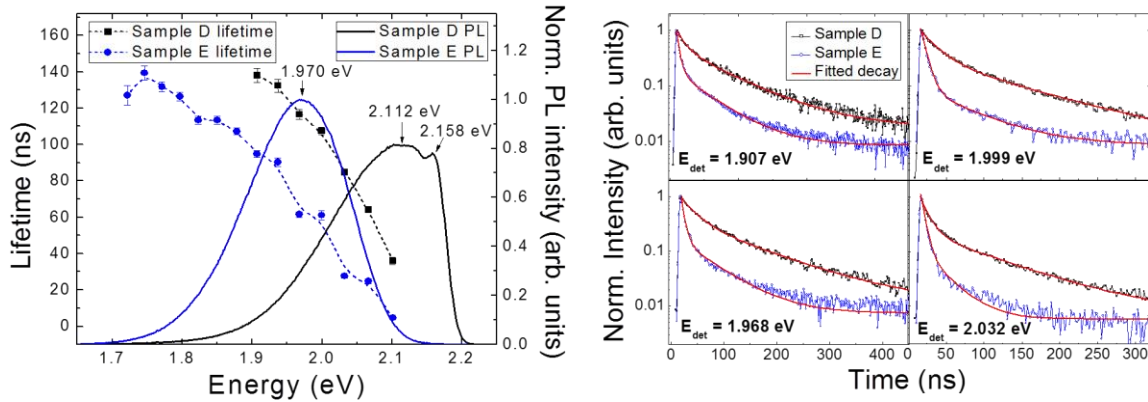


**Figure 5:** Left: Solid lines denote the PL spectra normalized to PL peak of sample E and the symbols connected with dotted lines are the extracted radiative lifetime of samples D and E. Right: Experimental and fitted decay curves at various detection energies

Figure 5 shows that narrower photoluminescence with a better yield was obtained for the sample with improved vertical correlation, indicating smaller QD size distribution along with partial suppression of non-radiative recombination paths. Observed reduction in radiative lifetimes and supportive calculations demonstrate enhanced hole-hole wavefunction overlap pointing towards possibility of miniband formation, an advantageous feature for an intermediate band solar cell.

## Future Plans

We plan to continue to investigate the potential for type-II ZnTe/ZnCdSe materials in IBSCs. Toward this end, we will grow Nitrogen doped structures of ZnTe/ZnCdSe materials, which will be investigated to enhance below bandgap absorption. We will also grow samples with larger QDs in order to enhance miniband formation. Incorporation of these QD structures within a p-n junction will be investigated.

We will also begin to explore refinements in the structural characterization of our samples using HRXRF and TEM techniques. We will explore methodologies to obtain data on the shape, chemical composition and elastic strain distributions within the dots. Initially we will conduct XRR and HRXRD and reciprocal lattice mapping measurements on NSLS X20-A and analyze these data to achieve such refinements.

## References:

1. Y. Gong, W. MacDonald, G. F. Neumark, M. C. Tamargo and I. L. Kuskovsky, *Optical properties and growth mechanism of multiple type-II ZnTe/ZnSe quantum dots grown by migration-enhanced epitaxy*, Phys. Rev. B **77**, 155314-155316 (2008)
2. M.S. Mukhin, Ya.V. Terent'ev, L.E. Golub, M.O. Nestoklon, B.Ya. Meltser, A.N. Semenov, V.A. Solov'ev, A.A. Sitnikov, A.A. Toropov and S.V. Ivanov, *Magneto-Optical Studies of*

*Narrow Band-Gap Heterostructures with Type II Quantum Dots InSb in an InAs Matrix*, Acta Polonica A **120** 868-869 (2011)

3. A. Luque and A. Martí, *Increasing the efficiency of ideal solar cells by photon induced transitions at intermediate levels*, Phys. Rev. Lett. **78**, 5014 (1997)
4. Luque, A. Martí, and C. Stanley, *Understanding intermediate-band solar cells*, Nat. Photonics **6**, 146 (2012)
5. S. Dhomkar, I.L. Kuskovsky, U. Manna, I.C. Noyan, and M.C. Tamargo, *Optimization of growth conditions of type-II Zn(Cd)Te/ZnCdSe submonolayer quantum dot superlattices for intermediate band solar cells*, J. Vac. Sci. Technol. B **31**, 03C119 (2013)
6. S. Dhomkar, U. Manna, L. Peng, R. Moug, I.C. Noyan, M.C. Tamargo, and I.L. Kuskovsky, *Feasibility of submonolayer ZnTe/ZnCdSe quantum dots as intermediate band solar cell material system*, Sol. Energy Mater. Sol. Cells **117**, 604 (2013)

### **DoE Sponsored Publications in the Last Two Years**

1. U. Manna, I. C. Noyan, Q. Zhang, I. F. Salakhutdinov, K. A. Dunn, S. W. Novak, R. Moug, M. C. Tamargo, G. F. Neumark, and I. L. Kuskovsky, *Structural properties and spatial ordering of multilayered ZnMgTe/ZnSe type-II quantum dot structures*, Journal of Applied Physics **111**, 033516 (2012)
2. B. Roy, H. Ji, S. Dhomkar, F. J. Cadieu, L. Peng, R. Moug, M. C. Tamargo, and I. L. Kuskovsky, *Determination of excitonic size with sub-nanometer precision via excitonic Aharonov-Bohm effect in type-II quantum dots*, Applied Physics Letters **100**, 213114 (2012) (Partial DOE support)
3. U. Manna, Q. Zhang, S. Dhomkar, I. F. Salakhutdinov, M. C. Tamargo, I. C. Noyan, G. F. Neumark and I. L. Kuskovsky, *Radiative transitions in vertically correlated type-II ZnMgTe/ZnSe multilayer quantum dot structure*, J. Appl. Phys. **112**, 063521 (2012).
4. B. Roy, H. Ji, S. Dhomkar, F. J. Cadieu, L. Peng, R. Moug, M. C. Tamargo, I. L. Kuskovsky, *Distinguishability of stacks in ZnTe/ZnSe quantum dots via spectral analysis of Aharonov-Bohm oscillations*, Eur. Phys. J. B **86**, 31 (2013). (Partial DOE support)
5. S. Dhomkar, I. L. Kuskovsky, U. Manna, I. C. Noyan, M. C. Tamargo, *Optimization of growth conditions of type-II Zn(Cd)Te/ZnCdSe submonolayer quantum dot superlattices for intermediate band solar cells*, J. Vac. Sci. Technol. B **31**, 03C119 (2013).
6. S. Dhomkar, U. Manna, L. Peng, R. Moug, I. C. Noyan, M. C. Tamargo, I. L. Kuskovsky, *Feasibility of submonolayer ZnTe/ZnCdSe quantum dots as intermediate band solar cell material system*, Sol. Energy Mater. Sol. Cells **117**, 604 (2013).
7. H. Ji, B. Roy, S. Dhomkar, R. T. Moug, M. C. Tamargo, A. Wang, I. L. Kuskovsky, *Tuning Between Quantum-Dot- and Quantum-Well-Like Behaviors in Type II ZnTe Submonolayer Quantum Dots by Controlling Tellurium Flux During MBE Growth*, J. Electron. Mater. **Published Online**, DOI 10.1007/s11664-013-2729-2 (2013).
8. S. Dhomkar, U. Manna, I. C. Noyan, M. C. Tamargo, I. L. Kuskovsky, *Vertical correlation and miniband formation in submonolayer Zn(Cd)Te/ZnCdSe type-II quantum dots for intermediate band solar cell application*, Appl. Phys. Lett. **Accepted** (2013).

9. B. Roy, H. Ji, S. Dhomkar, M. C. Tamargo, I. L. Kuskovsky, *Observation of oscillations in energy of Aharonov-Bohm excitons in type-II ZnTe/ZnSe stacked submonolayer quantum dots*, *Phys. Status Solidi C* **Submitted** (2013). (Partial DOE support)

## **Inverse Optimization Techniques for Targeted Self-Assembly**

**Salvatore Torquato and Frank H. Stillinger**

**Department of Chemistry and Princeton Institute for the Science and Technology of  
Materials**

**Princeton University, Princeton, N.J. 08544 USA**

**torquato@princeton.edu**

**fhs@princeton.edu**

**<http://cherryvit.princeton.edu>**

### **Program Scope**

Conventional applications of the principles of statistical mechanics (the “forward” problems), start with particle interaction potentials, and proceed to deduce local structure and macroscopic properties [1]. Other applications that may be classified as “inverse” problems, begin with targeted configurational information, such as low-order correlation functions that characterize local particle order, and attempt to back out full-system configurations and/or interaction potentials [2]. The latter inverse approach is the thrust of our research and applications are directed toward self-assembling colloidal systems, spin systems, and the reconstruction of material microstructures. Once inverse solutions for targeted configurations are obtained, forward methods are still employed to study the properties of the systems.

Inverse approaches could revolutionize the manner in which materials are designed and fabricated. There are a number of very tangible applications of targeted self-assembly. Examples include photonic band-gap applications, materials with negative or vanishing thermal expansion coefficients, materials with negative Poisson ratios, materials with optimal transport and mechanical properties, mesoporous solids for applications in catalysis, separations, sensors and electronics. In the case of spin systems, one could imagine designing materials to have desired magnetic properties. Perhaps the greatest applications are as yet un-foreseen – as the interest in and usefulness of nanosystems grow, as will the need for them to themselves form structures with desired behaviors.

In the case of many-particle systems, output from these optimization techniques could then be applied to create *de novo* colloidal particles or polymer systems with interactions that yield these structures at the nanoscopic and microscopic length scales. Colloidal particles suspended in solution provide an ideal experimental testbed to realize the optimized potentials, since both repulsive and attractive interactions can be tuned (e.g., via particle surface modification or the addition of electrolytes) and therefore offer a panoply of possible potentials that far extends the range offered by molecular systems.

### **Recent Progress**

The research program has been aimed at first devising completely new inverse statistical-mechanical methods and then applying them for novel material design. We have also used lessons learned from the inverse approach to characterize of a variety of disordered systems. The following is a list of the highlights of our accomplishments during last two years:

- Development of inverse methods for unusual ground states [3, 4];
- Optimized isotropic pair interactions for novel crystal ground states [3, 4];
- Collective-coordinate inverse methods for unusual ground states [5];
- Designer spin systems via inverse statistical mechanics [6];
- Inverse techniques for material microstructure reconstructions [7, 8];
- Characterization of hyperuniform materials, including amorphous silicon [9, 10];
- Identification of nonequilibrium static growing length scales in supercooled liquids on approaching the glass transition [11];
- Understanding hydration and percolation at the setting point of cement [12];
- Identification of families of tessellations of space by elementary polyhedra [13].

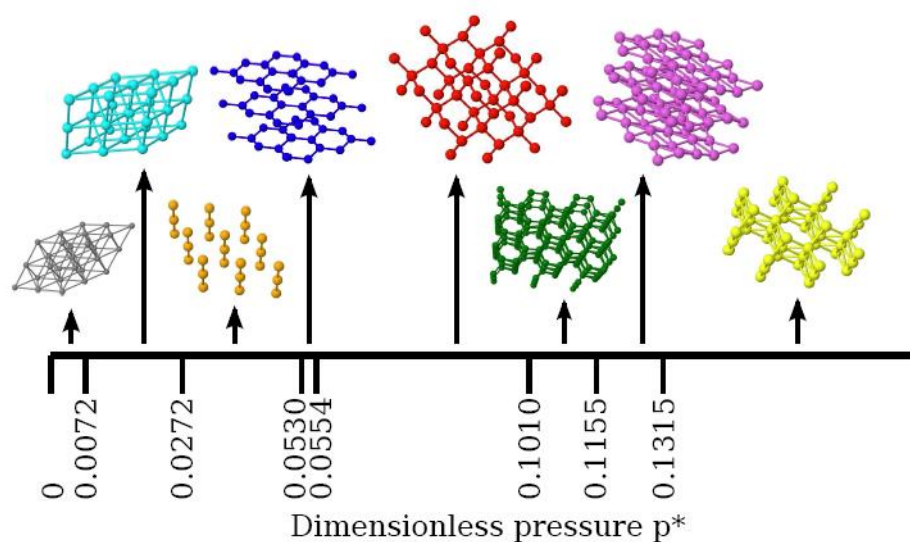


**Figure 1.** Monotonic radial pair potentials whose ground states for a range of pressures include the targeted diamond crystal (red) as well as other generally low-coordinated crystals for other pressures [3].

To illustrate our application of inverse statistical-mechanical methods, we describe three different recent research projects. Figure 1 summarizes results of our investigation to find a simple family of optimized isotropic, monotonic pair potentials (that may be experimentally realizable) whose classical ground state is the diamond crystal for the widest possible pressure range, subject to certain constraints (e.g., desirable phonon spectra) [3]. We also ascertained the ground-state phase diagram for a specific optimized potential to show that other crystal structures arise for pressures outside the diamond stability range. Cooling disordered configurations interacting with our optimized potential to absolute zero frequently led to the desired diamond crystal ground state, revealing that the capture basin for the global energy minimum is large and broad relative to the local energy minima basins.

In a subsequent investigation, we further tested the fundamental limitations of radial pair potentials by targeting crystal structures with appreciably less symmetry, including those in which the particles have different local structural environments [4]. Using a modified optimization

technique, we designed short- ranged radial pair potentials that stabilize the two-dimensional kagomé crystal, the rectangular kagomé crystal, and rectangular lattices, as well as the three-dimensional structure of  $\text{CaF}_2$  crystal inhabited by a single particle species. We presented general principles that offer guidance in determining whether certain target structures can be achieved as ground states by radial pair potentials.

The final example considers the first application of inverse statistical mechanics to designing radial two- state Ising interactions of finite range to produce targeted spin configurations as ground states [6]. We considered a general family of striped phase spin configurations comprised of alternating parallel bands of up and down spins of varying thicknesses and a general family of rectangular block checkerboard spin configurations with variable block size, which is a generalization of the classic anti-ferromagnetic Ising model. Our findings demonstrate that the structurally anisotropic striped phases, in which the thicknesses of up and down spin bands are equal, are unique ground states for isotropic short-ranged interactions. By contrast, many of the block checkerboard targets are degenerate ground states. It will be interesting to explore whether such inverse statistical-mechanical techniques could be employed to design materials with desired spin properties.

## Future Plans

Future work will focus on finding the interaction potential, not necessarily pairwise additive or spherically symmetric, that optimally stabilizes a targeted many-body system, which may be a crystal, disordered or quasicrystal structure, by incorporating structural information that is not limited to the pair correlation function and generally accounts for complete configurational information. Our primary interest is in the possible many-body structures that may be generated, some of which may include interesting but known structures, while others may represent entirely new structural motifs. We plan on extending our inverse methods to multicomponent systems. Moreover, the inverse methods described here can be employed to find targeted structures for metastable states as well as nonequilibrium configurations. Finally, an important component of future research will be the development of robust potentials (even if not optimal) for targeted structures and bulk properties that can be synthesized experimentally with colloids or other soft matter systems as well as solid state systems.

## References

1. J. P. Hansen and I. R. McDonald. *Theory of Simple Liquids*. Academic Press, New York, 1986.
2. S. Torquato. Inverse optimization techniques for targeted self-assembly. *Soft Matter*, 5:1157-1173, 2009.
3. É. Marcotte, F. H. Stillinger, and S. Torquato. Designed diamond ground state via optimized isotropic monotonic pair potentials. *J. Chem. Phys.*, 138:061101, 2013.
4. G. Zhang and F. H. Stillinger and S. Torquato. Inverse statistical mechanics: Probing the limitations of isotropic pair potentials to produce ground-state structural extremes. *Phys. Rev. E*, 2013.
5. S. Martis, É. Marcotte, F. H. Stillinger, and S. Torquato. Exotic ground states of directional pair potentials via collective-density variables. *J. Stat. Phys.*, 150:414, 2013.
6. R. Distasio, É. Marcotte, R. Car, F. H. Stillinger, and S. Torquato. Designer spins systems via inverse statistical mechanics. *Phys. Rev. B*, 2013.
7. C. J. Gommès, Y. Jiao, and S. Torquato. Density of states for a specified correlation function

- and the energy landscape. *Physical Review Letters*, 108:080601, 2012.
8. C. J. GOMMES, Y. JIAO, and S. TORQUATO. Microstructural degeneracy associated with a two-point correlation function and its information content. *Phys. Rev. E*, 85:051140, 2012.
  9. M. HEJNA, P. J. STEINHARDT, and S. TORQUATO. Nearly hyperuniform network models of amorphous silicon. *Phys. Rev. B*, 87:245204, 2013.
  10. R. XIE, G. G. LONG, S. J. WEIGAND, S. C. MOSS, T. CARVALHO, S. ROORDA, M. HEJNA, S. TORQUATO, and P. J. STEINHARDT. Hyperuniformity in amorphous silicon based on the measurement of the infinite-wavelength limit of the structure factor. *Proc. Nat. Acad. Sci.*, 110:13250, 2013.
  11. É. MARCOTTE, F. H. STILLINGER, and S. TORQUATO. Nonequilibrium static growing length scales in super-cooled liquids on approaching the glass transition. *J. Chem. Phys.*, 138:12A508, 2013.
  12. G. W. SCHERER, J. ZHANG, J. A. QUINTANILLA, and S. TORQUATO. Hydration and percolation at the setting point. *Cem. Concr. Res.*, 42:665, 2012.
  13. R. GABBRIELLI, YANG JIAO, and S. TORQUATO. Families of tessellations of space by elementary polyhedra via retessellations of face-centered-cubic and related tilings. *Phys. Rev. E*, 86:041141, 2012.

### DoE Sponsored Publications in the Last Two Years

1. C. J. GOMMES, Y. JIAO, and S. TORQUATO. Density of states for a specified correlation function and the energy landscape. *Physical Review Letters*, 108:080601, 2012.
2. C. J. GOMMES, Y. JIAO, and S. TORQUATO. Microstructural degeneracy associated with a two-point correlation function and its information content. *Phys. Rev. E*, 85:051140, 2012.
3. G. W. SCHERER, J. ZHANG, J. A. QUINTANILLA, and S. TORQUATO. Hydration and percolation at the setting point. *Cem. Concr. Res.*, 42:665, 2012.
4. R. GABBRIELLI, YANG JIAO, and S. TORQUATO. Families of tessellations of space by elementary polyhedra via retessellations of face-centered-cubic and related tilings. *Phys. Rev. E*, 86:041141, 2012.
5. É. MARCOTTE, F. H. STILLINGER, and S. TORQUATO. Designed diamond ground state via optimized isotropic monotonic pair potentials. *J. Chem. Phys.*, 138:061101, 2013.
6. S. MARTIS, É. MARCOTTE, F. H. STILLINGER, and S. TORQUATO. Exotic ground states of directional pair potentials via collective-density variables. *J. Stat. Phys.*, 150:414, 2013.
7. É. MARCOTTE, F. H. STILLINGER, and S. TORQUATO. Nonequilibrium static growing length scales in supercooled liquids on approaching the glass transition. *J. Chem. Phys.*, 138:12A508, 2013.
8. M. HEJNA, P. J. STEINHARDT, and S. TORQUATO. Nearly hyperuniform network models of amorphous silicon. *Phys. Rev. B*, 87:245204, 2013.
9. R. XIE, G. G. LONG, S. J. WEIGAND, S. C. MOSS, T. CARVALHO, S. ROORDA, M. HEJNA, S. TORQUATO, and P. J. STEINHARDT. Hyperuniformity in amorphous silicon based on the measurement of the infinite-wavelength limit of the structure factor. *Proc. Nat. Acad. Sci.*, 110:13250, 2013.
10. G. ZHANG and F. H. STILLINGER and S. TORQUATO. Inverse statistical mechanics: Probing the limitations of isotropic pair potentials to produce ground-state structural extremes. *Phys. Rev. E*, 2013.
11. R. DISTASIO, É. MARCOTTE, R. CAR, F. H. STILLINGER, and S. TORQUATO. Designer spins systems via inverse statistical mechanics. *Phys. Rev. B*, 2013.

## Four-Dimensional Analysis of the Evolution of Complex Dendritic Microstructures During Coarsening

J. Gibbs, C. Park\*, K. Thornton\* and P. Voorhees  
Department of Materials Science and Engineering  
Northwestern University, Evanston IL, 60208

\*Department of Materials Science and Engineering  
University of Michigan, Ann Arbor MI, 48109

### Program Scope

Dendrites are tree-like structures that frequently form during solidification of castings. Dendrites possess secondary and, sometimes, even tertiary side branches. While the tip radius and tip velocity of the dendrite are set by the growth conditions, the side branches behind the tip undergo a coarsening process under nearly isothermal conditions. The resulting two-phase mixtures are morphologically complex. These dendritic two-phase mixtures are one example from a large class of morphologically complicated structures found in nature that undergo coarsening. Included in this class are the bicontinuous two-phase mixtures produced following phase separation. Understanding the coarsening process in these systems requires theory, simulation, and experiments that capture their three-dimensional (3D) morphology.

At the core of the investigation is a four-dimensional (4D) characterization and analysis approach, which follows the morphological evolution process in three dimensions and in time (an additional dimension). A combined theoretical and experimental program is employed to examine the nature of the coarsening process in these highly complex, dendritic microstructures. The experiments examine the time-dependent evolution of the dendritic mixtures in three dimensions *in situ* through X-ray microtomography. The results of these experiments are used both to provide insights into the coarsening process and to guide the development of theory. Simulations of coarsening in bicontinuous mixtures are used to develop a theory of coarsening in these systems that can elucidate the role of the complicated morphology found in dendritic systems on the coarsening process.

### Recent Progress

X-ray computed tomography allows for 4D measurements of the locations of solid-liquid interfaces within a solid-liquid mixture that is being held at a constant temperature. The 3D reconstruction of this solid-liquid mixture is shown in Fig. 1. This allows us to

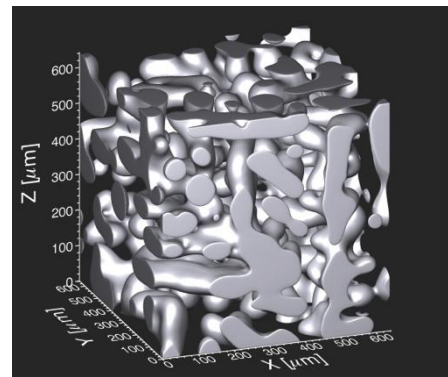


**Fig. 1.** A solid-liquid mixture used to determine interfacial velocities; the volume fraction of solid is 35%.

capture both the curvature of the interface, which sets its chemical potential, and the resulting evolution of the sample.

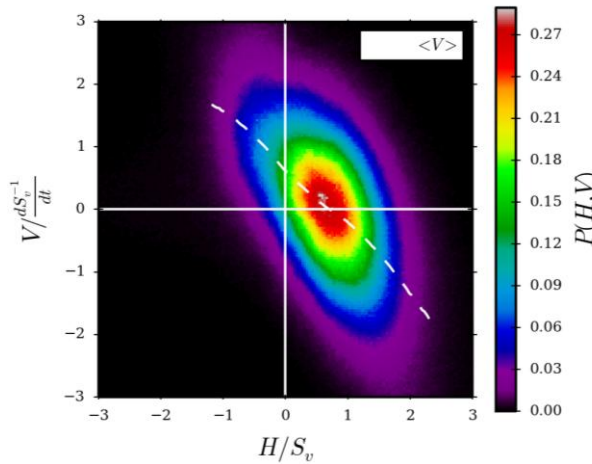


**Fig. 2.** Interfacial velocities,  $V$ , scaled on the characteristic coarsening rate,  $dS_v^{-1}/dt$ , as a function of the scaled mean curvature  $H$ .  $P$  is the probability of finding a patch of interface with a given pair of  $H$  and  $V$ , and  $S_v$  is the surface area per volume.

Using the 3D reconstructions at two different times, we determine the interfacial velocities and show that, on average, the normal velocity of an interface is approximately proportional to its mean curvature, see the dotted line on Fig. 2 that shows the average  $V$  for a given  $H$ . The mean curvature of a patch sets the value of the chemical potential in the liquid, but the velocity at a point on the interface also depends on the surrounding diffusion field. Thus, the qualitative dependence on the average velocity with  $H$  implies that the chemical potential plays a surprisingly important role in setting the velocity at a point on the interface. This result indicates that diffusion is affecting all the mean curvatures more or less uniformly.

However, diffusional interactions are still important. From Fig. 2, it is evident that for a particular mean curvature value, there is a significant dispersion of velocities; for example, at  $H = 1.0$  in Fig. 2,  $V$  can have a value between  $-1.5$  and  $+1.0$ . If we examine the distribution of velocities for given pair of mean ( $H$ ) and Gaussian ( $K$ ) curvatures, the geometry of the patch is fixed, and thus if there is a dispersion in velocity it is due to diffusional interactions between interfacial patches. Fig. 3 shows that there is, in fact, a distribution of velocities for that pair of curvatures and that this distribution is very nearly a Gaussian distribution, implying that the interactions are random despite the non-random microstructure. Most interestingly, this is a very general result: the distribution is

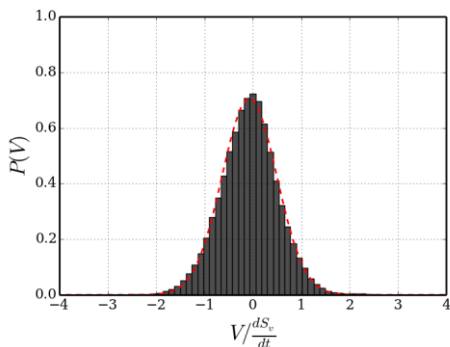


**Fig. 3.** The distribution of velocities for given  $H$  and  $K$ . The dashed line is the best fit to a Gaussian distribution.

Gaussian for all values of  $H$  and  $K$ , regardless of volume fraction, stage of coarsening, or whether those patches are shrinking or growing on average.

To assess the generality of these results, we are investigating how the normal velocity is affected by the local curvature and the curvature of the surrounding interfaces during coarsening in a completely different structure: the bicontinuous structure produced following spinodal decomposition. Fig. 4 shows (a) the interfacial shape distribution (ISD) of the

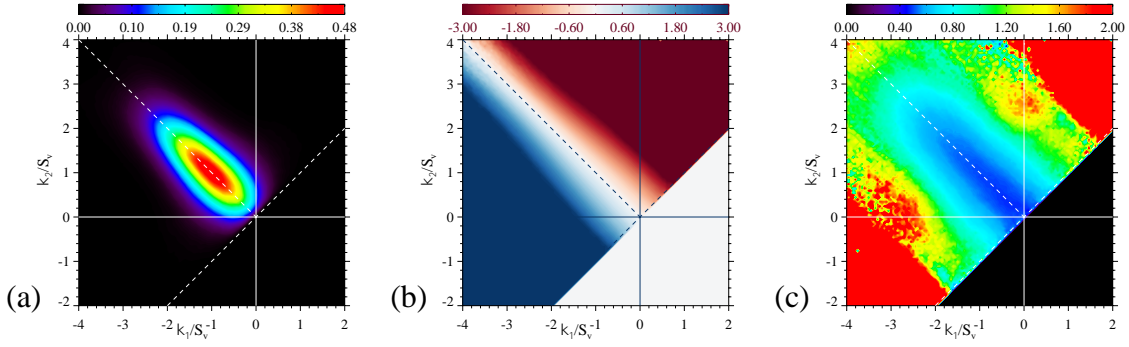


**Fig. 4.** (a) The interfacial shape distribution of the simulated bicontinuous structure, where  $\kappa_1$  and  $\kappa_2$  are the principal curvatures of a patch of interface (b) the scaled interfacial velocity averaged over all interfaces with a given  $\kappa_1$  and  $\kappa_2$  and (c) standard deviation of Gaussian fit of the velocities with a given  $\kappa_1$  and  $\kappa_2$ .

simulated structure. The ISD shows that nearly all the interfaces have negative  $K$ , or are saddle-shaped, which is very different from the experimental microstructures.

Figure 4(b) shows that the interfacial velocity is strongly coupled to  $H$  as the average velocity rapidly changes in the direction perpendicular to the  $H = 0$  line (where  $k_1 = -k_2$  and  $\kappa_1$  and  $\kappa_2$  are the principal interfacial curvatures), but not along a line of constant  $H$ . The strong dependence of interfacial velocity on the mean curvature is natural, since the chemical potential at the interface is related to the mean curvature of the interface. However, we also find that the magnitude of the average velocity increases, albeit less rapidly, along a constant  $H$ -line as the net curvature,  $d = \sqrt{k_1^2 + k_2^2}$ , increases. This increase in the magnitude of average velocity could be due to interfaces with same mean curvature having varying net curvature, which represents from overall bend of the surface as  $d$  increases. Thus, one could hypothesize that the velocity of the interfaces with complex geometry cannot be described by the mean curvature alone, but requires additional parameters such as net curvature and the morphologies of the surrounding interfaces.

Despite the very different morphologies, we also find for the simulated microstructure that the interfacial velocity distribution is well described by a Gaussian distribution for a fixed pair of  $H$  and  $K$  (or  $\kappa_1$  and  $\kappa_2$ ), in agreement with the experimental results shown in Fig. 3. To determine how this Gaussian distribution varies as a function of  $\kappa_1$  and  $\kappa_2$ , we plot the standard deviation of the distribution on the curvature space in Fig. 4c. The standard deviation increases with increasing magnitude of the mean curvature. Similar to the average velocity values, the standard deviation of the velocity distribution also increases with increasing net curvature at constant  $H$ . Possible explanations for the increase in the standard deviation of velocity with increasing mean curvature and net curvature are: (a) highly curved interfaces may experience longer-range interaction with surrounding interfaces than flatter interfaces, and/or (b) highly curved interfaces may have higher probability of being surrounded by wider range of morphological environments.

## Future Plans

Using the experimental data and simulations, we shall explore the reasons underlying the observed Gaussian distribution of interfacial velocities. For example, it is not clear why interfaces interact randomly, even though the structures themselves are far from random. Using the simulations, we shall determine if this same random distribution of velocities is present when the system is coarsening by nonconserved dynamics, where there are no diffusional interactions. In addition, we will use the combination of local and statistical analyses to fully understand the combined effect of mean curvature and the net curvature of interfaces on the interfacial velocity in structures resulting from evolution via conserved dynamics and more complex microstructures obtained from experiments.

## DoE Sponsored Publications in the Last Two Years

1. J.L. Fife, J.W. Gibbs, E.B. Gulsoy, C.-L. Park, K. Thornton, and P.W. Voorhees, *The Dynamics of Interfaces During Coarsening in Solid-Liquid Mixtures*, submitted.
2. C.-L. Park, P. W. Voorhees, K. Thornton, *Application of the Level-Set Method to the Analysis of an Evolving Microstructure*, submitted
3. D.J. Rowenhorst, and P.W.Voorhees, *Measurement of Interfacial Evolution in Three Dimensions*, Ann. Rev. Mater. Res. **42** 105-124 (2012).
4. L.K. Aagesen, A.E. Johnson, J.L. Fife, P.W. Voorhees, M.J. Miksis, S.O. Poulsen, E.M. Lauridsen, F. Marone and M. Stampanoni, *Pinch-Off of Rods by Bulk Diffusion*, Acta Mater., 59 4922-4932 (2011).

# Directed Assembly of Rod-Coil Block Copolymers by Combined External Fields

*Qiang (David) Wang and David S. Dandy*  
*Department of Chemical and Biological Engineering*  
*Colorado State University, Fort Collins, CO 80523-1370*

## Program Scope

The overall goal of our DOE project DE-FG02-07ER46448 is to understand, predict, and ultimately control the self-assembled nanostructures of rod-coil (RC) block copolymers in bulk, under thin-film confinement and with applied magnetic field. Photovoltaic (PV) energy obtained using  $\pi$ -conjugated (semiconducting) polymers is very attractive due to its cheap materials, low processing cost, and ease of large-scale manufacture. Control of the polymer morphology and structure at the nanoscale is critically important for optimizing the efficiency of polymer optoelectronic devices. The underlying hypothesis of this research is that such control can be achieved with magnetic-field directed assembly in thin films of RC block copolymers containing conjugated rod blocks. Using judiciously designed models and carefully selected methods, including 3D real-space parallel self-consistent field (SCF) calculations with high accuracy and newly proposed fast off-lattice Monte Carlo (FOMC) simulations with soft potentials that allow particle overlapping<sup>1</sup>, we examine in detail the effects of key factors (rod block length and volume fraction, RC incompatibility, orientational interaction between rod blocks, bending rigidity of rod blocks, and system fluctuations/correlations) on the self-assembled morphology of RC diblock copolymers (DBC) in bulk, as well as the effects external conditions (surface preference, film thickness, substrate topology, and applied magnetic field strength) for obtaining the optimal structures of bulk heterojunction in RC DBC thin films optimal for PV cells. This research will allow knowledge-based rational design of these nanomaterials, instead of trial-and-error experiments in a large parameter space, which will advance their integration into a range of technologically important applications, including the fabrication of polymer-based PV cells, light-emitting diodes, field-effect transistors, and chemical and biological sensors.

## Recent Progress

Since our project began on August 15th, 2011, we have made significant progress mainly in two directions: model development and quantification of fluctuation/correlation effects. To address the issue of lack of exact treatment of orientational interactions between rod blocks, we proposed a novel soft spherocylinder model that takes into account the degree of overlap between two spherocylinders (Model B), instead of a simpler model that depends only on the shortest distance  $d_{\min}$  between two spherocylinders (Model A). In particular, for two spherocylinders 1 and 2 both of diameter  $\sigma$  and length  $L$  ( $L=0$  corresponds to spheres), the pair potential in Model A is given by  $\beta u_A(d_{\min}) = \varepsilon \geq 0$  if the shortest distance between two line segments representing the spherocylinders  $d_{\min}(\mathbf{r}_1 - \mathbf{r}_2, \mathbf{u}_1, \mathbf{u}_2, L) < \sigma$  and 0 otherwise, while that in Model B is given by  $\beta u_B(\mathbf{r}_1 - \mathbf{r}_2, \mathbf{u}_1, \mathbf{u}_2, L) = \varepsilon \int_{-1/2}^{1/2} dt_1 \int_{-1/2}^{1/2} dt_2 \beta u_0(|\mathbf{r}_1 + t_1 L \mathbf{u}_1 - \mathbf{r}_2 - t_2 L \mathbf{u}_2|; \sigma)$ ; here  $\beta = 1/kT$  with  $k$  denoting the Boltzmann constant and  $T$  the thermodynamic temperature,  $\mathbf{r}_i$  ( $i=1,2$ ) is the spatial position of the center of spherocylinder  $i$ ,  $\mathbf{u}_i$  is a unit vector denoting the orientation

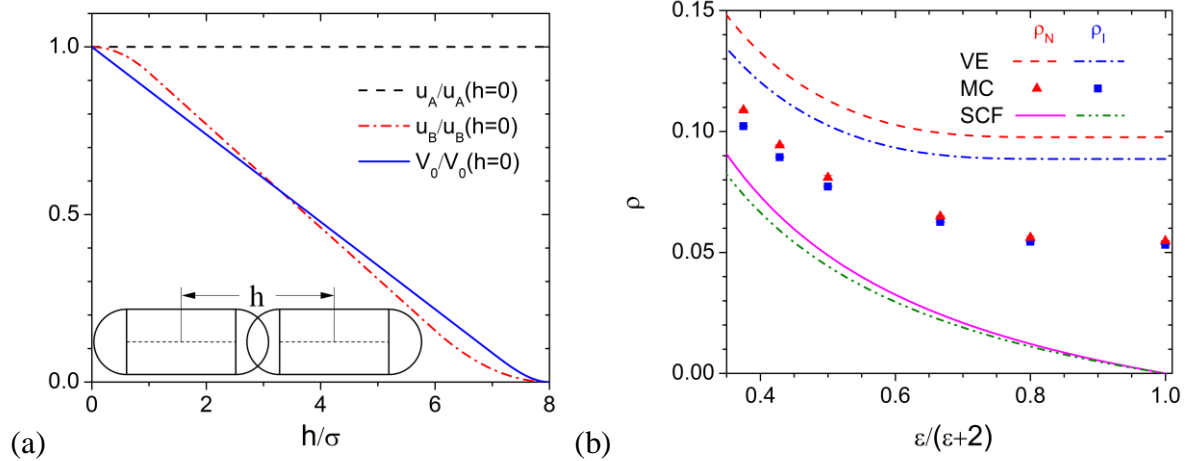


**Fig. 1.** Comparisons of (a)  $u_A$  and  $u_B$  with the actual overlapping volume  $V_0$  between two spherocylinders having their axes on the same line and their centers separated at distance  $h$  (as shown in the inset), where each quantity is normalized by its (maximum) value at  $h=0$ , and (b) the ensemble-averaged number density (per volume of  $\sigma^3$ ) of spherocylinders in the co-existing isotropic and nematic phases,  $\rho_I$  and  $\rho_N$ , respectively, obtained from FOMC simulations, VE and SCF calculations, where Model A is used.  $L/\sigma=7$  in both (a) and (b).

of spherocylinder  $i$ , and the integrations over  $t_1$  and  $t_2$  include the repulsion between all pairs of points (one on each line segment representing a spherocylinder) via a normalized isotropic pair potential  $\beta u_0$  depending on the distance  $r$  between the two points given by  $\beta u_0(r; \sigma) = 3/4\pi\sigma^3$  if  $r < \sigma$  and 0 otherwise. Note that  $\beta u_B$  can be evaluated analytically and thus efficiently, and that in the limit of  $\varepsilon \rightarrow \infty$  both Model A and B recover the standard model of hard spherocylinders for liquid crystals. Fig. 1(a) clearly shows that Model B captures the degree of overlap between two spherocylinders while Model A does not. Note that in general the overlapping volume  $V_0$  between two spherocylinders is unknown, and that  $d_{\min} < \sigma$  in the case shown in Fig. 1(a); any soft spherocylinder model depending only on  $d_{\min}$  therefore gives the same result as our Model A.

We further extended the above Model B for RC DBC, where  $\varepsilon^{RR}$ ,  $\varepsilon^{CR}$ , and  $\varepsilon^{CC}$  are introduced to control the repulsion strength between rod-rod, coil-rod, and coil-coil segments, respectively, and  $\sigma^R$ ,  $(\sigma^R + \sigma^C)/2$ , and  $\sigma^C$  are used for the corresponding repulsion range of  $\beta u_0$ . In addition, each coil segment is modeled as a sphere, and the connectivity of coil segments and the two blocks on a chain is taken into account by the discrete Gaussian chain model. Since this generic, coarse-grained model for RC DBC is based on an isotropic pair potential  $\beta u_0$ , it is computationally very efficient and can be used in SCF and virial expansion (VE) calculations as well as FOMC simulations, thus enabling unambiguously quantification of fluctuation/correlation effects by direction comparisons among the results obtained using these methods without any parameter-fitting.

Using FOMC simulations in an isothermal-isobaric ensemble with replica exchange at different pressures<sup>2</sup> and multiple histogram reweighting<sup>3</sup>, we studied the isotropic-nematic transition of both Model A and B and mapped out their phase diagrams; the results for Model A is shown in Fig. 1(b). This helps us in selecting appropriate parameter values in our subsequent study of RC DBC. In addition, Fig. 1(b) compares our FOMC results with the predictions from SCF theory (a mean-field theory neglecting the system fluctuations and correlations) and VE

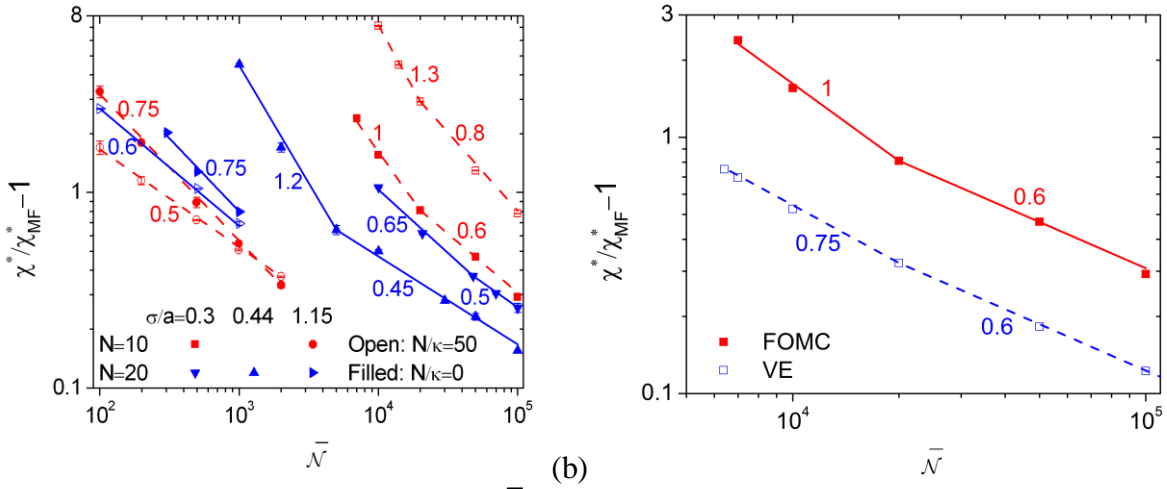


**Fig. 2.** ODT shift of symmetric DBC vs.  $\bar{N}$  obtained from (a) our FOMC simulations, where  $N$  is the number of segments on each chain,  $a$  is the effective bond length in our chain model, and  $\kappa$  is the Helfand compressibility<sup>6</sup>; and (b) our FOMC simulations and VE calculations, where  $N=10$ ,  $\sigma/a=0.3$  and  $N/\kappa=0$  are used. In both plots, the  $k$ -value is given next to each line.

analogous to Onsager’s original work<sup>4</sup> (which takes into account the leading order, two-body correlations), and clearly indicates the importance of properly treating the fluctuation/correlation effects on the orientation-dependent excluded-volume interactions between spherocylinders, which play a crucial role in the self- and directed assembly of RC DBC.

The only way to unambiguously quantify the system fluctuations/correlations is by comparing simulation results with mean-field theories based on exactly the same model system, as shown in Fig. 1(b). Unfortunately, this has rarely been done even in the case of flexible, linear and symmetric DBC melts in bulk. We therefore took a model DBC system of discrete Gaussian chains interacting with soft, finite-range repulsions as commonly used in dissipative-particle dynamics simulations<sup>5</sup>. Using FOMC simulations and mean-field calculations both based on this model system, we unambiguously quantified the effects of fluctuations/correlations on the shift of the order-disorder transition (ODT)  $\chi^*$  of symmetric DBC from the mean-field value  $\chi_{MF}^*$ , which is a classic yet unsolved problem in polymer physics. In particular, Fig. 2(a) shows that, while  $\chi^*/\chi_{MF}^* - 1 \propto \bar{N}^{-k}$  is found with  $\bar{N}$  denoting the invariant degree of polymerization controlling the system fluctuations,  $k$  decreases around the  $\bar{N}$ -value corresponding to the face-centered cubic close packing of polymer segments as *hard* spheres, indicating the short-range correlation effects. This is the first systematic study on the ODT shift of symmetric DBC with experimentally accessible fluctuations, and provides solid data for testing/developing advanced fluctuation theories for inhomogeneous polymers.

Theories are needed in order to further understand the fluctuation/correlation effects revealed in our FOMC simulations. Based on the above model system, we quantitatively compared the commonly used Gaussian-fluctuation (GF) theory, which includes fluctuations only at the Gaussian level, and the Reference Interaction Site Model (RISM) theory<sup>7</sup> with our FOMC simulations for the disordered phase of symmetric DBC, to unambiguously reveal the consequences of the theoretical approximations employed for treating the system fluctuations/correlations. In particular, we find that, while GF theory does not give good

predictions in most cases, RISM theory with the commonly used atomic Percus-Yevick closure<sup>8</sup> (which includes non-Gaussian fluctuations in an approximate way) can qualitatively explain the trends of ODT shift found in our FOMC simulations at  $\bar{N} \geq 10^3$  (accessible in most experiments on DBC). This theory, however, is only applicable to the homogeneous (disordered) phase and thus cannot describe the change of the negative slope  $k$  shown in Fig. 2(a). Therefore, we have further developed a VE theory for polymer melts that can be applied to both homogeneous and inhomogeneous systems. Our preliminary results shown in Fig. 2(b) indicate that this theory is very promising for properly (although not quantitatively) treating the fluctuations/correlations in inhomogeneous polymers. Another advantage of our VE theory is that it can be readily implemented in the well developed and widely used SCF calculations<sup>9</sup> [which gives  $\chi^* = \chi_{MF}^*$  in Fig. 2(b)]; the only modification is to replace the segment pair potential  $\beta u(r)$  by  $1 - \exp[-\beta u(r)]$ . We therefore expect the wide application of our VE theory to many polymeric systems.

## Future Plans

With our computationally very efficient models and methods developed, in the next year we will focus on the 3D parallel SCF and VE calculations to examine the effects of various key factors on the self- and directed assembly of RC DBC. Guided by these theoretical results, we will also perform FOMC simulations for selected cases to unambiguously quantify the fluctuation/correlation effects by direct comparisons among SCF, VE and FOMC results based on the same model system of RC DBC.

## References

1. Q. Wang and Y. Yin, **J. Chem. Phys.** **130**, 104903 (2009).
2. N. C. Ekdawi-Sever, P. B. Conrad, and J. J. de Pablo, **J. Phys. Chem. A** **105**, 734 (2001).
3. A. M. Ferrenberg and R. H. Swendsen, **Phys. Rev. Lett.** **63**, 1195 (1989).
4. L. Onsager, **Ann. N.Y. Acad. Sci.** **51**, 627 (1949).
5. P. J. Hoogerbrugge and J. M. V. A. Koelman, **Europhys. Lett.** **19**, 155 (1992).
6. E. Helfand and Y. Tagami, **J. Polym. Sci., Part B: Polym. Lett.** **9**, 741 (1971).
7. D. Chandler and H. C. Andersen, **J. Chem. Phys.** **57**, 1930 (1972).
8. J. K. Percus and G. J. Yevick, **Phys. Rev.** **110**, 1 (1958).
9. G. H. Fredrickson, **The Equilibrium Theory of Inhomogeneous Polymers**, Oxford University Press, 2006.

## Publications

- A. Q. Wang, "Theory and Simulation of Self-Assembly of Rod-Coil Block Copolymer Melts: Recent Progress", **Soft Matter** **7**, 3711 (2011).
- B. D. Meng and Q. Wang, "Stimuli-Response of Charged Diblock Copolymer Brushes", **J. Chem. Phys.** **135**, 224904 (2011).
- C. J. Zong, X. Zhang, and Q. Wang, "Fast Off-Lattice Monte Carlo Simulations of Soft-Core Spherocylinders: Isotropic-Nematic Transition and Comparisons with Virial Expansion", **J. Chem. Phys.** **137**, 134904 (2012).

- D. *P. Sandhu, J. Zong, D. Yang, and Q. Wang*, “On the Comparisons Between Dissipative Particle Dynamics Simulations and Self-Consistent Field Calculations of Diblock Copolymer Microphase Separation”, **J. Chem. Phys.** **138**, 194904 (2013).
- E. *J. Zong and Q. Wang*, “Fluctuation/Correlation Effects on the Order-Disorder Transition of Symmetric Diblock Copolymers”, **J. Chem. Phys.** **139**, 124907 (2013).

# Quantum Dot Sensitized Solar Cells Based on Ternary Metal Oxide Nanowires

J. Chen, Y. Yang, L. Lu, S. Maloney, Q. Dai, S. Horoz, J. Tang, and Wenyong Wang\*  
Department of Physics and Astronomy  
University of Wyoming, Laramie, WY 82071  
\*Email: [wwang5@uwyo.edu](mailto:wwang5@uwyo.edu)

## Program Scope

In this project we investigate quantum dot sensitized solar cells (QDSSCs) based on ternary metal oxide nanowires. Published work on nanostructure-based photovoltaic devices has mainly focused on binary metal oxides [1,2]. Compared with simple binary materials, ternary metal oxides offer certain advantages. For example, optimizing their band alignment with respect to the electrochemical potentials of the redox couples can reduce back electron transfer and create an improved photovoltage that is one of the major factors affecting the efficiencies of QDSSCs [3,4]. We also inspect non-solution based synthesis and deposition of quantum dots (QDs) on nanowires. Conventional solution-based QD synthesis methods involve linker molecules that present transport barriers for photo-generated electrons, and the ligand exchange processing is also challenging for certain types of QDs. In this project we utilize physical methods such as pulsed laser deposition (PLD) to assemble QDs on nanowires, which can avoid the use of ligand molecules and could possibly lead to solar cells with improved performance. In addition, it is well known that liquid electrolytes in QDSSCs have issues such as being volatile and corrosive, which causes QD corrosion and decreases the long-term stability of the cells. Therefore, another effort of this project is to investigate the synthesis of solid-state electrolytes, especially novel polymer electrolytes, for the creation of all-solid-state QDSSCs.

## Recent Progress

We have synthesized several types of ternary metal oxide nanowires such as  $\text{Zn}_2\text{SnO}_4$  and  $\text{Zn}_2\text{GeO}_4$  nanowires. The synthesis of  $\text{Zn}_2\text{GeO}_4$  nanowires was carried out in a 1-inch quartz tube that was mounted on a single-zone furnace. The molar ratio of the source

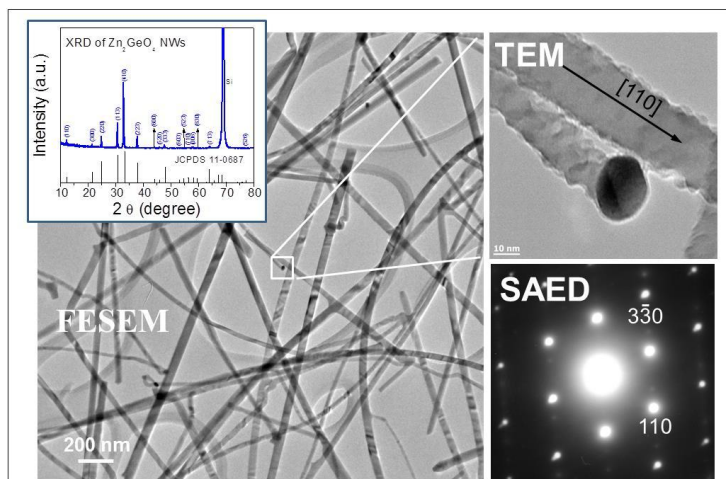


Fig. 1. FESEM, TEM, and XRD examination of  $\text{Zn}_2\text{GeO}_4$  nanowires.

materials was  $\text{ZnO}:\text{GeO}_2:\text{C} = 2:1:3$ , which were placed at the center of the quartz tube. The FTO substrate for nanowire growth was first cleaned and coated with 3-nm Au, and then was placed at the edge of the furnace tube where the local temperature during the growth was  $550\text{ }^\circ\text{C}$ . The furnace was kept at  $1000\text{ }^\circ\text{C}$  and under a pressure of 2 Torr, and the carrying gas mixture was  $\text{N}_2$  (100 sccm) and  $\text{O}_2$  (2 sccm). Figure 1 shows the field-emission scanning electron

microscopy (FESEM), transmission electron microscopy (TEM), and x-ray diffraction (XRD) examination results of the synthesized  $\text{Zn}_2\text{GeO}_4$  nanowires. It can be seen from the FESEM examination that the  $\text{Zn}_2\text{GeO}_4$  nanowires were uniform and had a relatively long length, with diameters in the range of tens of nanometers. All of the peaks in the XRD pattern, except those labeled by the star symbols, were indexed to be  $\text{Zn}_2\text{GeO}_4$  rhombohedral structure, with lattice constants of  $a = b = 1.423$  nm,  $c = 0.953$  nm,  $\alpha = \beta = 90^\circ$ , and  $\gamma = 120^\circ$  from JCPDS card 11-0687. The peaks labeled by the stars were from the FTO substrate. In this work impurity peaks such as those from ZnO or  $\text{GeO}_2$  were not observed, indicating a good yield of the  $\text{Zn}_2\text{GeO}_4$  phase in the final product.

We have investigated PLD deposition of magnetically doped quantum dots such as Mn-doped ZnS QDs. The primary reason to study doped QDs is that doping may alter the energy levels of the QDs and introduce spin-polarized states that may suppress unwanted hot carrier relaxation. We have been pursuing both PLD in vacuum and laser ablation in liquid

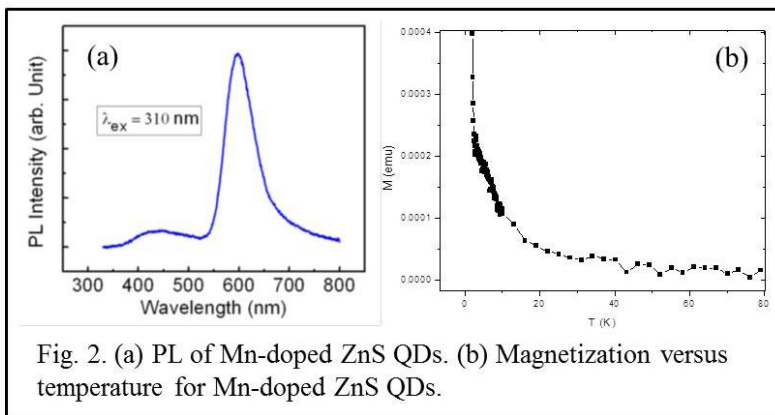


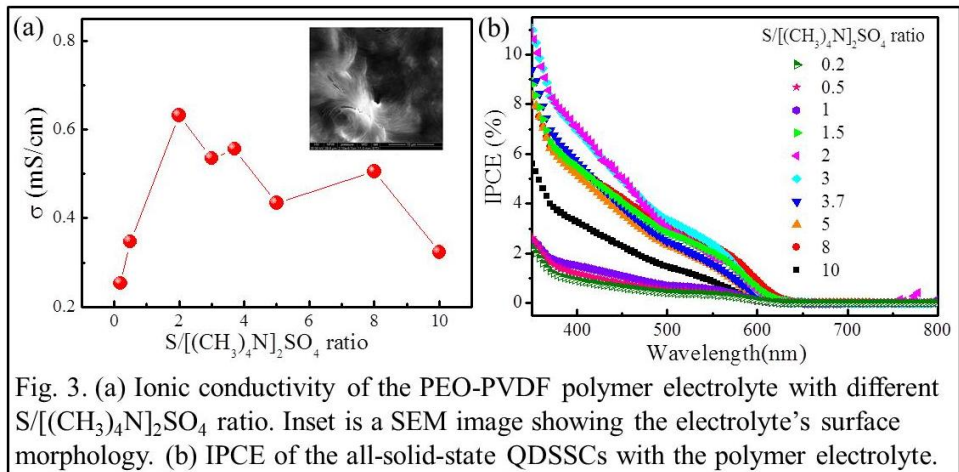
Fig. 2. (a) PL of Mn-doped ZnS QDs. (b) Magnetization versus temperature for Mn-doped ZnS QDs.

for this purpose, and such laser-facilitated, non-equilibrium growth will allow higher doping level to be achieved in the QDs than what is typically limited by the small size of the nanoparticles. ZnS QDs is benign with minimal environmental impact and at the same time the target is easy to make using

conventional chemical methods. To prepare Mn-doped ZnS target,  $\text{Zn}(\text{CH}_3\text{COO})_2 \cdot 2\text{H}_2\text{O}$  and  $\text{Mn}(\text{CH}_3\text{COO})_2 \cdot 2\text{H}_2\text{O}$  were dissolved in deionized water under stirring at room temperature. After drying, the powders were pressed into a pellet and annealed at  $900^\circ\text{C}$  for 8 hr. TEM and XRD results showed QDs of average particle size of  $\sim 3$  nm of zincblende cubic structure for the 5% Mn-doped ZnS. Figure 2(a) shows the photoluminescence (PL) emission spectrum of 5% Mn-doped ZnS QDs prepared by laser ablation in water. The smaller broad peak at 445 nm was from the excitonic emission of ZnS, while the main emission peak at 597 nm was due to the internal Mn d-d transition ( ${}^4\text{T}_1 - {}^6\text{A}_1$ ) [Figure 2(b)]. The Mn-doped ZnS exhibited Curie-Weiss behavior and showed an antiferromagnetic transition at about 2.7 K. The details of their magnetic properties are currently being investigated along with their optical properties and QDSSC applications.

We have also synthesized a novel polymer electrolyte based on S and  $[(\text{CH}_3)_4\text{N}]_2\text{SO}_4$ . The polymer frame is poly(ethylene oxide) (PEO) blended by poly(vinylidene fluoride) (PVDF). PEO is an important polymer for applications in lithium ion batteries and has a high molecular weight of  $\sim 10^6$  g/mol. By blending it with PVDF the obtained composite polymer frame exhibited improved mechanical and electrical properties. To dope this PEO-PVDF polymer frame we used S and  $[(\text{CH}_3)_4\text{N}]_2\text{SO}_4$ , which introduced the redox couple. After doping, the polymer electrolyte became a hydrogel and could be applied to the QD/nanowire structures. The structures could then be dried in an oven at a temperature of  $\sim 80^\circ\text{C}$  to remove the solvent and create QDSSCs containing the solid-state electrolyte. Figure 3(a) shows our preliminary result of this polymer electrolyte's ionic conductivity as a function of

S: $[(\text{CH}_3)_4\text{N}]_2\text{SO}_4$  ratio, and Figure 3(b) shows the corresponding incident photon-to-current conversion efficiency (IPCE) of the all-solid-state QDSSCs fabricated using this electrolyte. These results revealed that a S: $[(\text{CH}_3)_4\text{N}]_2\text{SO}_4$  ratio of 2:1 yielded the best electrolyte performance.



### Future Plans

Photovoltaic cells based on ternary metal oxide nanowires and semiconductor QDs are promising energy harvesting structures, and we will continue our investigation of this important subject. For nanowire synthesis, we will continue the synthesis of metal oxide nanowires for applications in QDSSCs, including other types of ternary metal oxide nanowires and magnetically doped nanowires. For QD synthesis, we will continue investigating the utilization of PLD method to create magnetically doped QDs such as Mn-doped CdSe or PbS QDs. As discussed previously, such doping can alter the energy levels of the QDs and introduce spin-polarized states, which may benefit the performance of QDSSCs. For polymer electrolyte synthesis, we will investigate several methods to improve their ionic conductivity, such as doping with magnetic nanoparticles and introducing magnetic field treatment. We will also investigate carrier transport mechanisms in the fabricated prototype PV cells using a variety of experimental methods such as Intensity-Modulated Photocurrent/Photovoltage Spectroscopy.

### References

1. M. Gratzel, "Solar energy conversion by dye-sensitized photovoltaic cells", *Inorg. Chem.* 44, 6841 (2005).
2. M. Law, L. E. Greene, J. C. Johnson, R. Saykally, and P. Yang, "Nanowire dye-sensitized solar cells", *Nature Materials*, 4, 455 (2005).
3. S. Y. Huang, G. Schlichthorl, A. J. Nozik, M. Graetzel, and A. J. Frank, "Charge Recombination in Dye-Sensitized Nanocrystalline TiO<sub>2</sub> Solar Cells", *J. Phys. Chem. B*, 101, 2576 (1997).
4. G. Schlichthorl, S. Y. Huang, J. Sprague, and A. J. Frank, "Band Edge Movement and Recombination Kinetics in Dye-Sensitized Nanocrystalline TiO<sub>2</sub> Solar Cells: A Study by Intensity Modulated Photovoltage Spectroscopy", *J. Phys. Chem. B*, 101, 8141 (1997).

## DOE Sponsored Publications in 2011-2013 from Current Grant

1. L. Lu, J. Chen, and W. Wang, "Wide Bandgap  $\text{Zn}_2\text{GeO}_4$  Nanowires as Photoanode for Quantum Dot Sensitized Solar Cells," *Applied Physics Letters*, 103, 123902 (2013).
2. J. Chen and W. Wang, "Carrier Transport Processes in Dye Sensitized Solar Cells Based on  $\text{Zn}_2\text{SnO}_4$  Nanostructures Studied by Intensity Modulated Photocurrent/Photovoltage Spectroscopy," *Applied Physics Letters*, 102, 213904 (2013).
3. Q. Dai, J. Chen, L. Lu, J. Tang, and W. Wang, "PbS Quantum Dots Prepared by Pulsed Laser Deposition for Photovoltaic Applications and Ligand effects on Device Performance," *Applied Physics Letters*, 102, 203904 (2013).
4. S. Horoz, L. Lu, Q. Dai, J. Chen, B. Yakami, J. Pikal, W. Wang, and J. Tang, "CdSe Quantum Dots Synthesized by Laser Ablation in Water and Their Photovoltaic Applications," *Applied Physics Letters*, 101, 223902, (2012).
5. A. Pimachev, G. Kolesov, J. Chen, W. Wang, and Y. Dahnovsky, "Internal Relaxation in Dye Sensitized Solar Cells Based on  $\text{Zn}_2\text{SnO}_4$  Nanostructures," *Journal of Chemical Physics*, 137, 244704, (2012).
6. H. Yu, C. M. Eggleston, J. Chen, W. Wang, Q. Dai, and J. Tang, "Optical Waveguide Lightmode Spectroscopy (OWLS) as a Sensor for Thin Film and Quantum Dot Corrosion," *Sensors*, 12, 17330, (2012).
7. Q. Dai, J. Chen, L. Lu, J. Tang, and W. Wang, "Pulsed Laser Deposition of CdSe Quantum Dots on  $\text{Zn}_2\text{SnO}_4$  Nanowires and Their Photovoltaic Applications," *Nano Letters*, 12, 4187, (2012).
8. L. Lu, J. Chen, L. Li, and W. Wang, "Direct Synthesis of Vertically Aligned ZnO Nanowires on FTO Substrates Using a CVD Method and the Improvement of Photovoltaic Performance," *Nanoscale Research Letters*, 7, 293 (2012).
9. J. Chen, L. Lu, and W. Wang, " $\text{Zn}_2\text{SnO}_4$  Nanowires as Photoanode for Dye Sensitized Solar Cells and the Improvement on Open-Circuit Voltage," *Journal of Physical Chemistry C*, 116, 10841 (2012).

# Surface-Reaction-Limited Pulsed Chemical Vapor Deposition for Growing Nanowires inside Highly-Confined Spaces

Xudong Wang

Department of Materials Science and Engineering  
University of Wisconsin – Madison, Madison, WI 53706

## Program Scope

Three-dimensional (3D) nanowire (NW) networks are promising architectures that can effectively project the extraordinary properties of one-dimensional objects into a 3D space. This structure requires NWs to be grown densely and uniformly as well as bridged among themselves. However, growing such a structure is very challenging due to the coupling between crystal growth rate and precursor concentration, which is intrinsic to almost all NW synthesis techniques. Recently, we have overcome this challenge by the surface-reaction-limited pulsed chemical vapor deposition (SPCVD) technique, which mimics the self-limited growth mechanism of atomic layer epitaxy (ALE). Through this technique, single-crystalline anatase  $\text{TiO}_2$  NWs were uniformly grown, covering the entire inner surfaces of anodic aluminum oxide (AAO) nanochannels and dense Si NW arrays. The formation of NW morphology is believed to be due to a combined effect of surface recombination and restructuring. The SPCVD is another example of adapting conventional thin film growth techniques to NW synthesis that inherits the merits from its parent technologies (conformal coating in this case).

This research project is to obtain in-depth understanding of the nanoscale crystal growth behavior in a SPCVD process, and thereby achieve well-controlled syntheses of 3D NW arrays inside highly-confined spaces. Scanning transmission electron microscopy, atomic force microscopy and in-situ X-ray absorption will be applied to study the atomic recombination and restructuring on  $\text{TiO}_2$  crystal surfaces, and thereby understand the nucleation and anisotropic crystal growth mechanisms of  $\text{TiO}_2$  and reveal how a continuous polycrystalline ALE film is evolved into discrete NW arrays. This understanding will then be applied to controlling the composition and dimensionality of  $\text{TiO}_2$  NWs and eventually to the growth of other functional materials. This project will set a knowledge ground of the SPCVD that can uniformly grow NW arrays of controlled composition and morphology inside 3D-confined and submicron-sized spaces, thus enabling the creation of a variety of new functional nanomaterial architectures.

## Recent Progress

The SPCVD technique presents a unique growth behavior that does not follow the conventional growth models of polycrystalline or epitaxial oxides *via* ALE or atomic layer deposition (ALD).[1] It thus provides a valuable platform for studying and comparing phase evolution during ALD process. We did a comprehensive atomistic study of crystal nucleation and growth behaviors of  $\text{TiO}_2$  nanostructures grown by SPCVD/ALD.[2] By applying aberration-corrected scanning transmission electron microscopy (STEM) and TEM characterization, we revealed the transformation process and sequence of atom arrangement during high-temperature  $\text{TiO}_2$  ALD growth, where the Ostwald-Lussac Law was found to be the governing rule of phase evolution. At high temperature, the amorphous-crystalline ALD mixture

can enable a unique anisotropic crystal growth behavior forming TiO<sub>2</sub> nanorods *via* the principle of vapor-phase oriented attachment.

Crystal evolution was first investigated from TiO<sub>2</sub> nanostructures deposited at 600 °C on single-crystalline ZnO and Si NW surfaces. Figure 1 shows a series of high resolution high-angle annular dark-field STEM (HR HAADF STEM) images taken at the interfaces between TiO<sub>2</sub> and supporting Si NWs, where different growth stages are indexed by the growth cycles. At the beginning of growth (1~5 cycles), there are no noticeable TiO<sub>2</sub> morphologies such as films or islands (Figs. 1a and 1b); whilst electron energy loss spectroscopy (EELS) analysis reveals the existence of Ti elements from the Si NW edge. At 10 cycles, three typical morphologies emerged as shown in Fig. 1c: cloudy and loosen amorphous flakes with diameters ranging from 1 to 2 nm; ultrathin amorphous film covering the surface of Si NW with a thickness of several angstroms (inset of Fig. 1c); and sparsely distributed fuzzy amorphous particles with a diameter of ~ 1 nm. When growth proceeds to 20 cycles, amorphous particles and ultrathin films became the dominating morphologies (Fig. 1d). The density of amorphous particles at the 20-cycle stage largely increased compared to the 10-cycle samples, while similar diameters remained. In addition, no cloudy flakes were observed at this stage suggesting that the flakes are unstable transient morphology. After 35 cycles of growth, the NW surfaces were covered with larger nanoparticles (5-10 nm), which were agglomeration of small crystallites shelled by thin amorphous layers (Fig. 1e). As the growth proceeded to 50 cycles, the integrated nanoparticle assemblage became larger and its elongated shape appeared like embryos of NRs (~10 nm wide and ~20 nm long, Fig. 1f). Both HR HAADF STEM image and its Fast Fourier Transform (FFT) (right inset of Fig. 1f) show that most small crystallites in the nanoparticle assemblage had the same orientation. A thin amorphous layer was also observed in the outmost region of the bulk embryos. At 75 cycles, high-density miniature NR-like single crystals of ~ 20 nm wide and ~ 40 nm long started to form (Fig. 1g). Eventually, typical high-aspect ratio TiO<sub>2</sub> NRs (width: ~ 40 nm; length: ~ 200 nm) were received after longer growth cycles (Fig. 1h). The entire NR evolution process is schematically shown in Fig. 1i.

HR HAADF STEM observation suggests that the formation of TiO<sub>2</sub> NRs at 600 °C consists of two processes: evolution of crystallites from amorphous nanoparticles via phase transformation; and self-organization of the crystallites into polycrystalline nanoparticles assemblage. It suggests that the entire TiO<sub>2</sub> crystal evolution pathway at high-temperature (high-T) can be summarized as: amorphous film/flakes → amorphous particles → anatase → rutile. The formation of transient metastable TiO<sub>2</sub> phases during the nucleation pathway follows the empirical Ostwald-Lussac Law.[3] This law states that an unstable system does not necessarily

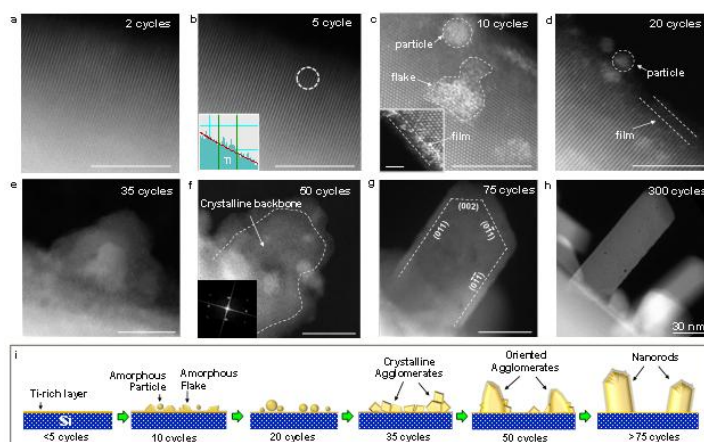


**Figure 1.** Evolution of TiO<sub>2</sub> NRs at different SPCVD cycles at 600 °C revealed by HR HAADF STEM from 2 to 300 cycles (a-h). i. Schematic illustration the entire evolution process of TiO<sub>2</sub> NRs. Scale bars are 5 nm unless otherwise noted.

transform directly into the most stable phase, but likely into one that most closely resembles itself. In terms of energy, the phase transformation is always accompanied by the minimum energy loss. Such a non-equilibrium process therefore involves more kinetic concepts.

For a kinetically-limited chemical process, the nucleation rate can therefore be presented as

$$J_n = A \exp\left(-B \frac{\gamma^3}{(\ln S)^2}\right),$$

where  $\gamma$  is the surface free

energy of nucleus and  $\ln S$  is supersaturation. Figure 2 shows the nucleation rates of amorphous film/flakes, amorphous particles, anatase, and rutile phases of TiO<sub>2</sub> versus activity product of the precursors divided by the equilibrium product of amorphous particles. The color dash lines are applied to qualitatively illustrate the normalized equilibrium products of amorphous nanoparticles, anatase and rutile structures and the precursor activity. According to Fig. 2, though the supersaturation of anatase TiO<sub>2</sub> is higher than amorphous nanoparticles at any randomly-chosen

considerable activity product ( $\ln S_{\text{anatase}} > \ln S_{\text{amorphous particle}}$ ), its nucleation rate is much lower than the amorphous nanoparticles. This perfectly agrees with our discovery from the 600 °C SPCVD/ALD results. The key factor yielding such a nucleation pathway is the drastic difference of surface free energies among different phases of TiO<sub>2</sub>, which has more influence (3rd power) on the nucleation rates. Literature reports revealed that the surface free energies of the three phases in Fig. 2 follow the relation:  $\gamma_{\text{amorphous particles}} < \gamma_{\text{anatase}} < \gamma_{\text{rutile}}$ . Therefore, although Gibbs free energy change of anatase is larger than that of amorphous flakes/films, the much lower  $\gamma$  of amorphous flakes/films makes their nucleation energy barrier lower than that of direct formation of anatase phase, rendering a preferable nucleation route towards unstable amorphous phase at the beginning. This numerical analysis, together with the experimental observation, evidences that the TiO<sub>2</sub> SPCVD or ALD growth at 600 °C follows the Ostwald-Lussac Law.

To further understand the anisotropic growth phenomenon that is responsible for NR formation, samples obtained from longer growth cycles were investigated. After 75 cycles of growth, HR HAADF STEM images revealed that the entire surface of single crystalline NR is covered with a ~2 nm thick percolated film (a mixture of polycrystalline TiO<sub>2</sub> with amorphous intercalation, Fig. 3a). This is considered as the secondary nucleation on the surface of evolved TiO<sub>2</sub> crystals, which still follows the Ostwald-Lussac Law. From the 200-cycle sample, the base portion of the NR exhibited a clean and smooth surface – no percolated film or other defects were observed (Fig. 3b-i). The percolated film started to appear at the middle region of the NR. It was a transient morphology with its thickness varying from a few angstroms (the bottom side) to ~ 1 nm (the top side) (Fig. 3b-ii). Fully evolved percolated film was only found at the top portion of NR (Fig. 3b-iii). EELS line scan demonstrated that the outmost tip of NR contained much less Ti and O, indicating this was the region under development, or actively growing (Fig. 3b-iv). After 400 cycles (Fig. 3c), the NR's body (i), side surface (ii), and front (iii, iv) all exhibited high

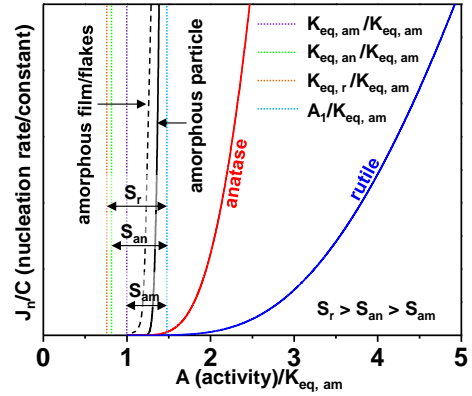


**Figure 2.** Nucleation rate of different phases of TiO<sub>2</sub> versus the precursor's activity product.  $K_{\text{eq}}$  is the equilibrium products,  $\ln S$  are defined as the supersaturations under the fixed activity  $A_1$  ( $\ln S = A_1 / K_{\text{eq}}$ ). Subscripts am, an and r stand for amorphous, anatase and rutile phases of TiO<sub>2</sub>, respectively.

quality crystallinity and no percolated film could be observed (the amorphous layer observed in Fig. 3c-iv is due to carbon deposition in STEM chamber). TEM images show that the NR builds its body by sacrificing the surface percolated layers. When the mobility of surface crystallites becomes high enough (e.g. under high temperature, 600 °C and hydroxyl group-rich environment), they could travel on the crystal surface and organize themselves to attach to appropriate NR surfaces following oriented attachment mechanism, as schematically shown in Fig. 3d.

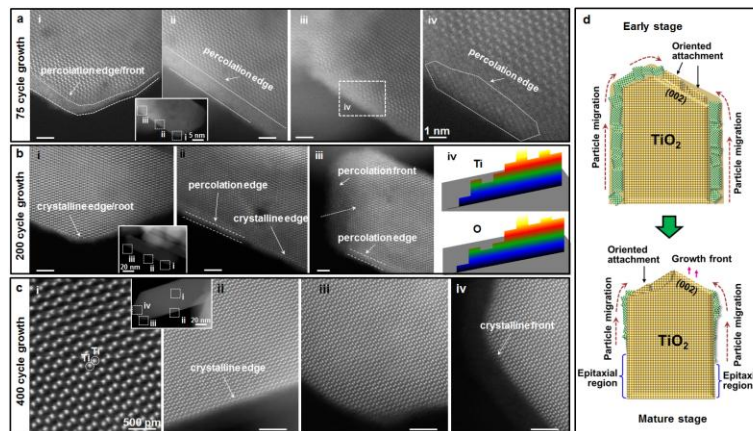


**Figure 3.** Vapor phase oriented attachment growth of TiO<sub>2</sub> NR by 600 °C ALD. **a-c**, Atomic structure of NR grown at 75, 200, and 400 cycles, respectively. **d**, Schematics showing the oriented attachment process for the anisotropic growth of a TiO<sub>2</sub> NR. Scale bars are 2 nm unless otherwise noted.

## Future Plans

We plan on continuously studying the nucleation and growth behavior of SPCVD/ALD at high temperature for different materials and compositions. For example, doping capability of SPCVD in the growth of N-doped TiO<sub>2</sub> NWs and the SPCVD growth mechanism of other oxide materials, including ZnO, SnO<sub>2</sub>, and V<sub>2</sub>O<sub>5</sub> will be studied. Meanwhile, we will also setup a portable ALD system that allows in-situ X-ray absorption near-edge structure (XANES) spectroscopy characterization on TiO<sub>2</sub> crystal evolution in SPCVD process, which will be performed at Argonne national laboratory.

## References

- [1] J. Shi, C. Sun, M.B. Starr, X.D. Wang “Growth of Titanium Dioxide Nanorods in 3D-Confined Spaces”, *Nano Lett.*, 11, 624-631 (2011).
- [2] J. Shi, Z. Li, A. Kvit, S. Krylyuk, A.V. Davydov, X.D. Wang “Electron Microscopy Observation of TiO<sub>2</sub> Nanocrystal Evolution in High-Temperature Atomic Layer Deposition”, submitted (2013).
- [3] Ostwald, W. Studien über die Bildung und Umwandlung fester Körper. *Z. Phys. Chem* 22, 289-330 (1897).

## Publications resulting from work supported by the DOE grant over the previous two years.

- (1) J. Shi, Z. Li, A. Kvit, S. Krylyuk, A.V. Davydov, X.D. Wang “Electron Microscopy Observation of TiO<sub>2</sub> Nanocrystal Evolution in High-Temperature Atomic Layer Deposition”, submitted (2013).

- (2) Z. Li, C. Yao, Y. Yu, Z. Cai, X.D. Wang “Highly-Efficient Capillary Photoelectrochemical Water Splitting Using Cellulose Nanofiber-Templated TiO<sub>2</sub> Photoanodes”, *Adv. Mater.*, Accepted (2013).

## **Boron-Based Nanostructures: Stability, Functionality and Synthetic Routes**

**Boris I. Yakobson and Pulickel Ajayan,  
Department of Mechanical Engineering &  
Materials Science, Department of Chemistry,  
and Smalley Institute for Nanoscale Science and  
Technology, Rice University, Houston, TX**

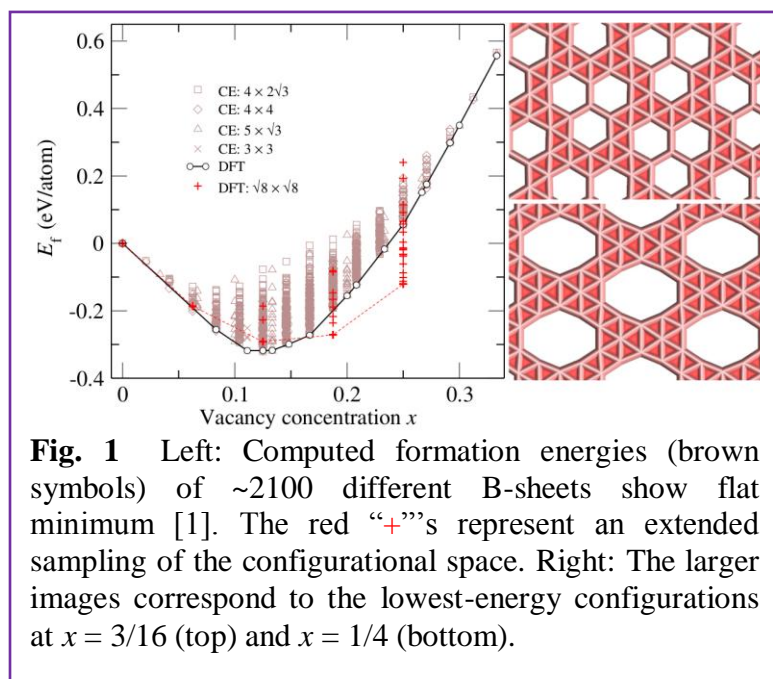
### **Program Scope**

The charisma of the B<sub>80</sub> Buckyball not only motivated our own work within the initial stage of this program but has fueled substantial research efforts worldwide. It has exploded into hundreds of detailed studies of the family of large clusters, especially hollow cages, with theoretical analysis still emerging almost weekly. Moreover, over the years of this project, the “unfolding of the fullerene” [1] in the case of boron proceeded in a way very similar to actual chronological developments in carbon research: first the C<sub>60</sub> Buckyball, then carbon nanotubes, and then graphene. As if copy-cat of these decades long development, boron research interests also evolved—pretty quickly—from fullerenes to planar monoatomic sheets and their folded form, boron nanotubes, and recently to probing the synthetic routes by employing first principles calculations. This latter aspect—exploration of possible synthetic approaches—is perhaps most relevant to this Program and also aligns well with recent general interests of materials genome initiative, MGI.

Despite the impressively fast (albeit not always easy) progress in the theoretical lane, the experiment was lagging behind with fewer groups attempting and yet less succeeding in producing novel nanostructures of pure boron. Boron chemistry is rather different, in some respects more complex, and its practicality is often much more challenging. Suffice it to mention that no pure boron forms are available in nature, while there is plenty of carbon, or that boron precursors used to experiment with nanostructure synthesis, those precursors are often toxic. Handling this in experimental lab, especially in academic setting, requires safety permits, certification etc. Still, what is accomplished in our team and worldwide is quite significant. While larger part of theoretical studies focus on predicting possible stable (metastable) structures and their physical properties, we have added at later stage first example of probing the feasibility of synthesis, with the hope to assist experimental efforts. The approach allowed us to determine most efficient catalyst-substrates where pure boron is more likely to assemble into 2D-monolayer, and yet to remain separable from such a substrate. This success leads us to expand this theoretical-computational analysis and to apply it to other boron-based nanostructures, in particular 2D-materials, presently of intense interest in the general quest for novel 2D materials “beyond graphene”.

### **Recent Progress**

Propositions of various B-layer models come from density-functional theory (DFT) calculations. These models are derived from a parent B lattice by selective removal of B atoms—a procedure that results in hexagonal voids, or “vacancies” (V), and ultimately leads to a colossal configurational space. Exploring the later poses a daunting combinatorial problem, and was considered eventually “infeasible”, hampering the use of first-principles methods.



undertaken in our very recent works [1,2] has uncovered a finite range of compositions  $x$  (Fig. 1, left) where the ground-state energy is essentially independent of  $x$ , identifying a variety of stable B-layer phases (all apparently metallic) and suggesting polymorphism, in stark contrast to graphene or hexagonal BN (h-BN, also being explored in this project).

This discovery of polymorphism has brought us to the next challenging issue: how the stability of different forms is affected by the presence of substrates, and—even more interesting from practical point of you—how and which substrate may be able to facilitate the assembly of 2D-layers of boron. In the broader context of “beyond graphene” era, the synthesis of novel 2D materials has attracted increasing interest because of their anticipated unique properties. While the production of 2D boron ( $^{2D}B$ ) sheets remains a challenge, it is even more important to investigate theoretically the possible fabrication methods. Recently, we explored the formation of B sheets on metal (Cu, Ag, Au) and metal boride ( $MgB_2$ ,  $TiB_2$ ) substrates using first-principles calculations. Our results suggest that B sheets can be grown on the Ag(111) or Au(111) surfaces by deposition. B atoms decomposed from a precursor, and driven by the gradient of the chemical potential, will assemble into 2D clusters and further grow into a larger sheet, while formation of three-dimensional boron ( $^{3D}B$ ) structures could be impeded owing to a high nucleation barrier. In addition, saturation of a boron-terminated  $MgB_2$  surface in a boron-rich environment can also lead to the formation of B sheets. These sheets are weakly bound to the substrates (Fig. 2), suggesting a feasible post synthetic separation into the free-standing forms. Our work proposes feasible approaches to synthesize  $^{2D}B$ , and could possibly pave the way towards its application in nano-electronics. This investigation is possibly a turning point for our future work within this project and even generally for synthesis of 2D materials of various compositions.

The experimental part of the project has dealt with different approaches to grow pure boron nanostructures as well as boron containing nanostructures, guided by the insights gained from the

Recently, we have demonstrated [2] that the structural stability and diversity of elemental B-layers can be evaluated by treating them as  $B_{1-x}V_x$  pseudo-alloy. This approach allows for an elegant use of the cluster expansion method in combination with DFT calculations, leading to a thorough exploration of the configurational space. To render various V patterns we have used carefully chosen rhombic and rectangular supercells. In the preceding funding period, we have used a minimal supercell sizes as a proof of concept and for basic hypothesis testing. The subsequent large-scale effort

theoretical investigations. Our efforts so far have led to the synthesis of amorphous boron nanowires by vapor transfer method.

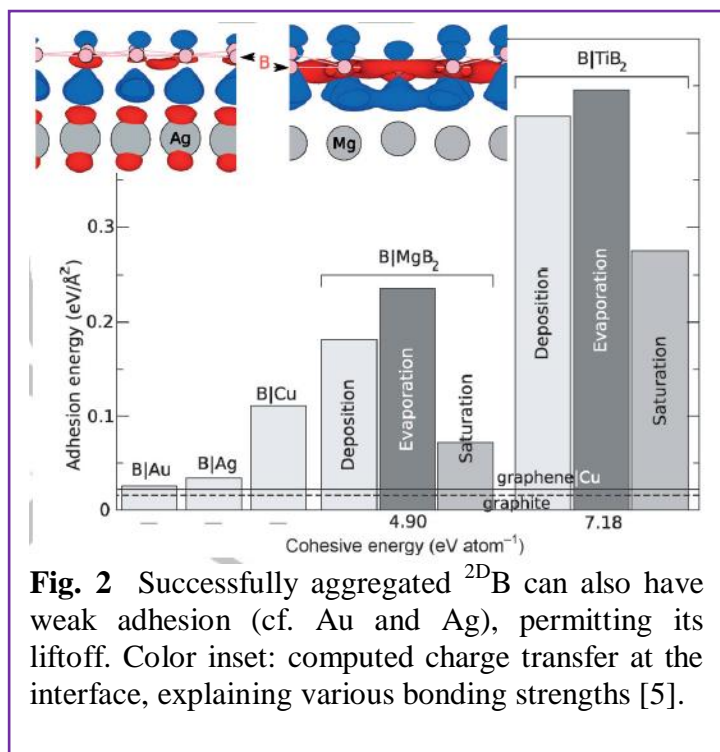


**Fig. 2** Successfully aggregated <sup>2D</sup>B can also have weak adhesion (cf. Au and Ag), permitting its liftoff. Color inset: computed charge transfer at the interface, explaining various bonding strengths [5].

Gold coated single crystal Si(100) wafers with a thermal oxide layer were used as growth substrate. The boron source material was a mixture of pure boron powder, boron oxide and Mg powder. The mixture and substrates were heated in sealed quartz tube to 1150°C (source) and 900°C (substrate) for 60-120 minutes. Dark brown layer (Fig. 3A, inset) is formed on the surface of the substrate, which is characterized to contain high yield of amorphous boron nanowires. Electrical and optical measurements on these boron nanowires as well as photoconductivity measurements will be reported in an upcoming paper [8].

Although the preparation of pure boron nanostructures was challenging,

we have had great success in synthesizing atomic layers containing hybridized domains of graphene and hexagonal boron nitride (h-BNC) that constitute a new kind of disordered 2D electronic system [9]. Magnetolectric transport measurements performed at low temperature in vapor phase synthesized h-BNC atomic layers show a clear and anomalous transition from an insulating to a metallic behavior upon cooling. The observed insulator to metal transition [9] can be modulated by electron and hole doping and by the application of an external magnetic field.

### Future Plans

Our past and ongoing work resulted now, besides the research discoveries, in a capable facility for accelerated research of boron-based nanostructures. Our initially pure-boron research evolved

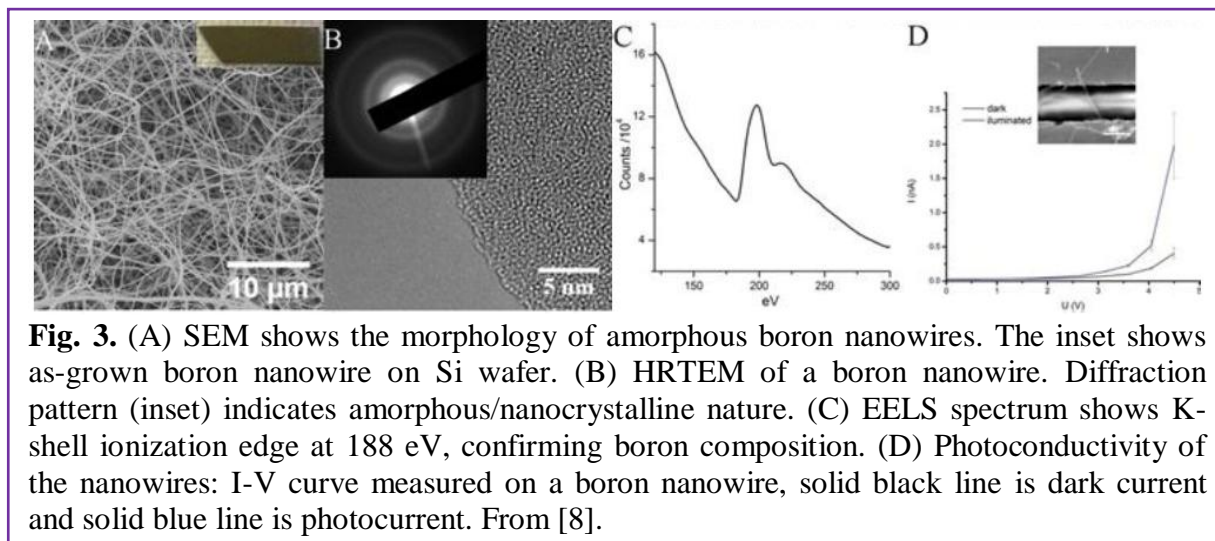


**Fig. 3.** (A) SEM shows the morphology of amorphous boron nanowires. The inset shows as-grown boron nanowire on Si wafer. (B) HRTEM of a boron nanowire. Diffraction pattern (inset) indicates amorphous/nanocrystalline nature. (C) EELS spectrum shows K-shell ionization edge at 188 eV, confirming boron composition. (D) Photoconductivity of the nanowires: I-V curve measured on a boron nanowire, solid black line is dark current and solid blue line is photocurrent. From [8].

while being influenced by concurrent broader developments in the research community. Within the emerging area of 2D materials our project focus has been mainly on two important examples, representing in certain way two extreme cases: pure elemental B as most subtle and not yet synthesized in the laboratories, and h-BN—hexagonal boron nitride, also known as “white graphene”—very stable compound, with the array of useful properties available for experiments. This compels us to extend search to a broad spectrum of 2D boron-rich compounds whose synthesis can be rationalized, and properties explored in detail. We will generalize our recently found approach, the first-principles computations of a layer-substrate system to offer a rational design of synthetic route for variety of 2D-compounds. Based on this approach we aim to achieve, through theoretical modeling and experiments, both synthesis and property characterization of several boron-based nanostructures, primarily monolayers: pure B layers (including two-dimensional crystals of B<sub>12</sub>) remain important lines of work; well-established stable h-BN; and novel layers of BC<sub>3</sub>, BSi, B<sub>2</sub>O<sub>3</sub>, and B<sub>x</sub>S<sub>y</sub> composition. We will mainly focus on 2D-materials, while also continue exploration of nanowires of pure B as well as coaxial B/BO<sub>x</sub>, already obtained in our labs, but calling for deeper characterization and understanding. Moreover, while pursuing our well planned quest, we will also keep an eye open for potential detection of the hotly-debated boron Buckyball isomers, where serendipity must be a factor.

### DoE Sponsored Publications in the Last Two Years

1. E.S. Penev, V.I. Artyukhov, F. Ding and B.I. Yakobson, “Unfolding the fullerene: Nanotubes, graphene and poly-elemental varieties by simulations” *Adv. Mater.* **24**, 4956–4976 (2012).
2. E.S. Penev, S. Bhowmick, A. Sadrzadeh, and B.I. Yakobson, "Polymorphism of the two-dimensional boron", *Nano Lett.* **12**, 2441–2445 (2012).
3. Y. Liu, X. Zou, and B. I. Yakobson, Dislocations and grain boundaries in two-dimensional boron nitride”, *ACS Nano* **6**, 7053–7058 (2012).
4. A.K. Singh and B.I. Yakobson, “First principles calculations of H-storage in sorption materials”, *J. Mater. Science* **47**, 7356-7366 (2012).
5. Y. Liu, E.S. Penev, and B.I. Yakobson, “Probing the synthesis of two-dimensional boron by first-principles computations”, *Angew. Chem. Int. Ed.* **52**, 3156–3159 (2013).
6. Y. Liu, V. I. Artyukhov, M. Liu, A. R. Harutyunyan, and B.I. Yakobson, “Feasibility of Lithium Storage on Graphene and Its Derivatives”, *J. Phys. Chem. Lett.* **4**,1737–1742 (2013).
7. Y. Liu, X. Zou, and B. I. Yakobson, “Dislocations and grain boundaries in two-dimensional boron nitride”, *ACS Nano* **6**, 7053–7058 (2012).
8. L. Ge, S. Lei, R. Vajtai and P.M. Ajayan, "Synthesis and photocurrent measurements of amorphous boron nanowires", unpublished (2013).
9. L. Song, L. Balicas, D.J. Mowbray, R.B. Capaz, K. Storr, L. Ci, D. Jariwala, S. Kurth, S. G. Louie, A. Rubio, and P.M. Ajayan, "Anomalous Insulator-Metal Transition in Boron Nitride-Graphene Hybrid Atomic Layers", *Phys. Rev. B* **86**, 075429 (2012).

# Atomic Layer Deposition (ALD) of Metal and Metal Oxide Films: A Surface Science Study

Francisco Zaera

Department of Chemistry, University of California, Riverside, CA 92521, zaera@ucr.edu

## i) Program Scope

The general objective of our project is to develop a molecular-level understanding of the thermal reactions that organometallic compounds used for atomic layer deposition (ALD) follow on surfaces. ALD is poised to become one of the dominant technologies for the growth of nanometer-sized conformal films in many industrial applications. In microelectronics in particular, the growth of diffusion, adhesion, and protection barriers and of metal interconnects is central to the buildup of diodes, transistors, and other elements within integrated circuits. All these processes require the deposition of isotropic films on complex topographies under mild conditions and with monolayer control. ALD is particularly suited to satisfy all those conditions, but many questions concerning the underlying surface chemistry need to be answered before it can find widespread use.

Our mechanistic studies of the ALD-related reactions is being pursued with the aid of a number of surface-sensitive techniques, including X-ray photoelectron (XPS), Auger electron (AES), low-energy ion scattering (LEIS), temperature programmed desorption (TPD), and infrared (IR) spectroscopies. Our present focus is on the study of processes for the deposition of copper metal interconnects, a central need in the microelectronics industry. Specific questions are being addressed in terms of the kinetics and mechanisms of the reactions involved, and also in connection with the composition and morphology of the resulting films. This knowledge will be directed to the design of ALD processes that operate under the mildest conditions possible and deposit stoichiometric and pure films with good density, low resistance, and smooth surfaces.

## ii) Recent Progress

In the initial stages of this project, we have characterized the thermal chemistry of copper(I)-*N,N'*-di-*sec*-butylacetamidinate on Ni(110) single-crystal and cobalt polycrystalline surfaces under ultrahigh vacuum (UHV) conditions by XPS and TPD [1; 2]. This chemistry was later tested on a Cu(110) surface in order to probe the chemistry associated with the build up of the metal film once the first copper layer has been grown [3].

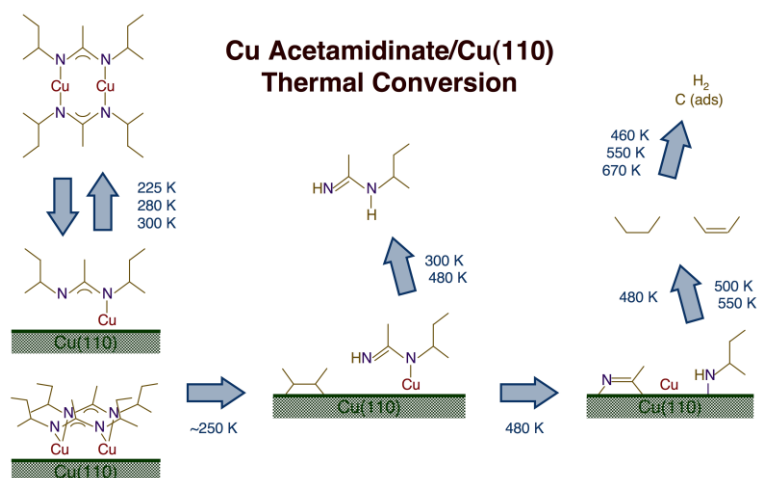


Figure 1. Schematic depiction of the proposed thermal chemistry of the copper acetamidinate ALD precursor on Cu(110) surfaces.

Like on the other surfaces, a series of thermal stepwise conversions were identified on this substrate, starting with the partial dissociative adsorption of the copper acetamidinate dimers into a mixture of monomers and dimers on the surface. An early dissociation of a C–N bond leads to the production of N-sec-butylacetamidine, which is detected in TPD experiments in three temperature regimes, the last one centered around 480 K. Butene, and a small amount of butane, is also detected above approximately 500 K, and hydrogen production, an indication of dehydrogenation of surface fragments, is observed at 460, 550 and 670 K. In total, only about 10% of the initial copper(I)-N,N'-di-sec-butylacetamidinate adsorbed monolayer decomposes, and only about ~3% of carbon is left behind on the surface after heating to high temperatures. It is interesting to note that deposition of copper films with this precursor is dirtier on Cu(110) than on Ni(110). The overall mechanism derived from our studies for the chemistry on copper surfaces is shown schematically in Figure 1.

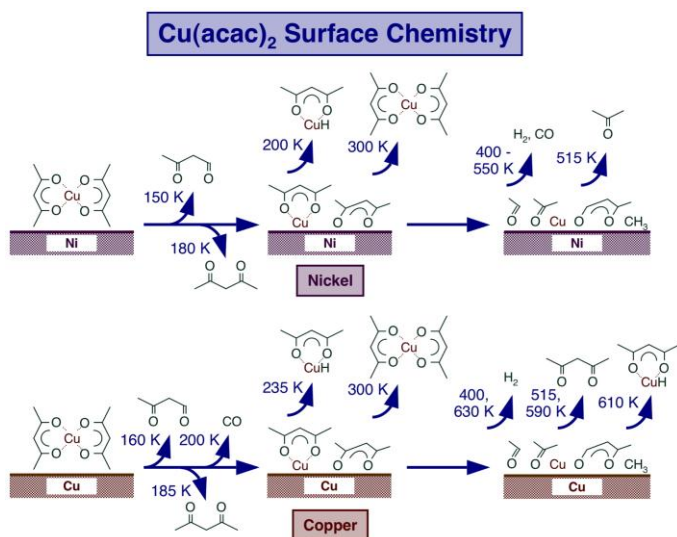


Figure 2. Schematic depiction of the proposed thermal chemistry of  $\text{Cu}(\text{acac})_2$  on Ni(110) and Cu(110) surfaces.

likely change in adsorption geometry were seen next, with the possible production of  $\text{HCu}(\text{acac})$ , which desorbs at 200 and 235 K from the nickel and copper surfaces, respectively. Molecular  $\text{Cu}(\text{acac})_2$  desorption is observed on both surfaces at approximately 300 K, probably from recombination of  $\text{Cu}(\text{acac})$  and  $\text{acac}$  surface species. The remaining copper atoms on the surface lose their remaining  $\text{acac}$  ligands to the substrate and become reduced directly to metallic copper. At the same time, the organic ligands follow a series of subsequent surface reactions, probably involving several C–C bond-scissions, to produce other fragments, additional  $\text{HCu}(\text{acac})$  and  $\text{HCu}(\text{acac})$  in the gas phase in the case of the copper surface, and acetone on nickel. A significant amount of  $\text{acac}$  must nevertheless survive on the surface to high temperatures, because  $\text{HCu}(\text{acac})$  peaks are seen in the TPD at about 515 and 590 K and the C 1s XPS split associated with  $\text{acac}$  is seen up to close to 500 K. In terms of ALD processes, this suggests that cycles could be design to run at such temperatures as long as an effective hydrogenation agent is used as the second reactant to remove the surface  $\text{acac}$  as  $\text{HCu}(\text{acac})$ . Only a small fraction of carbon is left behind on Ni after heating to 800 K, whereas more carbon and additional oxygen remains on the surface in the case of Cu.

To expand on our knowledge on the ALD of copper, and to test the behavior of Cu(II) precursors, in particular their potential for disproportionation reactions, the thermal chemistry of copper(II)acetylacetonate,  $\text{Cu}(\text{acac})_2$ , was also studied on both Ni(110) and Cu(110) single-crystal surfaces (Figure 2) [4]. Like with the acetamidinate, stepwise chemical transformations were identified covering a temperature range from 150 to 630 K. The desorption of  $\text{HCu}(\text{acac})$  and a 3-oxobutanal ( $\text{CH}_3\text{COCH}_2\text{CHO}$ ) byproduct was observed first, at 150 and 180 K on Ni(110) and at 160 and 185 K on Cu(110), respectively. Partial loss of the acetylacetonate ( $\text{acac}$ ) ligands and a

In a separate direction of research, we have been exploring non-thermal ways of activating ALD precursors as a way to trigger cleaner surface chemistry at lower temperatures. In the past, we investigated the possibility of using electron bombardment excitation in the gas phase to activate stable cyclopentadienyl precursors. Here we looked into the possibility of using photon-based excitations of adsorbed or condensed species. In many applications, the deposition of solid films requires control over thickness, conformality, and possibly spatial resolution [5]. Polymeric films are often grown on surfaces with the aid of X-rays or other excitation sources, one example being the deposition of photoresist masks. Polymerization is also possible via the use of catalysts, typically metalorganic compounds based on early transition metals. Here we report on a way to grow solid films by combining X-ray excitation with early-transition-metal promotion, for the particular case of the polymerization of pentakis(dimethylamido)tantalum (PDMAT) on tantalum foils initiated by radiation with soft X-rays (Al  $K_{\alpha}$  radiation,  $h\nu = 1486.6$  eV). Detailed mechanistic studies led to the conclusion that the initial excitation is triggered by the secondary electrons generated from, the underlying surface, and propagated to form polymeric films, via the catalytic action of the tantalum atom in the metalorganic precursor. This dual-functionality polymerization process may offer an alternative for film deposition at low temperatures and with great control on film thickness and spatial resolution. The synergistic effect derived from our studies is explained in the diagram in Figure 3.

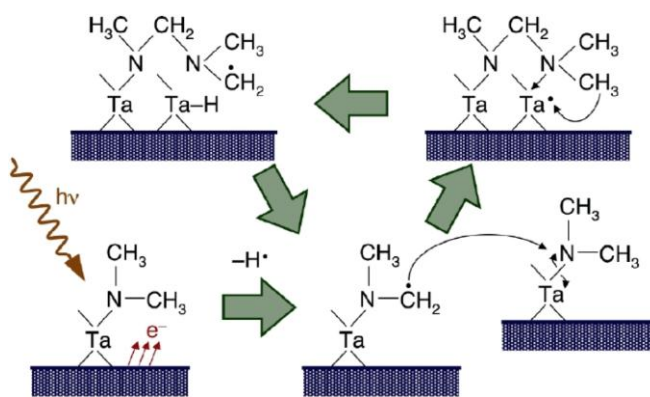


Figure 3. Schematic representation of the X-ray-induced surface chemistry observed for PDMAT.

Finally, we were also invited to offer a perspective on our studies on the surface chemistry of ALD processes for *The Journal of Physical Chemistry Letters* [6]. In our view, atomic layer deposition (ALD) is one of the most promising methodologies available for the growth of solid thin films conformally on complex topographies and with atomic-level control on thickness. However, as a chemical process, ALD can lead to the incorporation of impurities and to the growth of poor-quality films. In that article, we discussed some possible complications associated with the chemistry of ALD, including its ill-defined stoichiometry, the stepwise and extensive surface conversion possible with the ligands of most ALD metalorganic precursors, the need for the reduction or oxidation of the deposited elements, the poor understanding of the role of the co-reactants, the dominant activity of specific minority surface sites in starting ALD processes, and the development of complex layered or 3-D structures within the deposited films. We believe that the resolution of these issues, a general focus in our laboratory, should help with the development of a more systematic approach for the selection of ALD precursors and for the design of ALD processes.

### iii) Future Plans

In the next year, we plan to continue along the research directions already ongoing in this project. Specifically, we intend to extend our initial studies on copper deposition to:

- Extension of the studies on the surface chemistry of the original copper acetamidates to contrast with other new related precursors, obtained from the laboratory of Prof. Seán Barry at Carleton University. He is a synthetic chemist, and our collaborator in this project.
- Extension of the studies on the surface chemistry of these copper acetamidates to other metal surfaces, in particular copper surfaces in order to understand the film growth once the first layer has been deposited, and silicon to better mimic the conditions encounter in the early stages of deposition.

In addition, we propose to develop our GC/MS approach to the study of the thermal chemistry of copper ALD precursors.

#### iv) References

- [1] Q. Ma, H. Guo, R. G. Gordon, F. Zaera, *Chem. Mater.* 22 (2010) 352-359.
- [2] Q. Ma, H. Guo, R. G. Gordon, F. Zaera, *Chem. Mater.* 23 (2011) 3325-3334.
- [3] Q. Ma, F. Zaera, R. G. Gordon, *J. Vac. Sci. Technol. A* 30 (2012) 01A114/1-101A114/10.
- [4] Q. Ma, F. Zaera, *J. Vac. Sci. Technol., A* 31 (2013) 01A112/1-01A112/10.
- [5] T. Kim, F. Zaera, *J. Phys. Chem. C* 116 (2012) 8594-8600.
- [6] F. Zaera, *J. Phys. Chem. Lett.* 3 (2012) 1301-1309.

#### v) Publications Sponsored by This DOE Grant, 2012-2013

1. Qiang Ma, Roy G. Gordon, and Francisco Zaera, Thermal Chemistry of Copper(I)-N,N'-di-sec-butylacetamidate on Cu(110) Single-Crystal Surfaces, *J. Vac. Sci. Technol. A*, **30(1)**, 01A114/1-01A114/10 (2012). SPECIAL ISSUE: ALD
2. Xiangdong Qin, Huaxing Sun, and Francisco Zaera, Thermal Chemistry of Mn<sub>2</sub>(CO)<sub>10</sub> during Deposition of Thin Manganese Films on Silicon Oxide and on Copper Surfaces, *J. Vac. Sci. Technol. A*, **30(1)**, 01A112/1-01A112/10 (2012). SPECIAL ISSUE: ALD
3. Taeseung Kim and Francisco Zaera, X-Ray-Initiated Metal-Promoted Thin Film Growth, *J. Phys. Chem. C*, **116(15)**, 8594-8600 (2012).
4. Francisco Zaera, The Surface Chemistry of Atomic Layer Depositions of Solid Thin Films, *J. Phys. Chem. Lett.*, **3**, 1301-1309 (2012). INVITED
5. Huaxing Sun, Xiangdong Qin, and Francisco Zaera, Activation of Metalorganic Precursors by Electron Bombardment in the Gas Phase for Enhanced Deposition of Solid Films, *J. Phys. Chem. Lett.*, **3**, 2523–2527 (2012).
6. Qiang Ma and Francisco Zaera, The Chemistry of Cu(acac)<sub>2</sub> on Ni(110) and Cu(110) Surfaces: Implications for Atomic Layer Deposition (ALD) Processes, *J. Vac. Sci. Technol. A*, **31(1)**, A01A112/1-A01A112/10 (2013).
7. Huaxing Sun and Francisco Zaera, Chemical Deposition of Manganese Metallic Films on Silicon Oxide Substrates, *J. Phys. Chem. C.*, **116 (44)**, 23585–23595 (2012).

## Utilizing Molecular Self-Assembly to Tailor Electrical Properties of Si Nanomembranes

Pengpeng Zhang

[Zhang@pa.msu.edu](mailto:Zhang@pa.msu.edu)

Department of Physics and Astronomy

Michigan State University, East Lansing, MI 48824

### Program Scope

The program is focused on understanding and control of hetero-interfaces between organic and inorganic materials. Integrating organic molecules of desired orientation and long-range ordering with inorganics is essential to the development of organic electronics, molecular electronics, molecular/biological sensors and energy harvesting devices. We choose Si nanomembranes as the prototype inorganic system to explore the interfacial phenomena as the membrane's transport properties are sensitive to the surface and interface condition, thus offering a great opportunity to unravel the nature of electronic interactions at the hetero-interface. Specifically, we aim to 1) explore the nucleation and growth mechanisms of organic molecular thin films on Si surfaces; 2) create long-range ordered molecular structures with desired orientation on the substrate; and 3) control the electronic properties of Si nanomembranes at the molecular scale via regulation of surfaces and interfaces.

### Recent Progress

This report will focus primarily on our most recent efforts in achieving highly ordered molecular thin films on deactivated Si surfaces. Control of highly ordered organic molecular thin films with extended  $\pi$  systems is currently of intense interest for integration into modern electronics due to the tunable nature of organic molecules.<sup>1</sup> Selection of molecules and substrates can lead to desired transport properties such as charge transfer, charge injection, exciton diffusion, etc., at the hybrid heterointerface, which is central to the development of organic and molecular electronics.<sup>2</sup> However, achieving large-scale molecular ordering remains a significant challenge. Strong molecule-substrate interaction can hinder molecular diffusion and organization on the surface, while strong molecule-molecule interaction results in island growth and the formation of polycrystalline or polymorphic films.<sup>3</sup> Therefore, it is desirable to tip the balance between molecule-molecule and molecule-substrate interactions, and to grow organic thin films that are ordered in both the perpendicular and in-plane directions.<sup>4,5</sup>

We have recently discovered an anisotropic crystalline organic step-flow growth on deactivated Si surfaces that exhibits no true commensurism despite a single dominate long-range ordered relationship between the organic crystalline film and the substrate, uniquely distinct from

inorganic epitaxial growth (see Fig. 1). Our results indicate that the interaction between molecules and the substrate is sufficiently weak to allow the molecules to diffuse across  $\mu\text{m}$ -wide terraces at room temperature, but sufficiently strong to induce in-plane azimuthal ordering and long-range ordered growth, as shown in Fig. 2. Access to this growth mode offers the potential for improved performance for organic electronic and energy harvesting devices since the formation of twin boundaries of the adjacent stripe structures is preferred over randomly orientated grain boundaries (often observed during the island growth) for achieving superior electrical and excitonic transport.<sup>6</sup> This achievement is also crucial for our long-term goal in the DOE funded research, i.e., to achieve precise control of carrier concentration and charge transport in nanoscale Si membranes via modulation of surfaces and interfaces.<sup>7</sup>

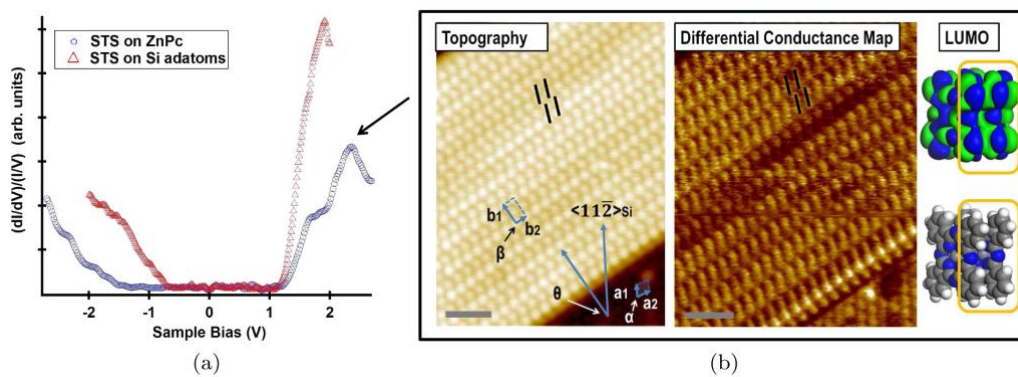


Figure 1. (a) Normalized STS spectra. The peak in the ZnPc spectra near +2.5 V was used for the simultaneous imaging of topology and differential conductance map in (b). (b) Partial imaging showing both the ZnPc overlayer and the Si surface, where  $\Theta$  defines the azimuthal relation between the two. Black lines represent individual molecules. Inset: atomic model of a ZnPc dimer in observed tilted orientation and LUMO of free ZnPc molecules calculated using density functional theory. Grey scale bars are 3nm.

We attribute the step-flow growth mode to the large diffusivity of organic molecules and the low defect density of the deactivated Si surface which allow molecules to fully explore the surface at room temperature to find preferential nucleation sites at the steps. The high molecular diffusivity is achieved largely due to two contributing factors: (i) the Si (111)-B surface is deactivated without any density of states present at the Fermi level, leading to a relatively weak molecule-substrate interaction and the noncommensurate molecular registration to the substrate;

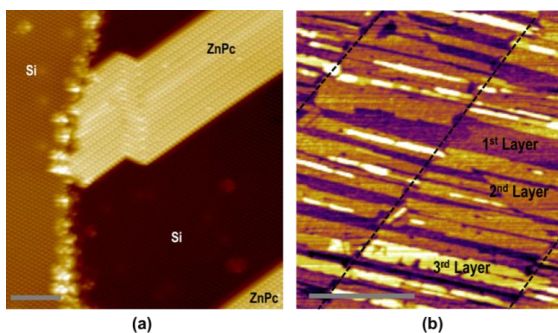


Figure 2: (a) STM image of the initial anisotropic step-flow growth of ZnPc on the deactivated Si surface. Two parallel stripes are observed extending from the same Si step edge. The gray scale bar is 8 nm. (b) Tapping mode AFM image of multiple layers of ZnPc. The anisotropic step-flow growth mode is maintained up to 3 layers with a single dominant stripe growth direction. The gray scale bar is 500 nm.

(ii) the geometric parameters of the molecule, including its size and symmetry, do not match with the substrate. As a consequence, the effective surface potential corrugation is smeared out over the size of the molecule which effectively reduces the activation barrier for diffusion.

In addition to the step-flow growth at room temperature, we have mapped the temperature dependence of this novel growth regime for different organic molecules, which shows a reversal trend from that observed in inorganic growth (see Fig. 3). Intuitively, one would expect a longer molecular diffusion length and thus continued step-flow growth as the substrate temperature is increased.<sup>8</sup> However, we find that the growth begins to shift away from anisotropic step-flow growth to two-dimensional islands nucleation on the terrace and eventually to random rough growth as a result of the competition between diffusion and nucleation processes.

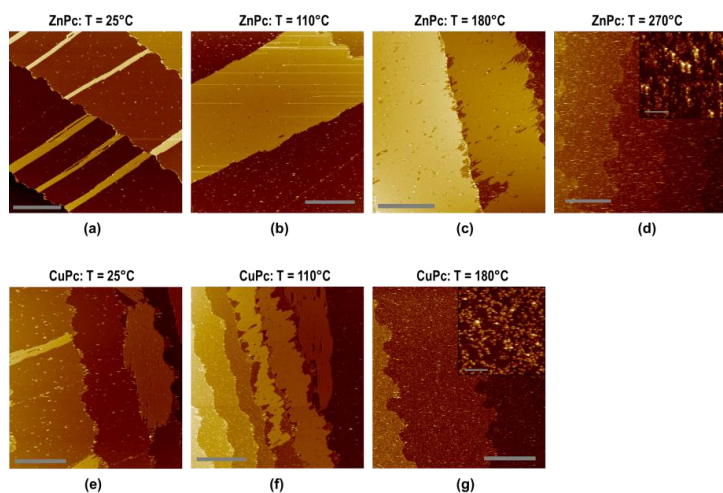


Figure 3: (a)-(d) STM images of ZnPc deposited on Si with varying substrate temperature during deposition. From the observations there are transitions in the growth mode from step-flow growth to 2D island growth to random rough growth. (e)-(g) STM images of CuPc on Si. CuPc growth displays the same temperature dependent growth trend as in ZnPc, but there is a relative shift in the temperatures at which growth mode transitions are observed which can be attributed to the different molecule-molecule and molecule-substrate interactions that impact the nucleation and growth behaviors. The gray scale bars in (a)-(g) are 300 nm (13nm for the inset).

Beyond the initial sub-monolayer growth, a highly ordered multilayered thin film has been achieved in both in-plane and out-of-plane directions on Si substrates studied by STM and LEED. Moreover, as known in the inorganic growth, energetics and kinetics both play important roles in controlling the thin film morphology. To provide a more generalized understanding of the organic growth mechanism on the deactivated Si(111)-B surface, we have investigated how the grain boundary crossing and Ehrlich-Schwöebel barriers influence the growth evolution with temperature.

## Future Plans

We will continue to explore the microscopic mechanisms of molecular diffusion and nucleation on the Si(111)-B surface and intentionally tune the molecule-molecule and molecule-substrate interactions to tailor the growth behaviors. We will investigate the interfacial electronic structure and charge transfer behaviors between molecular overlayer and Si substrates, including both the bulk and Si nanomembranes, by Kelvin probe force microscopy (KPFM) and/or

ultraviolet photoelectron spectroscopy (UPS). We will further conduct *in-situ* transport measurements to evaluate the effects of surface chemical functionalization and interfacial charge transfer on electronic properties of Si nanomembranes. Our goal is to utilize the molecular scale precision of surface structures to control the transport properties of Si nanomembranes to an unprecedented extent.

## References

---

1. G. Witte and C. Wöll, *J. Mater. Res.* **19**, 1889 (2004).
2. J. Hwang, A. Wan, and A. Kahn, *Mater. Sci. Eng. R* **64**, 1 (2009).
3. J. V. Vath, *Annu. Rev. Phys. Chem.* **58**, 375 (2007).
4. G. E. Thayer, J. T. Sadowski, F. Meyer zu Heringdorf, T. Sakurai, and R. M. Tromp, *Phys. Rev. Lett.* **95**, 256106 (2005).
5. S. Kowarik, A. Gerlach, F. Schreiber, *J. Phys.: Condens. Matter* **20**, 184005 (2008).
6. A. B. Chwang and C. D. Frisbie, *J. Appl. Phys.* **90**, 1342 (2001).
7. P. P. Zhang, E. Tevaarwerk, B.-N. Park, D. E. Savage, G. K. Celler, I. Knezevic, P. G. Evans, M. A. Eriksson, and M. G. Lagally, *Nature* **439**, 703 (2006).
8. M. H. Xie, S. M. Seutter, W. K. Zhu, L. X. Zheng, H. Wu, and S. Y. Tong, *Phys. Rev. Lett.* **82**, 2749 (1999).

## DoE Sponsored Publications in the Last Two Years

1. S. R. Wagner, R. R. Lunt, and P. P. Zhang, Anisotropic Crystalline Organic Step-Flow Growth on Deactivated Si Surfaces, *Phys. Rev. Lett.* **110**, 086107 (2013).
2. S. R. Wagner and P. P. Zhang, Surfaces and Interfaces of Nanoscale Silicon Materials, *Mater. Res. Soc. Symp. Proc.* **1550**, 609 (2013).
3. S. R. Wagner and P. P. Zhang, Formation of Highly Ordered Zinc Phthalocyanine Thin Films on Deactivated Si Surfaces by STM and LEED, submitted.
4. S. R. Wagner and P. P. Zhang, Characterization of Ehrlich-Schwöebel Barriers and Grain Boundary Crossing Barriers in Organic Thin Film Growth on Deactivated Si Surfaces, in preparation.

# **Giant Electrocaloric Effect In Ferroelectric Polymers With Tailored Polar-Nanostructures**

Q. M. Zhang

Department of Electrical Engineering and Materials Research Institute  
The Pennsylvania State University, University Park, PA 16802

## **Program Scope**

When an electric field is applied to an insulation material, it will induce a change of polar states and consequently, a change in the entropy or temperature of the material. Such an electric field induced temperature and entropy change in a dielectric material is known as the electrocaloric effect (ECE). The electrocaloric effect is attractive because refrigeration based on ECE approach is more environmentally friendly and has the promise of achieving higher efficiency if the ECE is large. Although ECE in ferroelectric materials have been studied for many decades, the relatively small ECE, up to 2.5 K in the adiabatic temperature change  $\Delta T$ , demonstrated in bulk ceramics at high temperature ( $>250$  °C) during the second half of the 20<sup>th</sup> century was unimpressive for practical applications. In the DoE BES program, we demonstrated that near ferroelectric-paraelectric transition, a large ECE, i.e.  $\Delta T > 12$  °C, can be induced near the ferroelectric-paraelectric transition. Moreover, by defects modification which converts the normal ferroelectric P(VDF-TrFE) into a relaxor, a large ECE, i.e.,  $\Delta T > 16$  °C can be obtained over a broad temperature near room temperature. The results indicate the potential of dielectric materials, with tailored nanostructures, in achieving giant ECE.

It is the objective of this DoE BES program to develop understanding of what are the “optimal” molecular and nano-structures of polar-dielectrics in order to achieve a giant ECE as well as a giant EC coefficient, i.e., a large ECE induced under a low electric field. A combined thermodynamic analysis and experimental study are employed in this program to investigate ECE in dielectric polymer compositions with built-in inhomogeneity, polar-dielectrics with weak inter-molecular interactions such as dielectric liquids and organic ferroelectrics. In addition to ECE, dielectric and structure characterizations are carried out to provide insights of molecular and nano-structure mechanisms of ECE in these strong dipolar coupled systems. Thermodynamic analyses and theoretical modeling are developed to elucidate the experimental results and to provide guidance to the experimental study.

## **Recent Progress**

One critical issue in developing ferroelectric materials to achieve high electrocaloric (EC) response is to understand what are the key material requirements and how to design and tailor the nano-structure of the materials since the EC is closely related to the “randomness” of the dipoles in the molecular and nano-scales. In this program, a theoretical model was developed which shows that the isothermal entropy change  $\Delta S$  of an EC material is related to the polarization P as

$$\Delta S = \frac{\ln \Omega}{3\varepsilon_0 \Theta} P^2$$

where  $\Omega$  is the number of available polar-states and  $\Theta$  is the Curie-constant, which is directly related to the dipole correlation length.<sup>1</sup> Indeed, a large ECE has been demonstrated by operating a ferroelectric material near its ferroelectric-paraelectric transition.<sup>2-3</sup> By defects modification to reduce the polar-correlation length and to convert the normal ferroelectric into relaxor ferroelectric, we have demonstrated a large EC response in the relaxor ferroelectric polymer over a broad temperature range (see Fig. 1).<sup>3-4</sup>

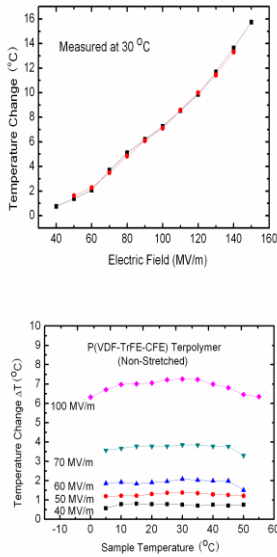


Fig. 1. The ECE (adiabatic temperature change) vs. applied field at 30 C (a) and vs. temperature under different fields for a P(VDF-TrFE-CFE) relaxor polymer

Moreover, basic materials consideration and a theoretical analysis indicate that a promising approach to significantly increase  $\Omega$  is to operate the material near a multi-phase coexisting phase diagram region, especially near the critical point at which the energy barriers for the phase switching

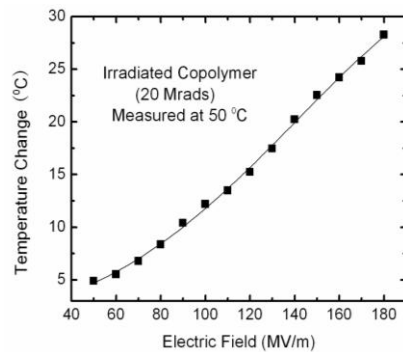


Fig. 2. The ECE (adiabatic temperature change) vs. applied field at 50 C for an electron irradiated P(VDF-TrFE) 65/35 mol% copolymer

become comparable to the thermal energy, leading to large EC response under low applied field.<sup>5</sup> Based on these considerations, we investigated ECE in the modified P(VDF-TrFE) at 65/35 mol%, which is a composition between the ferroelectric phase and a low temperature phase (besides the paraelectric phase). As shown in Fig. 2, an exceptionally large ECE ( $\Delta T=28$  °C) can be induced in the high energy electron irradiated P(VDF-TrFE) 65/35 mol% copolymer.<sup>6</sup>

For the dielectrics with large ECE reported, the ECE such as the isothermal entropy change  $\Delta S$  and adiabatic temperature change  $\Delta T$  is proportional to the square of applied field. Hence at low fields, ECE is low and a high field is required to induce a large ECE (see Fig. 1 and 2). One interesting question is can one engineer an EC material so that a large EC response can be induced at low field. In this program, we are investigating approaches to establish internal DC bias fields using the blend. We demonstrated that the blend approach, in which a small amount of normal ferroelectric polymer is blended with a relaxor terpolymer, is effective in establishing internal DC bias field which can significantly improve the ECE, especially at low field. In this program, we first investigate the blends of P(VDF-TrFE-CFE) with small amount of P(VDF-TrFE) copolymer, which also provide a model system to study how the random defects in the terpolymer influence the polarization response in the copolymer and consequently ECE in the blends. Since P(VDF-TrFE) copolymer is a normal ferroelectric, in which large remanent polarization will exist after poling, the copolymer may provide an internal electric field in the blends, thus generating higher polarization and enhancing ECE at low fields. The experiment results of the blends show, indeed, a large enhancement in the polarization response after the poling of the blend of P(VDF-TrFE-CFE)/P(VDF-TrFE) (65/35mol%) (see Fig. 3), indicating that

the internal DC bias field has increased the polarization response. The experimental results also reveal that the internal DC bias field effect and the enhancement of the polarization depend critically on the P(VDF-TrFE) copolymer composition (Fig. 3), indicating complicated interplay between the terpolymer and copolymer. Further studies, including micro-structure characterizations, will

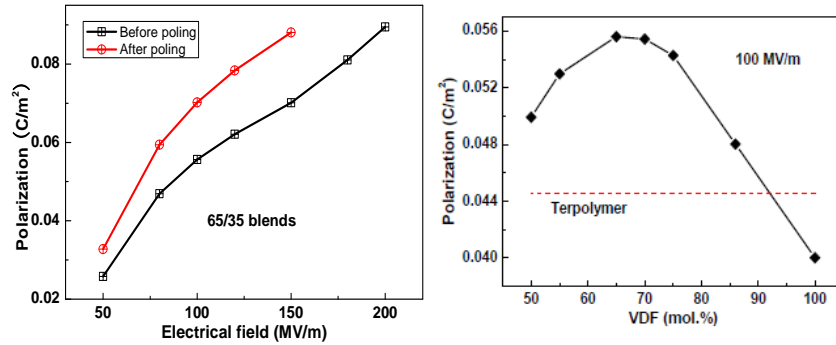


Fig. 3. (left) The enhanced polarization level in a terpolymer/(65/35 mol% copolymer) blend vs. applied field and (right) the enhanced polarization (measured at 100 MV/m) in the blend (after the poling) vs. the copolymer composition (the polarization of the neat terpolymer is also shown).

be conducted to understand the observed behavior. Nevertheless, the results demonstrate the effectiveness of this internal DC bias field approach in improving the ECE.

In developing EC materials, another interesting question is besides the polymers and ceramics, whether large ECE can also be obtained in dielectric liquids and organic ferroelectrics. There are several materials considerations suggest the potential of these materials in achieving large ECE under low electric fields. In this DoE BES program, we have started investigating ECE in a class of dielectric liquids: liquid crystals. Preliminary experimental results already showed a large ECE (Fig. 4, where a  $\Delta T = 5.2$  C has been obtained) in the liquid crystal 5CB (Fig. 5).<sup>7</sup>

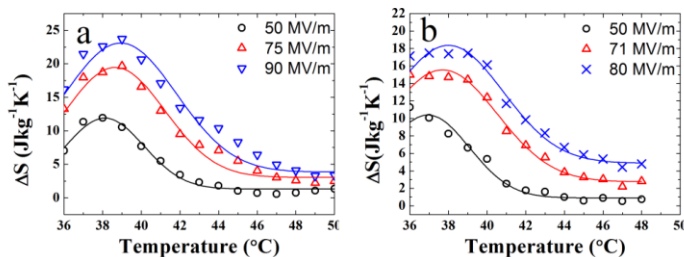


Figure 4. The electrocaloric effect for (a) isothermal entropy change  $\Delta S$  of 5CB LCs in NA-Cells, and (b)  $\Delta S$  of 5CB LCs in homogeneously aligned LC cells (HA-Cells) as functions of temperature.

## Future plans

Investigate ECE in the terpolymer/P(VDF-TrFE) copolymer blends (as well as nanocomposites with normal ferroelectric ceramics) to develop optimal material compositions and nano-morphologies for establishing internal DC bias field and generating large ECE under

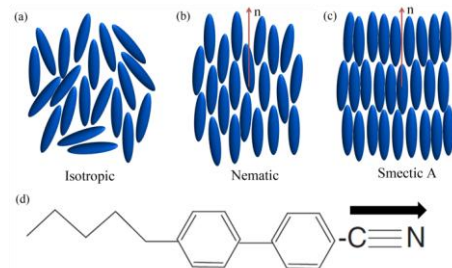


Figure 5. Schematic of various mesophases for rodlike LC molecules which are of interest for generating large ECE: (a) an isotropic, (b) nematic, and (c) smectic A phases, (d) Molecular structure of 5CB.

low electric fields and conduct fundamental studies on various couplings (between dipoles, at interphases and interfaces) on the ferroelectric and EC responses.

Expand the studies on liquid crystals, including studies on liquid crystals possessing a large dielectric constant (dielectric constant >100) and dielectric anisotropy, possible defects modification to liquid crystals as we have done in the past in the ferroelectric polymers.

## References

1. R. Pirc, Z. Kutnjak, and R. Blinc and Q. M. Zhang. *Appl. Phys. Lett.* 98, 021909 (2011).
2. S. G. Lu, B. Rožič, Q. M. Zhang, Z. Kutnjak, Bret Neese, *Appl. Phys. Lett.* 98, 122906 (2011).
3. Bret Neese, Baojin Chu, Sheng-Guo Lu, Yong Wang, E. Furman, and Q. M. Zhang, *Science*, 321, 821-823 (2008).
4. Xinyu Li, Xiao-shi Qian, S. G. Lu, Jiping Cheng, Zhao Fang and Q. M. Zhang. *Appl. Phys. Lett.* 99, 052907 (2011).
5. Z. K. Liu, Xinyu Li, and Q. M. Zhang. *Appl. Phys. Lett.* 101, 082904 (2012).
6. Xinyu Li, Xiao-shi Qian, Haiming Gu, Xiangzhong Chen, S. G. Lu, Minren Lin, Fred Bateman, and Q. M. Zhang. *Appl. Phys. Lett.* 101, 132903(2012).
7. Xiao-Shi Qian, S. G. Lu, Xinyu Li, Haiming Gu, L-C Chien, Q. M. Zhang, *Adv. Funct. Mater.* 23, 2894 (2013).

## DoE Sponsored Publications in the Last Two Years

- S. G. Lu, B. Rozic, Z. Kutnjak, and Q. M. Zhang, *Integrated Ferro.* 125, 176 (2011).
- Xinyu Li, Xiao-shi Qian, S. G. Lu, Jiping Cheng, Zhao Fang and Q. M. Zhang, *Appl. Phys. Lett.* 99, 052907 (2011).
- Brigita Rozic, Marija Kosec, Hana Ursic, Janez Holc, Barbara Malic, Q. M. Zhang, Robert Blinc, Rasa Pirc, and Zdravko Kutnjak, *J. Appl. Phys.* 110, 064118 (2011).
- R. Pirc, Z. Kutnjak, and R. Blinc, Q. M. Zhang. *J. Appl. Phys.* 110, 074113 (2011).
- B. Rozic, B. Neese, S. G. Lu, Q. M. Zhang, and Z. Tutnjak, *Ferro.* 416, 139-143 (2011) .
- B. Rozic, S. G. Lu, Z. Kutnjak, B. Neese, and Q. M. Zhang. *Ferro.* 422, 81 (2011).
- S. G. Lu, J. Z. Jin, X. Zhou, Z. Fang, Q. Wang, and Q. M. Zhang. *J. Appl. Phys.* 110, 104103 (2011).
- S. G. Lu, B. Rozic, Q. M. Zhang, Z. Kutnjak, R. Pirc. *Appl. Phys.* A106(4) (2012).
- V. Bobnar, X. Li, G. Casar, A. Erste, S. Glinsek, X. Qian, and Q. M. Zhang. *J. Appl. Phys.* 111, 083512 (2012).
- Z. K. Liu, Xinyu Li, and Q. M. Zhang. *Appl. Phys. Lett.* 101, 082904 (2012).
- Xinyu Li, Sheng-Guo Lu, Xiang-Zhong Chen, Haiming Gu, Xiao-shi Qian and Q. M. Zhang. *J. Mater. Chem. C.* 1, 23 (2013).
- S. G. Lu and Q. M. Zhang, *J. Adv. Diel.* 2(3), 1230011 (2012).
- S. G. Lu, B. Rozic, Q. M. Zhang, Z. Kutnjak, and R. Pirc, *Appl. Phys. A: Mater. Sci. & Proc.* 107, 559-566 (2012).
- Xinyu Li, Xiao-shi Qian, Haiming Gu, Xiangzhong Chen, S. G. Lu, Minren Lin, Fred Bateman, and Q. M. Zhang. *Appl. Phys. Lett.* 101(13), 132903(2012).
- B. Rozic, B. Malic, H. Ursic, J. Holc, M. Kosec, S.-G. Lu, Q. M. Zhang, and Z. Kutnjak. *Ferro.* 430, 98-102 (2012).

- Xiao-Shi Qian, S. G. Lu, Xinyu Li, Haiming Gu, L-C Chien, Q. M. Zhang, *Adv. Funct. Mater.* 23, 2894 (2013).
- Goran Casar, Xinyu Li , Jurij Koruza, Q. M. Zhang, Vid Bobnar, *J. Mater. Sci.* 48, 7920 (2013).

# ***In Situ* Visualization and Theoretical Modeling of Early-Stage Oxidation of Metals and Alloys**

Guangwen Zhou

[gzhou@binghamton.edu](mailto:gzhou@binghamton.edu)

Department of Mechanical Engineering, State University of New York, Binghamton, NY 13902

## **Program Scope**

Oxidation, with effects both beneficial and deleterious, plays an enormous role in technology, from causing serious corrosion problems, to providing protection against corrosion attack. Acquiring the ability to manipulate the microscopic processes governing the surface oxidation via either controlling the reaction environment or modifying the materials has huge technological implications. This project encompasses an atomic-scale study of the oxidation of metals and alloys ranging from the initial stage of oxygen surface chemisorption to the subsequent stages of nucleation and growth of bulk oxide. These studies exploit the unique *in situ* capabilities of scanning tunneling microscopy (STM), transmission electron microscopy (TEM) and x-ray photoelectron spectroscopy (XPS) to dynamically measure the surface structure and chemistry under a wide range of oxidation conditions. Particularly, we address oxygen chemisorption induced surface phase transitions, the crossover from on-surface oxygen chemisorption to subsurface oxygen incorporation, and surface/interface effect on growth morphologies of oxide nanoislands from the comparative study of the oxidation of Cu, Cu-Au, and Cu-Ni. Each of the experiments is coordinated closely by a number of theoretical modeling techniques ranging from the first-principles calculations to continuum elastic theory for developing direct insight into the reaction mechanism, including adsorption sites, diffusion path, reaction barrier, and surface/interface effects. Due to the decisive role of the environment in determining the reaction behavior, incorporation of the temperature and pressure effect into the first-principle thermodynamics calculations allows for identifying how the interplay between thermodynamics and kinetics determines the final structure, composition, and oxidation mechanism.

## **Recent Progress**

We have undertaken a combined in-situ microscopy experimental and theoretical program aimed at elucidating the atomistic processes governing oxide island formation during the oxidation of metals. We find that oxidation of Cu occurs via  $\text{Cu}_2\text{O}$  islanding on a 2D oxide wetting layer at a critical thickness of two atomic layers. Our results provide the first experimental observation of the structure transition, on the atomic scale, of the nucleation and growth of 3D oxide islands and reveals both heterogeneous and homogenous processes are involved leading to oxide islanding, where the heterogeneous process controls the nucleation of the oxide wetting layer at defect sites (e.g., surface steps) of the metal surface while the homogeneous process controls the nucleation of 3D oxide islands on the oxide wetting layer driven energetically by the metal-oxide interfacial strain.

Generally, the oxidation of metals involves hierarchical multiple length scales proceeding from oxygen surface chemisorption to oxide nucleation and growth and then to the formation of continuous oxide film. One of the most poorly understood and disputable phenomena in metal oxidation is its transient early stages, i.e., how oxide films nucleate and start to grow, which are inaccessible by both the traditional surface science (which is typically limited to ultrahigh

vacuum and monolayer oxygen adsorption) and "bulk" materials science techniques. Previous studies have shown that the early stages of metal oxidation typically involve oxide islanding, however, significant controversies exist regarding homogeneous or heterogeneous nucleation of oxide films. It was suggested that oxide nuclei should form at surface defect sites where threading dislocations or stacking faults intersect the surface (i.e., a process controlled by heterogeneous island nucleation), but in most cases the evidence has been purely inferential<sup>1-4</sup>. Although oxide nuclei were observed to form at some dislocations, most nuclei do not show one-on-one correlation with dislocations and many dislocations have no oxide nuclei associated with them (i.e., a process controlled by homogeneous island nucleation)<sup>5-7</sup>. A key challenge in resolving these controversies is the absence of direct observation of the structural transition in real space during oxidation due, in large part, to the inability of traditional experimental approaches to monitor the surface structure evolution and oxide formation with the desired spatial and temporal resolution.

Using dynamic real-time TEM observations of the nucleation and growth of  $\text{Cu}_2\text{O}$  islands during the oxidation of Cu, here we demonstrate that oxide islanding occurs homogeneously on an oxide wetting layer at a critical thickness of two atomic layers, which resembles the Stranski-Krastanov mechanism in heterogeneous thin film epitaxy<sup>8</sup>. Fig. 1 depicts *in situ* HRTEM images of a Cu(100) surface, seen edge-on under the oxidation condition of  $p\text{O}_2 = 5 \times 10^{-3}$  Torr and  $T = 350^\circ\text{C}$ . As seen in Fig. 1(a), some oxide has already developed on the surface from the oxidation before the *in situ* TEM movie was captured, where the lattice spacing matches well with the  $\text{Cu}_2\text{O}$  structure and can be used as a "fingerprint" for identifying the new oxide formed at later stages on the slightly lower left-hand side, where a two-atomic-layer-thick oxide wetting layer is visible. The top-left inset is a zoom-in TEM image from the location where a Cu step is present at the  $\text{Cu}_2\text{O}$ -Cu interface in the region indicated by the dashed box. Due to their different lattice spacings, the  $\text{Cu}_2\text{O}(200)$  plane (dashed red line) is slightly higher than the Cu surface (solid red line), thereby forming a disconnection at the Cu step and giving rise to slight lattice distortion across the stepped region. This is illustrated in the corresponding

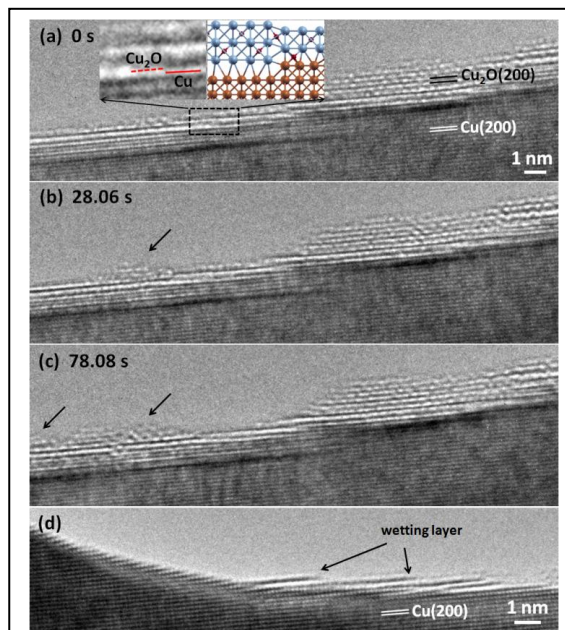


Fig. 1: (a-c) *In situ* TEM observations of the nucleation and growth of a  $\text{Cu}_2\text{O}$  island on the oxide wetting layer during oxidation of Cu(100) at  $350^\circ\text{C}$  and  $p\text{O}_2 = 5 \times 10^{-3}$  Torr (see *in situ* TEM movie S1 in the Supplementary Material). Inset in (a) shows the formation of a disconnection at the buried Cu-Cu $_2$ O interface due to the presence of an atomic Cu surface step. (d) TEM image revealing that the oxide wetting layers initiate at Cu surface steps.

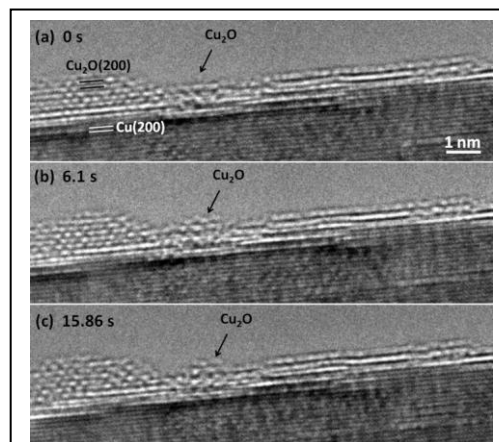
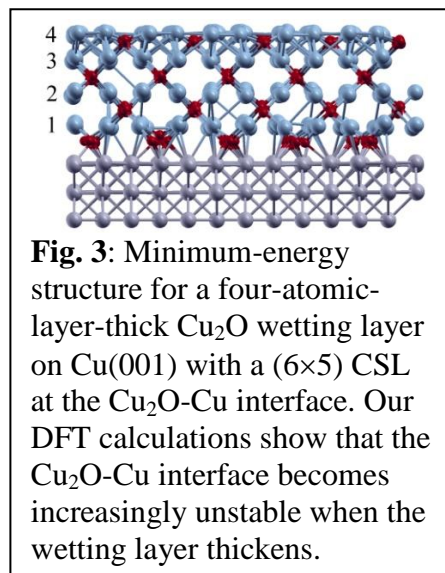


Fig. 2: (a) *In situ* TEM images showing the evolution of an initially three-atomic-layer-thick oxide wetting layer to a 3D  $\text{Cu}_2\text{O}$  island during the oxidation at  $350^\circ\text{C}$  and  $p\text{O}_2 = 5 \times 10^{-3}$  Torr.

structure model (top-right inset). It can be seen that two complete  $\text{Cu}_2\text{O}$  wetting layers have developed on the lower Cu terrace (i.e., the left hand side) while the third oxide layer still shows some discrete fuzzy feature. The time sequence of TEM images in Fig. 1(b-c) shows the nucleation and growth of a 3D  $\text{Cu}_2\text{O}$  island on the  $\text{Cu}_2\text{O}$  wetting layer in the course of the oxidation. It is interesting to note that the 3D island nucleates on a flat surface region rather than atop the distorted  $\text{Cu}_2\text{O}$  layer above the buried Cu step, suggesting a homogenous process of oxide island nucleation on the wetting layer. However, it is noted that the nucleation of the oxide wetting layer is via a heterogeneous process at surface defects, as seen in Fig. 1(d), which shows that all the wetting layers can be traced back to Cu surface steps at the corner. The *in situ* TEM images also reveal that the thickness of the  $\text{Cu}_2\text{O}$  wetting layer is two atomic thick for the transition to the 3D  $\text{Cu}_2\text{O}$  island growth. Fig. 1(c) shows that a second  $\text{Cu}_2\text{O}$  island (part of it is out of the TEM view) forms adjacent to the existing island and their coalescence would result in a bigger island similar as the one seen on the right-hand terrace.

Fig. 2 presents a time sequence of *in situ* TEM images showing the oxide wetting layer thickness evolution leading to the nucleation of a 3D  $\text{Cu}_2\text{O}$  island during the oxidation at  $p\text{O}_2 = 5 \times 10^{-3}$  Torr and  $T = 350^\circ\text{C}$ . In Fig. 2(a), a large  $\text{Cu}_2\text{O}$  island along with a  $\text{Cu}_2\text{O}$  wetting layer has already formed across the terrace before the *in situ* TEM movie was captured. The presence of atomic steps on the original Cu surface results in a slightly uneven surface morphology of the  $\text{Cu}_2\text{O}$  wetting layer. We focus on the wetting layer in the region having the flat surface as indicated by the black arrow in the figures. While the lattice fringe contrast of the wetting layer in this region appears slightly fuzzy, its thickness can be seen to be equivalent to three atomic layers by comparing with the well-resolved lattice fringe contrast in the adjacent large  $\text{Cu}_2\text{O}$  island. As seen in Figs. 3(a-c), the oxide wetting layer undergoes some fluctuation in height and eventually evolves into a stable 3D oxide island over time. Meanwhile, it can be noted that the oxide wetting layer between the large existing island and the newly formed  $\text{Cu}_2\text{O}$  island changes gradually from the originally three-atomic-layer thick to two-atomic-layer thick, where the atoms from the wetting layer are dislodged to the adjacent regions for oxide islanding. Such thickness reduction suggests that a continuous, three-atomic-layer-thick wetting layer is energetically unstable and transforms spontaneously to a more stable configuration by oxide islanding.

The natural lattice misfit between Cu and  $\text{Cu}_2\text{O}$  is 15.4% and this large misfit makes the formation of coherent metal-oxide interface energetically unfavorable. We have previously shown that the epitaxial growth of  $\text{Cu}_2\text{O}$  thin films on Cu substrates results in a  $(5 \times 6)$  coincidence site lattice (CSL) at the  $\text{Cu}_2\text{O}$ -Cu interface, in which 5 Cu spacings in  $\text{Cu}_2\text{O}$  overlayer match 6 Cu spacings in Cu substrate<sup>9</sup>. While the interfacial strain is significantly reduced to  $\sim 1.48\%$  by adopting this CSL interface configuration, the associated strain energy still increases rapidly as the oxide wetting layer thickens. To relieve the strain, oxide island formation occurs on the oxide wetting layer, by which the reduction in strain energy is greater than the concomitant cost of increased surface energy associated with creating the oxide island. The critical thickness of the wetting layer at which oxide islanding initiates is two atomic layers,



as seen in Figs. 1 and 2. To give further insight, we used density functional theory (DFT) to investigate the stability of the Cu<sub>2</sub>O wetting layer for different thicknesses up to 4 Cu<sub>2</sub>O layers. As shown in Fig. 3, in the optimized structure for the Cu/Cu<sub>2</sub>O system with 4 Cu<sub>2</sub>O layers, the interplanar spacings, from bottom to top, are 2.26 Å (the spacing between the Cu substrate and the bottom Cu<sub>2</sub>O layer), 1.96 Å, 2.04 Å and 1.49 Å, respectively. Note that the bulk Cu<sub>2</sub>O (100) interplanar distance is 2.15 Å from our DFT calculation. The distance between the top and second Cu<sub>2</sub>O layers is small compared to the bulk value, which can be attributed to the surface effect. Energetically, starting from a Cu slab with one Cu<sub>2</sub>O layer on top, we find that it costs 2.7, 1.5 and 1.1 eV per Cu<sub>2</sub>O to add 1, 2 and 3 additional layers. These DFT energies show that the interfacial energies are relatively large and the Cu-Cu<sub>2</sub>O interface becomes increasingly unstable with increasing the thickness of the wetting layer, and likely to transform into an island as shown in the experiments. Further investigations to elucidate this transformation are still ongoing.

### Future plans

We will continue to address a number of critical issues for controlling the oxide formation at the atomic level. The extensive interest in the initial-stage oxidation is motivated by seeking a fundamental understanding of the crossover between oxygen surface chemisorption and oxide formation. Such knowledge has great importance for understanding the initial oxidation kinetics (i.e., the ease or resistance to oxide formation). Unfortunately, this understanding is still very shallow for everything that goes beyond on-surface chemisorption of oxygen at low coverage. An intriguing phenomenon revealed recently from the oxidation of several metals is that surface oxidation does not proceed beyond the oxygen chemisorbed phase, despite the favorable thermodynamic conditions for bulk oxide formation<sup>10-13</sup>. By employing in-situ microscopy and spectroscopy (particularly ambient-pressure XPS), we will determine the critical oxygen pressure and temperature required for initiating oxygen subsurface incorporation and how the critical oxygen pressure and temperature are related to the surface orientations and alloy composition. Systematic experiments in conjunction with DFT calculations using the nudged energy band method will allow for identifying the origin of the kinetic hindrance limiting the crossover from on-surface oxygen chemisorption to subsurface oxygen adsorption for initiating bulk oxide nucleation.

### References

- <sup>1</sup> P. H. Holloway and J. B. Hudson, *Surf. Sci.* **43**, 141 (1974).
- <sup>2</sup> S. Zalkind, M. Polak, and N. Shamir, *Surf. Sci.* **513**, 501 (2002).
- <sup>3</sup> K. Heinemann, D. B. Rao, and D. L. Douglass, *Oxid. Met.* **9**, 379 (1975).
- <sup>4</sup> R. H. Milne and A. Howie, *Philos. Mag. A* **49**, 665 (1984).
- <sup>5</sup> J. C. Yang, M. Yeadon, B. Kolasa, and J. M. Gibson, *J. Electrochem. Soc.* **146**, 2103 (1999).
- <sup>6</sup> G. W. Zhou, L. Wang, and J. C. Yang, *J. Appl. Phys.* **97**, 063509 (2005).
- <sup>7</sup> K. R. Lawless, *Rep. Prog. Phys.* **37**, 231 (1974).
- <sup>8</sup> E. Bauer, *Z. Kristallogr.* **110**, 372 (1958).
- <sup>9</sup> G. W. Zhou, *Appl. Phys. Lett.* **94**, 233115 (2009).
- <sup>10</sup> E. Lundgren, J. Gustafson, A. Mikkelsen, J. N. Andersen, A. Stierle, H. Dosch, M. Todorova, J. Rogal, K. Reuter, and M. Scheffler, *Phys. Rev. Lett.* **92**, 046101 (2004).
- <sup>11</sup> J. A. Eastman, P. H. Fuoss, L. E. Rehn, P. M. Baldo, G. W. Zhou, D. D. Fong, and L. J. Thompson, *Appl. Phys. Lett.* **87**, 051914 (2005).

- <sup>12</sup> K. Lahtonen, M. Hirsimäki, M. Lampimäki, and M. Valden, *J. Chem. Phys.* **129**, 124703 (2008).
- <sup>13</sup> G. W. Zhou, *Phys. Rev. B* **81**, 195440 (2010).

### DOE Sponsored Publications in the Last Two Years

- 1 G.W. Zhou, L.L. Luo, L. Li, J. Ciston, E.A. Stach, W.A. Saidi, J.C. Yang, "In situ atomic visualization of oxide islanding during oxidation of Cu surfaces", *Chem. Comm.* (submitted)
- 2 L. Li, G.W. Zhou, "Oxygen subsurface adsorption on the Cu(110)-c(6×2) surface", *Surf. Sci.* **615**, 67-74 (2013)
- 3 W.A. Al-Saidi, M.Y. Lee, L. Li, G.W. Zhou, A.J.H. McGaughey, "Ab initio atomistic thermodynamics study of the early stages of Cu(100) oxidation", *Phys. Rev. B* **86**, 245429 (2012)
- 4 G.W. Zhou, L.L. Luo, L. Li, J. Ciston, E. Stach, J.C. Yang, "Step edge induced oxide growth during the oxidation of Cu(100)", *Phys. Rev. Lett.* **109**, 235502 (2012)
- 5 L.L. Luo, Y.H. Kang, J.C. Yang, G.W. Zhou, "Effect of oxygen gas pressure on the orientations of Cu<sub>2</sub>O nuclei during the oxidation of Cu(100), (110) and (111)", *Surf. Sci.* **606**, 1790-1797(2012)
- 6 L.L. Luo, Y.H. Kang, J.C. Yang, G.W. Zhou, "Influence of the surface morphology on the early stages of Cu oxidation", *Appl. Surf. Sci.* **259**, 791-798 (2012)
- 7 J.C. Yang, G.W. Zhou, "In situ UHV TEM studies of early-stage oxidation of Cu and Cu Alloy thin films", *Micron* **43**, 1195(2012)
- 8 L.L. Luo, Y.H. Kang, J.C. Yang, G.W. Zhou. "Effect of Au composition on the orientations of oxide nuclei during the oxidation of Cu-Au alloys", *J. Appl. Phys.* **111**, 083533 (2012)
- 9 L. Li, M. Xi, Y.F. Shi, G.W. Zhou, "Precursor to the bulk oxide formation during the oxidation of Cu(100)", *Phys. Rev. Lett.* **108**, 176102 (2012)
- 10 N. Cai, G.W. Zhou, K. Müller, D.E. Starr, "Tuning the limiting-thickness of a thin oxide layer on Al (111) with oxygen gas pressure", *Phys. Rev. Lett.* **107**, 035502 (2011)
- 11 N. Cai, G.W. Zhou, K. Müller, D.E. Starr, "Effect of oxygen gas pressure on the kinetics of alumina film growth during the oxidation of Al(111) at room temperature", *Phys. Rev. B* **84**, 125445 (2011)
- 12 L.L. Luo, Y.H. Kang, Z.Y. Liu, J.C. Yang, G.W. Zhou, "A pressure gap in the nucleation orientations of oxide islands during the initial oxidation of metals", *Phys. Rev. B* **83**, 155418 (2011)
- 13 L. Yuan, Y.Q. Wang, R. Mema, G.W. Zhou, "The driving force and growth mechanism for spontaneous oxide nanowire formation during the thermal oxidation of metals", *Acta Mater.* **59**, 2491 (2011)
- 14 L. Liang, G.W. Zhou, "3D kinetic Monte Carlo simulations of crater growth during the reduction of oxide nanoislands on metal surfaces", *Surf. Sci.* **605**, 54 (2011)
- 15 L.L. Luo, Y.H. Kang, Z.Y. Liu, J.C. Yang, G.W. Zhou, "Effect of Oxygen Pressure on the Initial Oxidation Behavior of Cu and Cu-Au Alloys", *Advances in Spectroscopy and Imaging of Surfaces and Nanostructures, Mater. Res. Soc. Proc.* **318**, 31-36 (2011)

# Growth And Properties Of New Epitaxial Metal/Semiconductor Nanocomposites

Joshua M. O. Zide

Department of Materials Science and Engineering,  
University of Delaware, Newark, DE 19716

## Program Scope

Nanocomposites consisting of semi-metallic nanoparticles (such as ErAs) within III-V semiconductors represent a useful alternative to conventional materials for a variety of applications. The incorporation of nanoparticles into semiconductors can pin the Fermi level, drastically altering the electronic properties in ways that are fundamentally [1], [2] different from conventional doping. This can reduce carrier lifetimes and also increase (or decrease) electrical conductivity (depending on the semiconductor matrix and the specific composition of the nanoparticle). Additionally, nanoparticles can scatter phonons, reducing thermal conductivity. These materials have been studied using molecular beam epitaxy (MBE)-grown materials and have been shown to be promising for applications such as photoconductive switches for terahertz sources and detectors, [3], [4], [5] thermoelectrics, [6], [7] tunnel junctions for multijunction solar cells, and several others. [8]

The epitaxial relationship between the rocksalt crystal structure of the nanoparticles and the zincblende structure of the matrix (Figure 1) allows high quality interfaces, [9], [10] allowing the study of the fundamental charge transfer mechanisms in nanostructured electronic composites.

Although the prior work by MBE has enabled significant advances in the understanding of a

subset of this class of composite materials, the hallmarks of MBE-grown material are a lack of flexibility in composition, a slow growth rate, and very high cost. *To these ends, this project is focused on creating epitaxial nanocomposites via a hybrid approach in which nanoparticles are produced using inert gas condensation (IGC) and incorporated epitaxially into semiconductor films using liquid phase epitaxy (LPE).* This hybrid approach has several advantages. First, there is considerable flexibility in what materials are grown; unlike the MBE approach, in which both particle and film are

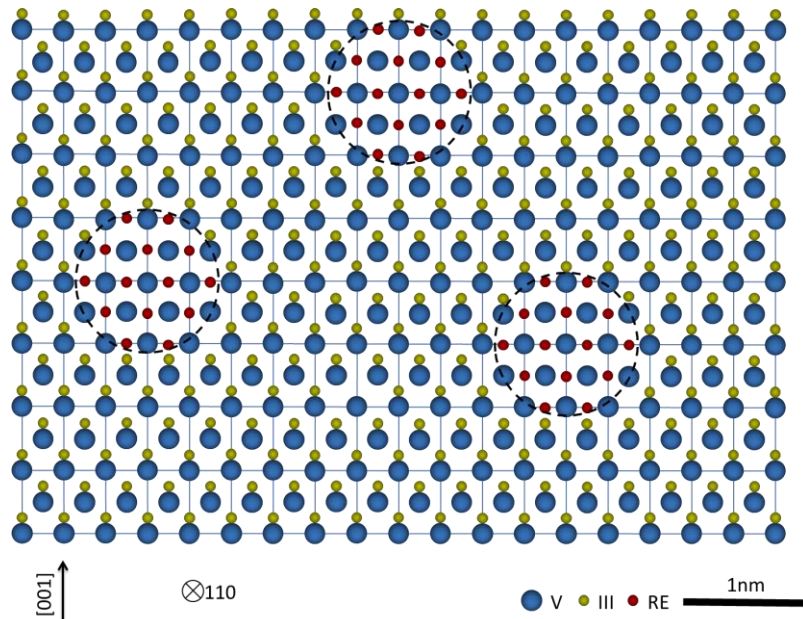


Figure 1: (110) projection view of rocksalt rare-earth-group V nanoparticles within a III-V matrix.

produced together, the hybrid IGC/LPE approach allows separate production of the nanoparticles. This means different group V elements are possible (e.g. ErAs in GaP), and the IGC approach (as described below) allows more rare-earth elements (e.g. Tb, Yb, Nd, Gd, etc.) to be explored. From a technological point of view, the hybrid approach should allow growth rates of micrometers per minute rather than micrometers per hour, thus allowing thicker films and scaling of materials. Finally, there is nothing limiting this approach to this particular class of materials; we hope to establish a new paradigm in nanocomposites for electronic materials.

### Recent Progress

To date, our efforts have focused on design and fabrication of the IGC system. We have completed all laboratory infrastructure changes (including the creation of safety protocols for IGC production of arsenic containing materials) and assembled the system. Currently, we are in the commissioning stage; we have a functional system, but are working out the final few technical challenges before producing nanoparticles. Briefly, we are using a valved cracker effusion cell (Veeco) for an arsenic source and a pulsed Nd-YAG laser system producing 850mJ per pulse (10Hz repetition rate) to ablate rare earth species such as erbium. This is a departure from our initial design, but allows improved flexibility in rare-earth source selection; the low vapor pressures of many rare-earth species would be a limitation of resistive heating. A schematic diagram of the IGC system is shown in Figure 2(a), while a photograph of the system is shown in Figure 2(b). We have finalized the details and fabricated the system to collect particles in a petri dish containing epoxy (for characterization of particles) or molten gallium (for LPE). We expect to produce nanoparticles within the next few months. This work has been conducted primarily by graduate student Matthew Lewis (who has developed expertise in equipment design as well as research methods) in collaboration with undergraduate researcher Chelsea Shockey, who is funded by the University of Delaware through the Undergraduate Research Program.

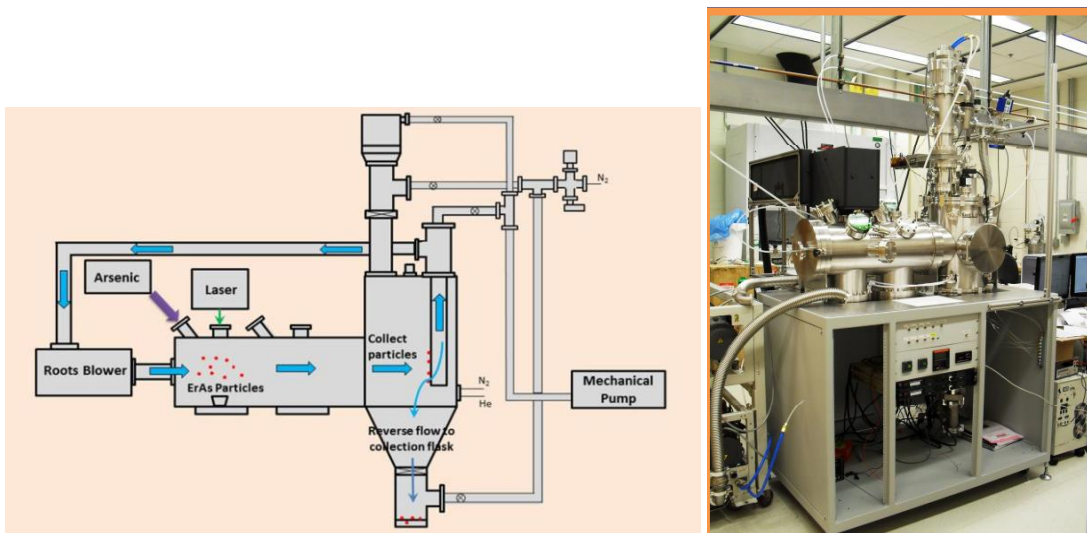


Figure 2 (a) Schematic view of inert gas condensation (IGC) system for production of RE-V nanoparticles. (b) photograph of IGC system in the Zide lab at the University of Delaware.

In parallel, we have begun commissioning of the liquid phase epitaxy (LPE) system for the growth of project materials. We are using an existing system and have begun the design stage for modifications required for project materials. Photographs of that system are given in Figures 3(a) and (b), while a schematic is included in Figure 3(c). The progress to date puts us within the timeline established on the GANTT chart within the original research proposal.

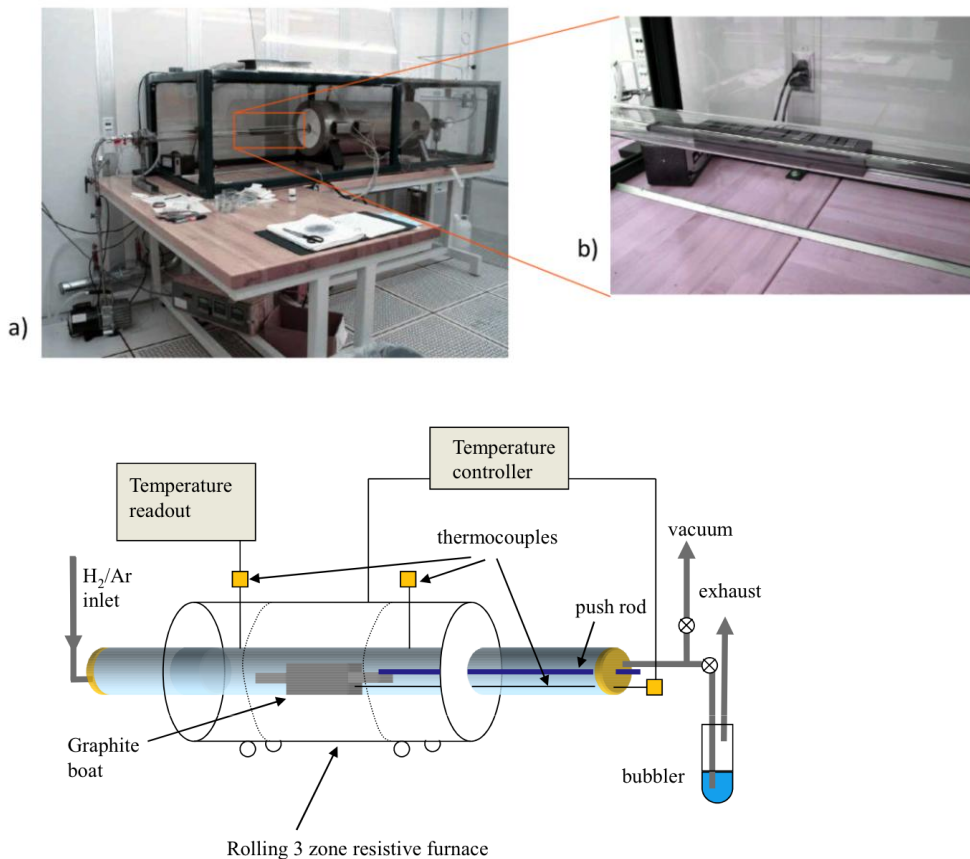


Figure 3 (a) photograph of liquid phase epitaxy (LPE) system for the growth of nanocomposites and semiconductors. (b) close-up of graphite boat, (c) schematic view of system.

### Future Plans

Our short-term future plans are to produce nanoparticles via IGC and begin growth of matrix materials (GaAs initially) using LPE. On the IGC side, our primary goal is to determine growth conditions to allow relatively mono-dispersed particles for tunable sizes, which will depend on the relative fluxes of the rare-earth and arsenic and also the pressure of the inert gas (helium). These particles will be capture in epoxy and characterized using x-ray diffraction (XRD) and electron microscopy to determine structure and morphology. Additionally, once basic growth conditons for high-quality LPE (as determined by rocking curves and high-resolution XRD) are determined, we will begin the fabrication of nanocomposites. Longer term, we hope to generalize this

approach first to other combinations of RE-V nanoparticles and III-V semiconductor and, eventually, to other material systems.

## References

- [1] J. M. O. Zide, A. Kleiman-Shwarsstein, N. C. Strandwitz, J. D. Zimmerman, T. Steenblock-Smith, A. C. Gossard, A. Forman, A. Ivanovskaya, and G. D. Stucky, "Increased efficiency in multijunction solar cells through the incorporation of semimetallic ErAs nanoparticles into the tunnel junction," *Applied Physics Letters*, vol. 88, no. 16, p. 162103, Apr. 2006.
- [2] P. Pohl, F. Renner, M. Eckardt, A. Schwanhäusser, A. Friedrich, Ö. Yüsekdağ, S. Malzer, G. H. Döhler, P. Kiesel, D. Driscoll, M. Hanson, and A. C. Gossard, "Enhanced recombination tunneling in GaAs pn junctions containing low-temperature-grown-GaAs and ErAs layers," *Applied Physics Letters*, vol. 83, p. 4035, 2003.
- [3] J. F. O'Hara, J. M. O. Zide, A. C. Gossard, A. J. Taylor, and R. D. Averitt, "Enhanced terahertz detection via ErAs : GaAs nanoisland superlattices," *Applied Physics Letters*, vol. 88, Jun. 2006.
- [4] E. R. Brown, F. W. Smith, and K. A. McIntosh, "Coherent Millimeter-Wave Generation by Heterodyne Conversion in Low-Temperature-Grown GaAs Photoconductors," *Journal of Applied Physics*, vol. 73, pp. 1480–1484, 1993.
- [5] A. K. Azad, R. P. Prasankumar, D. Talbayev, A. J. Taylor, R. D. Averitt, J. M. O. Zide, H. Lu, A. C. Gossard, and J. F. O'Hara, "Carrier dynamics in InGaAs with embedded ErAs nanoislands," *Applied Physics Letters*, vol. 93, no. 12, p. 121108, 2008.
- [6] J. M. O. Zide, J.-H. Bahk, R. Singh, M. Zebarjadi, G. Zeng, H. Lu, J. P. Feser, D. Xu, S. L. Singer, Z. X. Bian, A. Majumdar, J. E. Bowers, A. Shakouri, and A. C. Gossard, "High efficiency semimetal/semiconductor nanocomposite thermoelectric materials," *Journal of Applied Physics*, vol. 128, no. 12, p. 123702, 2010.
- [7] W. Kim, J. Zide, A. Gossard, D. Klenov, S. Stemmer, A. Shakouri, and A. Majumdar, "Thermal Conductivity Reduction and Thermoelectric Figure of Merit Increase by Embedding Nanoparticles in Crystalline Semiconductors," *Physical Review Letters*, vol. 96, no. 4, pp. 1–4, Feb. 2006.
- [8] M. Hanson, S. Bank, J. Zide, J. Zimmerman, and A. Gossard, "Controlling electronic properties of epitaxial nanocomposites of dissimilar materials," *Journal of Crystal Growth*, vol. 301–302, pp. 4–9, Apr. 2007.
- [9] D. O. Klenov, D. C. Driscoll, A. C. Gossard, and S. Stemmer, "Scanning transmission electron microscopy of ErAs nanoparticles embedded in epitaxial  $\text{In}_{0.53}\text{Ga}_{0.47}\text{As}$  layers," *Applied Physics Letters*, vol. 86, no. 11, p. 111912, 2005.
- [10] D. O. Klenov, J. M. Zide, J. D. Zimmerman, A. C. Gossard, and S. Stemmer, "Interface atomic structure of epitaxial ErAs layers on (001) $\text{In}_{0.53}\text{Ga}_{0.47}\text{As}$  and GaAs," *Applied Physics Letters*, vol. 86, Jun. 2005.

## Publications

N/A

# **Invited Programs' Abstracts**

This page is intentionally blank.

## **Morphology, carrier transport and device performance of thiophene based solar cells**

**Peter F. Green**

**Department of Materials Science and Engineering and Department of Chemical Engineering, Applied Physics**

University of Michigan, Ann Arbor, MI 48108

### **Program Scope:**

Theoretical and experimental research in the Energy Frontier Research Center (EFRC) at the University of Michigan, Center for Solar and Thermal Energy Conversion (CSTEC), is devoted to the design and synthesis of materials for high efficiency photovoltaic (PV) and thermoelectric (TE) devices. Insights into the design and synthesis rely on fundamental insights from equilibrium and non-equilibrium processes that occur in materials over various spatial and temporal scales. To this end, CSTEC is organized around three thrusts. (1) thrust area 1: structure absorption and carrier transport in low dimensional inorganic systems; (2) thrust area 2: fundamental mechanisms governing carrier transport processes and energy conversion efficiency in low-dimensional (single-molecular junctions, quantum-dot structures, and thin films) and a specific class of bulk thermoelectric materials; (3) thrust Area 3: the molecular design, and synthesis, nanoscale characterization of structure and dynamics, and device efficiency. Specific efforts include materials synthesis (caged systems, self-aligning polythiophene derivative based organic polymers, small molecule organic/C<sub>60</sub> systems) with the goal of understanding and improving charge transport at different length scales. This presentation will be devoted to carrier transport and device performance of conjugated polymer-based systems with controlled nano- and macro-scale morphology. It will be divided into three main areas: (1) Out-of-plane carrier transport in conjugated thin films; (2) use of a super critical solvent to control the morphology and hence bulk heterojunction (BHJ) device performance; (3) the use of a random copolymer to control the structure and hence device performance in BHJ devices.

### **Recent Progress**

The performance and reliability of polymer-based organic electronic devices is strongly dependent on the morphology of the active material. One of our first studies was an investigation of the out-of-plane carrier (hole) transport in the conjugated polymer poly(3-hexylthiophene) (P3HT).<sup>1</sup> Prior experiments were performed by others to determine the in-plane carrier transport. The out-of-plane hole carrier transport was measured in films, many microns in thickness, using time-of-flight spectroscopy. These publications reveal the existence of a small thickness dependence of the in-plane hole carrier mobility; there was virtually no experimental evidence of a film thickness dependence of out-of-plane hole mobility.

We used the charge extraction for linearly increasing voltage (CELIV) technique to show for the first time the existence of a significant film thickness dependence of the out-of-plane mobility; over the thickness range of 100 nm to 800 nm the mobility increased an order of magnitude (Figure 1).

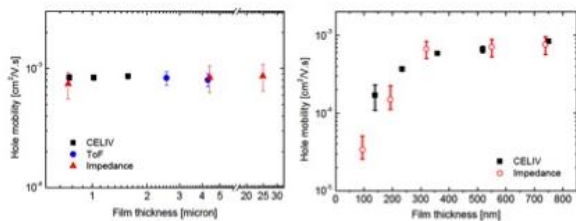


**Figure 1:** The film thickness dependence of the hole carrier mobility in P3HT is shown here. A comparison of the hole carrier mobilities measured in P3HT films using different techniques is also shown.

Through a combination of X-ray scattering, optical anisotropy studies and simulations, we showed that the carrier transport was extremely sensitive to the local morphology. In the thinnest films the structure was highly oriented (an edge-on dominant morphology, see Fig. 2), due to the influence of the substrate, and for distances further from the substrate, where the substrate-induced order was less effective, the average structure became more anisotropic.

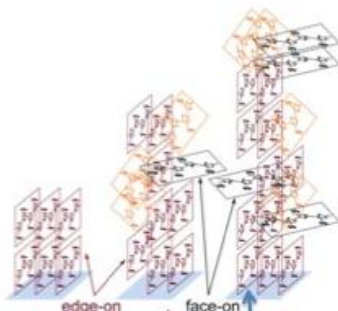


**Figure 2:** Schematic of the edge-on orientation in P3HT thin films close to the substrate (silicon Oxide). Sketches left to right show the increase in anisotropy of the structure, away from the substrate, as the film increases in thickness

We also developed a method of analysis to extract the carrier mobilities in poly(3-hexylthiophene) (P3HT) using Impedance Spectroscopy (IS).<sup>2</sup> The carrier mobilities measured using this technique are in excellent agreement with the results from the techniques: time-of-flight (ToF) and of charge extraction in a linearly increasing voltage (CELIV) (see Fig. 1). In addition to the mobilities we also extracted the conductivity and charge carrier densities, which are very difficult to extract, together, in organics. In addition we used IS, combined with conductive atomic force microscopy (CAFM), to show how carrier transport in P3HT is sensitive to changes of the morphological structure of films thinner than 100 nm.

Considering that the carrier transport is sensitive to structure we examined ways to manipulate the morphology and to control the efficiency of the archetypal bulk heterojunction solar cell P3HT/phenyl-C<sub>61</sub>-butyric acid methyl ester (PC<sub>61</sub>BM) system. With the use of supercritical carbon dioxide (scCO<sub>2</sub>) we achieved comparable, in some cases, better device performance than that achieved using the conventional high temperature procedures. The solvent quality of ScCO<sub>2</sub> was varied through changes in

pressure,  $P$ , and temperature,  $T$ .<sup>3</sup> To this end, changes in the pressure, 6.2 MPa – 13.8 MPa, and temperature, 35°C – 70°C, afforded us the ability to achieve various morphological structures. These structures were characterized using energy filtered transmission electron microscopy (EF-TEM), UV-vis spectroscopy and conductive and photoconductive atomic force microscopy. We determined that an optimum condition of  $T=50^{\circ}\text{C}$ ,  $P=10.34$  MPa processed for 45 min, could be achieved for the P3HT/PC<sub>61</sub>BM system. These conditions yielded comparable or better performance than the conventional procedure involving heat at 150 degrees centigrade (Fig. 3). Photoconductive AFM studies showed that the active area of the devices prepared using Sc-CO<sub>2</sub> is larger than that of the conventionally prepared device.<sup>3</sup>

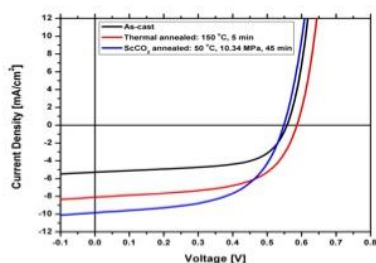


**Figure 3.** Current density-voltage curves of P3HT/PC<sub>61</sub>BM devices under different processing conditions. The scCO<sub>2</sub> annealed device shows a higher short circuit current (current density at 0 V), consistent with possessing larger fractions of photoactive regions.

In another series of experiments we blended a random copolymer of poly(3-hexylthiophene) (P3HT) and poly(3-((hexyloxy)methyl)thiophene) (P3HOMT) with the P3HT homopolymer and indene-C<sub>60</sub> bisadduct (ICBA). The morphologies of the mixtures were characterized using energy-filtered transmission electron microscopy (EFTEM), UV-visible spectroscopy (UV-vis) and conductive atomic force microscopy (C-AFM). The power conversion efficiency (PCE) increased by 20% with the addition of 10 wt.% of the random copolymer; beyond this composition it decreased (Fig. 4).

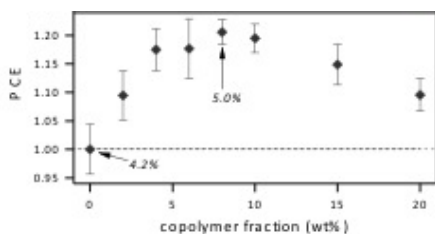


**Figure 4:** The PCE is plotted as a function of the weight fraction of the random copolymer added to the P3HT/ICBA BHJ

Non-trivial increases in the open circuit voltage and short-circuit current were also reported. These data are consistent with reductions in the carrier recombination measured using the photo-CELIV measurements.

## References

1. Huang, B; Glynos, E; Frieberg, B; Yang, H; Green P.F., "Effect of Thickness-Dependent Structural Evolution on Out-of-plane Hole Mobility in Poly(3-hexylthiophene) Films." ACS APPLIED MATERIAL & INTERFACES, 2012, 4 (10): p. 5204-5210.
2. Yang, H; Glynos, E; Huang, B; Green P.F., "The Out-of-Plane Carrier Transport in Conjugated Polymer Thin Films: Role of Morphology." JOURNAL OF PHYSICAL CHEMISTRY C, 2013, 117 (19): p.9590.
3. Amonoo, J; Glynos, E; Chen, X.C.; Green P.F., "An Alternative Processing Strategy for Organic Photovoltaic Devices Using Supercritical Fluid." JOURNAL OF PHYSICAL CHEMISTRY C, 2012, 116 (39): p. 20708-20716.

## Publications

1. Huang, B; Glynos, E; Frieberg, B; Yang, H; Green P.F., "Effect of Thickness-Dependent Structural Evolution on Out-of-plane Hole Mobility in Poly(3-hexylthiophene) Films." ACS APPLIED MATERIAL & INTERFACES, 2012, 4 (10): p. 5204-5210.
2. Yang, H; Glynos, E; Huang, B; Green P.F., "The Out-of-Plane Carrier Transport in Conjugated Polymer Thin Films: Role of Morphology." JOURNAL OF PHYSICAL CHEMISTRY C, 2013, 117 (19): p.9590.
3. Amonoo, J; Glynos, E; Chen, X.C.; Green P.F., "An Alternative Processing Strategy for Organic Photovoltaic Devices Using Supercritical Fluid." JOURNAL OF PHYSICAL CHEMISTRY C, 2012, 116 (39): p. 20708-20716.
4. Kim, B.G.; Ma, X.; Chen, X.C.; le, Y; Coir, E.W.; Hashemi, H; Aso, Y.; Green, P.F.; Kieffer, J; Kim J, "Energy Level Modulation of HOMO, LUMO, and Band-Gap in Conjugated Polymers for Organic Photovoltaic Applications." ADVANCED FUNCTIONAL MATERIALS, 2012, 23 (4): p.439-445.
5. Barito, A., Sykes, M.E., Bilby, D., Amonoo, J., Jin, Y., Morris, S.E., Green, P.F., Kim, J., Shtein, M., "Recovering Lost Excitons in Organic Photovoltaics Using a Transparent Dissociation." JOURNAL OF APPLIED PHYSICS, 2013, 113 (20): p.203110.
6. Agrawal, K.L.; Sykes, M.E.; An, K.H.; Frieberg, B; Green P.F.; Shtein, M, "Influence of Exciton Lifetime on Charge Carrier Dynamics in an Organic Heterostructure." APPLIED PHYSICS LETTERS, 2013, 102 (11): p.113304.

**Joint Center for Energy Storage Research (JCESR):  
Understanding Fundamental Structural Transformation and Electrochemical  
Reactions Using In-Situ TEM and NMR**

Jun Liu, Chongmin Wang, Nigel Browning, Meng Gu, Karl Mueller,  
Yuyan Xiao, Jie Xiao, Jianzhi Hu, Tianbiao Liu, Guosheng Li, Jiguang Zhang,  
Wei Wang, Larry Pederson, John Lemmon, Xilin Chen, Wu Xu  
Pacific Northwest National Laboratory  
Richland, WA 99352

### **Program Scope**

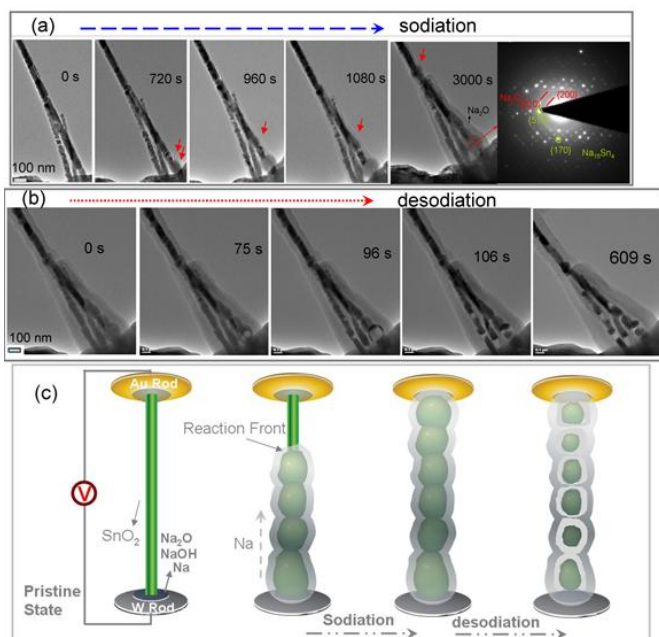
The Joint Center for Energy Storage Research (JCESR) aims to go beyond today's best Li-ion systems to provide five times the energy storage at one-fifth the cost within five years. The team will develop new energy storage chemistries through an atomic-level understanding of energy storage phenomena and the development of universal design rules for battery performance. JCESR will speed innovation by applying fundamental scientific advances of the last decade to battery R&D and uniting discovery science, materials design, battery system design, and advanced prototyping in a single highly interactive process. PNNL will contribute to JCESR using advanced synthesis and modeling capabilities and the state-of-the-art facilities in the Environmental and Molecular Sciences Laboratory (EMSL). PNNL will also contribute to the three fundamental storage chemistries: multivalent intercalation focuses on working ions, such as magnesium or yttrium, that carry twice or triple the charge of lithium and have the potential to store two or three times as much energy, chemical transformation based on using the chemical reaction of the working ion to store many times the energy of today's lithium-ion batteries, and non-aqueous redox flow is based on reversibly changing the charge state of ions held in solution. One emphasis of PNNL research is developing state-of-the-art TEM and NMR characterization tools to gain understanding of the structural transformation and reaction mechanisms in order to overcome the fundamental barrier of the materials and devices.

### **Recent Progress**

#### 1. In-situ TEM study of Ion Insertion for Beyond Li-Chemistry

In-situ transmission electron microscopy (TEM) has been used to characterize the structural changes of the anode materials used in Li-ion batteries. Storage mechanism using other cations, such as Na and Mg, are much more complex and requires significant breakthroughs in the fundamental understanding of the insertion chemistry and failure mechanisms. Various SnO<sub>2</sub> nanostructures, including SnO<sub>2</sub> nanorod and nanowires, have been studied for Na ion insertion. How each phase structurally and chemically evolves during subsequent electrochemical cycling is not very clear. Especially, the sodiation characteristic and the failure mechanism of SnO<sub>2</sub>-based anode are largely unknown. We employed a state-of-the-art in-situ TEM electrochemical testing technique to directly observe the structural and chemical evolution of SnO<sub>2</sub> nanowire upon sodiation/desodiation. Using in-situ TEM, in combination with DFT calculation, we

probed the lattice structural and chemical evolutions of SnO<sub>2</sub> nanowire anode in Na-ion batteries and compared quantitatively with the case of Li-ion. Upon Na insertion into SnO<sub>2</sub>, a displacement reaction occurs, leading to the formation of amorphous Na<sub>x</sub>Sn nanoparticles covered by crystalline Na<sub>2</sub>O shell. With further Na insertion, the Na<sub>x</sub>Sn core crystallized into Na<sub>15</sub>Sn<sub>4</sub> (x=3.75). Upon extraction of Na (desodiation), the Na<sub>x</sub>Sn core transforms to Sn nanoparticles; associated with the volume shrinkage, nanopores appear and metallic Sn particles are confined in hollow shells of Na<sub>2</sub>O. The pores greatly increase electrical impedance, therefore accounting for the poor cyclability of SnO<sub>2</sub>. In contrast to the lithiation of SnO<sub>2</sub>, no dislocation plasticity was seen ahead of the sodiation front. DFT calculations indicate that Na<sup>+</sup> diffuses 30 times slower than Li<sup>+</sup> in



SnO<sub>2</sub>, in agreement with in-situ TEM measurement; it is also ~40% larger in volume, and chemo-mechanically softened the reaction product to greater extent than in lithiation. Comparing the results of Na and Li, the observation highlights the critical role of ionic size and electronic structure of the ionic carrying ion on charge/discharge rate and failure mechanism of battery.

Figure 1. TEM images showing the sodiation (a) and desodiation (b) processes at different times; (c) schematic drawing showing the setup of the in-situ experiment and the structural changes after cycling. The diffraction pattern in the end of panel (a) shows the formation of Na<sub>15</sub>Sn<sub>4</sub> core and Na<sub>2</sub>O shell; and the red arrows label the location of the reaction fronts. (Nano Letters, 2013)

## 2. First Demonstration in-situ TEM Study of True Liquid Cells

One of the fundamental challenges for the battery research is the direct observation of the structural and chemical evolution of the components of the battery and how this directly correlates with the battery properties. Over the last few years, tremendous progress has been made towards developing methodologies for in-situ direct observation of structural and chemical evolution of electrodes used for lithium ion batteries. Most notably, the development of an in-situ TEM cell that is based on an open-cell configuration using a single nanowire and either an ionic liquid or Li<sub>2</sub>O as the electrolyte. Previous work carried out based on the open-cell has provided insightful information on structural and chemical evolution of electrodes upon lithiation/delithiation. However,

three typical deficiencies are associated with the open-cell configuration. Firstly, for the open-cell, the electrolyte is only in point contact with the electrode, which may inadvertently modify the diffusion pattern of Li ion in the electrode, and therefore, what has been obtained is not necessarily representative of the case where the electrode is fully immersed in the liquid electrolyte in a real battery. Secondly, for the case of using  $\text{Li}_2\text{O}$  as the electrolyte, a large overpotential is normally applied in order to drive the Li ions into the electrode, which may change the kinetics and phase behaviors of solid-state electrode lithiation. Thirdly, the use of the ionic liquid or  $\text{Li}_2\text{O}$  electrolyte excludes some of the fundamental processes which only occur in real electrolytes and the battery operating conditions, such as the interaction between electrolyte and electrode and the SEI layer formation. To address the short-comings of the open cell, we developed a liquid-cell based approach for in-situ or more precisely operando TEM studies of lithium ion batteries using a battery relevant liquid electrolyte and a lithium metal counter electrode. We used this new approach to observe the structural evolution of a single Si nanowire upon lithiation/delithiation with controlled battery operating conditions. This approach opens the door for in-situ TEM studies of both dynamic structural and chemical evolution of the electrodes and the SEI layer formation in batteries using real battery relevant electrolytes. Some of lithiation/delithiation behaviors of Si obtained using the liquid-cell are consistent with the results from the open-cell studies. However, we also discovered new insights different from the open cell configuration - the dynamics of the electrolyte and, potentially, a future quantitative characterization of the SEI layer formation and structural and chemical evolution.

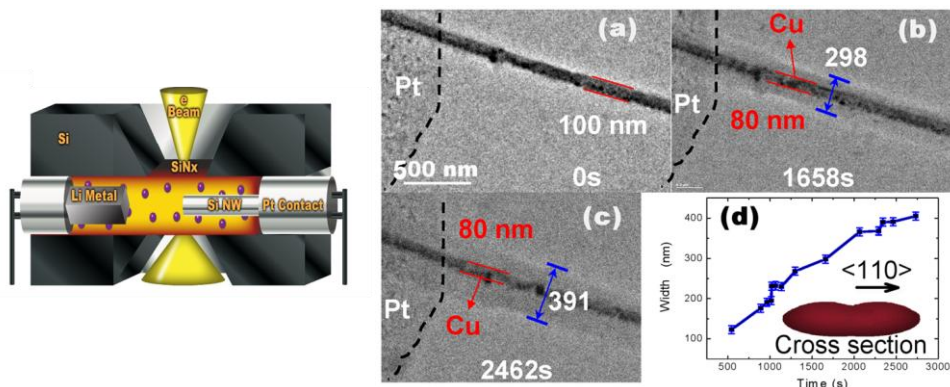


Figure 2. Left panel: schematic drawing showing the setup of the liquid cell battery In-situ liquid-cell TEM observation of the lithiation of the Cu-coated Si nanowire. Right panel: (a) TEM image showing the pristine state of the Si-Cu NW at 0s; (b) core-shell formation of the Si-Cu NW during lithiation at 1658s; (c) TEM image of the Si-Cu NW at 2462s; (d) plotted width changes of the NW as a function of time; Note in all image from (a-c), the Pt contact region is labeled by the black lines in the left of the image. The inset in panel (c) illustrating the cross sectional image after anisotropic swelling of the Si nanowire upon lithium insertion with maximum volume expansion along the  $\langle 110 \rangle$  direction (manuscript submitted).

### 3. NMR Study of the MG Electrolyte Chemistry

Magnesium batteries could potentially provide high volumetric capacity due to the divalent nature of  $Mg^{2+}$  (3832 mAh/cm<sup>3</sup>Mg vs. 2062 mAh/cm<sup>3</sup>Li and 1136 mAh/cm<sup>3</sup>Na), improved safety (dendrite-free Mg deposition), and low cost by using earth abundant Mg element. Electrolytes play a pivotal role in all battery systems, particularly for Mg batteries. Conventional electrolytes by mixing Mg salts (e.g.,  $Mg(ClO_4)_2$ ) and nonaqueous solvents (e.g., propylene carbonate), a typical approach to preparing electrolytes for lithium batteries, do not produce reversible plating/stripping of Mg. There are only a limited number of electrolytes that show reversible Mg plating/stripping. Fundamental understanding of the structure-property relationship in Mg electrolytes is critical for the design and development of new electrolytes with improved performance.

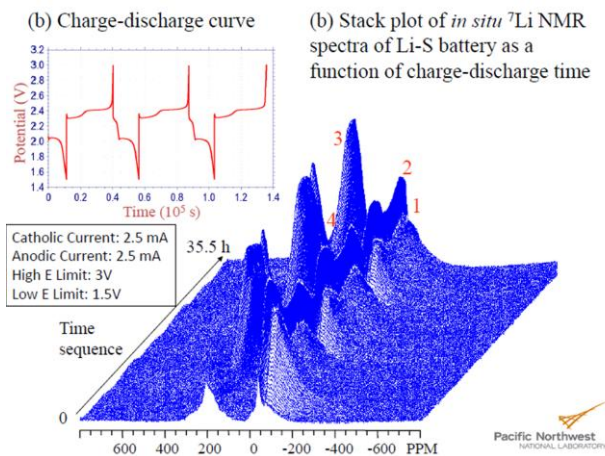
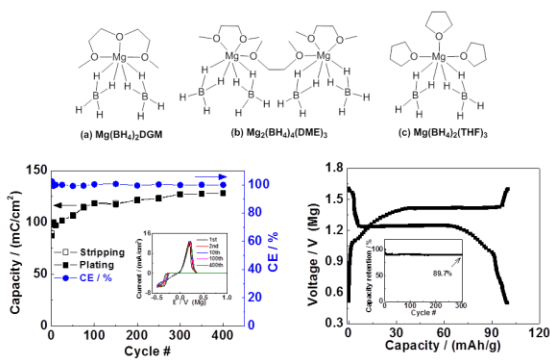


Figure 3. (a) Coordination structures of  $Mg(BH_4)_2$  in DGM (diglyme), DME and THF derived from NMR. (b) Cycling stability of  $Mg(BH_4)_2$ -LiBH<sub>4</sub>-DGM for reversible Mg plating/stripping; c) Discharge/charge profiles of an Mg-Mo<sub>6</sub>S<sub>8</sub> cell using the  $Mg(BH_4)_2$ -LiBH<sub>4</sub>-DGM electrolyte (inset: cycling stability).

As a result, a new electrolyte based on  $Mg(BH_4)_2$  and diglyme (DGM) is studied. LiBH<sub>4</sub> is also employed as an additive. This electrolyte with 0.1M  $Mg(BH_4)_2$  and 1.5M LiBH<sub>4</sub> in DGM demonstrates close to 100% coulombic efficiency (CE) for reversible Mg plating/stripping under the preliminary electrochemical test condition. A well-known cathode material Mo<sub>6</sub>S<sub>8</sub> Chevrel phase is used to evaluate the electrolyte for Mg insertion/de-insertion which shows high reversibility and stability. We focused on the fundamental understanding of the structure-property relationship for the Mg electrolyte through the study of the coordination chemistry of  $Mg^{2+}$  with ligands (solvent and BH<sub>4</sub><sup>-</sup>) in DGM and comparison with that in DME and THF. The performance of electrolytes



was found to be strongly correlated with the coordination structures and binding of the surrounding molecules of the electrochemically active  $Mg^{2+}$  species in the solutions.

We are also developing new in-situ NMR characterization techniques to study the chemical species formed during the electrochemical reaction. In Li-S systems, we are able to quantify the reactions

products that cannot be observed in ex-situ experiments.

Figure 4. New in-situ NMR study in Li-S revealed reaction species that cannot be observed in ex-situ experiments.

**Publications:**

1. “Probing the Failure Mechanism of SnO<sub>2</sub> Nanowires for Sodium-ion Batteries,” Meng Gu, Akihiro Kushima, Yuyan Shao, Ji-Guang Zhang, Jun Liu, Nigel D. Browning, Ju Li, Chongmin, Nano Letters, accepted, 2013.
2. “Coordination Chemistry in magnesium battery electrolytes: how ligands affect their performance,” Yuyan Shao, Tianbiao Liu, Gusheng Li, Jun Liu, submitted and in revision, 2013.
3. “Demonstration of an Electrochemical Liquid Cell for Operando Transmission Electron Microscopy Observation of the Lithiation/Delithiation Behavior of Si Nanowire Battery Anodes,” Meng Gu, Lucas R. Parent, Layla Mehdi, Raymond R. Unocic, Matthew T. McDowell, Robert L. Sacci, Wu Xu, Justin Grant Connell, Pinghong Xu, Patricia Abellan, Xilin Chen, Yaohui Zhang, Daniel E. Perea, Lincoln J. Lauhon, Ilke Arslan, Ji-Guang Zhang, Jun Liu, Yi Cui, Nigel D. Browning, and Chong-Min Wang, submitted, 2013.

## **Critical Materials Institute – A Energy Innovation Hub The Role of Synthesis & Processing in reducing criticality**

Thomas A. Lograsso  
Ames Laboratory, Ames IA 50011

To meet the expanding, urgent challenge, and to avoid delayed development and deployment of clean energy technologies that depend on the supply of and access to critical elements, their alloys and oxides, the Critical Materials Institute (CMI) has created an Energy Innovation Hub for critical materials – a team of multi-disciplinary, world-class researchers, together with industry, dedicated to finding innovative solutions and carving creative, transformational paths to eliminate criticality through the diversification of supplies, development of substitutes, and improvement of usage efficiency, reuse and recycling. CMI has organized sustained, coordinated, cross-disciplinary efforts to identify urgent problems and develop short-, intermediate- and long-term solutions across the entire life cycle of critical materials driving our energy future. CMI's mission is to eliminate materials criticality as an impediment to the commercialization of clean energy technologies for today and tomorrow.

Recently, DOE conducted detailed studies of many 'critical materials' essential for America's transition to clean energy technologies and identified five rare earths – neodymium, europium, terbium, dysprosium, and yttrium – as 'high risk.' While Nd and Dy are indispensable at present for advanced permanent magnets, Eu, Tb, and Y are vital in phosphors for energy efficient lighting. Economic projections indicate that these elements could experience worldwide supply deficits of up to 30% by 2016, stalling domestic manufacturing and preventing the adoption of emerging clean energy products. DOE also identified other elements such as lithium and tellurium as near-critical. Lithium plays a crucial role in emerging energy storage and battery technologies, particularly important for use in hybrid and electric vehicles; tellurium is essential in certain photovoltaic thin-films, but its geochemical scarcity and production supply risks threaten future U.S. leadership in photovoltaic manufacturing.

CMI is a partnership of 18 institutions consisting of national laboratories, universities, not-for-profit Association and industry. Through its four overlapping and mutually supporting Focus Areas (FA1 Diversifying Supply, FA2 Developing Substitutes, FA3 Improving Reuse and Recycling and FA4, Crosscutting Research), CMI's research and development (R&D), and demonstration and deployment (D&D) will attack short-, intermediate- and long-term goals. Crosscutting Research will develop validated scientific tools and materials databases, assess and develop techniques to reduce environmental impacts, and to carry out supply chain and economic analysis, supporting the other focus areas.

This presentation will provide an overview of goals of the CMI, specific technical challenges being undertaken by each the focus areas and details of some the approaches CMI research teams that rely on synthesis and processing methods in meeting the objectives of the CMI to reduce the reliance of clean energy technologies on critical materials.

# Participant List

This page is intentionally blank.

## Participant List

<u>Name</u>	<u>Organization</u>	<u>E-Mail Address</u>
Arnold, Michael	University of Wisconsin-Madison	msarnold@wisc.edu
Bent, Stacey	Stanford University	sbent@stanford.edu
Bhattacharya, Anand	Argonne National Laboratory	anand@anl.gov
Božović, Ivan	Brookhaven National Laboratory	bozovic@bnl.gov
Chabal, Yves	University of Texas at Dallas	chabal@utdallas.edu
Chambers, Scott	Pacific Northwest National Laboratory	sa.chambers@pnnl.gov
Chason, Eric	Brown University	eric_chason@brown.edu
Chen, I-Wei	University of Pennsylvania	iweichen@seas.upenn.edu
Chumanov, George	Clemson University	gchumak@clemson.edu
Clarke, Amy	Los Alamos National Laboratory	aclarke@lanl.gov
Click, Tammy	Oak Ridge Institute for Science and Education	tammy.click@ornl.gov
Crockett, Teresa	U.S. Department of Energy	teresa.crockett@science.doe.gov
Colby, Ralph	The Pennsylvania State University	rhc5@psu.edu
Csathy, Gabor	Purdue University	gcsathy@purdue.edu
Dierolf, Volkmar	Lehigh University	vod2@lehigh.edu
Du, Yingge	Pacific Northwest National Laboratory	yingge.du@pnnl.gov
Dudney, Nancy	Oak Ridge National Laboratory	dudneynj@ornl.gov
Ediger, Mark	University of Wisconsin-Madison	ediger@chem.wisc.edu
Eom, Chang-Beom	University of Wisconsin-Madison	eom@engr.wisc.edu
Eres, Gyula	Oak Ridge National Laboratory	eresg@ornl.gov
Fedorov, Andrei	Georgia Institute of Technology	AGF@gatech.edu
Fichthorn, Kristen	The Pennsylvania State University	fichthorn@psu.edu
Garofalini, Stephen	Rutgers University	shg@rutgers.edu
Geohegan, David	Oak Ridge National Laboratory	geohegandb@ornl.gov
Gersten, Bonnie	U.S. Department of Energy	bonnie.gersten@science.doe.gov
Green, Peter	University of Michigan	pfgreen@umich.edu
Han, Jung	Yale University	jung.han@yale.edu
Hart, A. John	Massachusetts Institute of Technology	ajhart@mit.edu
Hertz, Joshua	University of Delaware	hertz@udel.edu
Huang, Hanchen	Northeastern University	h.huang@neu.edu
Jain, Himanshu	Lehigh University	h.jain@lehigh.edu
Kaspar, Tiffany	Pacific Northwest National Laboratory	tiffany.kaspar@pnnl.gov
Katiyar, Ram	University of Puerto Rico	rkatiyar@hpcf.upr.edu
Koh, Carolyn	Colorado School of Mines	ckoh@mines.edu
Kramer, Matthew	Ames Laboratory	mjkramer@ameslab.gov
Lagally, Max G.	University of Wisconsin-Madison	lagally@engr.wisc.edu
Li, Jing	Rutgers University	jingli@rutgers.edu
Liang, Chengdu	Oak Ridge National Laboratory	liangen@ornl.gov
Liu, Feng	University of Utah	fliu@eng.utah.edu
Liu, Jun	Pacific Northwest National Laboratory	jun.liu@pnnl.gov
Liu, Yong	Ames Laboratory	yliu@ameslab.gov

Lograsso, Thomas	Ames Laboratory	lograsso@ameslab.gov
Lunt, Richard	Michigan State University	rlunt@msu.edu
Manfra, Michael	Purdue University	mmanfra@purdue.edu
Mangolini, Lorenzo	University of California, Riverside	lmangolini@engr.ucr.edu
Markowitz, Michael	U.S. Department of Energy	mike.markowitz@science.doe.gov
Mendeleev, Mikhail	Ames Laboratory	mendeleev@ameslab.gov
Mueller, Karl	The Pennsylvania State University	ktm2@psu.edu
Navrotsky, Alexandra	University of California, Davis	anavrotsky@ucdavis.edu
Nolas, George	University of South Florida	gnolas@usf.edu
Olevsky, Eugene	San Diego State University	eolevsky@mail.sdsu.edu
Paiella, Roberto	Boston University	rpaiella@bu.edu
Perepezko, John	University of Wisconsin-Madison	perepezk@engr.wisc.edu
Petrovic, Cedomir	Brookhaven National Laboratory	petrovic@bnl.gov
Poudeu, Ferdinand	University of Michigan	ppoudeup@umich.edu
Puretzky, Alex	Oak Ridge National Laboratory	puretzkya@ornl.gov
Reinhard, Bjoern	Boston University	bmr@bu.edu
Rioux, Robert	The Pennsylvania State University	rioux@engr.psu.edu
Schlom, Darrell	Cornell University	schlom@cornell.edu
Sennett, Michael	U.S. Department of Energy	michael.sennett@science.doe.gov
Siegrist, Theo	Florida State University	tsiegrist@fsu.edu
Switzer, Jay	Missouri University of Science & Technology	jswitzer@mst.edu
Tamargo, Maria	The City College of New York	mtamargo@ccny.cuny.edu
Thallapally, Praveen K.	Pacific Northwest National Laboratory	praveen.thallapally@pnnl.gov
Tringides, Michael	Ames Laboratory	tringides@ameslab.gov
Uher, Ctirad	University of Michigan	cuher@umich.edu
Voorhees, Peter	Northwestern University	p-voorhees@northwestern.edu
Wang, Qiang	Colorado State University	q.wang@colostate.edu
Wang, Wenying	University of Wyoming	wwang5@uwyo.edu
Wang, Xudong	University of Wisconsin-Madison	xudong@engr.wisc.edu
Watson, Chekesha	Cornell University	cml66@cornell.edu
Xiao, Jie	Pacific Northwest National Laboratory	jie.xiao@pnnl.gov
Xing, Qingfeng	Ames Laboratory	qxing@ameslab.gov
Yakobson, Boris I.	Rice University	biy@rice.edu
Yoon, Mina	Oak Ridge National Laboratory	myoon@ornl.gov
Zaera, Francisco	University of California, Riverside	zaera@ucr.edu
Zhang, Pengpeng	Michigan State University	zhang@pa.msu.edu
Zhang, Qiming	The Pennsylvania State University	qxz1@psu.edu
Zhou, Guangwen	Binghamton University	gzhou@binghamton.edu
Zide, Joshua	University of Delaware	zide@udel.edu

# Author Index

This page is intentionally blank.

## Author Index

Ajayan, Pulickel .....	267	Gibbs, J.....	249
Arnold, Michael S.....	83	Gibbs, P. J.....	18
Bader, Sam .....	3	Goldman, A. I.....	35, 53
Banerjee, Debasis .....	92	Gomez, M.....	165
Bedewy, Mostafa.....	148	Green, Peter F.....	140, 295
Bent, Stacey F.....	88	Gu, Meng.....	299
Besara, T. ....	231	Gujral, A.....	119
Bhattacharya, Anand.....	3	Gupta, P.....	161
Bollinger, Anthony T.....	7	Han, Jung.....	144
Božović, Ivan .....	7	Hart, A. John.....	148
Browning, Nigel .....	299	Henry, Matthew .....	127
Canepa, Pieremanuele.....	92	Hertz, Joshua L. ....	153
Chabal, Y. J.....	92	Ho, K. M.....	31, 35, 71
Chambers, S. A.....	13	Horoz, S.....	258
Chason, Eric .....	98	Hu, Jianzhi.....	299
Chen, I-Wei.....	103	Huang, Hanchen .....	157
Chen, J.....	258	Hupalo, M.....	71
Chen, Xilin .....	299	Imhoff, S. D.....	18
Chi, Miaofang.....	26, 76	Ishikawa, Y.....	165
Chisholm, Matthew .....	62	Jain, H. ....	161
Chumanov, George.....	107	Jiang, Yun.....	136
Clarke, A. J.....	18	Kaspar, T. C.....	13
Cohen, Itai.....	178	Katiyar, R. S.....	165
Colby, R. H. ....	13, 110	Kim, Yoongu .....	22
Csathy, Gabor.....	114	Knorr, B.....	161
Dai, Q.....	258	Koh, Carolyn A.....	169
Dalal, S. S.....	119	Kramer, M. J.....	31, 35, 53
Dandy, David S. ....	253	Kumar, A. ....	165
Dierolf, V. ....	161	Kuskovsky, I. K. ....	240
Droubay, T. C.....	13	Lagally, Max G.....	174
Du, Y.....	13	Lemmon, John .....	299
Dudney, Nancy J. ....	22, 39	Leung, Benjamin.....	144
Duscher, Gerd.....	26, 62, 76	Li, Guosheng .....	299
Ediger, M. D.....	119	Li, Jing .....	92
Eom, Chang-Beom .....	123	Li, Juchuan .....	22
Eres, Gyula.....	26, 62, 76	Li, Xiaolin .....	43
Eriksson, Mark A.....	174	Liang, Chengdu .....	22, 39
Escobedo, Fernando.....	178	Liddell Watson, Chekesha M. ....	178
Exarhos, Gregory J. ....	43	Lin, Zhan .....	39
Fang, X. W. ....	31	Liu, Feng .....	183
Fedorov, Andrei G. ....	127	Liu, Jian.....	67
Fennie, Craig J.....	226	Liu, Jun.....	43, 67, 299
Fichthorn, K. A.....	131	Liu, Tianbiao .....	299
Fonseca, L. ....	165	Liu, Yong .....	48
Garofalini, Stephen H. ....	136	Liu, Zengcai.....	39
Geohegan, David B.....	26, 62, 76	Lograsso, Thomas A. ....	48, 304

Lu, L. ....	258	Song, X. Y. ....	35, 53
Lunt, Richard R. ....	187	Stillinger, Frank H. ....	245
Ma, Ying ....	136	Sum, Amadeu K. ....	169
Mahjouri-Samani, Masoud. ....	26, 76	Sun, Y. ....	31, 35
Makrov, V. ....	165	Sushko, Maria ....	43
Maloney, S. ....	258	Sushko, P. V. ....	13
Manfra, Michael ....	114	Switzer, Jay A. ....	236
Mangolini, Lorenzo ....	190	Tamargo, M. C. ....	240
Maranas, J. K. ....	110	Tan, Kui. ....	92
McBrearty, I. ....	31	Tang, J. ....	258
Mendeleev, M. I. ....	31, 35, 53	Teichert, Kendall ....	148
Meriles, C. A. ....	240	Thallapally, Praveen K. ....	43, 67
Morell, G. ....	165	Thiel, P. A. ....	71
Moustakas, T. D. ....	208	Thomas, R. ....	165
Mueller, K. T. ....	110	Thornton, K. ....	249
Mueller, Karl ....	299	Thouhauser, Timo ....	92
Muller, David A. ....	226	Tian, Jian ....	67
Napolitano, R. E. ....	31, 35, 53	Tian, Mengkun. ....	26, 76
Navrotsky, Alexandra ....	195	Tomar, M. S. ....	165
Nijem, Nour. ....	92	Torquato, Salvatore. ....	245
Nolas, George S. ....	199	Tringides, M. C. ....	71
Noyan, I. C. ....	240	Uher, Ctirad ....	217
Olevsky, Eugene A. ....	204	Van der Ven, Anton ....	217
Otaño, W. ....	165	Velev, J. ....	165
Ott, R. T. ....	31, 35, 53	Voorhees, P. ....	249
Paiella, R. ....	208	Walters, D. M. ....	119
Palai, R. ....	165	Wang, C. Z. ....	31, 35, 71
Park, C. ....	249	Wang, Chongmin ....	299
Pederson, Larry ....	299	Wang, Qiang (David) ....	253
Perales, O. ....	165	Wang, Wei. ....	299
Perepezko, J. H. ....	213	Wang, Wenyong ....	258
Petrovic, Cedomir ....	57	Wang, Xudong. ....	262
Poudeu, Pierre F. ....	217	Wilson, S. R. ....	53
Puretzky, Alex ....	26, 62, 76	Winey, K. I. ....	110
Ramirez, D. ....	231	Wu, Haohan. ....	92
Regmi, Murari ....	62	Wu, Jie ....	7
Reinhard, Bjoern. ....	221	Xiao, Jie. ....	43, 299
Rioux, R. M. ....	131	Xiao, Yuyan. ....	299
Rouleau, Christopher M. ....	26, 62, 76	Xing, Qingfeng ....	48
Runt, J. ....	110	Xu, Wu ....	299
Savytskyy, D. ....	161	Ya'Akobovitz, Assaf ....	148
Schiffer, Peter. ....	226	Yakobson, Boris I. ....	267
Schlom, Darrell G. ....	226	Yang, Y. ....	258
Shao, Yuyan ....	43	Ye, Z. ....	31, 35
Shin, Yongsoon ....	43	Yoon, Mina. ....	26, 62, 76
Siegrist, T. ....	231	Zaera, Francisco. ....	271

Zhang, F. ....	31, 35
Zhang, H. K. L.....	13
Zhang, Jiguang .....	299
Zhang, Pengpeng .....	275
Zhang, Q. M. ....	279
Zhou, Guangwen .....	284
Zide, Joshua M. O.....	289
Zuluaga, Sebastian.....	92